

Conference Proceedings of the Society for Experimental Mechanics Series

Shamim Pakzad *Editor*

# Dynamics of Civil Structures, Volume 2

Proceedings of the 38th IMAC, A Conference  
and Exposition on Structural Dynamics 2020



 Springer

The Springer logo consists of a white chess knight icon positioned to the left of the word "Springer" in a white serif font.

# **Conference Proceedings of the Society for Experimental Mechanics Series**

*Series Editor*

Kristin B. Zimmerman, Ph.D.

Society for Experimental Mechanics, Inc.,

Bethel, CT, USA

The Conference Proceedings of the Society for Experimental Mechanics Series presents early findings and case studies from a wide range of fundamental and applied work across the broad range of fields that comprise Experimental Mechanics. Series volumes follow the principle tracks or focus topics featured in each of the Society's two annual conferences: IMAC, A Conference and Exposition on Structural Dynamics, and the Society's Annual Conference & Exposition and will address critical areas of interest to researchers and design engineers working in all areas of Structural Dynamics, Solid Mechanics and Materials Research.

More information about this series at <http://www.springer.com/series/8922>

Shamim Pakzad  
Editor

# Dynamics of Civil Structures, Volume 2

Proceedings of the 38th IMAC, A Conference and Exposition  
on Structural Dynamics 2020

*Editor*

Shamim Pakzad  
Department of Civil & Environmental Engineering  
Lehigh University  
Bethlehem, PA, USA

ISSN 2191-5644                      ISSN 2191-5652 (electronic)  
Conference Proceedings of the Society for Experimental Mechanics Series  
ISBN 978-3-030-47633-5              ISBN 978-3-030-47634-2 (eBook)  
<https://doi.org/10.1007/978-3-030-47634-2>

© The Society for Experimental Mechanics, Inc. 2021

This work is subject to copyright. All rights are reserved by the Publisher, whether the whole or part of the material is concerned, specifically the rights of translation, reprinting, reuse of illustrations, recitation, broadcasting, reproduction on microfilms or in any other physical way, and transmission or information storage and retrieval, electronic adaptation, computer software, or by similar or dissimilar methodology now known or hereafter developed.

The use of general descriptive names, registered names, trademarks, service marks, etc. in this publication does not imply, even in the absence of a specific statement, that such names are exempt from the relevant protective laws and regulations and therefore free for general use.

The publisher, the authors and the editors are safe to assume that the advice and information in this book are believed to be true and accurate at the date of publication. Neither the publisher nor the authors or the editors give a warranty, expressed or implied, with respect to the material contained herein or for any errors or omissions that may have been made. The publisher remains neutral with regard to jurisdictional claims in published maps and institutional affiliations.

This Springer imprint is published by the registered company Springer Nature Switzerland AG  
The registered company address is: Gewerbestrasse 11, 6330 Cham, Switzerland

# Preface

*Dynamics of Civil Structures* represents one of eight volumes of technical papers presented at the 38th IMAC, A Conference and Exposition on Structural Dynamics, organized by the Society for Experimental Mechanics, and held in Houston, Texas, February 10–13, 2020. The full proceedings also include volumes on *Nonlinear Structures and Systems; Model Validation and Uncertainty Quantification; Dynamic Substructures; Special Topics in Structural Dynamics & Experimental Techniques; Rotating Machinery, Optical Methods & Scanning LDV Methods; Sensors and Instrumentation, Aircraft/Aerospace, Energy Harvesting & Dynamic Environments Testing; and Topics in Modal Analysis & Testing*.

Each collection presents early findings from analytical, experimental, and computational investigations on an important area within Structural Dynamics. Dynamics of Civil Structures is one of these areas which cover topics of interest of several disciplines in engineering and science.

The Dynamics of Civil Structures Technical Division serves as a primary focal point within the SEM umbrella for technical activities devoted to civil structures analysis, testing, monitoring, and assessment. This volume covers a variety of topics including structural vibrations, damage identification, human-structure interaction, vibration control, model updating, modal analysis of in-service structures, innovative measurement techniques and mobile sensing, and bridge dynamics among many other topics.

Papers cover testing and analysis of different kinds of civil engineering structures such as buildings, bridges, stadiums, dams, and others.

The organizers would like to thank the authors, presenters, session organizers, and session chairs for their participation in this track.

Bethlehem, PA, USA

Shamim Pakzad

# Contents

<b>1</b>	<b>Graphene-Rubber Layered Functional Composites for Seismic Isolation</b> .....	<b>1</b>
	Maria Rosaria Marsico and Julián Mauricio Londoño Monsalve	
<b>2</b>	<b>What Rollercoasters Can Teach Us About Fatigue Life of Bridge Connections</b> .....	<b>5</b>
	Sofia Puerto Tchomodanova and Masoud Sanayei	
<b>3</b>	<b>Using Resonance Decay Responses to Model the Nonlinear Behaviour of Telecom Monopoles Via Backbone Curves</b> .....	<b>15</b>
	Jose A. Jimenez Capilla and Julian M. Londono Monsalve	
<b>4</b>	<b>Trench Warfare! The Battle Against Ground-borne Vibration</b> .....	<b>21</b>
	Michael J. Wesolowsky and Melissa W. Y. Wong	
<b>5</b>	<b>Vibration-Based Damage Detection Using Input-Output and Output-Only Environmental Models: A Comparison</b> .....	<b>29</b>
	Pernille Lysgaard, Sandro D. R. Amador, Silja Tea Nielsen, Evangelos Katsanos, and Rune Brincker	
<b>6</b>	<b>Techniques for Simulating Frozen Bearing Damage in Bridge Structures for the Purpose of Drive-by Health Monitoring</b> .....	<b>39</b>
	Robert Locke, Laura Redmond, and Sez Atamturktur	
<b>7</b>	<b>The Minimum Detectable Damage as an Optimization Criterion for Performance-Based Sensor Placement</b> .....	<b>53</b>
	Alexander Mendler, Michael Döhler, Carlos E. Ventura, and Laurent Mevel	
<b>8</b>	<b>Vibrations Assessment of Existing Building Foundations Due to Moving Trains in Underground Tunnels</b> .....	<b>65</b>
	Onur Avci, Ashish Bhargava, Nikolaos Nikitas, and Daniel J. Inman	
<b>9</b>	<b>Ambient Vibration Tests and Modal Response Analysis of Guayaquil Metropolitan Cathedral in Guayaquil, Ecuador</b> .....	<b>75</b>
	M. Motamedi, C. E. Ventura, O. Lara, and J. H. Barredo	
<b>10</b>	<b>An Overview on Floor Vibration Serviceability Evaluation Methods with a Large Database of Recorded Floor Data</b> .....	<b>91</b>
	Mohammad Royvaran, Onur Avci, and Brad Davis	
<b>11</b>	<b>Comparative Study of Floor Serviceability Methodologies</b> .....	<b>103</b>
	C. Chen, P. Duffour, and A. Margnelli	
<b>12</b>	<b>Experimental Modal Analysis of Double Tee Floors in a Fire Damaged Parking Deck for Post-Fire Vibration-Based Condition Assessment</b> .....	<b>113</b>
	Matthew Whelan, Nicole Braxtan, Glenda Mayo, and Brett Tempest	
<b>13</b>	<b>Occupant Localization in Obstructive Indoor Environments Using Footstep-Induced Floor Vibrations</b> .....	<b>121</b>
	Mostafa Mirshekari, Jonathon Fagert, Shijia Pan, Pei Zhang, and Hae Young Noh	

<b>14</b>	<b>Time-Frequency Analysis of Crowd Lateral Dynamic Forcing from Full-Scale Measurements on the Clifton Suspension Bridge</b> .....	125
	R. E. White, N. A. Alexander, and J. H. G. Macdonald	
<b>15</b>	<b>Validation of Deflection Monitoring for Ancillary Traffic Structures via Wireless Accelerometers</b> .....	135
	Delaney C. Thompson, Rodrigo Sarlo, and Matthew H. Hebdon	
<b>16</b>	<b>Localization of Stationary Source of Floor Vibration Using Steered Response Power Method</b> .....	141
	Mohammad Royvaran, Kevin D. Donohue, and Brad Davis	
<b>17</b>	<b>Predictions of Footbridge Vibrations and Influencing Load Model Decisions</b> .....	151
	Lars Pedersen and Christian Frier	
<b>18</b>	<b>A Damage Detection Strategy on Bridge External Tendons Through Long-Time Monitoring</b> .....	159
	Alfredo Cigada, Francescantonio Lucà, Marzia Malavisi, and Giuseppe Mancini	
<b>19</b>	<b>Structural Health Monitoring of a Damaged Operating Bridge: A Supervised Learning Case Study</b> .....	169
	A. Cigada, F. Lucà, M. Malavisi, and G. Mancini	
<b>20</b>	<b>Comparison of Time-Domain and Time-Frequency-Domain System Identification Methods on Tall Building Data with Noise</b> .....	179
	Ronwaldo E. R. Aquino, Mohamed Barbosh, and Ayan Sadhu	
<b>21</b>	<b>Fatigue Life Analysis of Main Shaft Bearings in Wind Turbines Using Strain Measurements Collected on Blades</b> .....	185
	Bridget Moynihan, Sauro Liberatore, Babak Moaveni, and Usman Khan	
<b>22</b>	<b>Towards the Detection and Localization of Multiple Occupant Footsteps from Vibroacoustic Measurements</b> .....	193
	Sa'ed Alajlouni, Murat Ambarkutuk, and Pablo Tarazaga	
<b>23</b>	<b>An Augmented Risk-Based Paradigm for Structural Health Monitoring</b> .....	201
	Aidan J. Hughes, Robert J. Barthorpe, Charles R. Farrar, and Keith Worden	
<b>24</b>	<b>Running Safety Analysis Considering Track Irregularities on an Open-deck Steel Plate Girder Bridge Using Finite Element Multibody Dynamics</b> .....	213
	Sanghyun Choi, Sooho Chae, Kyoungho Kim, and In-Chul Back	
<b>25</b>	<b>Influence of State-Switching Rotational Inertia Dampers on the Natural Frequencies and Response of Structures</b> .....	217
	Abdollah Javidialesaadi and Nicholas Wierschem	
<b>26</b>	<b>Towards Population-Based Structural Health Monitoring, Part VI: Structures as Geometry</b> .....	221
	Keith Worden	
<b>27</b>	<b>Comparison of Modal Parameters of a Concrete Slab Floor from EMA and OMA</b> .....	237
	Ellis Kessler, Vijaya V. N. Sriram Malladi, Rodrigo Sarlo, Luke A. Martin, and Pablo A. Tarazaga	
<b>28</b>	<b>Modeling Human Jumping Force on a Flexible Structure Using Control Models</b> .....	241
	Ahmed T. Alzubaidi and Juan M. Caicedo	
<b>29</b>	<b>Control of Traffic-Induced Ground Vibrations in a Residential Structure</b> .....	251
	Brad Pridham, Tom Normile, Christian Kronenwetter, Paul Reynolds, and Emma Hudson	



# Chapter 1

## Graphene-Rubber Layered Functional Composites for Seismic Isolation



Maria Rosaria Marsico and Julián Mauricio Londoño Monsalve

**Abstract** Elastomeric isolators are special devices used for seismic isolation of structures. Typically, they are made of alternate layers of steel and rubber and they positioned between the structure and its foundations to decouple them. Novel Graphene-Reinforced Elastomeric Isolators, GREI, are proposed in this study to overcome the heavy weight and long manufacturing process of elastomeric isolators currently used.

This manuscript presents an experimental dynamic analysis on rubber pads reinforced with a few layer graphene. Experimental modal analysis is performed on a mass-spring-damper system and the dynamics of the system and the mechanical properties essential to characterize the specimens are extracted from the measured frequency response function.

Results show that a few layer graphene transferred on a rubber pad increase stiffness and damping of the graphene-rubber composite; hence natural rubber can be used in lieu of high-damped rubber, saving the cost of reinforcing rubber with particulate fillers. Also results show that the mechanical properties of the graphene-rubber composite alter when varying the thickness of a few layer graphene transferred on rubber pads.

**Keywords** Elastomeric isolators · Frequency response function · Graphene-rubber composite · Modal analysis

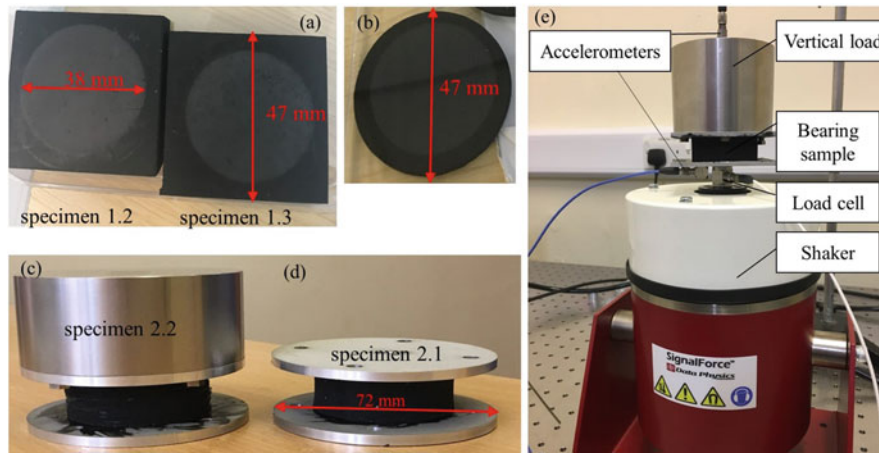
### 1.1 Introduction

The concept of interposing Elastomeric isolators (EIs) between a structure and its foundations to decouple them is known as base isolation; it is accepted by all major international seismic codes and enables structures to survive potentially devastating seismic events. Current technologies for base isolation use steel-reinforced elastomeric isolators (SREI) which are made of alternate layers of steel and rubber and are used mainly in strategic and public buildings due to high cost of designing, production and installation. The primary weight in a SREI is due to the reinforcing steel plates which are used to provide the rubber-steel composite with high vertical stiffness, and to the end steel plates at the bottom and top which are used to secure the device to the structure and the foundations. Studies have been conducted to investigate the dynamic behaviour of isolators reinforced with fibre sheets e.g. glass or carbon fibres (Fibre-Reinforced Elastomeric Isolators, FREI), which are lighter than steel shims, and without end steel plates [1–4]. However, aspects such as the design, alignment and behaviour of the fibres, the dependence of FREI to preloading history would require further investigation.

An attractive alternative to using fibres to reinforce rubber is graphene. Graphene, a one-atom thick layer of carbon, is the strongest known material, which is also mechanically flexible. The idea behind this research is to reinforce pure rubber with a few-layer graphene and to create Graphene-Reinforced Elastomeric Isolator (GREI). The dynamic response of square and circular graphene-rubber specimens with applied vertical load is investigated and experimental results are discussed.

---

M. R. Marsico (✉) · J. M. Londoño Monsalve  
College of Engineering, Mathematics and Physical Sciences, University of Exeter, Exeter, UK  
e-mail: [m.r.marsico@exeter.ac.uk](mailto:m.r.marsico@exeter.ac.uk)



**Fig. 1.1** (a) Specimens 1.2 and 1.3 made of a square rubber pad 15 mm thick. (b) Circular sample 1.5 mm thick rubber pad with a few layer graphene on top. (c) Specimen 2.2 made of nine circular rubber pads with 1 kg applied vertical load. (d) Specimen 2.1 made of nine circular rubber pads. (e) Experimental setup

## 1.2 Composition of Specimens and Experimental Setup

Two sets of samples, with circular and square geometries were manufactured. Set 1 samples are confined to two  $72 \times 72$  mm square steel plates 3 mm thick, while Set 2 samples are confined to two circular steel plates 3 mm thick with 72 mm diameter. Set 1 consists of three specimens. Specimen 1.1 is made of a square pure rubber pad 47 mm side and 15 mm thick; Specimen 1.2 is made of a square rubber pad 47 mm side and 15 mm thick with a circular thick layer of graphene on the top with diameter of 38 mm; and Specimen 1.3 is made of a square rubber pad 47 mm side and 15 mm thick with a circular thin layer of graphene on the top with diameter of 38 mm (Fig. 1.1a). Set 2 consists of two specimens made with nine circular pads of rubber each with diameter 47 mm and thickness 1.5 mm. Specimen 2.1 is made of nine pads of pure rubber bonded together using a cold vulcanizing agent. Specimen 2.2 is made of nine pads of rubber alternated to eight circular thin layers of graphene with diameter 38 mm (Fig. 1.1b–d).

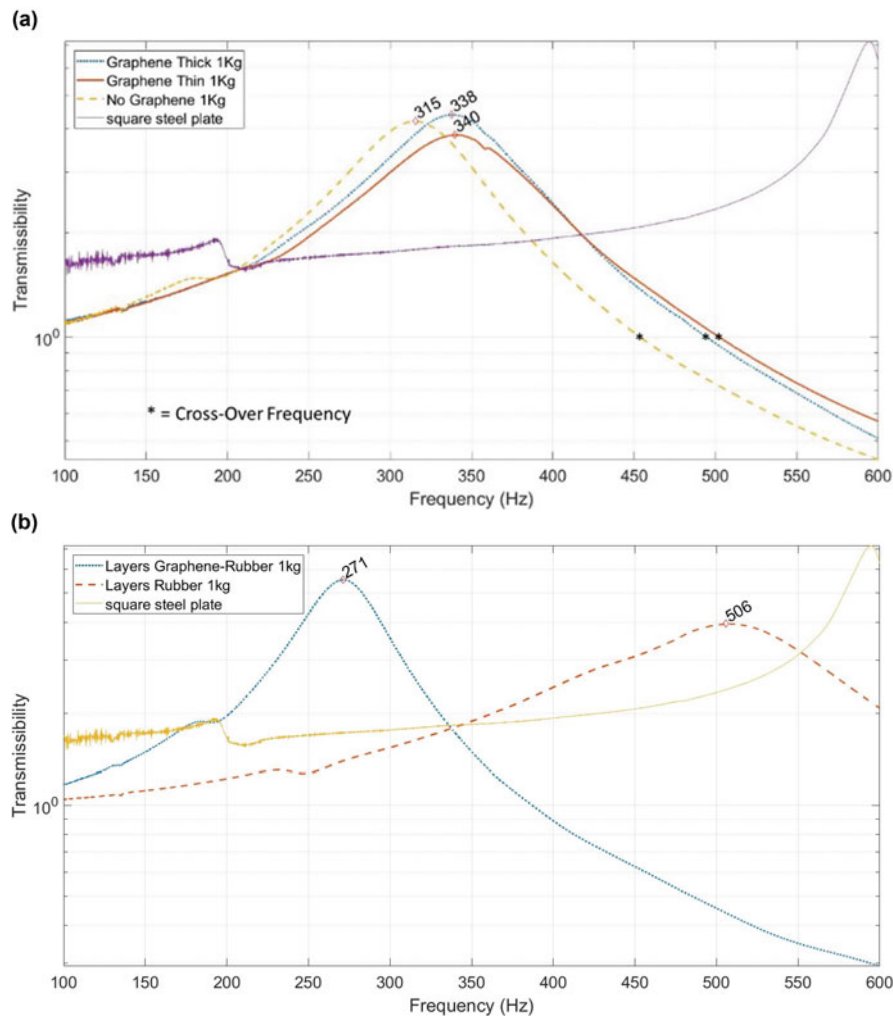
Graphene deposition on rubber was achieved by an isopropyl alcohol assisted direct transfer method [5]. To vary the thickness of the graphene films on rubber, multiple transfers of graphene films were used (i.e. 3 transfers for the thin films and 6 transfers for the thick films). The elastomer used in the samples is natural rubber with hardness  $70^\circ$  Shore A Degree, measured experimentally using a RS Pro digital durometer.

The experimental setup shown in Fig. 1.1e can be seen as a single-degree-of-freedom (SDOF) mass-spring-damper system with accelerations recorded at the bottom of the lower steel plate bonded to the specimen and at the top of the added mass. Experimental modal analysis was performed and the dynamics of the system and the mechanical properties essential to characterize the specimens were extracted from the measured Frequency Response Function (FRF).

Gravity loads are applied on the specimens in the form of a solid stainless steel cylinder bolted on the upper steel plate (1 kg and 2 kg at a time). Vibration tests were also performed on one of the 3 mm steel plate alone to define its natural frequency and ultimately to assess any dynamic interaction with the dynamic behaviour of the graphene-rubber compound.

## 1.3 Analysis

FRFs of Set 1 samples were used to evaluate the specimens' mechanical behaviour and to extract dynamic properties such as natural frequency and damping. FRFs show that the vertical natural frequency of the two specimens 1.2 and 1.3 made of a rubber pad and layers of graphene on top (either thin or thick) is higher than the natural frequency of the specimen made of pure rubber (specimen 1.1). This result proves that specimens 1.2 and 1.3 are stiffer vertically than specimen 1.1, and that the increase in vertical stiffness is due likely to the added layers of graphene. The vertical natural frequency of the three specimens is plotted in Fig. 1.2a, also showing that for exciting frequencies less than 250 Hz (i.e. a frequency ratio less than 0.7) the dynamic response of the specimens is disturbed by the dynamic response of the confining steel plates.



**Fig. 1.2** (a) Set 1 samples with vertical load 1 kg: transmissibility and cross-over frequency at transmissibility  $T = 1$ . (b) Transmissibility of Set 2 samples with vertical load 1 kg

The damping ratios of the specimens 1.2 and 1.3 are higher (0.73% and 17% respectively) than that of the specimen 1.1. Such an increase in damping ratio is likely due to the presence of graphene and it is beneficial to vibration isolation systems made with rubber, as it would enable using low damping natural rubber in lieu of expensive high damping rubber.

The natural frequency of the specimen made of nine rubber pads (specimen 2.1) was found to be higher than the frequency of the specimen made of rubber pads alternated with eight layers of graphene (specimen 2.2). This may indicate that eight layers of graphene are added at the expenses of the vertical stiffness of the layered specimen. Vertical natural frequency of Set 2 samples with vertical load 1 kg are depicted in Fig. 1.2b, also showing the transmissibility. As the natural frequency is lower in specimen 2.2 than in specimen 2.1, the vertical stiffness calculated experimentally is also lower in the graphene-reinforced rubber specimen compared to that in the specimen made of rubber pads only. Besides that, experimental results indicate a lower damping factor of the specimen reinforced with graphene compared to the damping factor of the specimen made of rubber pads only. Such a decrease of vertical frequency, vertical stiffness and damping factor in the specimen reinforced with graphene is likely due to an excessive quantity of graphene present in the specimen 2.2, provoking loss of adhesion between layers of graphene-reinforced rubber and unexpected inner behaviour between the graphene particles. A similar result was found in experimental tests on nanoengineered concrete reinforced with graphene [6].

## 1.4 Conclusion

Experimental results conducted on the three Set 1 samples with 1 kg vertical load applied showed that when adding a few layer graphene on the top of a 15 mm thick rubber pad the vertical stiffness of the specimen increases. In particular, the vertical stiffness increases by 15.7% when a thin layer of graphene is added on the top of the rubber pad and by 14.5% when a thick layers of graphene is added. Experimental results also show an increase of 17.7% in the damping of the composite rubber-thin layer of graphene and of 0.7% in the composite rubber-thick layer of graphene. Adding a few layer graphene is shown to be a viable and lowcost alternative to reinforce elastomeric isolators and to replace heavy steel plates. Results also show that a few layer graphene transferred on top of the specimen enhance the damping; hence natural rubber can be used in lieu of high-damped rubber, saving the cost of reinforcing rubber with particulate fillers.

Unwanted behaviour of the rubber pad due to an excessive added quantity of graphene is evident from the experimental results on Set 2 samples. The sandwich made with nine rubber pads alternated with eight layers of graphene exhibits lower vertical stiffness and damping factor than the specimen made of nine rubber pads only. Eight layers of graphene worsen the performance of the rubber, although it is likely that less layers would enhance its mechanical properties, as it has seen in the response of specimen 1.3 with a thin layer of graphene on top. The quest for future research is to find the exact quantity of graphene to be transferred homogenously on the rubber pad that would enhance its mechanical properties.

**Acknowledgements** The authors would like to acknowledge Prof. Monica F. Craciun for providing the graphene samples and Dr. Dong-Wook Shin for transferring a few layer graphene on rubber pads.

## References

1. Strauss, A.: Experimental investigations of fiber and steel reinforced elastomeric bearings: shear modulus and damping coefficient. *Eng. Struct.* **75**, 402–413 (2014)
2. Osgooei, P.M., et al.: Experimental and finite element study on the lateral response of modified rectangular fiber-reinforced elastomeric isolators (MR-FREIs). *Eng. Struct.* **85**, 293–303 (2015)
3. Marsico, M.R., et al.: Tension buckling in rubber bearings affected by cavitation. *Eng. Struct.* **56**, 656–663 (2013)
4. Angeli, P., Russo, G., Paschini, A.: Carbon fiber-reinforced rectangular isolators with compressible elastomer: analytical solution for compression and bending. *Int. J. Solids Struct.* **50**(22), 3519–3527 (2013)
5. Shin, D.W., et al.: A new facile route to flexible and semi-transparent electrodes based on water exfoliated graphene and their single-electrode triboelectric Nanogenerator. *Adv. Mater.* **30**, 1802953 (2018)
6. Dimov, D., et al.: Ultrahigh performance Nanoengineered graphene–concrete composites for multifunctional application. *Adv. Funct. Mater.* **28**, 1705183 (2018)

**Dr. Maria Rosaria Marsico** is presently a Senior Lecturer in Structural Engineering at the College of Engineering, Mathematics and Physical Sciences of the University of Exeter, UK. She conducts research in Earthquake Engineering, Structural Dynamics, Structural Health Monitoring, Control Systems and Energy Dissipation.

# Chapter 2

## What Rollercoasters Can Teach Us About Fatigue Life of Bridge Connections



Sofia Puerto Tchemodanova and Masoud Sanayei

**Abstract** Rollercoasters are challenging structures. Although the ever-changing geometry can guarantee a thrilling ride, the complexity of loading patterns due to the intricate geometry make testing and analysis of these structures challenging. Fatigue-induced damage is one of the most common types of damage experienced by civil engineering structures subjected to cyclic loading such as bridges and rollercoasters. Fatigue cracking eventually occurs when structures undergo a certain number of loading and unloading recurrences. This cyclic loading under stresses above a certain limit induces microcracking that can eventually propagate into failure of a member or connection. Because of the geometric and structural similarities between rollercoasters and bridge connections, similar techniques can be used for structural health monitoring and estimation of remaining fatigue life. Uniaxial fatigue analysis methods are widely used for the analysis of bridge connections. However, there is little guidance for the analysis of complex connections. They can experience variable amplitude, multiaxial, and non-proportional loading. In such cases uniaxial fatigue methods are insufficient and can lead to underestimates. A framework for the understanding and analysis of multiaxial fatigue damage using strain data collected from strain rosettes is presented. Uniaxial and multiaxial fatigue analysis methods proposed for non-proportional loading are compared. Methods proposed are applicable to both rollercoaster and bridge connections. The critical plane method is used for the estimation of multiaxial fatigue life. Results show that non-proportional loading and the accuracy of the critical plane estimation can cause a significant decrease in the estimates of remaining fatigue life. This methodology is anticipated to be used for real-time fatigue prognosis and evaluation tools for bridge networks.

**Keywords** Fatigue life assessment · Complex connections · In-service loading · Non-proportional loading · Multiaxial stresses · Strain rosettes measurements · Rollercoaster connections · Bridge connections

### 2.1 Introduction

Cyclic loading occurs in civil structures under in-service loading such as rollercoaster and bridges. Loading and unloading effects in such structures and its components can be due to the passage of vehicles, wind loadings, and movement of mechanical parts. Continuous application of this types of loads may induce microcracking that can eventually propagate and produce failure of structural components. This type of damage is known as fatigue and has been found to be cumulative and irreversible.

Fatigue damage can be classified into two categories based on the type of deformations experienced by a structure. High cycle fatigue (HCF) occurs when low stress amplitude cycles result in elastic deformations leading to longer fatigue life estimates. On the other hand, repeated plastic deformations in each stress cycle are characteristic of low cycle fatigue (LCF), such deformations can occur in extreme seismic events or high winds. In service structures normally experience HCF and are designed to never undergo fatigue failure throughout their life or in other words to have infinite fatigue life. However, fatigue cracking is still notorious during the lifetime of common civil structures as rollercoasters and bridges.

Fatigue damage can be quantified with S-N curves. These curves were first introduced by August Wöhler [1] and directly relate the number of cycles a material or connections can withstand under stress cycles at a given amplitude. These S-N curves were developed under cyclic uniaxial loading tests. Subsequently, they can be used to assess remaining fatigue life of structural components in which stresses in one direction are evident or predominant.

---

S. Puerto Tchemodanova · M. Sanayei (✉)  
Department of Civil and Environmental Engineering, Tufts University, Medford, MA, USA  
e-mail: [sofia.puerto@tufts.edu](mailto:sofia.puerto@tufts.edu); [masoud.sanayei@tufts.edu](mailto:masoud.sanayei@tufts.edu)

In-service loads can cause a combination of bending, torsional, and axial stresses in a connection. Multiaxial behavior of stresses occurs when combinations of these stresses take place. If the orientation of the principal stresses due to this combined loading remains constant in time, the loading history is characterized as proportional. Contrarily, if the orientation of principal stresses varies through time, the connection or structural component experiences non-proportional multiaxial loading. Multiaxial effects are known to significantly reduce fatigue life of a member or a connection [2].

Based on physical observation of the initiation and orientation of fatigue cracks under multiaxial loading, Findley formulated a model that combine the interaction of normal and shear stresses acting on the maximum shear stress plane [3]. Using Findley's criterium, a critical plane can be defined. This plane is defined as the most damaging fatigue orientation leading to the least fatigue life [4]. The critical plane approach consists of examining the detailed stress and strain states on all potential critical planes of a structural component. Stresses at the critical plane location are used for estimation of the number of stress reversals induced by live loads and the number of associated cycles using the rain-flow method [5].

In this study, a method for fatigue life assessment of complex connections is presented. The proposed method was initially evaluated for a rollercoaster connection. A connection was instrumented with strain rosettes to compute estimates of remaining fatigue life. Strain histories collected suggest multiaxial non-proportional behavior. Therefore, uniaxial fatigue methods are insufficient to reliability determine remaining fatigue life. A more realistic approach is considered to better represent the interaction of loads in the connection. The critical plane method is used for the estimation of remaining fatigue life using strain rosette data. Given that bridge connections also experience multiaxial interaction of stresses, the methodology proposed is similarly applied to a bridge connection. Uniaxial and multiaxial fatigue analysis methods are compared for the instrumented connections. Remaining fatigue life estimates show that non-proportional loading can result in a decrease in the estimates of remaining high cycle fatigue life. Therefore, current methodologies used in complex connections that are based on uniaxial stresses for the estimation of fatigue life can overestimate the fatigue life of a connection.

## 2.2 Testing

### 2.2.1 Rollercoaster Case Study

Roller coaster structures are by nature systems that undergo continuous cyclic loading. Therefore, fatigue cracking is commonly identified by inspectors in these types of structures. Current design and evaluation standards such as the American Society for Testing and Materials (ASTM) committee F24 and the German Institute for Standardization (DIN in German) DIN4112 recommends procedures for the estimation of fatigue stresses of welded steel structures [6]. However due to the complex geometry of these structures, estimation of live loads on the structure becomes cumbersome requiring many simplifications. A more realistic estimate of the remaining fatigue damage of a structure can be obtained by measuring the stress levels that the structure undergoes due to different load patterns.

For a rollercoaster structure in the US, an instrumentation system including sensors, using battery powered wireless data acquisition unit, is used to measure the structure's response to moving loads. A portable, battery-powered DAQ.

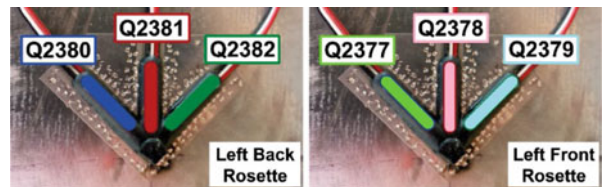
system was used for the collection of data. Strain rosette gages using quarter arm bridges, accelerometers, thermistors, and an optical sensor were installed on a connection of interest. Figure 2.1 shows the location of the connection instrumented in a section of the rollercoaster and the location of the left-front strain rosette. The connection consists of a bracket and is located near the midspan between two columns and approximately 10 m (32.8 ft) high. Two circular rails, running along the rollercoaster structure, guide the rollercoaster train. These rails are connected to a 38.1 mm (1.5 inch) thick steel plate bracket which connects to the main support girder located in the lower part of the rollercoaster's superstructure. The rail tubes, the brackets, and the support girder are welded and made of ASTM A572 grade 50 steel. Data collected from 10 rides under 4 different loading conditions is used for the estimation of fatigue life of the connection.

Four strain rosettes are installed at 50.8 mm (2 inches) from the weld toe connecting the bracket to the main girder. Figure 2.2 shows a close view of two strain rosettes installed mirroring each other on the left side of the bracket. These are color coded to match the measured response graph lines colors. Mean values of strains recorded with a full train from the strain rosettes located in the left side of the bracket are shown in Fig. 2.3. The optical sensor signal peaks downward when the rollercoaster train arrives and leaves the bracket. Tension and compression strain cycles are evident in all arms of the strain rosette when the train crosses the bracket. In addition, collected strains are mirroring each other in about the same magnitude experiencing tension in one side while compression in the other side of the bracket. Therefore, it is evident that the instrumented bracket is experiencing flexure stresses, mainly in the range of 4–6 seconds as shown in Fig. 2.3.

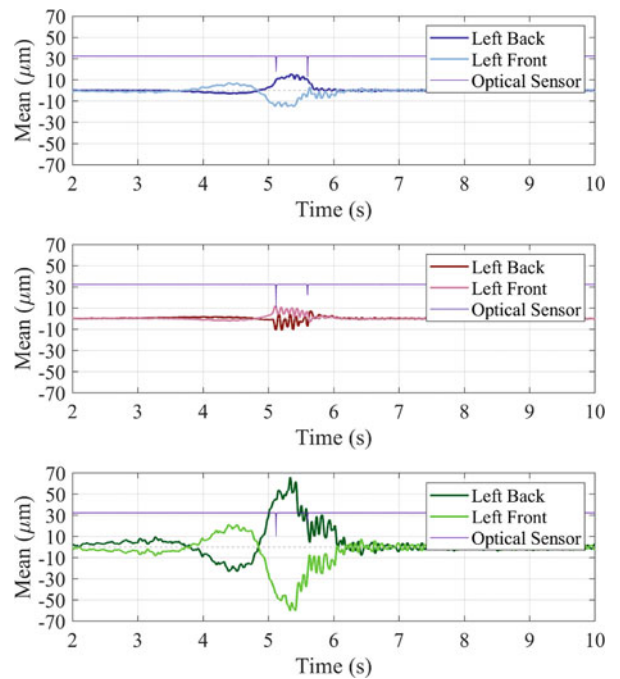
**Fig. 2.1** Instrumented bracket location. Close-up view of instrumentation



**Fig. 2.2** Left side strain rosettes installed on the roller coaster instrumented bracket



**Fig. 2.3** Strain data sample from the left-back and left-front rosette



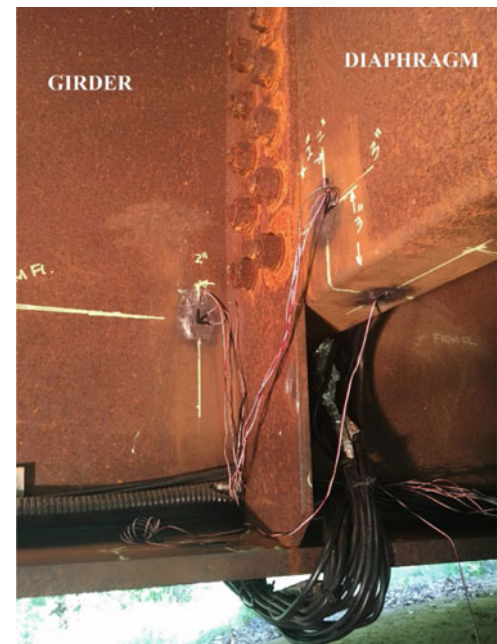
### 2.2.2 Steel Bridge Case Study

The Powder Mill Bridge (PMB), shown in Fig. 2.4, is a three-span steel-girder bridge located in Barre, Massachusetts. The PMB is 47 m (154 ft) long and it carries two lanes of traffic over the Ware river. The PMB was instrumented during its



**Fig. 2.4** Powder Mill Bridge (PMB) over the Ware River in Barre, MA

**Fig. 2.5** Instrumented connection



construction in 2009. An instrumentation system comprised of strain gauges and other transducers was installed as a research prototype for the development of an SHM system. The onsite Data Acquisition (DAQ) system located underneath the bridge collects strain and temperature data 24/7 at 200 Hz. The bridge is a full-scale outdoor laboratory for SHM using short-term and long-term bridge response measurements.

A connection was instrumented to determine the effect of multiaxial stresses and fatigue life. The connection instrumented connects a diaphragm near the south abutment to an interior girder (see Fig. 2.5). Two strain rosettes and two single strain gauges were placed. Strain rosettes are located on the web of the girder and the diaphragm while single strain gauges are located on the flanges.



## 2.3 Fatigue Analysis: Uniaxial Versus Multiaxial Procedures

### 2.3.1 Rollercoaster Case Study

Yield criteria based on principal stresses or Von Mises stresses is typically used for fatigue life estimations when assuming a uniaxial behavior. However, when a component is subjected to multiaxial non-proportional loading, the orientation and magnitude of principal stresses vary with time leading to overestimates of remaining fatigue life [7]. When multiaxial non-proportional stresses are evident, the critical plane method has shown to be effective at predicting remaining fatigue life [8]. The critical plane is defined as the plane orientation that causes the most fatigue damaging. This approach consists of examining the detailed stress states on several potential planes of a component based on a previously determined fatigue criterion. The critical plane approach has been found to be applicable to components subjected to both non-proportional and proportional multiaxial loadings [9]. In addition, it can be applied to different types of material besides steels such as elastomeric materials [10].

Figure 2.6 shows the variation of the principal stress orientation calculated using strains collected in the left-front side rosette for one full ride. In the range of 4–6 seconds, this graph demonstrates that the orientation of principal stresses does change. This variation was observed in all four rosettes. Outside that range, measured strains were close to ambient levels as shown in Fig. 2.3; Thus, such changes in the orientation as shown in Fig. 2.6 shall not be considered when determining if multiaxial effects should be assumed. This figure demonstrates that multiaxial non-proportional effects should be considered for this connection when estimating remaining fatigue life.

Furthermore, Fig. 2.7 compares shear and normal strains the front-left side rosette. For proportional loading histories this comparison will result in a linear relationship [11]. However, the strains experienced by the rollercoaster shown to be randomly out of phase. Therefore, to determine the multiaxial fatigue life a critical plane is first located to determine orientation of the most critical fatigue prone plane. In addition, for comparison purpose, remaining fatigue life is calculated using principal stresses.

Findley's parameter is used to determine the location of the critical plane. Findley proposed a linear combination of shear stress amplitude and the maximum normal stress experience during that cycle. The maximum value of the combination of cyclic shear stress amplitudes and maximum normal stress determines the location of the critical plane [3].

$$\left( \frac{\Delta\tau}{2} + k\sigma_{n,\max} \right)_{MAX} = \tau_f^* (N_f)^b \quad (2.1)$$

where,

$$\tau_f^* = \tau_f' \sqrt{1 + k^2} \quad (2.2)$$

The constant  $k$  is the material coefficient. This constant is found to be between 0.2 and 0.3 for ductile materials (Bruun and Härkegard 2015) [12].  $\tau_f'$  is torsional fatigue strength,  $b$  the fatigue exponent, and  $N_f$  the number of cycles to fatigue failure of the material. The right side of Eq. (2.1) corresponds to the elastic part of a torsion-based S-N curve. The number of stress cycles within the shear stress history at the critical plane is determined using a rain-flow counting algorithm. For

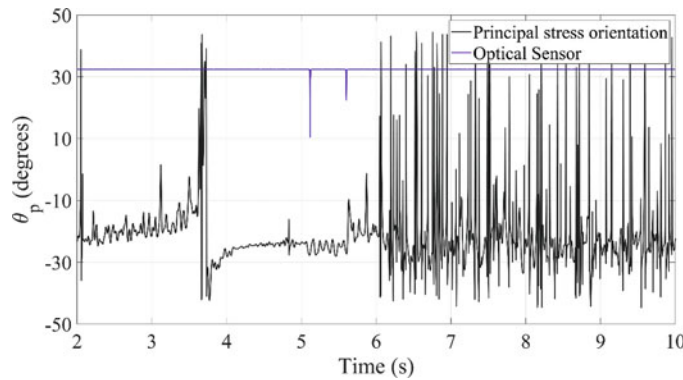


Fig. 2.6 Rollercoaster's variation of principal stress orientation over time at left-front rosette

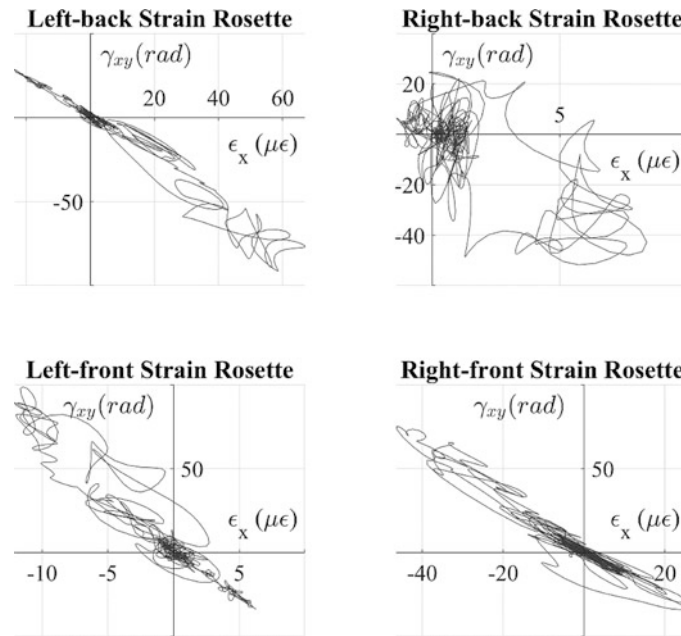


Fig. 2.7 Rollercoaster's normal versus shear strains

Table 2.1 Rollercoaster's summary of remaining fatigue life

Method	Strain rosette location (remaining fatigue life in years)			
	Left-back	Right-back	Left-front	Right-front
Critical plane	3.4E+13	2.7E+14	9.4E+14	3.8E+16
Principal stresses	8.3E+14	4.6E+15	7.6E+17	1.2E+18

comparison purpose, uniaxial fatigue life is calculated using a grade 50 steel axial based S-N curve [13] and the rain-flow counting algorithm using principal stresses. Failure is assumed to occur when the ratio of number of cycles of operation at a stress range to the total number of cycles reaches a value of one.

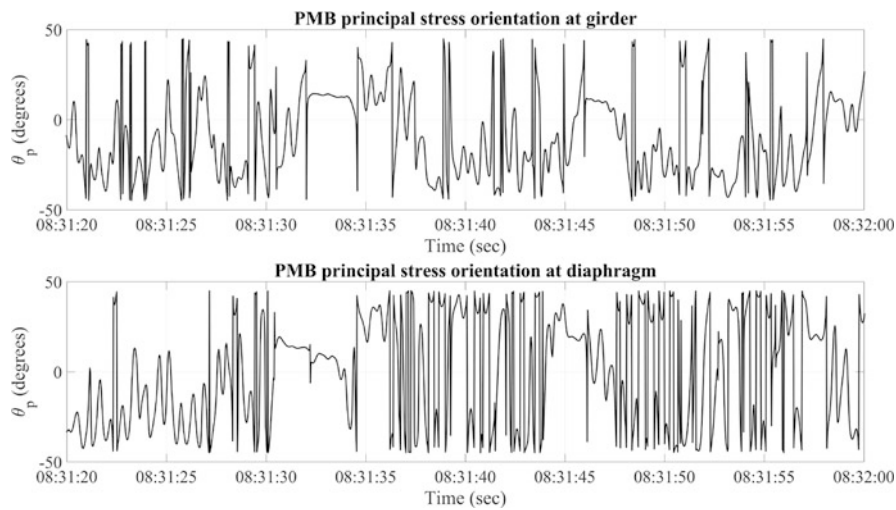
Fatigue life estimates obtained show infinite fatigue life at all strain rosette locations using both the critical plane method and principal stresses. However, the years of remaining fatigue life estimated using the critical method are consistently less than the years calculated using uniaxial fatigue procedures. It should be noted that fatigue life predictions presented in Table 2.1 exclude the presence of the weld. This simplification was made for comparison of fatigue predictions using the critical plane and principal stress methods.

### 2.3.2 Steel Bridge Case Study

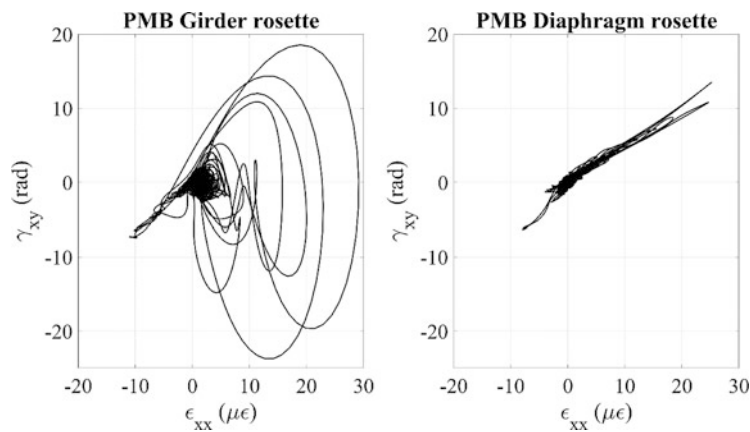
Given the complexity of bridge structures, connections can experience multiaxial distribution of stresses. Evaluation of bridge fatigue life is usually performed using a single strain gage. Typically, when placing strain gages the orientation of tensile stresses is first well known for the member or the component tested. Therefore, strain gages are placed in this orientation [14–16]. However, in more complex details or connections such as the bridge diaphragm to girder connection shown in Fig. 2.5 orientation of principal stresses might vary through a loading history. In this type of connections strain rosettes should be placed to have a better understanding of the distribution of stresses.

Data from the strain rosettes placed on the web of the girder and the web of the diaphragm are used to determine if multiaxial stresses are evident in this connection. Figure 2.8 shows the variation of principal stresses orientation over 40 seconds of data collected at the PMB. During this time about three traffic events are evident in strain histories. These plots show a high variation of principal stresses over time.

A direct comparison between normal and shear strains can also be used to describe multiaxial stresses. If there is a linear relationship between these strains or stresses, multiaxial stresses act proportionally. On the contrary, if the interaction is close to a circle time history of normal and shear stresses are about  $90^\circ$  out of phase. Figure 2.9 shows the interaction of shear



**Fig. 2.8** PMB’s variation of principal stress orientation over time at main girder and diaphragm



**Fig. 2.9** PMB’s normal versus shear strains at rosettes located on the girder and diaphragm

**Table 2.2** PMB’s summary of remaining fatigue life at strain rosettes

	Strain rosette location (remaining fatigue life in years)	
Method	Girder	Diaphragm
Critical plane	8.8E+14	2.7E+15
Principal stresses	1.5E+20	6.2E+19

and normal strains for the strain rosettes located on the girder and the diaphragm at the PMB. The plots show that there is a high phase difference between time histories of normal and shear strains at the girder. Although, the relationship between shear and normal strains at the diaphragm shows to be closer to a line, representing proportional multiaxial stresses, principal stresses orientations show some variation.

Remaining fatigue life is estimated using principal stresses and Findley’s parameter to determine the effect of multiaxial stresses at the location of the strain rosettes. Generalized axial and torsional S-N curves for grade 50 steel tested by Kurath and Fatemi (1990) are used to estimate remaining fatigue life. Table 2.2 summarizes remaining fatigue life estimates. These estimates are based solely on the data collected from strain rosettes.

Remaining fatigue life is estimated to be infinite. However, when looking at the finite number of remaining fatigue life lower values are obtained if multiaxial effects are taken into consideration. These preliminary estimates show that there is a significant difference when non-proportional stresses are evident. Such is the case with estimates base on data collected in the girder’s web. Fatigue life estimates are lower when using the critical plane method compared to estimates based on the rosette located at the diaphragm. However, when using principal stresses fatigue life seems to be overestimated.

## 2.4 Conclusions and Future Work

Remaining fatigue life is estimated based on data collected from two different connections. A rollercoaster connection was instrumented and tested under different loading configurations while a steel bridge connection was instrumented and tested under daily traffic. Multiaxiality was determined by comparing shear and normal strains and the orientation of principal stresses. Uniaxial and multiaxial fatigue life assumptions were used to examine the effect of multiaxial stresses acting in the instrumented connections. Uniaxial and multiaxial fatigue analysis methods are compared. The critical plane method is used for the estimation of multiaxial fatigue life and compared to results obtained assuming a uniaxial behavior. As expected, both methodologies resulted in infinite life estimates. However, when the critical plane method is used the total number of estimated remaining fatigue years is lower than estimated remaining fatigue assuming that the orientation of principal stresses is constant. Therefore, it is concluded that:

1. Commonly used uniaxial fatigue analysis methods are insufficient in complex structures that experience variable amplitude, multiaxial, and non-proportional loading.
2. Although, simplifications were made to make a fair and direct comparison possible between fatigue analysis methods, preliminary results demonstrate that assuming uniaxial behavior can lead to overestimates of remaining fatigue life. Fatigue estimates using the critical plane method resulted in lower fatigue life estimate compared to uniaxial estimate for the connections studied.
3. Multiaxial stresses present in complex connections can reduce the fatigue life. Therefore, generalized S-N curves based on uniaxial estimates shall not be used when multiaxial non-proportional stresses are present. Given the lack of torsional S-N curves available for different types of connections, further work is needed to determine the effect of multiaxial stresses on different connection geometries and types.
4. The presence of welds and bolts cause stress concentrations that significantly decrease in fatigue life and should be considered in final estimates of remaining fatigue life. Although several design codes and standard account for different types of geometries, the curves provided are insufficient in complex structures that experience variable amplitude, multiaxial, and non-proportional loading.
5. The methodology proposed is anticipated to be used for realistic fatigue prognosis of any complex connection. Having a realistic approach will help in assessing critical needs related to maintenance procedures of complex structures, visual inspection techniques, and evaluation tools for infrastructure networks.

## References

1. Wohler, A.: Bericht über die Versuche, welche auf der Königl. Niederschlesisch-Märkischen Eisenbahn mit Apparaten zum Messen der Biegung und Verdrehung von Eisenbahnwagen-Achsen während der Fahrt angestellt wurden. *Zeitschrift für Bauwes.* **8**, 641–652 (1858)
2. Skibicki, D.: *Phenomena and Computational Models of Non-Proportional Fatigue of Materials*. Springer, Cham (2014)
3. Findley, W.N.: A theory for the effect of mean stress on fatigue of metals under combined torsion and axial load or bending. *Engineering Materials Research Laboratory, Division of Engineering, Brown University* (1958)
4. Bannantine, J.A., Socie, D.F.: A multiaxial fatigue life estimation technique. STP1122-EB *Advances in Fatigue Lifetime Predictive Techniques*. 249–275 (1992). <https://doi.org/10.1520/STP24163S>
5. Socie, D.F.: Critical plane approaches for multiaxial fatigue damage assessment. *ASTM Spec. Tech. Publ.* **1191**, 7–36 (1993)
6. Atzori, B., Manara, G., Meneghetti, G.: Experimental analysis of the fatigue strength of a tubular welded joint adopted in a Roller Coaster Structure. In: *International Conference on CRACK PATHS*, 2009, pp. 1049–1056.
7. Shamsaei, N., Fatemi, A.: Effect of hardness on multiaxial fatigue behaviour and some simple approximations for steels. *Fatigue Fract. Eng. Mater. Struct.* **32**(8), 631–646 (Aug. 2009)
8. Chu, C.-C., Conle, F., Bonnen, J.: Multiaxial stress-strain modeling and fatigue life prediction of SAE Axle shafts. *Adv. Multiaxial Fatigue*, no. ASTM STP 1191, 37–54 (1993)
9. Li, J., Zhang, Z.P., Sun, Q., Li, C.W.: Multiaxial fatigue life prediction for various metallic materials based on the critical plane approach. *Int. J. Fatigue.* **33**(2), 90–101 (2011)
10. Mars, W.V., Fatemi, A.: Multiaxial fatigue of rubber: Part I: equivalence criteria and theoretical aspects. *Fatigue Fract. Eng. Mater. Struct.* **28**(6), 515–522 (2005)
11. Meggiolaro, M.A., De Castro, J.T.P., De Oliveira Miranda, A.C.: Evaluation of multiaxial stress-strain models and fatigue life prediction methods under proportional loading. *Proc. Second Int. Symp. Solid Mech.*, pp. 365–384 (2009)
12. Socie, D., Marquis, G.: *Multiaxial Fatigue*. Warrendale, Pa, Society of Automotive Engineers (2000)
13. Kurath, P., Fatemi, A.: Cracking mechanisms for mean stress/strain low-cycle multiaxial fatigue loadings. *Quant. Methods Fractography. ASTM(STP 1085)*, 123–143 (1990)
14. Saberi, M.R., Rahai, A.R., Sanayei, M., Vogel, R.M.: Bridge fatigue service-life estimation using operational strain measurements. *J. Bridg. Eng.* **21**(2013), 04016005 (2016)

15. Zhou, Y.E.: Assessment of bridge remaining fatigue life through field strain measurement. *J. Bridg. Eng.* **11**(6), 737–744 (2006)
16. Alampalli, S., Lund, R.: Estimating fatigue life of bridge components using measured strains. *J. Bridg. Eng.* **11**(6), 725–736 (2006)

**Sofia Puerto Tchemodanova** is a registered Professional Engineer (PE) in the USA and currently a PhD candidate (2020) at Tufts University in Medford, Massachusetts. Her current research focus is on structural health monitoring, analysis, and assessment of complex steel structures such as rollercoasters and bridges.

**Prof. Masoud Sanayei** is a leading researcher in the field of structural health monitoring for bridge condition assessment using static, dynamic, and operational measured data. He is also an expert in building floor vibrations and structure-borne noise for human comfort, operation of sensitive equipment, and precision manufacturing.



# Chapter 3

## Using Resonance Decay Responses to Model the Nonlinear Behaviour of Telecom Monopoles Via Backbone Curves

Jose A. Jimenez Capilla and Julian M. Londono Monsalve

**Abstract** During the last two decades development of mobile/telecoms technologies has meant an increased number of antennas anywhere we are in order to be always connected. In addition, the forthcoming implementation of 5G networks will require the use of bigger and heavier antenna-equipment which would compromise the structural integrity of current structures. Between all the existing types in the market, Monopoles are sensitive and vulnerable structures in this sense, since the dynamics induced by the tip-lumped mass increment, the slenderness and increasing loading due to higher wind resistances would dare the current knowledge and more exhaustive analyses of stiffness and damping in fatigue and other matters like vortex shedding will be necessary. Nonlinear behaviour has already been found in the dynamic response of several monopoles under demanding operational conditions.

This paper presents a technique for the extraction of backbone curves from field tests using quick external Pull and Release excitation on calm weather conditions. Backbone curves are useful to set a vision around the behaviour of nonlinear systems with significant information about any coupling between the primary linear modes in their response. Decaying acceleration records, obtained following tuned steady-state oscillation of actual monopole owned by Arqiva, one of the biggest telecom-structures portfolio in the UK, are processed to estimate the instantaneous frequency, the envelope amplitude of the structural response and the physical behaviour of structural damping, thus extracting the monopole's characteristic backbone curve. Results obtained from those analyses considering several types, geometries and boundary conditions demonstrate the implication of numerous non-linearities sources on the system. Soil-Foundation influence and connections frictions at different levels are able to determine completely the behaviour and modify with high impact the current standards and methodologies in structural engineering.

**Keywords** Backbone curves · Telecoms structures · Non-linearities introduction

### 3.1 Introduction

Nowadays we live in a world of continuous changes, the high degree of innovation makes engineering to keep finding solutions which satisfy the society with reliability and safety. Telecoms could potentially be one of the most continuously changing branch of engineering, new developed networks influence secondary affected fields like masts and towers structural engineering. The new technology requirements oblige either an improvement on the structural designs of already placed buildings or the replacement of high percentage due to new dynamics. In some cases, this second option could put in danger the viability of customer programmes. This conference paper pretends to provide value knowledge of structural non-linear behaviour of monopoles which could help on new designing approaches, especially in terms of fatigue, and be applicable to other civil engineering fields. This exercise is part of a PhD research which pretend to settle new understanding of damping on several types of telecoms structures.

Monopoles, Fig. 3.1, are considered the weakest structure in this matter, the main frequencies of those structure are excited under the spectrum density of wind loading, and the low mass distribution are compatible with high wind resistances to induce high vibrations which act as principal and ultimate limit state. In addition, previous points agree perfect conditions to have resonance under human excitation.

---

J. A. Jimenez Capilla (✉) · J. M. Londono Monsalve  
College of Engineering, Mathematics and Physical Sciences, University of Exeter, Exeter, Devon, UK  
e-mail: [jj379@exeter.ac.uk](mailto:jj379@exeter.ac.uk)



**Fig. 3.1** Left. F&Li Monopole. Right. Portasilo monopole

The study will control excitation, response and external factors, avoiding ambient loading with the purpose of obtaining a perfect free response decays either with climber agitation or, better, with the application of sharp tugs on a rope attached to a point close to the top of the structure, timed to build up a strong (resonant) response before letting the structure under free vibration. Accompanying this excitation with portable acceleration acquisition on the structure, two pair of OPALS (APDM) in this exercise, it is relatively easy to capture the dynamic behaviour.

Any Operational Modal Analysis (OMA) would provide key main parameters important for a dynamic designing, but acquired data can give much more information around some aspects of the structure in terms of stiffness and damping, defining their behaviour related to amplitudes. Those aspects are local defects, connections, influence of soil-foundation conjunction and asymmetries between others. The method backbone curve [1, 2] is applied to extract the energy dependency of nonlinear normal modal curves and their frequencies from decaying time series.

This paper shows an estimation of non-linearities in stiffness and damping for different acceleration measurements carried out on a monopole with the application of backbone curve methodologies (Zero Crossing and Wavelets [3]) after a postprocess based on accelerations integration and OMA, extracting displacement decays working modal coordinates.

### 3.2 Field Tests and Acquisition

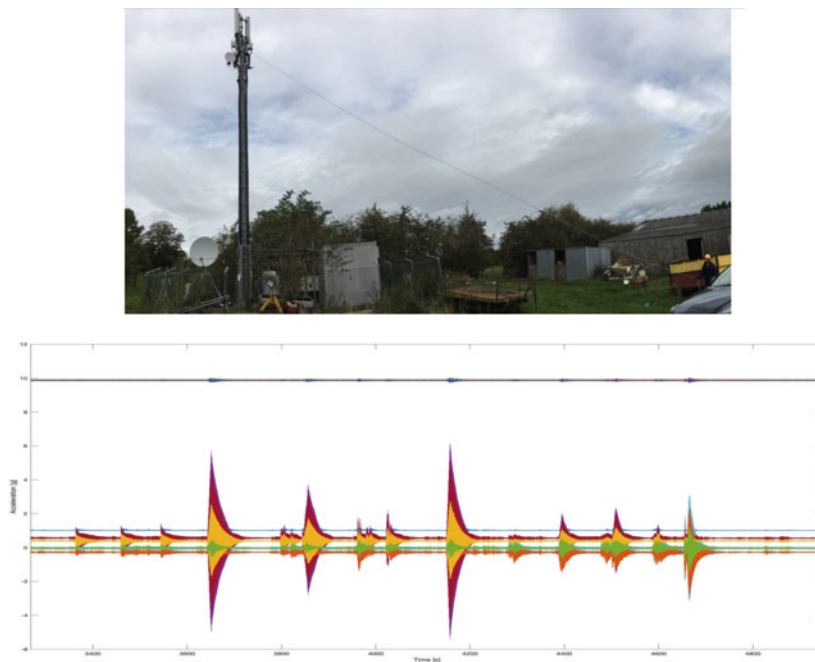
In this exercise, the measurements were obtained from a monopole tested in Norwich, United Kingdom. The structure is a monopole comprising S275J0 steel for main core and plates of 25 mm thick S355J2. There are two sections: a tubular tapered panel between ground level and 14.3 m and a triangular steelwork headframe suitable to accommodate mobile antennas. Also, there is an external spine ladder with latchway fall arrest system. For loading, three panels are installed at the upper part, with a small plate antenna at 14.3 m, with all necessary cables run internally. This structure is joined to the foundation through a flange plate and 12 Grade 8.8 M24 bolts, without grouting.

The acquisition of the data was carried out using a system of synchronized APDM Opal accelerometers as Fig. 3.2. Opals are wireless inertial measurement units including triaxial accelerometers with noise floor  $\sim 120 \mu\text{g}/\text{Hz}^{0.5}$ . Four Opals (i.e. four triaxial accelerometers) were placed at different level locations as shown in Fig. 3.2. Working at 128 Hz sample frequency, these provide the best approach to measure the mode shape of the structure. These devices are wireless sensors that synchronise over short distances typical for mast measurements, and by keeping one Opal at the top of the monopole and ‘roving’ the remaining three Opals to other height-wise locations on the mast it is possible to identify the vibration mode shapes very efficiently. Alternatively, the set of four can be left in place to track variation of mode shapes with vibration decay. Alternatively, an optical acquisition system based on HD cameras focused on dashboard placed at OPALS level was set to verify that the displacements calculate are correct. These checks were satisfactory.

The excitation induced by each pull is appreciated on the acceleration time history, Fig. 3.3, different amplitudes were achieved after single pulls applying different forces, although to acquire really high amplitudes there is need to apply several pulls at the main frequency of the system until resonance.



**Fig. 3.2** Left. Acquisition Scheme using OPAL system. Centre. OPALs installed in monopole. Right. OPAL sensor



**Fig. 3.3** Pull test time raw in Norwich

This type of monopole is characterized by high level of deterioration of inner connections between the shaft column and the flange base. Few failures were identified during last 10 years due to quick fatigue events under normal wind buffeting response which modified the current procedure in dealing with those structures i.e. extra conservative factors in terms of tension resistance at base elements and more maintenance and inspections required before new installations. This paper reveals as well that the estimated main frequencies through structural assessments do not satisfy the current ones on site by a large margin of error which can be an evidence of this deterioration or other similar issues. A knowledge of the non-linearities source in the structure will help to understand that conduct.



### 3.3 Application of Nonlinear SDOF Backbone Procedure

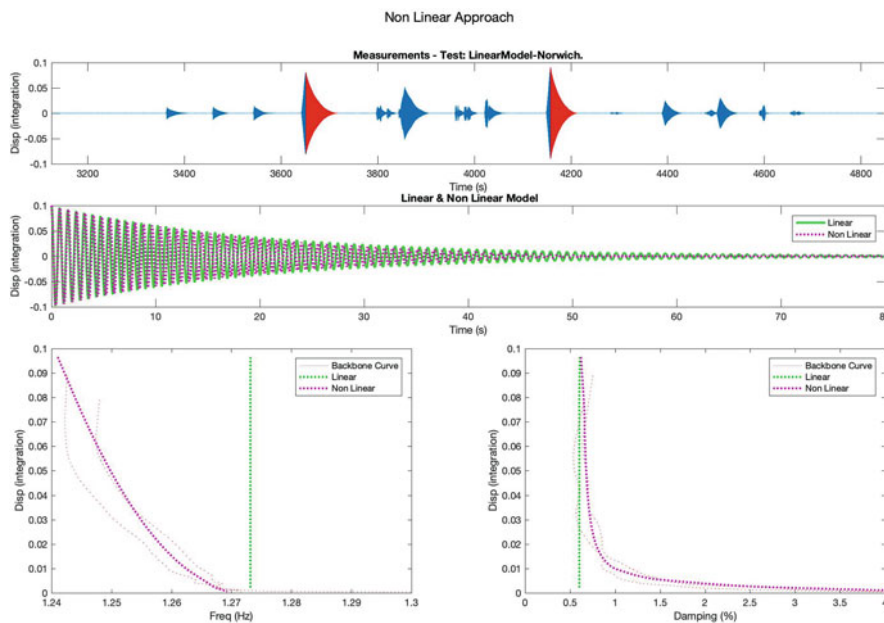
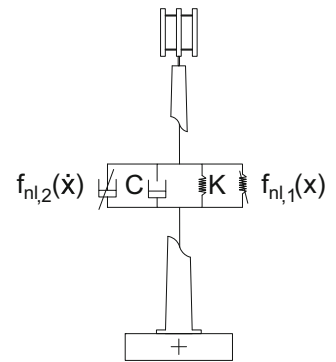
Backbone curve is a method to understand the behaviour on non linear systems looking at the shape of the natural frequencies and damping as a function of response when no forcing is present i.e. during a free vibration decay response after an initial forcing or conditions. In this methodology a force pattern at a predefine relevant frequency in the range of the analysed mode is used to harmonically excite the test structure. After achieving the desire response, the forcing is removed and the required decay is recorded. The resonance decay is then analysed by the linear modal space and instantaneous frequency, damping and amplitude envelope is saved.

A SDOF system is created to illustrate the applicability of the backbone procedure introduced by [2, 4] as Fig. 3.4. The non-linear simplified system taken this case satisfies:

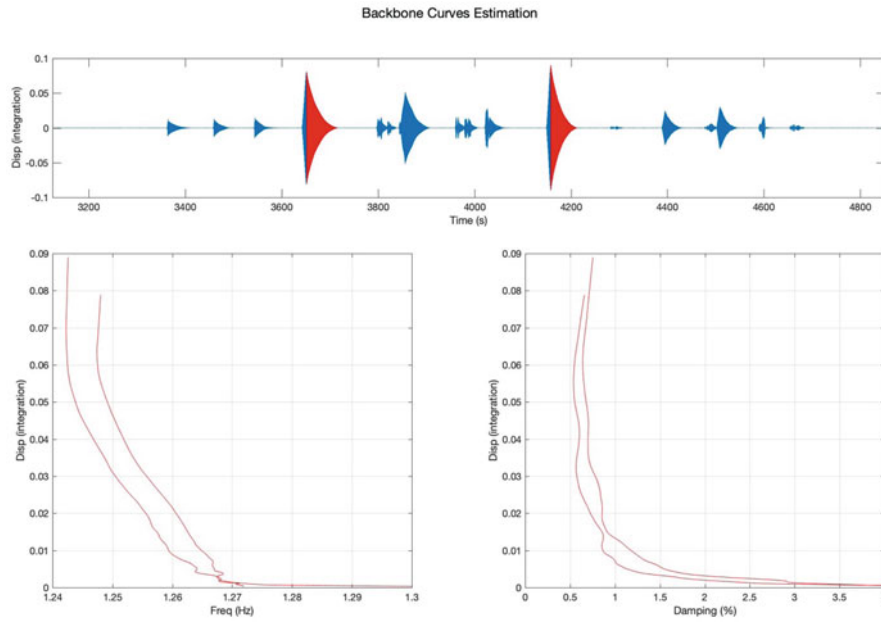
$$M\ddot{x} + C\dot{x} + Kx + f_{nl,1}(x) + f_{nl,2}(\dot{x}) = 0$$

The experimental backbone curves at very low amplitude are used here to define the parameters which defines the underlying linear system (green approach appeared on Fig. 3.5) and initial conditions of deflections. Later, they are used to set the stiffness and damping functions that capture the form of the nonlinearity as Fig. 3.7, which needs to be traduced into an analytic expression in the main equation via Harmonic Balance.

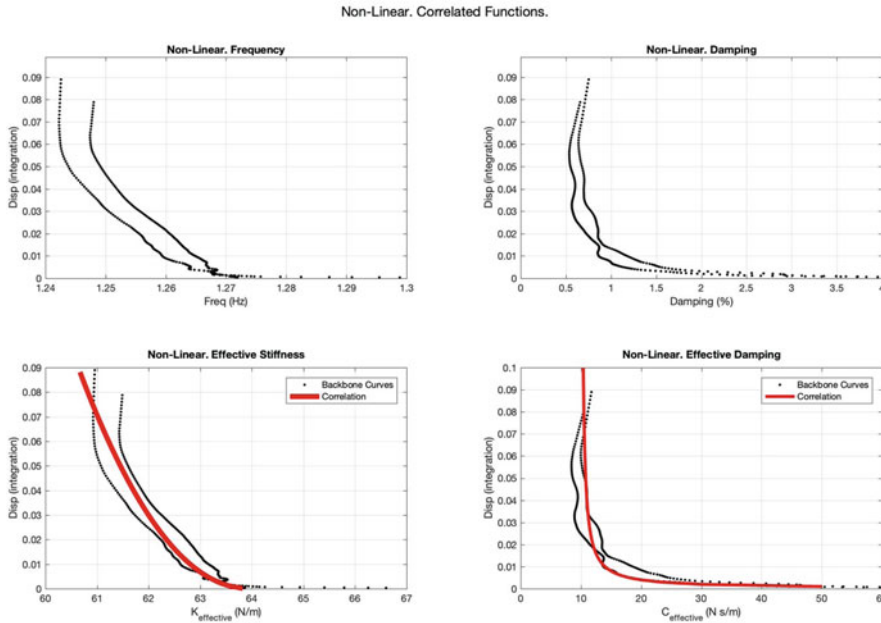
**Fig. 3.4** Non-Linear simplified model



**Fig. 3.5** Non-linear model fitted to current behaviour of measured backbone curves



**Fig. 3.6** Backbone curves from measurements. Upper. Displacements time raw. Down Left. Frequency behaviour. Down Right. Damping behaviour



**Fig. 3.7** Correlated functions of damping and frequency from measured backbone curves

**Table 3.1** Nonlinearities considered in the example SDOF system

System's nonlinearity	$f_{nl,1}(x)$	$f_{nl,2}(\dot{x})$
Nonlinear stiffness	$k_0 \sqrt{x}$	0
Dry friction	0	$c_0 \text{sign}(\dot{x})$

This field survey counts on two large resonance responses which are suitable for the analysis covering a good range of displacements. As mentioned, any data requires post-process to convert accelerations into displacements in modal coordinates.

Therefore, those decays are considered large enough to active the nonlinearity as the backbone procedure obtain on Fig. 3.6. The estimated effective and damping and each respective correlated function are shown on Fig. 3.7 and Table 3.1.

The non-linearities found in terms of stiffness based on a square root function means a softening performance with the displacements. The approach could be improved as a bilinear function which induce more complexity on the expressions. Chosen function describe a low level of restore stability induced by a reduction inertia forces or help from Soils-foundation components.

On the other hand, damping function shows a typical Dry friction or Coulomb-type damping behaviour which is expected from demountable structures and bolts connections based on a interfacial motion as defined on [5]. This source provides high damping at low levels when the movement starts and disappear at high levels where the system behaves nominally linearly. Results agree with current statements of structural damping mainly defined by material and connections components. No evidences of foundation and soils interaction is found which should be specifically analysed with other tools or examples.

The exercise has been proved as an excellent tool to know advanced detailing of structures abroad standard OMA, which could help to develop tools of deterioration analysis interesting for those type of flexible structures under a high range of loading cycles and likely fatigue issues. A SDOF is capable of achieving an accurate estimation of the backbone curve sufficient to represent with high precision in linear and non-linear terms.

Further exploration in different sites would determine if the behaviour found is standard and applicable to different geometries and boundary conditions.

**Acknowledgements** The authors would like to acknowledge Dr. Julian Londono and Prof. James Brownjohn for their mentorship and guidance throughout the duration of this PhD research and the length on this exercise, Mr. Duncan Gould and Mr. Mike Thompson for their continuous support for directing this program, and the entirety of Arqiva Ltd. for sponsoring our fellowship and offering us an opportunity of a lifetime.

## References

1. Cammarano, A., Hill, T.L., Neild, S.A., Wagg, D.J.: Bifurcations of backbone curves for systems of coupled nonlinear two mass oscillator. *Nonlinear Dyn.* **77**(1–2), 311–320 (2014)
2. Londoño, J.M., Cooper, J.E., Neild, S.A.: Identification of systems containing nonlinear stiffnesses using backbone curves. *Mech. Syst. Signal Process.* **84**, 116–135 (2017)
3. Wright, J.R., Cooper, J.E., Desforges, M.J.: Normal-mode force appropriation—theory and application. *Mech. Syst. Signal Process.* **13**(2), 217–240 (1999)
4. Londono, J.M., Neild, S.A., Cooper, J.E.: Systems with bilinear stiffness: extraction of backbone curves and identification, pp. 307–313 (2016).
5. Worden, K.: *Nonlinearity in Structural Dynamics: Detection, Identification and Modelling*. CRC Press, London (2019)

**Jose A. Jimenez Capilla** MENG Structural Engineer by University of Granada and Polytechnical University of Madrid. Currently PhD candidate on Dynamic structures by University of Exeter, UK. Research focused on damping behaviour of wind sensitive telecoms structures.

**Julian M. Londono Monsalve** is a lecturer in Mechanical Engineering at the University of Exeter. His research focuses on experimental testing and nonlinear structural dynamics. His work extends across developing technologies for reducing vibration levels in structures, to the study of nonlinear vibration phenomena naturally occurring in them.

# Chapter 4

## Trench Warfare! The Battle Against Ground-borne Vibration



Michael J. Wesolowsky and Melissa W. Y. Wong

**Abstract** Floor motions can disturb occupants, leading to frequent complaints and loss of functionality. In especially vibration-sensitive facilities, this issue can be more critical, as high-resolution imaging equipment with stringent vibration criteria are often employed. As urban intensification increases, new buildings are being constructed in close proximity to existing vibration sources, such as rail lines and industrial facilities. While a number of vibration mitigation options are feasible to properly isolate these sensitive facilities, vibration trenches can provide a cost-effective solution if the space is available to allow its installation.

In this paper, three case studies are presented of buildings that required trenches to mitigate ground-borne vibration. The first is an office building that was to be located directly adjacent to a currently unused rail line. The owners were concerned that at some point in the future, the line would be reactivated, and wanted to address the potential issue proactively. A hollow open trench was designed which could be implemented in the future. The second project involved a performing arts centre located in close proximity to a rail switching line. Measurements on site indicated that ground-borne vibrations were likely to cause audible rumbles in the theatre. A solid concrete trench was designed to run parallel to the tracks along the property line to mitigate the vibrations. The third project involved an existing industrial facility that had recently installed a new stamping press. The facility was located adjacent to a row of residential single-family dwellings. Two parallel foam-filled trenches were designed and installed to address the ground-borne impulsive vibrations. Validation testing was completed which indicated close agreement with the modelled vibration attenuation.

**Keywords** Vibration serviceability · Ground-borne vibration · Vibration measurements · Model validation · Sensitive floors · Dynamic loading · Vibration trench

### 4.1 Introduction

As urban intensification increases, new buildings are being constructed in close proximity to existing vibration sources, such as rail lines and industrial facilities. While a number of vibration mitigation options are feasible to properly isolate these sensitive facilities, vibration trenches can provide a cost-effective solution if the space is available to allow its installation.

In this paper, three case studies are presented of buildings that required trenches to mitigate ground-borne vibration. The first is an office building that was to be located directly adjacent to a currently unused rail line. The second project involved a performing arts centre located in close proximity to a rail switching line. The third project involved an existing industrial facility that had recently installed a new stamping press. Validation testing was completed on the third project which indicated close agreement with the modelled vibration attenuation.

---

M. J. Wesolowsky (✉) · M. W. Y. Wong  
Swallow Acoustic Consultants Ltd./Thornton Tomasetti, Mississauga, ON, Canada  
e-mail: [mwesolowsky@thorntontomasetti.com](mailto:mwesolowsky@thorntontomasetti.com)

## 4.2 Case Study #1

Case Study #1 involves a proposed office building that will be located directly adjacent to an existing abandoned rail line. The owners were concerned that at some point in the future, the line may be reactivated with either freight or Light Rail Transit (LRT) trains. While both were evaluated for the study, only the freight line will be presented in this paper.

### 4.2.1 *Applicable Vibration Criteria*

The vibration criteria, as recommended by the Federal Transit Administration's (FTA) Transit Noise and Vibration Impact Assessment guidelines [1], is dependent on the type of development, as well as the frequency of the rail vibration events. The development is expected to house retail, a 3-storey parking garage and commercial office space. As such, this development falls under Vibration Category 3 – Institutional. This category is used for schools, churches, quiet offices and other institutional land uses with mainly daytime use.

The frequency of the rail events were assumed to be “Infrequent Events” for the freight train scenario. “Frequent Events” are defined as more than 70 events per day, while “Infrequent Events” are defined as fewer than 30 events per day. Although the FTA Manual is typically used to assess transit, specific guidelines are also presented such that freight trains can also be evaluated using the manual. Using Table 8.1 from the FTA Manual, the ground-borne vibration impact criteria for general assessment was taken to be 83 VdB.

These criteria are based on limiting ground vibrations such that they will not be uncomfortable/ distracting for the building's occupants. These limits are not associated with building damage (including cosmetic damage), which would require much higher levels of vibration.

### 4.2.2 *General Vibration Assessment*

As per the FTA Manual, screening distances are used to determine if a development falls within the critical distance from a rail corridor. As a Category 3 building, the critical distance for freight is 120 feet. Given that the façade of the building is located 25 feet from the rail corridor, a general assessment is required.

To predict the vibration levels at the façade of the building, the generalized ground surface vibration curves from the FTA guideline, was used. For the freight train scenario, the “Locomotive Powered Passenger or Freight” was used. The curve states that at 25 feet, a RMS velocity level of 89 VdB can be expected. Note that that these curves represent the predicted velocity for a train operating at 50 mph.

To account for speed, track conditions and building foundations, the following assumptions and adjustments were made:

- Freight trains operating at 20 mph
- Existing tracks are worn with age
- Normal propagation in soil
- No soil to building coupling loss
- No floor loss

Given the proximity of the rail corridor to the development, as well as the significant curve in the track adjacent to the proposed building, it is highly unlikely that the freight trains will be operating at speeds as high as 50 mph. It has been assumed that the freight trains will be operating at a maximum speed of 20 mph. For a conservative analysis, it has been assumed that the existing rail tracks will be used, should the line be re-activated, and that the track conditions are worn out with age.

To achieve a general understanding of the soil on site, the geotechnical report was reviewed. Efficient vibration propagation within soil is typically associated with bedrock located less than 30 feet below the surface, as well as with stiff clayey soils. According to the geotechnical report, the bedrock is located at approximately 77 feet below the surface. In addition, the majority of the soils are soft as evident through the soil penetration tests. As such, it was deemed that the site does not have efficient propagation within the soil.

Often, a loss of vibration energy can be expected as the waves propagate from the soil to the building foundation. However, given that the building is set to be placed on piles down to the bedrock, it has been assumed that there is no coupling loss.

In addition, there is often a loss in energy as the vibration traverses up floors. Given that the development will have no basement, it has been assumed that there will be no loss to the ground floor.

Based on the above assumptions, it is predicted that a freight train operating at 20 mph on the existing tracks will result in a RMS velocity of 91 VdB at the face of the building. This is 8 dB higher than the vibration criteria, and as such, vibration impact is probable. A Detailed Analysis can be conducted using site-specific propagation in the future, to obtain a more precise prediction of vibration levels.

### 4.2.3 Trench Design

To predict the effect of other mitigation strategies, a more detailed understanding of the vibration sources was required. In particular, frequency-based velocity levels were required as opposed to an overall RMS velocity value, as certain mitigation strategies are more effective at different frequencies.

To determine the frequency-based vibration source levels, a collection of historical vibration measurements taken by the authors were used. These measurements included freight trains, LRTs, and commuter rail trains. A total of 18 freight and 9 LRT/commuter rail train measurements taken at 6 different sites were used to obtain a representative velocity spectrum.

Each of these measurements' spectra were taken and scaled to match that of the FTA predicted vibration levels. This is because the measurements taken had a variety of train speeds, distances from the track centreline, and often had much lower velocity levels compared to the predicted levels. The FTA curves represent the upper range of the expected vibration levels from the different vehicles. Thus by scaling the measurements' spectra to the FTA predicted level, this ensures the conservative upper range is maintained, as well as the general soil propagation. A more detailed assessment could be carried out by determining the site-specific propagation curves. However, as that information is unavailable, the FTA propagation curves were used.

Two mitigation strategies were considered: open trenches and in-filled trenches. These trenches would be placed between the rail corridor and the edge of the building. These trenches are shown in Fig. 4.1. Analysis indicated that the open trench would be more effective.

To obtain a reasonable estimate of the size of the trenches required, a variety of assumptions were made.

- Soil Poisson's ratio = 0.25
- Soil density = 115 lb/ft<sup>3</sup>
- Soil Young's modulus = 21,755 psi

To understand the soil located between the rail corridor and the building, the information from the two boreholes located closest to the rail were used. As the soil was found to be a mix of fine sand and sandy clay, the Poisson's ratio was estimated to be approximately 0.25. Based on the soil penetration tests, the soil is quite soft, and as such, the density of the soil was assumed to be 115 lb/ft<sup>3</sup>, which is typical for loose sand. Finally, the Young's modulus was assumed to be 21,755 psi, which is the upper limit for loose sand and gravel. The upper limit was used for a conservative analysis. From these assumptions, the Rayleigh (surface) wave velocity was able to be determined as 371 mph.

Based on these parameters, the maximum required trench depth was determined using "Simplified Design for Vibration Screening by Open and In-Filled Trenches" [2]. All 27 train measurements' spectra were used to determine the trench depth as the trench efficiency varies with frequency. The overall recommended open trench dimensions are 1.6' wide and 22'

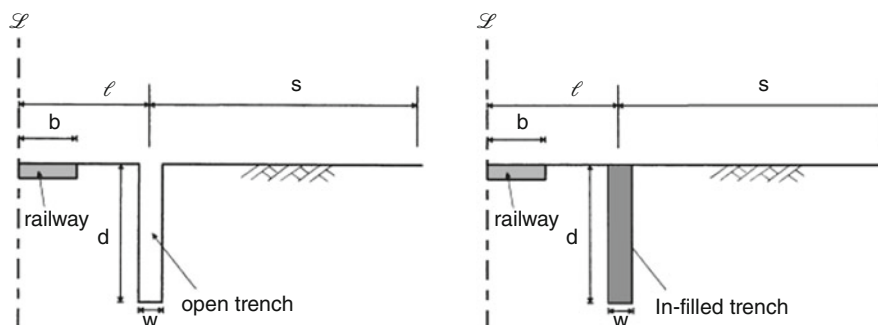
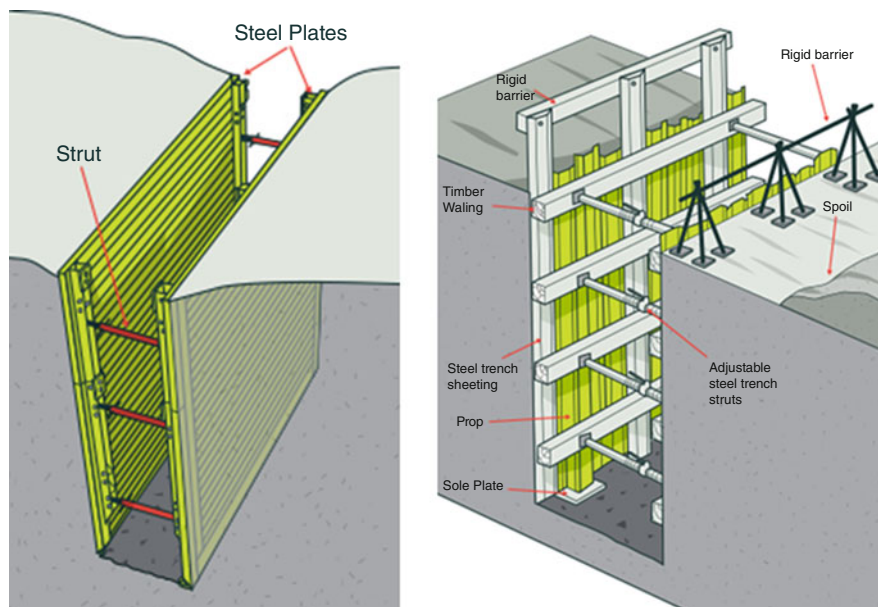


Fig. 4.1 Trench Schematic Drawings



**Fig. 4.2** Detail of two open trench configuration options

deep. To maximize the efficiency of the open trench, it is recommended that the trench be placed as close to the building as possible. To effectively isolate the building from the rail corridor, it is recommended that this trench be constructed along the entire south side of the building. Figure 4.2 shows detailed schematic drawings for two possible open trench configurations. It should be noted that the top should be capped with a plate affixed to one side of the trench, and free to move on the other.

The project is currently under construction at the time of writing this paper.

### 4.3 Case Study #2

The second project involved a performing arts centre located in close proximity to a rail switching line. Initial site vibration measurements indicated that the ground-borne motions would be radiated as noise within the building, which would interfere with the operations of the centre.

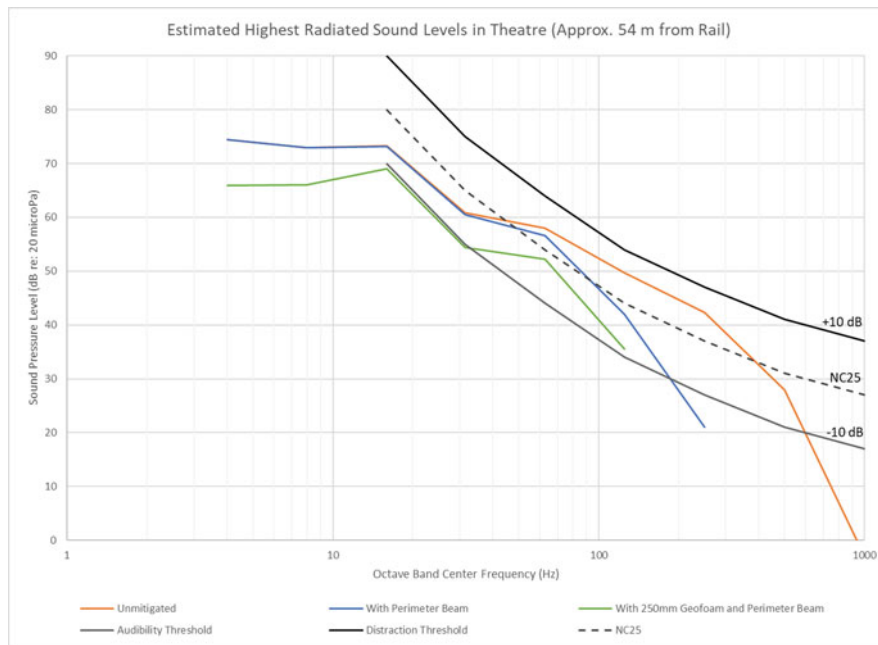
#### 4.3.1 *Ground-borne Vibration Effects*

Ground-borne vibration can have three potential effects on a building:

- The first is perceptible vibration that would be felt by a person standing or sitting on the structure.
- The second is the vibration of elements within the building such as light fixtures or items on a desk, possibly creating rattling noises.
- The third is sound that is radiated into the building by the structure itself (floor and walls) vibrating.

#### 4.3.2 *Rail Vibration Assessment*

Based on vibration measurements at the site, it was determined that the first effect (perceptible vibration) will not be of concern. Even with no mitigation, the highest vibration levels measured at the closest point to the rail line are only barely perceptible as vibration and are low enough to be appropriate for residences where people would be sleeping.



**Fig. 4.3** Comparison of proposed mitigation strategies

The second effect (vibration of light fixtures and other small building elements) should be anticipated, regardless of how the building is constructed or what mitigation strategies are employed. This is because even extremely small vibration levels, far below human perceptibility, can cause loose fixtures or small elements to vibrate in a way that could create rattling or shuddering noises. If issues like this do arise, they can generally be easily dealt with at the source (for example, by tightening the light fixture or securing it to a second point on the structure).

Of primary concern in this case, particularly due to the inclusion of the theatre in the design, is radiated noise from the structure. Estimated radiated sound levels due to the unmitigated vibration levels could be disruptive or distracting to occupants of the building. As a mitigation strategy, a concrete perimeter beam (originally proposed for structural reasons, but effective as a vibration barrier) will be constructed in the ground on the north, west, and south sides of the site. Additionally, the possibility of using 100–200 mm of geofoam (a rigid foam insulation) on the outside of the perimeter beam to further mitigate vibration had been proposed.

### 4.3.3 Comparison of Mitigation Strategies

Figure 4.3 shows the estimated radiated sound levels in the theatre from a train passing for completely unmitigated vibration levels; vibration levels with the perimeter beam alone; and vibration levels with 250 mm of geofoam and the perimeter beam. The line labelled ‘NC25’ represents the background sound level of a typical theatre or performing space. The line labelled ‘+10 dB’ represents the threshold for sounds that would typically be considered ‘distracting’ in that space, meaning that they would have the potential to interrupt a conversation or activity requiring concentration. Our goal is to keep sound levels as far below this ‘+10 dB’ line as possible. The line labelled ‘-10 dB’ represents the threshold for sounds that would be completely inaudible in the space, even if you were listening closely for them. Regardless of mitigation strategy, achieving sound levels this low is not practical, and as such, some amount of train noise will be audible if someone is listening closely for it.

Because the perimeter beam will be installed, radiated sound levels caused by passing trains (the blue line in Fig. 4.3) are expected to be below the threshold for ‘distracting’ noise. This means that, although the trains would be audible if one was intentionally listening for them, they likely would not disrupt most activities. This level of noise may be distracting in the specific scenario where a quiet performance is occurring in the theatre and a train happens to pass at the same time. It was understood that this is of concern because the end users of the theatre anticipate performing mostly drama with small casts, which are expected to be quiet performances.



The proposed additional mitigation strategy of adding 100–200 mm of geofoam is expected to further reduce sound levels. The green line in Fig. 4.3 shows the radiated sound levels expected if 250 mm of geofoam were added (the closest scenario that can be reliably calculated based on available data), placing the expected radiated sound levels for 100–200 mm in the range between the green and blue lines. Although this is an improvement over implementing the perimeter beam alone and may reduce the likelihood of performance being disturbed, even with the geofoam implemented, it should be noted that trains will still be audible if one was listening for them and could still be slightly noticeable during quiet performances in the theatre.

The project is currently under construction at the time of writing this paper.

## 4.4 Case Study #3

The third project involved an existing industrial facility that had recently installed a new stamping press. The facility was located adjacent to a row of residential single-family dwellings, and several complaints were registered from homeowners.

### 4.4.1 *Vibration Criteria*

The vibration requirements outlined in MECP document NPC-207 [3] were used for assessing vibration acceptability. According to NPC-207, the vibration limit on the average peak vertical vibration velocity is 0.3 mm/s. It is understood that this limit applies to all receptor locations within a residence.

### 4.4.2 *First Vibration Isolation Trench*

Based on an initial study conducted by the authors, a vibration isolation trench was constructed between the industrial building and the residences to the west of the building. The final trench dimensions were 87 m in length, 4 m deep and 1.2 m wide. The trench was constructed approximately 6 m away from the edge of the industrial building and was filled with foam with a density of 11.2 kg/m<sup>2</sup>.

After the installation of the trench, vibration measurements within the residence were conducted to determine if the vibration isolation trench reduced the vibration levels to the NPC-207 criterion. The vibration levels within the three receptor residences all met the NPC-207 criterion if arithmetic averaging of the peaks was used. However, it was later understood that MOCP preferred the use of logarithmic averaging. With logarithmic averaging, it was found that the vibration levels within one of the residences marginally exceeded the criterion. In addition, one resident continued to complain about the level of vibrations entering her residence. In an effort to minimize the complaints and meet the NPC-207 criterion using logarithmic averaging, the client requested a second vibration isolation trench.

### 4.4.3 *Second Vibration Isolation Trench*

A second vibration isolation trench was then designed having dimensions of 60 m in length, 4 m deep and 1.2 m wide. Similar to the first trench, the second trench was to be filled with a low-density foam of 11.2 kg/m<sup>3</sup>.

The trench dimensions were determined by modelling the soil in the finite element software ABAQUS. The soil properties including the Young's modulus and Poisson's ratio were found from data obtained from nearby well records. The soil density was assumed to be 1700 kg/m<sup>3</sup> for the first trench design. However, after soil samples were taken during the installation of the first trench, the actual soil density of 1820 kg/m<sup>3</sup> was used for the design of the second trench.

The predicted reductions at the primary complainant's residence due to one and two foam-filled trenches are shown in Fig. 4.4. The black line shows the pre-trench reference line, while the blue line is the reduction due to Trench One and the red line is the reduction due to Trench Two.

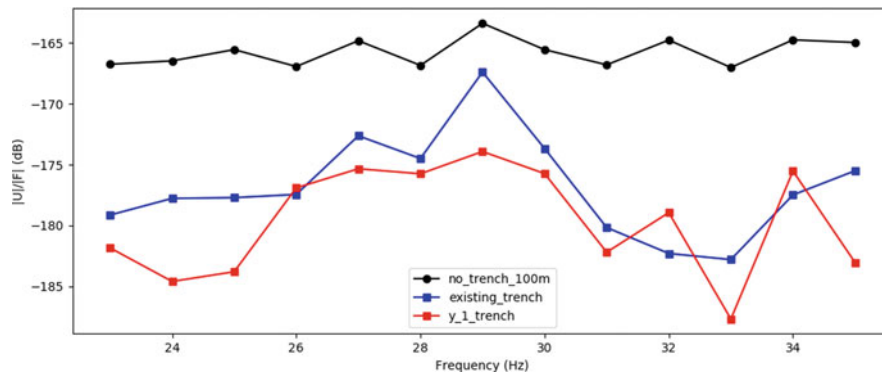


Fig. 4.4 Predicted vibration reduction

Table 4.1 Measured peak particle velocities

Measurement location	Maximum peak particle velocity (mm/s)		
	Original	Post – trench one installation	Post – trench two installation
Property #1	0.49	0.32	0.29
Property #2	Not measured	0.32	0.23

It can be seen that the addition of the second trench was expected to have a reduction between 9 and 20 dB from the pre-trench conditions. This is equivalent to a reduction range of 65% to 90%, depending on the excitation frequency. Comparing the first and second trench, the addition of the second trench was expected to range between a reduction of 7 dB and an amplification of 2 dB, as compared to the first trench. However, on average, it was expected that the second trench would provide a further 2–3 dB reduction from the first trench. This is equivalent to an additional reduction of 20–29% from the first trench.

#### 4.4.4 Verification Measurements

Vibration testing was then conducted post-trench installation at the primary complainant’s residence. The measured peak particle velocities (PPV) are shown in Table 4.1. Note that there are no pre-trench vibration measurements available for Property #2. Note that only the vertical vibration levels are stated here, as the NPC-207 criterion only refers to the vertical direction.

As can be seen from Table 4.1, the maximum PPV reduced with each additional trench installation. In particular, the second trench made a significant reduction (28%) in the maximum vibrations measured at Property #2. This is consistent with the design’s predicted reduction of 20–29%.

### 4.5 Conclusion

Three case studies have been presented which illustrate that vibration trenches, both open and filled, can be an effective mitigation strategy for ground-borne vibration, both from rail and industrial processes. Verification testing was conducted to validate the design in one of the cases.

## References

1. Federal Transit Administration: Transit Noise and Vibration Impact Assessment Manual, FTA Report No. FTA-VA-90-1003-06, May 2006
2. Ahmad, S., Al-Hussaini, T.: Simplified design for vibration screening by open and in-filled trenches. *J. Geotech. Eng.* **117**(1), (1991)
3. Ontario Ministry of the Environment, Conservation and Parks, "NPC-207: impulse vibration in residential buildings", Revised November 1983

**Michael J. Wesolowsky** A senior member of Thornton Tomasetti's acoustics, noise and vibration control engineering team, Dr. Wesolowsky has 20 years of experience in research, analysis, project management and design.

**Melissa W. Y. Wong** Ms. Melissa Wong joined Swallow Acoustic Consultants Ltd. in June 2013 where she has been involved in a wide range of acoustic, noise and vibration related projects. Melissa has a Master of Science in structural engineering from the Hong Kong University of Science and Technology.



## Chapter 5

# Vibration-Based Damage Detection Using Input-Output and Output-Only Environmental Models: A Comparison

Pernille Lysgaard, Sandro D. R. Amador, Silja Tea Nielsen, Evangelos Katsanos, and Rune Brincker

**Abstract** In vibration-based structural health monitoring the natural frequencies of the monitored structures are subjected to different sources of change including: (i) varying environmental conditions (i.e., temperature, humidity, and wind conditions) and (ii) structural degradation and damage. Thus, an accurate detection of structural degradation and damage depends on removing any influence from the environmental conditions on the natural frequencies. If such an influence is not removed, there is a risk of false positive or negative damage diagnosis and thus the damage detection is not robust and reliable. In this study, removal of the environmental conditions and the following damage detection are conducted by applying an output-only principal component analysis as well as an input-output multi linear regression model. The purpose of this study is to assess robustness of these methods by highlighting their advantages and disadvantages in terms of modeling the environmental conditions and detecting structural changes. The investigation is based on vibration data of a wooden mast structure subjected to natural loads and induced with damage at different levels.

**Keywords** Vibration-based monitoring · Natural frequencies · Environmental effects · Damage detection

## 5.1 Introduction

It is a well-known challenge in vibration-based damage detection, that the modal parameters are influenced both by actual variation of the structural changes as well as variations in the environmental and operational conditions (e.g. temperature, humidity, wind, and loads) [1–3]. Whilst it is generally acknowledged that these modal parameters reflect the state of the monitored structure [1, 4], it is therefore of great importance to differentiate the influence caused by environmental and operational variability from the ones caused by structural changes. In order to make this differentiation various methods including, among others, the multi linear regression (MLR) [5], principal component analysis (PCA) [1, 6], and auto-regressive (AR) models [7, 8] have been already introduced and applied. When considering especially the effect of environmental variability, it is common to consider, at least, a full calendar year as the necessary time period for appropriate modeling. This strategy is adopted in several damage detection related studies as, for instance, [6, 8, 9]. In fact, the underlying reason for considering such a long period is to formulate an environmental model capable of describing not only the daily, but also the seasonal variability of the environmental factors. However, it is sometimes necessary or beneficial to begin evaluating the monitored parameters sooner compared to the full year period. This is particularly beneficial in cases where a faster condition monitoring is needed. In Andersen, Nielsen et al [10], an MLR based input-output environmental model formulated from the observations acquired only over a month was efficiently used to detect damage in a wooden mast structure.

In this paper, the efficiency in terms of damage detection of an environmental model created from observations obtained over the time period of only one month is investigated. The environmental model is based on two of the aforementioned methods, namely the MLR approach and the PCA approach. The purpose of the present study is to elaborate further on the two methods. This is done as an investigation and presentation of which considerations should be made with regard to their

---

P. Lysgaard (✉) · S. D. R. Amador · E. Katsanos · R. Brincker  
Technical University of Denmark, Kgs. Lyngby, Denmark  
e-mail: [pelan@byg.dtu.dk](mailto:pelan@byg.dtu.dk); [sdio@byg.dtu.dk](mailto:sdio@byg.dtu.dk); [vakat@byg.dtu.dk](mailto:vakat@byg.dtu.dk); [runeb@byg.dtu.dk](mailto:runeb@byg.dtu.dk)

S. T. Nielsen  
Ramboll Group A/S, Copenhagen, Denmark  
e-mail: [sitn@ramboll.com](mailto:sitn@ramboll.com)

implementations and, on the other hand, to assess the benefits and drawbacks of the implementation of each method in the framework of damage detection by means of short term vibration based monitoring campaigns.

For this study, it is chosen to perform the investigations on experimental obtained in a previous study presented by Andersen, Nielsen et al [10].

## 5.2 Methodology

For this study, two different approaches will be applied to model the environmental variation in the observed natural frequencies namely a MLR model and a PCA model approach.

The available data is the observed natural frequencies ( $\mathbf{f}_n$  [Hz]) and the observed environmental parameters; temperature ( $\mathbf{T}$  [°C]), relative humidity ( $\mathbf{RH}$  [-]), wind speed ( $\mathbf{WS}$  [ $\text{ms}^{-1}$ ]), and wind direction ( $\mathbf{WD}$  [°]). For the wind direction, it is chosen to transform it into a modified parameter that will take the periodicity of the wind direction measure into account. This is done by the parameter  $\overline{\mathbf{WD}} = \sin(\mathbf{WD}) + \cos(\mathbf{WD})$ . It is chosen to also represent the second order of the environmental parameters, for the wind direction this is applied as  $\overline{\mathbf{WD}}_2 = \sin(2\mathbf{WD}) + \cos(2\mathbf{WD})$ . The observed parameters are then arranged as

$$\mathbf{X} = [\mathbf{f}_1 \ \mathbf{f}_2 \ \mathbf{f}_3 \ \mathbf{f}_4 \ \mathbf{f}_5] \quad , \quad \mathbf{P} = [\mathbf{T} \ \mathbf{RH} \ \mathbf{WS} \ \overline{\mathbf{WD}} \ \mathbf{T}^2 \ \mathbf{RH}^2 \ \mathbf{WS}^2 \ \overline{\mathbf{WD}}_2] \quad (5.1)$$

The MLR considers one frequency time series at a time and is defined as

$$f_n(p_j(t)) = \beta_{0,n} + \sum_{j=1}^J \beta_{j,n} p_j(t) + \varepsilon_n(t) \quad (5.2)$$

where  $p_j(t)$  refers to each environmental parameter in  $\mathbf{P}$ ,  $\beta_{j,n}$  is the coefficient of the  $j^{\text{th}}$  parameter in modeling the  $n^{\text{th}}$  mode, and  $\varepsilon_n(t)$  is the error of the modeling of the  $n^{\text{th}}$  mode.

The PCA approach is applied as an output-only method and hence, is only applied to the frequencies. Since the frequencies have quite different magnitude, it is necessary to standardise the data to avoid scaling issues in the PCA. This is done as

$$\mathbf{X}_S = \frac{\mathbf{X} - \mu_X}{\sigma_X} \quad (5.3)$$

where  $\mu_X$  and  $\sigma_X$  is the mean and standard deviation of the columns in  $\mathbf{X}$  respectively. The decomposition is then performed on the covariance matrix  $\mathbf{C}_X$

$$[\mathbf{USV}] = \text{svd}(\mathbf{C}_X) \quad \text{where} \quad \mathbf{C}_X = \mathbf{X}_S^T \mathbf{X}_S \quad (5.4)$$

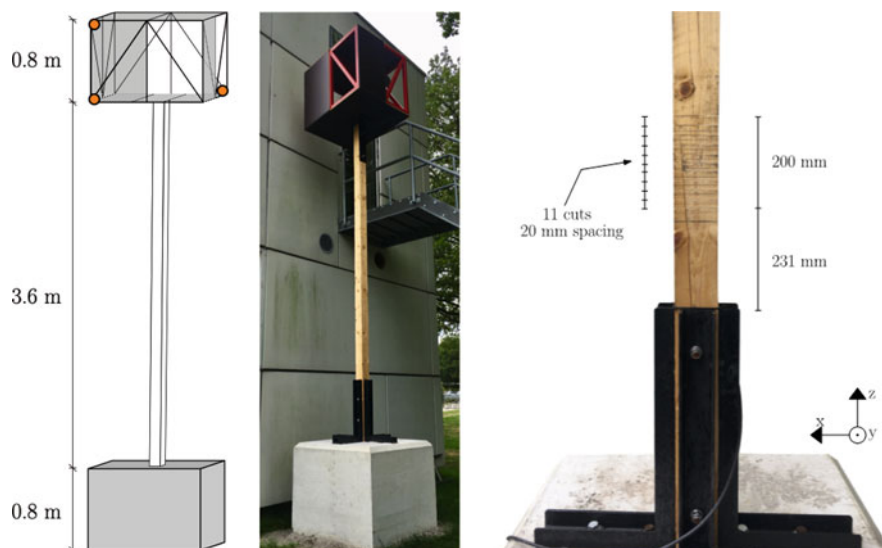
where  $\mathbf{U}$  is a matrix holding principal component vectors in the columns,  $\mathbf{S}$  is a matrix holding the singular values in the diagonal and  $\mathbf{V}$  is a matrix holding the remaining vectors to complete the decomposition. From these the chosen  $m$  singular values are used to make a low rank estimate as follows

$$\hat{\mathbf{X}}_S = \mathbf{X}_S (\mathbf{T} \mathbf{T}^T) \quad \text{where} \quad \mathbf{T} = [\mathbf{u}_1 \ \dots \ \mathbf{u}_m] \quad (5.5)$$

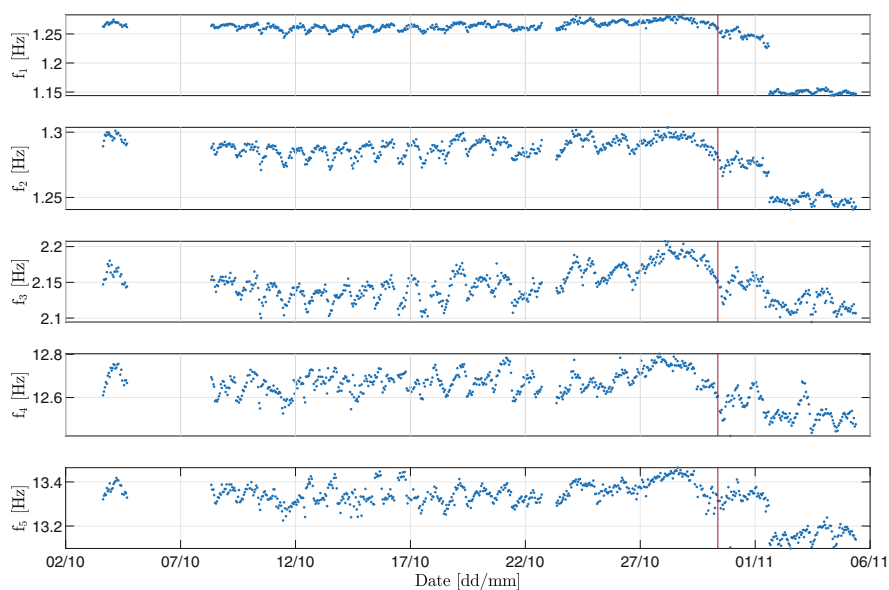
where  $u_i$  is the  $i^{\text{th}}$  column of  $\mathbf{U}$ , corresponding to the  $i^{\text{th}}$  singular value in  $\mathbf{S}$ .

## 5.3 Applied Data

For this study, data collected from a previous monitoring campaign with damage detection is used. This monitoring campaign was recently presented in the paper by Andersen, Nielsen et al [10]. In short summary, the campaign was carried out as monitoring the dynamic response of a medium sized monopile-like structure consisting of a wooden mast and a steel girder top-site founded on a concrete block. The monitoring campaign was initiated on the 3rd of October 2018 and finalised on the



**Fig. 5.1** Presentation of the experimental set-up from where the data used for the presented analysis is obtained [10]. (Left) A model representation with orange dots indicating the position of the three dimensional geophone sensors. (Middle) Photo of the experimental set-up. (Right) Zoom photo of the foundation level of the wooden mast with the induced damages



**Fig. 5.2** Natural frequencies identified during monitoring campaign. The red line indicates when damage induction was initiated

5th of November 2018, while damage was gradually induced to the structure from the 30th of October 2018. The vibration responses of each data set were acquired using nine geophone sensors attached to top-site of the mast structure and recorded with a sampling frequency of 100 Hz during 20 min. The experimental set-up and induced damage from the previous study is presented in Fig. 5.1. Each data set underwent a quality check to ensure reliable results. The vibration responses were then used as primary data by the time domain poly reference (TDPR) [11] operational modal analysis (OMA) identification method to identify the natural frequencies from each data set. The obtained time series of frequencies are the basis for the analysis conducted herein and they are presented for the full length of the monitoring campaign in Fig. 5.2.

## 5.4 Best Model

The MLR and PCA models should be reliable, not only on the data where the model is fitted, but also on other data where e.g. the structural state is unknown. It is important that the two models perform quite well when predicting the general trend and thus it is important to avoid over fitting of the models. Generally speaking, this is done by separating the data into four parts where each one will be used for a different purpose: training, testing, validation, and prediction. Training, testing, and validation are all to be in the part of data that can be considered the reference state of the structure. Thus, prediction is the part that the model is extrapolated onto and this is where the state of the structure is unknown. As the amount of reference state observations in this particular data set is small in terms of model building (528 observations) it is decided to let the testing and validation part be one and the same. It is chosen to use a 80/20 percent split between the training and testing part and thus the amount of observations for each part are 422, 106, and 142 for training, testing, and prediction respectively.

### 5.4.1 Multiple Linear Regression

To determine the best model for correction of environmental effects using the MLR approach it is first important to avoid co-linearity between the predicting parameters. Therefore, no parameter may coexist with its own second order component. With this in mind, all possible model combinations are fitted and tested based on the root mean square (rms) error on the test part defined as

$$E_{rms} = \sqrt{\frac{\sum_{i=1}^N (f_i - \hat{f}_i)^2}{N}} \quad (5.6)$$

where  $N$  is the number of data points in the considered time series. And such for the model where this error is lowest on the test data, is the model that will be used. The models found herein for each mode are presented in Table 5.1 and Fig. 5.3.

As can be seen from Fig. 5.3, the MLR models seem to fit the two first modes quite well and the third mode somewhat reasonable. While the fits of the fourth and the fifth mode are significantly worse. These tendencies are also reflected from the rms error presented in Table 5.1.

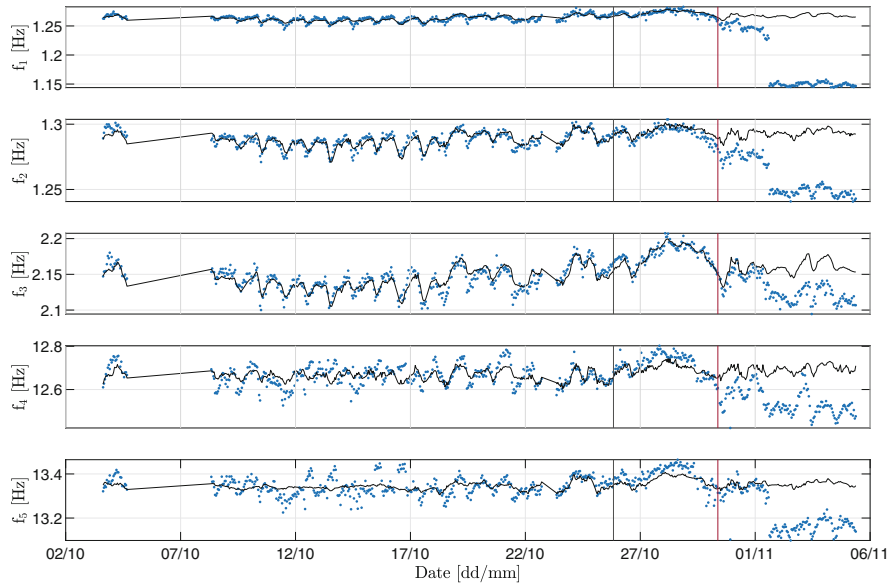
### 5.4.2 Principal Component Analysis

Choosing the best model for the PCA is not as well-defined as for the case of linear regression. The PCA is based on explaining variance and thus, one can describe how much variance in the signal is explained by each principal component (PC). The latter can be seen in Fig. 5.4. It is a common practise to use the amount of variance explained as a criteria for choosing the PCA model [6]. However, it is not necessarily clear where to draw the line in order to model the problem better, as some of the variance is, inevitably, noise. A different approach is therefore to investigate the model's sensitivity to change. This can be done by making simulated changes to the test set of the data, similar to the one used for the MLR best model investigation.

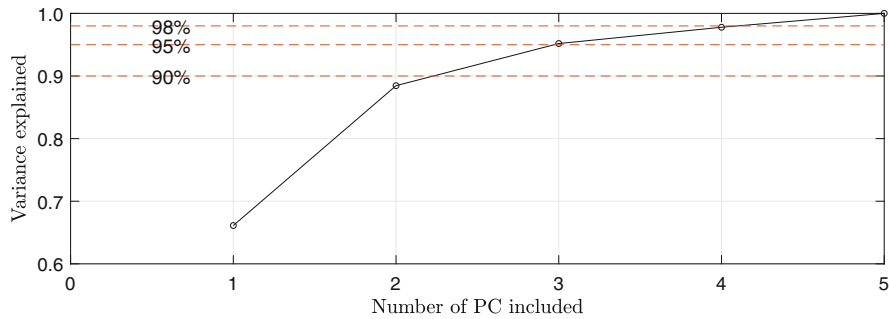
For the case presented here, the model sensitivity will be evaluated in the part of the data set where the structure is in its damaged state. Due to the nature of the PCA approach, the error will be randomly distributed over all five modes. Thus, to

**Table 5.1** Found regression coefficients,  $\beta_{j,n}$ , used for the best model for each mode. Here presented with a subscript of which parameter it relates to instead of the  $i, j$  notation. The rms error,  $E_{rms}$ , is given for each mode

Mode	$\beta_0$	$\beta_T$	$\beta_{RH}$	$\beta_{WS}$	$\beta_{\overline{WD}}$	$\beta_{T^2}$	$\beta_{RH^2}$	$\beta_{WS^2}$	$\beta_{\overline{WD}^2}$	$E_{rms}$
[-]	[-]	[ $10^{-4}$ ]	[ $10^{-4}$ ]	[ $10^{-4}$ ]	[ $10^{-4}$ ]	[ $10^{-4}$ ]	[ $10^{-4}$ ]	[ $10^{-4}$ ]	[ $10^{-4}$ ]	[ $10^{-2}$ ]
1	1.284	-14.876	-	-	-4.982	-	-0.0057	-	-	0.351
2	1.314	-	-1.492	-11.556	-	-0.765	-	-	-8.628	0.391
3	2.222	-52.044	-	-	-	-	-0.024	-1.417	-	0.584
4	12.774	-63.387	-	-107.483	-112.925	-	-	-	-	4.019
5	13.479	-53.071	-	-61.610	-	-	-0.087	-	-	3.845



**Fig. 5.3** Natural frequencies fitted with the multiple linear regression model. The split between training and test data is shown with the vertical dark grey line. The beginning of the induced damage is shown with the vertical red line



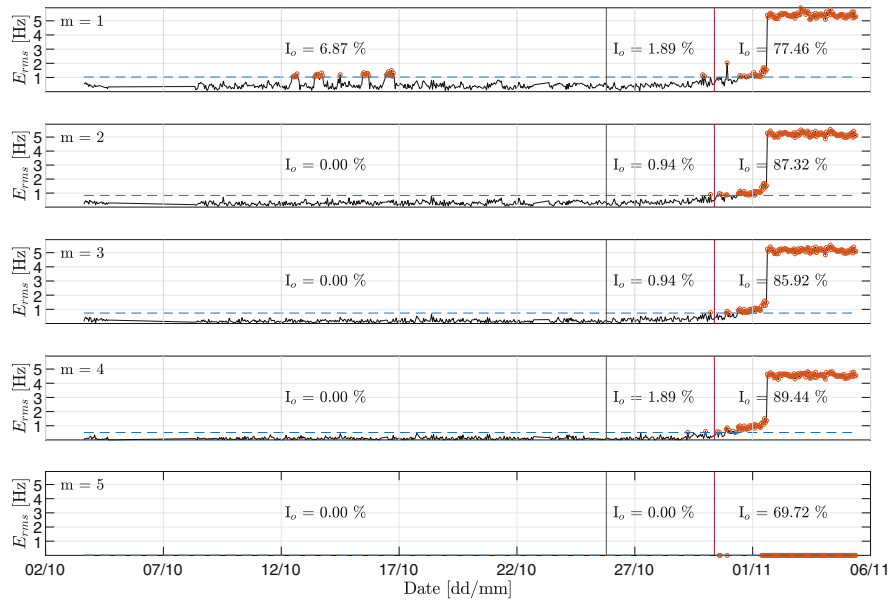
**Fig. 5.4** Cumulative variance explained by the principal components

investigate the sensitivity, the root means square (rms) error across all five modes is computed. To investigate the sensitivity, a limit of three times the standard deviation of the rms error from the test data is applied. These results are presented in Fig. 5.5, from where the outlier intensity for each part of the data can be seen.

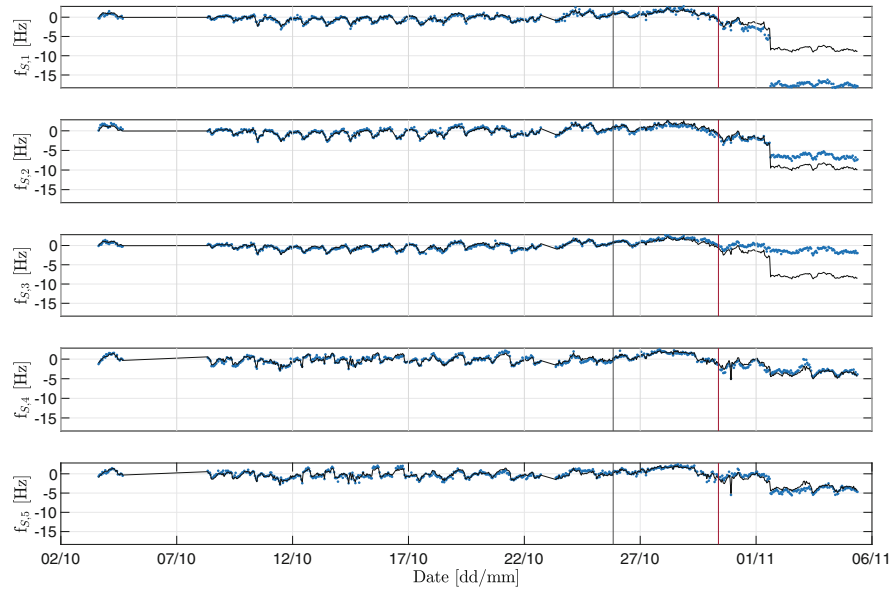
Based on these results, a number of different observations can be made. First of all, it can be seen that it requires more than the first principal component to model the behaviour well enough to avoid outliers in the training set. It also observed, that in the test set, only the model with all PCs provides no outliers and that the error on this model is practically numerical zero, so the outlier detection in the prediction state is a little meaningless. Generally speaking, the models using two, three, and four PCs seem to be reasonably sensitive to change, while yielding very few outliers in the test part of the data. Thus, all of these could be considered reasonable models to facilitate a damage detection campaign. If the relation between the outlier intensities in the damaged prediction state and the healthy test state is determined, it can be seen that the model using just two PCs is the one that has the highest ratio and can be considered more sensitive. This model fit is presented in Fig. 5.6. For this choice of the best model, it should be noticed that with just two PCs, the variance explained is less than 90%, as can be seen from Fig. 5.4. This might be considered a low amount of variance explained and illustrates well, how basing the choice of model on the amount variance explained could be misleading.

From the PCA fitting presented in Fig. 5.6 the effect of the aforementioned random distribution of error from this fitting method can be seen, as large errors are detected between the fit and the measured frequencies on the third mode, where the observed frequencies are not seen to change much due to the induced damage. Furthermore, it can be seen that the fitted model predicts much lower frequencies than the observed, indicating that they are not related to the actual changes of the system.





**Fig. 5.5** Sensitivity analysis when using different number of principal components ( $m$ ). The rms error given as a black line, the limit of three standard deviations given as a dashed blue line, outliers outside of this limit marked with red circles



**Fig. 5.6** Standardised natural frequencies fitted with the PCA model using two principal components

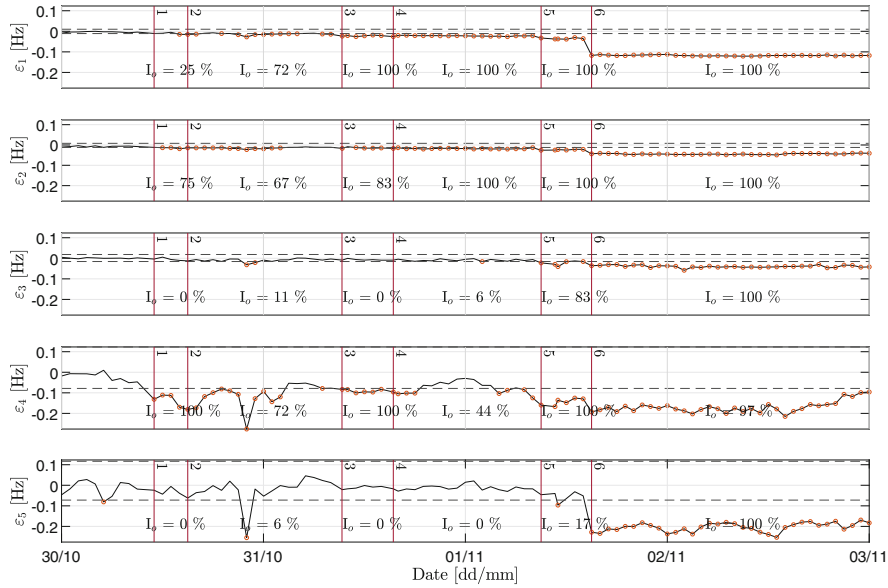
## 5.5 Evaluate Models

In order to further evaluate the models, the sensitivity to each of the six damage steps is to be investigated. However, as previously stressed, the two models are different in the distribution of error and thus it can be said that the MLR model should be evaluated on the basis of each mode, whereas the PCA model should be evaluated across all modes. To investigate what this means for the interpretation of results, both considerations are presented in this section. For both cases, the statistical consideration is kept simple, by considering the intensity of outliers as an indication of sensitivity and defining outliers as values that lie above three standard deviations from the mean, based on the measurements in the test part of the data.

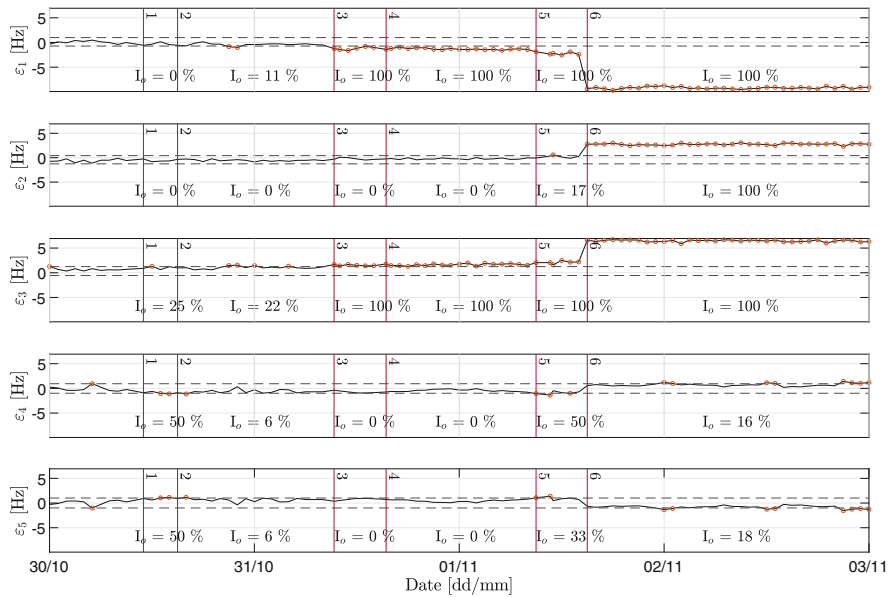
### 5.5.1 Individual Mode Consideration

First, the consideration where each mode is evaluated on its own is presented in Figs. 5.7 and 5.8. From these figures, the outlier intensity for each damage step can be seen. Considering the MLR fitting error first in Fig. 5.7, many things can be seen. The first and second modes are showing outliers already from the first damage step, and with an almost consistent increase in the outlier intensity with increase of damage step, both ending at an intensity of 100%. Next, the third mode also shows a consistent increase in outlier intensity, however it starts at later damage steps. Then the fourth and fifth mode show, first of all much larger errors, and later, less consistent outliers intensity.

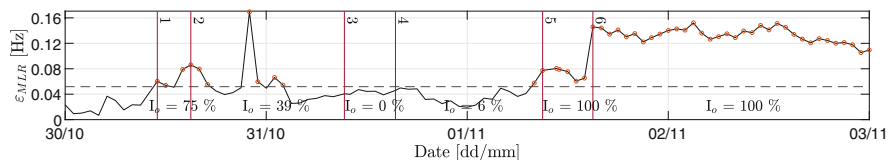
By considering the mode error when modeled by the PCA approach as presented in Fig. 5.8, it can be seen that large values of outlier intensities are generally observed at later damage steps. However, it is interesting to see that the third mode



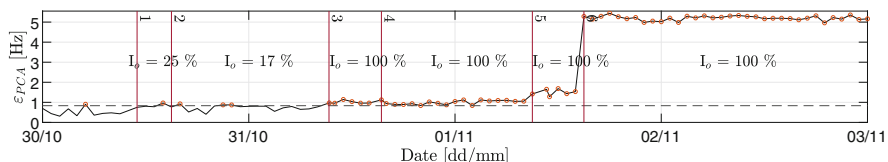
**Fig. 5.7** Error on the individual frequencies based on the MLR approach. The applied limits of three standard deviations are shown with dashed lines and outliers are marked with red circles



**Fig. 5.8** Error on the individual frequencies based on the PCA approach with two PCs. The applied limits of three standard deviations are shown with dashed lines and outliers are marked with red circles



**Fig. 5.9** Error on the combined frequencies based on the MLR approach. The applied limits of three standard deviations are shown with dashed lines and outliers are marked with red circles



**Fig. 5.10** Error on the combined frequencies based on the PCA approach with two PCs. The applied limits of three standard deviations are shown with dashed lines and outliers are marked with red circles

is actually the mode here that seems to react at the earliest damage step, closely followed by the first mode. What can also be observed from this presentation is that, when the outlier intensity is high, it is often equals 100%. So when this method seems to indicate damage, it does it very consistently.

For this consideration, in terms of sensitivity, it seems reasonable to conclude that the MLR approach can detect damage at the first damage step (1.1% cross section reduction [10]) and the PCA approach can detect damage at the third damage step (6.9% cross section reduction [10]). In terms of considering the damage influence on the structure, from Andersen, Nielsen et al [10] it is known that the damage is induced at a point of the structure that will affect mainly the first bending modes (first and second natural frequency modes). Thus, it appears that this consideration through the MLR approach reflects well the changes inflicted by the induced damage. Whereas, the PCA approach is showing the third mode as sensitive in the damage which is not a reflection of the induced damage. This, as has been already mentioned, has to do with the random distribution of error from this method. And so, the disadvantage of the PCA not reflecting clearly how the structure is effected by the damage is confirmed.

### 5.5.2 Combined Mode Consideration

For this consideration, the rms error across the error of all five modes is computed and presented in Figs. 5.9 and 5.10. From the rms error of the MLR fitting presented in Fig. 5.9, it can be seen that, even though there are high outlier intensities in the two first damage steps, it can be seen that they drop dramatically at the third and fourth damage step, before then increasing to convincing damage detection for the fifth and sixth damage step. Despite the fact that this consideration for the MLR fits eventually yield damage detection, it cannot be considered robust and reliable. This is most likely because the poor fitting of the fourth and fifth mode affects the overall interpretation. On the other hand, the PCA approach presented in Fig. 5.10 for this consideration yields a very consistent result with a low outlier intensity at the two first damage steps and then maintained 100% outlier intensity for the remaining damage steps. This means that this consideration of the MLR approach lowers the sensitivity of the damage detection whereas it maintains the sensitivity for the PCA approach.

## 5.6 Discussion

For the overall consideration the above presented investigations and results regarding the MLR and the PCA fitting approach for removing the effects of environmental influences on the natural frequencies should be considered with respect to the overall goal: Robust and reliable damage detection in long term structural health monitoring. For this purpose it must first be noted that the data used for the presented comparison is not long term and there could be differences in the results when considering long term data.

In order to have robust damage detection in long term monitoring, it is necessary to have processes that run automatically with no or very little on-going manual input and checkups. At the same time, the damage detection should be reliable and

so the model applied for subtracting the effect of environmental parameters must ensure neither false negative nor false positives. Thus, it is important that the model approach does not unintentionally model changes caused by damages to the structure. In order to have the best possible implementation during a monitoring campaign the model must be kept a jour, updated on new data, without including data from a damaged structure. In order to ensure this, the model should be updated with some delay, this delay period should be determined based on the sensitivity of the model as a more sensitive model will react to a smaller change and thus be able to choose not to include new data sooner.

With these considerations in mind, each of the presented approaches to this modeling can be considered. First there is the MLR approach, this has the clear advantage of modeling something that is related to the measured input why it gives a better understanding of the cause of change. Thus, the risk of modeling changes caused by developing damages to the structure is low. In return, it struggles to fit the complexity of the frequency dependency as can be seen from the relatively poor fitting, especially of the higher modes. There are several ways this could be improved, incorporating dynamics or linear trends into the modeling. However, all of this would increase complexity of the modeling as well as additional man-made assumptions, possibly incorporating bias into the modeling. This method is however strong on its lack of bias in the choice of the best suitable model, which strengthens its ability to be reliably applied with little manual interactions. When the modeling is reasonably good, as seen in the presented data for the first and second mode, the sensitivity of this approach is seen to be good. Making it most usable when considering each mode individually, where only the well fitted modes can be used. However, it cannot be ensured, that the well fitted modes are where the damage will be most detectable, though it is the case in the present data.

Considering the PCA approach, the case is almost opposite to the one of the MLR approach. This method has no way of including an interpretation of the cause for changes in the system as it is only output driven and relies heavily on the relation between the included modes as well as distributes the error in the modeling randomly. This means that the individual interpretation is rather meaningless. When considered together, it is however seen that the sensitivity is kept, and thus it can still be a good damage detector. From this detection indication, other methods may be considered to understand better the influence of the damage. Another main drawback of the PCA approach is the lack of unbiased choosing of the best model. It relies on the sensitivity test made by the implementer and therefore, further studies could be carried out in order to determine a more objective way of choosing the best model.

## 5.7 Conclusion

The present study shines light on some of the considerations that should be made when working with correcting natural frequencies for the influence of environmental and operational conditions. The study comprises the application of an input-output MLR method and of an output-only approach based on PCA to the experimental natural frequencies of a wooden mast structure with increasing damage levels. From these implementations it is highlighted how the damage influence on the structure is better interpreted in the MLR approach, and how the choice of the best model is clearer from this perspective. However, this method faces difficulties modeling the complexity of the influence from operational conditions. On the other hand, whilst the PCA approach shows to model the behaviour of the frequencies better, the choice of the best model shows to be difficult and subjective, which may easily result in over-fitting that will in turn, compromise the damage assessment of the monitored structure. Over all, this study shows that these methods must be used with caution and the goal of monitoring should always be considered when these methods are applied.

**Acknowledgments** The authors acknowledge the funding received from Centre for Oil and Gas – DTU/Danish Hydrocarbon Research and Technology Centre (DHRTC).

## References

1. Magalhães, F., Cunha, A., Caetano, E.: Vibration based structural health monitoring of an arch bridge: from automated oma to damage detection. *Mech. Syst. Signal Process.* **28**, 212–228 (2012)
2. Carden, E.P., Brownjohn, J.M.W.: Fuzzy clustering of stability diagrams for vibration-based structural health monitoring. *Comput. Aided Civ. Infrastruct. Eng.* **23**(5), 360–372 (2008)
3. Koo, K.-Y., Brownjohn, J.M.W., List, D.I., Cole, R.: Structural health monitoring of the tamar suspension bridge. *Struct. Control. Health Monit.* **20**(4), 609–625 (2013)

4. Rainieri, C., Gargaro, D., Fabbrocino, G.: Statistical tools for the characterization of environmental and operational factors in vibration-based shm. In: *Structural Health Monitoring and Damage Detection*, vol. 7, pp. 175–184. Springer, Cham (2015)
5. Laory, I., Trinh, T.N., Smith, I.F.C., Brownjohn, J.M.W.: Methodologies for predicting natural frequency variation of a suspension bridge. *Eng. Struct.* **80**, 211–221 (2014)
6. Diord, S., Magalhães, F., Cunha, Á., Caetano, E., Martins, N.: Automated modal tracking in a football stadium suspension roof for detection of structural changes. *Struct. Control. Health Monit.* **24**(11), e2006 (2017)
7. Ramos, L., Mevel, L., Lourenço, P.B., De Roeck, G.: Dynamic monitoring of historical masonry structures for damage identification. In: *Proceedings of 26th International Modal Analysis Conference*, Orlando (2008)
8. Peeters, B., De Roeck, G.: One-year monitoring of the z24-bridge: environmental effects versus damage events. *Earthq. Eng. Struct. Dyn.* **30**(2), 149–171 (2001)
9. Yan, A-M., Kerschen, G., De Boe, P., Golinval, J-C.: Structural damage diagnosis under varying environmental conditions—part I: a linear analysis. *Mech. Syst. Signal Process.* **19**(4), 847–864 (2005)
10. Andersen, P.L., Nielsen, S.T., Amador, S.D.R., Katsanos, E., Brincker, R.: Oma-based structural health monitoring of a wooden mast structure exposed to ambient vibrations. In: *Proceedings of 8th International Operational Modal Analysis Conference (IOMAC)*, Copenhagen, Denmark (2019)
11. Brincker, R., Ventura, C.: *Introduction to OPERATIONAL MODAL Analysis*. Wiley, Chichester (2015)

**Pernille Lysgaard** is PhD student at the Dept. of Civil Engineering of the Technical University of Denmark. Her research interests are focused on structural dynamics, operational modal analysis and structural monitoring with damage detection.

**Sandro D. R. Amador** is Assistant Professor at the Dept. of Civil Engineering of the Technical University of Denmark. His research interests are focused on structural dynamics, experimental dynamics, operational modal analysis and structural health monitoring.

**Silja Tea Nielsen** is an Engineer at Dept. of Monitoring and Analyses of Existing Structures in Ramboll. She mainly works with structural health monitoring and probability-based assessment of bridges and structures.

**Evangelos Katsanos** is Assistant Professor at the Dept. of Civil Engineering of the Technical University of Denmark. His research interests are focused on structural dynamics, earthquake engineering and nonlinear analysis, operational modal analysis and structural health monitoring.

**Rune Brincker** is Professor at Professor at the Dept. of Civil Engineering of the Technical University of Denmark. His research interests are focused on structural dynamics, random vibrations, experimental dynamics, operational modal analysis and structural health monitoring.



# Chapter 6

## Techniques for Simulating Frozen Bearing Damage in Bridge Structures for the Purpose of Drive-by Health Monitoring

Robert Locke, Laura Redmond, and Sez Atamturktur

**Abstract** Drive-by Health Monitoring (DBHM) is a relatively new mobile health monitoring strategy that employs vehicle mounted sensors to monitor the health of bridge systems in an efficient and economical manner. Before DBHM can be realized as a viable health monitoring strategy, however, an approach for managing environmental and operational noise needs to be developed. In traditional health monitoring, machine learning techniques, such as neural networks, have been shown to reduce the effect environmental and operational noise has on damage detection accuracy; though, these methods typically require training on damage data, which can be difficult if not impossible to obtain for healthy structures. To resolve this issue, the authors proposed a methodology that utilizes a neural network architecture trained on realistic vehicle-bridge simulations to detect damage in physical highway bridges. For a simulation trained neural network to be able to detect physical bridge damage, numerical models must be able to accurately represent the behavior of a system when damaged. Therefore, the motivation of this work is to identify and validate physics-based techniques for modeling damage induced fluctuations in the dynamic response of highway bridge structures. This study focuses on one of the most common types of bridge damage, frozen support bearings. The authors introduce methods for modeling frozen bearing damage, and discuss the variety of variables that must be considered under certain environmental and operating conditions. The study concludes with demonstrating how to generally apply frozen bearing damage in healthy bridge models to represent possible future damage states.

**Keywords** Highway bridges · Structural damage · Frozen support bearings · Drive-by health monitoring · Finite element models

### 6.1 Introduction

Drive-by Health Monitoring (DBHM), a form of indirect structural health monitoring (SHM), is the practice of using vehicle mounted sensors (e.g. accelerometers) to detect structural degradation in highway bridges. Because vehicles and bridges create a coupled system, vehicle acceleration data contains information about bridge frequencies that can be used as health indicators. First demonstrated to be a feasible form of SHM in the early 2000s, DBHM was initially developed for the purpose of continuously monitoring structural degradation across multiple bridges in a more efficient, cost effective, and less labor-intensive manner than traditional visual inspection or SHM practices [1, 2]. Traditional visual inspections are interval in nature and typically rely on qualitative data and expert opinion to make decisions regarding maintenance, rehabilitation, and replacement [3–5]. Studies have shown this subjective nature can render inspections ineffective as inspectors may fail to detect certain types of damage or make inconsistent and unrepeatable assessments [6, 7]. What's more, visual inspections occur in intervals between two to five years, meaning structural degradation may go undetected for long periods of time [3–5]. Traditional SHM addresses these issues by utilizing a collection of bridge mounted sensors and intelligent diagnostics to continuously analyze bridge response data for the purpose of monitoring localized and global damage over time. Traditional SHM has the benefit of allowing experts to make more informed life-cycle management decisions that can extend a bridge's service life [8, 9]; nonetheless, traditional SHM has not been realized as a competitive alternative to visual inspections

---

R. Locke (✉) · L. Redmond  
Glenn Department of Civil Engineering, Clemson University, Clemson, SC, USA  
e-mail: [wlocke@g.clemson.edu](mailto:wlocke@g.clemson.edu); [lmredmo@clemson.edu](mailto:lmredmo@clemson.edu)

S. Atamturktur  
Department of Architectural Engineering, Pennsylvania State University, University Park, PA, USA

predominantly due to significantly higher costs associated with equipment, installation, and routine maintenance [1, 9–11]. DBHM addresses the above mentioned issues with traditional practices by allowing as little as a single vehicle outfitted with SHM sensors to monitor an entire network of bridges continuously. Before this form of indirect health monitoring can be employed as a viable substitute to traditional practices, however, complications with the method first need to be addressed.

DBHM research has shown that operational and environmental parameters, such as bridge deck surface roughness, vehicle speed, traffic, and temperature, can prohibit the accurate and reliable classification of damage from the dynamic response of moving vehicles. Researchers have attempted to limit the effect of these noise inducing parameters through the implementation of supervised and unsupervised machine learning techniques [12]. Supervised machine learning relies on training a classification model on a set of healthy and damaged data to develop rules that can be applied towards a test data set for the purpose of classifying a structures current damage state [13, 14]. This method of machine learning is the most popular in SHM as researchers often have labeled data to work with and wish to learn functional relationships between inputs [14]. An issue with this methodology, however, is the fact that damage data is required for training, which can be difficult if not impossible to obtain for healthy structures. Unsuperised machine learning is typically employed when only data from a healthy structure is available; however, this method of learning is less popular in SHM due to the fact that labels for input data must be ignored for clustering [13, 14]. Additionally, understanding how to interpret clustered data may not be intuitive and, depending on the severity of noise inducing parameters, it may be extremely difficult to distinguish between clusters. To address the aforementioned issues with DBHM and the limitations associated with machine learning, Locke et al. proposed a supervised machine learning approach to DBHM that first trains a neural network (NN) on healthy and damaged vehicle-bridge models, and then applies the trained network to classify damage states on physical bridge structures.

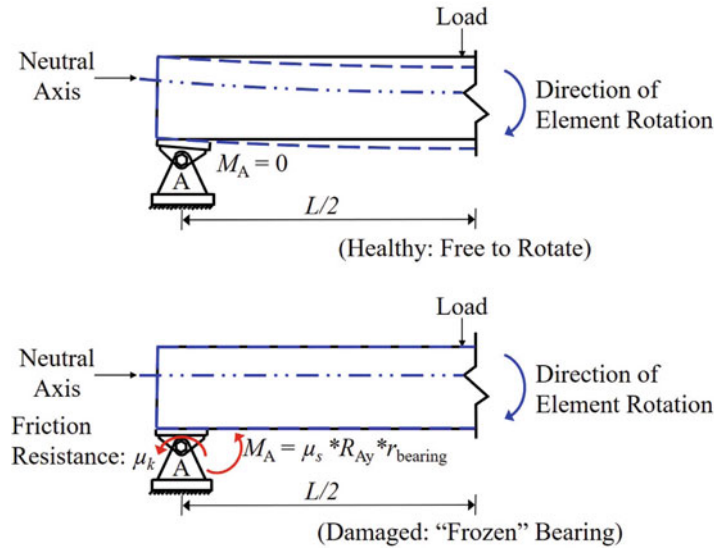
Using known vehicle and bridge properties, along with small sets of initial experimental data, model refinement techniques can first be employed to create realistic yet simplified vehicle-bridge models that accurately simulate the dynamic behavior of physical systems. If a bridge is healthy, various forms of damage can then be simulated in regions prone to degradation; if a bridge has existing damage and it is detectable from initial tests, damage can be introduced during model refinement and then further degradation can be introduced to simulate possible future damage states. Through this approach, a NN can then be trained on vehicle data obtained from the healthy and damaged simulations. Once a sufficient amount of training has been performed, the goal is to then employ the NN to detect physical bridge degradation over time using measured vehicle acceleration data. The success of this approach is dependent on the ability of the simulations to accurately capture the dynamic behavior of the damaged vehicle-bridge system. Therefore, in this study, focus is placed on identifying and validating physics-based techniques for modeling structural damage.

In highway bridge structures, damage can occur on any of three major components, the deck, superstructure, or substructure. This paper focuses on deck and superstructure degradation as these components have a greater influence on damage induced fluctuations in the dynamic response of vehicle-bridge systems. Per the Manual for Bridge Element Inspections and the Bridge Inspectors Reference Manual, the types of damage that can occur on deck and superstructure elements is dependent on the construction material and design; however, frozen bearings, cracking, corrosion, overloading, and impact damage are common types of damage that can occur for almost all construction materials and designs [5, 15]. This paper will focus exclusively on frozen bearings as they are typically a symptom of corrosion damage and can cause cracking and overload damage [5, 15].

The remainder of this paper is organized as follows: Sect. 6.2 discusses methods for modeling frozen bearing damage; Sect. 6.3 provides a model validation case for frozen bearings on a laboratory scale bridge; Sect. 6.4 provides a model validation case for frozen bearings on a full scale bridge; Sect. 6.5 generalizes levels of freezing damage in terms of friction; and Sect. 6.6 summarizes the results from the study and provides suggestions for future research.

## 6.2 Frozen Bearing Damage

Support bearings, such as pinned and rocker bearings, are used in highway bridge systems to provide a means of transferring loads from the superstructure to the substructure. When functioning properly, bearings help prevent the buildup of stresses between superstructure and substructure components by allowing the superstructure to displace relative to the substructure [5]. When deterioration occurs in the form of corrosion or the accumulation of debris, the coefficient of friction ( $\mu_s$ ) within the bearings increases, preventing the superstructure from displacing properly. This freezing effect has been shown to have both a positive and negative impact on a subject bridge's overall health. Studies have shown that frozen bearings can have a positive impact on a bridge structure by resisting rotations at the supports caused by bending moments, effectively increasing the stiffness and, therefore, load bearing capacity of the superstructure [16]. Studies have also shown that frozen bearings cause the unintentional buildup of stresses, which has been shown to cause adverse effects



**Fig. 6.1** Indicates both the healthy and damaged states of the pinned support of a simply-supported superstructure element. The damaged state demonstrates the development of a negative bending moment when  $\mu_k$  resists rotation in the superstructure element

in both superstructure and substructure elements (e.g. tearing and buckling in girders, and cracking in abutments and pier caps) [5, 17, 18]. The deterioration of these components adversely affects the load bearing capacity for a subject bridge. Because frozen bearings have such an impact on bridge health, whether positive or negative, engineers and inspectors place an emphasis on preventative measures for ensuring bearings are seated correctly, free of debris, and free of and protected from corrosion [5]; despite this fact, debris and corrosion can still go undetected during routine visual inspections. However, if models can be developed to accurately model bearing restraint effects for the purpose of informing a NN-trained DBHM approach, frozen bearing damage may be more frequently detected.

As the coefficient of friction increases in pinned bearings, friction forces begin to resist positive rotations caused by internal and external forces (e.g. self weight and vehicle traffic). This resistance to rotation acts as a partial fixity that increases the load bearing capacity and stiffness of superstructure elements. Figure 6.1 demonstrates this process for the pinned support of a simply-supported structure. As can be seen, the resulting negative moment at the support is a function of friction and is governed by the equation below:

$$M_A = \mu_s \cdot R_{Ay} \cdot r_{\text{bearing}}, \quad (6.1)$$

where  $R_{Ay}$  is the vertical reaction at the support, and  $r_{\text{bearing}}$  is the radius of the pin in the bearing. To model the restraining moment  $M_A$  in a finite element (FE) simulation, a rotational spring of stiffness  $K_{\text{rot}}$  can be introduced at the subject support's rotational degree-of-freedom. The resulting negative moment at the support now becomes a function of rotational stiffness and is governed by the equation below:

$$M_A = K_{\text{rot}} \cdot \theta, \quad (6.2)$$

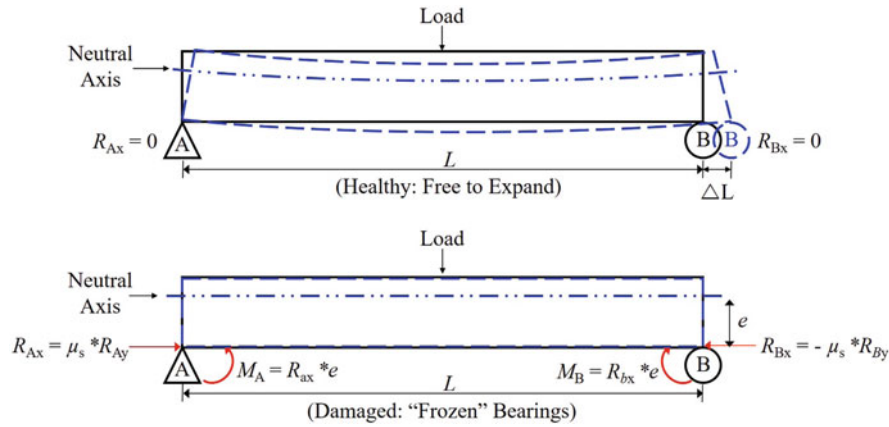
where  $\theta$  is the rotational displacement at the subject support. If a subject structure's frequencies and moment  $M_A$  are known,  $K_{\text{rot}}$  and  $\theta$  can both be solved for using conventional beam theory and the Euler-Bernoulli equation of motion below:

$$[M]\{\ddot{x}\} + [K_s]\{x\} = \{F_{\text{ext}}\}, \quad (6.3)$$

where  $[M]$ ,  $[K_s]$  and  $\{F_{\text{ext}}\}$  represent the structures global mass matrix, stiffness matrix, and external force vector, respectively. Vectors  $\{\ddot{x}\}$  and  $\{x\}$  represent the acceleration and displacement associated with vertical and rotational degrees-of-freedom.

As the coefficient of friction increases in rocker bearings, friction forces begin to develop at the base of superstructure elements. Because these forces are offset from the neutral axis by an eccentricity ( $e$ ), negative moment reactions are introduced to the system. Negative moments introduce a partial fixity in the system that causes an increase in the load bearing





**Fig. 6.2** Indicates both the healthy and damaged states of a simply-supported superstructure element. The damaged state demonstrates the development of negative bending moments when compression friction forces ( $FF$ ) restrict rotation in the superstructure element

capacity and stiffness of superstructure elements by resisting rotational displacements caused by internal and external forces. Figure 6.2 demonstrates this process for a simply-supported structure. Bakht and Jaeger demonstrated that bearing moments induced by eccentrically applied axial loads can be modeled in simulation using a linear spring offset from the neutral axis at the lower flange [16]. The benefit of this approach is that rotational restraints at the bearings can be calculated directly as a function of the measured axial force; however, the issue with this method is it requires identifying an appropriate spring stiffness and offsetting the spring from the neutral axis, which cannot be directly modeled in a simplified one dimensional FEM [18]. Another approach for introducing rotational restraints in simulation is to again employ rotational springs at the bridge supports. The benefits of this approach are rotational springs can be easily included at rotational degrees-of-freedom and do not need to be offset from the neutral axis, making it an ideal approach for simplified one dimensional models. Additionally, by computing the support-to-midspan moment ratio of the system, an analysis can be performed to identify a spring constant that provides the same ratio. Lastly, if the bridge structure is simply-supported, a relationship between the rotational spring stiffness and the subject structure's length ( $L$ ), modulus of elasticity ( $E$ ), and moment of inertia ( $I$ ) can be identified by virtue of the ratio of the simply-supported fixed-end moment to the fixed-end moment of a fixed-fixed structure [18, 19]. An issue with this approach, however, is that it removes the effects of axial forces on the structure, which have been shown to have a significant impact on changes in bridge load bearing capacity and frequencies [20].

Clough and Penzien explain the phenomena of axial forces influencing structural frequencies through the single-degree-of-freedom equation shown below:

$$\omega_n = \frac{n}{L} \sqrt{\frac{n^2 \cdot \pi^2 \cdot E \cdot I}{L^2} + P}, \quad (6.4)$$

where  $P$  is the axial force that is positive in tension and negative in compression,  $m$  is the mass per unit length, and  $n$  is the mode number (e.g.  $n = 1$  for mode 1) [20]. As can be seen by equation 6.4, the change in frequency is proportional to the square-root of the magnitude of the axial force. This relationship is derived from the fact that axial forces affect a structure's buckling capacity and, therefore, bending stiffness [20]. When tension forces are present, the stiffness of the system increases, resulting in an increase in buckling capacity and frequencies; intuitively, the opposite is true for compression forces. Having identified a relationship that explains the change in bridge frequencies caused by axial forces, a method for including these changes in a multi-degree-of-freedom FE simulation is needed. In their book, Clough and Penzien introduce a geometric stiffness matrix that can be subtracted from the four degree-of-freedom Euler-Bernoulli stiffness matrix ( $[K_s]$ ) to account for changes in system stiffness caused by axial loads [20]. Equations 6.5 and 6.6 respectively indicate the coefficients for the geometric stiffness matrix and the updated Euler-Bernoulli equation of motion:

$$[K_g] = \frac{P}{30L} \begin{bmatrix} 36 & 3L & -36 & 3L \\ 3L & 4L^2 & -3L & -L^2 \\ -36 & -3L & 36 & -3L \\ 3L & -L^2 & -3L & 4L^2 \end{bmatrix}, \quad (6.5)$$

$$[M]\{\ddot{x}\} + ([K_s] - [K_g])\{x\} = \{F_{\text{ext}}\}, \quad (6.6)$$

where  $[K_g]$  is the geometric stiffness matrix. For the case outlined above, the axial force used for the geometric stiffness matrix can be calculated using equation 6.7 below:

$$P = \mu_s \cdot R_y. \quad (6.7)$$

By including the geometric stiffness matrix in addition to a rotational spring at the support's rotational degree-of-freedom, a simplified FE model should be able to account for all the changes in a subject structure's load bearing capacity and frequencies when frozen bearing damage introduces axial and rotational effects. The following model validation studies demonstrate how frozen bearings can be simulated for a lab scale and full scale structure.

### 6.3 Lab Scale Study

The following laboratory setup was constructed at Carnegie Mellon University for the purpose of employing DBHM concepts to characterize vehicle-bridge interaction patterns and detect changes in bridge health caused by various types of damage, including frozen bearings. For the purpose of validating the frozen bearing bridge model, this study ignores vehicle-bridge interactions and focuses exclusively on the bridge free of any vehicles. The subject bridge, as seen in Fig. 6.3, is a 2.44 m (8 ft) long single span simply-supported structure, where pinned and roller supports are respectively located on the left and right of the structure. The bridge has a  $m$  of  $7.5062 \frac{\text{kg}}{\text{m}}$  ( $.4203 \frac{\text{lb}}{\text{in}}$ ), with an  $E$  of 68.9 GPa (10000 ksi) and an  $I$  of  $8.15e^{-8} \text{m}^4$  ( $.1956 \text{in}^4$ ). From free-vibration testing, the fundamental frequency and damping ratio of the bridge were identified to be 7.23 Hz and 3.6%, respectively. For more details regarding bridge design and dimensions, please see the following reference [21].

To simulate frozen bearing damage in the physical structure, a rotational restraint mechanism (lever arm) was attached to the corners of the supports. The lever arms were constructed using an aluminum bar that was milled down through part of the cross section to provide a partial restraint near the supports. The arms were installed by attaching one end to the main girders and by fastening the other end to the adjacent support using aluminum bolts. A technical drawing and picture of the mechanism can be seen in Fig. 6.4. In this study, focus is placed on two damage cases tested in the original study that



Fig. 6.3 Elevation views of laboratory bridge setup

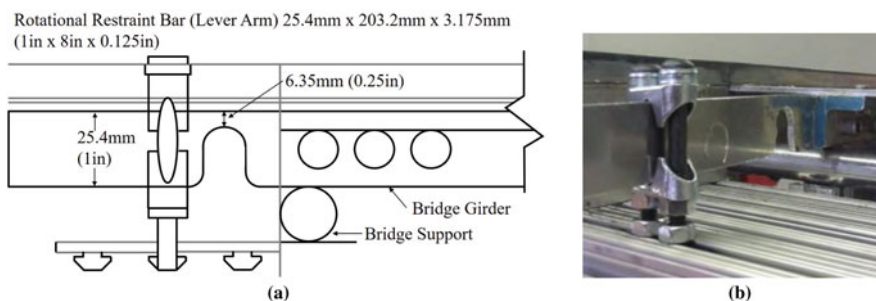



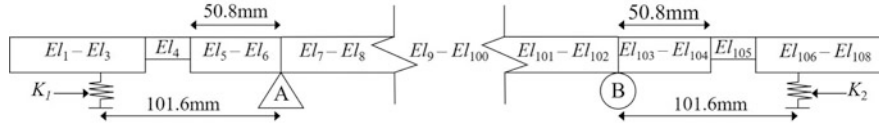


Fig. 6.4 Rotational restraint at roller support condition. (a) Indicates technical drawing of system. (b) Image showing physical system

**Table 6.1** Damage cases for lab-scale bearing damage

Damage condition	Frequency [ $\omega$ ] Hz	Diagram
Healthy	7.23	
1	7.66	
2	8.56	

**Fig. 6.5** Element ( $EI$ ) meshing scheme demonstrating how the lever arms are integrated into the bridge structure**Table 6.2** Section properties for lever arm and bridge elements

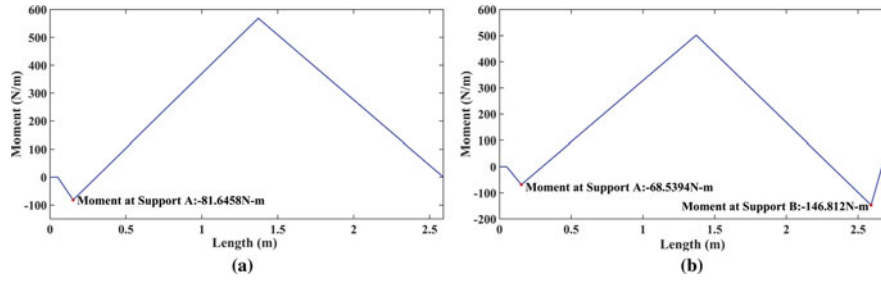
Elements	Damage condition 1		Damage condition 2	
	MoI [ $I$ ]	Mass [ $m$ ]	MoI [ $I$ ]	Mass [ $m$ ]
$EI_1 - EI_3, EI_5 - EI_6$	$8.671e^{-9}$ (.0208)	$.446$ (.013)	$8.671e^{-9}$ (.0208)	$.446$ (.013)
$EI_4$	$1.355e^{-10}$ ( $3.255e^{-4}$ )	$.446$ (.013)	$1.355e^{-10}$ ( $3.255e^{-4}$ )	$.446$ (.013)
$EI_7 - EI_8$	$1.126e^{-7}$ (.2705)	$7.95$ (.445)	$1.126e^{-7}$ (.2705)	$7.95$ (.445)
$EI_9 - EI_{100}$	$8.150e^{-8}$ (.1956)	$7.51$ (.420)	$8.150e^{-8}$ (.1956)	$7.51$ (.420)
$EI_{101} - EI_{102}$	$8.150e^{-8}$ (.1956)	$7.51$ (.420)	$1.126e^{-7}$ (.2705)	$7.95$ (.445)
$EI_{103} - EI_{104}, EI_{106} - EI_{108}$	N.A.	N.A.	$8.671e^{-9}$ (.0208)	$.446$ (.013)
$EI_{105}$	N.A.	N.A.	$1.355e^{-10}$ ( $3.255e^{-4}$ )	$.446$ (.013)
$EI_{106} - EI_{108}$	N.A.	N.A.	$8.671e^{-9}$ (.0208)	$.446$ (.013)

The properties in Table 6.2 consider the combined effects of the parallel lever arms for the cantilever sections, and the combined effects of the parallel lever arms and bridge for the sections where the lever arms connect to the bridge girders

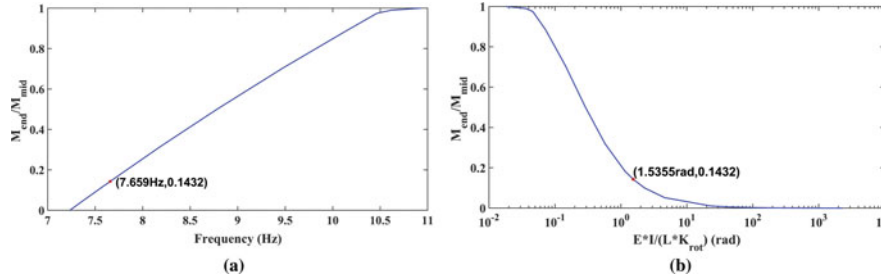
constitute symmetric damage in the transverse direction of the bridge, Table 6.1 provides a diagram of the subject damage cases and reports the associated resonant frequency [21].

To demonstrate that a rotational spring can be employed to represent the lever arm mechanism shown in Fig. 6.4, a FE study first needs to be conducted to determine the magnitude of rotational restraint introduced by the lever arms. In this study, equation 6.3 is employed to model the behavior of the subject bridge. The main structure is modeled as a one dimensional simply-supported beam that is discretized into 96 Euler-Bernoulli beam elements, while the lever arms are modeled as cantilevered sections that are discretized into 6 Euler-Bernoulli beam elements. The mesh size is chosen such that the size of all elements will be equal to 25.4 mm (1 in), this is to accommodate the change in MoI at the milled sections, which are estimated to be approximately 25.4 mm wide. Information regarding the distance of the milled sections from the supports was not provided in the original research; therefore, it is assumed that the milled cross sections are located two elements before and after the pinned and roller supports, respectively. Additionally, information regarding the length of connection between the lever arms and main girders was not provided, this overlap distance is assumed to encompass the first and last two elements of the main structure. The connection between the lever arms and girders causes an increase in mass and MoI near the supports, this change is accounted for by increasing the mass and MoI of the first and last two elements of the main structure. Please reference Fig. 6.5 and Table 6.2 to visualize the aforementioned meshing scheme and observe the section properties assigned to elements across the structure. It should be noted that the above mentioned assumptions are based on visual inspections of photographs provided for the original test setup [21].

As can be seen in Fig. 6.5, linear springs ( $K_1$  and  $K_2$ ) are used in simulation to model the vertical restraints introduced by the aluminum bolts on the physical structure. The springs are located at the beginning of the element before the milled section on the pinned side, and at the end of the element after the milled section on the roller side (i.e. at the beginning and end of  $EI_3$  and  $EI_{106}$ , respectively). Because the stiffness of the actual bolts is dependent on tension, for which no data was provided, it is difficult to physically calculate the equivalent stiffness of the bolts acting in parallel. Because of this, a trial



**Fig. 6.6** Moment diagrams of bridge system when a point load is applied at the midspan of the main structure. (a) Moment diagram for Damage Condition 1. (b) Moment diagram for Damage Condition 2



**Fig. 6.7** Demonstrates how the equivalent spring stiffness can be determined for Damage Condition 1. (a) Relationship between resonant frequency and support-to-midspan moment ratio. (b) Relationship between support-to-midspan moment ratio and the inverse of equivalent spring stiffness

and error procedure is performed to identify the equivalent spring stiffness needed in simulation to match the frequencies of the physical system observed in Table 6.1. From this trial and error procedure, stiffness  $K_1$  and  $K_2$  are calculated to be  $4.4e^5 \frac{N}{m}$  ( $2512.5 \frac{lb}{in}$ ) and  $1.3e^6 \frac{N}{m}$  ( $7423.2 \frac{lb}{in}$ ), respectively. It should be noted that the significant difference between the stiffness of  $K_1$  and  $K_2$  can be attributed to different levels of tension being applied to the aluminum bolts of each lever arm. As there was no mention of using a calibrated torque wrench to tighten the bolts in the original research, it is assumed that all bolts were not tightened equally and thus introduced significantly different changes in stiffness.

Having calculated the stiffness of the linear springs, it is now possible to determine the rotational restraint being introduced at the supports. To do this, an analysis is conducted to calculate the moment diagrams for both damage conditions when a point force of 1000 N (225 lb) is applied at the midspan of the main structure. Figure 6.6a, b indicate the calculated moment diagram for Damage Conditions 1 and 2. Figure 6.6a indicates the restraining moment at Support A ( $M_A$ ) is  $-81.64N\cdot m$  ( $-722.6lb\cdot in$ ), while Fig. 6.6b indicates the restraining moments  $M_A$  and  $M_B$  are  $-68.53N\cdot m$  ( $-606.5lb\cdot in$ ) and  $-146.79N\cdot m$  ( $-1299.2lb\cdot in$ ), respectively. By knowing the magnitude of the restraining moment at the supports, an equivalent rotational spring stiffness ( $K_{rot}$ ) can be calculated via equation 6.2 above. For Damage Condition 1,  $\theta_A$  is calculated to be  $-.0544rad$ , meaning  $K_{rot,A}$  is equal to  $1500 \frac{N\cdot m}{rad}$  ( $1.33e^{-4} \frac{lb\cdot in}{rad}$ ). For Damage Condition 2,  $\theta_A$  and  $\theta_B$  are respectively calculated to be  $-.0457rad$  and  $.0402rad$ , meaning  $K_{rot,A}$  is  $1500 \frac{N\cdot m}{rad}$  ( $1.33e^{-4} \frac{lb\cdot in}{rad}$ ) and  $K_{rot,B}$  is  $3651.5 \frac{N\cdot m}{rad}$  ( $3.23e^{-4} \frac{lb\cdot in}{rad}$ ). Substituting these stiffness constants into a model of the simply-supported bridge free of any lever arms, the subsequent eigen-value analysis indicates that the resonant frequency of the system matches the values outlined in Table 6.1 for each damage condition. Thus, this process demonstrates that rotational springs can be employed in lieu of more complex modeling strategies to introduce changes in system frequency caused by rotational restraints at support conditions. Furthermore, when an analysis is performed to identify the relationship between change in frequency and the support-to-midspan moment ratio, the equivalent rotational spring stiffness can easily be determined; Fig. 6.7 demonstrates this procedure for Damage Condition 1. As can be seen, by identifying the support-to-midspan ratio that causes the frequency to change to 7.66 Hz, the equivalent spring stiffness can be found by virtue of the relationship between support-to-midspan ratio and the inverse of the equivalent spring stiffness.

The above example provides a good demonstration for how rotational springs can be employed in simulation to model changes in a bridge structure caused by rotational restraints at the supports, which is analogous to the case outlined in Fig. 6.1. However, this example does not provide a demonstration showing how axial forces affect the system as no axial effects were introduced by the lever arms. The next model validation study addresses this issue by analyzing the effects of axial forces introduced by frozen bearing damage in a full scale bridge system.

## 6.4 Full Scale Study

The following bridge is a 60 m (196.8 ft) long two-span continuous structure with simply-supported boundary conditions. The deck is composed of .179 m (7 in) thick reinforced concrete with a .064 m (2.5 in) bituminous (asphalt) overlay. The superstructure is composed of seven welded plate girders that are supported by rocker bearings at all the supports; the exterior rocker bearings allow for both longitudinal and rotational movement, while the central bearing only allows for rotational movement. The outermost girders are spaced at 1.93 m (6.33 ft) on center from the interior girders, while the interior girders are spaced at 2.06 m (6.75 ft) on center from each other. All seven girders are non-prismatic across the length of the structure, meaning their cross sections change at approximately the middle of each span. The sections of the bridge ranging from the exterior supports to the middle of each span make up one cross section (S1), while the interior section of the bridge ranging from midspan to midspan makes up another cross section (S2). Tables 6.3 and 6.4 indicate the material properties of the bridge components and the different cross sectional dimensions of the steel girders, respectively. From ambient vibration testing, the first three bending frequencies of the bridge were identified to be 3.6 Hz, 5.3 Hz, and 14.1 Hz [22, 23]. It should be noted that the temperature at the time of ambient testing was 4.4 °C (40 °F).

The bridge is modeled in simulation as a one dimensional FE model by taking the structure's cross section and transforming it into a square cross section of equivalent area and MoI. The area and MoI of the square cross section are calculated by transforming the asphalt and reinforced concrete layers into equivalent areas of steel. Because the girders have two different cross sectional properties, an equivalent area and MoI have to be calculated for each cross section. The area and MoI for S1 are respectively .6371 m<sup>2</sup> (987.5 in<sup>2</sup>) and .2001m<sup>4</sup> (48.09<sup>4</sup> in<sup>4</sup>), while the area and MoI for S2 are respectively .7613 m<sup>2</sup> (1180 in<sup>2</sup>) and .2894 m<sup>4</sup> (69.52<sup>4</sup> in<sup>4</sup>). The mass for each section is calculated using the density values outlined in Table 6.3 and the non-transformed sectional properties. Barrier mass is incorporated into the total mass of each section by approximating it to be equal to that of a typical New Jersey style Type B barrier (i.e. 507.5  $\frac{\text{kg}}{\text{m}}$  (341  $\frac{\text{lb}}{\text{ft}}$ )). The total mass for cross sections S1 and S2 are 10700  $\frac{\text{kg}}{\text{m}}$  (7190  $\frac{\text{lb}}{\text{ft}}$ ) and 11674  $\frac{\text{kg}}{\text{m}}$  (7845  $\frac{\text{lb}}{\text{ft}}$ ), respectively. Lastly, the FE model is discretized into 20 Euler-Bernoulli beam elements. The mesh size is chosen such that the properties for cross sections S1 and S2 can be easily applied to their respective regions across the length of the structure. Through an eigen-value analysis, the first three bending frequencies of the simulated bridge are identified to be 3.59 Hz, 5.65 Hz, and 14.54 Hz. These values compare well against the first three bending modes of the physical structure measured at 4.4°C (40°F), with the percent differences being .22%, 6.6%, and 3.1%, respectively.

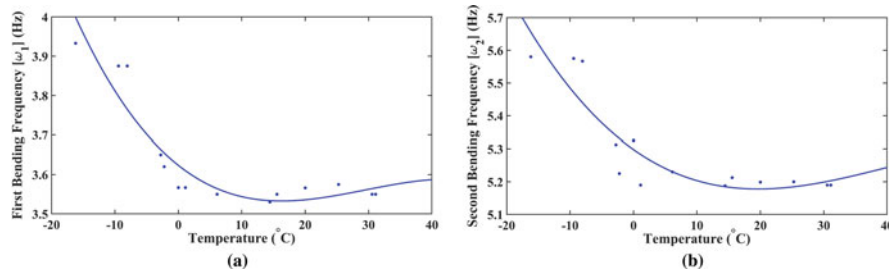
In the original study, researchers identified the subject structure's frequencies varied non-linearly with temperature; an example of the observed relationship for the first two bending frequencies can be seen in Fig. 6.8a, b, respectively [22, 23]. Through an analysis of the longitudinal displacements of the seven superstructure elements, the team concluded that the observed temperature-frequency trends were caused by freezing in the external bearings that resisted axial deformations caused by thermal expansion and contraction. The team was able to come to this conclusion by comparing the difference between the measured coefficient of thermal expansion,  $7.556e^{-6}/^{\circ}\text{C}$  ( $4.198e^{-6}/^{\circ}\text{F}$ ), and that of steel,  $1.17e^{-5}/^{\circ}\text{C}$  ( $6.50e^{-6}/^{\circ}\text{F}$ ). Because the measured coefficient was  $4.14e^{-6}/^{\circ}\text{C}$  ( $2.3e^{-6}/^{\circ}\text{F}$ ) less than the coefficient of the superstructure elements, it meant that the exterior supports were not displacing completely due to friction forces resisting movement [22, 23]. To model changes in frequencies as a function of temperature in simulation, the researchers modified the single-degree-of-freedom equation outlined in equation 6.4 to calculate axial forces as a function of temperature. Equation 6.8 indicates the new single-degree-of-freedom equation:

**Table 6.3** Material properties for components of full scale structure

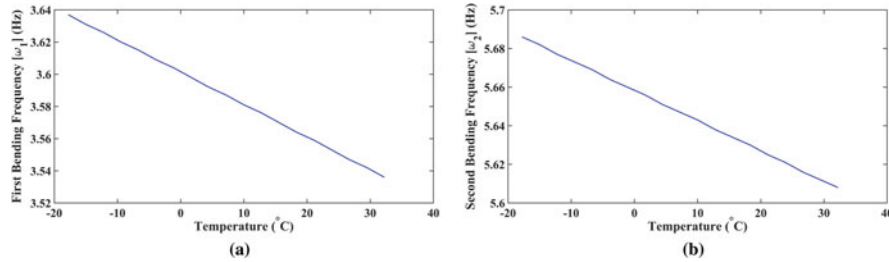
Material	Modulus of elasticity [E]	Density [ $\rho$ ]
	GPa (ksi)	$\frac{\text{kg}}{\text{m}^3}$ ( $\frac{\text{lb}}{\text{ft}^3}$ )
Asphalt overlay	13.79 (2000)	2243 (140)
Reinforced concrete	26.20 (3800)	2400 (150)
Steel	200 (29000)	7844.1 (490)

**Table 6.4** Steel girder dimensions for the two different cross sections

Elements	Section 1		Section 2	
	Height [H] mm (in)	Width [W] mm (in)	Height [H] mm (in)	Width [W] mm (in)
Flanges	25.4 (1)	508 (20)	42.86 (1.69)	508 (20)
Web	1320.8 (52)	9.53 (.375)	1320.8 (52)	9.53 (.375)



**Fig. 6.8** Demonstrates relationship between physical structural frequencies and temperature. (a) Relationship between first bending mode and temperature. (b) Relationship between second bending mode and temperature



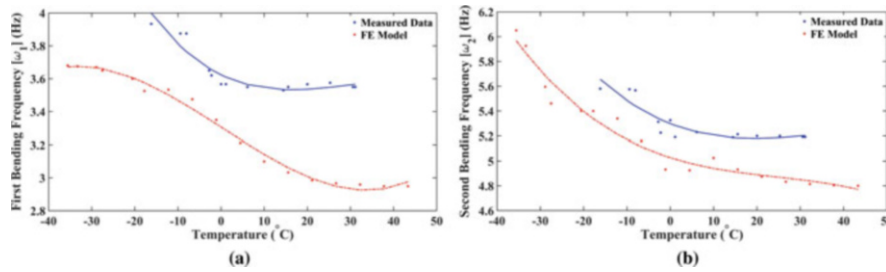
**Fig. 6.9** Demonstrates linear relationship between model frequencies and temperature. (a) Linear relationship between first bending mode and temperature. (b) Linear relationship between second bending mode and temperature

$$\omega_n = \frac{n}{L} \sqrt{\frac{n^2 \cdot \pi^2 \cdot E \cdot I}{L^2} + (\alpha \cdot E \cdot A \cdot \Delta T)}, \quad (6.8)$$

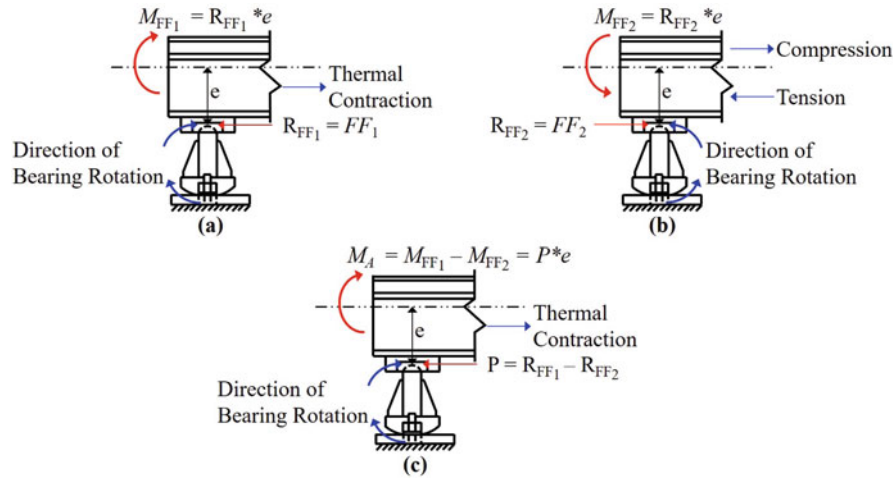
where  $\alpha$  is the net coefficient of thermal expansion,  $4.14e^{-6}/^{\circ}\text{C}$ ;  $A$  is the average cross sectional area of the transformed section,  $.6992 \text{ m}^2$  ( $1083.8 \text{ ft}^2$ ); and  $\Delta T$  is the change in temperature from  $4.4^{\circ}\text{C}$ , where the values are negative as temperature decreases and positive as temperature increases. It should be noted that the reference temperature,  $4.4^{\circ}\text{C}$ , is an arbitrary reference point and does not necessarily represent the temperature at which no axial forces are present, it is simply the temperature at which data acquisition originally commenced. As can be seen by Fig. 6.9a, b, the magnitude of frequency change calculated from equation 6.8 does not equal the magnitude of change observed on the physical structure. What's more, the frequency trends calculated by the simulation appear to be perfectly linear and do not match the apparent trends observed in Fig. 6.8a, b. The reason for the lack of trend correlation between the model and the physical structure can be attributed to the fact that the axial load calculated in equation 6.8 varies linearly with temperature, meaning the frequencies also vary linearly.

In an attempt to get their model frequencies to match the nonlinear relationship with temperature observed on the physical structure, Fu and DeWolf altered the MoI of the transformed girders about their moment inflection points [23]. In the negative moment regions, the deck was assumed to be under-reinforced and cracked due to tension forces, meaning only the MoI contribution from the steel girders was considered. In the positive moment regions, the deck was assumed to be intact, meaning the full composite MoI was considered. As the magnitude of the eccentric moments at the supports varied with temperature, so did the location of the inflection points and, therefore, MoI across the length of the structure. As can be seen by Fig. 6.10a, b, the results from the study demonstrate that this modeling approach does yield a nonlinear relationship between simulation frequencies and temperature that is comparable to the relationship observed on the physical structure. However, the results also demonstrate that this approach causes both frequencies to decrease too much at temperatures above  $4.4^{\circ}\text{C}$ , and increase too little at temperatures below  $4.4^{\circ}\text{C}$ . Additionally, the models nonlinear temperature-frequency relationship for the first bending mode tapers off as temperatures continue to decrease, which is not a trend that can be observed from the measured data [23].

An issue with the above mentioned modeling strategies is that friction forces resisting rotational displacements are not considered. Based on the design of the rocker bearing supports, the friction forces that resist axial deformations would also partially resist rotational displacements caused by the eccentric moments at the supports. An example of this phenomena can be observed in Fig. 6.11. Figure 6.11a provides an illustration for how the exterior rocker bearings resist axial deformation caused by thermal contraction. As can be seen, the moment resulting from the eccentric friction force introduces positive



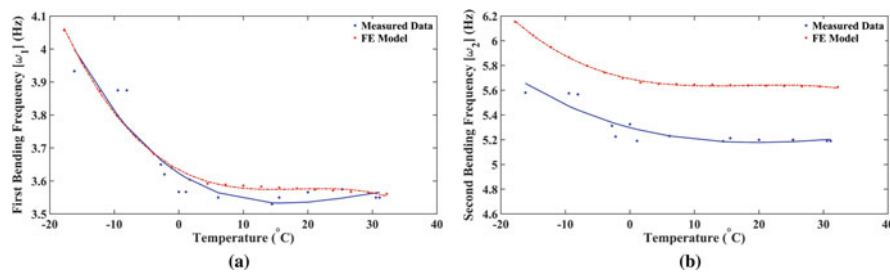
**Fig. 6.10** Demonstrates nonlinear relationship between frequencies and temperature from Fu and DeWolf’s FE model. (a) Nonlinear relationship between first bending mode and temperature. (b) Nonlinear relationship between second bending mode and temperature



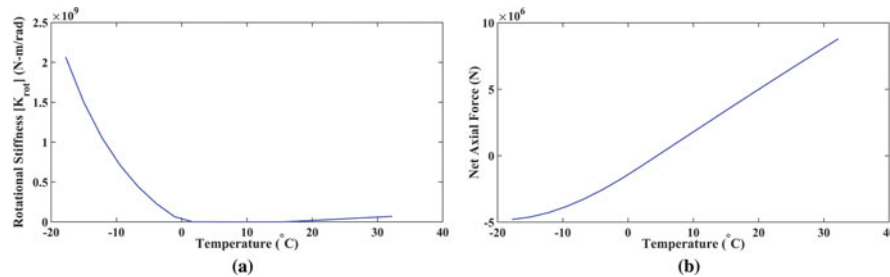
**Fig. 6.11** Example demonstrating how friction forces in the exterior rocker bearings of the full scale structure can resist both axial and rotational displacements. (a) Demonstrates how friction forces resist axial deformations caused by thermal contraction. (b) Demonstrates how friction forces resist rotational displacements caused by eccentric moments in (a). (c) Demonstrates how the forces and moments in Fig. 6.11a, b balance out in the system. As can be seen, the negative moment introduced in Fig. 6.11b partially counteracts the positive moment introduced in Fig. 6.11a; this is analogous to a partial fixity in the supports, and indicates that a rotational spring may be used in the simulation to model rotational restraining effects.

bending in the structure, causing the top cord to go into compression and the bottom cord to go into tension, meaning the top cord displaces inward while the bottom cord displaces outward. Figure 6.11b provides a demonstration for how friction in the bearings also resists the outward displacement of the bottom cord caused by the positive moment introduced in Fig. 6.11a. As can be seen, the friction force that resists the bottom cord displacement also introduces a negative eccentric moment at the support. Lastly, Fig. 6.11c provides a demonstration for how the forces and moments in Fig. 6.11a, b balance out in the system. As can be seen, the negative moment introduced in Fig. 6.11b partially counteracts the positive moment introduced in Fig. 6.11a; this is analogous to a partial fixity in the supports, and indicates that a rotational spring may be used in the simulation to model rotational restraining effects.

Based on the example outlined in Fig. 6.11, a final study is conducted to identify if employing rotational springs in addition to the geometric stiffness matrix helps better capture the behavior of the physical system in FE simulation. As strain data was not collected during the original research study, the spring stiffness can not be calculated by subtracting the measured moment at the support from the moment introduced by the eccentric axial force (e.g.  $M_{FF2} = M_A - M_{FF1}$ ). Because of this, an optimization routine is performed to determine the rotational spring stiffness required to cause the FE model frequencies to approximately match the measured frequencies measured on the physical structure. Figure 6.12a, b indicate the results from this study. As can be seen, by using rotational springs to introduce partial fixities at the supports, the FE model is now able to accurately capture not only the magnitude of change in the frequencies with temperature, but also the nonlinear relationship. It should be noted that the frequencies in Fig. 6.12b are higher than the frequencies observed on the physical structure in Fig. 6.8b due to the initial modeling error of 6.6%; however, this is not an issue as the magnitude of change across the temperature range is still the same (i.e. from the coldest temperature to the hottest, the second bending frequency changes in both the simulation and the physical structure by a magnitude of approximately 5 Hz). Figure 6.13a, b respectively indicate how the rotational spring stiffness and the net axial force change as a function of temperature in order to obtain the results observed in Fig. 6.12.



**Fig. 6.12** Demonstrates final nonlinear relationship between FE model frequencies and temperature caused by inclusion of rotational springs at the exterior supports. (a) Nonlinear relationship between first bending mode and temperature. (b) Nonlinear relationship between second bending mode and temperature



**Fig. 6.13** Demonstrates final nonlinear relationship between FE model frequencies and temperature caused by inclusion of rotational springs at the exterior supports. (a) Nonlinear relationship between first bending mode and temperature. (b) Nonlinear relationship between second bending mode and temperature

As can be seen by Fig. 6.13a, the rotational stiffness decreases as temperatures increase from  $-20^{\circ}\text{C}$  to  $4.4^{\circ}\text{C}$ , after which the stiffness appears to begin to increase again at a slower rate. It should be noted that the stiffness of the rotational spring was expected to change at the same rate on either side of the reference temperature as the measured coefficient of expansion on the physical structure does not change across the temperature range (i.e. the coefficient of friction resisting axial and rotational deformations must be the same across the subject temperature range). An explanation for this is that changes in the modulus of elasticity of the deck and superstructure materials are not considered during the analysis. Studies have shown that at lower temperatures, the modulus of elasticity of concrete and asphalt increases, thus requiring less rotational restraint at the supports to prevent the frequency from increasing to much, while at higher temperatures, the modulus of elasticity of concrete and asphalt decreases, thus requiring higher rotational restraint at the supports to prevent the frequency from decreasing to much. Whats more, concrete and asphalt temperature-modulus relationships have been observed to be nonlinear under certain conditions, which would help to further equalize the rate of stiffness change on both sides of the reference temperature [24–26]. It is believed that if temperature-modulus relationships were incorporated into the FE model, the rate of change in rotational stiffness would be equal on each side of the reference temperature. To implement this effect in simulation, detailed strain and temperature data taken directly from the structure are needed in order to match the magnitude of the internal moments, and correctly modify the modulus of concrete and asphalt; however, this approach is outside the scope of this project as no strain and direct temperature data were provided by the original research team.

The above example provides a good demonstration for how rotational springs and the geometric stiffness matrix can be employed in FE simulation to model changes in a physical bridge structure caused by frozen bearings. However, for this modeling strategy to be viable in terms of training neural networks for DBHM, the above methodology needs to be generalized so it can be applied towards healthy bridges to represent possible future damage states. For this to occur, rotational stiffness needs to be defined as a function of friction, and levels of damage need to be related back to the magnitude of the friction coefficient. The next section provides a brief discussion for relating rotational stiffness to the coefficient of friction.

## 6.5 Generalized Model

If frozen bearing damage is modeled for a bridge as friction resisting rotation in a pinned support, such as the case outlined in Fig. 6.1, the magnitude of rotational stiffness can be written as a function of friction by combing equations 6.1 and 6.2 as seen below:



$$K_{\text{rot}} = \frac{\mu_s \cdot R_{Ay} \cdot r_{\text{bearing}}}{\theta}. \quad (6.9)$$

Through equation 6.9, a generalized study can be conducted to identify the expected change in a subject structure's rotational stiffness at the support associated with a certain level of friction. Additionally, if the subject structure is simply-supported, the relationship between friction and stiffness can be employed along with the support-to-midspan ratio, like the one outlined in Fig. 6.7a, to identify the expected change in frequency associated with a level of friction damage. To conduct such a study, however, a benchmark structure is required in order to relate realistic magnitudes of friction to measured changes in frequency and rotational stiffness. As the full scale structure in this paper is not simply-supported, and the lab scale structure does not represent realistic friction effects at the support, a generalized benchmark study is out of the scope of this project and should be explored in future work.

If frozen bearing damage is modeled for a structure as friction resisting rotation in a rocker support, such as the case outlined in Fig. 6.2, the magnitude of the rotational stiffness can be written by replacing the  $r_{\text{bearing}}$  term in equation 6.9 with the eccentricity ( $e$ ) from the neutral axis; however, this assumes that the friction force resists all of the axial deformation, which will not hold true for most cases. To account for situations where axial deformations are not completely restrained, a relationship between  $\mu_s$  and displacement must also be determined. In equation 6.8 of Sect. 6.4, the axial force introduced by temperature is calculated using the equation below:

$$P = \alpha \cdot E \cdot A \cdot \Delta T, \quad (6.10)$$

meaning  $\mu$  can be rewritten as follows:

$$\mu_s = \frac{\alpha \cdot E \cdot A \cdot \Delta T}{R_y}. \quad (6.11)$$

Since  $\alpha$  is the difference between the coefficient of thermal expansion of the superstructure elements and the measured coefficient of thermal expansion, it can be represented by the equation below:

$$\alpha = \frac{\Delta L_{\text{exp-temp}} - \Delta L_{\text{meas-temp}}}{L \cdot \Delta T}, \quad (6.12)$$

where  $\Delta L_{\text{exp-temp}}$  is the expected displacement caused by thermal loads and  $\Delta L_{\text{meas-temp}}$  is the measured displacement caused by thermal loads. Using equation 6.12, equation 6.11 can be rewritten as seen below:

$$\mu_s = \frac{(\Delta L_{\text{exp-temp}} - \Delta L_{\text{meas-temp}}) \cdot E \cdot A}{R_y \cdot L}. \quad (6.13)$$

Having derived a relationship between  $\mu_s$  and temperature induced displacements, the eccentric moment caused by the temperature induced axial loads can be calculated as follows:

$$M_{\text{FFI}} = \mu_s \cdot R_y \cdot e = \frac{(\Delta L_{\text{exp-temp}} - \Delta L_{\text{meas-temp}}) \cdot E \cdot A \cdot e}{L}. \quad (6.14)$$

If the moment at the support is known, rotational stiffness at the support can now be calculated using the equation below:

$$K_{\text{rot}} = \frac{M_A - \frac{(\Delta L_{\text{exp-temp}} - \Delta L_{\text{meas-temp}}) \cdot E \cdot A \cdot e}{L}}{\theta}. \quad (6.15)$$

If the moment at the support is unknown, however, force balancing needs to be done to identify the net axial force introduced by the difference between the friction force and the axial force required to introduce an axial displacement equivalent to that caused by bending. Equations 6.16 and 6.17 indicate the formula for calculating the expected bending force, and  $K_{\text{rot}}$ , respectively:

$$P_{\text{axial-bend}} = \frac{(\Delta L_{\text{exp-bending}} - \Delta L_{\text{exp-meas}}) \cdot A \cdot E}{L}, \quad (6.16)$$

$$K_{\text{rot}} = \frac{P_{\text{axial-bend}} \cdot e}{\theta}, \quad (6.17)$$

where  $\Delta L_{\text{exp-bending}}$  is the expected axial displacement caused by the bending loads,  $\Delta L_{\text{exp-meas}}$  is the measured or allowed axial displacement caused by bending loads, and  $P_{\text{axial-bend}}$  is the equivalent axial force required to cause expected axial displacement. Variable  $\Delta L_{\text{exp-bending}}$  is solved for by solving the differential moment/curvature relationship for the full scale structure, while  $\Delta L_{\text{exp-meas}}$  is measured from a subject structure or is set as an assumed value. A  $\Delta L_{\text{exp-meas}}$  of zero indicates a subject support is completely fixed against movement, while  $\Delta L_{\text{exp-meas}}$  equal to  $\Delta L_{\text{exp-bending}}$  indicates a completely unrestrained support. As the differential moment/curvature relationship would need to be derived for the subject structure, which is out of the scope of this work, a comparison will not be done to demonstrate how  $K_{\text{rot}}$  changes as a function of friction. The above equations demonstrate that rotational stiffness can be represented as a function of friction for a full scale bridge structure; thus, magnitudes of friction can now be used to define generalized frozen bearing damage classes for training NNs for DBHM.

## 6.6 Conclusion

The goal of this study was to identify and validate physics based approaches for modeling frozen bearing damage in bridge structures for the purpose of validating a new drive-by health monitoring approach. In this study, frozen bearing damage was represented by employing rotational springs at a supports rotational degree-of-freedom to introduce a restraint caused by friction. For situations where axial forces were also introduced at the supports due to freezing effects, a geometric stiffness matrix was incorporated into the bridge equation of motion in addition to the rotational springs at a support's rotational degree-of-freedom. The purpose of the geometric stiffness matrix was to introduce an increase or decrease in stiffness and buckling capacity caused by tension or compression forces, respectively. To validate the aforementioned modeling approaches, both a lab scale and full scale validation study were conducted. In the lab scale study, lever arms were attached at the supports of an aluminum bridge to simulate two different damage cases, in one case freezing was present at only one support and in the other case freezing was present at both supports. From the lab scale study, it was demonstrated that rotational springs could be effectively employed to capture the change in both the subject structure's frequency and bending capacity. In the full scale study, a continuous bridge was subjected to axial restraints at its exterior supports due to the development of friction in the rocker bearings. From the study, it was demonstrated that both rotational springs and the geometric stiffness matrix could successfully be employed in simulation to represent realistic variations in bridge frequency; however, the study also showed that temperature effects on asphalt and concrete material properties needs to be included in future studies. Having validated that rotational springs and the geometric stiffness matrix can be used to successfully model freezing effects in simplified models, the methodology was generalized by deriving a mathematical relationship between rotational stiffness and friction. Through this process, frozen bearing damage classes can now be defined as a function of the magnitude of friction present in the system. By being able to classify damage based on the magnitude of friction, NN models can be trained on simulation data to identify changes in a system associated with various levels of freezing. Once a sufficient amount of training has been performed, the goal is to then employ the NN to detect physical damage and its severity.

Moving forward, additional studies should be conducted to evaluate physics based methods for modeling other common types of damage, such as open and breathing cracks. Additionally, a benchmark study needs to be conducted to identify realistic magnitudes of friction that can exist in physical bridge structures and the severity of change in the system's static and dynamic properties. As mentioned, future studies should also consider incorporating temperature effects on the material properties of concrete and asphalt. Lastly, a study needs to be conducted that demonstrates the effectiveness of employing simulation trained NNs to detect damage on physical bridge systems.

**Acknowledgments** The authors gratefully acknowledge the support of the National Science Foundation under grant #1633608.

## References

1. Yang, Y., Lin, C., Yau, J.: Extracting bridge frequencies from the dynamic response of a passing vehicle. *J. Sound Vib.* **272**, 471–493 (2004)
2. Lin, C., Yang, Y.: Use of a passing vehicle to scan the fundamental bridge frequencies: an experimental verification. *Eng. Struct.* **27**, 1865–1878 (2005)

3. Hearn, G., Puckett, J., Friedland, I., Everett, T., Hurst, K., Romack, G., Christian, G., Shepard, R., Thompson, T., Young, R.: Bridge preservation and maintenance in Europe and South Africa, Technical Report (2005)
4. Everett, T.D., Weykamp, P., Capers Jr, H.A., Cox, W.R., Drda, T.S., Hummel, L., Jensen, P., Juntunen, D.A., Kimball, T., Washer, G.A.: Bridge evaluation quality assurance in Europe, Technical Report (2008)
5. FHWA, F.H.A.: National bridge inspection standards (NBIS). Fed. Regist. **69**, 74438 (2009)
6. Moore, M., Phares, B.M., Graybeal, B., Rolander, D., Washer, G., Wiss, J., et al.: Reliability of visual inspection for highway bridges, volume I, Technical Report, Turner-Fairbank Highway Research Center (2001)
7. Phares, B.M., Washer, G.A., Rolander, D.D., Graybeal, B.A., Moore, M.: Routine highway bridge inspection condition documentation accuracy and reliability. *J. Bridg. Eng.* **9**, 403–413 (2004)
8. Farrar, C.R., Worden, K.: An introduction to structural health monitoring. In: *New Trends in Vibration Based Structural Health Monitoring*, pp. 1–17. Springer, Vienna (2010)
9. Agdas, D., Rice, J.A., Martinez, J.R., Lasa, I.R.: Comparison of visual inspection and structural-health monitoring as bridge condition assessment methods. *J. Perform. Constr. Facil.* **30**, 04015049 (2015)
10. Lynch, J.P., Loh, K.J.: A summary review of wireless sensors and sensor networks for structural health monitoring. *Shock Vib. Dig.* **38**, 91–130 (2006)
11. Lynch, J.: *Smart bridges: expert q/a*, NOVA (2008)
12. Yang, Y., Yang, J.P.: State-of-the-art review on modal identification and damage detection of bridges by moving test vehicles. *Int. J. Struct. Stab. Dyn.* **18**, 1850025 (2018)
13. Farrar, C.R., Worden, K.: *Structural Health Monitoring: A Machine Learning Perspective*. Wiley, Chichester (2012)
14. Smarsly, K., Dragos, K., Wiggenbrock, J.: Machine learning techniques for structural health monitoring. In: *Proceedings of the 8th European Workshop on Structural Health Monitoring (EWSHM 2016)*, Bilbao, pp. 5–8
15. AASHTO: *Manual for bridge element inspection 2* (2019)
16. Bakht, B., Jaeger, L.G.: Bearing restraint in slab-on-girder bridges. *J. Struct. Eng.* **114**, 2724–2740 (1988)
17. Jacobsen, F.: *Investigation of Bridge Approach Spans to Poplar Street Bridge*, Technical Report (1975)
18. Chajes, M.J., Mertz, D.R., Commander, B.: Experimental load rating of a posted bridge. *J. Bridg. Eng.* **2**, 1–10 (1997)
19. Gerstle, K.H., Ackroyd, M.H.: Behavior and design of flexibly-connected building frames. *Eng. J.* **27**, 22–29 (1990)
20. Clough, R.W., Penzien, J.: *Dynamics of Structures*, 2nd edn, p. 738. McGraw-Hill, New York (1993). isbn:0-07-011394-7
21. Cerda, F., Chen, S., Bielak, J., Garrett, J.H., Rizzo, P., Kovacevic, J.: Indirect structural health monitoring of a simplified laboratory-scale bridge model. *Smart Struct. Syst.* **13**, 849–868 (2014)
22. Con, P.: *Monitoring the vibrations of a continuous structure*, Ph.D. thesis, University of Connecticut (1996)
23. Fu, Y.: *Analytical evaluation of experimental bridge vibration behavior*, Ph.D. thesis, University of Connecticut (1996)
24. Peeters, B., Maeck, J., De Roeck, G.: Vibration-based damage detection in civil engineering: excitation sources and temperature effects. *Smart Mater. Struct.* **10**, 518 (2001)
25. Xia, Y., Hao, H., Zanardo, G., Deeks, A.: Long term vibration monitoring of an RC slab: temperature and humidity effect. *Eng. Struct.* **28**, 441–452 (2006)
26. Moser, P., Moaveni, B.: Environmental effects on the identified natural frequencies of the dowling hall footbridge. *Mech. Syst. Signal Process.* **25**, 2336–2357 (2011)

**Robert Locke** is a doctoral student in the department of Structural Engineering at Clemson University. His primary research focuses on resilient interconnected infrastructure systems, where he focuses on developing a new approach to drive-by health monitoring that employs simulation trained techniques to detect physical bridge damage.

**Dr. Laura Redmond** is an assistant professor of Civil Engineering at Clemson University. Her research focuses on creating new, test-validated models to analyze complex material and structural behavior that enable the design and structural health monitoring of civil, mechanical, and aerospace structures.

**Dr. Sez Atamturktur** is the Harry and Arlene Schell Professor and Department Head of Architectural Engineering at The Pennsylvania State University. Dr. Atamturktur's research focuses on uncertainty quantification in scientific computing as applied to the analysis and design of engineering systems. Her work has been supported by numerous federal agencies and documented in over 100 peer-reviewed publications in some of the finest engineering science journals and proceedings.

# Chapter 7

## The Minimum Detectable Damage as an Optimization Criterion for Performance-Based Sensor Placement



Alexander Mendler, Michael Döhler, Carlos E. Ventura, and Laurent Mevel

**Abstract** Selecting the right sensor locations is pivotal for the effectiveness of vibration-based damage detection as part of structural monitoring under unknown excitation. Traditional optimization criteria aim to increase the signal-to-noise ratio and information content carried by ambient vibrations, or to identify modal parameters with minimal uncertainty and optimal mode distinguish ability. None of the existing criteria appear to consider a relative decrease in material strength, although this is the decisive quantity for structural design, structural health, and thus safety. This paper fills this gap for stochastic subspace-based damage diagnosis methods. It introduces an optimization criterion that ensures that a minimum damage extent can be detected in each structural component while maintaining a probability of detection that meets the national design standards. The presented strategy helps to find an acceptable number of sensors as well as their optimal layout. Further advantages are that the optimization can be done based on the simulated vibration data from the healthy structure and that the criterion can be tuned so the resulting sensor layout becomes more sensitive to damage hotspots.

**Keywords** Output-only · Stochastic subspace-based damage detection · Minimum measurement duration · Fisher information

### 7.1 Introduction

There is an increasing demand for developing damage detection and localization methods for structural components of safety-critical infrastructure, e.g. lifeline bridges in areas of high seismic hazards [1]. An important part of the efficiency of the damage diagnosis is the sensor placement strategy. Optimal sensor placement has been subject to extensive research in both the engineering and the automatic control community, see [2, 3] and [4]. Recent literature reviews conclude that the existing optimization criteria suffice to pre-condition the signal with respect to the signal-noise ratio and the quality and uncertainty of the modal identification, but also outline that there is a demand for new, method-specific performance criteria that directly target the detectability of damage [5]. This paper proposes the *measurement duration*  $T$  [s] as a performance criterion for damage detectability and is written for *stochastic subspace-based damaged detection (SSDD)* [6–8]. It continues the line of work of previous authors [9, 10] that employed the Fisher information as a measure for the information content of ambient vibrations with respect to characteristic system parameters. This is equivalent to increasing the probability of detection and decreasing the false-alarms. It combines the approach with a formula for the minimum detectable damage, see [11], which is used to interpret the Fisher information as a minimum measurement duration that is necessary to achieve a desired probability of detection. This paper is organized as follows: Sect. 7.2 recaps how a damage-sensitive criterion can be formed in the subspace of covariance functions, Sect. 7.3 derives the formula for the minimum measurement duration and Sects. 7.4 and 7.5 optimize the sensor placement on a pin-supported beam and discuss the results.

---

A. Mendler (✉) · C. E. Ventura  
University of British Columbia, Vancouver, BC, Canada  
e-mail: [alexander.mendler@ubc.ca](mailto:alexander.mendler@ubc.ca); [ventura@civil.ubc.ca](mailto:ventura@civil.ubc.ca)

M. Döhler · L. Mevel  
Inria, Ifsttar COSYS/SII, University Rennes, Rennes, France  
e-mail: [michael.doehler@inria.fr](mailto:michael.doehler@inria.fr); [laurent.mevel@inria.fr](mailto:laurent.mevel@inria.fr)

## 7.2 Background

### 7.2.1 Stochastic System Model

Let the vibration signal be a realization of a linear and time-invariant (LTI) dynamic system with  $m$  degrees of freedom

$$\mathcal{M}\ddot{z}(t) + C\dot{z}(t) + \mathcal{K}z(t) = v(t) \quad \text{where } \mathcal{K} = f(E_1, \dots, E_H) \quad (7.1)$$

where  $z(t)$  is the displacement under random disturbances  $v(t)$  in continuous-time and  $\mathcal{M}$ ,  $C$  and  $\mathcal{K} \in \mathbb{R}^{m \times m}$  are the mass, damping and stiffness matrices. This paper assumes that structural damage is limited to changes in the stiffness matrix, which are a function of the stiffness of each structural component, i.e. the modulus of elasticity  $E_h$  [MPa] for  $h \in [1, \dots, H]$ .

### 7.2.2 Subspace-Based Residual

The residual is formed based on measurement data in discrete-time, i.e. displacement, velocity, or acceleration data at some of the degrees of freedom of Eq. (7.1). For each time instant  $k$ , the data is stored in the measurement vector  $y_k \in \mathbb{R}^r$  where  $r$  is the number of sensors. To analyze the similarity of the wave pattern at different time instances and sensor locations, the output covariances  $R_i = E(y_{k+i}y_k^T)$  are estimated through  $\hat{R}_i = \frac{1}{N-i} \sum_{k=1}^{N-i} y_{k+i}y_k^T$  where  $i$  is the time lag. Output covariances can be interpreted as impulse response functions that model the system output under random excitation for  $i \geq 1$ , see [12, 13]. To capture the (hidden) vibration model of the dynamic system, the covariances are arranged in an (output) block Hankel matrix.

$$\hat{\mathcal{H}}_{p+1,q} = \begin{bmatrix} \hat{R}_1 & \hat{R}_1 & \dots & \hat{R}_q \\ \hat{R}_2 & \hat{R}_1 & \dots & \hat{R}_{q+1} \\ \vdots & \vdots & \ddots & \vdots \\ \hat{R}_{p+1} & \hat{R}_{p+2} & \dots & \hat{R}_{p+q} \end{bmatrix} = [\hat{S}_1 \ \hat{S}_0] \begin{bmatrix} \hat{V}_1 & 0 \\ 0 & \hat{V}_0 \end{bmatrix} \begin{bmatrix} \hat{D}_1^T \\ \hat{D}_0^T \end{bmatrix} \quad (7.2)$$

The time lag parameters  $p$  and  $q$  are set large enough so all modes (in particular low-vibration modes) are observable with  $qr > 2m$  and typically  $p+1 = q$ . Since the modes of vibration merely have to be observable but not identifiable, considerably shorter time lags are required for damage detection in comparison to modal identification. Applying a singular value decomposition (SVD) to the block Hankel matrix leads to several desirable effects. Firstly, more dominant trends, such as structural vibrations are stored in the upper part  $\hat{S}_1\hat{V}_1\hat{D}_1^T$  and the lower part models noise, so  $\hat{V}_0 \approx 0$ . Secondly, the singular vectors are orthogonal to one another and multiplying orthogonal vectors yields zero. That means that pre-multiplying the left null space (i.e. the vector space  $\hat{S}_0$  corresponding to the singular values in  $\hat{V}_0$ ) of the block Hankel matrix in the reference state eliminates all information related to structural vibrations in the reference state

$$\varepsilon^0 = \text{vec}(\hat{S}_0^T \hat{\mathcal{H}}_{p+1,q}^0) \approx 0. \quad (7.3)$$

This approximation becomes exact if the measurement is sufficiently long ( $N \rightarrow \infty$ ) because then the estimated covariances approximate the theoretical one  $\hat{R}_i \rightarrow R_i$  and so do the block Hankel matrix  $\hat{\mathcal{H}}_{p+1,q} \rightarrow \mathcal{H}$  and the null space  $\hat{S}_0 \rightarrow S_0$ . Using the central limit theorem, a Gaussian residual vector can be formulated with respect to the sample size  $N$  [6],

$$\hat{\zeta} = \sqrt{N}\varepsilon^0 \sim \begin{cases} \mathcal{N}(0, \Sigma) & (\text{healthy}) \\ \mathcal{N}(\mu, \Sigma) & (\text{damaged}) \end{cases} \quad (7.4)$$

In other words, the residual vector  $\hat{\zeta}$  follows a Gaussian distribution with a mean value of zero and the covariance  $\Sigma$  if both matrices  $\hat{S}_0$  and  $\hat{\mathcal{H}}_{p+1,q}$  are calculated based on the same healthy structure. Damage, on the other hand, manifests itself in a deviation from the zero mean condition by  $\mu$ .

### 7.2.3 Link to Finite Element Model

Let the structural system be characterized by  $H$  health parameters. These parameters could, for example, be the stiffness and mass values of different structural components, which can be taken from an equivalent finite element (FE) model and have a direct relation to the system matrices  $\mathcal{M}$  or  $\mathcal{K}$  from Eq. (7.1). Since damage is assumed to exclusively affect the stiffness parameters, i.e. the material's modulus of elasticity, the structure can be characterized through the parameter vector

$$\theta = [E_1 \cdots E_H]^T, \quad (7.5)$$

where  $\theta \in \mathbb{R}^H$ . The superscript "0" indicates that the parameter vector is in its reference state. The Gaussian residual from Eq. (7.4) is purely data-driven and statistical in nature, but its mean value vector can be linked to the physical parameters change in Eq. (7.5). This process is called parametrization. The deviation in the mean residual is replaced by  $\mu = \mathcal{J}\delta$ , where  $\delta$  is the statistical change vector and  $\mathcal{J} = \frac{\partial}{\partial \theta^0} E(\varepsilon^0)$  is the sensitivity (or Jacobian) matrix of the mean residual with respect to the chosen parametrization. The statistical change vector is a central element, as it transforms the change detection problem from the statistical domain (and monitoring the mean residual) into the physical domain of monitoring structural parameters, where [6]

$$\delta = \sqrt{N}(\theta - \theta^0). \quad (7.6)$$

In our case, the physical problem is to detect a decrease in the material stiffness  $E$ , which can be linked to a change in the mean residual through three consecutively performed first-order sensitivity analyses combined through the chain rule

$$\mathcal{J} = \mathcal{J}(\varepsilon^0, \theta_d^0) \cdot \mathcal{J}(\theta_d^0, \theta_c^0) \cdot \mathcal{J}(\theta_c^0, \theta^0). \quad (7.7)$$

The first term links the mean residual to the modal parameters in discrete-time in  $\theta_d^0$ , the second term links the modal parameter in discrete-time to the modal parameters of the FE model in continuous-time in  $\theta_c^0$ , and the third one links the modal parameters of the FE model to its structural parameters in  $\theta$ . More information on this can be found in the literature, see [7, 14, 15].

## 7.3 Method

### 7.3.1 Minimum Detectable Damage

To discriminate the healthy state from the damaged state, the residual vector has to be tested in regard to whether it is more likely to be the realization of the damaged rather than the healthy structure, see Eq. (7.4). This can be done through statistical hypothesis tests, e.g. the general likelihood ratio (GLR), see [16], where the null hypothesis  $\theta = \theta^0$  is tested against the alternate hypothesis  $\theta = \theta^0 + \delta/\sqrt{N}$  from Eq. (7.6). In the referenced literature, see [7], it is shown that the GLR unfolds to

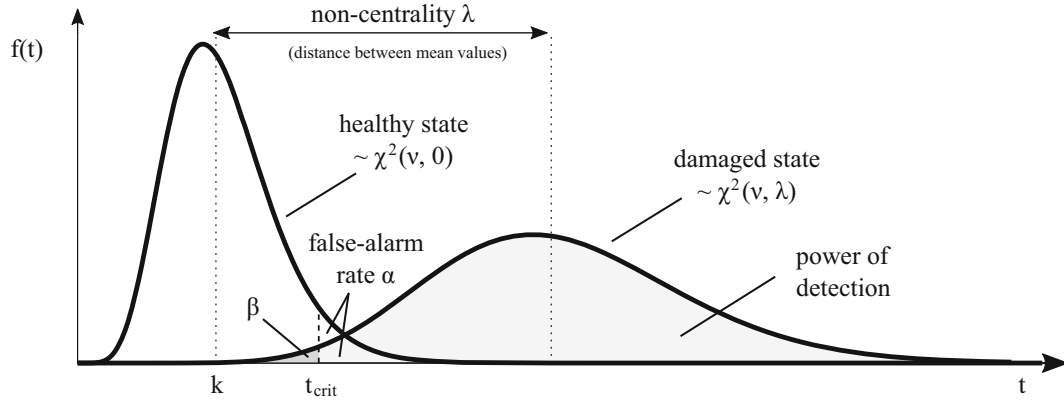
$$t = \hat{\xi}^T \Sigma^{-1} \mathcal{J} \left( \mathcal{J}^T \Sigma^{-1} \mathcal{J} \right)^{-1} \mathcal{J}^T \Sigma^{-1} \hat{\xi} \sim \begin{cases} \chi^2(\nu, 0) & (\text{healthy}) \\ \chi^2(\nu, \lambda) & (\text{damaged}) \end{cases} \quad (7.8)$$

Since the residual with well-defined Gaussian properties is squared up, the test statistic follows a  $\chi^2$ -distribution with  $\nu$  degrees of freedom and non-centrality  $\lambda = \delta^T F \delta$ , [7], where  $F \in \mathbb{R}^{H \times H}$  is the Fisher information matrix

$$F = \mathcal{J}^T \Sigma^{-1} \mathcal{J}. \quad (7.9)$$

The number of degrees of freedom  $\nu$  of the  $\chi^2$ -distribution is—in the simplest case—equal to the number of structural parameters  $H$ . This is only true if the Jacobian matrix is of full rank, which is assumed in this paper. Otherwise, it is given by

$$\nu = \text{rank}(F). \quad (7.10)$$



**Fig. 7.1** Statistical distribution of the test statistic from Eq. (7.8) in the healthy and damaged state, with reference to Eq. (7.13)

The non-centrality is the distance between the healthy and damaged state probability density function (PDF) with  $\lambda = 0$  and  $\lambda > 0$ , respectively, see Fig. 7.1. To ensure a sufficient degree of separation between the states, the desired non-centrality can be characterized by a minimum value for any parameter  $h$ ,

$$\lambda_h = F_{hh} \delta_h^2 \geq \lambda_{min} = const. \quad (7.11)$$

This is equivalent to prescribing a minimum probability of detection (POD) in each of the  $H$  health parameters, see Fig. 7.1. The non-centrality  $\lambda_{min}$  could, for instance, be calculated based on the maximum allowable false-alarm rate  $\alpha$  and false-positive rate  $\beta$  because both PDFs are mathematically well-defined, see Fig. 7.1. More on this follows in the subsequent section. Solving Eq. (7.11) for  $\delta_h$  and plugging it into Eq. (7.6) results in a formula for the minimum parameter change that can be detected reliably, [11].

$$\theta_h - \theta_h^0 \approx \sqrt{\frac{\lambda_{min}}{N \cdot F_{hh}}} \quad (7.12)$$

### 7.3.2 Minimum Reliability

The  $\chi^2$ -distribution in Fig. 7.1 is a function of two variables, i.e. the number of degrees of freedom  $\nu$  and the non-centrality  $\lambda$ , which is zero in the healthy state. The probability density functions (PDF) are defined as

$$f_{\chi^2(\nu,0)}(t) = \frac{1}{2^{\nu/2} \Gamma(\nu/2)} x^{\nu/2-1} e^{-t/2} \text{ (healthy)}, \quad f_{\chi^2(\nu,\lambda)}(t) = \sum_{n=0}^{\infty} e^{-\frac{\lambda}{2}} \frac{(\lambda/2)^n}{n!} f_{\chi^2(\nu+2n,0)}(t) \text{ (damaged)} \quad (7.13)$$

where  $\Gamma(\gamma)$  is the Gamma function, satisfying  $\Gamma(\gamma) = (\gamma - 1)!$  for integer values of  $\gamma$ . The healthy state is uniquely defined with  $\lambda = 0$ , because the number of degrees of freedom  $\nu$  is a known constant that depends on the monitoring application, see Eq. (7.10). The minimum non-centrality  $\lambda_{min}$  is a user-defined value and, as explained in this section, can be set by requiring a minimum reliability regarding the damage diagnosis result.

The false-alarm rate  $\alpha$  is the probability that a false-alarm occurs, i.e. it quantifies how often the test diagnoses a healthy structure as damaged. Based on the acceptable false-alarm rate, a safety threshold value can be defined that discriminates the damaged from the healthy structure, see  $t_{crit}$  in Fig. 7.1. Our recommendation for civil engineering structures is to set the safety threshold corresponding to a false-alarm rate of  $\alpha \in [0.3\%, 5\%]$  or lower. In that case, one out of 20 - 333 tests diagnoses a healthy structure as damaged.

$$\alpha = 1 - \int_0^{t_{crit}} f_{\chi^2(\nu,0)}(t) dt \quad (7.14)$$

The false-positive rate  $\beta$  quantifies how often the test diagnoses the structure as healthy although damage is present, see Fig. 7.1. The consequences of setting the false-positive rate  $\beta$  too high can be fatal, as small damage to key components may cause the collapse of the structure and put human lives at risk. In other words, the false-positive rate is adjusted with respect to the damage consequences and the acceptable level of risk. For load-bearing components, we recommend choosing this value according to the national safety concept. In Canada and the U.S.A., the reliability index for assessment is prescribed as 3.25 and 2.5, which is equivalent to a false-negative rate of  $\beta = 0.06\%$  and  $\beta = 0.6\%$ , respectively. The Eurocode does not define a reliability index for assessment, but the ISO norm requires a reliability index of 4.7, so  $\beta = 10^{-6}$  [17].

$$\beta = \int_0^{t_{crit}} f_{\chi^2(v,\lambda)}(t) dt \quad (7.15)$$

The minimum non-centrality can be determined by sliding the theoretical distribution for the damaged state to the right until the  $\beta$ -th quantile aligns with the safety threshold that was fixed based on Eq. (7.14). The only unknown parameter in the curve-fitting process is the minimum non-centrality  $\lambda_{min}$  which can be solved for through numerical iteration, cf. Eq. (7.13) and Fig. 7.1. The non-centrality is the distance between the mean values, and the mean value of the healthy state PDF is  $\nu$ .

$$\lambda_{min} = \mu(f_{\chi^2(v,\lambda)}) - \nu \quad (7.16)$$

### 7.3.3 Minimum Measurement Duration

The basic formula from Eq. (7.12) can be rearranged and solved for the measurement duration  $T = N/f_s$ . Moreover, the parameter change can be normalized through the reference parameter to obtain an expression for a relative parameter change  $\Delta_h = (\theta_h^0 - \theta_h)/\theta_h^0$ . The resulting equation estimates the minimum measurement duration required to diagnose the user-defined (relative) damage level, e.g.  $\Delta_h = 5\%$ , in each stiffness parameter.

$$T_h(c) \approx \frac{\lambda_{min}}{f_s F_{hh}} \left( \frac{1}{\Delta_h \theta_h^0} \right)^2 \text{ [s]} \quad (7.17)$$

If the sampling frequency  $f_s$  and the minimum non-centrality  $\lambda_{min}$  are fixed, the measurement duration depends on the magnitude of the health parameter in the healthy state  $\theta_h^0$ , the desired minimum detectable damage  $\Delta_h$ , and the main diagonal of the Fisher information  $F_{hh}$ , which depends on the sensor configuration  $c$ . To indicate this dependency, the bracket term is added to the measurement duration  $T_h(c)$ . If the desired damage extent is to be detected in each parameter, the decisive parameter is the one with the longest measurement duration. In this sense, the performance criterion for sensor placement optimization writes

$$T_{max}(c) = \max_h \{T_1, \dots, T_H\}. \quad (7.18)$$

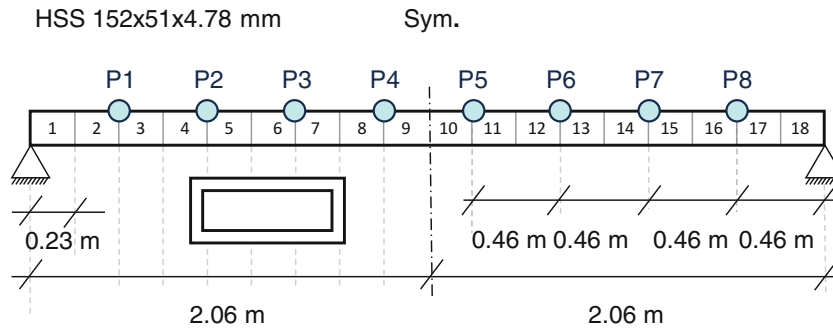
The higher the Fisher information, the higher the sensitivity towards small damages, see Eq. (7.9), and the shorter the maximum measurement duration. The optimization goal for sensor placement is, therefore, to find the sensor layout that minimizes the maximum measurement duration.

$$\min_c f = T_{max}(c) \quad (7.19)$$

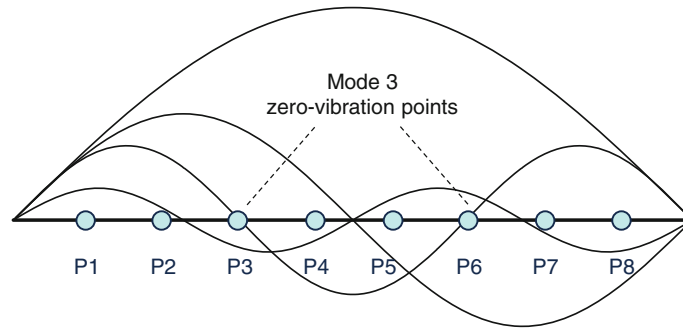
## 7.4 Numerical Application

For proof of concept, the sensor placement strategy is applied to a pin-supported beam discretized into 18 elements and nine materials. The overall goal is to find an acceptable number of sensors as well as the optimal sensor placement that allows for detecting a  $\Delta = 5\%$  stiffness decrease in any material. The minimum reliability is defined through the false-alarm rate of  $\alpha = 5\%$  and the false-positive rate of  $\beta = 0.6\%$ .





**Fig. 7.2** Pin-supported hollow structural steel (HSS) beam with possible sensor locations P1-P8



**Fig. 7.3** Zero-vibration points among the sensor locations P1-P8

#### 7.4.1 Pin-Supported HSS Beam

The structure under consideration is a 4.11 m-long pin-supported beam with a hollow structural steel section, HSS  $152 \times 51 \times 4.78$  mm. The 3-D beam model is divided into 18 finite beam elements with a length of 22.8 cm, see Fig. 7.2, where two consecutive elements are assigned to the same material (or health parameter) with a modulus of elasticity of  $E_h = 200,000$  MPa and  $h \in [1, \dots, 9]$ . The first four vertical modes of vibration are used to screen the beam for structural damage with natural frequencies of 8.97, 35.8, 80.3, and 142 Hz, a modal damping ratio of 1% critical damping, and the mode shapes visualized in Fig. 7.3. The system input is modeled as white noise and applied to all 104 degrees of freedom. To simulate measurement noise, uniformly distributed noise was added to the output with a magnitude corresponding to 5% of the output variance.

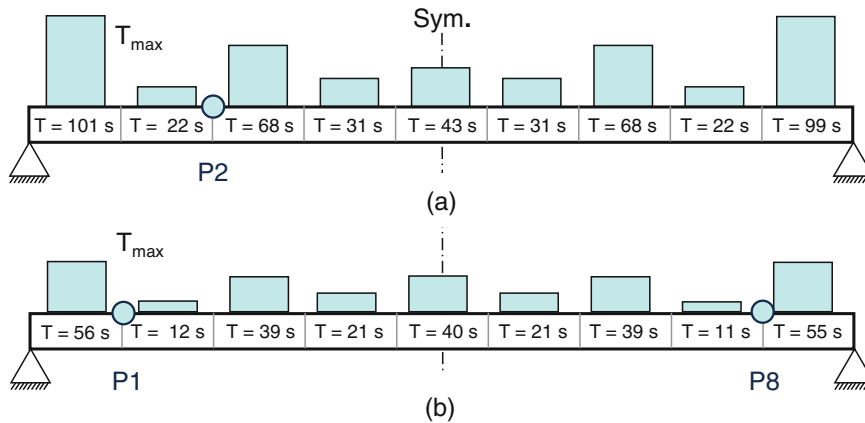
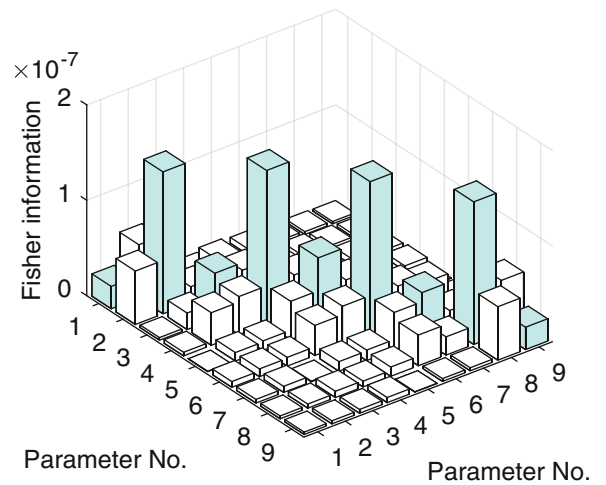
The required input for the sensor placement optimization is the vibration data from the healthy structure at all possible locations. Hence, one transient analysis is run while recording the velocity in the vertical direction at eight selected locations, see Fig. 7.2. The measurement time for the simulation is set to 60 min and the sampling frequency for the simulation is set to 1024 Hz and subsequently downsampled at 360 Hz. The resulting measurement matrix  $Y(\theta_0)$ , which is handed over to the sensor placement optimization algorithm, contains  $r$  columns and  $N$  rows where  $r$  and  $N$  are the number of sensors and samples, respectively.

$$Y(\theta_0) = \begin{bmatrix} y_{1,1} & y_{1,2} & \cdots & y_{1,r} \\ \vdots & \vdots & \ddots & \vdots \\ y_{N,1} & y_{N,2} & \cdots & y_{N,r} \end{bmatrix} \quad (7.20)$$

### 7.4.2 Measurement Duration for a Fixed Sensor Configuration

In this section, it is explained how the minimum measurement duration can be calculated for a fixed sensor configuration, for example, a single sensor at location P2. First, all input parameters are determined to calculate the performance criterion for the sensor placement, see Eq. (7.17). The minimum reliability requirements translate into a minimum non-centrality of  $\lambda = 33.7$ , which corresponds to the minimum distance between the mean of the healthy and damaged stated PDF, see Fig. 7.1. The re-sampling frequency  $f_s$  is fixed sufficiently high to capture all modes of vibration, so  $f_s = 360$  Hz, and the structural parameter to be monitored is the modulus of elasticity between each sensor, so  $\theta_h = 200,000$  MPa with  $h \in [1, \dots, 9]$ . The last input quantity is the Fisher information, which describes the sensitivity of the Gaussian residual towards changes in the structural parameters, scaled by the residual's (co-)variance. It is the only quantity that is estimated based on vibration data, see Fig. 7.4 as well as Eqs. (7.7) and (7.9). The main diagonal of the Fisher information (highlighted in blue colour) can be interpreted as a minimum measurement duration in each parameter using Eq. (7.17), and the results are visualized in Fig. 7.5a. On close inspection of the bar plot in this figure, it can be observed that the minimum measurement duration is almost symmetrical despite the asymmetrical sensor arrangement. Moreover, the measurement duration is the longest for parameters near low-vibration points, i.e. near the pin supports (with the decisive measurement time of  $T_{max} = 101$  s) and at mid-span, where Mode 2 and 4 exhibit low vibration points, cf. Fig. 7.3. More generally, the distribution of the measurement duration per element depends on the modes of vibration that are used to screen the structure for damage. For demonstration, a second sensor layout with two sensors at position P1 and P8 is shown in Fig. 7.5b. Due to the increased number of sensors, the maximum measurement duration  $T_{max}$  decreases from 101 to 56 s.

**Fig. 7.4** Fisher information for nine monitoring parameters and a typical sensor layout



**Fig. 7.5** Minimum measurement duration  $T_h$  from Eq. (7.17) for (a) one sensors at position P2, and (b) two sensors at P1 and P8

### 7.4.3 Optimal Sensor Placement for a Fixed Number of Sensors

In this section, the sensor placement strategy is outlined for a fixed number of sensors with varying sensor locations. The total number of sensor configurations is

$$N_c = \frac{r_{pos}!}{(r_{pos} - r)!r!} \quad (7.21)$$

where  $r_{pos}$  is the number of possible sensor locations and  $r$  is the number of sensors. For each sensor configuration, the maximum measurement time is evaluated using the approach that was described in the preceding section. Since the measurements at all sensor locations are available and stored in the measurement matrix from Eq. (7.20), the only thing left to do is to extract the respective columns, re-estimate the Fisher information, see Fig. 7.4, translate it into the minimum measurement duration, and find the decisive measurement duration among all elements as the one with the longest measurement duration. Ultimately, all configurations can be compared in an evaluation chart (Fig. 7.7).

The evaluation chart is shown for the simplest case with only one sensor and  $N_c = 8$  possible sensor configurations, see Fig. 7.7. The optimal measurement duration is the one with the shortest maximum measurement duration, i.e. configuration number one or eight (symmetry) with  $T_{max} = 101$  s. In contrast, the worst sensor configurations are configuration C(3) and C(6) with sensors at P3 and P6 and a measurement duration of  $T_{max} = 240$  s. The sensor locations coincide with vibration nodes (zero-vibration points) of Mode 3, see Fig. 7.3. Consequently, Mode 3 is non-observable and does not contribute to the Fisher information. According to Eq. (7.17), a lower Fisher information leads to a higher measurement duration.

Non-observable modes should be treated with caution. Since the null space  $S_0$  is estimated based on data, see Eq. (7.2), it is blind to Mode 3. Reducing the stiffness in any health parameter (apart from  $E_5$  at mid-span) introduces a non-symmetry in the system, which may cause the zero-vibration point of Mode 3 to shift and the mode to become observable. However, the null space is not orthogonal to Mode 3, meaning the residual will not have the expected statistical properties. Moreover, zero-vibration modes can cause linear dependencies in the column space of the Jacobian matrix, which falsifies the predictions of the minimum detectable damage. The latter can be avoided if zero-vibration modes are removed from the analysis, e.g.

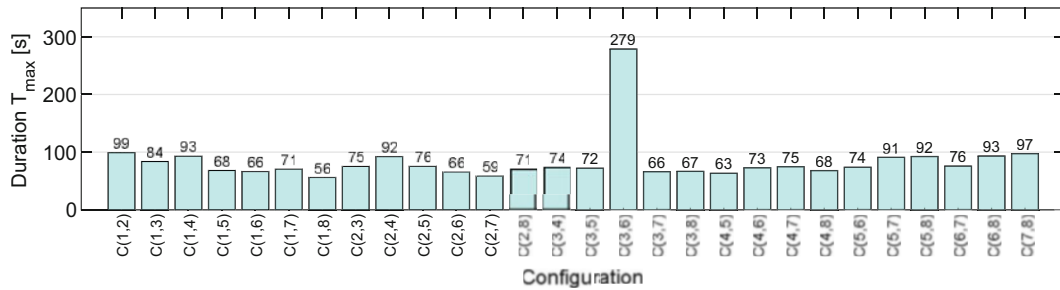


Fig. 7.6 Maximum measurement durations  $T_{max}$  from Eq. (7.18) for all sensor configurations with two sensors

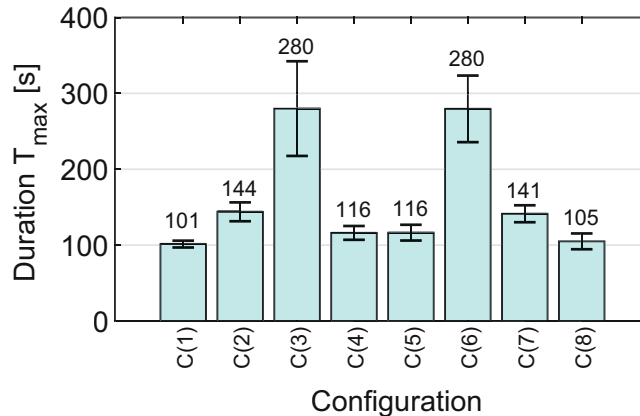
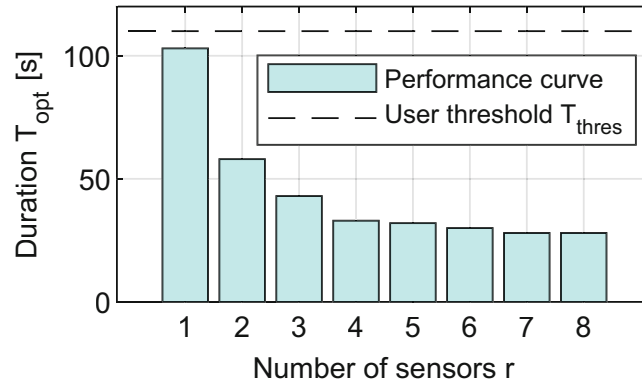


Fig. 7.7 Maximum measurement durations  $T_{max}$  from Eq. (7.18) and its standard deviation  $\sigma$  for one sensor



**Fig. 7.8** Optimal measurement time  $T_{opt}$  from Eq. (7.22) for a varying number of sensors

by overwriting the corresponding entries in the Jacobian matrix with zero entries. Since this does not remedy the problem regarding the missing modes in the null space, it is recommended to exclude sensor configurations from the optimization scheme that exhibit non-observable modes.

For the sake of example, the optimization scheme is also shown for sensor configurations with two sensors, see Fig. 7.6. Configuration C(3,6) has the longest measurement duration because the sensors are placed at P3 and P6, i.e. the zero-vibration points of Mode 3. The best sensor configuration is C(1,8) with a measurement duration of  $T = 56$  s. Note that the best sensor configurations for one and two sensors were already discussed in the previous section, see Fig. 7.5.

#### 7.4.4 Finding an Acceptable Number of Sensors

This section explains how to find an acceptable number of sensors. The main idea is to repeatedly evaluate the optimal sensor configuration for a fixed number of sensors, as explained in the previous section. For the problem at hand, there are eight sensor locations, and thus, we could use between one and eight sensors, so  $r \in [1, \dots, 8]$ . As a result, we obtain the optimal sensor configuration for each number of sensors  $r$  as well as the corresponding optimal measurement duration.

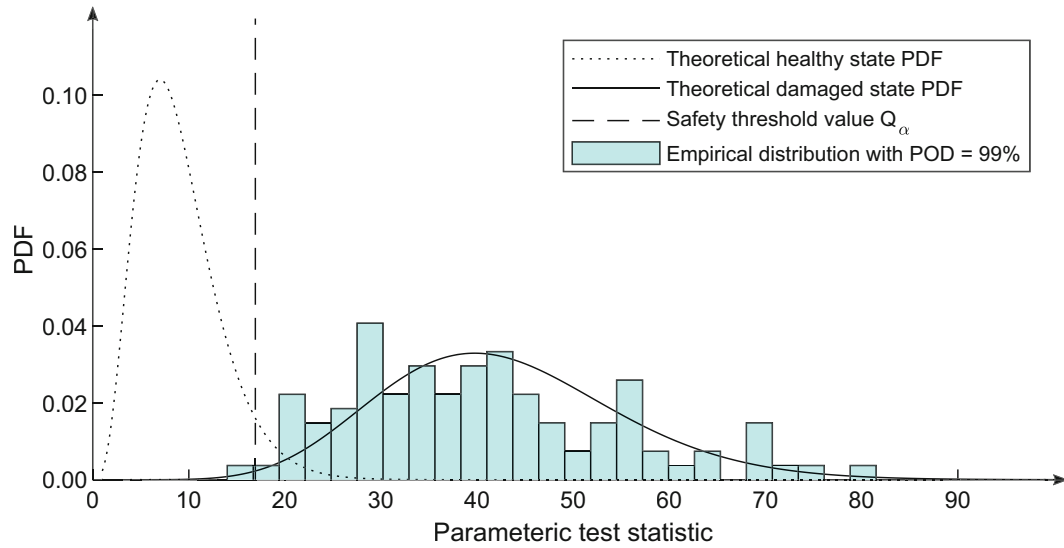
$$T_{opt}(r) = \min_c \{T_{max}(c)\} < T_{thres} \quad (7.22)$$

To find an acceptable number of sensors, the optimal measurement duration can be plotted over the number of sensors, see Fig. 7.8. Now, the maximum allowable measurement duration  $T_{thres}$  should be defined (based on the application and the user demand) and the optimal sensor configuration can be selected as the one with the next-lowest measurement time.

#### 7.4.5 Validating the Minimum Detectable Damage

The overall goal was to find the optimal sensor configuration and an acceptable number of sensors to detect a 5% stiffness decrease in any one beam element. For the sake of example, the optimal sensor configuration with one single sensor is chosen, because the measurement duration of  $T = 101$  s is deemed acceptable. To validate the effectiveness of the obtained sensor layout, the stiffness in the decisive element is decreased by 5%. Then, 100 new data sets with a duration of  $T = 101$  s are generated in the damaged state, the statistical test is applied to each record, and the empirical damaged state histogram is compared to the theoretical distribution. The measure used for evaluating the accuracy of the predicted minimum measurement duration is the probability of detection (POD), i.e. the probability that a damaged structure is correctly classified as damaged, see Fig. 7.1.

$$POD = 1 - \beta \quad (7.23)$$



**Fig. 7.9** Empirical probability density function (PDF) and power of detection (POD) for a 5% stiffness decrease in stiffness parameter  $E_9$

The validation technique is visualized in Fig. 7.9, where merely the damaged state for the decisive element is shown, i.e. the element with the greatest distance to the sensor at P1 right next to the support, so  $E_9$ . The empirical distribution (histogram in blue) aligns with the theoretical one and the POD is close to 99.4%, which is the complement of required false-positive rate  $\beta$  from Eq. (7.15). Hence, it can be concluded that the prediction based on healthy vibration was accurate. For completeness, the validation procedure is applied to all other stiffness parameters as well, but the results are not shown here. As expected, the test's response to a 5% stiffness decrease in any other parameter  $E_2, \dots, E_8$  is very strong and the non-centrality is beyond the minimum value, so  $\lambda > \lambda_{min}$ . That is because the minimum detectable damage in all other (non-critical) elements is below 5% and the monitoring system is tuned in a conservative manner.

## 7.5 Discussion

The main results can be summarized as follows. The minimum measurement time of the examined beam mainly depends on the mode shapes (see Sect. 7.4.2) and their visibility (see Sect. 7.4.3) at the candidate sensor locations. A non-symmetrical sensor arrangement can also lead to a symmetrical distribution for the minimum measurement duration in each health parameter and may lead to better performances than a classical symmetrical sensor placement.

*Uncertainties.* The Fisher information is a statistical quantity estimated based on data, and thus, subject to uncertainties. Consequently, the minimum measurement duration  $T_h$  and the maximum measurement duration over all elements  $T_{max}$  from Eqs. (7.17) and (7.18) are also scattered quantities. To quantify the uncertainties, the optimization procedure for one sensor and eight sensor locations P1-P8 was repeated 20 times with error bars shown in Fig. 7.7. It appears that the standard deviation is below 10% of the total measurement duration.

*Changing time lags.* Optimizing the sensor configuration for a fixed number of sensors is consistent because the same input parameters can be used, but for a varying number of sensors, inconsistencies are introduced. Due to the mathematical requirement regarding the model order  $\min\{pr, qr\} > 2m$ , the time lag parameters  $p$  and  $q = p + 1$  for the block Hankel matrix in Eq. (7.2), it is technically possible to reduce the minimum number of time lags for an increasing number of sensors  $r$  because the number of modes  $m$  remains the same. For eight sensors and four modes of vibration, the time lag is merely  $q = 3$ , so 8.3 milliseconds. An undesired consequence is that the block Hankel matrix changes in size, and so does the left null space and the residual vector which also influences all parameters derived from it (and their computation time), e.g. the Fisher information and the minimum measurement duration, see Eq. (7.17). A reduced number of time lags could cause that low-vibration waves do not have enough time to travel from one sensor to all others. Whether or not this is a problem remains an open question because, as shown in this paper, damage detection is also possible with a single sensor. Increasing

the time lag parameter can have a desirable effect but if computational efficiency is a problem, it is generally recommended to work with the minimum time lag values  $q = 2m/r$ .

*Changing excitation.* In the presented form, the optimal sensor placement depends on the excitation characteristics as well as the extent of noise contamination. The noise contamination during training will lead to spurious modes that might dominate the structural modes (indicated through noise components in the signal with greater singular values greater than the structural ones). As a result, the singular vectors corresponding to structural modes get pushed into the null space and bias the entire framework. The noise contamination during testing could also lead to spurious modes of vibration that are not orthogonal to the null space, so the residual vector from Eq. (7.4) will not attain the Gaussian properties. One way to enhance the robustness towards noise is to set the model order higher than  $2m$  to create space for noise modes. Another way is to use a Gaussian residual vector that is more robust to change in the excitation characteristics, see for example [8].

*Combinatorial explosion.* The exhaustive search approach—where every possible sensor configuration is analyzed—worked well for the examined pin-supported beam with eight sensor locations but might be computationally burdensome for large structures with many candidate sensor locations. For example, for a 100 m-long bridge with 60 possible sensor locations and 10 available monitoring channels, the number of sensor combinations increases to  $N_c = 7.5 \cdot 10^{10}$ , see Eq. (7.21). To overcome the problem of combinatorial explosion, the performance criterion has to be combined with efficient optimization approaches, e.g. genetic algorithms, simulated annealing or others, see [3, 5] for an overview.

## 7.6 Conclusions

A distinguishing characteristic of stochastic subspace-based damage detection (SSDD) is the profound mathematical theory that accurately models the healthy and, more importantly, the damaged state. The formula for the minimum detectable damage is a central element, as it links abstract statistical quantities (e.g. the Fisher information) to practical engineering units, such as the minimum measurement duration. Due to the statistical framework, the damage detectability increases (asymptotically) with increasing sample size  $N$ . Vice versa, the necessary measurement duration  $T = Nf_s$  can be interpreted as a performance criterion for the damage detectability.

A great advantage of the presented performance criterion is that it can be calculated based on vibration data from the healthy structure. In fact, only a single transient analysis under white noise excitation is necessary to generate the system output at all candidate locations. Simulations in the damaged state are merely necessary to validate the method's capability of finding the optimal sensor layout. Another advantage is that both the input and output parameters are intuitive to handle. The input parameter is the desired detectable damage in percent of a stiffness parameter. It can be linked to the material utilization rate of the structural analysis and defined individually for each structural component. Hence, the sensor placement can be tuned to become more sensitive to damage in vital structural components or damage hot spots. The output parameter, on the other hand, is the required measurement duration. It is a function of the desired damage detectability and might soon replace the general rules of thumb that can be found in the literature, see [18, 19].

**Acknowledgments** The financial support from the Natural Sciences and Engineering Research Council of Canada (NSERC), the German Academic Exchange Service (DAAD) and the Mitacs Globalink Research Award is gratefully acknowledged.

## References

1. Kaya, Y., Ventura, C., Huffman, S., Turek, M.: British columbia smart infrastructure monitoring system. *Can. J. Civ. Eng.* **44**(8), 579–588 (2017)
2. Boller, C., Chang, F-K., Fujino, Y.: *Encyclopedia of structural health monitoring*. Wiley, Chichester (2009)
3. Ostachowicz, W., Soman, R., Malinowski, P.: Optimization of sensor placement for structural health monitoring: a review. *Struct. Health Monit.* **18**(3), 963–988 (2019)
4. Van de Wal, M., de Jager, B.: A review of methods for input/output selection. *Automatica* **37**(4), 487–510 (2001)
5. Yi, T-H., Li, H-N.: Methodology developments in sensor placement for health monitoring of civil infrastructures. *Int. J. Distrib. Sens. Netw.* **8**(8), 612726 (2012)
6. Benveniste, A., Basseville, M., Moustakides, G.: The asymptotic local approach to change detection and model validation. *IEEE Trans. Autom. Control* **32**(7), 583–592 (1987)
7. Basseville, M., Abdelghani, M., Benveniste, A.: Subspace-based fault detection algorithms for vibration monitoring. *Automatica* **36**(1), 101–109 (2000)

8. Döhler, M., Mevel, L., Hille, F.: Subspace-based damage detection under changes in the ambient excitation statistics. *Mech. Syst. Signal Process.* **45**(1), 207–224 (2014)
9. Basseville, M., Benveniste, A., Moustakides, G., Rougee, A.: Optimal sensor location for detecting changes in dynamical behavior. *IEEE Trans. Autom. Control* **32**(12), 1067–1075 (1987)
10. Döhler, M., Kwan, K., Bernal, D.: Optimal sensor placement with a statistical criterion for subspace-based damage detection. In: *Proceedings of the IMAC – 31st International Modal Analysis Conference* (2013)
11. Mendler, A., Allahdadian, S., Döhler, M., Mevel, L., Ventura, C.: Minimum detectable damage for stochastic subspace-based methods. In: *IOMAC – International Operational Modal Analysis Conference* (2019)
12. James, G.H., Carne, T.G., Lauffer, J.P.: The natural excitation technique (next) for modal parameter extraction from operating structures. *Modal Anal. Int. J. Anal. Exp. Modal Anal.* **10**(4), 260–277 (1995)
13. Van Overschee, P., de Moor, B.: *Subspace Identification for Linear Systems: Theory-Implementation-Application*. Springer Science & Business, Berlin (2012)
14. Balmès, É., Basseville, M., Mevel, L., Nasser, H., Zhou, W.: Statistical model-based damage localization: a combined subspace-based and substructuring approach. *Struct. Control. Health Monit.* **15**(6), 857–875 (2008)
15. Basseville, M., Mevel, L., Goursat, M.: Statistical model-based damage detection and localization: subspace-based residuals and damage-to-noise sensitivity ratios. *J. Sound Vib.* **275**(3–5), 769–794 (2004)
16. Basseville, M.: Information criteria for residual generation and fault detection and isolation. *Automatica* **33**(5), 783–803 (1997)
17. Wenzel, H.: *Health Monitoring of Bridges*. Wiley, Chichester (2009)
18. Brincker, R., Ventura, C.E. (eds.): *Introduction to Operational Modal Analysis*. Wiley, New York (2015)
19. Rainieri, C., Fabbrocino, G.: *Operational Modal Analysis of Civil Engineering Structures*. Springer, New York (2014)

**Alexander Mendler** Ph.D. Candidate at the University of British Columbia

**Dr. Michael Döhler** Researcher at the French National Institute for Computer Science and Automatic Control.

**Dr. Carlos E. Ventura** Professor at the University of British Columbia and Director of the Earthquake Engineering Research Facility

**Laurent Mevel** Senior Researcher and Team Leader at the French National Institute for Computer Science and Automatic Control.



# Chapter 8

## Vibrations Assessment of Existing Building Foundations Due to Moving Trains in Underground Tunnels

Onur Avci, Ashish Bhargava, Nikolaos Nikitas, and Daniel J. Inman

**Abstract** Train movements generate oscillations that are transmitted as waves through the track support system into its surroundings. The waves reaching nearby structures may cause distractions for humans and/or result in equipment malfunctions. Dynamic characteristics of surrounding media affect the level of vibrations experienced in nearby buildings. In this paper, the authors are presenting a finite element analysis study performed to assess vibration levels due to train movements in nearby subway tunnels. The closer subway tunnel is located at an average horizontal distance of 50 ft (15.2 m) from an existing office building. While the authors focus on assessing vibration levels at the foundations of the office building, a plane strain finite element model is created to simulate the tunnel, surrounding rock and the soil stratum above the rock layer. The loading function is modeled as a sinusoidal point source and simulations are run for sensitivity analysis.

**Keywords** Finite element modeling · Vibrations serviceability · Railroad tunnels · Train vibrations · ANSYS

### 8.1 Introduction

Train vibrations can cause distractions for building occupants and result in equipment malfunctions. Propagation of train induced excitations and ground borne vibration serviceability is a topic of research for decades. The serviceability of building foundations and elevated floors against train vibrations are affected by several parameters [1–3]. Train suspension system, train and track components, rail and wheel smoothness, tunnel variables, surrounding rock and soil layers add up to a complicated engineering problem which can be simulated with a detailed finite element model [4].

An updated version of the Transit Noise and Vibration Impact Assessment Manual [5] is released in 2018 by Federal Transit Administration (FTA) describing the procedure to predict and assess noise and vibration impacts due to transit systems. The manual offers three different methods to quantify vibration impacts of ground-borne train excitations. Based on the scale of the project and environmental conditions, one of the methods is to be utilized: Vibration Screening Procedure (VSP); General Vibration Assessment (GVA); Detailed Vibration Analysis (DVA). The work presented in this paper is a predominant example for the DVA method in which the train excitations originating from tunnels embedded in rock are studied to ensure the response of the foundations of the neighboring office building do not exceed a certain threshold.

The office building is supported on pile foundations extending 70 ft (21.3 m) down to bedrock and it neighbors a parking garage. The railway tunnels are located within the bedrock at 97 ft (29.6 m) below the ground and are passing adjacent to the office building and under the parking garage as depicted in Fig. 8.1. The minimum horizontal distance between the railway centerline and the office structure is 25 ft (7.6 m) while the maximum horizontal distance is 90 ft (27.4 m), as depicted in Fig. 8.2. Both the office building and the parking garage are six-story structures. A comprehensive finite element (FE) model

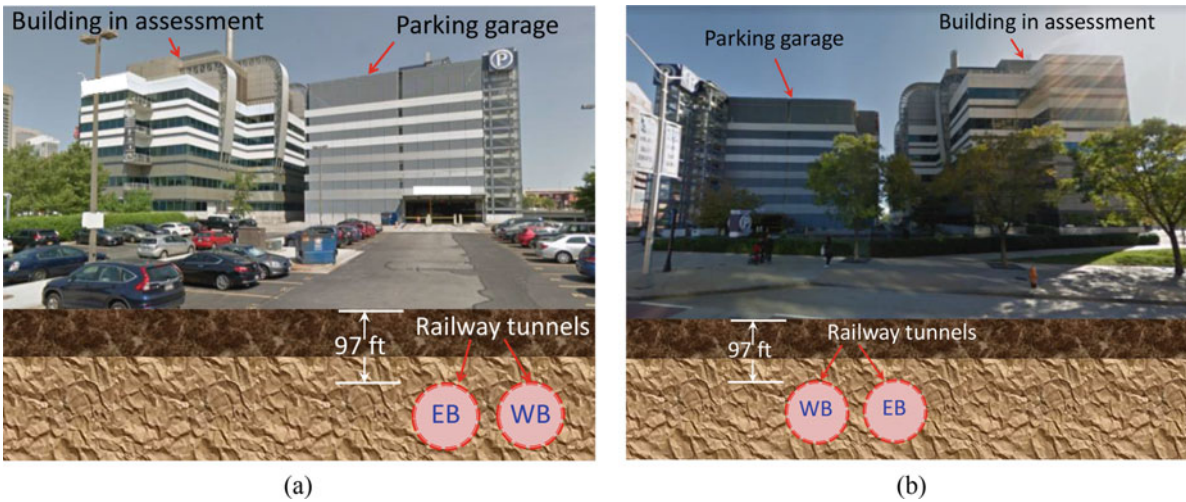
---

O. Avci (✉) · N. Nikitas  
School of Civil Engineering, University of Leeds, Leeds, UK  
e-mail: oavci@vt.edu

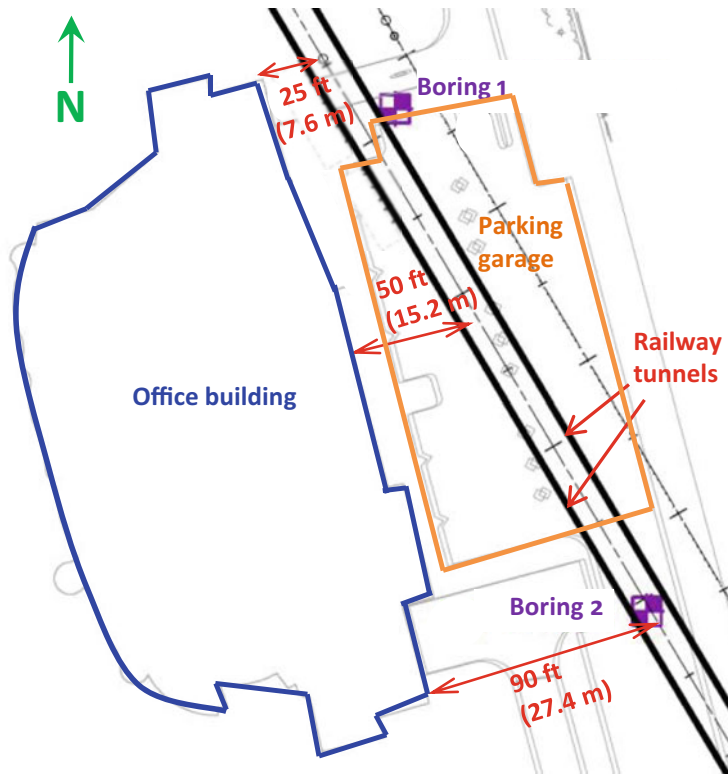
A. Bhargava  
AECOM USA, Inc., New York City, NY, USA

D. J. Inman  
Department of Aerospace Engineering, University of Michigan, Ann Arbor, MI, USA





**Fig. 8.1** Office building, parking garage and the railway tunnels (a) South view, (b) North view



**Fig. 8.2** Plan view of the office building, parking garage and railway tunnels

is created and dynamic loading from trains are simulated to assess the acceleration levels at the foundation level of the office building. FTA's DVA criteria and corresponding descriptions are shown in Fig. 8.3 and Table 8.1, respectively, per [5]. The FTA criteria have certain vibration velocity limits for which potential mitigations are to be implemented when the levels exceed a specific criterion. VC-A is found to be the best fit for the DVA runs of the office structure.

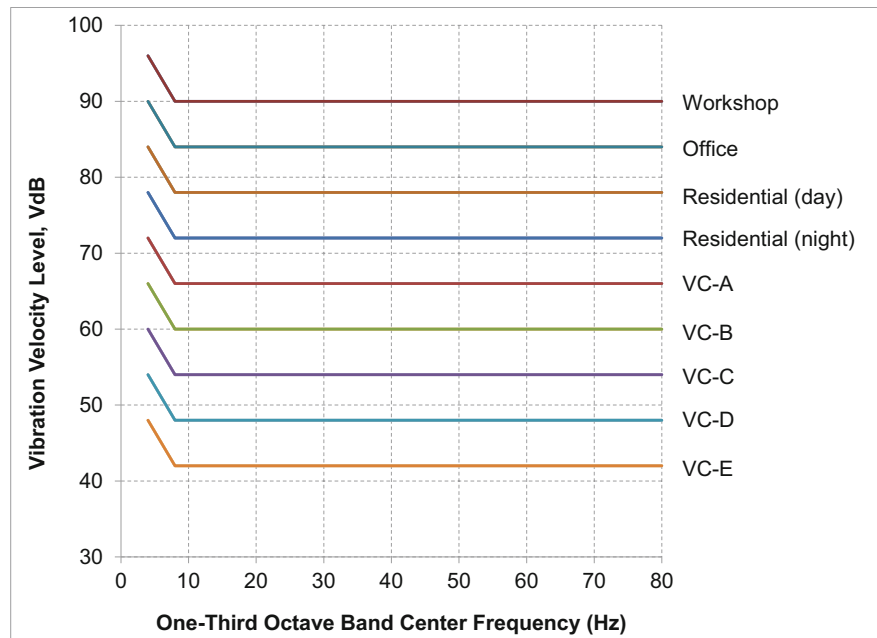


Fig. 8.3 Criteria for detailed vibration analysis. (Adapted from Fig. 6.2 of FTA Assessment Manual)

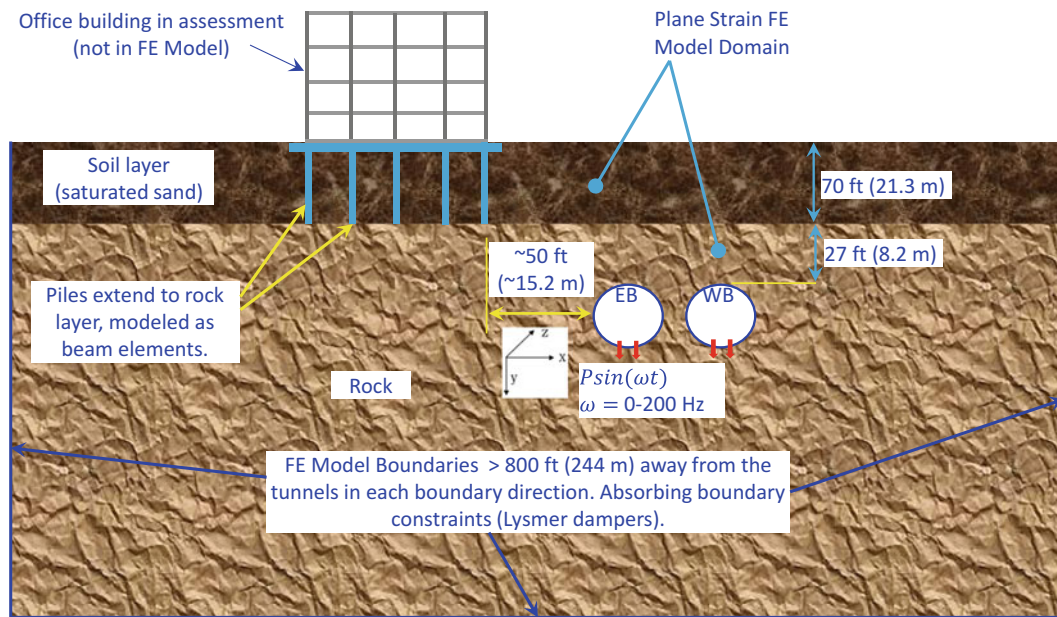
Table 8.1 Interpretation of vibration criteria for detailed vibration analysis

Criterion curve	Max Lv, VdB	Description
Workshop (ISO)	90	Vibration that is distinctly felt. Appropriate for workshops and similar areas not as sensitive to vibration
Office (ISO)	84	Vibration that can be felt. Appropriate for offices and similar areas not as sensitive to vibration
Residential day (ISO)	78	Vibration that is barely felt. Adequate for computer equipment and low-power optical microscopes (up to 20×)
Residential night, operating rooms (ISO)	72	Vibration is not felt, but ground-borne noise may be audible inside quiet rooms. Suitable for medium-power optical microscopes (100×) and other equipment of low sensitivity
VC-A	66	Adequate for medium-to high-power optical microscopes (400×), microbalances, optical balances, and similar specialized equipment
VC-B	60	Adequate for high-power optical microscopes (1000×) and inspection and lithography equipment to 3-micron line widths
VC-C	54	Appropriate for most lithography and inspection equipment to 1-micron detail size
VC-D	48	Suitable in most instances for the most demanding equipment, including electron microscopes operating to the limits of their capabilities
VC-E	42	The most demanding criterion for extremely vibration-sensitive equipment

Adapted from Table 6.6 of FTA Assessment Manual

## 8.2 Plane Strain Finite Element Model

While the primary purpose of this paper is to assess the vibrations at the office building foundations, ANSYS [6] finite element software is utilized to simulate the vibration waves propagating through railways, tunnels, rock layer, soil layers, and piles; assuming a plane strain model [7] and a harmonic line source for the train excitations. This software has successfully been utilized in similar work [8–13] by the authors. A general view of the plane strain 2D FE model is depicted in Fig. 8.4. The plane strain model is valid when the strain state of a point has non-zero components lying in one plane only. The office structure is not included in this model since the focus of the work is to find out vibrations at the foundation level. Lysmer dampers [14] are used as absorbing boundaries at the model edges placed at a reasonable distance from the tunnels.



**Fig. 8.4** 2D FE model

**Table 8.2** Shear wave velocity information

Material	Property	Symbol	US customary units	SI units
Soil	Shear wave velocity	$V_s$	400 ft/s	122 m/s
Rock	Shear wave velocity	$V_s$	13,000 ft/s	3963 m/s

Meanwhile, the Rayleigh damping option in ANSYS allows the user define frequency dependent damping ratios [15–17] for the FE model (3–5% damping for 2–30 Hz frequency range, for the initial run). Additional information for soil and rock layers is shown in Table 8.2. In the FE model, the train excitations are introduced as dynamic line loading. The train car properties used in the calculations are 95 ft (29 m) for the train car length; 80,000 lbs (36,288 kg) for the empty train car weight; 95,000 lbs (43,091 kg) for the total weight when hundred passengers are present in the train-car. This resulted in a dynamic loading function with amplitude of 0.5 kip/ft (7.3 kN/m) per track, varying within a frequency range of 0 to 200 Hz. For the “one train” condition in the FE model, the tunnel closer to the building is dynamically loaded; while the for the “two trains” condition both tunnels are dynamically loaded simultaneously.

Considering the analytical approaches available in the literature, there are recommendations for the loading function generated by a train [18–20]. Nevertheless, the complicated nature of dynamic interaction between the bogie, sleepers, rail-pads, rails, wheel-set, ballast and the train car tend to make this prediction difficult. Yet, the number of unknowns in material and dynamic properties of the tunnel construction materials and surrounding soil/rock layers make the use of analytical prediction methods questionable at times. All this brings up a need for a detailed FE model in which a loading function is introduced to represent the train excitations originating from the tunnels and the resulting vibration response at various locations of the foundation are determined and then compared to the FTA criterion [5]. This model is created in ANSYS with a sinusoidal loading function  $P \sin(\omega t)$  where:

$$\begin{aligned}
 P \sin(\omega t) &= \text{harmonic force function generated by the train pass} \\
 P &= \text{harmonic force amplitude} \\
 \omega &= \text{frequency range } 0\text{--}200 \text{ Hz}
 \end{aligned}$$

The loading function in ANSYS is based on a sine sweep run (chirp) for a range of frequencies per One-Third Octave Band Frequency of FTA criterion. The maximum response at specific frequencies are recorded and plotted for comparison. Vibration velocity levels in decibels are calculated per Eq. (8.1). The vibration levels presented in this paper are referenced to  $1 \times 10^{-6}$  inches/second.

$$L_{vel} = 20 \log \left( \frac{vel}{vel_{ref}} \right) \quad (8.1)$$

where:

$$vel_{ref} = 10^{-6} \text{ in/sec in the USA}$$

$$= 10^{-8} \text{ m/sec internationally}$$

$vel$  = RMS velocity amplitude

$L_{vel}$  = velocity level, VdB

### 8.3 Sensitivity Analysis and Discussion of Results

At a horizontal distance of about 50 ft (15.2 m) from the train line, the surface vibrations at the foundation level is plotted in Fig. 8.5 with respect to the VC-A criterion of the FTA manual. It is shown in the figure that in the frequency ranges of 20–30 Hz and 8–12 Hz, the vibration velocity levels tend to be the highest. While both one train and the two train loading conditions are below the VC-A criterion of 66 VdB; the peak for the two train loading condition (64 VdB) is higher than the peak for the one train loading condition (60 VdB) at 25 Hz. Conclusion for this ANSYS run is the fact that, for the foundation vibration serviceability, both loading conditions are within the acceptable range of VC-A criterion.

In an attempt to observe the VdB levels based on the variability of independent input items, a sensitivity study is performed. Three different analysis cases are studied in the sensitivity analysis:

- The amplitude of the one train loading condition is increased by 20%.
- The modal damping ratio is lowered from 3–5% range to 1–2% range.
- The horizontal distance from the train loading to the office structure is decreased from 50 ft (15.2 m) to 25 ft (7.6 m).

It should be emphasized that the three sensitivity items are purposely chosen to increase the VdB magnitudes at the foundation of the office building. The authors intended to see how much the vibrations would increase and whether they would exceed the 66 VdB limit of the VC-A criterion. For the first case of the sensitivity analysis, the amplitude of the one train loading is increased by 20% (Fig. 8.6). The figure shows that this results in a 2.7% increase in the VdB values (from 60 VdB to 61.6 VdB) at the most critical frequency (25 Hz). Both loading conditions are below the VC-A criterion limit of 66 VdB.

For the second case of the sensitivity analysis, the modal damping ratio range is lowered from 3–5% to 1–2%. Based on the Rayleigh damping model (Fig. 8.7), the modal damping ratio is frequency dependent. Running the FE model with lowered damping ratio range yielded higher vibration levels, as expected. Figure 8.8 shows that the VdB results increase by

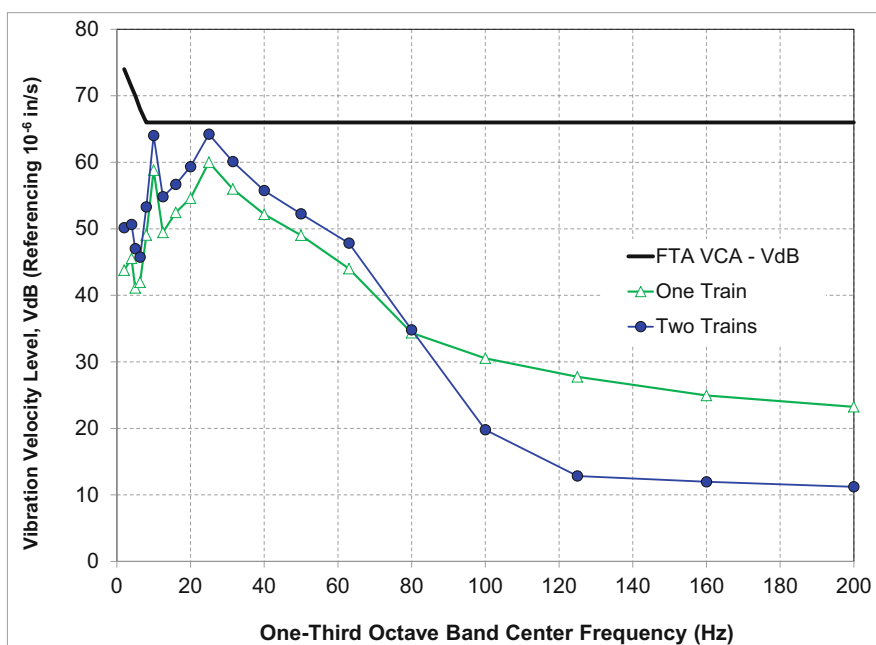


Fig. 8.5 Vibrations at the foundation level at 50 ft (15.2 m) from the train line

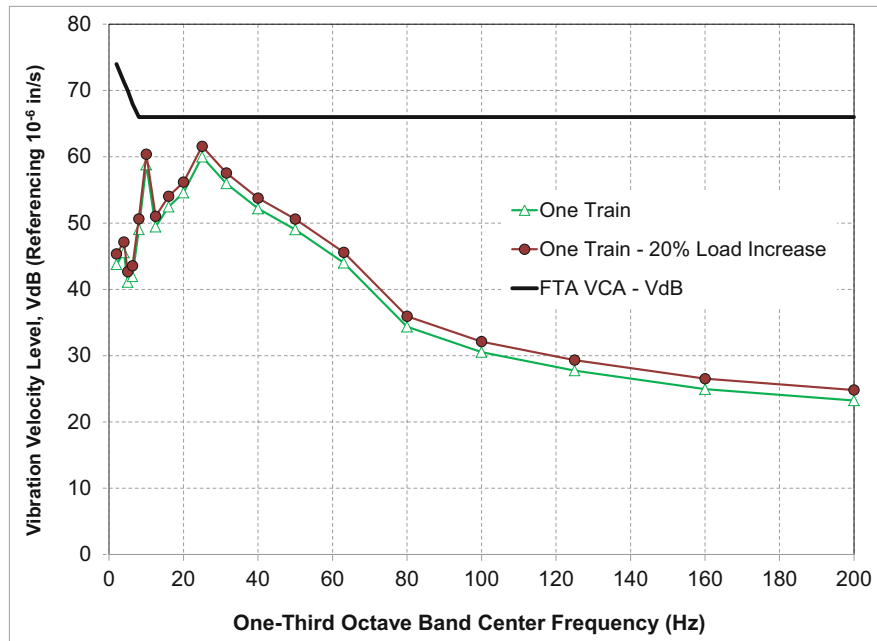


Fig. 8.6 Vibrations at the foundation level at 50 ft (15.2 m) from the train line with 20% load increase

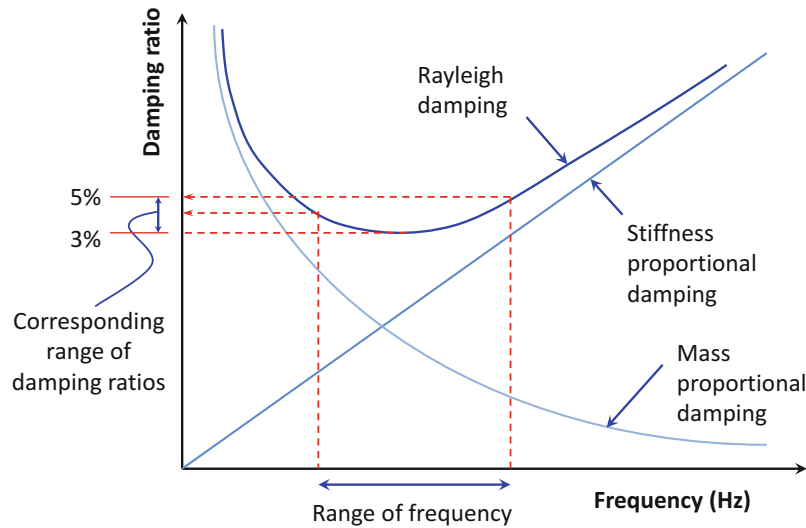


Fig. 8.7 Frequency dependent damping per Rayleigh model

2.7% (from 60 to 61.6 VdB) at the most critical frequency of 25 Hz. Both runs are below the VC-A criterion limit of 66 VdB, again.

For the third case of the sensitivity analysis, horizontal distance from the train loading to the office structure is decreased from 50 ft (15.2 m) to 25 ft (7.6 m). According to the results shown in Fig. 8.9, for the frequencies less than 50 Hz, vibrations at the foundations are not very sensitive to the distance between the train line and the building. For frequencies higher than 50 Hz, it is clear that the VdB levels drop for 50 ft distance. Based on Fig. 8.9, for 25 ft (7.6 m) distance, VdB results increase by 1.7% (from 60 to 61 VdB) at the most critical frequency of 25 Hz. Again, both runs are below the VC-A criterion limit of 66 VdB.

While this study focused on the vibrations at the foundation level only, the vibration serviceability of elevated floors is of great importance [21–28] and it has become a major parameter to be considered in structural design [29–33]. It should be noted again that in Figs. 8.5, 8.6, 8.8 and 8.9, all VdB values are below VC-A criterion limit of 66 VdB at the foundations.

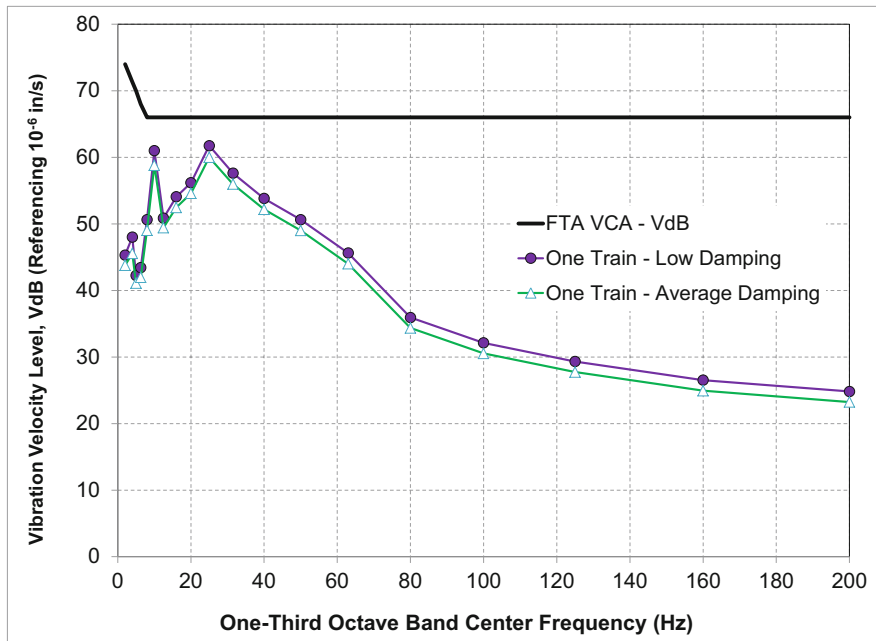


Fig. 8.8 Vibrations at the foundation level at 50 ft (15.2 m) from the train line with lower damping

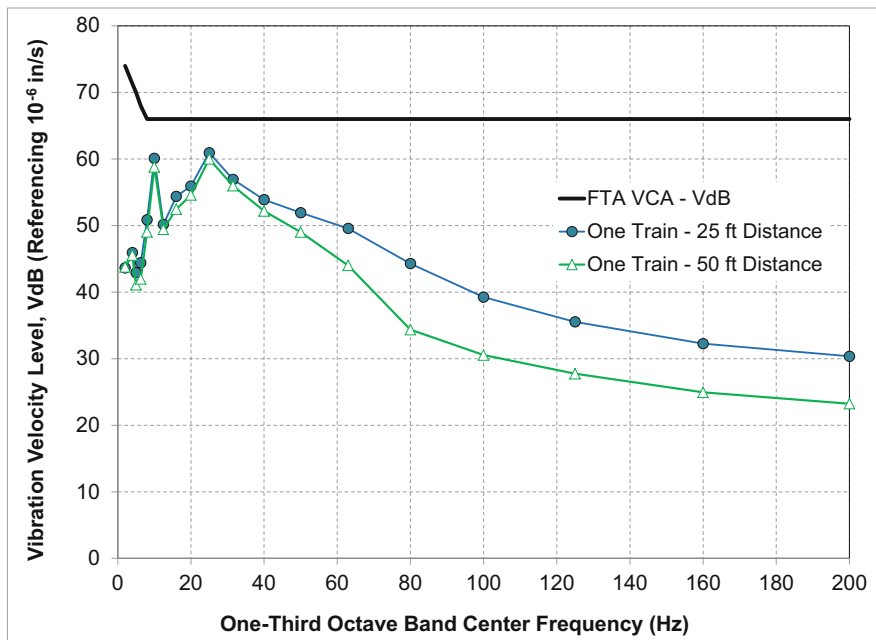


Fig. 8.9 Vibrations at the foundation level at 25 ft (7.6 m) from the train line

Since FTA manual [5] suggests that  $-2$  dB attenuation can be considered for each elevated story for the first five stories and  $-1$  dB for the next five stories, the elevated floors of the structure would be considered acceptable per the VC-A criterion. However, a more detailed FE model including the building structure and the elevated floors would provide more information and shed more light on the vibration response of individual floors.

## 8.4 Conclusions

In this paper, vibrations at the foundation level of an existing office building are studied in detail with a finite element model. The model included the train excitations as well as the soil and rock layers in a plane strain format. The simulations are carried out accompanying a sensitivity analysis. Namely, the amplitude of the one train loading condition is increased by 20%; the modal damping ratio is lowered from 3–5% range to 1–2% range; and the horizontal distance from the train loading to the office structure is decreased from 50 ft (15.2 m) to 25 ft (7.6 m) to see the effect on the vibrations response of the foundations. For all runs, the peak VdB values remained below the FTA VC-A criterion limit of 66 VdB; therefore, it can be concluded that the foundations of the existing office building will not be adversely affected by the moving trains in nearby tunnels.

## References

1. Lee, P.J., Hong, J.Y., Jeon, J.Y.: Assessment of rural soundscapes with high-speed train noise. *Sci. Total Environ.* (2014). <https://doi.org/10.1016/j.scitotenv.2013.07.026>
2. Connolly, D.P., Marecki, G.P., Kouroussis, G., Thalassinakis, I., Woodward, P.K.: The growth of railway ground vibration problems — a review. *Sci. Total Environ.* (2016). <https://doi.org/10.1016/j.scitotenv.2015.09.101>
3. Zou, C., Wang, Y., Wang, P., Guo, J.: Measurement of ground and nearby building vibration and noise induced by trains in a metro depot. *Sci. Total Environ.* (2015). <https://doi.org/10.1016/j.scitotenv.2015.07.123>
4. Alabbasi, S., Hussein, M.F.M., Abdeljaber, O., Avci, O.: Investigating the dynamics of a special type of floating-slab tracks. In: *COMPADYN 2019, 7th Int. Conf. Comput. Methods Struct. Dyn. Earthq. Eng.*, 2019
5. Hanson, C.E., Towers, D.A., Meister, L.D.: *Transit noise and vibration impact assessment manual* (Federal Transit Administration), Federal Transit Administration, 2018
6. ANSYS, *ANSYS Fluent 12.0 User's Guide*, Canonsburg, PA, 2009. <https://doi.org/10.1111/j.1600-0447.2011.01711.x>
7. Boreni, A.P., Schmidt, R.J., Sidebottom, O.M.: *Advanced Mechanics of Materials*, 5th edn, (1993). <https://doi.org/10.1115/1.3269509>
8. Avci, O., Al-Smadi, Y.M.: Unreinforced masonry Façade assessment of a historic building for excessive displacements due to a nearby subway construction. *Pract. Period. Struct. Des. Constr.* (2019). [https://doi.org/10.1061/\(ASCE\)SC.1943-5576.0000399](https://doi.org/10.1061/(ASCE)SC.1943-5576.0000399)
9. Avci, O., Bhargava, A.: Finite-element analysis of cantilever slab deflections with ANSYS SOLID65 3D reinforced-concrete element with cracking and crushing capabilities. *Pract. Period. Struct. Des. Constr.* (2019). [https://doi.org/10.1061/\(ASCE\)SC.1943-5576.0000411](https://doi.org/10.1061/(ASCE)SC.1943-5576.0000411)
10. Avci, O., Bhargava, A.: Investigation of uplift pressures on a drainage shaft using ANSYS SOLID185 elements and Drucker–Prager failure criterion for the surrounding rock stratum. *J. Perform. Constr. Facil.* (2019)
11. Al-Smadi, Y.M., Bhargava, A., Avci, O., Elmorsi, M.: Design of experiments study to obtain a robust 3D computational Bridge Model. In: *Conf. Proc. Soc. Exp. Mech. Ser.*, 2012. [https://doi.org/10.1007/978-1-4614-2413-0\\_29](https://doi.org/10.1007/978-1-4614-2413-0_29)
12. Bhargava, A., Isenberg, J., Feenstra, P.H., Al-Smadi, Y., Avci, O.: Vibrations assessment of a hospital floor for a magnetic resonance imaging unit (MRI) replacement. In: *Struct. Congr. 2013 Bridg. Your Passion with Your Prof. - Proc. 2013 Struct. Congr.*, 2013
13. Avci, O., Bhargava, A., Al-Smadi, Y., Isenberg, J.: Vibrations serviceability of a medical facility floor for sensitive equipment replacement: evaluation with sparse in-situ data. *Pract. Period. Struct. Des. Constr.* **124**(1), (2018)
14. Lysmer, J., Kuhlemeyer, R.L.: Finite Dynamic Model for Infinite Media. *J. Eng. Mech. Div. ASCE.* (1969)
15. Avci, O.: Effects of bottom chord extensions on the static and dynamic performance of steel joist supported floors, Virginia Polytechnic Institute and State University, 2005
16. Avci, O.: Amplitude-dependent damping in vibration serviceability: Case of a laboratory footbridge. *J. Archit. Eng.* **22**, (2016). [https://doi.org/10.1061/\(ASCE\)AE.1943-5568.0000211](https://doi.org/10.1061/(ASCE)AE.1943-5568.0000211)
17. Avci, O.: Nonlinear damping in floor vibrations serviceability: Verification on a laboratory structure. In: *Conf. Proc. Soc. Exp. Mech. Ser.*, 2017. [https://doi.org/10.1007/978-3-319-54777-0\\_18](https://doi.org/10.1007/978-3-319-54777-0_18)
18. Yang, Y.B., Hung, H.H., Chang, D.W.: Train-induced wave propagation in layered soils using finite/infinite element simulation. *Soil Dyn. Earthq. Eng.* (2003). [https://doi.org/10.1016/S0267-7261\(03\)00003-4](https://doi.org/10.1016/S0267-7261(03)00003-4)
19. Yang, Y.B., Hung, H.H., Hsu, L.C.: Ground vibrations due to underground trains considering soil-tunnel interaction. *Interact. Multiscale Mech.* (2007). <https://doi.org/10.12989/imm.2008.1.1.157>
20. Bin Yang, Y., Hung, H.H.: A 2.5D finite/infinite element approach for modelling visco-elastic bodies subjected to moving loads. *Int. J. Numer. Methods Eng.* (2001). <https://doi.org/10.1002/nme.208>
21. Avci, O.: Retrofitting steel joist supported footbridges for improved vibration response. In: *Struct. Congr. 2012 - Proc. 2012 Struct. Congr.*, 2012. <https://doi.org/10.1061/9780784412367.041>
22. Avci, O.: Modal parameter variations due to joist bottom chord extension installations on laboratory footbridges. *J. Perform. Constr. Facil.* **29**, (2015). [https://doi.org/10.1061/\(ASCE\)CF.1943-5509.0000635](https://doi.org/10.1061/(ASCE)CF.1943-5509.0000635)
23. Barrett, A.R., Avci, O., Setareh, M., Murray, T.M.: Observations from vibration testing of in-situ structures. In: *Proc. Struct. Congr. Expo.*, 2006. [https://doi.org/10.1061/40889\(201\)65](https://doi.org/10.1061/40889(201)65)
24. Avci, O., Setareh, M., Murray, T.M.: Vibration testing of joist supported footbridges. In: *Struct. Congr. 2010, 2010*. [https://doi.org/10.1061/41130\(369\)80](https://doi.org/10.1061/41130(369)80)
25. Davis, B., Avci, O.: Simplified vibration response prediction for slender monumental stairs. In: *Struct. Congr. 2014 - Proc. 2014 Struct. Congr.*, 2014. <https://doi.org/10.1061/9780784413357.223>

26. Avci, O., Davis, B.: A study on effective mass of one way joist supported systems. In: Struct. Congr. 2015 - Proc. 2015 Struct. Congr., 2015. <https://doi.org/10.1061/9780784479117.073>
27. Davis, B., Avci, O.: Simplified vibration serviceability evaluation of slender monumental stairs. J. Struct. Eng. (United States). **141**, (2015). [https://doi.org/10.1061/\(ASCE\)ST.1943-541X.0001256](https://doi.org/10.1061/(ASCE)ST.1943-541X.0001256)
28. Catbas, F.N., Celik, O., Avci, O., Abdeljaber, O., Gul, M., Do, N.T.: Sensing and monitoring for stadium structures: a review of recent advances and a forward look. Front. Built Environ. **3**, 38 (2017). <https://doi.org/10.3389/fbuil.2017.00038>
29. Younis, A., Avci, O., Hussein, M., Davis, B., Reynolds, P.: Dynamic forces induced by a single pedestrian: A literature review. Appl. Mech. Rev. **69**, (2017). <https://doi.org/10.1115/1.4036327>
30. Abdeljaber, O., Hussein, M.F.M., Avci, O.: In-service video-vibration monitoring for identification of walking patterns in an office floor. In: 25th Int. Congr. Sound Vib. Hiroshima, Japan., 2018
31. Abdeljaber, O., Hussein, M.F.M., Avci, O., Davis, B., Reynolds, P.: A novel video-vibration monitoring system for walking pattern identification on floors. Adv. Eng. Softw. **139**, (2020)
32. Do, N.T., Gul, M., Abdeljaber, O., Avci, O.: Novel framework for vibration serviceability assessment of stadium grandstands considering durations of vibrations. J. Struct. Eng. (United States). **144**, (2018). [https://doi.org/10.1061/\(ASCE\)ST.1943-541X.0001941](https://doi.org/10.1061/(ASCE)ST.1943-541X.0001941)
33. Muhammad, Z., Reynolds, P., Avci, O., Hussein, M.: Review of pedestrian load models for vibration serviceability assessment of floor structures. Vibration. (2018). <https://doi.org/10.3390/vibration2010001>

**Dr. Onur Avci** had his MS and PhD degrees at Virginia Tech. He is focused on dynamics of structures, smart structures and machine learning applications in structural engineering.

**Dr. Ashish Bhargava** received his PhD from George Washington University. He is a structural engineer at AECOM New York.

**Dr. Nikolaos Nikitas** received his PhDs from the University of Edinburgh (2008) and the University of Bristol (2011). He is an Associate Professor in structural dynamics and engineering at the University of Leeds working particularly on aeroelasticity and on complex, multibody dynamic interaction problems.

**Daniel J. Inman** received his PhD in mechanical engineering from Michigan State University in 1980 and is the Harm Buning Collegiate Professor in the Department of Aerospace Engineering at the University of Michigan. Since 1980, he has published eight books (on vibration, energy harvesting, control, statics, and dynamics), eight software manuals, 20 book chapters, over 375 journal papers, and 650 proceedings papers, given 68 keynote or plenary lectures, graduated 65 PhD students and supervised more than 75 MS degrees. He works in the area of applying smart structures to solve aerospace engineering problems including energy harvesting, structural health monitoring, vibration suppression, and morphing aircraft. He is a fellow of AIAA, ASME, IIAV, SEM, and AAM.





# Chapter 9

## Ambient Vibration Tests and Modal Response Analysis of Guayaquil Metropolitan Cathedral in Guayaquil, Ecuador

M. Motamedi, C. E. Ventura, O. Lara, and J. H. Barredo

**Abstract** This paper describes a series of ambient vibration tests and modal analysis conducted on Guayaquil Metropolitan Cathedral, located in Guayaquil, Ecuador. The Guayaquil Cathedral is composed of the reinforced concrete frames and masonry infills, constructed in mid 1920s. Modal response analysis was performed to identify the dynamic properties of the structure, including predominant natural frequencies and the corresponding mode shapes to support seismic assessment and upgrading of the Cathedral. The testing program consisted of several setups on different locations of the structure including the roof of the main building, towers, and the dome. Two series of sensors were used to carry out the vibration measurements: (1) Tromino<sup>®</sup> velocity/acceleration wireless sensors; and (2) Polytec<sup>®</sup> Laser Vibrometers. The sensors were placed on predetermined locations according to the test plan; The wireless sensors were located on top of the roof, along the height of the towers, and top of the dome whereas the Laser Vibrometers were reflected to the Diaphragms to study the flexibility and also to determine the modal frequencies of the Diaphragms. The computer program ARTEMIS version 4, was used to perform the system identification of the structure. The software allows to develop a 3D model of the structure and test points; the resulting mode shapes are displayed using this geometry. Two different techniques were used for modal identification: the Enhanced Frequency Domain Decomposition (EFDD) and the Stochastic Subspace Identification (SSI). These two modal identification techniques were used to cross-validate the results. The joint analysis of the signals measured in various strategic points of the structure made it possible to identify the modal configurations and the corresponding natural frequencies. As the results of this study, the vibration modes of the main building, towers and dome in translational and torsional directions, as well as the motions of the diaphragms were discussed. Also, the natural frequencies and corresponding dynamic mode shapes were presented.

**Keywords** Ambient vibration test · Modal analysis · Cathedral · Mode shape · Frequency

### 9.1 Introduction

Ambient Vibration Tests (AVTs) are widely used for system identification and damage detection in the structures [1]. Elyamani et al. [2] and Turek et al. [3] used this technique for model updating and modal analysis of cathedral structures before, respectively. The current study focuses on a series of Ambient Vibration Test those were conducted at the Guayaquil Metropolitan Cathedral, located in Guayaquil, Ecuador in order to determine the modal frequencies and the mode shapes of the structure. The sensors were placed on predetermined locations according to the test plan; on the roof of the building, on the towers, on the dome and inside the cathedral at the level of diaphragms. A series of vibration tests were then carried out using velocity sensors and laser vibrometers on October 31st to November 3rd, 2018. The main purposes of the AVTs were to determine the fundamental frequency and corresponding mode-shape of the towers in the current condition, as well as to estimate the site period.

The Metropolitan Cathedral of Guayaquil (officially San Pedro Cathedral) is located in the Guayaquil downtown, near the Seminary Park. It was originally built by wood around 1547 next to the Municipal Palace and in the “Plaza de Armas”, (nowadays Seminary Park). The temple was destroyed by a fire in 1692 and maintained the simple colonial style for long time until the twentieth century. It was rebuilt by reinforced concrete materials between 1924 and 1937 in neo-Gothic style.

---

M. Motamedi (✉) · C. E. Ventura  
Department of Civil Engineering, University of British Columbia, Vancouver, BC, Canada

O. Lara · J. H. Barredo  
Sismica Ingenieros Consultores, Guayaquil, Ecuador

On the facade of the original church, there was a carved wooden medallion with the image of the Apostle Santiago, patron of Guayaquil, which was removed from the old church and placed in the Office of the Mayor of Guayaquil, in the Municipal Palace of Guayaquil as decoration. The Cathedral has attached to the Archbishop's Palace of Guayaquil and the offices of the metropolitan curia, also in neo-Gothic style [4].

After the Ecuador Earthquake in 2016, the Cathedral suffered some damages in the structural and non-structural components. The Archdiocese of Guayaquil has repaired the damaged non-structural components and has carried out some studies on the structural components. This paper describes the ambient vibration tests and modal analysis that serves as the basis of the cathedral structure assessment proposal which is still under review by the Archdiocese [4].

## 9.2 Ambient Vibration Tests

AVTs were conducted at the Cathedral structure from October 31st to November 3rd, 2018 in order to determine the dynamic modal properties (modal frequencies and mode shapes) of the structure. The starting and ending time of the test setups, number of the sensors in each setup, recording time for each setup, and the average temperature at the time of the tests are presented in Table 9.1 [4].

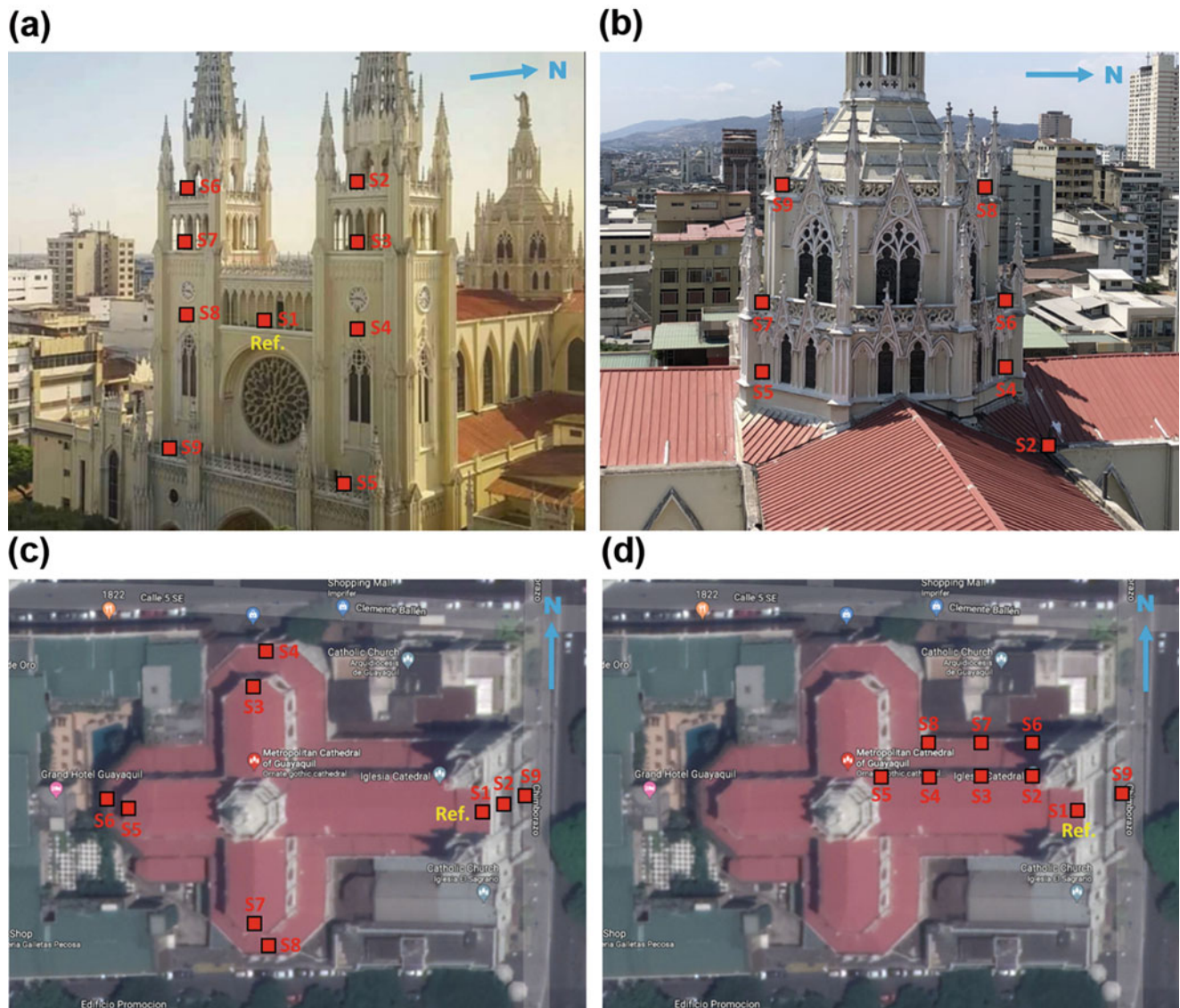
The testing program consisted of five measurement tests: Test 1 with four setups on the Towers, on the roof of the Main Building, and on the Dome using Tromino sensors; Test 2 was including five setups inside the Cathedral on the end walls in the North wing, East and West wings using Laser Vibrometers; Test 3 was including six setups inside the building on the North wall along the building using Laser Vibrometers; Test 4 was including two setups inside the building on the end walls of East and West wings using Laser Vibrometers; Test 5 including three single station Tromino sensors on ground inside and outside of the building to determine the site response. Figure 9.1 shows the layout of the measurement setups in the Test 1.

Tromino<sup>®</sup> velocity/acceleration sensors [5] were used to carry out AVTs in Test 1 and Test 5. The collected records were time synchronized with a radio antenna and amplifier in each sensor. This allowed the synchronization of the recordings both within each measurement setup and between setups. The Tromino sensors are suitable for high-resolution ambient vibration tests as they are fully portable, wireless, compact, and light instruments. Each sensor is equipped with two sets of three orthogonal high-resolution electro-dynamics sensors (high gain and low gain velocity meter) and one set of three orthogonal digital accelerometers with a frequency range of 0.1–300 Hz. For these tests the high-gain velocity data was used for the modal identification process. The sampling frequency of the recordings at each setup in Test 1 was 128 samples per second (sps), and the total recording duration for each setup was about 30–40 minutes. This testing approach allows to capture the most important vibration modes up to a frequency of about 64 Hz. The North component of each sensor was oriented to the North direction of the site for all setups. One stationary reference sensor was used for all setups in Test 1.

Laser Vibrometer System [6] was employed for ambient vibration measurements in Test 2, Test 3 and Test 4. These tests mainly used to identify the modal properties of the diaphragms. Vibrometer System is consisting of two Laser camera units that reflect Laser beam to the targets, and two controllers that record the signals receive from the subject. Figures 9.2 and 9.3 show the Laser targets layout on North diaphragm and South diaphragm, respectively. The sampling rate for Laser Vibrometers were 240 Hz.

**Table 9.1** Test information for each setup

	Test 1	Test 2	Test 3	Test 4	Test 5
Date of the test	October 31st	November 1st	November 2nd	November 2nd	November 3rd
Time of the test	11:13 to 14:10	20:50 to 22:15	12:45 to 16:48	19:00 to 19:42	8:18
Instrument type	Tromino	Laser Vibrometer	Laser Vibrometer	Laser Vibrometer	Tromino
Number of the setups	4	5	6	2	3
Number of the sensors	9	2	2	2	1
Recording duration (min.)	30–40	9.1	9.1	9.1	20
Temperature (°C)	25	26	31	24	23



**Fig. 9.1** Location of the Tromino sensors in Test 1: (a) on the Towers (Setup 1), (b) at the Dome (Setup 4), (c) at the roof levels (Setup 2), (d) at the roof levels (Setup 3)

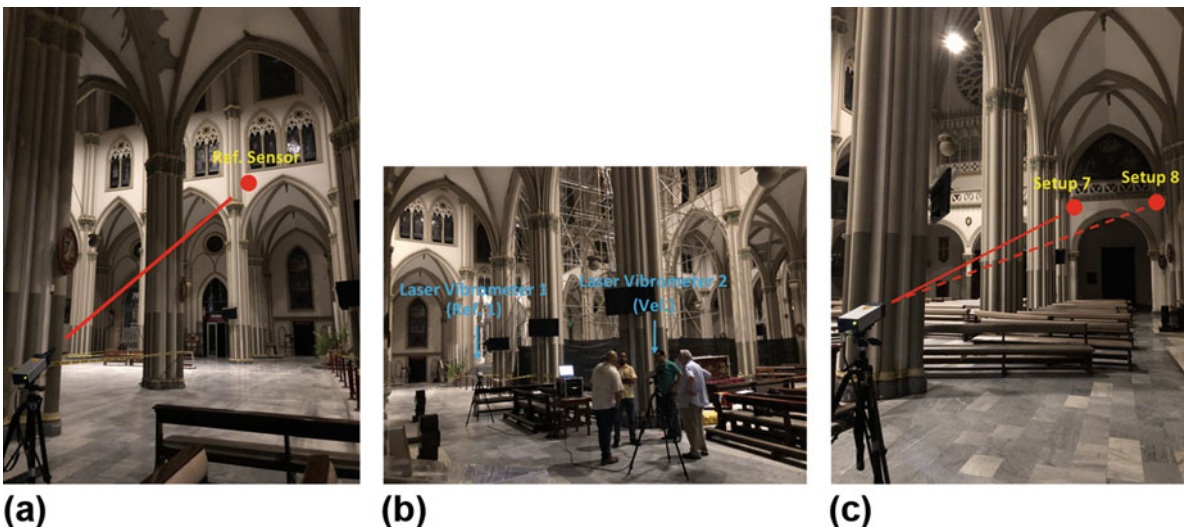
### 9.3 Methodology and Data Processing

The computer program ARTEMIS version 4 [7], was used to perform the modal identification of the structure. The software allows the user to develop a 3D model of the structure and test points; the resulting mode shapes are displayed using this geometry. Two different, complementary techniques are usually used for modal identification [8]: the Enhanced Frequency Domain Decomposition (EFDD) and the Stochastic Subspace Identification (SSI). These two modal identification techniques are used to cross-validate the results. The joint analysis of the signals measured in various strategic points of the structure makes it possible to identify the modal configurations and the corresponding natural frequencies.

The EFDD technique is an enhanced frequency domain method and the procedure consists of decomposing the system output into a set of systems of a specific degree of freedom, which are independent for each mode. The singular values are estimated from the spectral density of the specific degree of freedom system and the configuration of the modes is estimated from the singular vectors by selecting the highest peaks of the responses. The SSI technique is a time domain method which consists of adjusting a parametric model to the time series recorded by the sensors. SSI method takes a matrix of the time history data, and performs a series of geometric manipulations which results in a set of mathematical models that represent the system that produces the data; the analysis provides modes based on those models. The advantage of the SSI is more



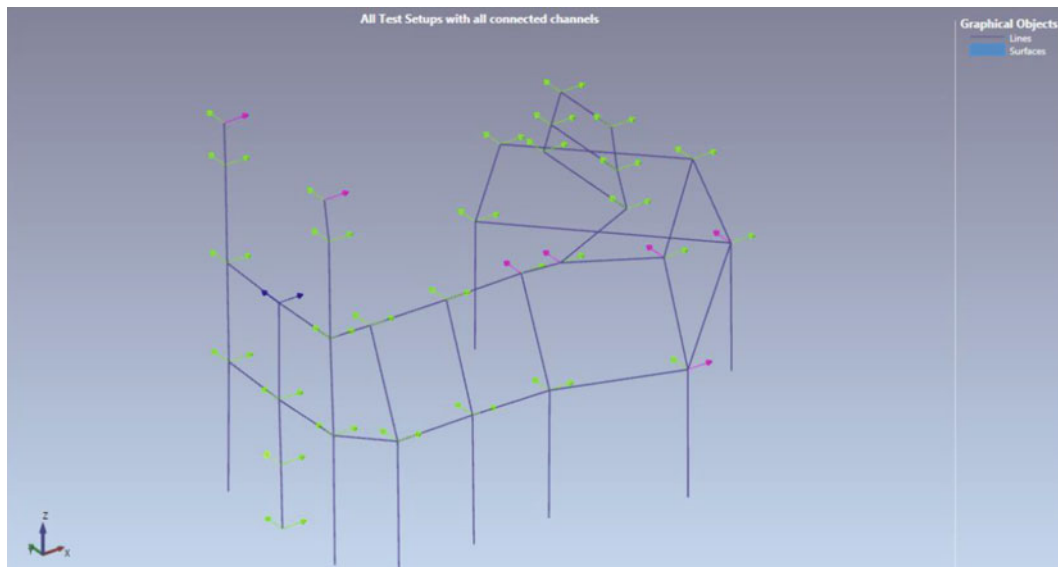
**Fig. 9.2** Location of the Laser Vibrometers' target in Test 3 at the North Diaphragm (Setups 1–6)



**Fig. 9.3** Location of the Laser Vibrometers' target in Test 4 at the South Diaphragm (Setups 7 and 8): (a) Location of reference sensor at West side; (b) Laser Cameras Station; (c) Location of Laser targets at East side

accurate modal estimations, especially in the lower frequencies when the data is properly decimated. The disadvantage is that the SSI method takes a considerable amount of time for analysis, and is not easily applied to broadband data. In contrast, the FDD method is very quick and allows for the user to pick modes anywhere in the frequency range of interest.

Ambient vibration data recorded on and off the Cathedral contains both noise and the response of the structure under ambient vibrations. The noise component of the recorded data is mainly due to mechanical imperfections in the sensors, instrument noise, installation, and other aspects in the sensor such as digitalization. The noise components of the vibration data, by its nature, usually appear as a random phenomenon in the data; however, the response of the Control Tower is not random, but consistent at certain frequencies due to resonance effects of the Control Tower to environmental excitations. Removing the noise components from the data is generally achieved by using signal processing tools such as decimation,



**Fig. 9.4** 3D ARTeMIS Full Model showing the location of the measurement points of the Cathedral structure

filtering, and data averaging. In order to identify the modal properties of the Cathedral structure correctly, the Towers Structure and the Dome were analyzed separately. To study the modal properties of the structure, the Full Model, including the Main Building, Towers Structure and the Dome, was also considered, and analyzed, as illustrated in Fig. 9.4.

The data collected at all measurement locations was processed and analyzed with ARTeMIS Modal. A 3D model (for animation purposes only) of the Structure was created using the structural geometry provided by Sismica Ingenieros Consultores. The model includes the discretized locations of measurement points on the structure. The blue arrows represent the location and orientation of the reference sensor for setups 1–4, while the green and pink arrows represent the location and orientation of the roving sensors. This estimation would be correct since the readings from all of the sensors had been fully synchronized. Therefore, this method would provide a reliable estimation of a mode shape.

## 9.4 Test Results

The results of the Cathedral structure analysis are presented in this section for the Main Structure, Towers Structure and the Dome, separately.

### 9.4.1 Main Building

The results of the analysis using the Enhanced Frequency Domain Decomposition method (EFDD) are shown in Fig. 9.5. This figure shows a plot of the spectral density of the peak singular values of all the data from setups 3 as a function of frequency. The peak values in this plot can be associated to dominant frequencies in the datasets, and some of these correspond to modal frequencies. However, the results of the analysis of the data using the SSI method can be used to determine with greater certainty the most dominant frequencies in the dataset.

Based on this analysis, the predominant frequency (the first natural frequency) of the structure is estimated to be 1.50 Hz, and it corresponds to the fundamental mode of the Main Building in the North-South direction. The corresponding mode-shape is shown in Fig. 9.6. Table 9.2 summarizes the modal frequencies extracted from the vibration data for which the confidence on the results is high from both the EFDD and SSI-UPC methods.

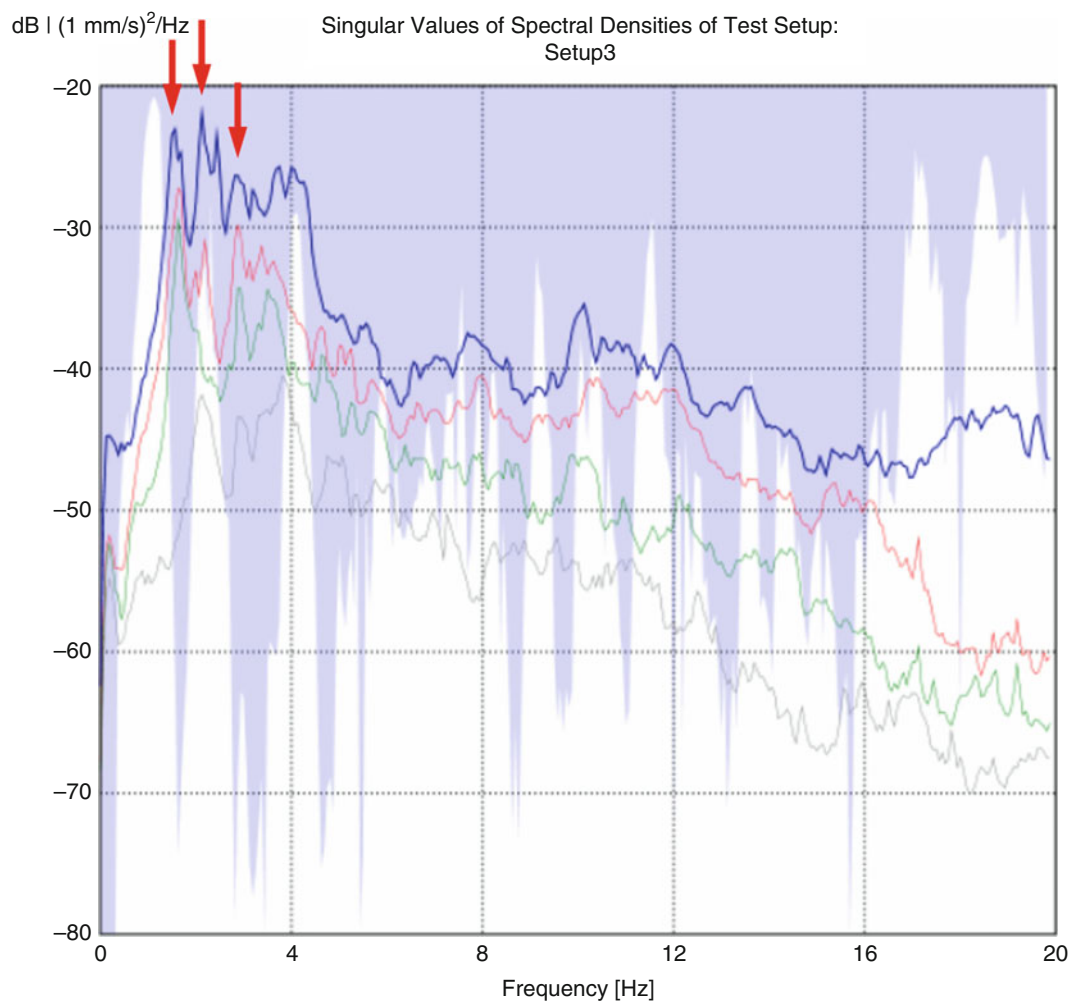


Fig. 9.5 Singular values of spectral densities of the structure in the frequency range of 0–20 Hz

#### 9.4.2 Towers Structure

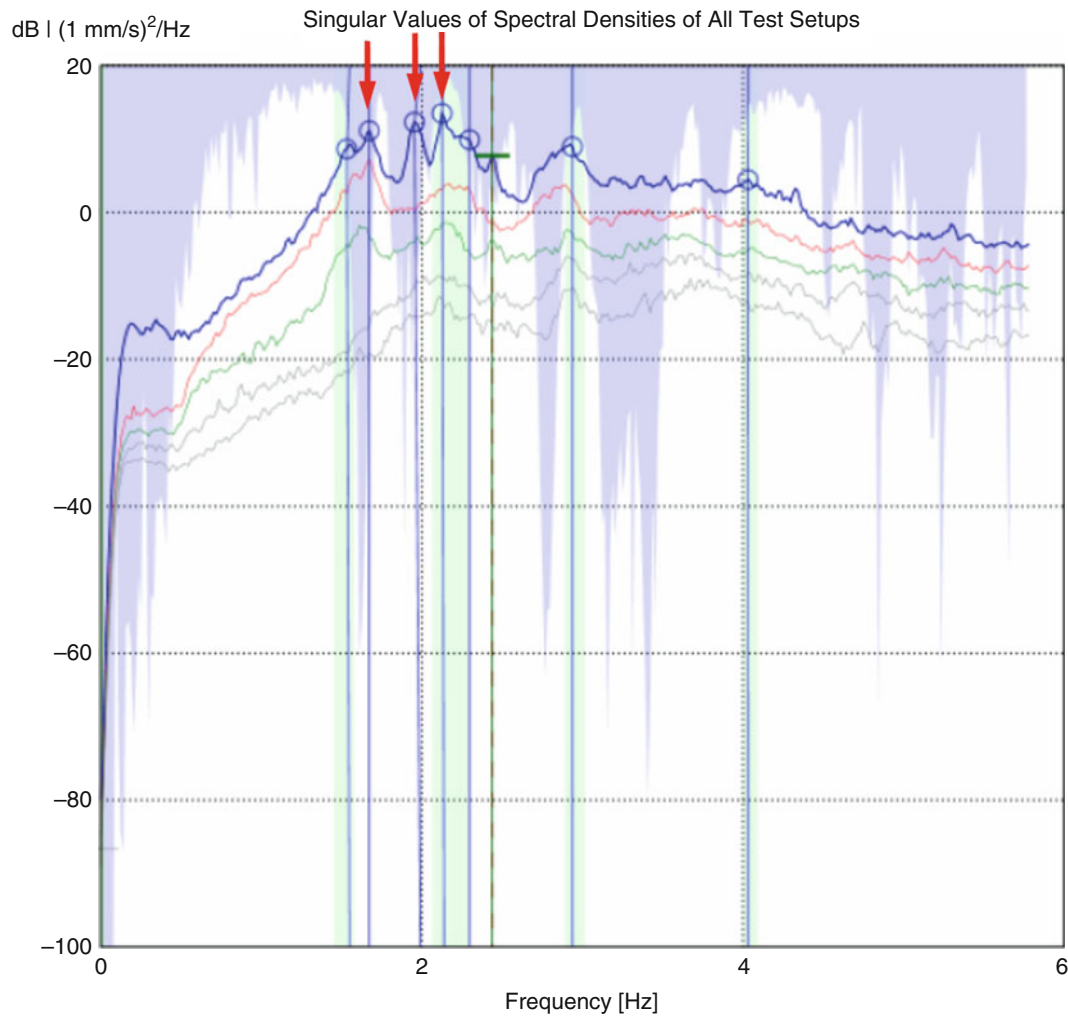
In order to identify the modal frequencies and mode shapes of the Towers Structure, the full model including the Towers Structure was used for modal analysis. Figure 9.6 shows the plot of the spectral density of the peak singular values of all the data from all setups as a function of frequency.

Figure 9.7 shows the Stabilization Diagram of all the data from setup 4. The vertical red dotted lines indicate the frequencies at which the modal frequencies are stable and can be associated to natural modes of the structure. By combining the results from both methods, it is possible to determine what peaks in Fig. 9.8 are associated to modal frequencies of the Towers [8]. The corresponding mode-shapes are shown in Fig. 9.8. Table 9.3 summarizes the modal frequencies extracted from the vibration data for which the confidence on the results is high from both the EFDD and SSI-UPC methods.

#### 9.4.3 Dome Structure

In order to identify the modal frequencies and mode shapes of the Dome, the full model including the Dome Structure was used for modal analysis. Figure 9.8 shows the plot of the spectral density of the peak singular values of all the data from all setups as a function of frequency.

The corresponding mode-shapes of the Dome are shown in Fig. 9.9. Table 9.4 summarizes the modal frequencies extracted from the vibration data for which the confidence on the results is high from both the EFDD and SSI-UPC methods.



**Fig. 9.6** Singular Values of Spectral Densities of the Full Model to identify the modal properties of the Towers Structure in the frequency range of 0–6 Hz using EFDD Method

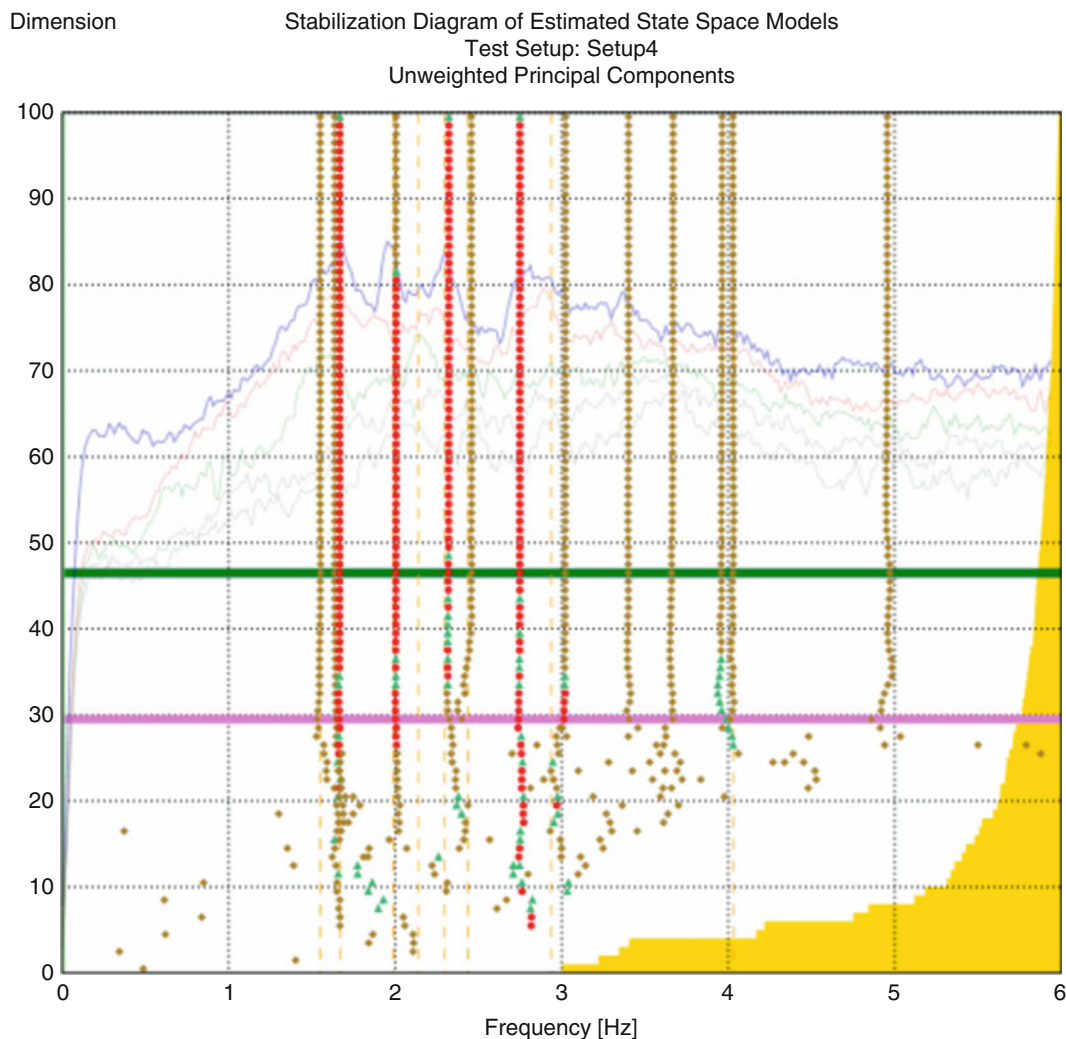
**Table 9.2** Modal frequencies of the Main Building obtained from modal analysis estimated by EFDD and SSI methods (Hz)

	EFDD method	SSI – PC method	Direction of the mode
1st mode	1.54	1.50	North-South
2nd mode	1.625	–	East-West
3rd mode	3.18–3.37	–	Torsion

#### 9.4.4 North Diaphragm in the East Wing Using Laser Vibrometers

In order to identify the modal frequencies and mode shapes of the North Diaphragm, an individual model including the North side wall (as shown in Fig. 9.2) was used for modal analysis. Figure 9.9 shows the plot of the spectral density of the peak singular values of all the data from all setups as a function of frequency. Figure 9.10 shows the Stabilization Diagram of all the data from setup 1.

The corresponding mode-shapes of the North Diaphragm are shown in Fig. 9.11. Table 9.5 summarizes the modal frequencies extracted from the vibration data for which the confidence on the results is high from both the EFDD and SSI-UPC methods.



**Fig. 9.7** Stabilization Diagram of Estimated State Space Models of the Full Model. This plot is for the Unweighted Principal Components (UPC) Test Setup 4 in the frequency range of 0–6 Hz

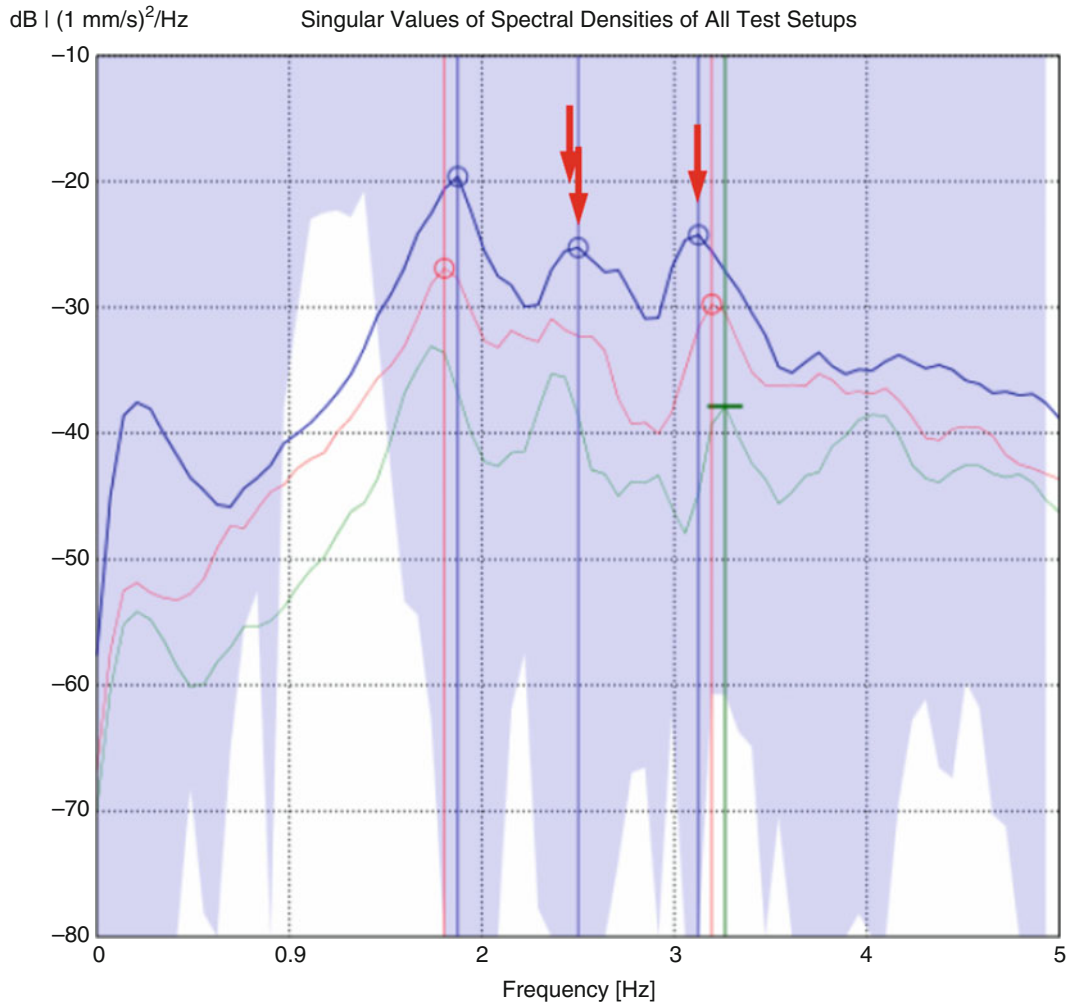
#### 9.4.5 South Diaphragm of the East Wing

In order to study the behavior of the South Diaphragm, an individual model including the East side Wall and West side Wall (as shown in Figs. 9.3) was used for modal analysis. Figures 9.12 and 9.13 show the plot of the spectral density of the peak singular values of all the data from Setup 7 and Setup 8, respectively as a function of frequency.

Also, the Fast Fourier Transform functions of data from Reference Sensor and other Sensor in Setup 7 are shown in Figs. 9.14 and 9.15, respectively. The modal frequencies obtained from Setups 7 and 8 confirm the test results of the other tests and provide higher level of confidence for the modal properties; Main Building frequency in East-West direction ( $f_2 = 1.64$  Hz); Tower Structure ( $f_1 = 1.82$  Hz,  $f_2 = 2.125$  Hz); and Dome ( $f_1 = 2.81$  Hz,  $f_2 = 2.875$  Hz,  $f_3 = 3.62$  Hz).

The measurements in Setups 7 and 8 show that the vibration of West side and East side of the South Diaphragm is not in the same order. The displacement of the West side was measured 3.5 times larger than the East side of the diaphragm. This observation confirms that the diaphragms in the Church are flexible and there is a potential risk of failure in diaphragm corners.





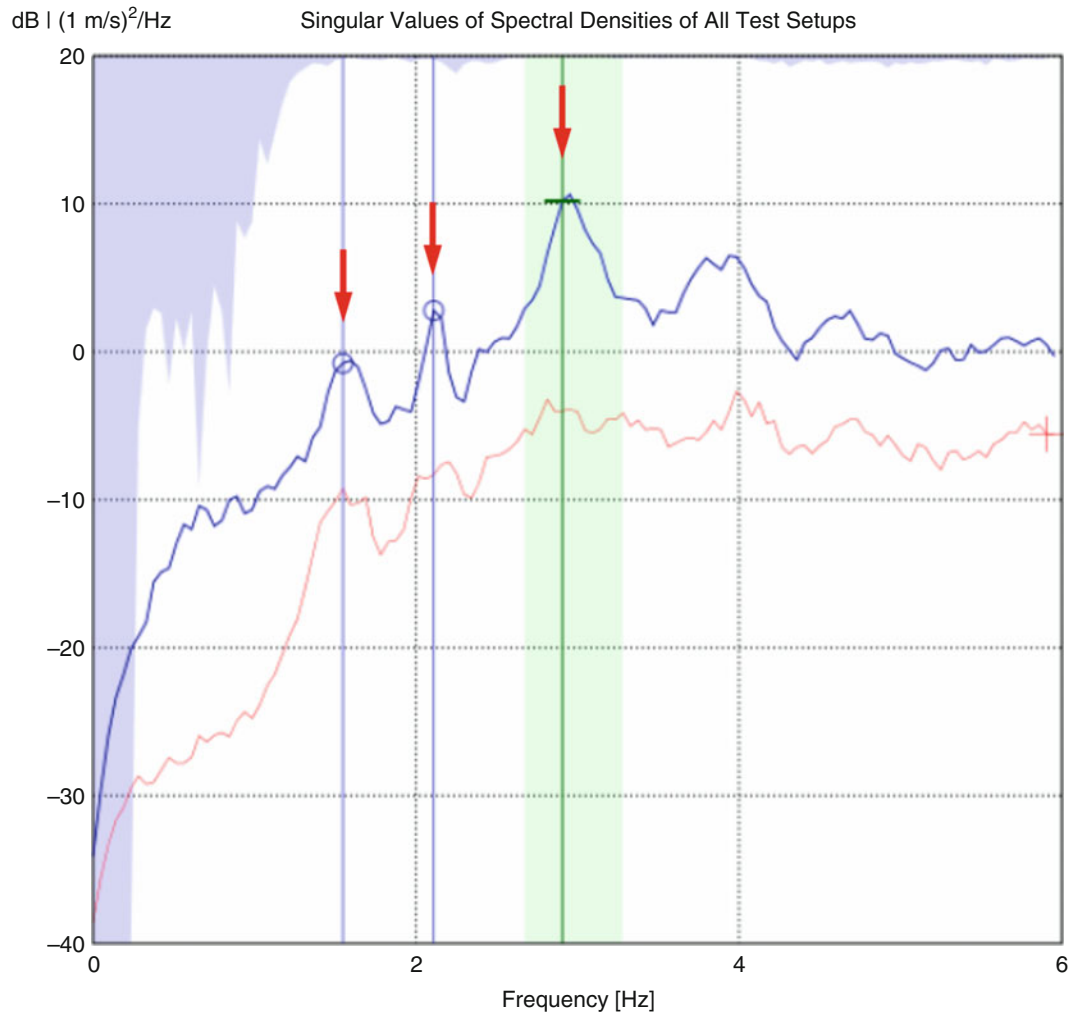
**Fig. 9.8** Singular Values of Spectral Densities of the Full Model to verify the modal properties of the Dome in the frequency range of 0–5 Hz using EFDD Method

**Table 9.3** Modal frequencies of the Towers Structures obtained from modal analysis estimated by EFDD and SSI methods (Hz)

	EFDD method	SSI – PC method	Direction of the mode
1st mode	1.50	1.610	North-South
2nd mode	1.938	1.990	East-West
3rd mode	2.125	2.138	Torsion

### 9.4.6 Site Response Analysis

The single instrument recording technique was used for site period estimation via horizontal-to-vertical (H/V) spectral ratio analysis [9]. A three-component ambient vibration recording was performed using three sensors that were placed on the ground inside the cathedral and also on the site nearby the Cathedral (at the Parque Seminario). The orientation of the sensors was consistent and was parallel to North direction. The GEOPSY software was used for modal analysis in frequency domain [10]. The observed response of the peak frequency suggests consistent ground conditions around the Cathedral. The peak frequency at the site ranges between 0.72 and 0.92 Hz (The average is 0.92 Hz (T = 1.087 Sec.)).



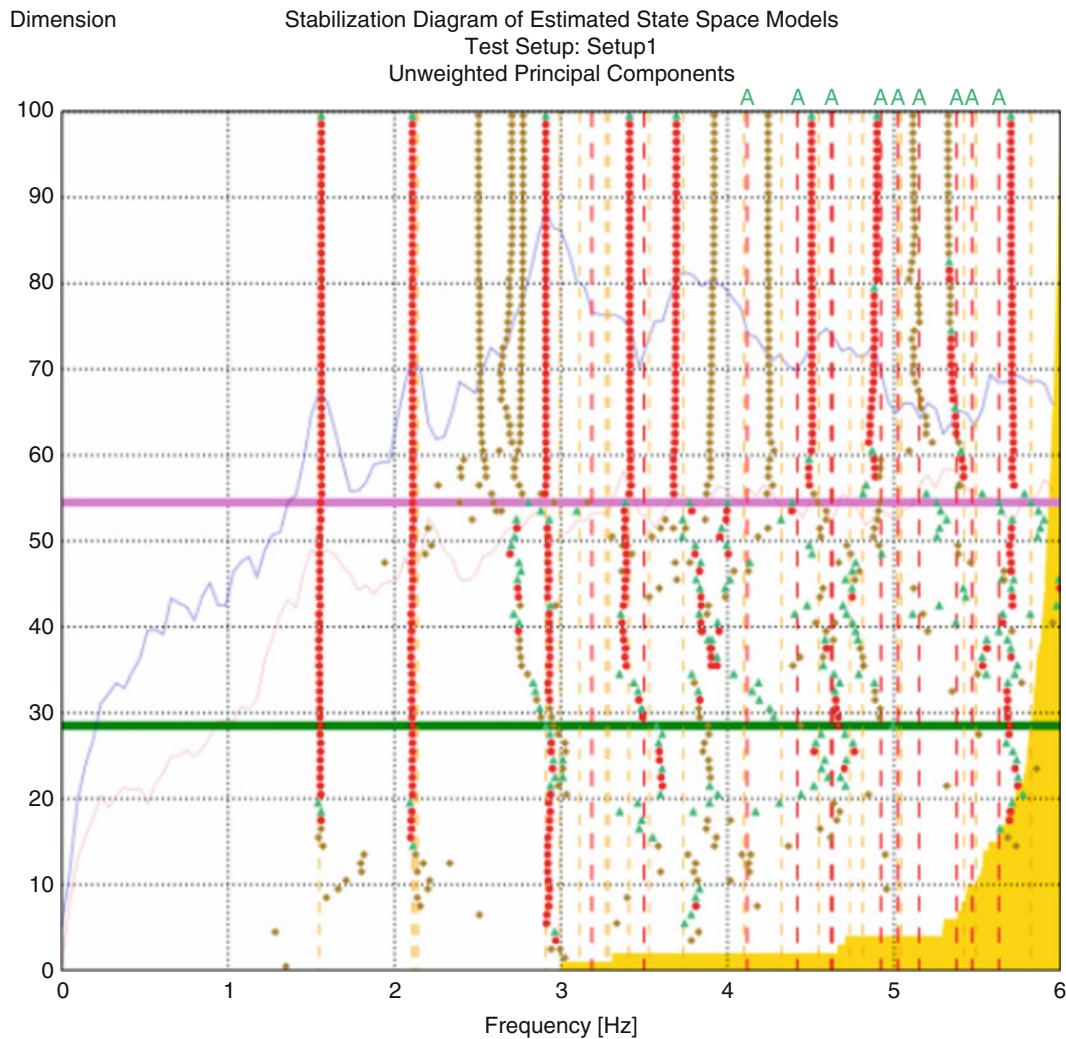
**Fig. 9.9** Singular Values of Spectral Densities of data setups 1–6 of Test 3 to identify the modal properties of the in-plane motion of the North diaphragm in the frequency range of 0–6 Hz using FDD Method

**Table 9.4** Modal frequencies of the Dome from modal analysis estimated by EFDD and SSI methods (Hz)

	EFDD method	SSI – PC method	Direction of the mode
1st mode	2.813	–	North-South
2nd mode	2.875	2.938	East-West
3rd mode	3.688	–	Torsion

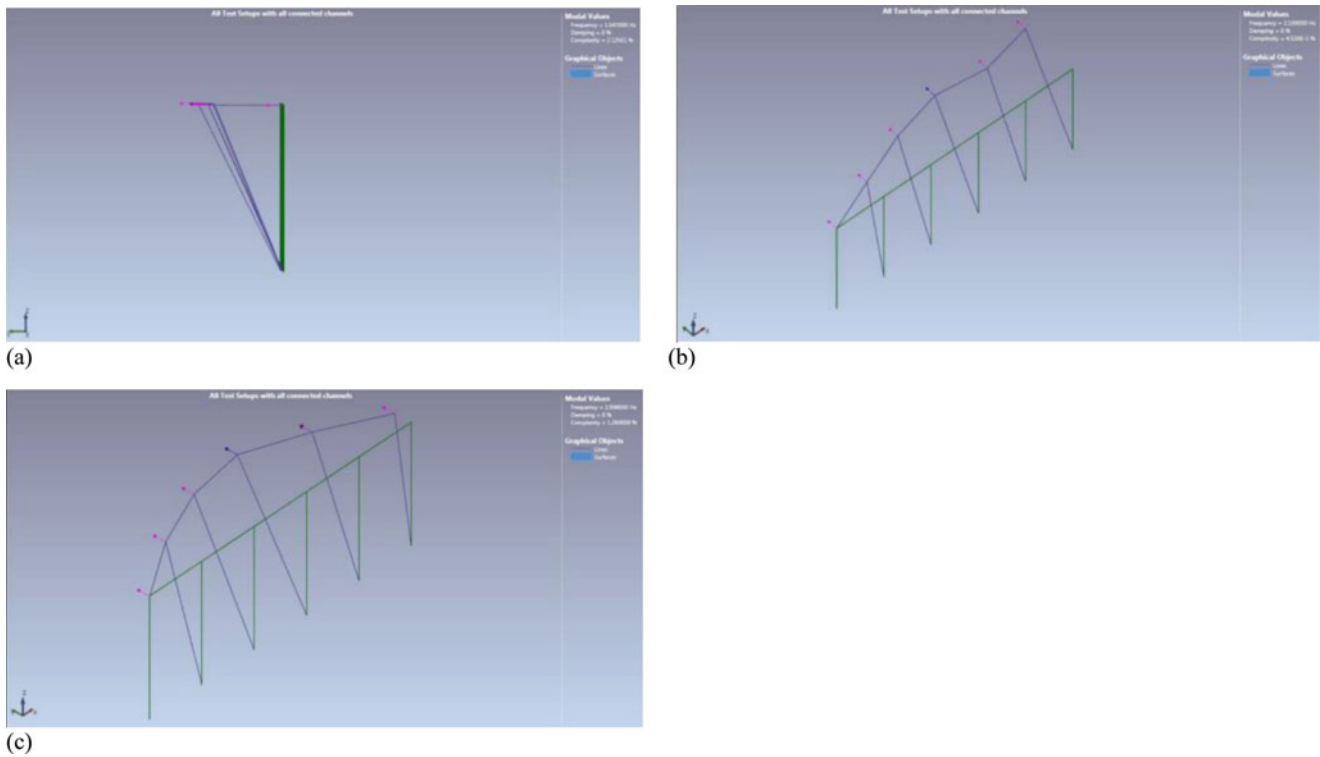
## 9.5 Conclusion

A series of Ambient Vibration Tests was conducted on the Guayaquil Metropolitan Cathedral from October 31st to November 3rd, 2018. The testing program consisted of five Tests using wireless digital seismometers and Laser Vibrometers placed on the roof of the Main Building, on the Towers structure, the Dome and reflected to the Diaphragms. Vibration of the structure was recorded for approximately 30–40 minutes in each setup for seismometers and 9 minutes for Laser Vibrometers. To identify the modal properties of the structure, the Towers, the Dome and the Diaphragms were analyzed separately. The



**Fig. 9.10** Stabilization Diagram of Estimated State Space Models of Test 3. This plot is for the Unweighted Principal Components (UPC) in Test Setup 1 in the frequency range of 0–6 Hz

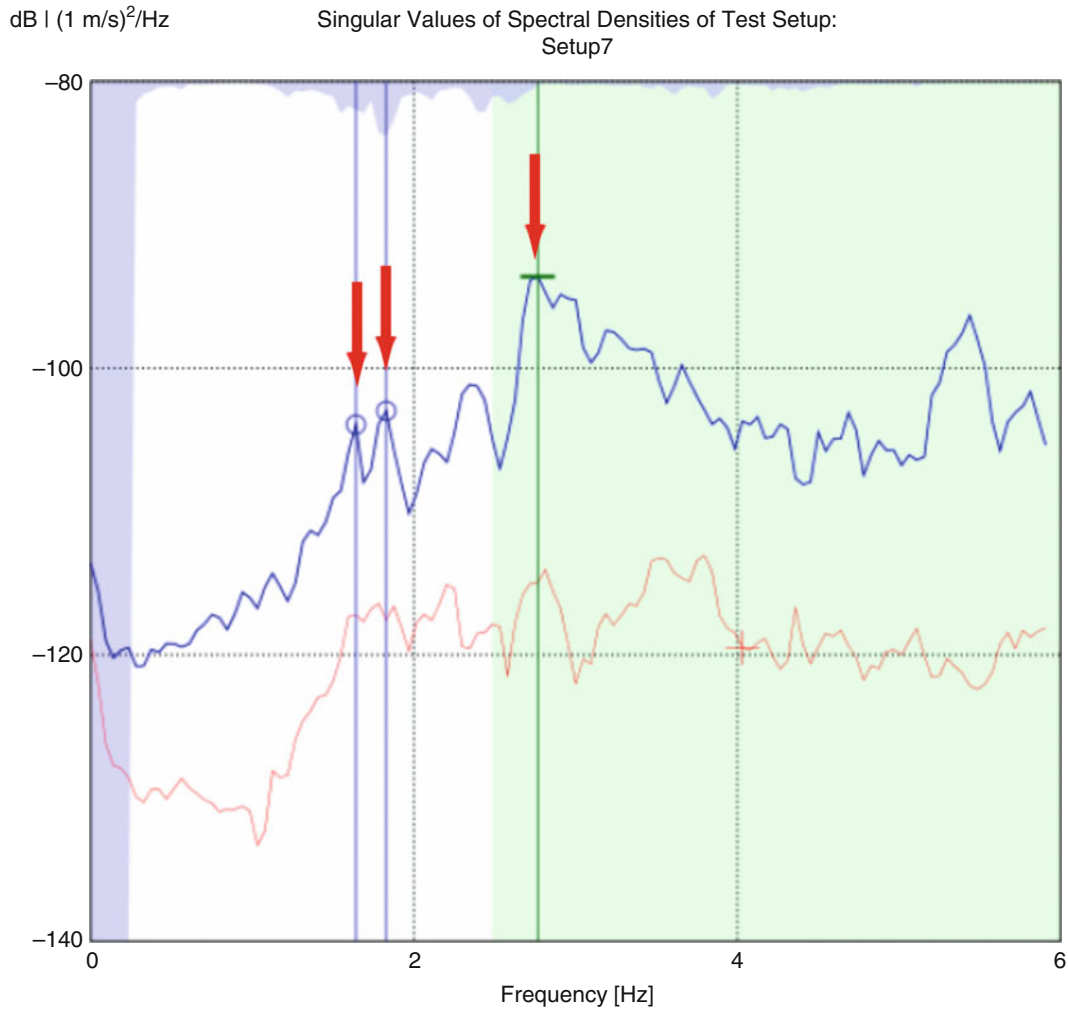
results from modal analysis indicated that the frequencies of the Main Building are 1.54 Hz and 1.64 Hz in North-South and East-West direction, respectively. The fundamental frequency of the Towers Structure in the North-South direction was identified as 1.50–1.61 Hz. The modal frequencies corresponding to the second and third modes of vibration are 1.938 Hz in East-West direction and 2.125 Hz in Torsional direction, respectively. The frequencies of the Dome were also identified as 2.813 Hz, 2.875 Hz, and 3.688 Hz for the first mode (North-South), second mode (East-West), and the third mode (Torsion), respectively. The analysis of data extracted from Laser Vibrometers on North Diaphragm indicates that the diaphragm is flexible and the frequency of in-plane bending mode is 2.95 Hz in North-South direction. The identified frequencies and periods of the Main Building, Towers Structure, and the Dome of the Cathedral are summarized in Table 9.6. The main direction of the associated mode shapes is also included in the table. The main direction of the associated mode shapes are also included in the table. By analyzing the site response, the average peak frequency of the H/V curves at the site was determined as 0.92 Hz.



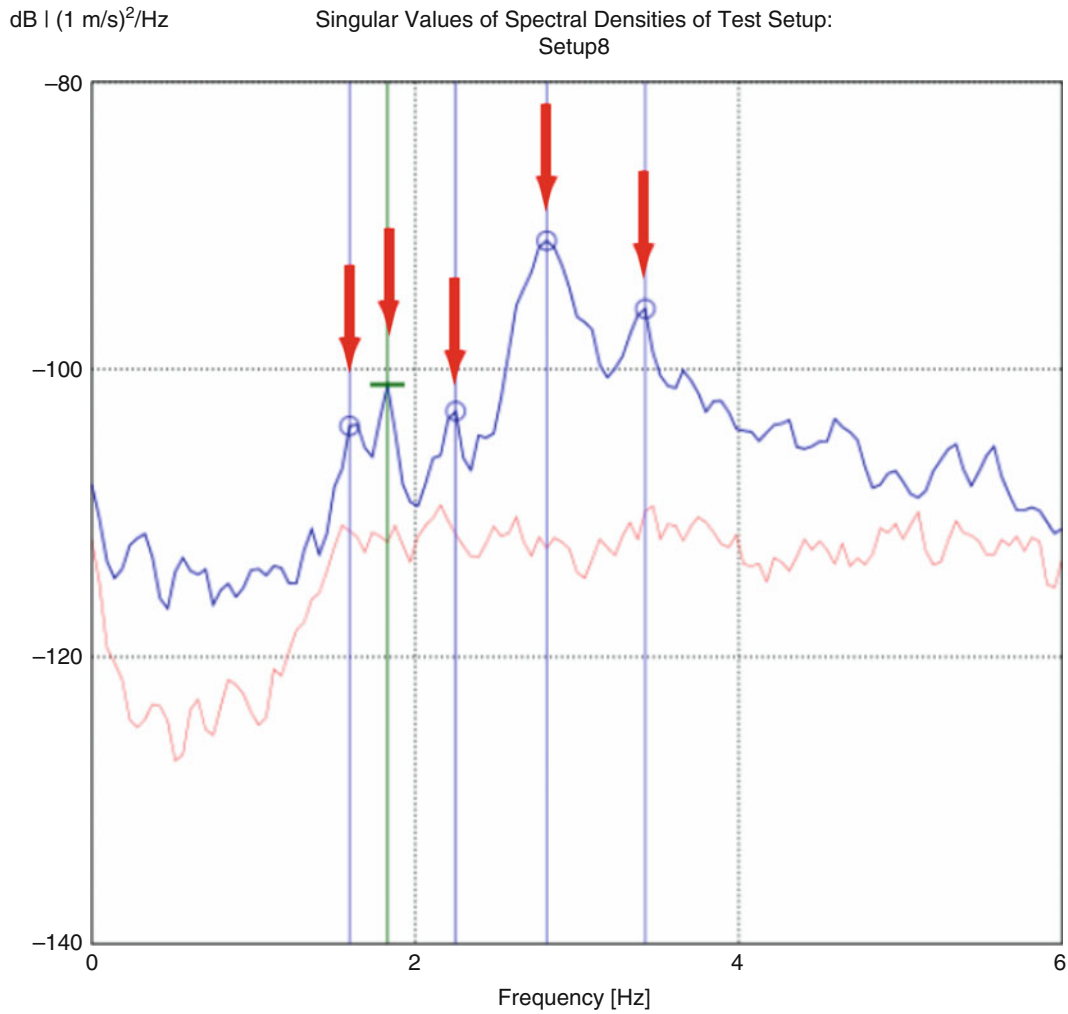
**Fig. 9.11** Mode shapes of the North Diaphragm in East wing: (a) Confirmation of the 1st mode of the building in Translational (North-South) direction-Elevation view ( $F = 1.55$  Hz); (b) 2nd mode of the building in Torsional motion of the East wing-Perspective view ( $F = 2.11$  Hz); (c) In-plane mode of the diaphragm at Elevation 15.7 m – Perspective view ( $f = 2.95$  Hz)

**Table 9.5** Modal frequencies of the North Diaphragm of the East wing estimated by FDD and SSI methods (Hz)

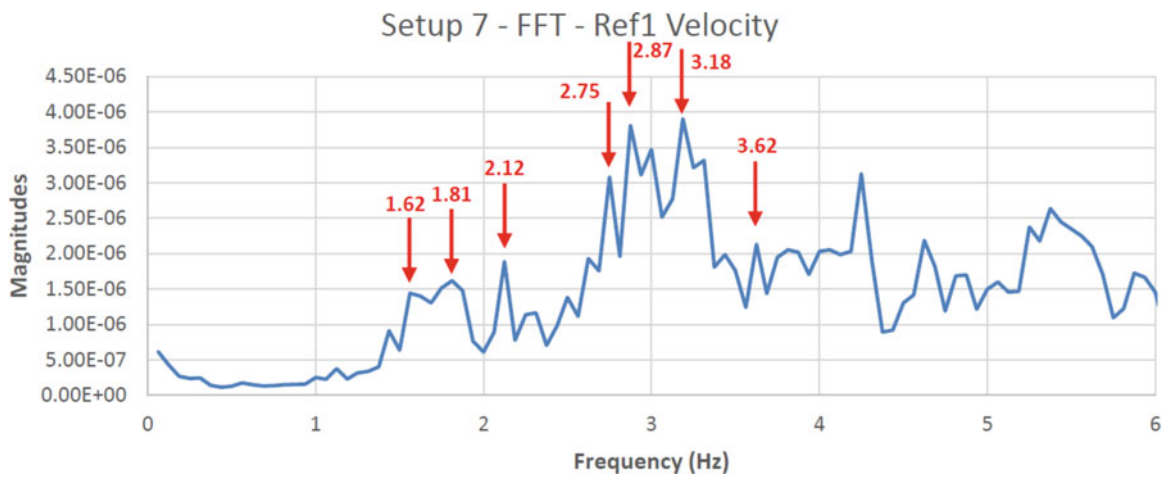
	FDD method	SSI – UPC method	Direction of the mode
1st mode	1.54	1.56	Translational (North-South) of the whole building (Confirmation of the Test 1 results)
2nd mode	2.11	2.11	Torsional of the East wing of the building
3rd mode	2.95	2.91	Out-of-Plane motion of North wall (In-plane motion of the diaphragm at elevation 15.7 m)



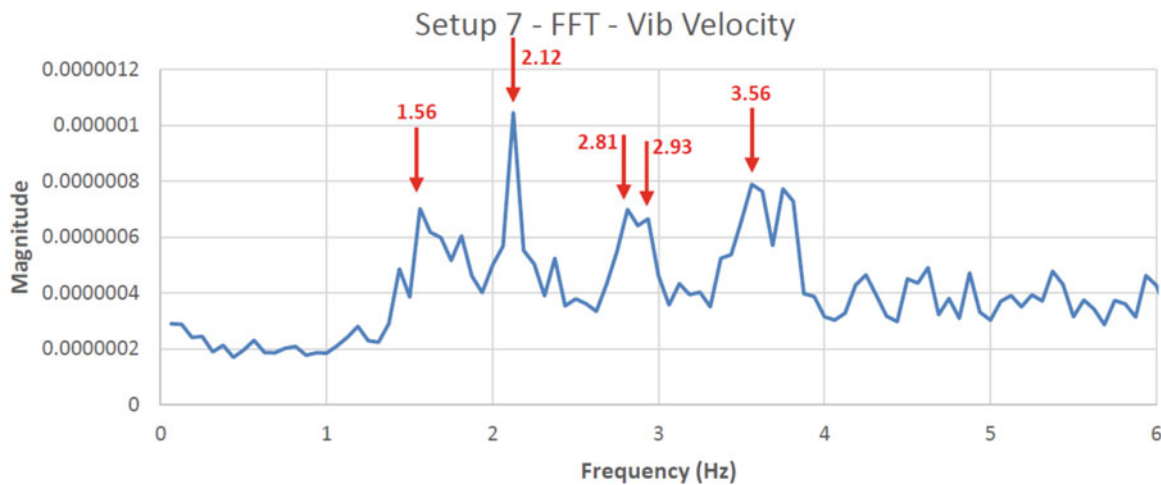
**Fig. 9.12** Singular Values of Spectral Densities of Setup 7 of Test 4 to identify the modal properties of the South diaphragm in the frequency range of 0–6 Hz using FDD Method ( $f_1 = 1.64$  Hz  $f_2 = 1.828$  Hz  $f_3 = 2.766$  Hz)



**Fig. 9.13** Singular Values of Spectral Densities of Setup 8 of Test 4 to identify the modal properties of the South diaphragm in the frequency range of 0–6 Hz using FDD Method ( $f_1 = 1.594$  Hz  $f_2 = 1.828$  Hz  $f_3 = 2.25$  Hz  $f_4 = 2.812$  Hz  $f_5 = 3.422$  Hz)



**Fig. 9.14** Fast Fourier Transform of Ref. [1] sensor of Setup 7 in Test 4



**Fig. 9.15** Fast Fourier Transform of Vel. 1 sensor of Setup 7 in Test 4

**Table 9.6** Summary of modal periods obtained from the ambient vibration tests

	Church component	Mode No.	Frequency (Hz)	Period (Sec.)	Mode & direction	
Global vibration modes	Whole structure	1st mode	1.54	0.649	Translational (North-South)	
		2nd mode	1.64	0.610	Translational (East-West)	
		3rd mode	3.18–3.37	0.314–0.297	Torsion	
Local vibration modes	Towers Structure	1st mode	1.50–1.61	0.666–0.621	Translational (North-South)	
		2nd mode	1.938	0.516	Translational (East-West)	
		3rd mode	2.125	0.471	Torsional	
	Dome Structure	1st mode	2.813	0.355	Translational (North-South)	
		2nd mode	2.875	0.348	Translational (East-West)	
		3rd mode	3.688	0.271	Torsional	
	North diaphragm (at elevation 15.7)	1st mode	2.95	0.33	Out-of-plane (In-plane diaphragm) Single curvature bending mode in (North-South)	
	Site			0.92	1.087	Average of peak frequencies of H/V curves

## References

1. Peeters, B.: System identification and damage detection in civil engineering. Ph.D. Thesis, Katholieke University of Leuven, Belgium (2000)
2. Elyamani, A., Roca, P., Caselles, O., Clapes, J.: Seismic safety assessment of historical structures using updated numerical models: the case of Mallorca cathedral in Spain. *Eng. Fail. Anal.* **74**, 54–79 (2017)
3. Turek, M., Ventura, C.E., Placencia, P.: Dynamic characteristics of a 17th century church in Quito, Ecuador. In: Proceedings of SPIE, The International Society for Optical Engineering (2002)
4. Motamedi, M., Ventura, C.E.: Ambient vibration tests and modal analysis of Guayaquil Metropolitan Cathedral, Ecuador. University of British Columbia, Earthquake Engineering Research Facility, Project No. EERF 18-07, 2018
5. Micromed: Tromino: Portable ultra-light acquisition system for seismic noise and vibration- User's manual, Macromed, Italy (2012)
6. Polytec GmbH: Laser Doppler Vibrometer, Model OFC-505/503 User Manual, Polytec, Germany (2009)
7. Structural Vibration Solutions, A/S, "ARTeMIS Modal Software", Version 4, Denmark, Copyright 1998–2014
8. Brincker, R., Ventura, C.E.: Introduction to Operational Modal Analysis. Wiley, West Sussex (2015)
9. Crow, H., Hunter, J.: Shear wave velocity measurement guidelines for Canadian seismic site characterization in soil and rock. Open File Report 7078, Geological Survey of Canada, pp. 77–110, 2012
10. Geopsy, "Geopsy Manual", <http://www.geopsy.org/documentation/geopsy/>, Copyright 2006

**Mehrtash Motamedi** has PhD in Structural & Earthquake Engineering and currently is Research Associate and Earthquake Lab Manager of the Department of Civil Engineering at the University of British Columbia. He has been involved in ambient vibration tests and modal response analysis of many structures during past years.



# Chapter 10

## An Overview on Floor Vibration Serviceability Evaluation Methods with a Large Database of Recorded Floor Data

Mohammad Royvaran, Onur Avci, and Brad Davis

**Abstract** In this paper, the accuracies of four well-established floor vibration evaluation methods developed over the last couple of decades are investigated by comparing predictions with observed acceptability of each bay. A large database of steel-framed floors subjected to walking excitation is used for the evaluations and comparisons. Detailed comparisons have been made among the methods of the American Institute of Steel Construction (AISC) Design Guide 11 Chapter 4 Method; Steel Construction Institute (SCI) P354 Simplified Method; Steel Construction Institute (SCI) P354 Vibration Dose Values; and Human Induced Vibration of Steel Structures (HIVOSS) Method. The floor bay database is based on data collected from real buildings and it contains 22 satisfactory and 28 unsatisfactory bays, a total of 50 bays.

**Keywords** Floor vibration serviceability · Walking excitations · Floor vibrations · Steel framed floors · Vibration evaluation methods

### 10.1 Introduction

For steel framed gravity systems, floor vibrations serviceability has become a major limit state for design in the last couple of decades thanks to the use of slender structural members and high-strength materials [1–4]. For open floor plans, for lightly furnished electronic offices, especially in the lack of full-height partitions complaints on floor vibrations are often brought-up [5–9]. Human walking is the typical excitation on slender stairs [10–12] and elevated floors (and other slender civil structures) which has the potential to cause annoying vibrations for occupants [13–18]. While there are various type of excitations for various civil structures [19–27], the primary goal of this paper is to assess four very well-known and widely used vibrations serviceability evaluation methods for walking excitations, evaluating the accuracies by comparing the observed and predicted acceptability of 50 real floor bays. All of the bays are part of W-shaped steel framed buildings. Engineers in design offices are mostly interested in final result of an analysis method to see whether the bay in consideration is “satisfactory” or “unsatisfactory”; however, it is very important to know the level of performance and accuracy of the existing popular methods. The four widely used simplified methods included in this paper are:

- American Institute of Steel Construction (AISC) Design Guide 11 Chapter 4, by Murray et al. [28].
- Steel Construction Institute (SCI) P354 Simplified Method, by Smith et al. [29].
- Steel Construction Institute (SCI) P354 Vibration Dose Values, by Smith et al. [29].
- Human Induced Vibration of Steel Structures (HIVOSS) Method [30].

---

M. Royvaran · B. Davis  
Department of Civil Engineering, University of Kentucky, Lexington, KY, USA

O. Avci (✉)  
Civil, Construction and Environmental Engineering, Iowa State University, Ames, IA, USA  
e-mail: [oavci@iastate.edu](mailto:oavci@iastate.edu)



## 10.2 Prediction Methods for Floor Vibration Serviceability

The AISC Design Guide 11 Chapter 4 [28], often referred to as DG11, is extensively used in North America and in the world. In DG11 approach, the bay is idealized as a single degree of freedom system and the walking excitation is basically the product of the curve-fit by Rainer et al. [31] dynamic coefficients and weight of the walking person, as discussed in [32]. The bay evaluation criterion in DG11 is based on Eq. (10.1); the bay is “satisfactory” if the peak acceleration,  $a_p$ , remains below the tolerance limit,  $a_o$ .

$$\frac{a_p}{g} = \frac{P_o e^{-0.35 f_n}}{\beta W} \leq \frac{a_o}{g} \quad (10.1)$$

where;

$f_n$  = bay fundamental frequency, Hz

$\beta$  = critical damping ratio

$W$  = bay effective weight, lb

The second evaluation method is per the Steel Construction Institute (SCI) P354, *Design of Floors for Vibration: A New Approach* [29]. In this method, the bay is also idealized as a single degree of freedom system. Per the Simplified Method of Chapter 7, the floor bay evaluation is satisfactory if the response factor,  $R$ , does not exceed the tolerance limit:

$$R = \frac{a_{w,rms}}{0.005 \text{ m/sec}^2} \quad (10.2)$$

where  $a_{w,rms}$  is the frequency-weighted root mean square (rms) acceleration due to walking.

The third evaluation method, SCI P354 Vibration Dose Values Method accounts for the infrequent and/or short vibration events. It is known that the building occupants tend to tolerate higher levels of accelerations for relatively shorter activities; therefore, the floor is counted satisfactory when the VDV does not exceed the limit. The VDV is calculated per Eq. (10.3):

$$VDV = \left[ \int_0^T [a_w(t)]^4 dt \right]^{1/4} \quad (10.3)$$

where

$T$  = exposure duration, taken as 16 hours for daytime occupancy of a building, sec.

$a_w(t)$  = acceleration at time,  $t$ , m/sec.<sup>2</sup>

The fourth evaluation method is based on the Human Induced Vibrations of Steel Structures Vibration Design of Floors Guideline. The HIVOSS [30] “hand calculation method” has the tolerance limits expressed in terms of floor classes. The floors in Classes A through D are recommended for offices, floors in Class E are critical, and floors in Class F are not recommended. This method is also per the response of a single degree of freedom system. There are two analytical approaches in HIVOSS: the Dunkerley approach and the self-weight deflection approach. The modal mass for this method is calculated with Eq. (10.4).

$$M_{\text{mod}} = \mu \int \delta^2(x, y) dx dy \quad (10.4)$$

where

$\mu$  = distributed mass, kg/m<sup>2</sup>

$\delta(x,y)$  = unity-normalized mode shape value

Using the beam deflections ( $\delta_x$ ) and girder deflections ( $\delta_y$ ), for the bays analyzed in this paper, Eq. (10.5) is used:

$$M_{\text{mod}} = M_{\text{total}} \left( \frac{\delta_x^2 + \delta_y^2}{2\delta^2} + \frac{8}{\pi^2} \frac{\delta_x \delta_y}{\delta^2} \right) \quad (10.5)$$

where  $\delta$  is the sum of beam and girder deflections and  $M_{total}$  is the total weight (kg) of the bay. For bays with unequal girders,  $M_{mod}$  was calculated based on the girder with the lower frequency.

In an attempt to research the accuracy of the HIVOSS method, the following four combinations of frequency and modal mass calculations were studied.

- Combination 1:  $f_n$  is calculated with the self-weight approach from HIVOSS Appendix A.4 and  $M_{mod}$  is calculated per HIVOSS Appendix A.6.
- Combination 2:  $f_n$  is calculated with the Dunkerley approach from HIVOSS Appendix A.5 and  $M_{mod}$  is calculated per HIVOSS Appendix A.6.
- Combination 3: natural frequency,  $f_n$ , is calculated from self-weight approach from HIVOSS Appendix A.4, and modal mass,  $M_{mod}$ , is based on the effective weight calculated based on DG11 Chapter 4 ( $M_{mod} = W / 2 g$ ).
- Combination 4:  $f_n$  is calculated with the Dunkerley approach in HIVOSS Appendix A.5, and  $M_{mod}$  is based on the effective weight from DG11 Chapter 4.

### 10.3 Floor Database

The database contains 50 bays with 28 unsatisfactory and 22 satisfactory cases as summarized in Table 10.1. Most of the data in the database were collected by Dr. Thomas M. Murray of Virginia Tech. The rest are from Pabian [33] and Davis [1]. In Table 10.1, the level of complaints is reported for all bays. It should be noted that from Bay 2 to Bay 5, “CP” indicates that the bay was under construction and exhibited lively vibration due to walking. Meanwhile, the rest of the bays (Bay 1, and Bay 6 to Bay 50) support quiet areas, such as offices, universities, hospitals. Bays with “NC” codes are considered satisfactory; all other bays are considered unsatisfactory. It should also be noted that the level of complaints was reported after occupant interviews. With that, “NC”, “FC”, “SC”, “MC” codes correspond to “no complaints”, “few complaints”, “some complaints”, and “many complaints”, respectively. When a bay is in service for at least 5 years without any complaints, the bay is coded “no complaints”. In presence of complaints, the engineer-of-record, architect, or occupants contacted Dr. Thomas Murray and asked for assistance to alleviate human discomfort due to vibrations. For bare slabs, “SDL + LL = 0” is used.

### 10.4 Observed and Predicted Evaluations

While the observed evaluations are coded as OK or NG (No Good); the predicted evaluations are coded as OK, B (borderline), or NG. Below are short discussions for the four methods.

#### 10.4.1 AISC Design Guide 11 Chapter 4 Method

It is shown in Table 10.2 that DG11 evaluations were accurate for 90.9% (20 of 22 bays) of satisfactory bays and 89.3% (25 of 28 bays) of unsatisfactory bays. As a result, DG11 predictions were accurate for 90% (45 of 50 bays) of the bays in the database (inaccurate for 5 bays). The inaccurate predictions of AISC DG11 correspond to the cases where the predicted  $a_p$  values are close to the limit of 0.5%g. Meanwhile, it is shown in Table 10.2 that the inaccurate five cases correspond to the predicted  $a_p$  values of 0.540 (bay 33), 0.591 (bay 35), 0.452 (bay 41), 0.519 (bay 47), and 0.439 (bay 48).

#### 10.4.2 SCI P354 Simplified Method

Table 10.3 presents the results of the P354 Simplified Method. P354 provided accurate evaluations for 18.2% (4 of 22 bays) of satisfactory bays and 100% (28 of 28 bays) of the unsatisfactory bays. In total, it resulted in accurate predictions for 64.0% (32 of 50 bays) of the bays in the database. As a result, the method inaccurately evaluated the bays observed to be satisfactory and very accurately evaluated the bays observed to be unsatisfactory, indicating that the method is a bit on the conservative side. Since P354 Simplified Method resulted in conservative predictions, it was investigated more to increase its accuracy. It

Table 10.1 Floor database

Bay	Length		Floor size (Width × Length)		Beam spacing (ft)	Girder size (left, right) (if different)	Slab depth (total/deck) (in/in)	Conc. weight ( $w_c$ ) (pcf)	Conc. strength ( $f'_c$ ) (ksi)	SDL + LL (psf)	$\beta$ (DG11 & SCI)/ (HIVOSS) (%)	Complaints
	Beam (ft)	Girder (ft)	Beam size	Beam × Length								
1	32.8	21.3	120 × 50.5	W16 × 31	10.7	W16 × 31, Wall	5.6/3.0	115	3.50	21	3.0/3.0	FC
2	30.0	30.0	120 × 90	W16 × 36	10.0	W21 × 55	5.5/2.0	145	4.00	0	1.0/1.0	CP
3	30.0	30.0	47 × 90	W16 × 36	10.0	W21 × 55	5.5/2.0	145	4.00	0	1.0/1.0	CP
4	30.0	30.0	120 × 90	W16 × 36	10.0	W21 × 55	5.5/2.0	145	4.00	0	1.0/1.0	CP
5	30.0	30.0	120 × 60	W16 × 36	10.0	W21 × 62	5.5/2.0	145	4.00	0	1.0/1.0	CP
6	32.8	21.3	100 × 50.5	W16 × 31	10.7	W16 × 26, W16 × 40	5.6/3.0	115	3.50	21	3.0/3.0	SC
7	40.0	36.2	111 × 120	W16 × 31	9.04	W21 × 101	6.0/2.0	145	3.00	12	2.5/3.0	MC
8	31.1	36.2	64.3 × 111	W14 × 22	9.04	W21 × 93, Wall	6.0/2.0	145	3.00	12	2.5/3.0	NC
9	36.0	28.0	140 × 140	W16 × 31	7.0	W24 × 62, W24 × 68	4.5/2.0	110	4.00	0	1.0/1.0	MC
10	38.8	30.0	120 × 57	W18 × 40	10.0	Wall, W21 × 44	4.5/2.0	145	3.50	15	3.0/4.0	SC
11	42.0	30.0	120 × 42	W21 × 44	10.0	Wall, W21 × 50	4.5/2.0	145	3.50	15	3.0/4.0	SC
12	30.0	30.0	90 × 81	W16 × 26	10.0	W18 × 50, W21 × 50	5.25/2.0	110	4.00	0	1.5/1.0	SC
13	30.0	30.0	90 × 71.9	W16 × 26	10.0	W18 × 50, W21 × 50	5.25/2.0	110	4.00	0	1.5/1.0	SC
14	30.0	30.0	90 × 71.9	W16 × 26	10.0	W18 × 50, W21 × 50	5.25/2.0	110	4.00	0	1.5/1.0	SC
15	30.0	30.0	60 × 90	W16 × 26	10.0	W18 × 50, W21 × 50	5.25/2.0	110	4.00	0	1.5/1.0	SC
16	30.0	30.0	60 × 90	W16 × 26	10.0	W18 × 50, W21 × 50	5.25/2.0	110	4.00	0	1.5/1.0	SC
17	30.0	30.0	90 × 90	W16 × 26	10.0	W18 × 50, W21 × 62	5.25/2.0	110	4.00	0	1.5/1.0	SC
18	30.0	40.8	105 × 150	W16 × 26	10.2	W24 × 68	5.25/2.0	115	3.00	11	5.0/4.0	NC
19	28.0	37.0	62 × 150	W18 × 35	12.3	W24 × 84	6.25/3.0	115	3.00	11	5.0/4.0	NC
20	40.0	32.0	40 × 150	W21 × 62	10.7	W21 × 62	6.25/3.0	115	3.00	11	5.0/4.0	NC
21	33.0	32.0	96 × 150	W18 × 40	10.7	W24 × 62, W21 × 44	6.25/3.0	115	3.00	11	5.0/4.0	NC
22	30.0	30.0	75 × 150	W16 × 26	7.5	W24 × 55, W36 × 135	6.25/2.0	115	3.00	5	2.0/2.0	NC
23	28.3	30.0	36 × 60	W16 × 26	7.5	W24 × 55	6.25/2.0	115	3.00	15	5.0/4.0	NC
24	30.0	30.0	60 × 60	W16 × 26	7.5	Wall, W24 × 55	6.25/2.0	115	3.00	11	4.0/4.0	NC

25	66.6	21.3	64 × 98.1	W36 × 135	10.7	W24 × 55	7.5/3.0	145	3.50	6	3.0/3.0	NC
26	66.6	21.3	64 × 98.1	W36 × 135	10.7	W24 × 55	7.5/3.0	145	3.50	10	3.5/3.0	NC
27	30.0	44.5	71.5 × 110	W14 × 30	8.9	W30 × 90	5.5/3.0	145	4.00	15	3.0/3.0	NC
28	40.0	30.0	90 × 40	W18 × 40	10.0	Wall, Wall	5.5/3.0	145	4.00	15	3.0/3.0	NC
29	40.0	44.5	120 × 110	W18 × 40	8.9	Wall, W30 × 90	5.5/3.0	145	4.00	15	3.0/3.0	NC
30	40.0	45.0	120 × 40	W18 × 40	9.0	Wall, Wall	5.5/3.0	145	4.00	15	3.0/3.0	NC
31	40.0	30.0	90 × 40	W18 × 35	10.0	Walls	6.25/3.0	110	3.00	22	2.5/3.0	SC
32	30.0	30.0	90 × 30	W16 × 26	10.0	Walls	5.5/3.0	145	3.50	4.5	2.5/3.0	NC
33	40.0	30.0	90 × 40	W18 × 40	10.0	Walls	5.5/3.0	145	3.50	4.5	2.5/3.0	NC
34	43.0	30.0	90 × 118	W21 × 50	10.0	Wall, W2784	5.25/2.0	115	3.00	15	2.5/2.0	NC
35	43.0	30.0	90 × 119.5	W21 × 50	10.0	Wall, W30x99	5.25/2.0	115	3.00	15	2.5/2.0	NC
36	43.0	30.0	90 × 119.5	W21 × 50	10.0	Wall, W30x99	5.25/2.0	115	3.00	15	1.0/1.0	SC
37	43.0	30.0	90 × 119.5	W21 × 50	10.0	Wall, W24 × 76	5.25/2.0	115	3.00	15	1.0/1.0	SC
38	45.8	30.8	267 × 129	W21 × 44	10.3	Wall, W27 × 84	5.25/2.0	115	3.50	24.5	2.5/3.0	NC
39	32.5	30.0	90 × 81	W16 × 31	7.5	Wall, W21 × 44	5.5/2.0	145	3.50	15	3.0/3.0	NC
40	32.5	30.0	90 × 48.5	W16 × 31	7.5	Wall, W21 × 44	5.5/2.0	145	3.50	15	3.0/3.0	MC
41	28.0	30.0	90 × 87	W16 × 26	10.0	W21 × 44, Wall	5.5/3.0	145	3.50	13	3.0/2.0	SC
42	30.0	30.0	90 × 87	W16 × 26	10.0	W21 × 44	5.5/3.0	145	3.50	15	3.0/3.0	SC
43	30.0	30.0	90 × 87	W16 × 26	10.0	W21 × 44	5.5/3.0	145	3.50	13	3.0/2.0	SC
44	30.0	30.0	90 × 90	W16 × 26	10.0	W21 × 62	7.5/2.0	115	3.00	0	1.5/1.0	FC
45	30.0	30.0	80 × 160	W16 × 26	10.0	W21 × 62, W21 × 57	5.25/3.0	145	4.00	12	2.5/2.0	SC
46	40.0	30.0	120 × 40	W18 × 40	10.0	Walls	5.25/3.0	145	4.00	12	2.5/2.0	SC
47	40.0	30.0	120 × 160	W18 × 40	10.0	Wall, W21 × 62	5.25/3.0	145	4.00	12	2.5/2.0	MC
48	42.0	30.0	90 × 120	W21 × 44	10.0	W21 × 50, W21 × 73	5.63/3.0	110	4.00	15	3.0/4.0	SC
49	30.0	52.5	52.5 × 85	W16 × 31	8.75	Wall, W30 × 132	4.0/3.0	145	4.00	26	3.0/3.0	NC
50	25.0	52.5	52.5 × 85	W16 × 26	8.75	W30 × 108	4.0/3.0	145	4.00	26	3.0/3.0	NC

**Table 10.2** Observations and predictions per AISC Design Guide 11 Chapter 4

Bay	Observed evaluation	Prediction			Evaluation	Correct prediction?
		$f_n$ (Hz)	$W$ (kips)	$a_p$ (%g)		
1	NG	4.35	65.5	0.761	NG	Yes
2	NG	4.95	98.8	1.165	NG	Yes
3	NG	4.95	97.9	1.176	NG	Yes
4	NG	4.95	98.8	1.165	NG	Yes
5	NG	5.12	80.3	1.350	NG	Yes
6	NG	4.45	65.8	0.729	NG	Yes
7	NG	2.94	137.0	0.679	NG	Yes
8	OK	3.50	151.7	0.504	B	Yes
9	NG	5.32	60.7	1.661	NG	Yes
10	NG	3.69	75.9	0.785	NG	Yes
11	NG	3.61	75.3	0.813	NG	Yes
12	NG	4.76	67.8	1.210	NG	Yes
13	NG	4.76	63.0	1.301	NG	Yes
14	NG	4.76	63.0	1.301	NG	Yes
15	NG	4.76	71.0	1.155	NG	Yes
16	NG	4.76	71.0	1.155	NG	Yes
17	NG	4.76	71.0	1.155	NG	Yes
18	OK	3.57	131.2	0.284	OK	Yes
19	OK	4.84	119.1	0.200	OK	Yes
20	OK	4.11	136.6	0.226	OK	Yes
21	OK	4.45	116.9	0.234	OK	Yes
22	OK	5.45	92.6	0.521	B	Yes
23	OK	5.06	81.3	0.272	OK	Yes
24	OK	4.93	89.8	0.323	OK	Yes
25	OK	3.83	253.3	0.228	OK	Yes
26	OK	3.75	264.2	0.192	OK	Yes
27	OK	3.54	172.0	0.364	OK	Yes
28	OK	4.56	102.4	0.429	OK	Yes
29	OK	3.17	198.6	0.359	OK	Yes
30	OK	4.76	100.8	0.406	OK	Yes
31	NG	4.21	107.4	0.554	NG	Yes
32	OK	6.68	54.2	0.463	OK	Yes
33	OK	4.93	85.7	0.540	NG	No
34	OK	4.12	132.5	0.463	OK	Yes
35	OK	4.43	93.3	0.591	NG	No
36	NG	4.27	132.0	1.106	NG	Yes
37	NG	4.19	97.1	1.545	NG	Yes
38	OK	3.28	177.6	0.465	OK	Yes
39	OK	4.19	103.8	0.481	B	Yes
40	NG	4.19	78.6	0.635	NG	Yes
41	NG	4.44	101.5	0.452	OK	No
42	NG	4.10	107.8	0.478	B	Yes
43	NG	4.16	104.7	0.482	B	Yes
44	NG	4.85	113.9	1.047	NG	Yes
45	NG	4.43	94.7	0.583	NG	Yes
46	NG	4.70	89.8	0.559	NG	Yes
47	NG	3.84	130.5	0.519	B	No
48	NG	3.94	124.6	0.439	OK	No
49	OK	3.47	159.5	0.403	OK	Yes
50	OK	3.44	170.5	0.382	OK	Yes

should be emphasized that this method uses a fairly high estimate of the dynamic coefficient (0.1), which explains why its predictions are conservative. Additional runs with dynamic coefficients ranging from 0.04 to 0.12 (instead of 0.1) revealed that the dynamic coefficient of 0.06 provides the highest accuracy [34]. Yet, the dynamic coefficient of 0.06 is very close to the average dynamic coefficient for the second through fourth harmonics of the walking force presented by Kerr [35], and summarized in Willford et al. [36].

### 10.4.3 SCI P354 Vibration Dose Values Method

Only the bays used as offices were evaluated with this method. This means, 33 bays were evaluated (13 satisfactory bays and 20 unsatisfactory bays). Table 10.4 presents the results of the P354 VDV method including the computed VDV if  $n_a$  is 1400 walking events in the 16 hours of exposure duration. After trying different values for  $n_a$  and comparing the computed VDV to the upper end limit per P354, it was found that the most optimum prediction accuracy occurred if  $n_a$  is between 1000 to 1400 walking events for 16 hours of exposure for offices. Using any number between 1000 to 1400 events for  $n_a$  resulted in accurate evaluations for 38.5% (5 of 13 bays) of satisfactory bays and 100% (20 of 20 bays) of unsatisfactory bays. As a result, the method provided accurate predictions for 75.8% of the bays (25 of 33 bays) identified as offices in the database. It is to be noted that the VDV method runs involve  $a_{w,rms}$  from the SCI P354 simplified method which means incorrect estimations of  $a_{w,rms}$  would play a role on the outcome of VDV method calculations.

### 10.4.4 HIVOSS Method

The results per the HIVOSS method are discussed here for the four combinations described earlier. Combination 1 correctly predicted that 63.6% of the satisfactory bays would be satisfactory; whereas only 25% of unsatisfactory bays would be unsatisfactory. As a result, this combination provided accurate predictions for 42% of the bays in the database. Combination 2 correctly predicted that 59.1% of the satisfactory bays would be satisfactory while it correctly predicted that only 3.6% of unsatisfactory bays would be unsatisfactory. This means it resulted in accurate predictions for 28% of the bays in the database. Combination 3 correctly predicted that 95.5% of the satisfactory bays would be satisfactory; however, it could not predict any of the unsatisfactory bays. As such, it provided accurate predictions for 42% of the bays in the database. Lastly, Combination 4 correctly predicted that 81.8% of the satisfactory bays would be satisfactory and it could not predict any of unsatisfactory bays. This resulted in accurate predictions for 36% of the bays in the database. A summary of HIVOSS results are shown in Table 10.5. More detailed information on the HIVOSS method run can be found in [34].

## 10.5 Conclusions

The accuracies of four widely recognized floor vibration serviceability evaluation methods (AISC DG11 Chapter 4 Method, SCI P354 Simplified Method, SCI VDV Method, HIVOSS Method) were investigated in this paper. A large database of 50 bays (22 satisfactory and 28 unsatisfactory bays) subjected to walking excitation was studied by comparing the observed acceptability to predictions by each method. The findings of the study are summarized and presented in Table 10.6.

According to the results on Table 10.6, it is noted that the DG11 Chapter 4 accurately predicted the acceptability of 90.9% of the satisfactory bays and 89.3% of the unsatisfactory bays in the database. The SCI P354 Simplified Method resulted in accurate predictions for 18.2% of the satisfactory bays and accurate predictions for 100% of the unsatisfactory bays, indicating that the method is a bit on the conservative side. Nevertheless, changing the dynamic coefficient from 0.1 to 0.06 remarkably enhanced the prediction accuracy for satisfactory bays from 18.2% to 50.0% which resulted in increase from 64.0% to 76.0% in the overall prediction accuracy of this method. On the other hand, the SCI P354 VDV approach, with the number of walking events selected to optimize the prediction accuracy provided correct predictions for 38.5% of the satisfactory bays and 100% of the unsatisfactory bays, indicating that the method is a bit on the conservative side. It is important to note that the optimization was conducted to maximize the prediction accuracy compared to observation in this set of data. Lastly, the HIVOSS method resulted in poor prediction accuracy for all unsatisfactory bays for all

**Table 10.3** Observations and predictions per SCI P354 simplified method

Bay	Observed evaluation	Predicted					Evaluation	Correct prediction?
		$f_o$ (Hz)	$W$	$M$ (lb)	$\rho$	$R$		
1	NG	5.430	1.000	24400	0.987	15.7	NG	Yes
2	NG	6.210	1.000	32600	0.904	32.3	NG	Yes
3	NG	6.210	1.000	24600	0.904	42.7	NG	Yes
4	NG	6.210	1.000	32600	0.904	32.3	NG	Yes
5	NG	6.520	1.000	28300	0.915	37.6	NG	Yes
6	NG	5.430	1.000	24500	0.987	15.6	NG	Yes
7	NG	3.880	0.850	40000	0.988	9.8	NG	Yes
8	OK	4.270	0.830	27600	0.985	13.8	NG	No
9	NG	7.140	1.000	18900	0.919	56.5	NG	Yes
10	NG	5.170	1.000	24100	0.997	16.0	NG	Yes
11	NG	5.270	1.000	26500	0.997	14.6	NG	Yes
12	NG	5.990	1.000	19500	0.966	38.4	NG	Yes
13	NG	5.970	1.000	19300	0.966	38.8	NG	Yes
14	NG	5.970	1.000	19300	0.966	38.8	NG	Yes
15	NG	5.860	1.000	16600	0.964	45.0	NG	Yes
16	NG	5.860	1.000	16600	0.964	45.0	NG	Yes
17	NG	5.860	1.000	19100	0.964	39.2	NG	Yes
18	OK	4.040	0.850	25300	1.000	7.8	B	Yes
19	OK	5.630	1.000	25800	1.000	9.0	NG	No
20	OK	5.200	1.000	30800	1.000	7.6	OK	Yes
21	OK	5.580	1.000	31800	1.000	7.3	OK	Yes
22	OK	7.190	1.000	27200	0.996	21.2	NG	No
23	OK	6.050	1.000	24900	1.000	9.3	NG	No
24	OK	6.000	1.000	25200	1.000	11.6	NG	No
25	OK	4.350	8.500	76600	0.970	41.7	NG	No
26	OK	4.260	0.840	79900	0.982	3.4	OK	Yes
27	OK	3.950	0.850	26300	0.989	12.4	NG	No
28	OK	4.660	0.860	23900	0.995	13.9	NG	No
29	OK	3.950	0.860	35700	0.997	9.3	NG	No
30	OK	4.860	0.950	23500	0.999	15.6	NG	No
31	NG	4.310	0.830	26100	0.983	14.5	NG	Yes
32	OK	6.720	1.000	18400	0.998	25.2	NG	No
33	OK	5.060	1.000	20700	0.992	22.3	NG	No
34	OK	5.420	1.000	27700	0.994	16.7	NG	No
35	OK	4.930	0.950	26300	0.990	16.7	NG	No
36	NG	5.350	1.000	27200	0.868	37.1	NG	Yes
37	NG	4.930	0.950	21500	0.845	43.4	NG	Yes
38	OK	4.090	0.850	40400	0.981	9.6	NG	No
39	OK	5.320	1.000	30800	0.998	12.5	NG	No
40	NG	5.320	1.000	28000	0.998	13.8	NG	Yes
41	NG	5.480	1.000	24900	0.997	15.5	NG	Yes
42	NG	5.290	1.000	24500	0.998	15.8	NG	Yes
43	NG	5.370	1.000	24700	0.998	15.7	NG	Yes
44	NG	6.380	1.000	33100	0.973	22.8	NG	Yes
45	NG	5.920	1.000	27000	0.996	17.1	NG	Yes
46	NG	4.800	0.950	24200	0.989	18.0	NG	Yes
47	NG	5.280	1.000	33300	0.993	13.9	NG	Yes
48	NG	5.140	1.000	25900	0.997	14.9	NG	Yes
49	OK	3.860	0.850	16700	0.987	19.5	NG	No
50	OK	3.590	0.850	16900	0.966	18.9	NG	No

**Table 10.4** Observations and predictions per SCI P354 VDV method

Bay	Observed evaluation	Prediction		Correct prediction?
		VDV (If $n_a = 1400$ ) $m/s^{1.75}$	Evaluation	
1	NG	0.47	NG	Yes
2	NG	1.05	NG	Yes
3	NG	1.39	NG	Yes
4	NG	1.05	NG	Yes
5	NG	1.23	NG	Yes
6	NG	0.47	NG	Yes
9	NG	1.81	NG	Yes
10	NG	0.52	NG	Yes
11	NG	0.47	NG	Yes
18	OK	0.25	OK	Yes
27	OK	0.40	OK	Yes
28	OK	0.45	NG	No
29	OK	0.33	OK	Yes
30	OK	0.55	NG	No
31	NG	0.47	NG	Yes
32	OK	0.82	NG	No
33	OK	0.73	NG	No
34	OK	0.54	NG	No
35	OK	0.54	NG	No
36	NG	1.21	NG	Yes
37	NG	1.41	NG	Yes
38	OK	0.31	OK	Yes
39	OK	0.41	OK	Yes
40	NG	0.45	NG	Yes
41	NG	0.50	NG	Yes
42	NG	0.51	NG	Yes
43	NG	0.51	NG	Yes
45	NG	0.56	NG	Yes
46	NG	0.59	NG	Yes
47	NG	0.45	NG	Yes
48	NG	0.49	NG	Yes
49	OK	0.63	NG	No
50	OK	0.59	NG	No

**Table 10.5** HIVOSS method summary

	Prediction accuracy			
	Combination 1	Combination 2	Combination 3	Combination 4
Observed satisfactory bays	63.6%	59.1%	95.5%	81.1%
Observed unsatisfactory bays	25.0%	3.6%	0.0%	0.0%
All bays	42.0%	28.0%	42.0%	36.0%

combinations. Combination 1 and 2 with modal mass computed by HIVOSS Appendix A.6 could only predict 63.4% and 59.1% of satisfactory bays, respectively. Nevertheless, when the modal mass computed per DG11 Chapter 4 is used in HIVOSS method, Combination 3 and 4, this method provided 95.5% and 81.1% correct prediction for satisfactory bays. Yet, the HIVOSS method is found to be on the unconservative side.



**Table 10.6** Summary of accuracies for the evaluation methods

	Evaluation method	Observed satisfactory bays	Observed unsatisfactory bays	All bays	
Guideline	AISC DG11 Chapter 4	90.9%	89.3%	90.0%	
	SCI P354 simplified method	18.2%	100%	64.0%	
	SCI P354 VDV method (only offices)	38.5%	100%	75.8%	
	HIVOSS	Combination 1	63.6%	25.0%	42.0%
		Combination 2	59.1%	3.6%	28.0%
		Combination 3	95.5%	0.0%	42.0%
		Combination 4	81.1%	0.0%	36.0%
Investigation to improve prediction accuracy	SCI P354 simplified method	50.0%	96.4%	76.0%	

**Acknowledgements** The authors would like to thank Dr. Thomas M. Murray for his support and providing most of the information in the database. The financial support for this research was provided by Qatar National Research Fund (a member of the Qatar Foundation) via the National Priorities Research Program (NPRP), Project Number NPRP8-836-2-353.

## References

- Davis, B.: Finite element modeling for prediction of low frequency floor vibrations due to walking, Virginia Polytechnic Institute and State University (2008)
- Hudson, M.J., Reynolds, P.: Implementation considerations for active vibration control in the design of floor structures. *Eng. Struct.* **44**, 334–358 (2012). <https://doi.org/10.1016/j.engstruct.2012.05.034>
- Murray, T.M.: Floor vibrations: the human tolerance side of the equation. In: 17th Int. Modal Anal. Conf., 1999
- Živanović, S., Pavić, A., Reynolds, P.: Probability-based prediction of multi-mode vibration response to walking excitation. *Eng. Struct.* **29**, 942–954 (2007). <https://doi.org/10.1016/j.engstruct.2006.07.004>
- Muhammad, Z.O., Reynolds, P., Hudson, E.J.: Evaluation of contemporary guidelines for floor vibration serviceability assessment. In: Conf. Proc. Soc. Exp. Mech. Ser., 2017. [https://doi.org/10.1007/978-3-319-54777-0\\_42](https://doi.org/10.1007/978-3-319-54777-0_42)
- Muhammad, Z., Reynolds, P., Avci, O., Hussein, M.: Review of pedestrian load models for vibration serviceability assessment of floor structures. *Vibration*. (2018). <https://doi.org/10.3390/vibration2010001>
- Barrett, A.R., Avci, O., Setareh, M., Murray, T.M.: Observations from vibration testing of in-situ structures. In: Proc. Struct. Congr. Expo , 2006. [https://doi.org/10.1061/40889\(201\)65](https://doi.org/10.1061/40889(201)65)
- Bhargava, A., Isenberg, J., Feenstra, P.H., Al-Smadi, Y., Avci, O.: Vibrations assessment of a hospital floor for a magnetic resonance imaging unit (MRI) replacement. In: Struct. Congr. 2013 Bridg. Your Passion with Your Prof. - Proc. 2013 Struct. Congr., 2013
- Younis, A., Avci, O., Hussein, M., Davis, B., Reynolds, P.: Dynamic forces induced by a single pedestrian: a literature review. *Appl. Mech. Rev.* **69**, (2017). <https://doi.org/10.1115/1.4036327>
- Davis, B., Avci, O.: Simplified vibration response prediction for slender monumental stairs. In: Struct. Congr. 2014 - Proc. 2014 Struct. Congr., 2014. <https://doi.org/10.1061/9780784413357.223>
- Davis, B., Avci, O.: Simplified vibration serviceability evaluation of slender monumental stairs. *J. Struct. Eng. (United States)*. **141**, (2015). [https://doi.org/10.1061/\(ASCE\)ST.1943-541X.0001256](https://doi.org/10.1061/(ASCE)ST.1943-541X.0001256)
- Avci, O., Davis, B.: A study on effective mass of one way joist supported systems. In: Struct. Congr. 2015 - Proc. 2015 Struct. Congr., 2015. <https://doi.org/10.1061/9780784479117.073>
- Catbas, F.N., Celik, O., Avci, O., Abdeljaber, O., Gul, M., Do, N.T.: Sensing and monitoring for stadium structures: a review of recent advances and a forward look. *Front. Built Environ.* **3**, 38 (2017). <https://doi.org/10.3389/fbuil.2017.00038>
- Do, N.T., Gul, M., Abdeljaber, O., Avci, O.: Novel framework for vibration serviceability assessment of stadium grandstands considering durations of vibrations. *J. Struct. Eng. (United States)*. **144**, (2018). [https://doi.org/10.1061/\(ASCE\)ST.1943-541X.0001941](https://doi.org/10.1061/(ASCE)ST.1943-541X.0001941)
- Abdeljaber, O., Hussein, M.F.M., Avci, O., Davis, B., Reynolds, P.: A novel video-vibration monitoring system for walking pattern identification on floors. *Adv. Eng. Softw.* **139** (2020)
- Avci, O., Bhargava, A., Al-Smadi, Y., Isenberg, J.: Vibrations serviceability of a medical facility floor for sensitive equipment replacement: evaluation with sparse in-situ data. *Pract. Period. Struct. Des. Constr.* **124**, 1 (2019)
- Avci, O.: Amplitude-dependent damping in vibration serviceability: Case of a laboratory footbridge. *J. Archit. Eng.* **22**, (2016). [https://doi.org/10.1061/\(ASCE\)AE.1943-5568.0000211](https://doi.org/10.1061/(ASCE)AE.1943-5568.0000211)
- Avci, O.: Effects of bottom chord extensions on the static and dynamic performance of steel joist supported floors. Ph.D. Dissertation, Virginia Polytechnic Institute and State University, Blacksburg (2005)
- Avci, O., Bhargava, A., Nikitas, N., Inman, D.: Vibrations assessment of train induced excitations from tunnels embedded in rock. *Sci. Total Environ.* **711** (2020)
- Avci, O., Bhargava, A., Nikitas, N., Inman, D.: Vibrations assessment of existing building foundations due to moving trains in underground tunnels. In: IMAC XXXVIII, Int. Modal Anal. Conf., 2020

21. Avci, O., Setareh, M., Murray, T.M.: Vibration testing of joist supported footbridges. In: Struct. Congr. 2010, 2010. [https://doi.org/10.1061/41130\(369\)80](https://doi.org/10.1061/41130(369)80)
22. Avci, O.: Retrofitting steel joist supported footbridges for improved vibration response, in: Struct. Congr. 2012 - Proc. 2012 Struct. Congr., 2012. <https://doi.org/10.1061/9780784412367.041>
23. Celik, O., Catbas, F.N., Do, N.T., Gul, M., Abdeljaber, O., Younis, A., Avci, O., Issues, codes and basic studies for stadium dynamics. In: Proc. Second Int. Conf. Infrastruct. Manag. Assess. Rehabil. Tech., Sharjah, 2016
24. Avci, O.: Nonlinear damping in floor vibrations serviceability: Verification on a laboratory structure. In: Conf. Proc. Soc. Exp. Mech. Ser., 2017. [https://doi.org/10.1007/978-3-319-54777-0\\_18](https://doi.org/10.1007/978-3-319-54777-0_18)
25. Celik, O., Do, N.T., Abdeljaber, O., Gul, M., Avci, O., Catbas, F.N., Recent issues on stadium monitoring and serviceability: a review. In: Conf. Proc. Soc. Exp. Mech. Ser., 2016. [https://doi.org/10.1007/978-3-319-29763-7\\_41](https://doi.org/10.1007/978-3-319-29763-7_41)
26. Abdeljaber, O., Hussein, M.F.M., Avci, O.: In-service video-vibration monitoring for identification of walking patterns in an office floor. In: 25th Int. Congr. Sound Vib. Hiroshima, Japan, 2018
27. Avci, O.: Modal parameter variations due to joist bottom chord extension installations on laboratory footbridges. *J. Perform. Constr. Facil.* **29**, (2015). [https://doi.org/10.1061/\(ASCE\)CF.1943-5509.0000635](https://doi.org/10.1061/(ASCE)CF.1943-5509.0000635)
28. T.M. Murray, D.E. Allen, E.E. Ungar, D.B. Davis, *Vibrations of Steel-Framed Structural Systems Due to Human Activity: Second Edition.*, American Institute of Steel Construction, 2016
29. Smith, A.L., Hicks, S.J., Devine, P.J.: Design of floors for vibration - A new approach SCI P354, Revised Ed, pp. 1–128. Steel Construction Institute, Ascot, Berkshire, U.K. SCI P354 (2009). <https://doi.org/10.13140/RG.2.2.29342.95048>
30. RFCS: Human Induced Vibrations of Steel Structures Vibration Design of Floors Guideline, Brussels, Belgium, 2009
31. Rainer, J.H., Pernica, G., Allen, D.E.: Dynamic loading and response of footbridges. *Can. J. Civ. Eng.* **15**, 66–71 (1988). <https://doi.org/10.1139/188-007>
32. Allen, D.E., Murray, T.M.: Design criterion for vibrations due to walking. *Eng. J.* **30**, 117–129 (1993)
33. Pabian, S.D.: Investigation of floor vibration evaluation criteria using an extensive database of floors. University of Kentucky, 2011
34. Royvaran, M., Avci, O., Davis, B.: Analysis of floor vibration evaluation methods using a large database of floors framed with W-shaped members subjected to walking excitation. *J. Constr. Steel Res.* **164**, 105764 (2020)
35. Kerr, S.C.: Human induced loading on flexible staircases. (1998). [https://doi.org/10.1016/S0141-0296\(00\)00020-1](https://doi.org/10.1016/S0141-0296(00)00020-1)
36. Wilford, M., Young, P., Field, C.: Predicting footfall-induced vibration: Part I. In: Proc. Inst. Civ. Eng. Build., 2007

**Dr. Onur Avci** had his MS and PhD degrees at Virginia Tech. He is focused on dynamics of structures, smart structures and machine learning applications in structural engineering.

# Chapter 11

## Comparative Study of Floor Serviceability Methodologies



C. Chen, P. Duffour, and A. Margnelli

**Abstract** With the advent of lighter floor systems and the drive to lower the embodied energy in structures, meeting vibration serviceability requirements for floor systems can be a challenge. A number of guidelines have been published in the UK over the past 15 years (e.g. SCI P345, CCIP-016) that have been helpful in providing a consistent methodology. Although these can differ slightly in the detail, they are essentially based around the concept of response factor. Other methodologies have been proposed in continental Europe. The better documented one is the One-Step RMS90 (OS-RMS90) developed as part of the Technical Steel Research of the European Commission (e.g. EUR 24084 EN). Although similar in spirit, OS-RMS90 differs from the UK methodologies in key aspects which can be categorized along three strands (1) Footfall force definition, (2) Floor modelling and estimation of the dynamic response of the floor; (3) Acceptability criteria. This paper proposes a detailed comparison between these methodologies in each of these aspects and concludes by applying the methods on a composite floor case study. Based on this comparison, the merits of various quick assessments are evaluated.

**Keywords** Floor vibration · Serviceability · Design methodologies

### 11.1 Introduction

Floor serviceability limit state (SLS) criteria play a key role in the design of lighter floor structures. The assessment of floor serviceability starts from the modelling of the dynamic forces applied to the floor which are usually associated with human walking. According to previous research [1–3], the frequency range of the excitation is in the range from 1.5 to 2.5 Hz with different root-mean-square (RMS) values. Expressions for the average values of the peaks in the force were given by [4] using Fourier components. Measurements were also carried out to statistically characterise the walking excitations [5]. Formulae have been proposed to determine approximately the modal properties of the floor structures. For example, the modal masses can be calculated by multiplying the total mass of the slab with some effective lengths and widths. The calculation of effective lengths and widths is dependent on the particular floor system (SCI, Canadian guide, and AISC). Alternatively a detailed finite element (FE) model can be used to determine the modal properties. The modal damping ratio is the sum of contributions from different components within the system which are distinguished according to the construction materials, the use of the floor and the potential presence of supplemental damping.

Several methods are currently available to calculate the floor dynamic response at the design stage. SCI P354 [6] considers the steady-state or impulse response of floors at different natural frequencies and uses modal superposition to determine the total dynamic response. The peak root mean square (RMS) values of the acceleration are then determined to obtain the R-factors. CCIP-016 [7] and CSTR43 App G are similar to the SCI method. The OS-RMS90 method (also called HiVoSS) developed by the Research Fund for Coal and Steel (RFCS) has been presented in varying degrees of detail in a number of publications [6, 8, 9]. In this method a more statistical response metrics is computed also using a frequency domain approach, in which the floor system is assumed to be composed of individual single degree of freedom (SDOF) systems. A useful overall comparison of serviceability assessments was carried out in [10]. This paper compares systematically and in more detail the SCI and the OS-RMS90 methods only as the other methods mentioned above are fairly similar to SCI.

---

C. Chen · P. Duffour (✉)

Department of Civil, Environmental and Geomatic Engineering, University College London, London, UK  
e-mail: [p.duffour@ucl.ac.uk](mailto:p.duffour@ucl.ac.uk)

A. Margnelli

AKT II, White Collar Factory, London, UK

## 11.2 Background: Description of the Two Methods

Both methods assume that the modal properties of the floor to be assessed have been determined from the material and geometrical properties of the floor. This can be done using either approximate formulae or by running a modal analysis on an FE model. More detail on this can be found from the references mentioned in the introduction section.

Both methods also follow essentially the same three-stage process:

1. Definition of the force excitation;
2. Estimation of the dynamic response of the system;
3. Comparison of the response level against thresholds of acceptability.

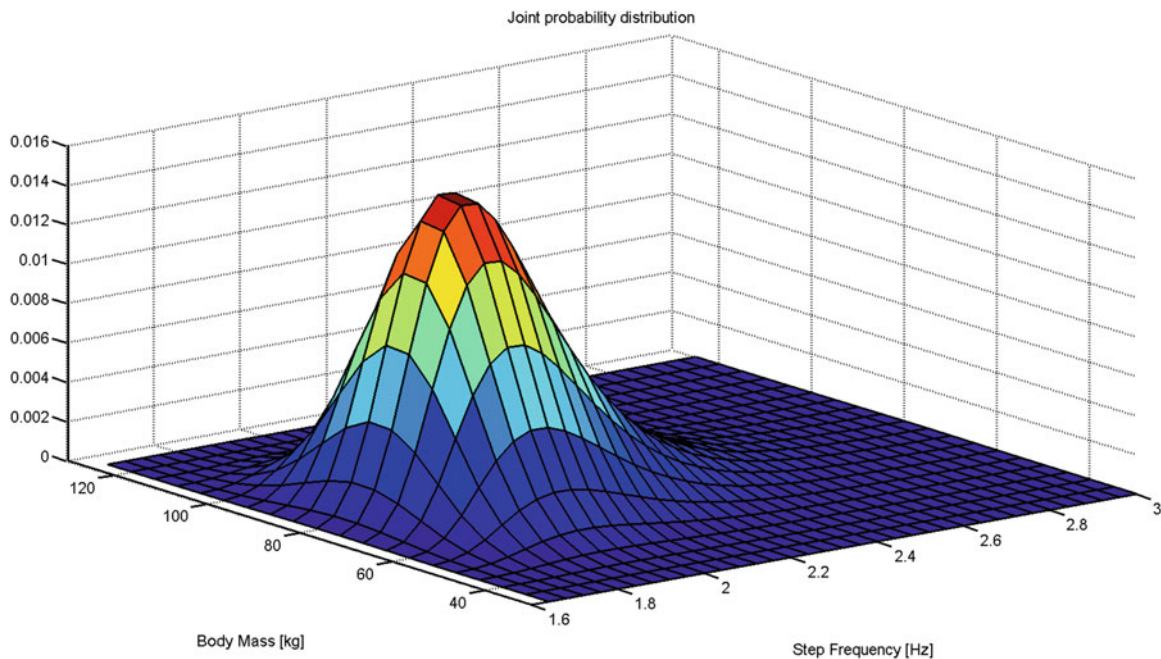
### 11.2.1 OS-RMS90

*Excitation* A person walking normally produces a vertical contact force with each foot. This contact force has two peaks corresponding to the heel drop and uplift of the feet. The detailed shape of the one-step force varies moderately but noticeably with the step frequency. OS-RMS90 defines this force through an 8-order polynomial function of time  $t$  as follows:

$$F(t) = M_b g \cdot \left( K_1 t + K_2 t^2 \cdots K_8 t^8 \right), \quad (11.1)$$

where  $M_b$  is the body mass,  $g$  is the acceleration of gravity and  $K_1 - K_8$  are coefficients dependent on the step frequency and fitted from experimental data. From this, a walking load time history can be obtained by superposing a series of single contact forces at a  $1/f_s$  time interval, where  $f_s$  is the step frequency. The statistics on the force step frequency and the walker body mass are provided in the form of empirical cumulative distributions. Assuming the two variables are independent, the joint distribution, whose probability density is illustrated in Fig. 11.1 can easily be calculated by multiplication.

*Response* As presented in the existing literature this method only considers one mode of the floor system at time. This assumes, either that the system is dominated by this mode and its behavior is well described by the corresponding single degree of freedom system or that a multimodal response can be obtained by some form of modal combination such as SRSS



**Fig. 11.1** Body mass and step frequency joint probability distribution used as a statistical input for the OS-RMS method. This gives an expected frequency of 2.0 Hz and a body mass of 78.2 kg

or CQC. The next step consists in calculating the response of this single degree of freedom to the walking load history just described. Little detail is provided on this particular step (although frequency domain is mentioned in [9]) but this can be done either in frequency domain or in the time domain using any direct integration technique (e.g. Newmark or any alpha-method). From this a raw velocity response time history, denoted  $\dot{X}(t)$  is obtained. A frequency weighting function is applied to this velocity signal to account for the dependence of human perception of vibration with the frequency content of the disturbance. The frequency weighting function used is that recommended in [11]. The weighting is implemented in frequency domain following a Fourier transform of the velocity:

$$\dot{X}_H(f) = \dot{X}(f)H_v(f), \quad (11.2)$$

where  $\dot{X}(f)$  is the Fourier transform of the velocity and  $H_v(f)$  is the filter transfer function.  $H_v(f)$  is defined by:

$$\left| H_v(f) = \frac{1}{v_0} 1/\sqrt{1 + \left(\frac{f_0}{f}\right)^2} \right|, \quad (11.3)$$

where  $v_0 = 1$  mm/s and  $f_0 = 5.6$  Hz. The weighted time domain response  $\dot{X}_H(t)$  is then obtained by inverse Fourier transform. The calculation of the OS-RMS for a specific step frequency  $f_{s,m}$  and modal mass  $M_n$  is done by finding the RMS value of response over a time window  $[t, t + T_s]$  starting at arbitrary time but after any initial transient that may have been caused by an artificially sudden onset of the force. This calculation is based on the following equation:

$$\text{OS-RMS}_{n,m} = \sqrt{\frac{1}{T_s} \int_t^{t+T_s} \dot{X}_H^2(t) dt}. \quad (11.4)$$

The value of OS-RMS90 requires the introduction of the probability distribution of the step frequency  $f_s$  and the body mass  $M_b$  shown in Fig. 11.1 and provided in tabulated format. OS-RMS90 is the value 90% percentile of the OS-RMS $_{n,m}$  values weighted by the corresponding value of the  $f_{s,m}$  and modal mass  $M_n$  joint-probability distribution. OS-RMS90 can be plotted for varying slab natural frequencies and modal masses (and damping as a parameter). Two-dimensional maps (with constant damping) have been published. They allow rapid assessment of a floor serviceability performance which is useful in early design stages.

### R-factor Based Assessment (SCI P354)

This method [6] describes the walking force as a periodic continuous function of time that is represented by a finite number of Fourier components at the walking fundamental frequencies and its harmonics. This set of frequencies excite the floor eigenmodes to varying degree depending on their relative proximity in frequency and the harmonic amplitudes. The method distinguishes between two types of responses: the modal response of a floor at an eigenfrequency much higher than the harmonic frequency considered is deemed to be impulsive while the modal response of the floor is considered to be in steady state when the floor eigenfrequency is lower than the force component frequency. The amplitude  $F_h$  of the  $h^{\text{th}}$  harmonics is expressed by:

$$F_h = \alpha_h Q, \quad (11.5)$$

where  $\alpha_h$  is the step frequency-dependent coefficient of the  $h^{\text{th}}$  harmonic and  $Q$  is the static force of an ‘‘average person’’ (normally 746N). Equivalent force for impulse excitation is calculated by

$$F_I = 60 \frac{f_s^{1.43}}{f_n^{1.30}} \frac{Q}{700}, \quad (11.6)$$

where  $f_n$  is the structure eigenfrequency of the  $n^{\text{th}}$  mode under consideration. For the steady-state response, the RMS value of the acceleration for  $n^{\text{th}}$  single mode and force of  $h^{\text{th}}$  harmonics is

**Table 11.1** Frequency weighting curve (Z – axis)

Z – axis vibrations weighting ( $W_h$ )	
$W = 0.4$	For $1\text{Hz} < f_s < 2\text{Hz}$
$W = f_s/5$	For $2\text{Hz} \leq f_s < 5\text{Hz}$
$W = 1.0$	For $5\text{Hz} \leq f_s \leq 16\text{Hz}$
$W = 16/f_s$	For $f_s > 16\text{Hz}$

$$a_{w,rms,e,r,n,h} = \mu_{e,n} \mu_{r,n} \frac{F_h}{M_n} D_{n,h} W_h, \quad (11.7)$$

where  $\mu_{e,n}$  and  $\mu_{r,n}$  are the mode shape amplitudes respectively at the excited point (subscript  $e$ ) and the response point (subscript  $r$ ),  $M_n$  is the modal mass,  $W_h$  is the frequency weighted factor defined according to [12].  $D_{n,h}$  is the dynamic magnification factor and expressed by

$$D_{n,h} = \frac{h^2 \beta_n^2}{\sqrt{(1 - h^2 \beta_n^2)^2 + (2h \zeta_n \beta_n)^2}}, \quad (11.8)$$

where  $\beta_n = f_s/f_n$ ,  $\zeta_n$  is the modal damping ratio. For impulse response, the RMS value has a similar expression and can be calculated by:

$$a_{w,peak,e,r,n,h} = 2\pi f_n \mu_{e,n} \mu_{r,n} \frac{F_I}{M_n} W_n \sqrt{1 - \zeta^2}. \quad (11.9)$$

The total response is then obtained by summing up the components for all modes considered and force harmonics. This can be done either using full time history or by SRSS combination. Using SRSS, the RMS of the steady-state response and the total acceleration is calculated by:

$$a_{w,rms,e,r} = \frac{\sqrt{2}}{2} \sqrt{\sum_{h=1}^H \left( \sum_{n=1}^H a_{w,rms,e,r,n,h} \right)^2}. \quad (11.10)$$

The RMS of the impulse response is calculated in the time domain by the following equation:

$$a_{w,rms,e,r} = \sqrt{\frac{1}{T} \int_0^T \sum_{n=1}^N a_{w,peak,e,r,n,h} \sin \left( 2\pi f_n \sqrt{1 - \zeta^2} \right) e^{-2\pi \zeta f_n t} dt}. \quad (11.11)$$

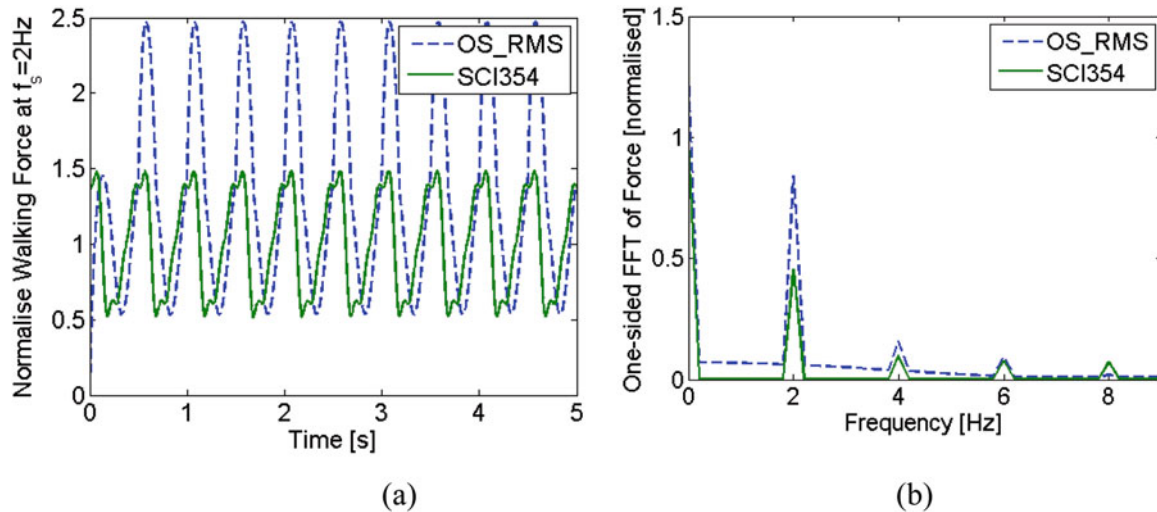
The RMS values calculated here also needs to be weighed using Table 11.1. According to [13], the R factor for z axis vibration can be finally determined by

$$R = \frac{a_{w,rms}}{0.005}. \quad (11.12)$$

### 11.3 Comparison of the Methods

- Force definition

SCI-P354 methods and OS-RMS90 use somewhat different force definitions. Both are parametrized, in time by the step frequency and in amplitude by the weight of a single walking person. The R-factor methods capture the footfall force using the first four Fourier components of the force as fitted from experimental data. OS-RMS90 stores the time profile of the force in terms of polynomial coefficients (although a Fourier decomposition is suggested an approximation in [8]). As a result, the



**Fig. 11.2** Comparison of walking force time histories (a) and spectra (b). The body mass was taken as unity and the step frequency as 2 Hz

latter does not bring out explicitly the significance of harmonics content of the force signal. R-factor methods use a single average person walking weight and a narrow range of frequencies with uniform probability of occurrence. The OS-RMS method offers a more developed statistical framework, providing a first step towards a firmer reliability basis.

Figure 11.2 compares walking forces in the time domain (a), and the frequency domain (b) for a footfall frequency of 2 Hz. From the time histories, it can be seen that the OS-RMS profile looks quite different and is significantly larger. This has been noted before in the literature [10]. The frequency spectra show that both the static components and the first harmonic are significantly higher (almost by a factor of 2) for the OS-RMS force. This difference increases further as the footfall frequency increases.

It should be noted that the range of walking frequencies given in the OS-RMS probably distribution goes up to 3 Hz. As the bell curve in Fig. 11.1 already hinted, walking at this pace is unlikely but in terms of calculation, care should be taken that the values of the coefficients  $K_i$  have been obtained by fitting experimental data over the range 2–2.25 Hz. Extrapolating linearly for higher frequencies (up to 3 Hz as suggested by the table defining the  $K_s$  in [5]) produces forces time histories which are clearly wrong. We tried to estimate better these  $K_s$  but a secondary fitting. This gave a walking forced with a plausible profile but their normalized amplitude reaches 6–7 which is clearly unrealistic.

- Calculation of the response

Both approaches are based on modal decomposition. With R-Factor methods the response for each mode to the various force harmonics is obtained separately and superimposed. OS-RMS90 only considers the response of one mode force by the footstep time history. For multimodal response an SRSS combination is recommended.

R-factor methods make a distinction between impulsive and steady state response of the floor. This distinction is not clearly made in OS-RMS90 but this distinction is not necessary if the equation of motion is directly integrated but this comes at a higher computational cost.

Although both methods assume that the walking person is effectively stationary (usually at the antinode of the mode shape considered to be conservative) R-Factor methods include an attenuation coefficient that accounts for the fact that a person walking over a typical slab dimension is unlikely to cause the system to reach a full steady-state amplitude. This coefficient depends on the damping, the walking speed and the characteristics length of the slab (its definition in SCI354 contains a typo as reported by [4]). No such coefficient is mentioned in OS-RMS90 methodology although the particular one-step interval chosen to compute the RMS value could be selected with this effect in mind. The criteria for selecting this interval currently remain vague.

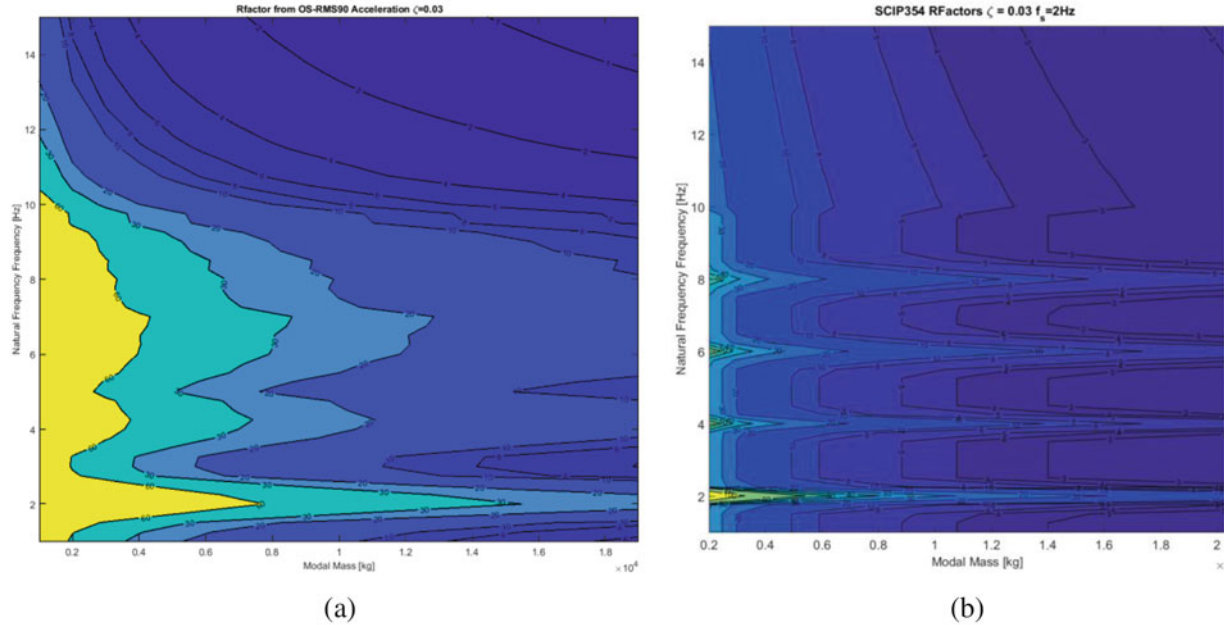
- Thresholds of acceptability

OS-RMS90 eventually produced results in terms of velocity whereas R-Factor methods work with acceleration. In principle both contain the same information but this means the direct comparison of the two methods is not straightforward. Different criteria of acceptability are provided in terms of floor usage. However Feldmann et al. [5] offer some elements of comparison which we have attempted to summarize in Table 11.2.

**Table 11.2** Main thresholds of acceptability for the two metrics considered

	Hospitals	Residential day	Residential night	Office
<i>R-Factor</i>	1	2–4	1.4	4
<i>OS-RMS90</i>	0.1	0.8–3.2		

Note that the R-factor and OS-RMS90 values quoted in this table cannot be directly compared



**Fig. 11.3** Contour maps of response factors in terms of floor modal masses and natural frequencies. Both maps were obtained with a constant damping ratio  $\zeta = 0.03$ . (a) R-Factor based on OS-RMS90 Accelerations. (b) Acceleration R-Factor following SCIP354

## 11.4 Single Degree of Freedom Contour Maps

To provide a quantitative comparison between the two methods, they were both adapted to produce results that can be related. The OS-RMS90 processed as described earlier was followed except that the force time histories were generated using the harmonics defined in SCI-P354. It was judged that the forced originally defined with the OSRM90 method were too high for  $f_s > 2.2$  Hz. Also the results were expressed in terms of acceleration rather than velocity. This acceleration was not filtered according to Eq. (11.3) as it is not clear what the equivalent transfer function for accelerations is. Instead the  $W_b$  filter [12] was applied in the frequency domain to the acceleration time series. The final acceleration levels obtained for each walking frequency and body mass pair were multiplied by the corresponding probability density value and the 90% percentile of the resulting sample values was calculated then divided by  $5 \text{ mm/s}^2$ . The process was repeated for a range of SDOF systems of varying modal mass and frequency. Newmark ( $\beta = 1/4$  and  $\gamma = 1/2$ ) with a time step of 1 ms was used for time integration. The results are plotted as a contour map in Fig. 11.3a.

The standard R-Factor method (SCI-P354) was applied to the same array of single degree of freedom systems with the same level of damping ( $\zeta = 0.03$ ). The walking frequency and body mass were kept constant at 2 Hz and 76 kg resp. The results, also presented as a contour map are shown in Fig. 11.3b.

The two contour plots show a number of similarities. The R-factor is fairly low for heavy floors and natural frequencies above 10 Hz. The two maps show horizontal ridges of high responses for light floors. These represent resonant responses at multiples of the walking frequency (harmonics of the force). These ridges are more clearly defined in the SCI-P354 map presumably because a single step frequency is used to define the force whereas a whole distribution comes into the OS-RMS90 calculation. Clear resonant ridges no longer feature for natural frequencies above 10 Hz for either method. In the case of SCI P354 this is because the response of the system is then governed by an impulsive behaviour (threshold of 10 Hz).

In terms of process the main remaining differences between the two methods are (1) the range of body masses and walking frequency for OSRMS90 vs one single mass and frequency in SCI P354, and (2) in OSRMS90 the response is obtained by



direct integration. It is reassuring that the 10 Hz frequency threshold is also clearly visible in the OSRMS90 map even though the method makes no distinction between impulsive and resonant response.

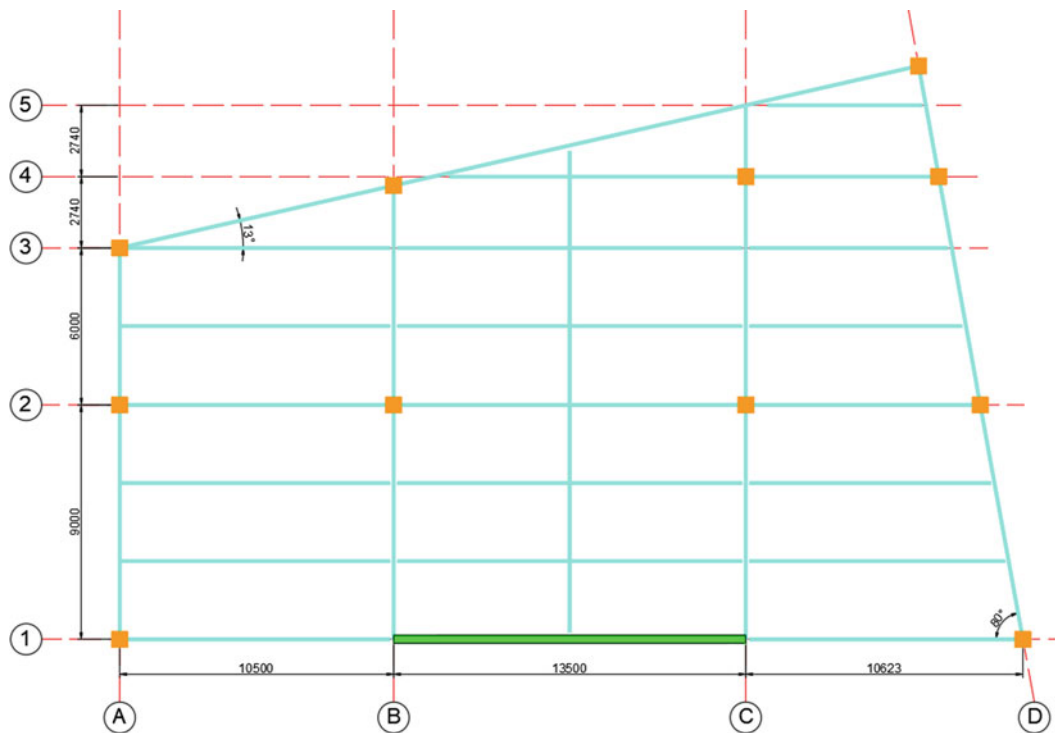
The detail of the contours can differ slightly, but more importantly, the OSRMS levels are consistently higher by almost about 50%. Two reasons explain this difference: (1) the wider range of walking frequencies is likely to broaden the ridges in all directions; (2) by definition the OS-RMS90 metric returns a value at the higher end of the distribution. In fact, a map showing the weighted average of the all the values obtained for the  $M_b$  and  $f_s$  range is closer in value to those of the SCI P354 map.

It should be noted that implemented with a time integration, the OSRM90 map takes a lot longer to generate than the SCI P354 one.

## 11.5 Case Study: Serviceability of a Composite Office Floor

This section compares the two methods on an office floor. The flooring system is a concrete slab supported by steel beams (with shear transfer) represented by blue lines, which are themselves supported by columns (yellow squares) and the side of a shear wall (green strip) as shown in Fig. 11.4.

The basic properties of the floor are described in Table 11.3. To obtain the modal properties of the floor system, the slab was first modelled in Robot Structural. Columns were modelled as pin supports. The slab was modelled with shell elements. A modal analysis was then carried out, producing the modal properties shown in Table 11.4. The low-to-high frequency



**Fig. 11.4** Schematic of the office floor plane

**Table 11.3** Basic information about the floor system

Design code	EN 1992-1-1:2004 Eurocode 2
Strength grade of concrete	C30
Slab thickness (mm)	130
Young's modulus (N/mm <sup>2</sup> )	26000
Poisson's ratio	0.17
Density of slab (t/m <sup>3</sup> )	2.453
Beams	UB533x165x85

**Table 11.4** Modal properties and R-Factors values from each mode and each method as read from the contour maps

Mode numbers	Frequency (Hz)	Modal mass (t)	SCI P354	OS RMS90
1	4.51	19.64	2.0	2.7
2	5.50	17.11	3.0	4.1
3	5.91	24.23	5.8	3.4
4	6.30	11.92	4.2	6.2
5	7.01	8.80	4.3	7.2

**Table 11.5** Modal combination results from various methodologies

	SCI-P354 chart	OS-RMS90 chart	SCI-P354 Matlab (mode shapes all 1)	SCI-P354 Matlab (mode shapes from Robot)	Robot footfall analysis
SRSS	9.6	11.2	15.7	7.7	9.1

cut-off for general floor (open offices *etc.*) is 10 Hz. This floor can be regarded as low-frequency floor. The damping ratio of the floor slab is selected as 3% based on the usage of the floor and the recommendation from [14].

Based on these modal properties, several calculations of the response factors can be attempted. First, using the SCI P354 contour map, values of each modes can be read off the chart and combined. The same process can be followed using the OS-RMS90 map. These two values were compared to results from a Matlab program that calculates the R-Factor according to the SCI P354 method first assuming that all the mode shapes have their maximum at the same location which is also the position of the walker and second taking into account the mode shape (as read from the Robot modal analysis results). The results are shown in Table 11.5.

It can be seen that a good estimate of the Matlab result can be obtained by combining the graph corresponding readings. The OS-RMS90 values are a little higher, reflecting the issues with the metrics highlighted earlier with the calculation of the force embedded in the method. The robot value is lower than the other two as expected since the program takes into account the fact that the mode shapes have maximum values at different locations. From this it is clear that combining values read-off the charts lead to reasonable estimates on this example. From the two Matlab results, it is also clear that including the mode shape in the calculation makes a significant difference and using 1 for all in the absence of better information can lead to a significant over estimate of the R-factor.

## 11.6 Conclusion

This paper carried out a systematic comparison of two available method to assess the vibration of floor system. OS-RMS90 has a more robust statistical framework but its force definition seems to be problematic. SCI P354 is simpler and quicker but it relies on the distinction between impulsive and resonant response which has been shown not to be so clear. OS-RMS90 could prove a better solution if it was based with a more reliable definition of the force.

## References

- Matsumoto, Y., Nishioka, T.S., Matsuzaki, K.H.: Dynamic design of footbridges. In: IABSE proceedings, p. P-17/78, pp. 1–15, (1978)
- Kerr, S.C., Bishop, N.W.M.: Human induced loading on flexible staircases. *Eng. Struct.* **23**(1), 37–45 (2001). [https://doi.org/10.1016/S0141-0296\(00\)00020-1](https://doi.org/10.1016/S0141-0296(00)00020-1)
- Pachi, A., Ji, T.: Frequency and velocity of people walking. *Struct. Eng.* **83**(3), 36–40 (2005)
- Živanović, S., Pavic, A., Reynolds, P.: Vibration serviceability of footbridges under human-induced excitation: a literature review. *J. Sound Vib.* **279**, 1–74 (2005). <https://doi.org/10.1016/j.jsv.2004.01.019>
- Feldmann, M. et al.: Design of floor structures for human induced vibrations, JRC–ECCS joint report. (2009). <https://doi.org/10.2788/4640>
- Smith, L., Hicks, L., D. P. J.: Design of Floors for vibration: (revised edition, February 2009). The Steel Construction Institute, Silwood Park, Ascot, Berkshire, UK (2009)
- Wilford, M., Young, P.: A design guide for footfall induced vibration of structures. Concrete Centre Report CCIP-016 (2006)
- Sedlecek, G., Heinemeyer, C., Butz, C., Voelling, B., Warrts, P., Van Duin, F., Hicks, S., Devine, P., Demarco, T.: Generalisation of criteria for floor vibrations of industrial, office, residential and public building and gymnastic halls - Final Report, EUR 21972 (2006)
- Galanti, F., Heinemeyer, C., Feldmann M., Lentzen, S.: Assessment of floor vibration using the OS-RMS90 method. In: Eurodyn 2011, Leuven, pp. 1072–1077 (2011)

10. Muhammad, Z.O., Reynolds, P.: Vibration serviceability of building floors: performance evaluation of contemporary design guidelines. *J. Perform. Constr. Facil.* **33**(2), 04019012 (2019)
11. ISO: Mechanical vibration and shock — Evaluation of human exposure to whole- body vibration — Part 2: Vibration in buildings (1 Hz to 80 Hz) Vibrations. International Organization for Standardization (2003)
12. British Standards Institute: BS 6481 Measurement and evaluation of human exposure to whole-body mechanical vibration and repeated shock (1997)
13. British Standards Institute: BS 6472:1992 Evaluation of human exposure to vibration in buildings (1 Hz to 80 Hz) - guide for the evaluation of human exposure to whole-body vibration (1992)
14. ISO: Bases for design of structures—Serviceability of buildings and walkways against vibration ISO 10137:2007. International Organization for Standardization (2007)

**Dr Philippe Duffour** is an Associate Professor in structural dynamics at UCL. He has extensive experience in vibration modeling and measurements in the areas of wind turbines, earthquake engineering and floor serviceability.



# Chapter 12

## Experimental Modal Analysis of Double Tee Floors in a Fire Damaged Parking Deck for Post-Fire Vibration-Based Condition Assessment

Matthew Whelan, Nicole Braxtan, Glenda Mayo, and Brett Tempest

**Abstract** Vibration-based structural health monitoring and damage detection has been long pursued as a multi-hazard tool for performance assessment and management of civil infrastructure. However, the majority of full-scale case studies have focused on the efficacy of vibration-based condition assessment to detect, localize, and quantify structural damage resulting from either overload or long-term deterioration mechanisms. To supplement the limited case studies of vibration-based condition assessment performed on fire damaged structures, experimental measurements obtained from a prestressed concrete parking deck following a large fire in an attached timber framed structure are presented. Experimental modal analysis was conducted on two elevations of prestressed concrete double tees in the parking deck using a stationary pair of shakers and a large array of uniaxial accelerometers. The two floor elevations were nominally identical in design, with one elevation featuring visible symptoms of localized fire damage across a portion of the span and the other exhibiting no visible evidence of fire damage. Impact echo testing was also performed on select double tees at each elevation to estimate reductions in the modulus of elasticity along the stems of each member. Coupled with camber measurements and visual condition surveys, the impact echo results are used to quantify the severity of the effects of the elevated temperatures on the double tees independent of the vibration-based condition assessment. Experimental estimates of the natural frequencies, damping ratios, and mode shapes for each elevation are developed and compared to illustrate empirical evidence of localized structural damage in the modal parameters of the elevation affected by the fire. The results suggest that the changes in experimental modal parameters resulting from fire damage are distinct from those typically associated with fracture or other localized forms of structural damage resulting from overload or deterioration and may necessitate the development of unique strategies specific to fire damage within multi-hazard structural health monitoring applications.

**Keywords** Structural health monitoring · Vibration-based damage detection · Prestressed concrete · Post-fire nondestructive evaluation · Experimental modal analysis

### 12.1 Introduction

Concrete, due to its thermal mass, offers inherent fire resistance that, in most cases, enables reinforced and prestressed concrete structures to withstand even severe fires without collapse. However, the mechanical properties of concrete, reinforcing steel, and prestressing strands are all adversely affected by exposure to elevated temperatures, with potentially significant reductions in residual elastic modulus and strength for each material [1, 2]. While the intrinsic fire resistance of concrete often permits reinforced and prestressed concrete structures to be rehabilitated and returned to service after exposure to elevated temperatures, post-fire evaluation of the structure is critical for determining the extent of structural damage to inform if continued use is permissible [3]. While thermo-mechanical finite element simulations have been used to predict the fire resistance of prestressed concrete components during exposure to elevated temperatures, few studies have produced guidance on predicting the residual properties or performance of such components after a fire [4]. Furthermore,

---

M. Whelan (✉) · N. Braxtan · B. Tempest

Department of Civil and Environmental Engineering, William States Lee College of Engineering, University of North Carolina at Charlotte, Charlotte, NC, USA

e-mail: [mwhelan3@uncc.edu](mailto:mwhelan3@uncc.edu); [nbraxtan@uncc.edu](mailto:nbraxtan@uncc.edu); [Brett.Tempest@uncc.edu](mailto:Brett.Tempest@uncc.edu)

G. Mayo

Department of Engineering Technology and Construction Management, William States Lee College of Engineering, Charlotte, NC, USA

e-mail: [Glenda.Mayo@uncc.edu](mailto:Glenda.Mayo@uncc.edu)

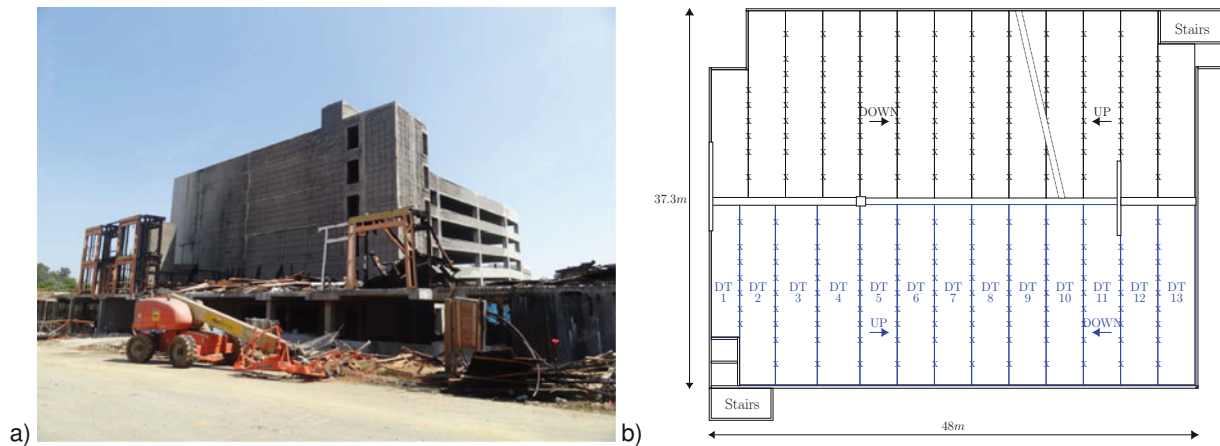
measurements of actual thermal loads are generally not available for structural fires and may be highly variable across a structure, so simulation-based approaches for structural evaluation are limited in predictive accuracy. Consequently, post-fire evaluations of prestressed concrete structures typically rely extensively on visual inspection, nondestructive testing, and, in some cases, proof load tests [3]. Various nondestructive evaluation techniques have been applied to detect and quantify the effects of fire and elevated temperatures on reinforced and prestressed concrete structures, including impact-echo [5, 6], ultrasonic pulse velocity [7], Schmidt hammer [8], and Windsor probe penetration resistance [6]. However, these methods only offer the ability to indirectly measure material properties at discrete locations rather than directly assess the effect of material degradation on the global structural response, require sampling at a large number of discrete locations to map the location and extent of deterioration, and are only suitable for assessing the residual properties of the concrete after the fire has been extinguished. In contrast, vibration-based damage detection may offer the ability to serve as a global damage identification technique for either real-time structural health monitoring during fires [9] or as a means of post-fire condition assessment.

Despite the potential advantages of applying vibration-based techniques for condition assessment of fire damaged structures and the demonstrated effectiveness of vibration-based damage detection for other extreme loads including seismic [10] and blast [11], few studies have explored the use of vibration-based methods for damage diagnosis of fire damaged reinforced or prestressed concrete structures. Whelan et al. [12] presented a case study where experimental modal parameter estimates were obtained for a prestressed concrete double tee roof with fire-induced damage. The experimental estimates were complemented by linear eigenanalysis of two finite element models: one of the as-built structure and one where estimates of the residual modulus of elasticity obtained through impact-echo nondestructive evaluation were used to produce an updated model. The modal parameters of the updated finite element model generally correlated well with the experimental measurements and suggested that the fire damage resulted in both significant reductions in natural frequencies and changes in the mode shapes in the region of visible fire damage. Although this is one of the few studies offering experimental insight into the effects of fire damage in structures on modal parameters, no guidance on the use of either nonparametric or parametric methods for vibration-based damage detection specific to fire damage was offered by the authors. The progression of changes in the fundamental natural frequency and mode shape of simply supported reinforced concrete beams under 60, 90, 120, and 150 min fire loads was experimentally measured in Liu et al. [13]. The fundamental natural frequency of the beams reduced by as much as 50%, while only nominal changes in the fundamental mode shape were observed. However, it should be noted that the entire beam specimen was placed in the test furnace. Consequently, the elevated temperatures were applied uniformly across the surface of the specimen and therefore no localized damage was specifically promoted. In a subsequent study, the authors used a support vector machine trained with numerical simulations performed on an updated finite element model of the beam to predict the time of exposure to a standardized heating curve using the measured modal parameters. The estimated time of exposure was then used in a numerical simulation to predict the residual flexural stiffness and capacity of the beams, which was found to correlate well with experimental measurements obtained from load tests of the fire damaged beams [14].

## 12.2 Case Study Structure

The focus of this experimental study is directed toward measurement of the residual performance of two elevations of prestressed concrete double-tee framing in a five story parking deck subjected to a five-alarm fire. The post-fire residual behavior of double-tee members is often a particular concern because the generally thin cross section often provides less concrete cover to the prestressing strands and the strands are located within stems that are subjected to elevated temperatures on both sides. At the time of the fire, the parking deck was newly built and part of a mid-rise apartment complex that was under construction. The apartment complex was designed as four stories of timber framing over a concrete podium. At the time of the fire, the framing for all stories was in place, but fire prevention systems had not yet been installed. Exterior walls, columns, and spandrels of the parking adjacent to the timber structure experienced extensive spalling as a result of the elevated temperatures (Fig. 12.1a). The extent of the spalling varied across the structure, but was severe enough to expose a significant area of steel reinforcement as well as prestressing strands in the southwest corner of the parking deck.

In this study, a suite of nondestructive evaluation techniques and inspection methods were applied to the 2nd and 4th elevations of double tee members within the parking deck. Based on a visual survey, the 4th elevation of double tees appeared to be subjected to the highest temperatures and greatest potential for structural damage, while the 2nd elevation of double tees appeared to be unaffected by the fire. These elevations are nominally identical in design, so the performance of the 2nd elevation serves as a baseline for the expected behavior of the 4th elevation of the parking deck prior to the fire. At each elevation in the parking deck, two rows of double tee members form a single helix ramp accommodating two-way traffic



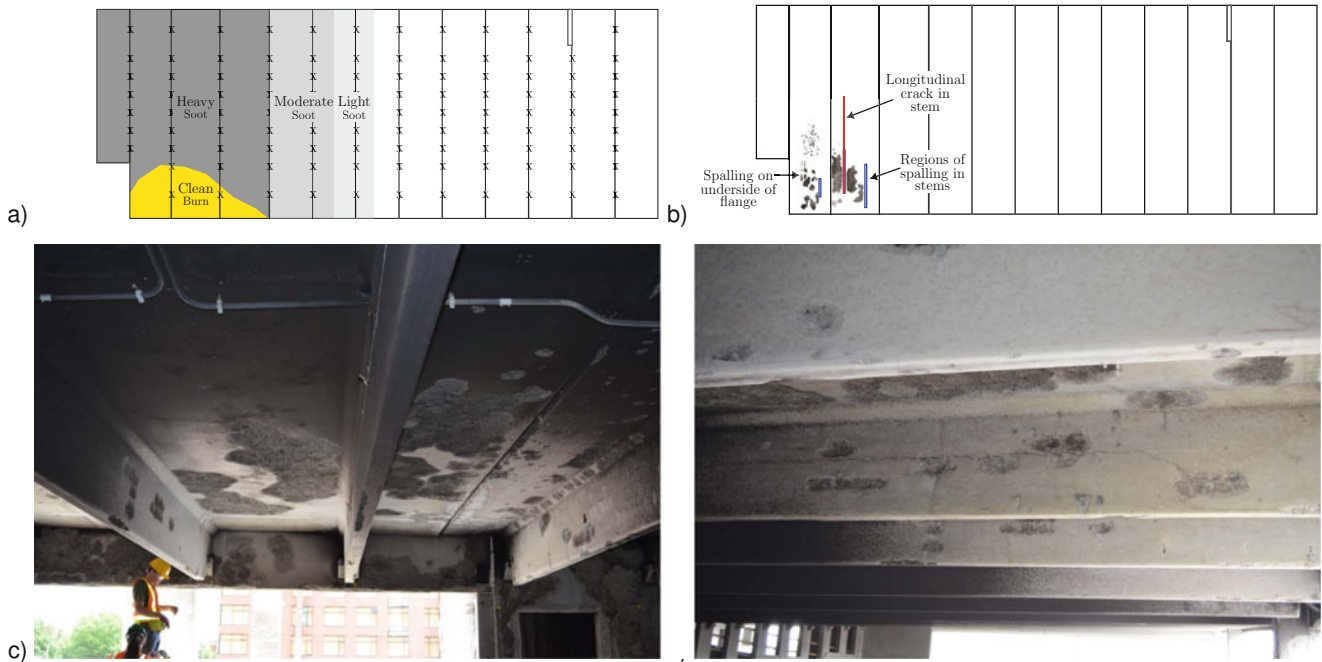
**Fig. 12.1** Case study structure: (a) photograph of exterior of parking deck after fire; (b) framing plan for a typical level

(Fig. 12.1b). Only the southern row of 13 double tees, denoted in blue within the figure, was experimentally tested for each elevation. The double tees were normal weight concrete and poured between seven and eight months prior to the fire. Although the flange width varied, all of the double tee members featured a 10.2 cm thick flange, stems spaced at 182.9 cm on-center, and a 76.2 cm total depth. The length of the double tees was approximately 18.2 m, with the exception of DT1, which was 13.3 m. The south end of each member was supported by corbels attached to the spandrels. The north end of members DT1-DT4 and DT11-12 were supported by inverted tee beams, while the north end of the remaining double tees were supported by corbels attached to wall panels. Flange-to-flange connections of adjacent members were developed by welds at the locations indicated by an “X” within Fig. 12.1b. Welded connections to the supporting spandrel, inverted tee beam, or wall panel were also present at the flange of every double tee directly over each stem and a continuous cast-in-place strip was poured along the perimeter of the floor.

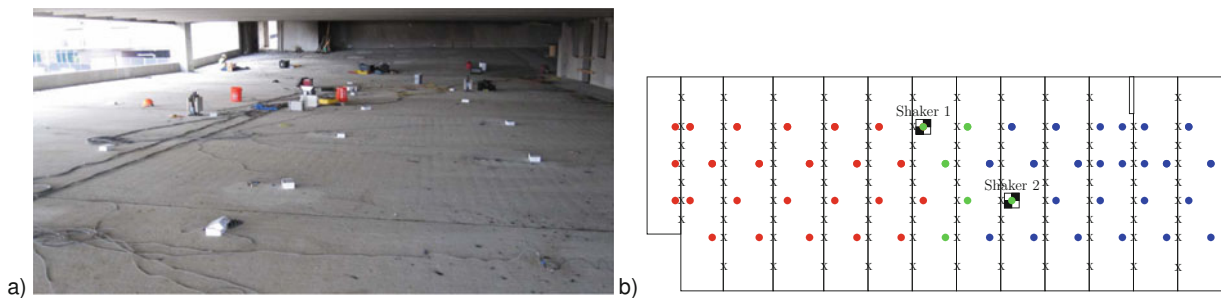
Visible symptoms of exposure to elevated temperatures and structural damage in the 4th elevation of double tees were generally limited to the four westernmost members. Figure 12.2a presents a map of the presence and relative density of soot observed on the 4th elevation members, as well as the location of a clean burn pattern in the southwest corner of the deck. The area of clean burn extended to approximately 5 m from the southern end of the member DT3. Clean burn patterns are often used in forensic investigations to identify regions of intense elevated temperatures, as the burning of soot and pyrolysis requires temperatures in excess of 600 °C [15]. Due to the temperatures required to develop clean burn, such surfaces are typically assumed to have been subjected to direct flame contact [16]. A summary of visual inspection of the double tees is provided in Fig. 12.2b, which indicates the location and approximate density of spalling observed on the underside of the members at the 4th elevation. Mapping of the spalling was facilitated by physical measurements as well as point clouds obtained through LiDAR scanning of the structure. This figure also indicates the location of a single longitudinal crack observed in the west stem of DT3. This longitudinal crack developed at the same elevation as the uppermost prestressing strand in the stem and extended from 1.8 to 10 m from the southern end of the member. Figure 12.2c provides a photograph of a portion of the longitudinal crack within the area of clean burn as well as representative spalling observed in the stems of this double tee. A photograph of the area with the most severe spalling in the flange of DT3 is provided in Fig. 12.2d.

### 12.3 Experimental Modal Analysis

As one component of the larger study, experimental modal analysis was performed on the double tee floors of the parking deck using a multiple-input, multiple-output (MIMO) approach. An array of 30 Measurement Specialties 4000 A uniaxial accelerometers were used to acquire the out-of-plane vibration response of the double tees at 54 locations using a reference-based approach to experimental modal analysis. These accelerometers feature a  $\pm 2g$  full-scale range, 0–200 Hz frequency bandwidth, and 1V/g sensitivity. The locations of the accelerometer placement is presented in Fig. 12.3, where red markers indicate the location of accelerometers in the first setup, blue markers indicate the location of the accelerometers in the second setup, and green markers indicate the location of the six stationary reference accelerometers. It is noted that the location of the reference accelerometers shared between the two test setups was constrained by the limited cable length of the instrumentation available at the site. The accelerometers were temporarily affixed to the top surface of the flange of



**Fig. 12.2** Visible symptoms of elevated temperature exposure in 4th elevation of double tees: (a) soot and clean burn patterns; (b) map of spalling and cracking; (c) photograph of clean burn of soot, longitudinal cracking, and spalling in stems; (d) photograph of spalling on the underside of the flanges of the same members



**Fig. 12.3** Experimental modal analysis of parking deck double tee floor: (a) photograph of setup; (b) instrumentation layout (red: accelerometers in setup 1; blue: accelerometers in setup 2; green: reference accelerometers common to both setups)

the double tees at locations directly over stems using bonding wax. A pair of APS Dynamics 113 Electro-Seis<sup>®</sup> long stroke shakers were used to generate prescribed excitation to the floor system. Each shaker was oriented in the gravitational direction and configured with 16 kg reaction masses. The shakers were independently driven in current mode with linear swept sine excitation over the 0.1 to 25 Hz frequency bandwidth over a 60 s duration. The swept sine signals used to control the electrodynamic shakers were generated with a pair of National Instruments PXI-5412 14-bit arbitrary waveform generators at an output rate of 50 kHz. Tests were performed with the shakers driven synchronously as well as asynchronously. National Instruments PXIe-4497 24-bit dynamic signal analyzers were used to digitize the voltage output from the array of distributed accelerometers and monitor outputs from the power amplifiers used to drive the shakers. A simultaneous sampling rate of 5 kHz was used to acquire all measurements.

### 12.3.1 Experimental Modal Parameter Estimates

The measurement data was first decimated to an effective sampling rate of 100Hz using multi-rate digital anti-alias filters prior to resampling. Experimental modal parameter estimates were obtained for each elevation using the combined

deterministic-stochastic subspace state-space system identification algorithm, originally formulated in Van Overschee and De Moor[17]. For each elevation, the algorithm was employed on data from three tests performed with the shakers driven synchronously and three tests performed with the shakers driven asynchronously. Stabilization diagrams were used to select three poles from each mode identified by the system identification algorithm for each individual test. The Modal Assurance Criteria (MAC) [18] was then used to identify consistent estimates of modal parameter estimates within a 1% undamped natural frequency deviation across all of the test perform for each elevation. Groups of modal parameter estimates exhibiting MAC correlations above 0.95 and meeting the proximity criteria for the undamped natural frequency were then averaged. The Modal Scale Factor (MSF) was used to normalize the phase and amplitude of mode shape estimates prior to this averaging.

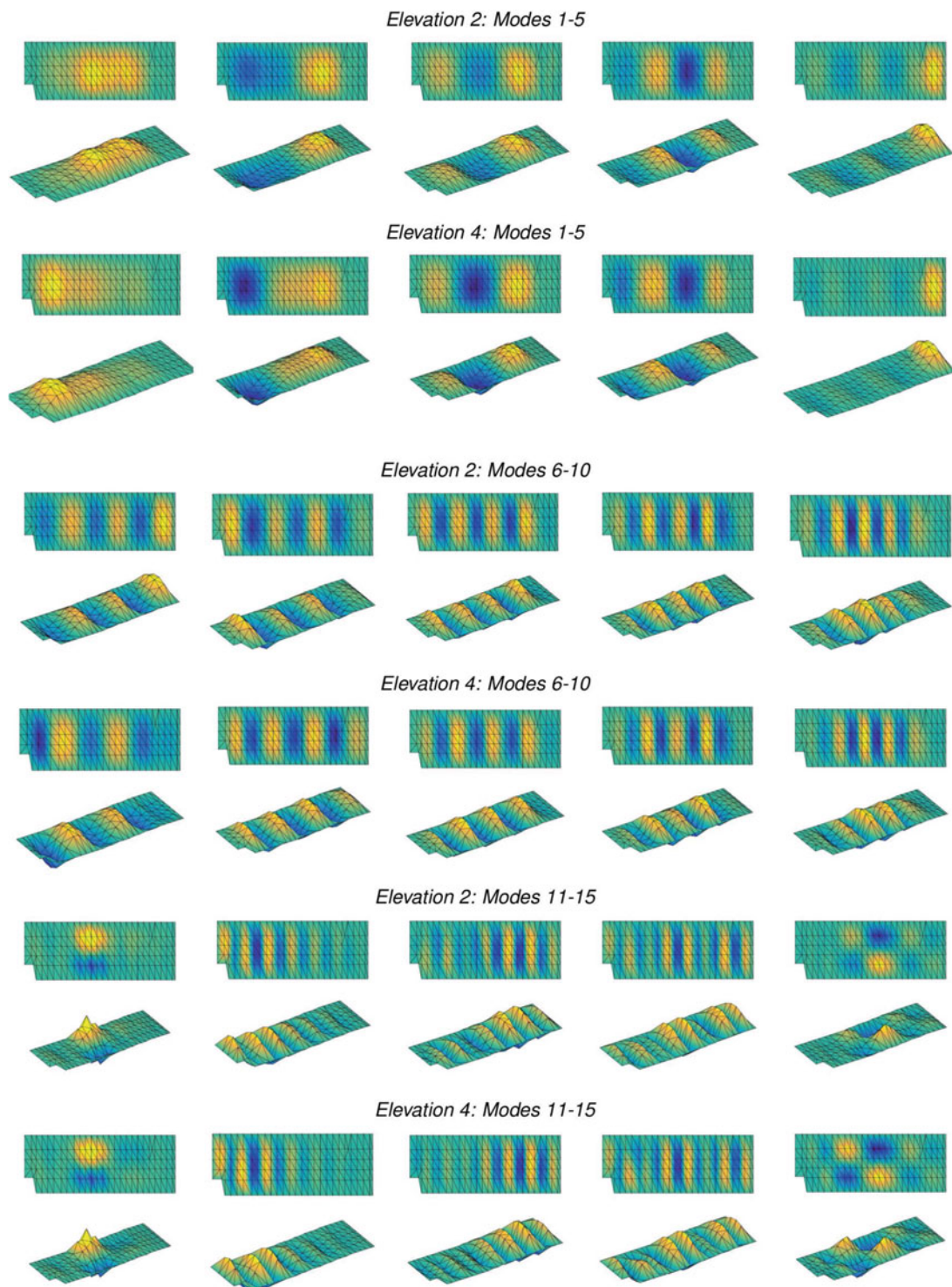
The first fifteen real-valued mode shape estimates obtained through the system identification for each elevation are presented in Fig. 12.4. The modes have been paired in this figure with the order of mode shapes established by the estimates obtained for the undamaged double tees at the 2nd elevation. The order of the mode shapes was identical for the damaged double tees at the 4th elevation, with exception of the fifth and sixth modes. Table 12.1 provides a summary of the experimental estimates of the natural frequencies corresponding with each mode shape. Within this table, the percentage change in natural frequency between the estimates obtained for the 2nd elevation and those obtained for the 4th elevation are shown. In addition, the diagonal entries of the Cross-MAC calculated using the corresponding mode shapes is presented to provide a measure of the consistency between the mode shapes obtained for each elevation. A pseudocolor plot of the full matrix of Cross-MAC values is provided in Fig. 12.5.

### 12.3.2 Discussion

This case study provides a unique experimental perspective on the effect of localized reductions in stiffness of fire damaged prestressed concrete on the modal parameters. This damage scenario is distinct from the majority of vibration-based structural health monitoring case studies within the existing literature because the deterioration likely produced moderate to significant reductions in the flexural stiffness distributed over a relatively large localized area. In contrast, most simulated damage scenarios applied in prior experiments have introduced very localized damage by utilizing saw cuts to simulate fatigue cracks [19–21], removal of bolts at connections[22], forced settlements at supports [22–24], or intentional overloading [24, 25]. In many of these studies, the damage scenarios typically introduced only minor changes in natural frequencies and modest changes in Cross-MAC correlations between mode shapes estimates obtained from the damaged and undamaged states, unless the extent of the damage was severe.

In the current study, the effect of reduced material stiffness in the region of clean burn associated with the highest elevated temperatures is visibly apparent in the changes in the measured modal parameters. Most notably, there are distinct increases in the relative modal displacements across double tees DT2 and DT3 observable in the first two mode shapes, as well as the sixth mode shape. These observations are consistent with the only known prior full-scale study on the effect of fire damage on the modal parameters of a prestressed concrete structure, where empirical evidence of the presence and location of the damage was noted in the experimentally measured mode shapes[12]. The Cross-MAC values presented in Table 12.1 provide a quantitative measure of the lack of consistency across these three mode shapes measured at the damaged and undamaged elevations. The Cross-MAC values for these modes are the lowest across all measured modes. Within the existing literature on vibration-based damage detection of full-scale structures, it is atypical to observe multiple Cross-MAC values indicating such low correlation between a subset of the damaged and undamaged mode shapes. This suggests that the relatively large localized area affected by the elevated temperatures, even if localized to a portion of the structure, may produce greater changes in the mode shapes than the typical damage scenarios utilized in most vibration-based damage detection studies. Consequently, vibration-based structural health monitoring and damage detection may be particularly well suited for structures vulnerable to fire damage. Furthermore, the significant changes in the lowest frequency mode shapes, and to a lesser extent the reductions in their natural frequencies, suggests that pseudo-flexibility methods for vibration-based damage detection and quantification are likely to be successful when applied to fire damaged structures. Interestingly, despite the significant differences observed in the lower frequency mode shapes, there is relatively strong correlation in the natural frequencies and mode shapes of the higher order modes between the two elevations. It is acknowledged that the comparisons presented and hypotheses developed are based on an assumption that the measured response of the nominally identical elevation of double tees without evidence of fire damage reasonably reflects, and can serve as a surrogate for the measurement of, the behavior of the fire damage elevation prior to the onset of structural damage. Future work will leverage finite element analysis of models constructed from the as-built plans, as well as supplemental measurements obtained from other nondestructive evaluation techniques applied to this structure, to support the plausibility of this assumption.





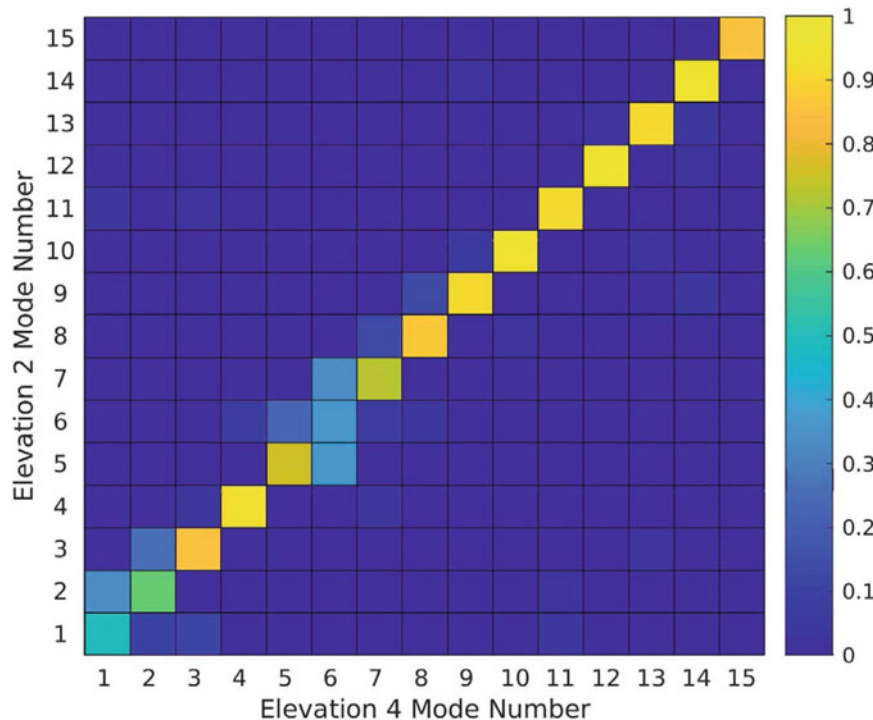
**Fig. 12.4** A subset of the experimental modal parameter estimates obtained for an undamaged and a damaged floor of the parking deck

## 12.4 Conclusion

Vibration-based methods for structural health monitoring and damage detection have been long proposed as potentially applicable to a wide range of civil infrastructure subject to various extreme loads as well as mechanisms of natural deterioration. However, while an increasing number of full-scale experimental studies have produced data with simulated

**Table 12.1** Experimentally estimated natural frequencies, percentage change in natural frequencies, and diagonal entries of the Cross-MAC

Mode	Elevation 2 $f_n$	Elevation 4 $f_n$	$\Delta f_n$ (%)	Cross-MAC $_{i,i}$
1	3.42	3.37	-1.5	0.50
2	3.61	3.50	-3.0	0.63
3	3.70	3.63	-1.9	0.85
4	4.04	4.04	-	0.94
5	4.32	4.36	0.9	0.76
6	4.35	4.22	-3.0	0.37
7	4.55	4.45	-2.2	0.73
8	4.79	4.76	-0.6	0.87
9	5.19	5.16	-0.6	0.92
10	5.53	5.52	-0.2	0.94
11	9.68	9.76	0.8	0.91
12	10.46	10.36	-1.0	0.94
13	11.05	11.05	-	0.92
14	12.02	11.95	-0.3	0.95
15	13.86	13.95	0.6	0.86



**Fig. 12.5** Cross-MAC calculated between mode shapes of double tee floor at elevation 2 and mode shapes of double tee floor at elevation 4

mechanically induced damaged on structures, there is a lack of published data on the effects of fire damage on modal parameters of actual structures. In this study, experimental modal analysis was performed on two nominally identical prestressed double tee floors in a parking deck adjacent to a large fire fueled by a timber framed mid-rise apartment under construction. Experimental modal parameters obtained from an elevation with visible evidence of elevated temperatures and structural distress were compared to the corresponding experimental modal parameters obtained from an elevation without visible evidence of structural distress. The experimental mode shape estimates exhibit empirical evidence of reduced stiffness in the region of fire damage in the form of increases in relative modal displacements. Although natural frequencies were only mildly reduced for the elevation of fire damaged double tees, Cross-MAC values for several modes quantify the significant changes in mode shape for several low frequency modes. Collectively, the observed changes in modal parameters are consistent with significant reductions in stiffness in a local region of the floor consistent with the location of the fire damage. The extent of the changes in modal parameters measured in this case study support the further pursuit of vibration-

based structural health monitoring and damage detection methodologies for structures vulnerable to fire damage. Future work will explore the efficacy of nonparametric and parametric approaches for vibration-based damage detection when applied to this unique case study.

**Acknowledgments** The research team would like to thank Mary Ann Griggas-Smith, Ladiel Vazquez, and Greg Force along with the Tindall Corporation for providing access to the structure and assisting with the research. Any opinions, findings, conclusions, or recommendations expressed in this paper are those of the authors and do not necessarily reflect the views of any acknowledged individuals.

## References

1. Chang, Y., Chen, Y., Sheu, M., Yao, G.: Residual stress-strain relationship for concrete after exposure to high temperatures. *Cem. Concr. Res.* **36**(10), 1999–2005 (2006)
2. Tao, Z.: Mechanical properties of prestressing steel after fire exposure. *Mater. Struct.* **48**(9), 3037–3047 (2015)
3. PCI: Design for fire resistance of precast/prestressed concrete, Precast/Prestressed Concrete Institute (PCI)
4. Kalaba, N., Bamonte, P., Felicetti, R.: Prestressed members under natural fires: a preliminary study on the residual behavior. In: *Applications of Structural Fire Engineering* (2015)
5. Epasto, G., Proverbio, E., Venturi, V.: Evaluation of fire-damaged concrete using impact-echo method. *Mater. Struct.* **43**, 235–245 (2010)
6. Whelan, M., Tempest, B., Scott, D.: Post-fire nondestructive evaluation of a prestressed concrete double-tee joist roof. *J. Perform. Constr. Facil.* **29**(2), 04014055 (2015)
7. Dilek, U.: Ultrasonic pulse velocity in nondestructive evaluation of low quality and damaged concrete and masonry construction. *J. Perform. Constr. Facil.* **21**(5), 337–344 (2007)
8. Chew, M.: The assessment of fire damaged concrete. *Build. Environ.* **28**(1), 97–102 (1993)
9. Duron, Z., Yoder, N., Kelcher, R., Hutchings, A., Markwardt, S., Panish, R.: Fire Induced Vibration Monitoring for Building Collapse. National Institute of Standards and Technology (NIST), (2005) [https://tsapps.nist.gov/publication/get\\_pdf.cfm?pub\\_id=101379](https://tsapps.nist.gov/publication/get_pdf.cfm?pub_id=101379)
10. Moaveni, B., Stavridis, A., Lombaert, G., Conte, J., Shing, P.: Finite-element model updating for assessment of progressive damage in a 3-story infilled RC frame. *J. Struct. Eng.* **139**(10) 1665–1674 (2013)
11. Kernicky, T., Whelan, M., Weggel, D., Rice, C.: Structural identification and damage characterization of a masonry infill wall in a full-scale building subjected to internal blast load. *J. Struct. Eng.* **141**(1) 1–13 (2015)
12. Whelan, M., Tempest, B., Scott, D.: Influence of fire damage on the modal parameters of a prestressed concrete double-tee joist roof. *Struct. Control. Health Monit.* **21**(11), 1335–1346 (2014)
13. Liu, C., Huang, X., Miao, J., Ba, G.: Modification of finite element models based on support vector machines for reinforced concrete beam vibrational analyses at elevated temperatures. *Struct. Control. Health Monit.* **26**(6), e2350 (2019)
14. Liu, C., Liu, C., Liu, C., Huang, X., Miao, J., Xu, W.: Fire damage identification in RC beams based on support vector machines considering vibration test. *KSCE J. Civ. Eng.* **23**(10), 4407–4416 (2019)
15. Hartman, J., Beyler, A., Riahi, S., Beyler, C.: Smoke oxidation kinetics for application to prediction of clean burn patterns. *Fire Mater.* **36**(3), 177–184 (2012)
16. Carman, S.: Clean burn fire patterns – a new perspective for interpretation. In: *4th International Symposium on Fire Investigations Science and Technology* (2010)
17. Van Overschee, P., De Moor, B.: *Subspace Identification for Linear System Theory, Implementation, Applications*. Kluwer Academic Publishers, Dordrecht (1996)
18. Allemang, R.J., Brown, D.L.: A correlation coefficient for modal vector analysis. In: *Proceedings of the 1st International Modal Analysis Conference*, Vol. 1, pp. 110–116 (1982)
19. Alampalli, S., Fu, G., Dillon, E.: On the use of measured vibration for detecting bridge damage. In: *Fourth International Bridge Engineering Conference* (1995)
20. Farrar, C., Jauregui, D.: Comparative study of damage identification algorithms applied to a bridge: I. experiment. *Smart Mater. Struct.* **7**(5), 704–719 (1998)
21. Lee, J., Yun, C.: Damage diagnosis of steel girder bridges using ambient vibration data. *Eng. Struct.* **28**(6), 912–925 (2006)
22. Whelan, M., Janoyan, K.: In-service diagnostics of a highway bridge from a progressive damage case study. *J. Bridg. Eng.* **15**(5), 597–607 (2010)
23. Maeck, J., Peeters, B., De Roeck, G.: Damage identification on the Z24 bridge using vibration monitoring. *Smart Mater. Struct.* **10**, 512–517 (2001)
24. Huth, O., Feltrin, G., Maeck, J., Kilic, N., Motavalli, M.: Damage identification using modal data: experiences on a prestressed concrete bridge. *J. Struct. Eng.* **131**(12), 1898–1910 (2005)
25. Toksoy, T., Aktan, A.: Bridge-condition assessment by modal flexibility. *Exp. Mech.* **34**(3), 271–278 (1994)

**Matthew Whelan** is an Associate Professor in the Department of Civil and Environmental Engineering at the University of North Carolina at Charlotte. His research focuses on full-scale performance testing of civil structures and structural health monitoring.



# Chapter 13

## Occupant Localization in Obstructive Indoor Environments Using Footstep-Induced Floor Vibrations

Mostafa Mirshekari, Jonathon Fagert, Shijia Pan, Pei Zhang, and Hae Young Noh

**Abstract** In this paper, we characterize the effects of obstructions on footstep-induced floor vibrations to enable obstruction-invariant indoor occupant localization. Occupant localization is important in smart building applications such as healthcare and energy management. In prior works, footstep-based vibration sensing has been introduced for non-intrusive occupant localization in open areas. However, real buildings have various types of obstructions (e.g., walls, furniture, etc.) which affect the wave propagation characteristics and significantly reduce localization accuracy. Requiring unobstructed paths between footsteps and sensors results in higher instrumentation and maintenance cost for these prior works. We have observed that the obstruction mass is one of the key factors affecting localization accuracy by altering wave propagation velocity. Therefore, to overcome the obstruction challenge, we (1) detect and estimate the mass of the obstruction by characterizing the attenuation rate, and (2) model the velocity-mass relationship to find the propagation velocities which in turn are used for occupant localization through non-isotropic multilateration. In field experiments, we achieved an average localization error of 0.61 m, which is a 1.6X improvement compared to the baseline approach.

**Keywords** Structural vibrations · Obstruction · Multilateration · Occupant localization

### 13.1 Introduction

Occupant localization is an important part of many smart building applications such as smart health care and adaptive energy management [1, 2]. Prior works have explored non-intrusive occupant localization using structural vibrations [2]. These works are based on the intuition that the footstep-induced vibration waves arrive at different sensors at different times. These Time Differences of Arrivals (TDoAs) are used to localize the occupants through multilateration. This approach assumes the floor is homogeneous and non-obstructed. However, obstructions (e.g., walls, furniture, etc.) change the floor structural properties and, in turn, the wave propagation velocity between the footstep and the sensors and thus, reduce the occupant localization accuracy [3]. Therefore, to maintain high localization accuracy in obstructed settings, the prior works need to ensure an unobstructed wave propagation path between the footstep and the sensors which increases the deployment and maintenance costs.

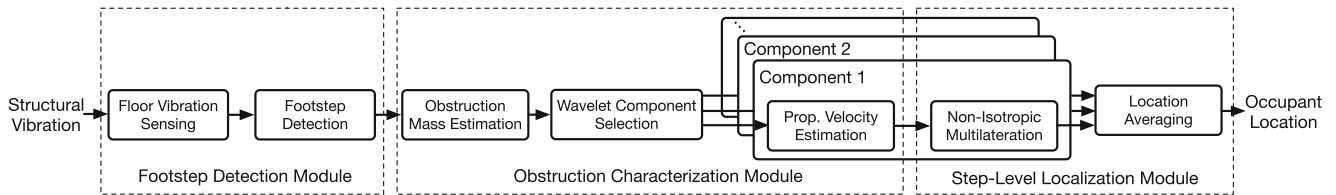
In this paper, we introduce a footstep-vibration-based occupant localization approach which is robust to obstructions and, therefore, significantly reduces sensing requirements in obstructive indoor settings. This approach achieves localization robustness by considering different wave propagation velocities between the footstep and various sensors based on the presence and mass of the obstruction on the wave path. The main challenge is that, for a specific footstep, we do not know the existence and mass of the obstruction and its effect on the wave propagation velocity. To overcome this challenge, we leverage the Lamb wave propagation properties to characterize how the addition of mass affects the signal energy (i.e., the

---

M. Mirshekari (✉) · J. Fagert · H. Y. Noh  
Department of Civil and Environmental Engineering, Carnegie Mellon University, Pittsburgh, PA, USA  
e-mail: [mmirshekari@cmu.edu](mailto:mmirshekari@cmu.edu); [jfagert@cmu.edu](mailto:jfagert@cmu.edu); [noh@cmu.edu](mailto:noh@cmu.edu)

P. Zhang  
Department of Electrical and Computer Engineering, Carnegie Mellon University, Moffett Field, CA, USA  
e-mail: [peizhang@cmu.edu](mailto:peizhang@cmu.edu)

S. Pan  
Department of Computer Science and Engineering, University of California, Merced, CA, USA  
e-mail: [span24@ucmerced.edu](mailto:span24@ucmerced.edu)



**Fig. 13.1** Overview of occupant localization approach in the obstructed indoor settings

attenuation rate) and the wave propagation velocity. Finally, we utilize these velocities to localize the occupants through a non-isotropic multilateration formulation which relaxes the assumption of similar propagation velocity in different directions. To validate the system performance, we use field experiments on a concrete slab on grade floor in a campus building with human participants.

## 13.2 Gait Balance Estimation Approach

Our approach enables obstruction invariant localization by accounting for velocity differences when obstructions are present. To this end, the approach consists of three main modules: (1) footstep detection, (2) obstruction characterization, and (3) step-level localization. The different stages of this approach are presented in Fig. 13.1.

### 13.2.1 Footstep Detection Module

The Footstep Detection module measures the ambient floor vibration and then isolates the parts of signal which are caused by footsteps. To measure the vibration, we use low cost geophone sensors that measure the vertical velocity of floor vibration. To isolate the footstep-induced signals, we first detect the part of the signal caused by impulsive excitations (e.g. footsteps, object falls, and door closings) using a Chi-squared-based anomaly detection. Then, among these impulsive excitations, we distinguish footsteps using a model-transfer-based SVM classifier [4].

### 13.2.2 Obstruction Characterization Module

Our obstruction characterization module (1) detects the obstruction in the wave propagation path and estimates its mass and (2) finds the wave propagation velocity based on this mass. To estimate and detect the obstruction mass, we characterize the wave attenuation rates caused by the obstruction. Intuitively, the addition of obstruction mass results in different levels of energy reduction across different frequency components. However, these component energies also depend on the footstep force which makes it challenging to find out whether the energy reduction is caused by an obstruction or a lighter footstep. To overcome this challenge, we have characterized the relationship between the energy ratios across different frequency components and the obstruction mass. Using these ratios, the footstep force cancels out as the energy of different frequency components is affected similarly by the footstep force (assuming a linear and elastic system).

Further, we characterize the mass-velocity relationship using Lamb wave propagation characteristics. To consider the dispersive and frequency-dependent wave propagation, we first decompose the signals using wavelet decomposition which is suitable for decomposing non-stationary signals such as footsteps [5]. Then, to ensure we are not choosing signals with low Signal-to-Noise Ratio (SNR), we choose a subset of the scale components with the highest energy across all the sensors. Finally, for each selected component, we estimate the wave propagation velocity as a function of the obstruction mass using Lamb wave equation.

### 13.2.3 Step-Level Localization Module

Our non-isotropic multilateration approach considers various propagation velocities in different directions. Specifically, our approach takes two main steps: (1) the simulation step and (2) the filtering step. The simulation step takes the propagation velocities found in the previous module to find the possible TDoA ranges when a footstep happens in the boundary of the room. The filtering step compares the measured TDoA with these possible TDoAs and finds the locations in the room where measured and possible TDoAs are similar. Finally, to improve the localization robustness, we average multiple location estimations from the scale components selected in the previous module.

## 13.3 Evaluation

To evaluate our occupant localization approach in obstructed indoor settings, we conducted real-world experiments on a slab-on-grade concrete floor in a campus building (shown in Fig. 13.2a). To mimic the effect of an obstruction mass, we used a plastic bin filled with sand. The sensing configuration is shown in Fig. 13.2b. We compare our localization errors with a baseline and unobstructed approaches. The baseline (1) averages the estimations across all the scale components, (2) does not account for the effect of the obstruction, (3) utilizes a Nonlinear Least Square (NLS) ToA-based multilateration. As shown in Fig. 13.2c, our approach results in a 0.61 m average localization error which is equivalent to a 1.6X improvement over the baseline approach. Further, our results are comparable to the results of the unobstructed approach, which means that we successfully negate the obstruction effect.

## 13.4 Conclusions

In this paper, we introduce a floor-vibration-based occupant localization approach which is robust to obstructions such as walls and furniture. Our approach characterizes how the obstruction mass affects the wave propagation velocity and the attenuation rate using the Lamb wave propagation properties. These characteristics are then used for estimating the wave propagation velocity in obstructed indoor environments which, in turn, is used for occupant localization through non-isotropic multilateration. Our approach resulted in a 0.61 m average location estimation error, which corresponds to a 1.6X improvement compared to the baseline that does not account for obstructions.

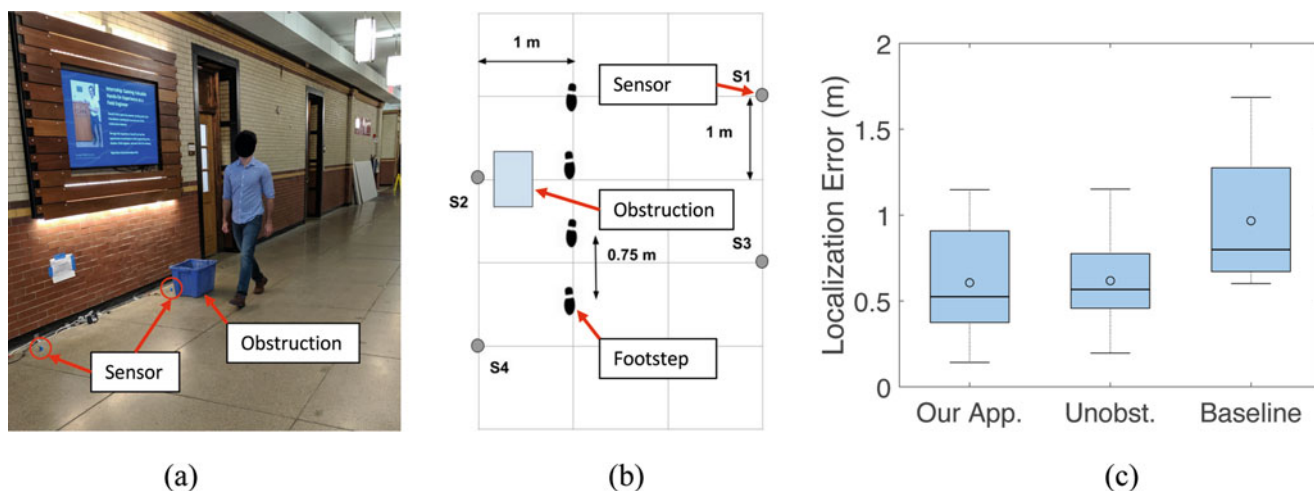


Fig. 13.2 Real world experimental evaluation. (a) Experimental location. (b) Sensing configuration. (c) Localization performance

## References

1. Bahroun, R., Michel, O., Frassati, F., Carmona, M., Lacoume, J.-L.: New algorithm for footstep localization using seismic sensors in an indoor environment. *J. Sound Vib.* **333**(3), 1046–1066 (2014)
2. Mirshekari, M., Pan, S., Fagert, J., Schooler, E.M., Zhang, P., Noh, H.Y.: Occupant localization using footstep-induced structural vibration. *Mech. Syst. Signal Process.* **112**, 77–97 (2018)
3. Achenbach, J.: *Wave Propagation in Elastic Solids*, Vol. 16. Elsevier, Amsterdam (2012)
4. Mirshekari, M., Fagert, J., Pan, S., Zhang, P., Noh, H.Y.: Step-level occupant detection across different structures through footstep-induced floor vibration using model transfer. *J. Eng. Mech.* **146**(3), 04019137 (2020)
5. Addison, P.S.: *The Illustrated Wavelet Transform Handbook: Introductory Theory and Applications in Science, Engineering, Medicine and Finance*. CRC press, Boca Raton, Florida (2002)

**Mostafa Mirshekari** I work on physics-guided data-driven models to characterize structural vibrations for occupant monitoring. I have published in both top-tier conferences and journals in Computer Science as well as Civil Engineering. Furthermore, I have received multiple awards and fellowships, including Bertucci fellowship, and six best paper and poster awards.



# Chapter 14

## Time-Frequency Analysis of Crowd Lateral Dynamic Forcing from Full-Scale Measurements on the Clifton Suspension Bridge

R. E. White, N. A. Alexander, and J. H. G. Macdonald

**Abstract** Pedestrian-induced vibrations have caused significant issues on various footbridges, over the past few decades, as it can lead to an abrupt growth in the amplitude of structural oscillations, i.e. lateral dynamic instability. Measurements were taken during two separate crowd loading events on the Clifton Suspension Bridge, UK, to characterise the human-structure interactions observed. Two lateral modes of the bridge were studied, previously found susceptible to pedestrian-induced excitation. A comparative study is performed to identify the different interactions observed for the differing bridge deck amplitude responses through a novel procedure based on time-frequency analysis. This enables the identification of the fluctuations on the instantaneous modal amplitude and resonant frequency during pedestrian loading. Previous measurements of Clifton Suspension Bridge during crowd loading leading to the onset of large-amplitude vibrations revealed a significant increase in the natural frequency of the two modes considered. The instantaneous frequency, of both modes, appeared to roughly mirror the displacement amplitude response during significant loading, >250 pedestrians. Recent measurements of Clifton Suspension Bridge during crowd loading, illustrated tentative evidence for the presence of human-structure interactions during low-amplitude responses. For high amplitude responses on the bridge the modal frequencies were observed to increase with an increase in amplitude displaying a complex non-linear hardening effect for the two modes of vibration.

**Keywords** Bridges · Structural dynamics · Full-scale testing · Human-structure interactions · Pedestrian-induced vibrations

### 14.1 Introduction

Pedestrian loading of footbridges has caused serious concern for vibration serviceability. Multiple footbridges have observed lateral dynamic instability, resulting in the onset of large amplitude vibrations. The London Millennium Footbridge (LMF) [1] and Clifton Suspension Bridge (CSB) [2] are examples of this phenomenon. Significant multi-modal excitation has been observed on the CSB [2]. Pedestrians have been observed to significantly alter a structure's properties: modal damping and frequency, which is reflected in fluctuations of a bridge's instantaneous amplitude and frequency respectively. Pedestrian lateral dynamic forcing can be characterised as the action of equivalent added mass or damping which may be positive or negative, depending on the pedestrian pacing to bridge forcing frequency ratio.

Decomposing a structure's modal properties may be difficult to successfully approximate, as pedestrian loading contains a frequency spectrum producing multi-modal excitation. This paper presents a time-frequency analysis procedure for evaluating lateral human-structure interactions from full-scale measurements on the Clifton Suspension Bridge, from two separate crowd loading events. The Hilbert transform is utilised to identify the instantaneous amplitude and frequency of two low-frequency lateral resonant modes, modes L2 and L3, previously shown to be susceptible to pedestrian-induced vibrations [2]. The evaluated amplitude and frequency time-histories, of each lateral mode, are quantitatively studied to characterise equivalent added mass and damping of pedestrians, for each crowd loading event. Comparisons are drawn between low- and high amplitude bridge responses. A complex instantaneous amplitude-frequency relationship is observed for the two lateral modes studied, for large amplitude bridge responses. The corresponding 'back-bone' curves are constructed from reduced-

---

R. E. White (✉) · N. A. Alexander · J. H. G. Macdonald  
Department of Civil Engineering, Queen's Building, University of Bristol, Bristol, UK  
e-mail: [rorry.white@bristol.ac.uk](mailto:rorry.white@bristol.ac.uk)



order, fifth order, polynomials, for both modes respectively, to characterise the lateral human-structure interactions. They both display a hardening effect, i.e. an increase in resonant frequency with an increase in amplitude.

## 14.2 Experimental Procedure

The Clifton Suspension Bridge spans the River Avon bridging from Clifton, Bristol, to Leigh Woods, North Somerset. It is approximately 2 km west of the centre of Bristol. The main span is 214.35 m, from centreline to centreline of the towers, with the suspended bridge length spanning 193.85 m. The roadway is 6.1 m wide between the two longitudinal stiffening girders. These are supported by vertical suspension rods spaced 2.44 m apart from each other along the bridge. Total deck width is 9.46 m including 1.1 m footways either side. A more complete description of the structure is given by Barlow [3]. The bridge layout and rod breakdown are displayed in Fig. 14.1.

The CSB was instrumented with accelerometers and displacement transducers at multiple rod locations: Rod 40LW, Rod 11LW and Rod 40C, as shown in Fig. 14.1. These sensors acquired both lateral and vertical responses during the crowd loading events. Measurements at rod 11LW are used for analysis in this study, as they represent close approximates of the total modal responses of modes' L2 and L3. See reference [4] for full details on the structural health monitoring system used on the CSB.

In 2003, the Clifton Suspension Bridge exhibited two crowd loading events, restricted to the footways, on the nights of Thursday 7th and Saturday 9th August. Data analysis is focused on the measurements acquired from the 7th August for the proposed time-frequency method of analysis. In 2017, the CSB observed a crowd loading event, open to roadway and footways, on the afternoon of Sunday 15th October.

### 14.2.1 Number of People

During the 2003 crowd loading event, the number of people were monitored by CCTV footage counting the accumulative number in three-minute intervals. The CCTV data was used to approximate the pedestrian counts during the crowd loading event. For the 2017 crowd loading event, the number of people were measured by two GoPro cameras, one either side of the bridge pillars, in conjunction with counting pedestrians on and off the bridge using the phone application, Timestamp, by four volunteers. Figure 14.2a, b display the number of people during the crowd loading events in 2003 and 2017 respectively. The maximum number of people, at any one given time, was approximated to be 488 and 151 people, during the 2003 and 2017 crowd loading events respectively. This corresponded to approximate pedestrian densities of  $1.1 \text{ m}^2/\text{ped.}$ , per walkway, and  $0.13 \text{ m}^2/\text{ped.}$ , across the roadway, respectively. This suggests that pedestrians, during the crowd loading event witnessing large-amplitude vibrations, displayed significantly small walking speeds corresponding to low pacing frequencies. The combination of pedestrian numbers and prolonged low stepping frequencies may have contributed to the onset of large amplitude vibrations. The 2017 event suggests that pedestrians were more free flowing, promoting larger walking speeds and comfortable pacing frequencies. The 2003 event on the Clifton Suspension bridge was observed to last approximately

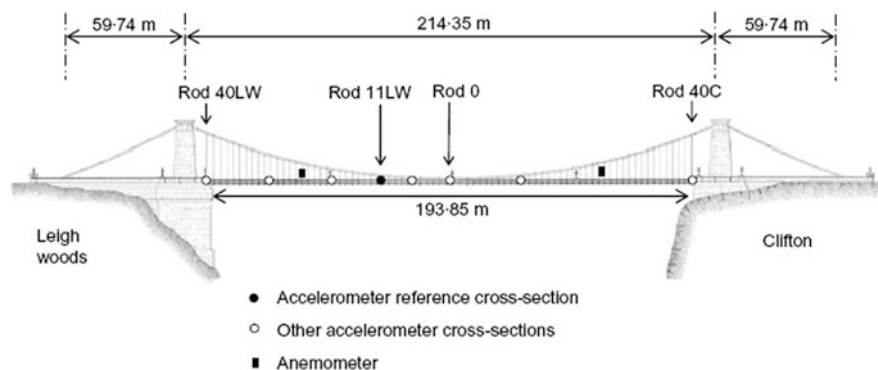
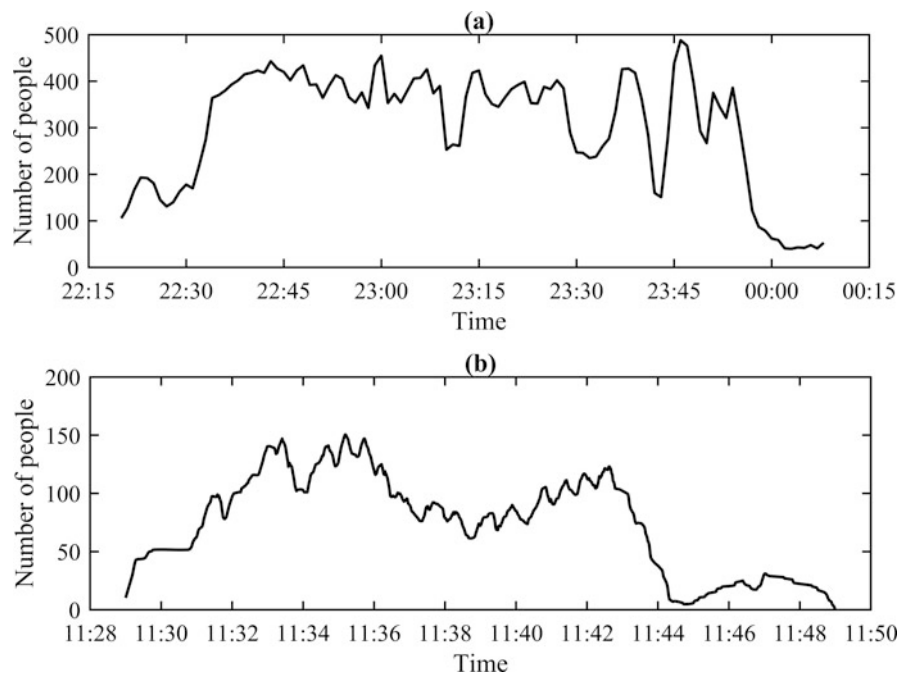


Fig. 14.1 Schematic and layout of the Clifton Suspension Bridge [3] displaying instrumented rod location



**Fig. 14.2** Number of people during the crowd loading events measured on the Clifton Suspension Bridge (a) 2003; (b) 2017

2 hours in comparison to 20 minutes during the 2017 event. This is reflected in the high and low acceleration amplitude responses measured from each experiment respectively [2, 5].

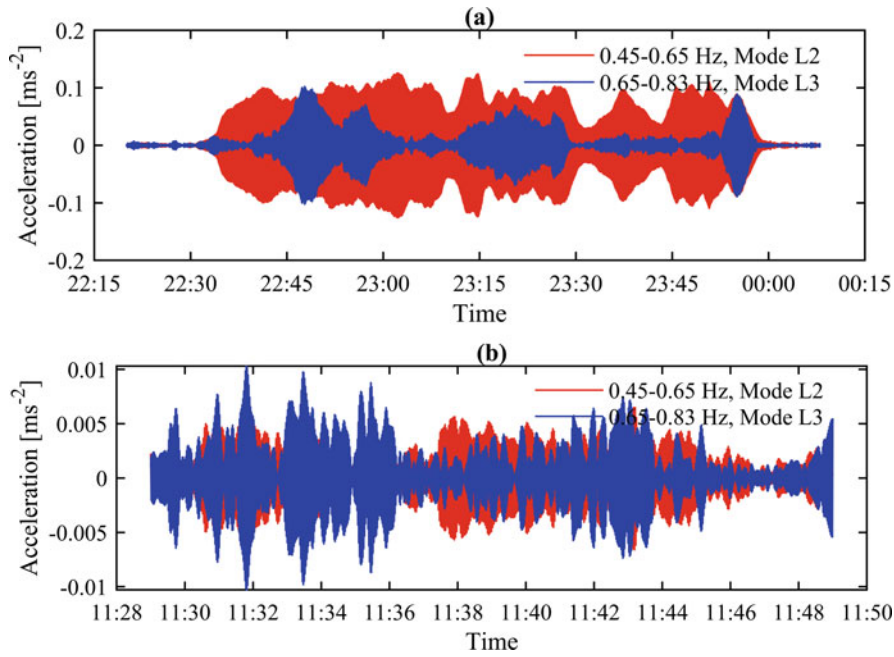
### 14.2.2 Bridge Response

The bridge deck was seen to oscillate in two of its low-frequency lateral modes: L2 (0.52 Hz) and L3 (0.75 Hz), during the 2003 crowd loading event. This was observed to occur simultaneously displaying multi-modal structural excitation by pedestrians. To be consistent with data processing from the 2003 event, the 2017 measurements were processed in the same manner to compare the two events and corresponding bridge responses. Sixth order bandpass Butterworth filters were applied to extract modes L2 and L3, in their prescribed bandwidths, to mitigate the effects of noise. Figure 14.3 displays the bridge deck accelerations measured at Rod 11, for modes L2 and L3 for each crowd loading event. Figure 14.3a indicates the 2003 event whilst Fig. 14.3b displays the 2017 event. The red indicates mode L2, whilst blue distinguishes mode L3. The amplitude response from the 2003 crowd loading event is observed to be significantly larger than the 2017 event.

Table 14.1 illustrates the modal properties of lateral modes L2 and L3 of the CSB, based on experimental system identification performed by Macdonald [2]. These two modes have significantly low damping ratios making them susceptible to pedestrian-induced vibrations. It should be clear, lateral modes from L1 through to L4, 0.25–0.965 Hz, have been previously identified. For this study, only modes L2 and L3 are analysed to identify the observed human-structure interactions.

## 14.3 Time-Frequency Analysis

Time-frequency analysis is beneficial in analysing the instantaneous frequency and amplitude of a structure's response to dynamical loading. During crowd loading, pedestrians have been observed to alter a structure's modal instantaneous frequency and amplitude [1, 2]. This corresponds to their dynamic forcing producing equivalent added mass and damping, positive or negative, depending on the frequency ratio, human pacing frequency to structural forcing frequency. Pedestrian forcing in-phase with acceleration corresponds to added mass, whilst forcing in-phase with velocity is equated to added damping. The Hilbert transform converts a real continuous, or discrete, signal into an analytic solution [6]. This allows



**Fig. 14.3** Bridge deck acceleration time-histories for lateral modes L2 and L3 on the Clifton Suspension Bridge (a) 2003 crowd loading event; (b) 2017 crowd loading event

**Table 14.1** Modal properties of lateral modes of the Clifton Suspension Bridge, evaluated from Macdonald [2]

Mode	Natural frequency [Hz]	Damping ratio [%]	Modal mass [Tonnes]
L2	0.524	0.58	538
L3	0.746	0.68	561

the evaluation of the instantaneous phase and amplitude of a structure's modal response. This time-frequency method only allows unimodal analysis, requiring measured structural responses to be filtered and decomposed into modal components. Lateral bridge acceleration measurements are first filtered to isolate modes L2 and L3 separately. For further understanding of the method, see reference [5].

Assuming a discrete complex signal,  $S_q(t)$ , for a single mode, of the form:

$$S_q(t) = x_q(t) + iy_q(t) \quad (14.1)$$

Where  $x_q(t)$  is the discrete input signal,  $y_q(t)$  is the Hilbert transformed input signal and  $i = \sqrt{-1}$ . The instantaneous amplitude,  $A_q(t)$ , and phase,  $\theta_q(t)$ , of the  $q$ th mode, can be evaluated from the modulus and argument respectively, using Pythagorean and trigonometric principles, as shown below:

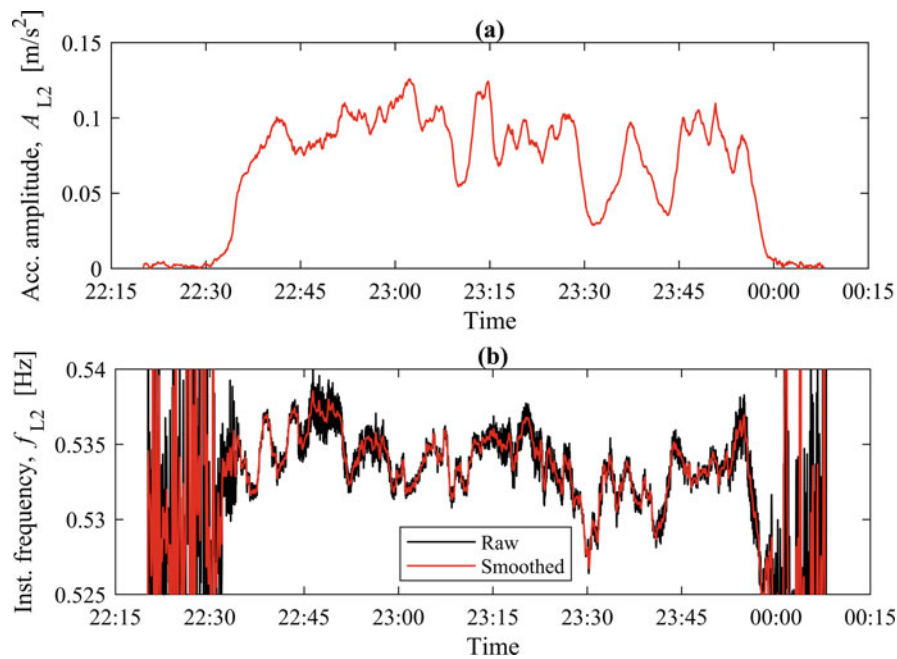
$$A_q(t) = \sqrt{x^2(t) + y^2(t)}, \quad \theta_q(t) = \tan^{-1} \frac{y(t)}{x(t)} \quad (14.2)$$

The instantaneous modal frequency,  $f_q$ , can then be approximated by differentiating the instantaneous frequency with respect to time, using the finite difference method, shown as:

$$f_q = \frac{1}{2\pi} \frac{d\theta_q}{dt} = \frac{1}{2\pi} \frac{\Delta\theta}{T_{p,s}} = \frac{1}{2\pi} \frac{\theta_i - \theta_{i-1}}{T_{p,s}} \quad (14.3)$$

Where  $T_{p,s}$  is the sampling period which is analogous to the inverse of the sampling frequency,  $f_s = 1/T_{p,s}$

This method provides a very good approximation of the response envelope making it very beneficial [6]. This allows the extraction of data from each sample in comparison to the conventional cycle-by-cycle zero-crossing maximum and minimum points of vibrations [7]. Fluctuations in the bridge modal frequency would suggest the presence of equivalent added mass whilst variations in the bridge amplitude would indicate equivalent added damping by pedestrians. There are limitations to



**Fig. 14.4** Comparison plot from 2003 crowd loading event, Mode L2 (a) Instantaneous amplitude time-history (b) Instantaneous frequency time

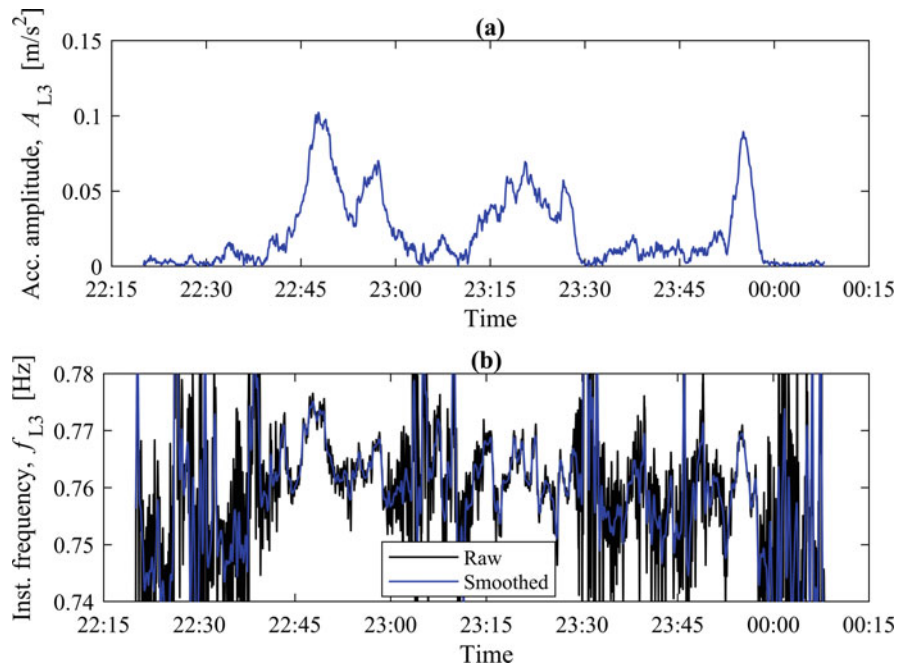
this time-frequency analysis method. Noise is attenuated at beginning and end conditions which can cause issues in accurate data extraction and analysis. Inherently noisy signals are amplified through this transform hence, a fourth order low pass Butterworth filter is used to smooth the instantaneous modal frequency responses and identify the underlying trends. To mitigate the end effects a larger window of the signal is used when applying the Hilbert transform which is then isolated about the crowd loading event.

### 14.3.1 Human Structure Interactions

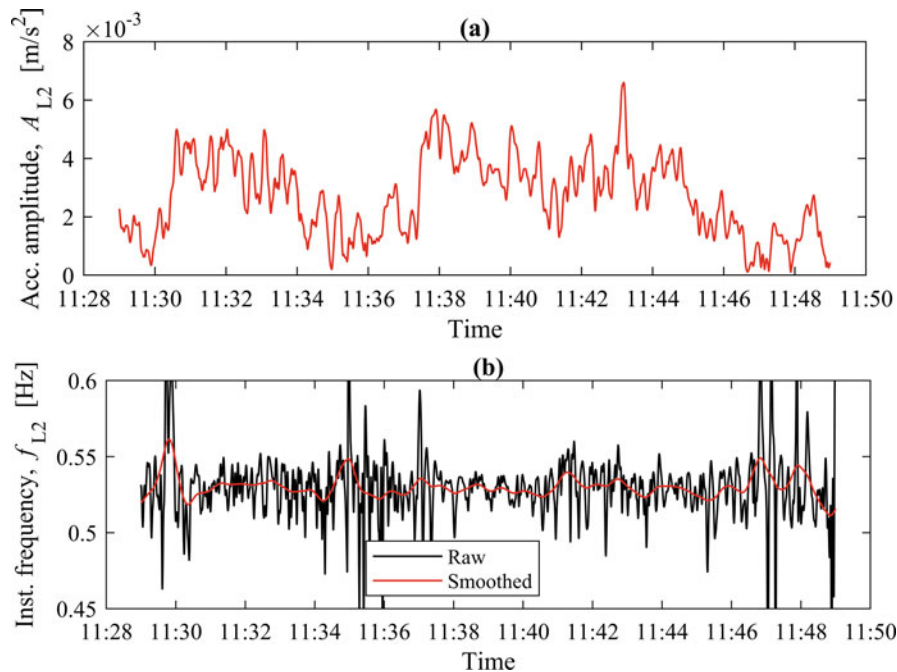
During the 2003 crowd loading event, a large-amplitude vibrational response was observed, a sudden onset in diverging large amplitude vibrations. This was a result of the number of people interacting on the bridge over a two-hour window. As detailed by Arup [1], the critical number of people were achieved for the two-low frequency lateral modes on the CSB. This is reflected in the number of people and bridge response in Figs. 14.2a and 14.3a. In 2017, the crowd loading event observed low-amplitude oscillations. The number of people interacting with the bridge were considerably less than the critical number of people for the onset of large amplitude vibrations to occur. The loading was observed over a 20-minute window. Figures 14.4 and 14.5 are breakdown plots of instantaneous amplitude, (a), and frequency, (b), time-histories for modes L2 and L3 respectively during the 2003 crowd loading event. Figures 14.5 and 14.6 are breakdown plots of instantaneous amplitude and frequency time-histories, for modes L2 and L3 respectively, during the 2017 crowd loading event.

In Fig. 14.4, the instantaneous modal frequency roughly mirrors the amplitude response, for mode L2. Interestingly, it reflects the loading, i.e. the number of people in Fig. 14.2a, reasonably well. The maximum instantaneous acceleration amplitude,  $0.13 \text{ m/s}^2$ , and frequency,  $0.539 \text{ Hz}$ , are not observed to correspond at the same instance. These correlate to approximately 350 and 400 pedestrians respectively, suggesting different phasing for the pedestrian, self-excited, forces. This mode observes a frequency increase of 2.8% at the maximum instantaneous frequency observed.

Figure 14.5 follows similar mirroring in amplitude and frequency response during the 2003 crowd loading event, however, not as well correlated to the number of people. Distinct mirroring is evident in three sections of the time histories during large amplitude responses,  $A(t) > 0.05 \text{ ms}^2$ . For mode L3, the maximum instantaneous acceleration amplitude,  $0.10 \text{ m/s}^2$ , and frequency,  $0.775 \text{ Hz}$ , are observed to correspond at roughly the same time. This correlates to an approximate pedestrian number of 350. This mode observes a frequency increase of 3.9% at the maximum instantaneous frequency observed. Interestingly, these instantaneous maxima occur at roughly the same instance, for modes L2 and L3, reinforcing that pedestrian synchronisation didn't occur during the 2003 event.

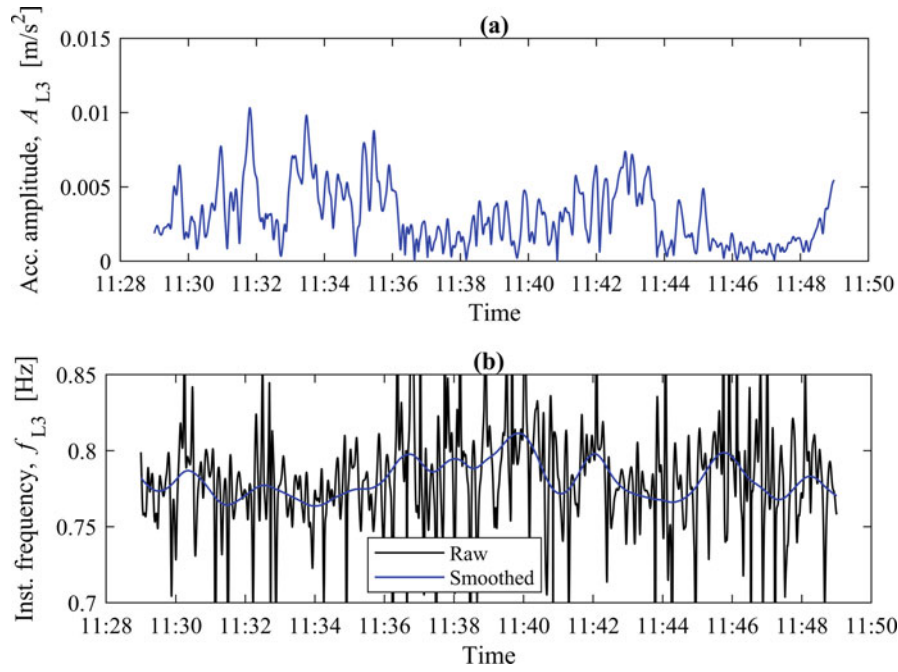


**Fig. 14.5** Comparison plot from 2003 crowd loading event, Mode L3 (a) Instantaneous amplitude time-history (b) Instantaneous frequency time-history



**Fig. 14.6** 2017 crowd loading event, Mode L2 (a) Instantaneous amplitude time-history (b) Instantaneous frequency time-history

Figures 14.6 and 14.7 display low-amplitude responses, making it more difficult to identify signs of human-structure interactions, nevertheless, subtle behaviour is observed. In the first 5 minutes of Fig. 14.6, the increase in amplitude is subtly reflected by an increase in frequency of mode L2. This corresponds to the initial rise in the number of people, during 11:30 am and 11:34 am, in Fig. 14.2b. Another region, between 11.38 am and 11.40 am, indicates a slight increase in amplitude and natural frequency for an increase in loading. This suggests that, at low-amplitude bridge responses, lateral human-structure interactions are still observed. In this case, corresponding to equivalent negative added mass and damping.



**Fig. 14.7** 2017 crowd loading event, Mode L3 (a) Instantaneous amplitude time-history (b) Instantaneous frequency time-history

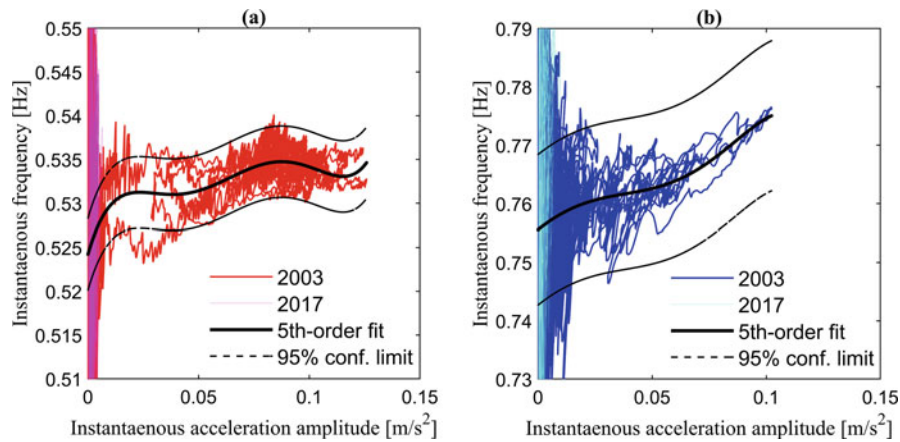
Figure 14.7 displays more erratic behaviour in the instantaneous acceleration amplitude of mode L3. The corresponding instantaneous frequency is also observed to be fluctuating considerably. However, it should be noted that the natural frequency is seen to shift by 5% over the 2017 crowd loading event. At instantaneous amplitude peaks of  $0.01 \text{ m/s}^2$ , observed just before 11:32 am and 11:34 am, the corresponding instantaneous frequency is seen to decrease. This may suggest equivalent positive added mass in comparison to mode L2. Interestingly, the equivalent added mass for mode L3, is observed to be positive at low-amplitude, whilst negative at high-amplitude responses. This may indicate that L3 is susceptible to both negative and positive added mass depending on the number of people and bridge deck amplitude.

### 14.3.2 Amplitude-Frequency Relationships

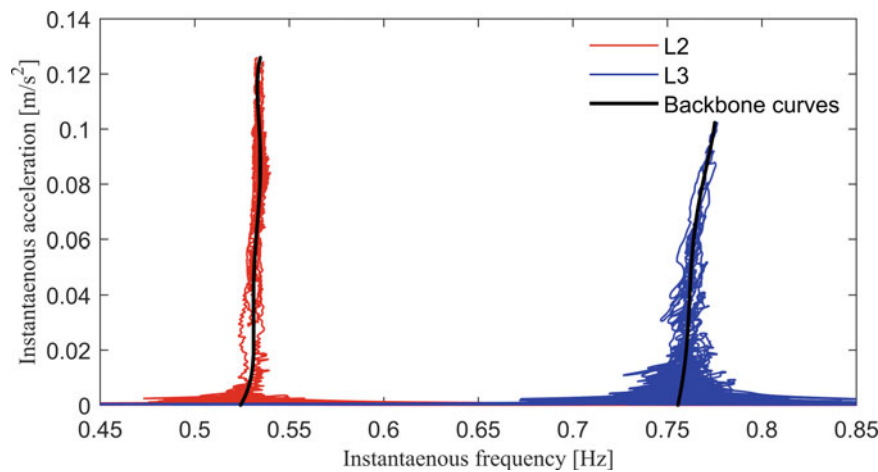
Using the transformed acceleration measurements of modes L2 and L3, as represented in Figs. 14.4, 14.5, 14.6, and 14.7, the amplitude-frequency relationships are evaluated for both the low and large amplitude bridge responses. Reduced order, fifth-order, polynomials are fitted to the large-amplitude bridge responses, using nonlinear least-squares approach, to characterise the complex interactions observed. This is displayed in Fig. 14.8. The low-amplitude bridge responses unfortunately do not display a clear relationship. For the 2003 crowd loading event, mode L2, Fig. 14.8a, is observed to show an obvious increase in frequency with increase in acceleration amplitude. The same effect is observed for mode L3, Fig. 14.8b, although its instantaneous frequency increases at a steeper rate, above an amplitude of  $0.05 \text{ m/s}^2$ . The reduced order models are quantified in Eqs. (14.4) and (14.5) and displayed in Fig. 14.9 as the approximated backbone curves of modes L2 and L3 respectively. Both modes observe nonlinear ‘hardening’ effects, i.e. an increase in frequency with an increase with amplitude. L3 witnesses a prominent hardening effect whilst L2 is seen to fluctuate around a frequency of 0.53 Hz however, still larger than its linear resonant frequency of 0.524 Hz.

$$f_{L2} = 0.524 + 0.867A_{L2} - 38.6A_{L2}^2 + 751A_{L2}^3 + 6.34 \times 10^3 A_{L2}^4 + 1.92 \times 10^4 A_{L2}^5 \quad (14.4)$$

$$f_{L3} = 0.756 + 0.307A_{L3} - 3.88A_{L2}^2 + 49.9A_{L2}^3 + 1.66 \times 10^3 A_{L2}^4 + 8.95 \times 10^4 A_{L2}^5 \quad (14.5)$$



**Fig. 14.8** Instantaneous acceleration amplitude – frequency relationships with reduced-order polynomial fitting (a) mode L2; (b) mode L3



**Fig. 14.9** Evaluated backbone curves of lateral modes L2 and L3 during high-amplitude pedestrian loading

## 14.4 Conclusion

This paper has presented a novel application of the time-frequency analysis technique, Hilbert transform, to qualitatively analyse and characterise the lateral human-structure interactions observed on the Clifton Suspension Bridge. The instantaneous acceleration amplitude and frequency are successfully extracted for two low frequency lateral vibration modes, shown to be susceptible to pedestrian-induced vibrations. The instantaneous frequencies, of both modes, are observed to approximately mirror the acceleration amplitudes during significant loading periods of the crowd loading event witnessing large-amplitude bridge responses. Equivalent negative added mass and damping of both modes are simultaneously observed. During the crowd loading event witnessing low-amplitude bridge responses, tentative evidence of human-structure interactions are observed for each mode. An initial increase in loading is mirrored in instantaneous amplitude and frequency, over brief time periods.

Amplitude-frequency relations are evaluated from reduced-order polynomial fitting to identify the backbone curves of each lateral resonant mode during the large-amplitude response crowd loading event. Nonlinear hardening effects are observed, for both modes, indicating an increase in instantaneous modal frequency with an increase in bridge deck acceleration amplitude.

**Acknowledgements** The authors gratefully acknowledge: the Clifton Suspension Bridge Trust for the research opportunities and cooperation throughout installation and decommissioning of the Structural Health Monitoring System; the Bridgemaster Mrs Trish Johnson and the bridge maintenance staff for their assistance; Mr Sam Gunner for the installation and decommissioning of his bespoke Structural Health Monitoring System; Miss Xioyang Wang, Dr Ute Leonards and Mr Artur Soczawa-Stronczyk for assisting in the data collection; Dr Matt Dietz for consultation on data processing and spectral analysis.

RW is supported by an EPSRC Doctoral Training Partnership studentship.

## References

1. Dallard, P., Fitzpatrick, A.J., Flint, A., Le Bourva, S., Low, A., Ridsdill Smith, R.M., Willford, M.: The London millennium footbridge. *Struct. Eng.* **79**(22), 17–21 (2001)
2. Macdonald, J.H.G.: Pedestrian-induced vibrations of the Clifton Suspension Bridge, UK. In: *Proceedings of the Institution of Civil Engineers-Bridge Engineering*, vol. 161(2), pp. 69–77 (2008)
3. Barlow W.H.: Description of the Clifton suspension bridge (including plate). In: *Minutes of the Proceedings of the Institution of Civil Engineers*, vol. 26(1867), pp. 243–257 (1867)
4. Gunner S., Vardanega P.J., Tryfonas T., Macdonald J.H.G., Wilson R.E.: Rapid deployment of a WSN on the Clifton Suspension Bridge, UK. In: *Proceedings of the Institution of Civil Engineers-Smart Infrastructure and Construction*, vol. 170(3), pp. 59–71 (2017)
5. White, R.E., Alexander, N.A., Macdonald, J.H.G.: Characterisation of crowd lateral dynamic forcing from full-scale measurements on the Clifton Suspension Bridge. Manuscript submitted for publication (2019). <https://doi.org/10.1016/j.istruc.2019.11.012>
6. Marple, L.: Computing the discrete-time “analytic” signal via FFT. *IEEE Trans. Signal Process.* **47**(9), 2600–2603 (1999)
7. Londoño, J.M., Neild, S.A., Cooper, J.E.: Identification of backbone curves of nonlinear systems from resonance decay responses. *J. Sound Vib.* **348**, 224–238 (2015)

**Rory Elias White** I am a PhD student at the University of Bristol with a research focus on structural dynamic, specifically to pedestrian-induced vibrations. My research interests broadly cover human-structure interactions in differing loading scenarios, such as walking and jumping.





# Chapter 15

## Validation of Deflection Monitoring for Ancillary Traffic Structures via Wireless Accelerometers

Delaney C. Thompson, Rodrigo Sarlo, and Matthew H. Hebdon

**Abstract** Large ancillary structures (e.g., traffic lights, light poles, signage structures) are prone to unusual or extreme dynamic behavior, especially during high winds events. The associated risks of fatigue failure and distractions to drivers require long-term dynamic monitoring solutions. Some of the major obstacles to wide-spread deployment are that traditional wired methods require lengthy lane closures, extensive data storage, and may measure only a single axis of vibration. This motivates the need for alternatives that are both easy to deploy and intuitive to interpret. The accuracy of the Embedor Technology XNode Smart Sensor for these purposes was studied using a 20-foot cantilevered traffic pole in the Thomas M. Murray Structures Lab at Virginia Tech. A double integrating and filtering approach was tested to estimate displacement from the acceleration readings and found to have a maximum uncertainty of one eighth of an inch when compared to a laser displacement sensor. The XNode's ability to integrate other hardware, perform data processing on the edge, communicate on its own wireless network and provide accurate displacement estimates has potential to unseat the current state of the art for dynamic monitoring of ancillary traffic structures.

**Keywords** Dynamic response · Oscillation · Fatigue · Acceleration monitoring · Ancillary traffic structures · Mast arm · Lifetime safety

### 15.1 Introduction

Ancillary traffic structures include cantilevered mast arms that house signs, streetlights, traffic signals and traffic monitoring equipment, luminary posts and bridge mounted signs. Due to the shape of the cantilever and the configuration of signage or traffic signals, mast arms in particular can experience large deflections when subjected to wind loading or traffic gust [1, 2]. This motion can cause large displacements of the system which can induce fatigue on the structure, cause motion of the objects attached to the structure, and distract drivers [3].

Monitoring can increase the lifetime of a structure as well as improve the safety of those around it [4]. For mast arms, fatigue failures are sudden and can happen under seemingly low loading [5, 6]. By monitoring structures of interest, government agencies can more accurately determine if maintenance or additional displacement damping is necessary before a failure occurs. In addition to preventing failure, monitoring can help ascertain that the displacement being experienced by the mast arm is within tolerance. Large, out-of-tolerance displacement events are distracting for drivers and can cause traffic accidents [3, 6]. The cost of repairs for fatigue related damage in cantilevered traffic structure and a concern for public safety necessitate an easy to deploy monitoring system for these structures.

Many different kinds of monitoring systems have been used for the purpose of monitoring displacement and fatigue. Strain gauges can be used to monitoring material fatigue, while laser displacement monitors and camera pixel intensity can be used to measure displacement directly [5, 7]. Due to the existence of these more direct measurement devices, accelerometers seem to be an unlikely choice; however, they prove to be extraordinarily useful. Because mast-arms are non-symmetric and experience loading in multiple directions, they are prone to complex three-dimensional motion [7]. Laser displacement sensors or cameras are unable to capture these multi-dimensional displacement responses; however, with suitable integration, a tri-axial accelerometer is able to capture three-dimensional displacements, without the need for a reference. In addition, accelerometers are less susceptible to environmental interference. Cameras tend to be rendered unable to capture motion in

---

D. C. Thompson · R. Sarlo (✉) · M. H. Hebdon  
Virginia Tech, Department of Civil and Environmental Engineering, Blacksburg, VA, USA  
e-mail: sarlo@vt.edu

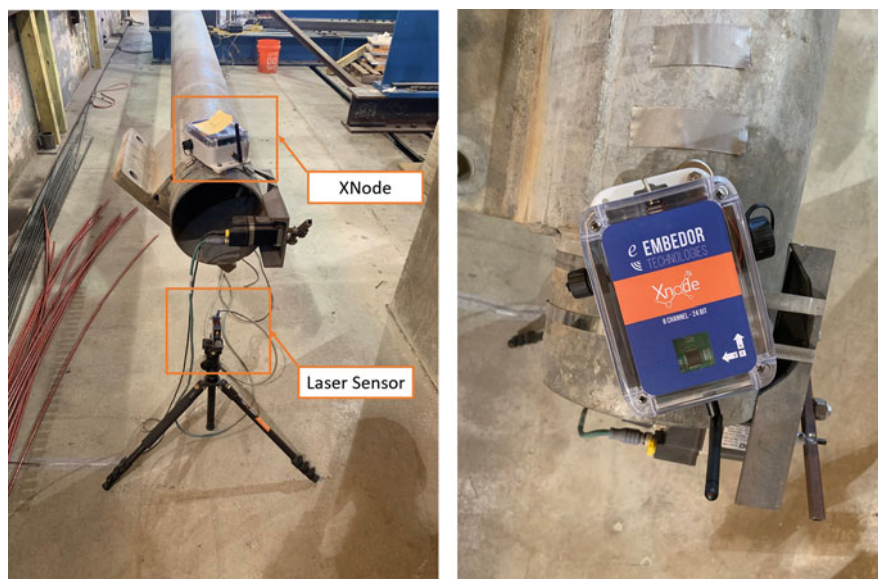
heavy rainfall or fog, while laser displacement monitors must be pointed at a fixed object (theoretically the ground) and can experience interference from moving traffic, pedestrians, or animals [7].

In previous work by the authors, wired accelerometers were used to continuously monitor a seven-lane, 78-ft span cantilevered traffic signal mast arm at the intersection of Military Highway and Lowery Road in Norfolk, VA to assess the need for deflection mitigation for the Virginia Department of Transportation (VDOT) [7]. The results of the field test supported the use of accelerometers as a monitoring device; however, the deployment of the field test was time-consuming and expensive. The original system required integration to the power grid, a purchased cellular data plan, several hours of lane closures and on-site system resets throughout the monitoring period. In addition, the raw data needed to be stored and exported before it could be processed and presented to VDOT as results. This difficulty motivated further investigation into a wireless accelerometer system with built-in automated data processing that could be intuitively operated by a VDOT engineer.

The Embedor Technology XNode wireless sensing system consists of deployable tri-axial accelerometer nodes and a central gateway. Each gateway is capable of communicating with six nodes at a time from a distance of up to 2 km [8]. Each node has built-in data processing capabilities and is equipped with eight analog output channels, the first three of which output acceleration in the X-, Y-, and Z-directions. The remaining five channels are available for integrating external sensors into the system [8]. The flexibility and ease of deployment of the XNode lends it to be an ideal system for monitoring of ancillary traffic structures; however, before it can be deployed, the validity of its results must be confirmed. By performing a validation test, an uncertainty value can be obtained to quantify the accuracy of the results.

## 15.2 Methods

To determine the accuracy of the Embedor Technologies XNode system for displacement monitoring, a 20-foot cantilevered traffic pole was instrumented, excited and monitored at the Thomas M. Murray Structures Lab at Virginia Tech as seen in Fig. 15.1. One XNode was mounted to the end of the cantilevered pole using high strength magnets; no additional sensors were integrated into the XNode. To ensure the least amount of rocking, the accelerometer was mounted on a diagonal; however, this did not impact the results because the axis of interest, the Z-axis, was unaffected. Mounted on the ground below the location of the accelerometer, an OPT2005 photoelectric laser sensor (Wenglor) connected to a CR5000 data acquisition system (Campbell Scientific), measured the displacement of the pole to the nearest 0.01 in. The XNode Gateway (Embedor Technologies) was connected to a computer equipped with the XNode data acquisition software to collect the acceleration data on the first three channels of the accelerometer.



**Fig. 15.1** Experimental set up including an Xnode and laser sensor

Three subsets of excitation were recorded: an impulse, a random excitation, and a sinusoidal excitation. Three responses each excitation type were recorded. The impulse was recorded by hitting the pole near the end with a rubber mallet; the random excitation was created by a researcher pushing on the end of the pole with varying amount of force; and the sinusoidal excitation was created by an eccentric mass motor oscillating at a given frequency. Two of the sinusoidal excitation occurred at frequencies slightly below resonance, and the third featured a sweep of frequencies up to the resonant frequency.

Calculating displacement from an acceleration signal requires double cumulative integration, which is susceptible to low-frequency measurement drift. This drift can then lead to large low frequency components in the calculated displacement signal. The issue can be mitigated by using filtering in the post-processing stage to attenuate any additional drift present in the data. Using a power spectral density, we were able to tailor the filters to the structure to remove interference from non-modal frequencies. While structures can exhibit vibration at non-resonant frequencies, because of the size of the pole and the relatively low amplitude of the forces used to excite it, it was assumed that this test structure only vibrated at frequencies very near to its resonant peaks. Thus, by filtering before, between, and after these peaks, it was possible to mitigate measurement drift in the cumulative integration process. In order to determine the best signal processing approach, different kinds of filters and initial conditions for integration were used. They are as follows:

1. A system of three filters: high pass, band stop, and low pass where the integration begins while the structure is at rest.
2. A system of two filters: a high pass and a band stop where the integration begins while the structure is at rest.
3. A single high pass filter where the integration begins while the structure is at rest
4. A single band stop filter where the integration begins while the structure is at rest
5. A system of three filters: high pass, band stop, and low pass where the integration begins while the system is in motion.

The acceleration signals were filtered and then cumulatively integrated using the MATLAB `cumtrapz` function to obtain the velocity signal. This filtering and cumulative integration process was repeated to obtain the estimated displacement in inches. Finally, a low pass filter was used to smooth the displacement signal from the photoelectric laser sensor to mitigate the error experienced due to the resolution of the equipment and subsequent quantization of the signal and the two signals were compared. One challenge posed in this portion of the validation was matching the two signals. The laser sensor monitored continuously between tests, while the accelerometers only ran for a minute at a time; further, the two signals were collected on different data acquisition systems. To match the signal, different segments of the displacement signal were cross correlated with the given estimated displacement. From there, the time lag was used to adjust the signal to fit.

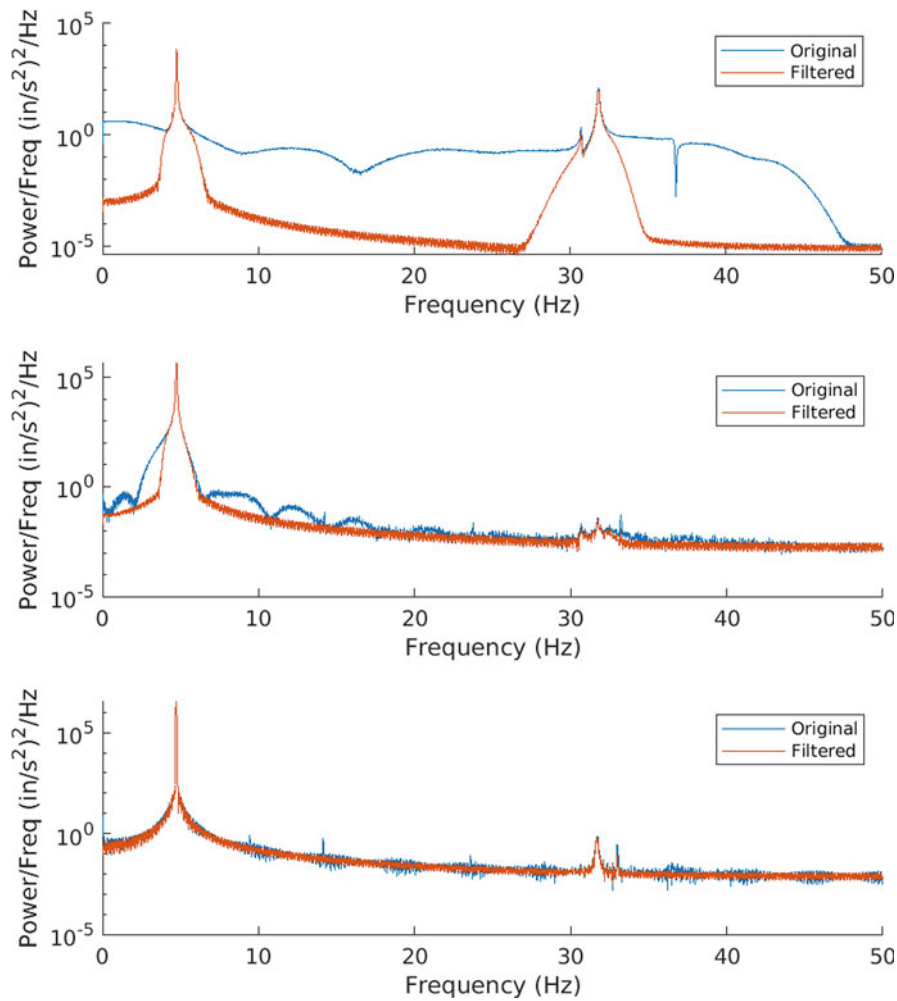
### 15.3 Results and Discussion

Figure 15.2 shows a representative power spectral density of each excitation type using three filters. From the unfiltered signal, we found the first frequency mode of the pole occurs at 4.761 Hz and the second to occur at 31.76 Hz (Fig. 15.3).

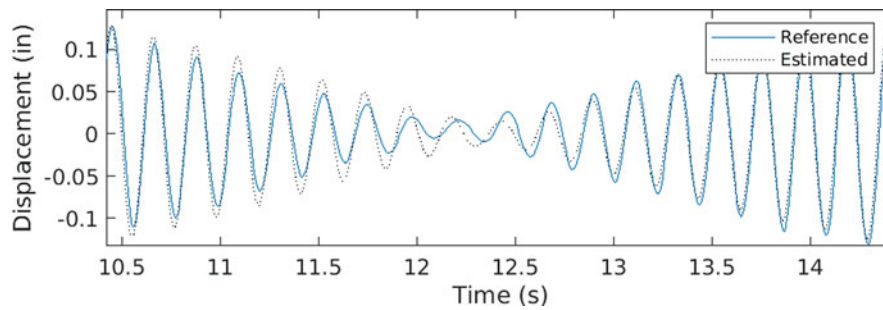
As seen in Fig. 15.4, the error, taken as the difference between the estimated displacement from the accelerometer and the laser displacement signal, is approximately normally distributed. Out of nine data samples collected, 7 had normally distributed error and 2 had uniformly distributed data. Thus, a  $\pm 2\sigma$  bound can be taken as a 95% confidence interval. Many signals experienced transient error at the beginning and end of data recording as a side effect of filtering, but this was disregarded in the error calculation. Outliers seen in the histograms can be attributed to these filtering effects.

In Table 15.1, the average uncertainty ( $\pm 2\sigma$ ) of each test type is recorded for each method of post-processing. From this, the accuracy of each method of post-processing can be analyzed. It is apparent that employing a low pass filter in addition to the high pass and the band stop has little noticeable impact on the quality of the estimation. Similarly, using a band stop filter in addition to the high pass filter only minimally increases the accuracy of the estimation. On the other hand, as seen in both Table 15.1 and Fig. 15.5, using only a band stop filter is not enough to prevent low-frequency drift from accumulating in the integration process. Thus, though employing additional filters such as the band stop and the low pass can refine results, doing may not be worth the computational effort and subsequent filtering error. The most important filter to implement in this type of analysis is a high pass filter.

All of the signals with varied filters began at rest before integration started. In a field deployment, it is incredibly unlikely that a mast arm will ever be fully at rest. Thus, it was vital to ensure that the methods employed in this study worked for structures that were already vibrating. As seen in Table 15.1, beginning the integration while the pole is already vibrating had minimal effect on the accuracy of the results. Nevertheless, from the methods employing at least a high-pass filter, the highest uncertainty was seen in the sinusoidal excitation with mid-vibration integration. Even so, one can be 95% confident that this measurement is within  $\pm 0.0673$  in.

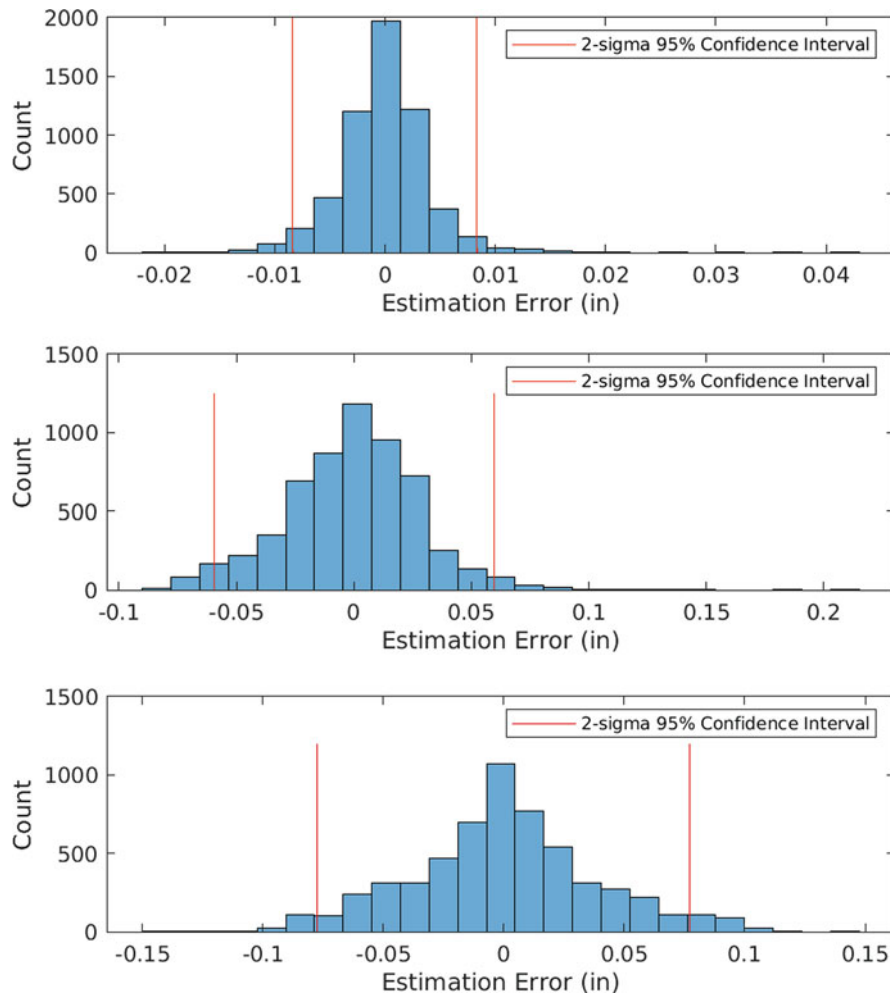


**Fig. 15.2** The power spectral density is a powerful tool for identifying the resonant frequencies of a structure. Here three filters are employed to isolate the first two frequency modes for an impulse, a random excitation and a sinusoidal excitation



**Fig. 15.3** A portion of displacement validation from doubly integrated accelerometer signal (Estimated) compared to photoelectric laser sensor signal (Reference) for a sinusoidal excitation with three filters

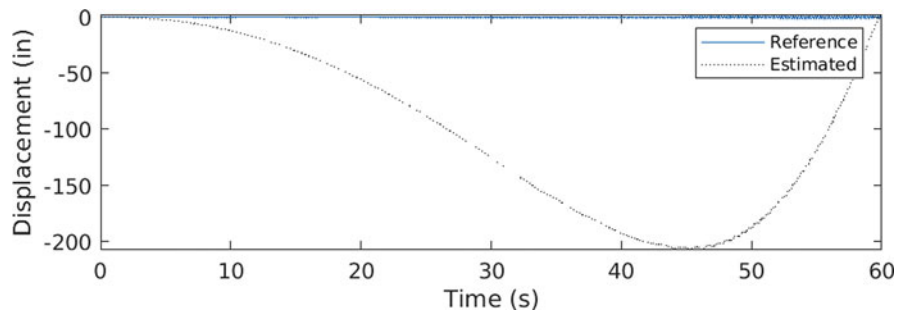
Future research on this topic will include exploring higher displacement events and the subsequent effect on the accuracy of this method. Additionally, in order to ease computational time and effort and create a deployable system for VDOT, time will be spent automating the data processing program and creating a MATLAB Graphic User Interface. To round out the creation of this monitoring system, additional exploration into the programmability of the XNode and how that could be incorporated with anemometers or traffic sensors will be done.



**Fig. 15.4** Difference (in.) between acceleration-estimated and laser-measured displacements

**Table 15.1** Average uncertainty ( $\pm$ in.) of each measurement based on a  $2\text{-}\sigma$  bound

Test type	3 filters	High pass + Band stop	High pass only	Band stop only	Mid-vibration integration
Impulse	0.0087	0.0108	0.0114	76.5427	0.0062
Random	0.0556	0.0533	0.0550	16.234	0.0352
Sinusoidal	0.0556	0.0561	0.0594	85.2668	0.0673



**Fig. 15.5** Low-frequency drift seen when employing only the band stop filter

## 15.4 Conclusions

In conclusion, this study has demonstrated the accuracy of double cumulative integration of accelerometer signals for mast arm displacement monitoring. The study was performed by exciting a 20-foot traffic pole in the Thomas M. Murray Structures Lab at Virginia Tech instrumented with an XNode and a photoelectric laser sensor. The estimated displacement results from the accelerometer signal were compared to the photoelectric laser displacement signal and found to have an uncertainty of 0.0673 in. It was found that the most important filter to employ in post-processing is a high pass filter with a cutoff frequency slightly below the resonant frequency of the structure. Future studies will be aimed at validation of the XNodes at larger amplitudes, creating an automated data processing program with a graphic user interface, and exploring the programmability of the XNode.

**Acknowledgements** The authors wish to acknowledge the generous support of the Virginia Department of Transportation which made this work possible. In addition, many thanks to Japsimran Singh and Ashutosh Kumar for their help in organizing and conducting the experiment.

## References

1. Zuo, D., Letchford, C.W.: Field observations of traffic signal structure vibration. Tech. Rep.
2. Pulipaka, N., Sarkar, P.P., McDonald, J.R.: On galloping vibration of traffic signal structures. Tech. Rep. **78** (1998)
3. Pulipaka, N.: Wind-induced vibrations of cantilevered traffic structures. Tech. Rep.
4. Lynch, J.P., Law, K.H., Kiremidjian, A.S., Carryer, E., Farrar, C.R., Sohn, H., Allen, D.W., Nadler, B., Wait, J.R.: Design and performance validation of a wireless sensing unit for structural monitoring applications. Tech. Rep. **4** (2004)
5. South, J.M.: Fatigue analysis of overhead sign and signal structures Illinois Department of Transportation Bureau of materials and physical research. Tech. Rep.
6. Rizzo, P., Zhu, X.: Sensing technology for damage assessment of sign supports and Cantilever Poles Commonwealth of Pennsylvania Department of Transportation. Tech. Rep. (2010)
7. Sarlo, R., Hebdon, M.H., Thompson, D.: Maximum deflection monitoring of a traffic signal via accelerometer-and camera-based approaches, Tech. Rep.
8. Zhu, L., Fu, Y., Chow, R., Spencer, B.F., Park, J.W., Mechitov, K.: Development of a high-sensitivity wireless accelerometer for structural health monitoring. *Sensors (Switzerland)*. **18**(1), 262 (2018)

**Delaney** is a Master's Candidate in the Charles E. Via Department of Civil and Environmental Engineering at Virginia Tech. She received her Bachelors of Science in Civil Engineering from Duke University.



# Chapter 16

## Localization of Stationary Source of Floor Vibration Using Steered Response Power Method

Mohammad Royvaran, Kevin D. Donohue, and Brad Davis

**Abstract** It is sometimes necessary to locate the source of machinery-induced vibrations in buildings when the generated vibration exceeds the acceptable limits. The objective of this study is to localize stationary source of vibration using floor vibration measurements with the steered response power (SRP) method. While this method has been used in microphone array processing and acoustic imaging systems, this paper describes the first application of this method to surface wave vibrations in structures. Source locations are derived from shifted and summed version of received signals by accelerometers to search and find the maximum likelihood of source location. Similar to the time difference of arrival (TDOA) method, the accuracy of the estimate is degraded by the frequency dependent propagation speed and attenuation of concrete floor, which lead to changes in the shape of the received signals. However, the SRP method is more robust than TDOA. Additional processing steps will be applied to reduce the effect of the aforementioned issues. The accuracy of the SRP method is validated through series of experiments in a building. To estimate the wave propagation speed, which is needed for SRP method, cross-correlation is used to compute delays between received signals. The accuracy of this method depends on the location of the source on the bay. Experiments showed an average error of 1 m or less for a single bay with a size of approximately 13.4 by 8.2 m when the source is located at mid bay. The results for SRP method as well as its advantages and shortcomings are discussed.

**Keywords** Vibration source localization · Steered response power (SRP) · Wave propagation speed · Time different of arrival (TDOA) · Smart structure

### 16.1 Introduction

Most floor systems are subjected to vibration caused by applied dynamic loads due to machinery-induced vibrations, e.g. chiller, fan, HVAC units, water pump etc., which are utilized in almost all buildings. Identification of the source of vibration, which is called localization, is not easy in some cases.

Localization of vibration source has twofold benefits. First, it has the capability to increase the level of comfort for occupants. For example, vibration monitoring systems help to enhance utilization of smart buildings by identifying a source of unusual levels of vibration that are causing discomfort for occupants, e.g. vibration due to the use of treadmill in a unit of an apartment building. Second, vibration measurements can help to localize the vibration source due to machinery induced vibration exceeding the sensitive equipment tolerance limit, for example MRI. In such cases, the source of vibration must be localized. This research presents a vibration localization method based on measurements of vertical accelerations at selected locations on the floor.

---

M. Royvaran (✉) · B. Davis  
Department of Civil Engineering, University of Kentucky, Lexington, KY, USA  
e-mail: [m.royvaran@uky.edu](mailto:m.royvaran@uky.edu)

K. D. Donohue  
Department of Electrical and Computer Engineering, University of Kentucky, Lexington, KY, USA

## 16.2 Background

One of the popular techniques for localizing the source of vibration is the Time Difference of Arrival (TDOA) method [1] where the location of sensors are known. This method relies on this assumption that waves propagate along the shortest and most direct path, which might not be the case in the presence of obstacles such as CMU walls or when there are columns, beams and girders. In addition, in solid media such as concrete floors the signal arrives at a receiver via two or more paths (direct and indirect transmission); such effects are called multipath effects [2]. Another challenge in the TDOA method is the estimation of time delay between the received signals of multiple receivers since in solid media, such as concrete floor, frequency components travel at different speeds [3], which is called dispersion. Philippidis and Aggelis [4] have shown that the type of aggregate content play an important role in wave propagation increasing considerably the wave velocity, while the aggregate size seems to control the attenuation, i.e. reduction in amplitude for each frequency traveled a known distance through material. Therefore, dispersion and frequency attenuation result in path dependent alterations in the spectral characteristics and distortions of the waveform received by different sensors from a single source [5]. There is another localization method called measure technique based on Received Signal Strengths (RSS), but Bahroun et al. [6] concluded that this method cannot lead to acceptable results due to the presence of boundaries causing echoes, modes, and interferences. He also indicates that TDOA accuracy depends on the distances between the source and the sensors.

## 16.3 SRP Method

Similar to the TDOA method, dispersion and attenuation effects remain a challenge for any technique that relies on matching similarities in received vibration patterns over spatially distributed sensors. The steered response power (SRP) method, however, has several advantages over TDOA at the cost of more computational requirement and additional sensors. It relies on beamforming (focusing) the array of sensors at a dense set of grid points in the space of interest and computing the power emanating from each of the grid points. For grid points close to an actual vibration source, the waveforms from each sensors will add up coherently (constructively) to result in a significantly higher power values at those grid points. This is a much more robust approach than TDOA that relies on a single time delay estimate that is easily confounded when multipath (secondary) reflections occur. SRP also has the ability to detect multiple simultaneous sources, which TDOA cannot [7].

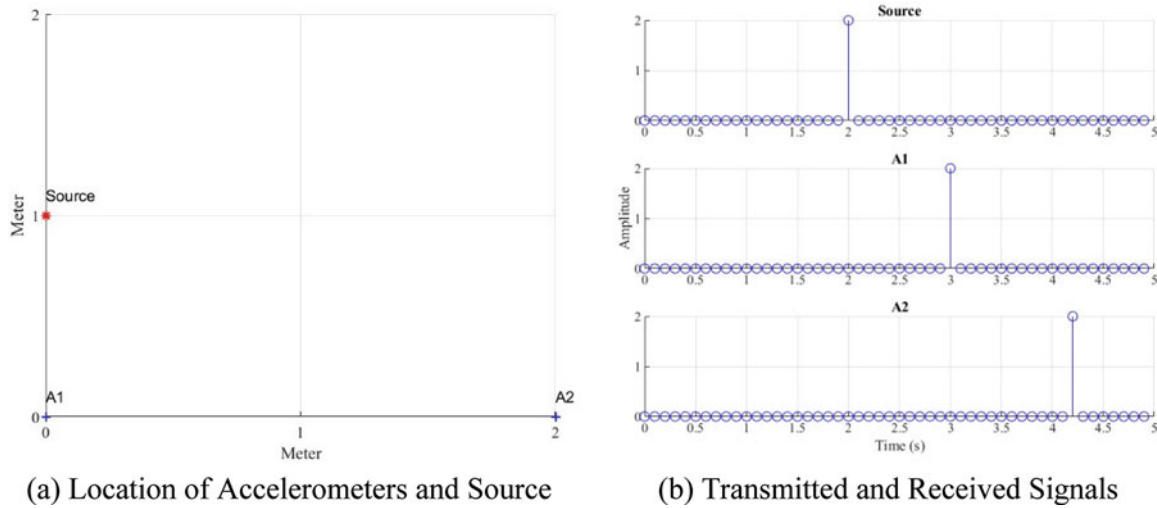
Beamforming is spatial filtering technique [8], used to steer signal transmission in a specific direction using more than one source in a way that signals at particular angles experience constructive interference while others experience destructive interference. The idea of beamforming can be generalized for receiving sensors as well to localize the source. Information from different sensors is shifted and summed to steer the arrays to various locations in order to search and find the maximum likelihood of source location. The following simulation will illustrate this idea in a form of an example. For simplicity, it is assumed the velocity of propagation is 1 m/s and sampling frequency is 10 samples per second. The chosen units in this example are arbitrary. The effect of damping is not considered in this example.

Figure 16.1a shows the location of two accelerometers and a source generating vibrations. The signal associated with the source is a single pulse with amplitude of two occurs at  $t = 2$  s. The total data acquisition is 5 s. Figure 16.1b shows the transmitted impulse signal generated by the source as well as signals received by A1 and A2, denoting accelerometer number one and two, respectively. All signals are in a form of row vectors. The distances between source and A1 and A2 are 1 and almost 2.2 m, respectively. Since the propagation speed is assumed 1 m/s, it takes 1 and 2.2 s for A1 and A2 to receive the signal, respectively.

All we need in this method for localization are propagation speed as well as the locations and received signals from A1 and A2, and the objective is locating the source. The spatial grid resolution is 1 m; therefore, the coordinate of all possible locations as the source are (1,0), (0,1), (1,1), (2,1), (0,2), (1,2), and (2,2) in this example. All these locations are tested for the presence of a source by calculating the distance of these assumed locations to the accelerometers and regarding propagation speed, received signals for A1 and A2 will be shifted, shown by “shiftA1” and “shiftA2” which will be added together and each element in this vector will be raised to the power of two. This process is shown in Fig. 16.2 for each point.

For case  $x = 0$  and  $y = 1$ , by shifting the received signals, recorded pulse of two signals are lined up; then, the two vectors are added to each other. Then, all elements in the new vector are squared (power) and the sum of elements results in the steered response power, which is the highest in this case. Equation 16.1 defines a new vector that represents the steered response power (SRP) in this research for each point.





**Fig. 16.1** Illustrative example for two accelerometers. (a) Location of accelerometers and source. (b) Transmitted and received signal

$$Z_{x,y} = \sum_{n=1}^T \left( \sum_{i=1}^M S_i (n + \tau_{i,x,y}) \right)^2 \quad (16.1)$$

where  $Z_{x,y}$  is the response power for each point on the  $x$ - $y$  plane spatial grid,  $M$  is the number of sensors (2 in this case),  $T$  is the total number of time samples, and  $\tau_{i,x,y}$  is the time delay associated with the spatial point the SRP is beamforming on for each sensor. As you can see, the location corresponding to the maximum  $Z$  value is the correct localization for the source. For this example, Fig. 16.3 shows the  $Z$  values regarding to  $x$ - and  $y$ -coordinates in form of 3-D plot and its top view.

By choosing a smaller number spatial resolution, the number of points needed to be searched increases, and the SRP plot will be smoother. However, this advantage comes with the cost of longer computation.

There are two ways to improve SRP plots. First, the more sensors used, the more accurate and robust the localization. Second, the more irregular the distances between the possible source locations and sensors, the better. Since the seismic accelerometers are expensive and using large quantity of accelerometers is generally not applicable, using limited number of accelerometers (seven in this research) can still give acceptable results if they are positioned judiciously. The objective of this research is to make the applicability of this study as general as possible. Performance is clearly affected by the array geometry [9, 10]. The optimal design of the array still needs more research.

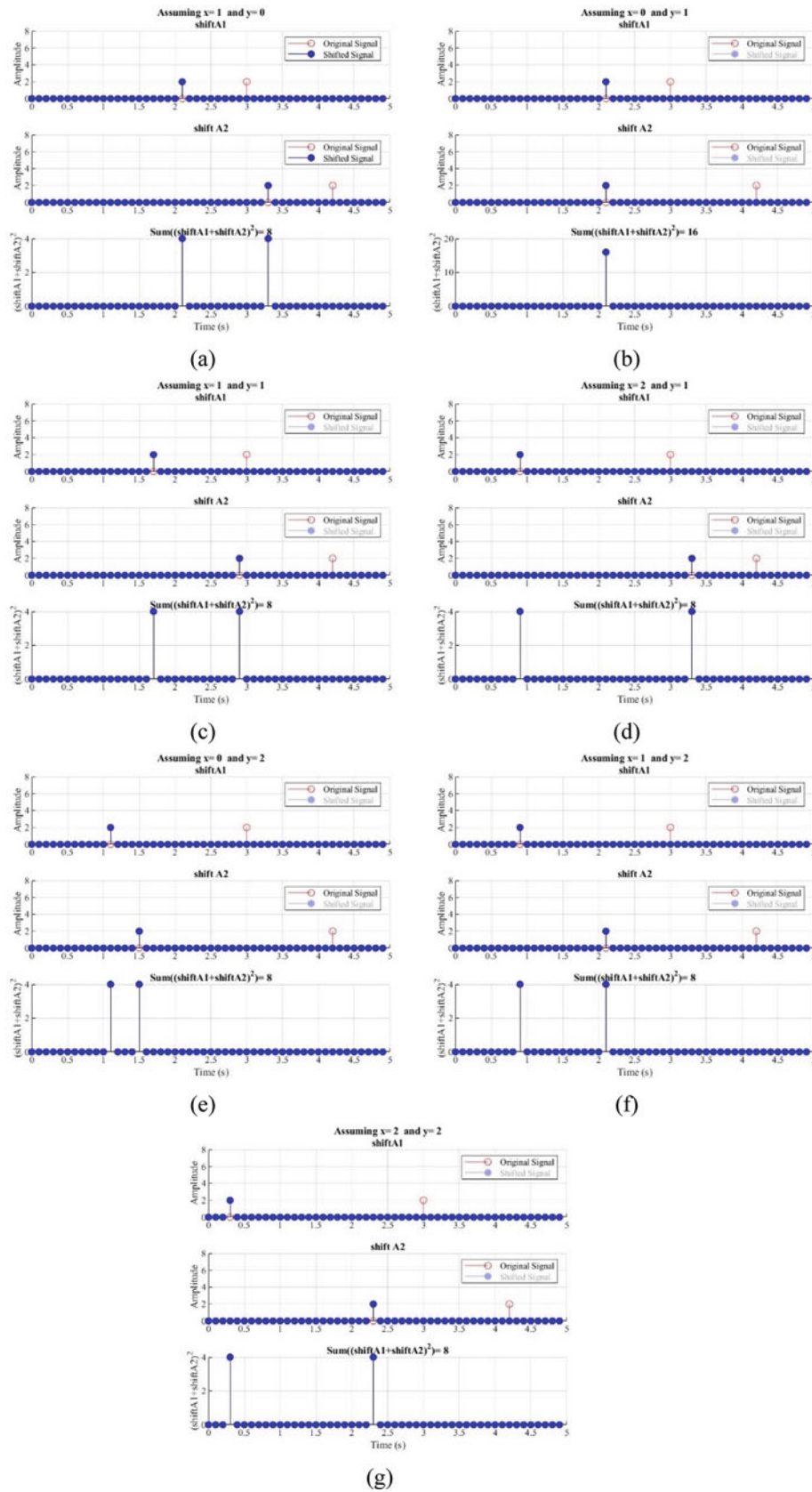
## 16.4 Experiment Description

### 16.4.1 Estimation of Wave Propagation Speed

Correct estimation of propagation speed is a crucial step in SRP method. Figure 16.4 shows the structural drawing of the tested bay between 3 and 4 and F-E axes as well as location of the shaker and accelerometers. A1 through A7 denote different accelerometers. Sampling frequency was set to 10,240 samples per second.

The procedure to estimate propagation speed involves finding a series of received signal delays between pairs of accelerometers using cross-correlations. Cross-correlation represents the similarity between two signals as a function of different shifts in time are applied to one of them. The coordinate of accelerometers are known. Simply, the distance between two accelerometers divided by time delay gives propagation speed. Since the multipath effect, presence of echo, dispersion, and attenuation change the shape of waveform and degrading the accuracy of cross-correlation, the time delay corresponding to the highest five peaks, representing the highest similarities, are considered to estimate the speed.

The generated vibrations are white noise and sinusoid. The objective of using white noise is that it is a random noise that has no similarity with itself except in zero lag. Therefore, cross-correlation function computes time delay more accurately. However, the cross-correlation of sinusoid is a sinusoid which is not our interest. To avoid this, in the first and last 10 s of



**Fig. 16.2** Illustrative example to find likelihood of source location by searching candidate locations at (a)  $x = 1$  and  $y = 0$ , (b)  $x = 0$  and  $y = 1$ , (c)  $x = 1$  and  $y = 1$ , (d)  $x = 2$  and  $y = 1$ , (e)  $x = 0$  and  $y = 2$ , (f)  $x = 1$  and  $y = 2$  and (g)  $x = 2$  and  $y = 2$

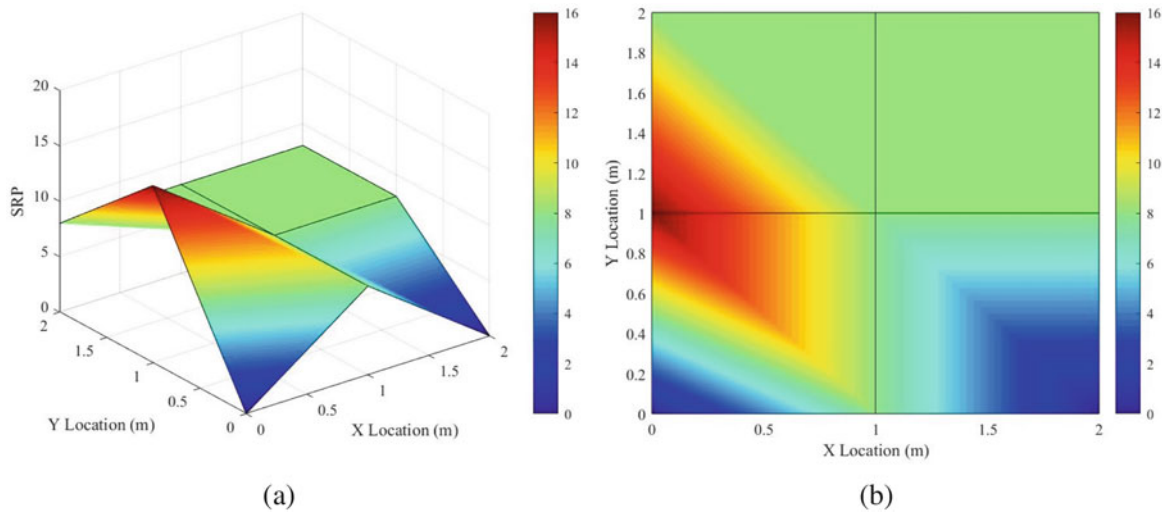


Fig. 16.3 SRP plot for the illustrative example. (a) 3D view. (b) Top view

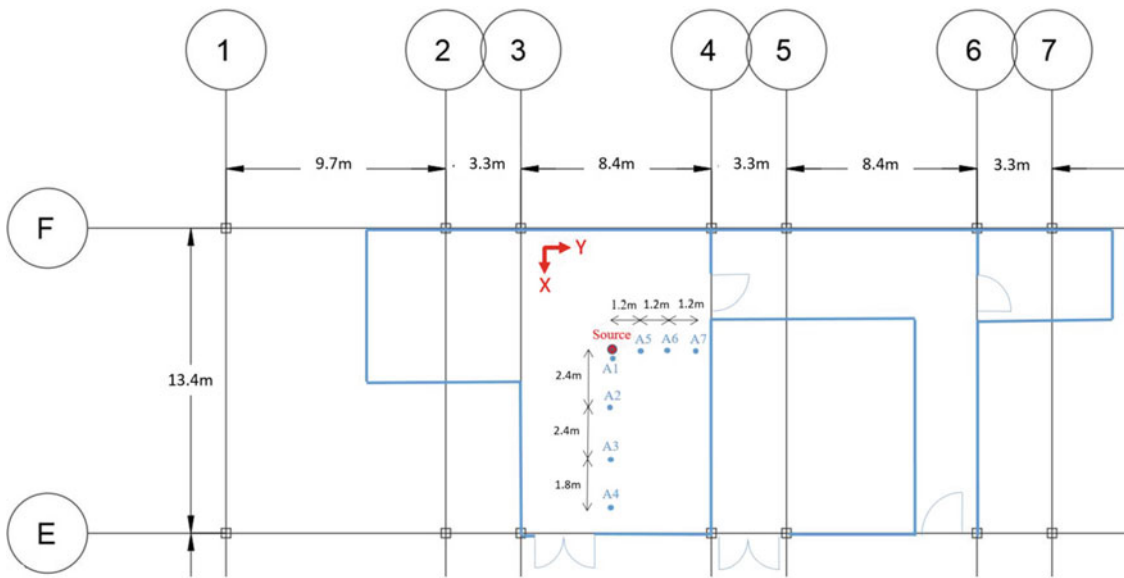


Fig. 16.4 Drawing for the tested floor and location of accelerometers and the source

data acquisition the shaker is not working and for 30 s in between the shaker is working, so the overall time acquisition is 50 s. Table 16.1 shows the speed estimation when the generated vibration is white noise from 4 to 200 Hz. The highest five peaks in cross-correlation representing the highest similarities are very close to each other. The number with is common among cross-correlation between all pairs is assumed estimated speed for accelerometers configured collinearly in X- and Y-direction shown in Table 16.1. For example, in X-direction, the propagation speed is almost between 200 and 214 m/s. It should be mentioned that a band-pass filter was applied to frequency domain for received responses in range of frequencies of excitation. In addition, for pairs of accelerometers with less than 2 m distance, estimated speed is not close to other estimations. In such cases, this estimation is ignored.

Table 16.2 shows the average speed for each test estimated with different pairs of accelerometers regarding Fig. 16.4.

**Table 16.1** Estimated speed based on the highest five peaks in cross-correlation

Direction	Cross-correlation	Distance (m)	Speed (m/s)				
			Highest	2nd	3rd	4th	5th
X	A1 and A2	2.36	124.7	208.5	88.6	590	69.1
	A1 and A3	4.80	297.9	200.6	152.2	558.6	123.2
	A1 and A4	6.63	212.8	392.4	672.1	277.1	170.6
	A2 and A3	2.44	509.6	198.2	123	89.5	70.5
	A2 and A4	4.27	338.7	214.2	809.2	156.6	123.1
	A3 and A4	1.83	120	237	4681.7	80.4	60.8
Y	A1 and A5	1.22	521.2	118	66.5	30.3	25.4
	A1 and A6	2.44	195.2	555.1	119	86.4	68.4
	A1 and A7	3.66	486.5	221.7	101	136.2	80.4
	A5 and A6	1.22	693.6	121.2	67.1	46.9	25.6
	A5 and A7	2.44	438.1	163.2	98.3	71.1	55.6
	A6 and A7	1.22	297.3	89.2	52.2	37.2	28.6

**Table 16.2** Estimated speed propagation for different vibrations and frequencies

Generated vibration	Vibration frequency (Hz)	Speed (m/s)	
		X-direction	Y-direction
White noise	4–200	206.8	107.8
	100–120	139.1	106.3
Sinusoid	70	107.7	79.4
	90	125.3	96.8
	110	133.8	108.4

#### 16.4.2 Localization of Vibration Source Using SRP Method

Based on the simulation developed for source localization, using irregular configuration for accelerometers placed on the floor results in less partial coherences between accelerometers to obtain less ambiguous power values and more accurate localization [9, 11]. Figure 16.5 shows location of accelerometers on structural drawing of the tested floor. Four locations on the floor are considered for the shaker in each test, denoted by L1, L2, L3, and L4, and the objective is to find the source just by using acceleration data recorded by accelerometers as well as location of accelerometers and propagation speed as input speed.

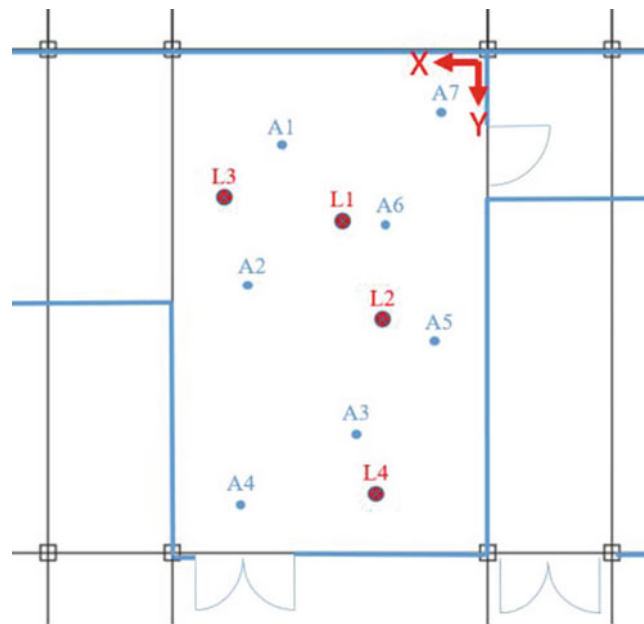
The same vibration with similar frequencies utilized in Sect. 16.4.1, e.g. white noise and sinusoid, are used in this section. One of shortcomings in this method is that computation is expensive and processing takes a long time first because sampling frequency is high, 12,800 samples per second. In addition, this method should search all possible points with 0.3 m increment in both X- and Y-direction, for the 13.4 by 8.4 m bay. This method needs speed as an input parameter.

Figure 16.6b shows the localization result using SRP method with 0.3 m error when vibration was a sinusoid with frequency of 70 Hz. The color bar on the right indicates the power for each point. Based on Table 16.2, the estimated speed in X-direction for the sinusoid with frequency of 70 Hz is 107.7 m/s. In this case, using estimated speed plus and minus 10% as input speed results in locating the source close enough to the real source.

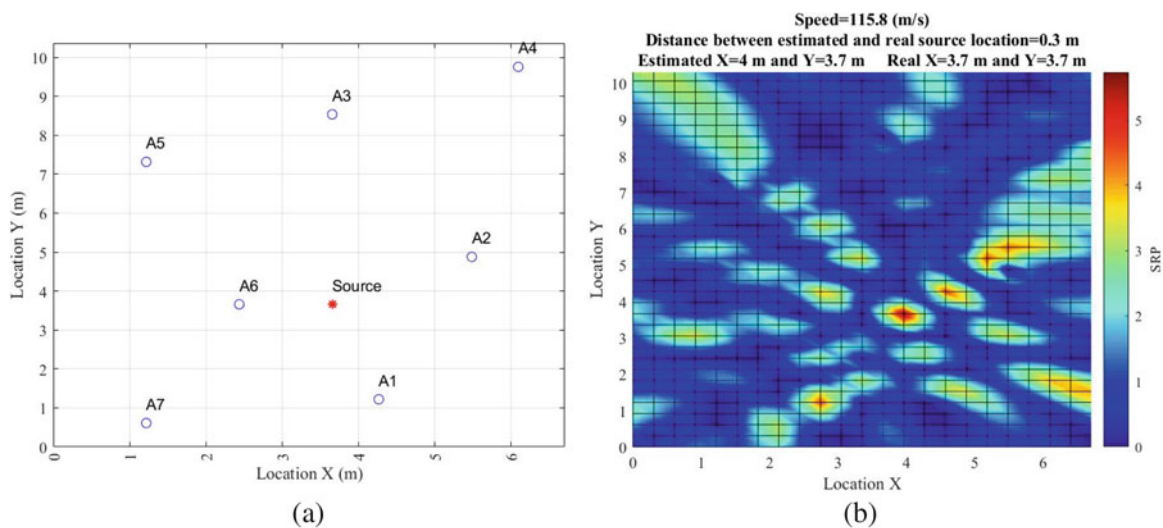
To reduce the power of the wrong peaks in this method, first band-pass filter was applied to the frequency domain of received signals match the frequency of excitation (remove out of band noise). Then, the received responses are weighted in a way that more weights are given to the closer accelerometers, according to the inverse distance beamformer [12].

For some cases where the shaker is placed at mid-bay, this method works well. However, when the shaker is placed near the wall or girder, error increases. For example, for the shaker located at L4 (see Fig. 16.5) generating sinusoid with frequency of 70 Hz, the least localization error is 2.8 m when the input speed is between 73.2 m/s, which is lower than the estimated speed for sinusoid with frequency of 70 Hz.

In some cases, source localization using speed estimated in Sect. 16.4.1 results in less than 1 m error. However, this does not happen for some other cases, which means more research is needed. Therefore, as a study, through trial-and-error procedure, different speeds in range of plus and minus 10% of estimated speed in Sect. 16.4.1 are considered as input speed. The results for the least error for different vibration excitation for the shaker placed at L1, L2, L3, and L4 is shown in Table 16.3.



**Fig. 16.5** Configuration of accelerometers and location of the shaker in each test



**Fig. 16.6** Result of source localization using SRP method for sinusoid vibration with frequency of 70 Hz. (a) Location of accelerometers and the source. (b) Result of SRP plot

Table 16.4 shows the averaged errors regarding the location of the shaker in the tested floor. The accuracy of this method is almost 1 m or less, except when the shaker is located at L4. This low accuracy might be because of the multipath effect near the wall or girder tended to generate more error.

### 16.5 Conclusion

The estimated propagation speed is different in X- and Y-direction, which means waves travel with different speeds in different angles. Table 16.2 shows the average estimated speed for different generated vibrations. For sinusoid vibration, higher frequencies travel faster than lower frequencies demonstrating that propagation speed is a function of frequency.

**Table 16.3** The least error for different vibration excitation using estimated speed

Generated vibration	Vibration frequency (Hz)	Shaker located at	Error (m)	Corresponding speed
White noise	4–200	L1	0.61	207.3
		L2	0.67	182.9
		L3	0.67	182.9
		L4	0.43	207.3
	100–120	L1	0.85	152.4
		L2	0.61	109.7
		L3	1.55	103.6
		L4	3.66	146.3
Sinusoid	70	L1	0.30	109.7
		L2	1.37	79.2
		L3	1.65	73.2
		L4	2.80	73.2
	90	L1	0.30	128.0
		L2	1.77	128.0
		L3	0.85	134.1
		L4	1.52	103.6
	110	L1	1.25	103.6
		L2	0.61	109.7
		L3	0.30	146.3
		L4	3.23	128.0

**Table 16.4** Averaged errors regarding the location of the shaker

Shaker placed at	Average error (m)
L1	0.66
L2	1.01
L3	1.00
L4	2.33

The accuracy of SRP method depends on the input speed. The estimated speeds plus and minus 10% were used as an input speed in SRP method to locate the source, and the least error was shown in Table 16.3. Instead of using a single number, consideration of two input speeds in X- and Y-direction in this method might improve its accuracy. SRP method can locate the source with good accuracy when the shaker was placed at mid bay. However, the accuracy of this method degrade when the shaker was placed at the edge of the bay which might be because of the interference of reflected waves near walls or girders.

## References

- Torrieri, D.J.: Statistical theory of passive location systems. *IEEE Trans. Aerosp. Electron. Syst.* **2**, 183–198 (1984)
- Shi, G., Ming, Y.: Survey of indoor positioning systems based on ultra-wideband (UWB) technology. In: *Wireless Communications, Networking and Applications*, pp. 1269–1278. Springer, New Delhi (2016)
- Sulaiman, A., Poletkin, K., Khong, A.W.: Source localization in the presence of dispersion for next generation touch interface. In: *2010 International Conference on Cyberworlds*, pp. 82–86. IEEE (2010)
- Philippidis, T.P., Aggelis, D.G.: Experimental study of wave dispersion and attenuation in concrete. *Ultrasonics*. **43**(7), 584–595 (2005)
- Thanasopoulos, I., Avaritsiotis, J.: Wavelet analysis of short range seismic signals for accurate time of arrival estimation in dispersive environments. *IET Sci. Meas. Technol.* **5**(4), 125–133 (2011)
- Bahroun, R., Michel, O., Frassati, F., Carmona, M., Lacoume, J.L.: New algorithm for footstep localization using seismic sensors in an indoor environment. *J. Sound Vib.* **333**(3), 1046–1066 (2014)
- Donohue, K.D., SaghaianNejadEsfahani, S.M., Yu, J.: Constant false alarm rate sound source detection with distributed microphones. *EURASIP J Adv Signal Process.* **2011**, 656494 (2011, 12 pages). <https://doi.org/10.1155/2011/656494>
- Van Veen, B.D., Buckley, K.M.: Beamforming: a versatile approach to spatial filtering. *IEEE ASSP Mag.* **5**(2), 4–24 (1988)
- Yu, J., Donohue, K.D.: Optimal irregular microphone distributions with enhanced beamforming performance in immersive environments. *J. Acoust. Soc. Am.* **134**(3), 2066 (2013)
- Brandstein, M.S., Adcock, J.E., Silverman, H.F.: Microphone-array localization error estimation with application to sensor placement. *J. Acoust. Soc. Am.* **99**(6), 3807–3816 (1996)

11. Yu, J., Donohue, K.D.: Geometry descriptors of irregular microphone arrays related to beamforming performance. *EURASIP J. Adv. Signal Process.* **2012**, 249 (2012). <https://doi.org/10.1186/1687-6180-2012-249>
12. Donohue, K.D., Hannemann, J., Dietz, H.G.: Performance for phase transform for detecting sound sources in reverberant and noisy environments. *Signal Process.* **87**(7), 1677–1691 (2007)

**Mohammad Royvaran** is a PhD Candidate in Structural Engineering at University of Kentucky. His research area is on floor vibration and he is working on localization of source of vibration using wave vibrations in structures including both data acquisition through experiment, using accelerometers and a shaker, and data post-processing using MATLAB.

# Chapter 17

## Predictions of Footbridge Vibrations and Influencing Load Model Decisions



Lars Pedersen and Christian Frier

**Abstract** Prior to erecting a footbridge it may be useful to quantify the future and to predict vibration levels of the footbridge, since the vibration levels to come will determine the serviceability of the bridge throughout its service life. For design stage predictions of pedestrian-generated vibrations of a footbridge, decisions need to be made in terms of how to model the load. If the load is modelled as being stochastic it entails that a set of walking parameters are to be modelled as random variables for the predictions. Fundamentally, walking parameters are load amplification factors, step frequency, walking speed, pedestrian weight etc. and the paper adapts this line of thinking and presents results in terms of footbridge vibration levels computed under various calculation assumptions. Since the studies treat walking parameters as random variables, it is the stochastic nature of footbridge vibrations, which is in focus when comparing vibrations. The stochastic nature is brought about by Monte Carlo simulations, and a central aim of the studies of the paper is to examine how two different load models perform in terms of predicting selected stochastic features of footbridge vibrations when subjected to single-person traffic.

**Keywords** Footbridge vibrations · Walking loads · Walking parameters · Stochastic load models · Serviceability-limit-state

### Nomenclature

$a$	Bridge acceleration
$i$	Integer
$v$	Pacing speed
$L$	Bridge length
$\alpha$	Dynamic load factor
$\sigma$	Standard deviation
$f_1$	Bridge fundamental frequency
$m_1$	Bridge modal mass
$t$	Time
$Q$	Modal load
$\zeta_1$	Bridge damping ratio
$\Theta$	Phase
$f_s$	Step frequency
$l_s$	Step length
$F$	Walking load
$W$	Weight of pedestrian
$\mu$	Mean value
$\Phi$	Mode shape

---

L. Pedersen (✉) · C. Frier  
Department of Civil Engineering, Aalborg University, Aalborg, Denmark  
e-mail: [lp@civil.aau.dk](mailto:lp@civil.aau.dk)



## 17.1 Introduction

A pedestrian exerts dynamic forces on the structure he walks on. When the structure is a footbridge and if the bridge is flexible and have one or more natural frequencies in the proximity of the dynamic forces generated by the pedestrian, resonance of the bridge structure may occur. This may lead to serviceability problems and probably the most well-known bridge that has experienced excessive vibrations is The Millennium Bridge in London [1].

This paper deals with load models for pedestrians with particular focus on the vertical action. Some years ago, these models were deterministic, for example the load models suggested in [2–4] and the calculation of walking loads were quite simple too. However, one drawback was that the load models did not account for the variability in walking forces imposed the bridge by different pedestrians (exchange the pedestrian and you have another set of parameters for pedestrian step frequency, step length and dynamic load factors being input parameters for your calculation of pedestrian forces). Variability in these parameters is known to exist [5–8].

It is considered useful to employ a load model that accounts for the stochastic nature of these parameters. Load models that embrace the uncertain input are employed in the studies of this paper. A load model that handles these parameters as random variables is already developed [9] but a somewhat simpler variant of that model is introduced and examined in this paper.

The outputs of both load models are quantiles of structural vibrations (more specifically quantiles for the vertical peak bridge accelerations occurring at bridge midspan), hence properties that describe bridge responses in a probabilistic sense. They are brought about by numerically simulating the action of a pedestrian crossing the bridge and by computing the resulting bridge vibrations. Repetitions of pedestrian crossings (established by Monte Carlo simulations) ensure that a cumulative distribution function for bridges vibration levels are established from which quantiles of interest are sampled.

This strategy is employed for both load models allowing direct comparison between estimates of acceleration quantiles of footbridge response.

The difference between the two load models is the level of detail in which they model the nature of walking. In one model the spreading of energy around the harmonic loads in the force spectrum observed in [10] is accounted for. This is not the case in the other load model. Nevertheless, it is introduced here as it has other advantages. The models are described in Sect. 17.2.

Section 17.3 outlines the methodology in more detail, covering a description of the artificial footbridges used for the investigations being pin-supported single-span footbridges. Section 17.4 presents the results in terms of acceleration quantiles of bridge vibrations obtained for the two load models and Sect. 17.5 provides conclusions and discusses the results.

## 17.2 Modelling of Walking Loads

As mentioned two different walking load models will be considered for the studies of this paper. They will be denoted load model I and II.

Common for both are that the vertical modal load,  $Q(t)$ , acting on the structure (on the footbridge and generated by the pedestrian) can be calculated using Eq. (17.1):

$$Q(t) = \Phi(t)F(t) \quad (17.1)$$

where  $F(t)$  is the vertical load at the point of action of the pedestrian when moving across the bridge.

The definition of  $\Phi(t)$  will be presented later in this paper as it will be common for both load models.

Hence, initially, focus is on the way in which  $F(t)$  is modelled in load model I and II, respectively.

### 17.2.1 Load Model I

This load model is the model introduced in [9]. The time-domain load model is believed to capture and model effects of the nature of walking not encompassed in time-domain load models proposed prior to the introduction of load model I.

The mathematical expression for  $F(t)$  is seen in Eqs. (17.2, 17.3, and 17.4):

$$F(t) = \sum_{i=1}^5 F_i(t) + \sum_{i=1}^5 F_i^S(t) \quad (17.2)$$

$$F_i(t) = W\alpha_i \sum_{\bar{f}_j=i-0.25}^{i+0.25} \bar{\alpha}_i(\bar{f}_j) \cos(2\pi\bar{f}_j f_s t + \theta(\bar{f}_j)) \quad (17.3)$$

$$F_i^S(t) = W\alpha_i^S \sum_{\bar{f}_j^S=i-0.75}^{i-0.25} \bar{\alpha}_i^S(\bar{f}_j^S) \cos(2\pi\bar{f}_j^S f_s t + \theta(\bar{f}_j^S)) \quad (17.4)$$

It is beyond the scope of this paper to define all parameters appearing in the load model. However, here it is useful to know that  $W$  represents the static weight of the pedestrian, and that  $f_s$  represents the step frequency. Also that five main load harmonics (introduced in Eq. (17.3) with associated dynamic load factors,  $\alpha_i$ ), and five subharmonics (introduced in Eq. (17.4) with associated dynamic load factors,  $\alpha_i^S$ ) constitute the basis of the load model. The presence of subharmonics is due to the fact that “the fundamental period of the force time history is equal to the time required to make two successive steps, rather than one”, [9]. Many of the other parameters in the model ensures that it accounts for the fact that energy is spreading around the main harmonics and subharmonics in the force spectrum. Reference is made to [9] for definition of the parameters not defined in this paper. Overall, the model has the advantage that it models the fact that the locomotion of a pedestrian is not fully period and that load energy leaks at the load harmonics in the force spectrum. In total 400 harmonics are used to calculate the load  $F(t)$ , following the line of procedure outlined in [9].

### 17.2.2 Load Model II

A simpler variant of load model I (denoted load model II) is one in which the leaking of load energy at harmonics is not accounted for. By disregarding this effect, the load model can be described by Eqs. (17.5, 17.6, and 17.7).

$$F(t) = \sum_{i=1}^5 F_i(t) + \sum_{i=1}^5 F_i^S(t) \quad (17.5)$$

$$F_i(t) = W\alpha_i \cos(2\pi i f_s t + \varphi_i) \quad (17.6)$$

$$F_i^S(t) = W\alpha_i^S \cos(\pi(2i-1)f_s t + \varphi_{i+5}) \quad (17.7)$$

The load model introduced here, in line with load model I, consists of five main load harmonics (introduced in Eq. (17.6) with associated dynamic load factors,  $\alpha_i$ ), and five subharmonics (introduced in Eq. (17.7) with associated dynamic load factors,  $\alpha_i^S$ ). The main load harmonics excite the supporting structure at the step frequency  $f_s$  and integer multiples hereof. The subharmonics excite at half of the step frequency and at  $1.5f_s$ ,  $2.5f_s$  etc. A frequency domain representation of this load model would show 10 spikes separated by  $0.5f_s$  along the frequency axis. This would also be the case for load model I, but in that load model energy would also exist between the spikes.

The model to some extent mimics the type of time domain load models suggested prior to the introduction of model 1, such as models suggested in [2–4] – which are models assuming fully periodic action. However, load model II respects that there are subharmonic load components exciting the supporting structure at frequencies between the frequencies of the main load harmonics.

There are other features of the model that differ from the load models introduced prior to the time of introduction of load model I. Firstly, five main load harmonic are considered whereas some earlier load models considered fewer main load

harmonics. In this paper, five main harmonics are considered for the sake of allowing meaningful comparisons to be made between structural responses calculated using load model I and load model II. Secondly, for the calculations of this paper, the walking parameters are modelled as random variables in load model II, as they are in load model I.

### 17.2.3 Common for Both Load Models

The mode shape function,  $\Phi(t)$ , need to be defined and regardless of the model assumed for  $F(t)$  is can be determined using Eq. (17.8):

$$\Phi(t) = \sin(\pi vt/L) \quad (17.8)$$

as this represents the mode shape function for a pin-supported single-span footbridge with a length of  $L$  between the supports.

In the equation,  $v$  represents the walking velocity of the pedestrian. Common for load models I and II is that it is determined using Eq. (17.9):

$$v = f_s l_s \quad (17.9)$$

In this equation,  $l_s$  represents the step length of the pedestrian and  $f_s$  represents step frequency of the pedestrian. These parameters are modelled as random variables. The way in which this is done is described later in this section.

Returning to the load models there are other parameters that need to be defined prior to calculations.

Focusing on the dynamic load factors of the modelled action, and starting with the dynamic load factor associated with the first main harmonic,  $\alpha_1$ , it is modelled as a random variable with a mean value,  $\mu$ , and a standard variation,  $\sigma$ , according to Eq. (17.10).

$$\mu = -0.2649 f_s^3 + 1.3206 f_s^2 - 1.7597 f_s + 0.7613; \sigma = 0.16\mu \quad (17.10)$$

The relationship is due to work in [7]. A Gaussian distribution is assumed.

This is also the assumption for the other main harmonic load factors,  $\alpha_i (i = 2, 3, 4, 5)$ , and the assumed mean values ( $\mu$ ) and standard deviations ( $\sigma$ ) for these parameters are listed in Table 17.1.

The subharmonic load factors  $\alpha_i^S$  are derived from the main harmonic load factor,  $\alpha_1$ , in the way described in [9].

A premise for load model I is that the pedestrian weight,  $W$ , is modelled as a deterministic property. Also, and as already mentioned, the step length and step frequency are modelled as random variables, and as independent random variables. Hence, these assumptions will also be made for load model II.

The assumptions made for both models are presented in Table 17.2.

In both load models the phases,  $\theta$  and  $\varphi$ , are modelled by a uniform distribution in the range  $[-\pi, \pi]$ .

## 17.3 Methodology

Above two load models have been outlined. The methodology is to employ both load models for calculating selected statistical properties associated with the vertical acceleration response of different footbridges. For the investigations is it

**Table 17.1** Mean values and standard deviations [7, 9]

–	$\alpha_2$	$\alpha_3$	$\alpha_4$	$\alpha_5$
$\mu$	0.07	0.05	0.05	0.03
$\sigma$	0.030	0.020	0.020	0.015

**Table 17.2** Mean values and standard deviations

–	$\mu$	$\sigma$	Reference
$W$	750 N	0 N	[9]
$l_s$	0.71 m	0.071 m	[9]
$f_s$	1.87 Hz	0.186 Hz	[9]

**Table 17.3** Modal properties of bridges and bridge lengths

Property	Unit	Bridge		
		A	B	C
$f_1$	Hz	1.875	2.35	2.80
$\zeta_1$	%	0.5	0.5	0.5
$m_1$	$10^3$ kg	44.9	28.6	20.2
$L$	m	45.9	36.6	30.7

chosen to consider pin-supported single-span footbridges. Instead of examining solely a single bridge, the responses of three different bridges are investigated.

Table 17.3 lists the modal properties assumed for the bridges considered in this paper. The natural frequency is denoted  $f_1$ , the damping ratio is denoted  $\zeta_1$ , and the modal mass is denoted  $m_1$ . These properties define the modal properties of the first vertical bending mode of the bridges. The assumed bridge length,  $L$ , is also shown in the table.

The motivation for choosing a bridge with a frequency of 1.875 Hz (bridge A) for investigation is that its natural frequency is close to the mean value of the assumed probability density function for the step frequency (1.87 Hz). Hence, it is a bridge, which is likely to be excited by the first main load harmonic. Bridge C is also likely to be excited but by the second subharmonic as this is at 1.5 times 1.87 Hz (approximately 2.80 Hz). Furthermore, it is of interest to investigate a bridge with a frequency in between the frequencies of bridge A and C. For this bridge, denoted B, a natural frequency of 2.35 Hz is assumed.

It is mentioned that the bridge modal masses and bridge lengths are set such that they increase as the bridge frequency decreases which it considered a realistic feature.

Based on the assumptions outlined above it is possible to numerically simulate load time histories for a pedestrian crossing the bridges using Newmark time-integration methods and Monte Carlo simulations allowing for repeating pedestrian crossings. For each simulated crossing of the bridge its vertical motion is computed and from this the vertical peak acceleration occurring at bridge midspan is tracked being a bridge feature relevant in the context of serviceability-limit-state evaluation.

In this way probability distribution functions for bridge peak accelerations are established for the three bridges and from these, the acceleration quantiles  $a_{95}$ ,  $a_{90}$  and  $a_{75}$  are extracted where the subscripts define the quantile. For example, the quantile  $a_{95}$  is the acceleration level exceeded in 5% of the pedestrian crossings.

For each bridge 100.000 simulations were conducted.

## 17.4 Results

This section is concerned with presentation of results in terms of acceleration quantiles derived from calculations.

For the presentation of results it is considered useful to introduce the ratio  $r_x$  defined in Eq. (17.11).

$$r_x = \frac{a_x^I}{a_x^{II}} \quad (17.11)$$

In Eq. (17.11),  $a$  represents the peak acceleration, and the superscript (I or II) represents the load model assumed for the calculations. The subscript  $x$  represents the quantile of peak acceleration.

Hence, for example,  $r_{95}$  defines the ratio between the acceleration quantile  $a_{95}$  computed employing load model I, and the corresponding value computed employing load model II. Introduction of the ratio eases identifying which load model delivers the highest bridge response and at the same time it provides information about the size of the difference.

A value of  $r_x$  higher than unity indicates that load model I (accounting for the leaking of energy at harmonics) provides higher estimates of bridge acceleration response than load model II (not accounting for leaking of energy).

Table 17.4 presents results for  $a_{95}$  and for the ratio  $r_{95}$  obtained for the three bridges (A, B, and C).

First item to notice is that bridge A vibrates the most (if evaluated based on  $a_{95}$ ). This is not surprising as this bridge is likely to be excited by the first main load harmonic. The energy in this load harmonic is significantly higher than the energy in the subharmonic exciting bridge C. For bridge A both load models (I and II) provide estimates of  $a_{95}$  which are almost identical - the value of  $r_{95}$  being close to 1. As the value is below 1, load model II provides the highest estimate of  $a_{95}$ . This is consistent with the modelling feature of load model I where load energy is modelled to leak around the load harmonic in the force spectrum.

**Table 17.4** Acceleration quantile  $a_{95}$  and ratio  $r_{95}$  for the three bridges

Property	Unit	Load model	Bridge		
			A	B	C
$f_1$	Hz	–	1.875	2.35	2.80
$a_{95}$	$\text{m/s}^2$	I	0.3281	0.1014	0.0713
$a_{95}$	$\text{m/s}^2$	II	0.3382	0.0806	0.0869
$r_{95}$	–	I/II	0.97	1.26	0.82

**Table 17.5** Ratio  $r_{95}$ ,  $r_{90}$  and  $r_{75}$  for the three bridges

Property	Unit	Load model	Bridge		
			A	B	C
$f_1$	Hz	–	1.875	2.35	2.80
$r_{95}$	–	I/II	0.97	1.26	0.82
$r_{90}$	–	I/II	0.97	1.32	0.88
$r_{75}$	–	I/II	1.16	1.34	1.24

A similar tendency is seen for bridge C, however, here the value of  $r_{95}$  is somewhat lower ( $r_{95} = 0.82$ ). Hence, the overestimation of  $a_{95}$  involved with employing load model II (not modelling the leaking of energy) is more pronounced for this bridge.

For bridge B, load model II is seen to underestimate the value of  $a_{95}$  and by a factor of 1.26. That load model I provides the highest estimate of  $a_{95}$  is explained by the spreading of load energy around the harmonics modelled in load model I – a spreading of energy that enters into the frequency region between the harmonics where bridge B is located for many pedestrian crossings of the bridge.

It can be seen that (for load model I) the value of  $a_{95}$  for bridge B is higher than the corresponding value computed for bridge C. This is believed to be a result of the fact that although the second subharmonic excites at a frequency close to the natural frequency of bridge C, the first main load harmonic will, for some pedestrian crossings, cause resonance of bridge B. This excitation is much higher than that of the second subharmonic, and hence the resulting effect will be a balance between likelihood of occurrence and size of excitation.

In order to widen the basis for discussion, Table 17.5 presents results for ratios  $r_{95}$ ,  $r_{90}$  and  $r_{75}$  obtained for the three bridges (A, B, and C).

The ratios  $r_{95}$  are those already presented in Table 17.4 but it is useful to align these with values computed for  $r_{90}$  and  $r_{75}$ .

It can be seen that for the higher quantiles of bridge response (represented by  $r_{95}$  and  $r_{90}$ ), the tendency is the same, namely that for bridge A and bridge C, load model II overestimates the acceleration quantiles but for bridge B it underestimates the acceleration quantiles. For bridge A and bridge C, the overestimation changes to an underestimation of the acceleration quantile  $a_{75}$ . In a serviceability-limit-state evaluation perspective it is most likely the higher bridge acceleration quantiles that are of interest.

Overall, the difference between the estimates of computed acceleration quantiles are within about 35%. If the bridge frequency is very close to the expected mean value of the probability density function for the step frequency of pedestrians (as the case for bridge A), the difference between estimates obtained using load model I and load model II is quite limited.

## 17.5 Conclusion and Discussion

In the paper two load models were examined with focus on their difference in predicting acceleration quantiles of bridge responses to single-person pedestrian traffic on single-span pin-supported footbridges. One model accounted for leaking of load energy around the load harmonics. The other model did not.

The results showed estimates of acceleration quantiles that differed up to 35%, however for some scenarios and acceleration quantiles, the difference in estimates was much smaller.

Generally, it seems most logical to employ the load model that best captures the nature of the pedestrian forces, which would be the load model that accounts for the leaking of load energy around the load harmonics in the force spectrum. However, the alternative load model introduced in this paper (not accounting for the leaking of energy) may be a useful alternative in that it does capture the nature of walking that suggests that subharmonic load components excite the supporting structure at frequencies between the excitation frequencies of the main load harmonics. For instance, it estimates acceleration quantiles of a bridge with a natural frequency likely to be present in the region where a subharmonic would be present fairly

accurately. This would not be accomplished by a fully periodic load model only accounting for load effects associated with the main harmonics.

Overall, the choice of load model is a trade-off between required accuracy in prediction, complexity of the nature of the mechanism to be modelled, other influencing uncertainties, programming and simulation time. That there are other influencing uncertainties associated with estimating acceleration quantiles for serviceability-limit-state evaluations are discussed in, for instance [8].

The benefits of the load model introduced in this paper (not accounting for the leaking of energy) is that it is simpler to program than the load model accounting for leaking of energy. Additionally that the simulations run about 40 times faster than the model accounting for spreading of energy at load harmonics. However, it would be useful to conduct a more compressive study of its limitations.

## References

1. Dallard, P., Fitzpatrick, A.J., Flint, A., Le Bourva, S., Low, A., Ridsdill-Smith, R.M., Wilford, M.: The London Millennium Bridge. *Struct. Eng.* **79**, 17–33 (2001)
2. Ellis, B.R.: On the response of long-span floors to walking loads generated by individuals and crowds. *Struct. Eng.* **78**, 1–25 (2000)
3. Bachmann, H., Ammann, W.: *Vibrations in Structures – Induced by Man and Machines: IABSE Structural Engineering Documents 3e*. IABSE, Zürich (1987)
4. Rainer, J.H., Pernica, G., Allen, D.E.: Dynamic loading and response of footbridges. *Can. J. Civ. Eng.* **15**, 66–78 (1998)
5. Matsumoto, Y., Nishioka, T., Shiojiri, H., Matsuzaki, K.: Dynamic design of footbridges. In: *IABSE Proceedings*, pp. 1–15. IABSE, Zürich. , No. P-17/78 (1978)
6. Živanovic, S.: *Probability-based estimation of vibration for pedestrian structures due to walking*. PhD Thesis, Department of Civil and Structural Engineering, University of Sheffield, UK (2006)
7. Kerr, S.C., Bishop, N.W.M.: Human induced loading on flexible staircases. *Eng. Struct.* **23**, 37–45 (2001)
8. Pedersen, L., Frier, C.: Sensitivity of footbridge vibrations to stochastic walking parameters. *J. Sound Vib.* **329**, 2683 (2009). <https://doi.org/10.1016/j.jsv.2009.12.022>
9. Živanovic, S., Pavic, A., Reynolds, P.: Probability-based prediction of multi-mode vibration response to walking excitation. *Eng. Struct.* **29**, 942–954 (2007). <https://doi.org/10.1016/j.engstruct.2006.07.004>
10. Brownjohn, J.M.V., Pavic, A., Omenzetter, P.A.: A spectral density approach for modelling continuous vertical forces on pedestrian structures due to walking. *Can. J. Civ. Eng.* **31**(1), 65–77 (2004)

**Lars Pedersen** has been with Aalborg University, Denmark since 2000. He received his Ph.D at the department where he is currently employed as associate professor.



# Chapter 18

## A Damage Detection Strategy on Bridge External Tendons Through Long-Time Monitoring

Alfredo Cigada, Francescantonio Lucà, Marzia Malavisi, and Giuseppe Mancini

**Abstract** In recent years, Structural Health Monitoring (SHM) has gained a lot of attention, given the need to detect a structure damage at an early stage. A series of technological advances, especially in the world of new sensors, has allowed more structures to be equipped with an always increasing number of monitoring systems of different nature. The state of the art of monitoring systems involves the interaction and cooperation of elements such as low-cost sensors, efficient communication networks, data transfer and storage, often based on cloud architectures.

If on the one hand the amount of data collected by the new SHM systems tends to be of considerable size, the search for damage passes through a process of information synthesis aimed at defining features able to describe the health of the monitored structure.

Although many papers in literature are focused on the definition of an early warning through the most suitable damage feature, less attention has been paid till now to the challenge of implementing a fully automatic monitoring system that can serve as a robust and reliable tool for decision making.

This paper presents a framework/architecture for a real-time data elaboration process, based on different alarm levels to track an ongoing and growing damage. Into details, data coming from a large number of MEMS accelerometers, installed on tensioning cables inside a box composite highway bridge, are continuously processed and analyzed at the sensor level. This is done on a microcontroller equipping each sensor, thanks to both fit-to-the-purpose algorithms that do not require huge computational effort and a strategy which can manage each sensor independently from the others.

At a first stage, the proposed strategy is able to identify every kind of anomalies in the collected data; then, the benign phenomena, such as the occurrence of heavy though not extraordinary loading conditions, are identified and separated from those which clearly point at a damage, such as the breaking of the strands of prestressed cables. As these events occurred during the monitoring and have been recorded, we have a check about the capability of the chosen algorithms to perform this clustering.

Different output examples are discussed in this paper in order to provide a significant case study where the effectiveness of a SHM system is discussed in a damage detection perspective.

**Keywords** SHM · Damage detection · MEMS sensors · Cable · Cable vibration

### 18.1 Introduction

Civil structures such as bridges and roads play an important role in the mobility of modern society, with the related effect that the integrity of these structures has direct repercussions on the safety of an enormous quantity of people who use them on a daily basis.

---

A. Cigada · F. Lucà  
Department of Mechanical Engineering, Politecnico di Milano, Milan, Italy

M. Malavisi (✉)  
Department of Structural, Geotechnical and Building Engineering, Politecnico di Torino, Torino, Italy  
e-mail: [marzia.malavisi@polito.it](mailto:marzia.malavisi@polito.it)

G. Mancini  
SafeCertifiedStructure Ingegneria s.r.l., Torino, Italy

The discipline known as “Structural Health Monitoring” (SHM) aims at defining strategies for damage detection, through a continuous assessment of structural integrity [1]. The development of new technologies in the field of sensors and telecommunications suggests a progressive transition from maintenance carried out with visual inspections to the automation of the diagnostic process. In this sense, the goal is to make the maintenance process more effective and more efficient at one time: moving from periodic visual inspections to an intervention “only when needed”, better results in terms of timing can be achieved. This reflects in a better allocation of the available resources for maintenance and, mainly, in higher safety standards [2].

However, if an increasing number of structures are being equipped with sensors for SHM purposes, new challenges have to be faced in terms of management and synthesis of the information contained in the huge amount of available data [3].

In literature, many techniques have been successfully developed to extract information from vibration data [4, 5]. If, on the one hand, low-cost accelerometers with unexpected good level performances for civil applications are currently available, the amount of data generated by dynamic measurements continuously acquired, for long time records, can be critical under different points of view: from the processing phase to the transferring, storing and querying of the data, it is necessary to adopt a strategy aimed at effectively summarizing the information contained in the monitoring data.

This paper describes an interesting case study, where a fully automated SHM system was installed on a highway concrete bridge located in Italy. In particular, following the failure of one of the external tendons located in the hollow section of the box girder, and due to the difficulty of accessing the site to carry out visual inspections, 88 triaxial accelerometers were installed directly on all the accessible external cables: since the consequences of the collapse of these elements are well known [6, 7], the goal was to detect any sign of early damage, to possibly anticipate further dangerous scenarios.

Taking into account the limits in terms of sensor performances and computational capability of the system components, but at the same time exploiting the possibility of processing the data at different levels, from the measurement nodes to gateways and the cloud environment, a strategy based on two different levels of alarm has been proposed. With reference to [8], a first check is carried out at the gateway level, in order to identify the occurrence of extraordinary events. When this first level alarm is produced, data are sent to the cloud to be further investigated. An algorithm based on the frequency domain decomposition (FDD) and peak picking is then adopted in order to verify the presence of a structural tendon change, producing a second level alarm when a variation in the natural frequency is recognized, out of the boundaries of environmental variations.

A description of the methodology and some interesting results from the application of this simple yet effective strategy are synthetically resumed in this work.

## 18.2 The Monitored Structure: A Pre-stressed Bridge

As above mentioned, a large-scale real time structural health monitoring system has been installed to monitor the external pre-stressed tendons of a composite box girder located in Italy.

As shown in Fig. 18.1c, the bridge is composed by five equally spaced continuous spans with a length of 120 m each and one simply supported end span 43 m long, for a total length of 580 m. Two abutments are located at the end points (SP1 and SP2) and five concrete piers (P1 to P5) support the spans.

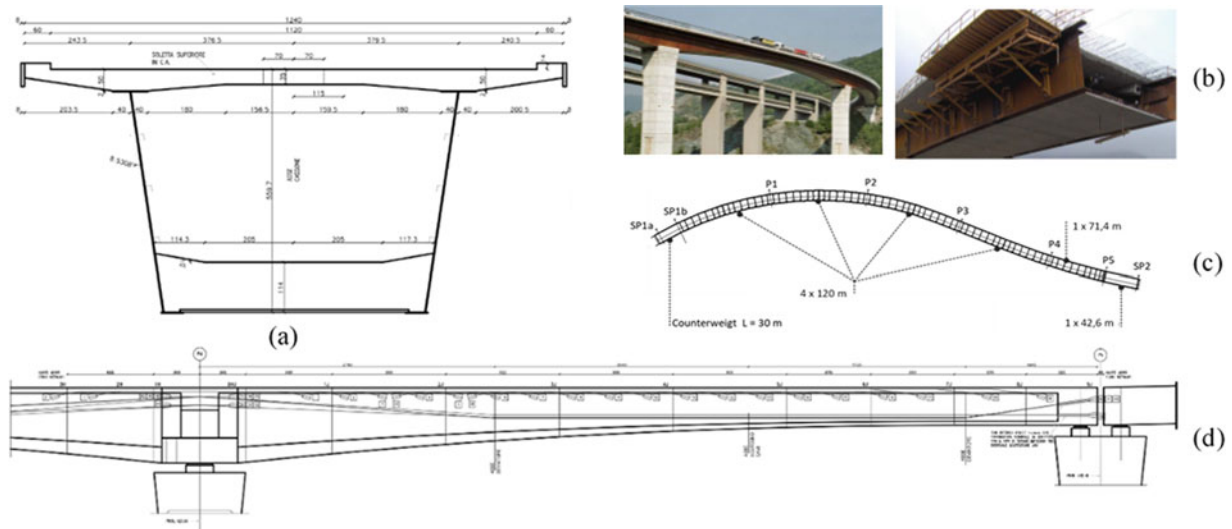
The section of the composite box girder, where corrugate steel plates replacing the concrete webs serve to reduce the self-weight of the structure, is shown in Fig. 18.1a. The height of the cross-section varies between 6.0 m (at the bearings) and 3 m (at the centerline); this is seen in Fig. 18.1c.

The bridge is strengthened by both internal and external pre-stressing [9]. In this work, the focus is on the unbounded tendons that can be found inside the hollow section of the box girder; each of the tendons is made of 27 strands and it is contained inside a polyethylene duct where a grout is injected to protect the cable. The interest followed the failure of one of the tendons, only 2 years after construction. The origin of this phenomenon has to be found in an incorrect grout composition that caused an accelerated corrosion of the strands [10]. A monitoring system was installed in order to help visual inspection inside the box girder, with the aim of identifying, and possibly anticipating, future collapse of the tendons.

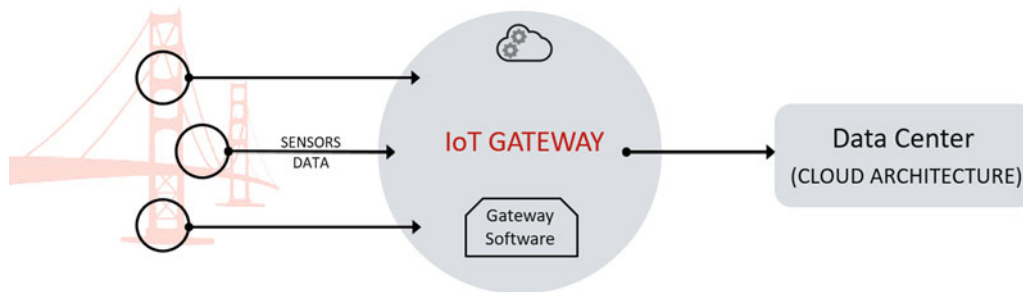
## 18.3 The Monitoring System

The monitoring system can be divided into three main parts: the sensor nodes, the IoT gateway and the Data Center (Fig. 18.2).

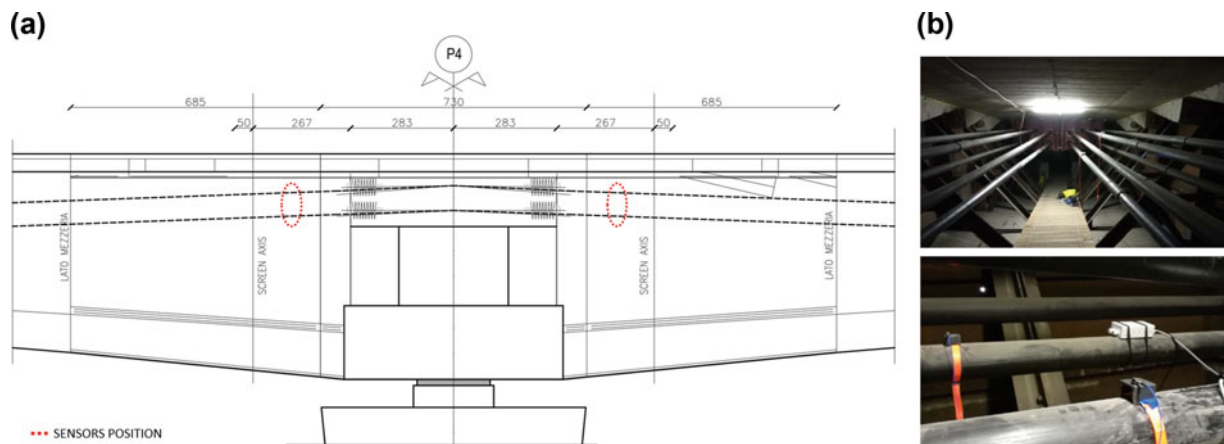




**Fig. 18.1** Structural drawings of the bridge. (a) Bridge cross-section; (b) bridge images after and during construction; (c) plan view of the highway bridge; (d) longitudinal section of a span



**Fig. 18.2** Gateway architectural overview



**Fig. 18.3** Layout of the monitoring system. (a) Typical sensors position; (b) MEMS Accelerometers installed on the external steel tendons

Each of the 88 sensor nodes is equipped with a tri-axial MEMS accelerometer, a sensor of humidity and temperature and a microcontroller, this latter mainly used for data sampling. A sensor node is something different from the traditional sensors adopted for SHM: in fact, in addition to the sensors, it also includes local sampling, the possibility of local data elaboration to compress information, the management of data transfer, through a cabled or wireless connection, to a gateway. The measurement nodes are placed in 10 cross-sections of the bridge, close to the steel protection screens as shown in Fig. 18.3a. More in detail, the device is placed on top of the pre-stressed cables and fastened to it (Fig. 18.3b).

The tri-axial accelerometers are characterized by a range of  $\pm 2.5$  g and a bandwidth of 50 Hz; the results of preliminary tests carried out in field proved the adopted MEMS sensors to be effective in measuring the vibration of the tendons (at least for the damage recognition needs). Indeed, the presence of ground vehicle traffic on the bridge during all the 24 hours is able to excite the tendons that are also characterized by a low damping at rather high levels. It is noted that the presence of one sensor node for each cable does not allow the user to carry out traditional modal analysis, but it has been preferred to mount only one sensor per cable, but on all cables.

The acceleration data are sampled at the sensor level at 25.6 kHz, filtered down and down sampled to finally obtain a sampling rate of 100 Hz; this sampling frequency is the maximum allowable sampling rate per channel, due to the limitation of the data streaming through the network. The acceleration data are encoded by the microcontroller into a CAN BUS network and sent to a local IoT gateway.

The IoT gateway is made to collect data from the measurement nodes, do some preliminary preprocessing and to send the information to the cloud. Pre-processing is especially aimed at filtering acceleration series, discarding corrupted data. Also, different parameters can be evaluated, for a preliminary quick inspection, such as maximum, minimum, root-mean-square; as it will be explained in the following, the IoT gateway represents an interesting stage of the monitoring system where a first step of the damage detection can be carried out at a higher level than just on the sensor; as at this level, more channels can be evaluated, accounting for the available cross sensor information.

Finally, the acceleration, temperature and humidity time series coming from the 88 measurement nodes are sent to the cloud monitoring infrastructure: this is considered of fundamental importance to eventually correct data for their effects. Data are then available to be accessed, downloaded or processed on a cloud environment.

Considering that the monitoring system is operating since September 20th 2017, in continuous except for occasional breaks due to maintenance of the system, the amount of stored data is already of noticeable dimensions; a high level of operation parallelism is needed, in order to process the data in short time and provide a reasonable warning.

Different levels of detail can be achieved analyzing data in the gateway rather than in the cloud; if the latter is the environment where more complex algorithms can be run, some limits on its usage are the cost related to the data transfer and storage. Therefore, the leading idea is that of storing all the raw data on local disks, sending only synthetic information and data worthy of further investigation to the cloud. The main challenge is, then, exploiting all the potentiality of the monitoring system, avoiding waste of resources. Being aware of the potentiality and limits of the different components, a strategy for early detection of tendon damage has been developed. The description of the methodology and some interesting results are shown in the following.

## 18.4 The Proposed Methodology: A Two Level of Alert Damage Detection

The main problem concerning the structural integrity of the monitored tendons is an ongoing corrosion process due to an incorrect grout composition. This phenomenon causes a progressive break of the strands until complete failure of the tendon is reached. Indeed, the progressive failure of the individual strands causes a progressive reduction of the tendon cross section and thus an increase in the tendon stress, which gradually leads to a failure of the tendon itself.

A methodology based on two alarm levels has been proposed, in order to fully exploit the potentiality of the monitoring system.

The first alarm level is checked at the gateway level, and its main output is to point out the presence of out of normal behavior in terms of tendon vibration energy. This because of the brittle nature characterizing the failure of the single strand, which can be associated with the release of energy that can be perceived as an impulse by some of the accelerometers in the surroundings. The monitoring of the vibration energy of the tendons is carried out evaluating the STD level during the data preprocessing at the gateway level.

Collecting and analyzing the data for a training period of 1 month, where only the data associated to a “normal” behavior of the structure (at least as the picture during that month, not considering eventual older damage) have been taken into account, it was possible to define and set a certain range of acceptable values that the STD can assume. The result of the training phase is shown in Fig. 18.4, where the maximum and minimum STD values, evaluated on windows 60 s long, are represented for each of the 88 sensors. As it can be seen, all the sensors belonging to the last span on the right side of the bridge (between piles P4 and SP2) are characterized by higher vibration level, while the other four spans, characterized by the same size, have a similar behavior.

A threshold has been defined for each sensor:

$$T_s = STD_i \quad (18.1)$$

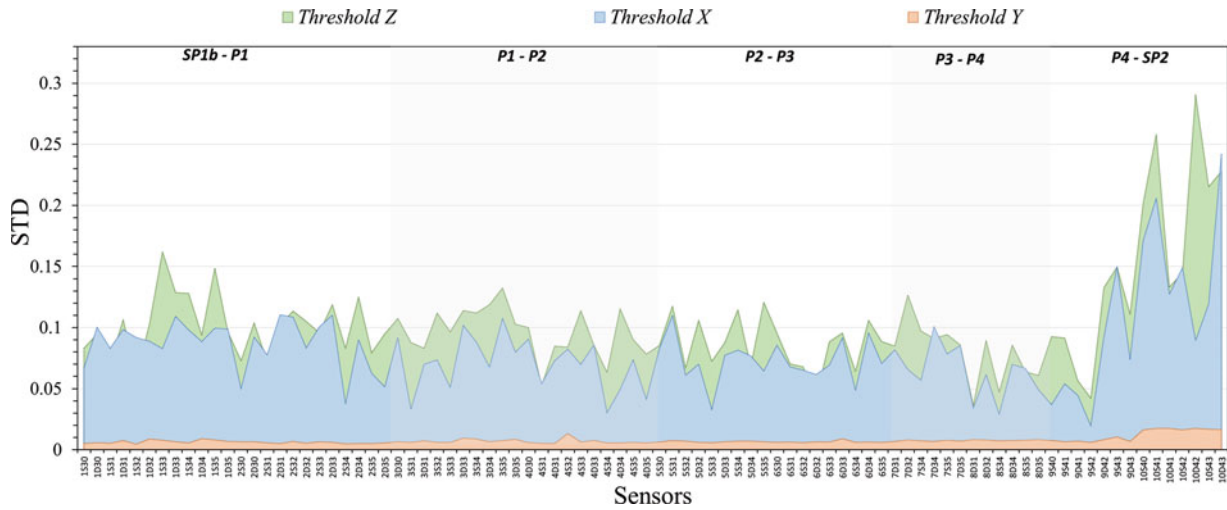


Fig. 18.4 Threshold values for all the 88 sensors – directions x, y, z

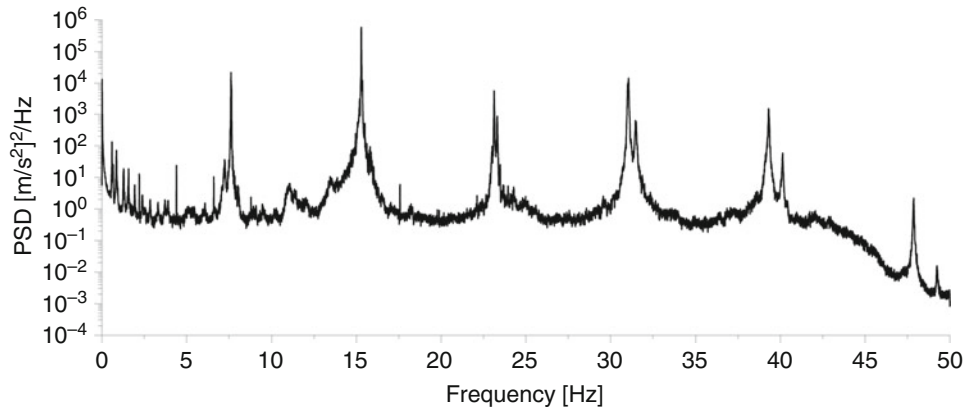


Fig. 18.5 Example of the PSD of the signal measured by one of the 88 accelerometers installed on the bridge

Where  $T_s$  is the threshold level for sensor  $i$ . The threshold values for each sensor of the structure in the three directions of measurement x, y and z are shown in Fig. 18.4.

If the first alarm level is reached, the analysis is then moved to the cloud environment, where a deeper insight in the portion of anomalous data can be carried out, with the aim of distinguishing high energy levels associated to exceptional operational loading (such as exceptional maintenance works on the bridge, earthquakes, . . . ) from those which can be associated to the release of energy due to the failure of a strand.

The second alarm level is based on a physical interpretation of the vibration data in the frequency domain. The random signals can be analyzed through the computation of the Power Spectral Density (PSD). The parameters of the analysis that can be adopted in order to get to a good estimate of the PSD were set after some preliminary tests where the data acquired through the tri-axial MEMS accelerometers were compared with signals acquired with low noise piezo accelerometers (24 bit A/D converter with anti-aliasing filter, sampling frequency of 2048 Hz). The averaging process is performed with a record length of 200 s, 66% of overlap and Hanning window. As it can be observed in Fig. 18.5, in the range 0–50 Hz it is possible to clearly identify the position of the peaks corresponding to the first natural frequencies of the tendon.

Considering the cables injected with cement grout, when a strand collapses, the cross section of the tendon is reduced; this causes a decrease in the axial force. Knowing that the analytical formulation of the natural frequencies of a cable [11]:

$$f_i = \frac{1}{2L_i} \sqrt{\frac{T_i}{m_i}} \tag{18.2}$$

where  $m_i$ ,  $L_i$  and  $T_i$  are respectively the mass, length and axial force of the cable, when the axial force is reduced a frequency shift should be observed.

Then the idea is that, when the gateway sends a warning because a high level of vibration has been observed, data are sent to the cloud where an algorithm runs to verify if any change in the natural frequencies suddenly occurred. In order to identify the natural frequency of the tendons, the frequency domain decomposition (FDD) has been adopted.

The FDD algorithm is a well-known technique [12] that allows to get to the modal identification of output-only systems basing the analysis on responses only, when the structure is loaded by a broad-banded excitation. The FDD goes through the decomposition of the PSD function matrix using a singular value decomposition (SVD). The spectral response is decomposed into a set of auto spectral density functions, each corresponding to a single degree of freedom (SDOF) system. The result is exact in the case where the excitation is white noise, the structure is lightly damped and when the mode shapes of close modes are geometrically orthogonal.

Considering a mechanical system characterized by constant coefficient, which is stable and linear, the relationship between the “ $r$ ” inputs  $x(t)$  and the “ $m$ ” measured responses  $y(t)$  is:

$$G_{yy}(j\omega) = H^*(j\omega) G_{xx}(j\omega) H(j\omega)^T \quad (18.3)$$

Where, if  $G_{xx}(j\omega)$  is the ( $r \times r$ ) PSD matrix of the input,  $G_{yy}(j\omega)$  is the ( $m \times m$ ) PSD matrix of the responses,  $H(j\omega)$  is the ( $m \times r$ ) frequency response function (FRF) matrix, the superscript “ $*$ ” is the complex conjugate and the superscript “ $T$ ” is the transpose.

With the assumption that the input is white noise, which means that the PSD is a constant matrix ( $G_{xx}(j\omega) = const$ ), and knowing that, in the case of a lightly damped structures, at a certain frequency  $\omega$  only a limited number of modes will contribute to the response, through the modal decomposition of the spectral matrix the PSD of the responses matrix can be expressed as:

$$G_{yy}(j\omega) = \sum_{k \in Sub(\omega)} \frac{d_k \phi_k \phi_k^T}{j\omega - \lambda_k} + \frac{d_k^* \phi_k^* (\phi_k^*)^T}{j\omega - \lambda_k^*} \quad (18.4)$$

Where  $d_k$  is a scalar constant,  $\phi_k$  is the mode shape vector,  $\lambda_k$  is the pole and  $Sub(\omega)$  is the set of modes that contribute significantly at a certain frequency  $\omega$ .

In the FDD identification, the starting point is, then, the estimate of the PSD matrix,  $\hat{G}_{yy}(j\omega)$ . By a singular value decomposition, this matrix which is known at discrete frequencies  $\omega = \omega_i$ , is decomposed as it follows:

$$\hat{G}_{yy}(j\omega_i) = U_i S_i U_i^T \quad (18.5)$$

where  $S_i$  is a diagonal matrix with the scalar singular values  $s_{ij}$  and the matrix  $U_i = [u_{i1}, u_{i2}, \dots, u_{im}]$  is a unitary matrix, with  $u_{ij}$  singular vectors. When the range of considered frequencies is near a peak corresponding to the  $k$ -th mode, only a few modes will be dominating; in correspondence of a natural frequency, where only one mode is dominating, there will only be one term in the Eq. (18.4). In this case, the first singular vector  $u_{i1}$  is an estimate of the mode shape, such that  $\hat{\phi}_k = u_{i1}$  and the corresponding singular value  $s_{i1}$  is the auto-PSD function of the corresponding SDOF system. Peaks of the first singular values  $s_{i1}(\omega)$  can be, then, found in correspondence of the natural frequency of the system through a peak-picking procedure.

In case a variation of the natural frequencies is noticed, the second level alert alarm is produced.

The damage identification in terms of natural frequency shifts has some limitations [13–15]; nevertheless, the results coming from the application of the proposed strategy are encouraging. Some of these results are described in the following paragraph.

## 18.5 Results and Discussion

The strategy has been adopted for monitoring the integrity of tendons in the period between September 2017 and July 2019. In this section, two main events are described which occurred respectively in November and December 2017.

On 19/11/2017 the first threshold level was exceeded by all the sensors of the structure. Figure 18.6 shows the STD values recorded in the 3 directions  $x$ ,  $y$  and  $z$  compared with the threshold values set for each sensor. As illustrated in the graph,

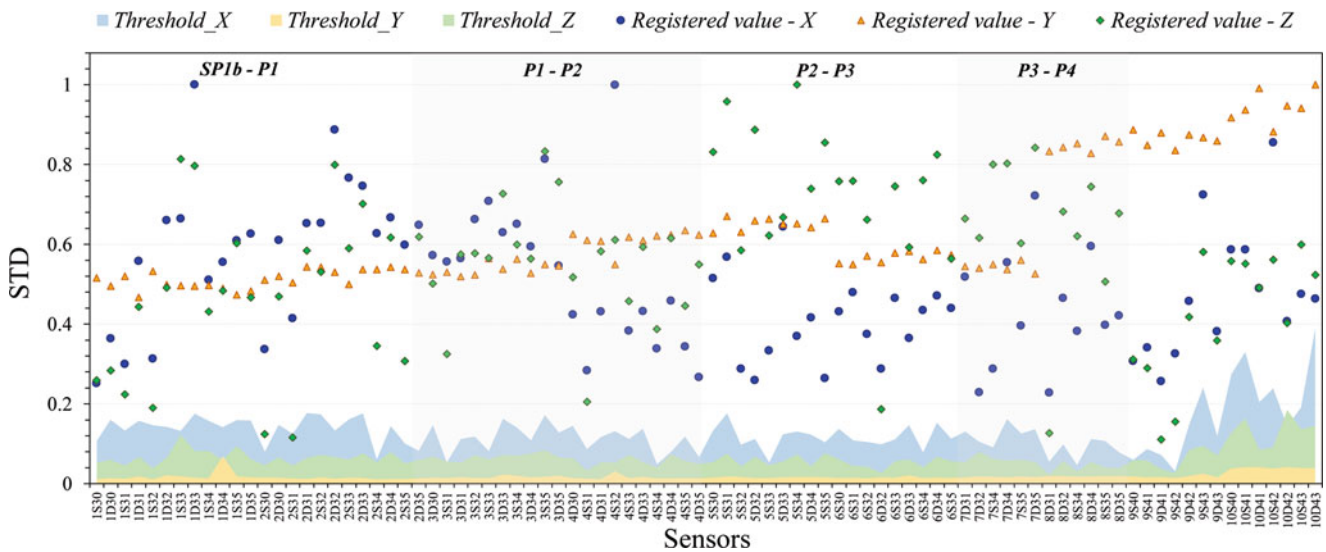


Fig. 18.6 STD values registered on 19/11/2017 by all the sensors

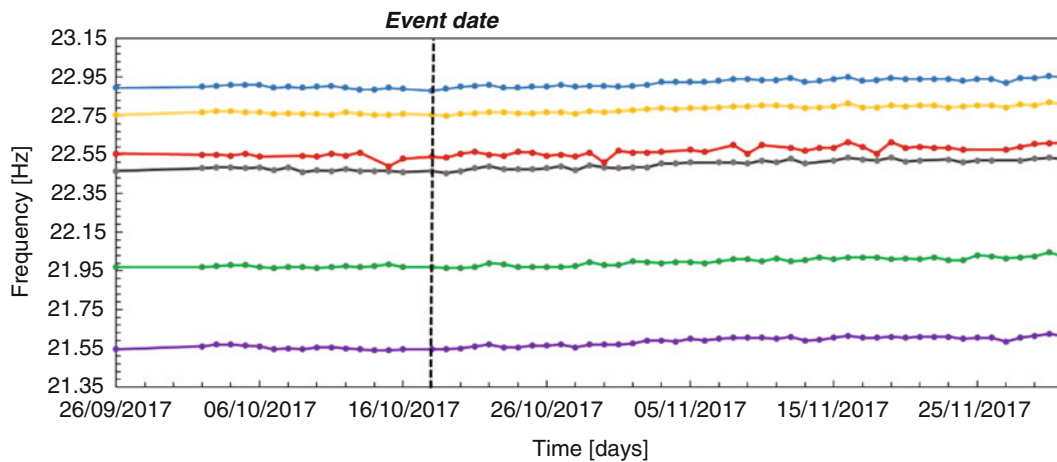


Fig. 18.7 Natural frequency evolution over time for some sensors installed on the structure

all the sensors showed STD values significantly higher than the pre-defined thresholds, indicating an anomaly condition that covered the whole bridge.

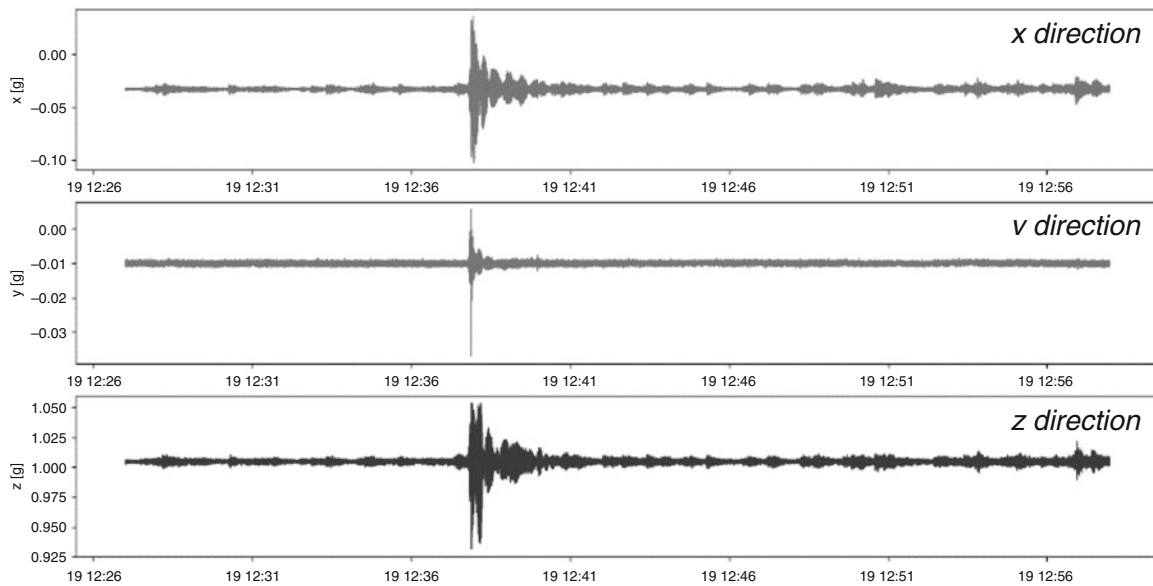
When the first level threshold was exceeded, the second level check was automatically activated in the cloud, in order to verify the frequency trend at the alerted time instant.

Figure 18.7 presents the evolution of the third natural frequency for some of the tendons during the period under analysis. A focus on this graph around the date in which the event occurred, for the natural frequency of the third mode, shows that frequencies did not change during the considered time period, remaining constant for all the tendons. The choice of the third peak is motivated by the highest accuracy in the identification phase, being the two peaks relative to the third mode well separated.

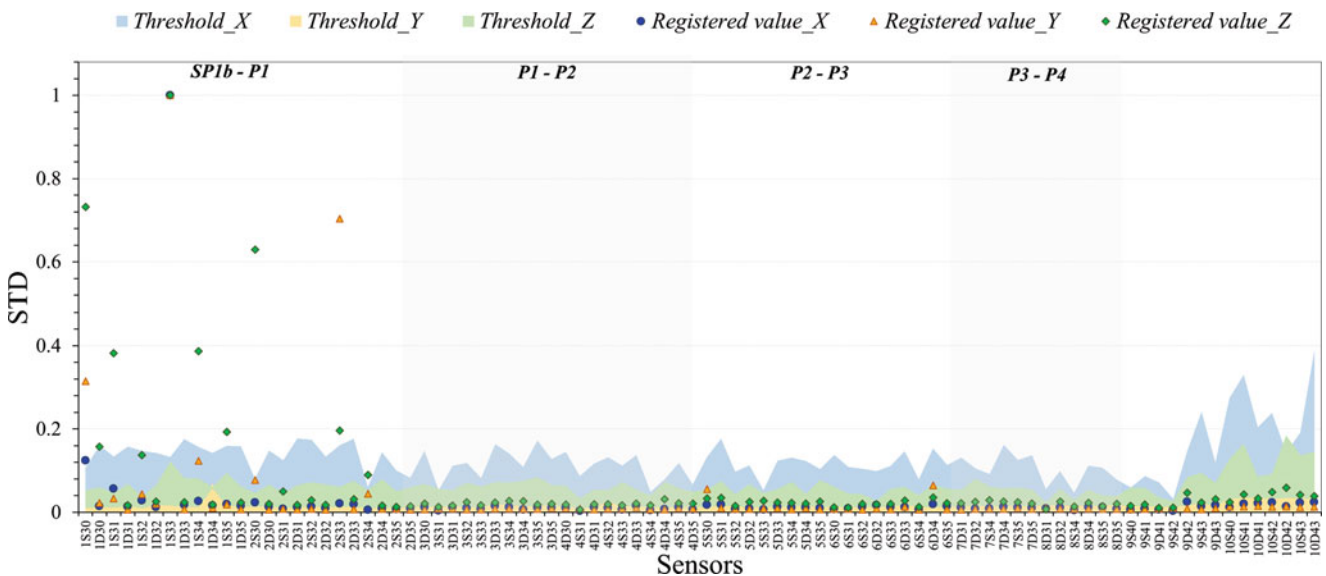
It is relevant to observe that frequencies are very well characterized by the algorithm for the automatic identification of modal parameters used for the second level check. At the sight of these observations, it is easy to deduce that the second level alert was not produced, meaning that no significant change in the axial load is observed.

Also, the occurrence of a tendon failure should involve a limited number of sensors, due to the local nature of the phenomenon; overcoming the first level threshold for all the sensors was in fact justified by the occurrence of an earthquake in the vicinity of the structure.

The STD values calculated on acceleration data recorded by sensors during the earthquake were, of course, out of bounds, due to the considerable amount of energy contained in the signal following the seismic input. In fact, as known, STD value is only related to the signal amplitude that, in this case, was extremely high due to the seismic shock (Fig. 18.8). However, the



**Fig. 18.8** Time signal related to the earthquake occurred in November 2017 near the monitored structure



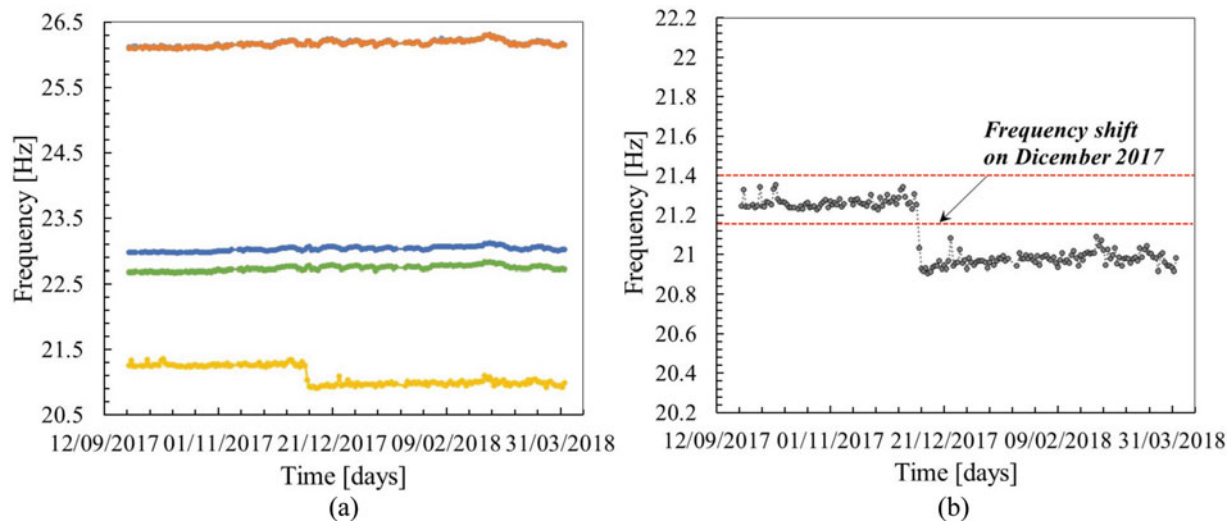
**Fig. 18.9** STD values registered on December 2017 by all the sensors

second threshold was not exceeded and no shifts in natural frequencies were observed; consequently, the automatic anomaly detection procedure did not report any structural alarms, demonstrating the reliability and robustness of the implemented methodology.

On December 2017 another significant event occurred on the monitored structure. In particular, the first level threshold was exceeded by some sensors installed in the first span of the bridge, as shown in Fig. 18.9.

The event was recorded mainly by one of the sensors installed in the first span, as highlighted in the graph, where it is possible to observe that only one sensor reaches the normalized STD value of 1. At the same time, all the sensors installed in the remaining spans did not show anomalous STD values, indicating that the event triggering the alarm affected only the first span of the bridge.

Following the first level alert, the natural frequency check has been automatically activated by the monitoring system for all the sensors that exceeded the first threshold. Figure 18.10 shows the evolution over time of the natural frequencies obtained from some of the sensors affected by the anomaly, with the indication of the date on which the event occurred.



**Fig. 18.10** (a) Natural frequency evolution over time for some sensors installed on the first span of the structure; (b) frequency shift registered for one tendon located in the first span

As can be observed from the graph, one of the cables installed in the first span of the monitored bridge exceeded the second threshold level, pointing at a possible structural damage. In fact, as highlighted by the zoom of the Fig. 18.10b, the frequency analysis showed a considerable shift in natural frequency values (at least considering the time lag in which the change occurred), which indicates a meaningful and sudden reduction in the element stiffness.

The registered shift in the frequency values could be caused by the failure of one of the strands of the tendon that exceeded the second level threshold. Indeed, a strand break causes a partial loss of pre-stress force in the tendon, which results in a stiffness reduction of the element itself. This reduction in stress distribution is a function of the severity of tendon damage (the number of strand breaks) and the location of the damage. Moreover, if a strand breaks, a significant amount of vibrational energy would be released, being recorded as a dynamic input by the immediately nearby sensors.

The effectiveness of the two levels monitoring approach discussed in this paper have been demonstrated through experimental evidences. The comparison between the two different events, described herein, shows that the system was able to automatically recognize (and activate the alarm procedure) only when there was an actual structural problem (the strand breakage). In the case of the earthquake indeed, no alarm was produced.

## 18.6 Conclusions

The monitoring program presented in this paper, in operation for about 2 years, has permitted collecting a very complete high quality database with the time evolution of the natural frequencies of all the tendons of the analyzed bridge. A framework for an automatic and real-time damage detection has been developed based on two levels of alarm, respectively characterized by a check on a statistical parameter, the signal STD, and a check on a physical parameter, the natural frequencies. The first level of alarm is verified at the gateway level, and its main output is highlighting the presence of anomalous behavior in terms of the vibration energy of the tendons. The second level of alarm, activated only if the first one is exceeded, is based on a physical interpretation of the vibration data in the frequency domain and it is performed in the cloud environment.

This methodology has been successfully adopted to monitor the external tendons of the bridge, proving to be able to highlight the occurrence of the damage that progressively leads to the bridge cables failure. Two different events that occurred on the structure were presented, showing how the implemented methodology was able to distinguish a non-structural problem, for which no alarm was sent to the operator, and a structural damage, for which a real-time alarm was generated. The proposed methodology therefore seems to be effective in terms of avoiding false positive and sufficiently reliable and robust for a continuous and automatic monitoring system.

**Acknowledgement** Authors would like to thank Dr. Diego Melpignano, Dr. Angelo Giani and Dr. Livio Gasparetto who provided insight and expertise that greatly assisted the research.

## References

1. Farrar, C.R., Worden, K.: An introduction to structural health monitoring. *Philos. Trans. R. Soc. A Math. Phys. Eng. Sci.* **365**(1851), 303–315 (2007)
2. Chang, P.C., Flatau, A., Liu, S.C.: Review paper: health monitoring of civil infrastructure. *Struct. Health Monit.* **2**(3), 257–267 (2003)
3. Tokognon, A.C., Gao, B., Tian, G.Y., Yan, Y.: Structural health monitoring framework based on internet of things: a survey. *IEEE Internet Things J.* **4**(3), 629–635 (2017)
4. Das, S., Saha, P., Patro, S.K.: Vibration-based damage detection techniques used for health monitoring of structures: a review. *J. Civ. Struct. Heal. Monit.* **6**(3), 477–507 (2016)
5. Amezquita-Sanchez, J.P., Adeli, H.: Signal processing techniques for vibration-based health monitoring of smart structures. *Arch. Comput. Methods Eng.* **23**(1), 1–15 (2016)
6. Anania, L., Badalà, A., D'Agata, G.: Damage and collapse mode of existing post tensioned precast concrete bridge: the case of Petrulla viaduct. *Eng. Struct.* **162**, 226–244 (2018)
7. Colajanni, P., Recupero, A., Ricciardi, G., Spinella, N.: Failure by corrosion in PC bridges: a case history of a viaduct in Italy. *Int. J. Struct. Integr.* **7**(2), 181–193 (2016)
8. Bertagnoli, G., et al.: A large scale SHM system: a case study on pre-stressed bridge and cloud architecture. In: *Dynamics of civil structures*, vol. 2, pp. 75–83. Springer, Cham (2020)
9. Miyamoto, A., Tei, K., Nakamura, H., Bull, J.W.: Behavior of prestressed beam strengthened with external tendons. *J. Struct. Eng.* **126**(9), 1033–1044 (2000)
10. Minh, H., Mutsuyoshi, H., Niitani, K.: Influence of grouting condition on crack and load-carrying capacity of post-tensioned concrete beam due to chloride-induced corrosion. *Constr. Build. Mater.* **21**(7), 1568–1575 (2007)
11. Cheli, F., Diana, G.: *Dinamica e vibrazione dei sistemi*. UTET Università, Torino (1993)
12. Brincker, R., Zhang, L., Andersen, P.: Modal identification of output-only systems using frequency domain decomposition. *Smart Mater. Struct.* **10**(3), 441–445 (2001)
13. Doebling, S.W., Farrar, C.R., Prime, M.B.: A summary review of vibration-based damage identification methods. *Shock and vibration digest.* **30**(2), 91–105 (1998)
14. Fan, W., Pizhong, Q.: Vibration-based damage identification methods: a review and comparative study. *Struct. Health Monit.* **10**(1), 83–111 (2011)
15. Farrar, C.R., Doebling, S.W., Nix, D.A.: Vibration-based structural damage identification. *Philos. Trans. R. Soc. London, Ser. A.* **359**(1778), 131–149 (2001)

**Prof. Alfredo Cigada** is Full Professor in Mechanical and Thermal Measurements at Politecnico di Milano, Italy.





# Chapter 19

## Structural Health Monitoring of a Damaged Operating Bridge: A Supervised Learning Case Study

A. Cigada, F. Lucà, M. Malavisi, and G. Mancini

**Abstract** The aging of materials, combined with the persistence and alteration of both operational loads and atmospheric conditions, cause a decrease of the structural properties of civil structures. This raises questions of considerable importance when it comes into play the safety of infrastructure users, mainly related to bridges and roads. Therefore, monitoring and evaluating the health of such structures becomes of central importance, allowing a more efficient maintenance, aimed at preserving or recovering the required structural properties.

This article describes a case study where a structural health monitoring system has been installed on a damaged operating bridge, where the signs of heavy wear were first detected through visual inspections. Therefore, a network of accelerometers has been designed and installed to the purpose of monitoring the evolution of deterioration phenomena and testing some new approaches related to the use of MEMS sensors. In particular, sensors readings were collected in real-time in order to gain useful information about the dynamic behavior of the structure under ambient and traffic loads.

Data obtained from the monitoring system were used to support the decision of carrying out maintenance operations aiming at reinforcing the bridge, increasing its structural stiffness.

This result was achieved through the post tensioned reinforcement of the bridge, by means of external tendons. The vibration data were collected at different points along the bridge, before and after the maintenance operations, so that both the damaged and undamaged information are now known, suggesting a supervised learning approach for future monitoring of the structure.

The modal parameters of the bridge, extracted from the data, have been used to verify the change in structural stiffness, confirming the effectiveness of the adopted intervention in improving the structural property.

**Keywords** SHM · Bridge · MEMS sensors · Structural dynamics · Supervised learning

### 19.1 Introduction

The research field named Structural Health Monitoring (SHM) deals with the development of strategies for the automatic identification of damage in mechanical, civil and aerospace systems [1]. The main goal of a SHM strategy is to synthesize the information coming from different type of sensors installed on the monitored structure to obtain a constant knowledge of its structural performances. In this way it is possible to move from a “time-based” to a “condition based” maintenance; this mainly results in a more punctual and effective actions, with consequent economic advantage.

By framing the problem in the field of large-scale civil structures, the natural aging of materials and the effect of operational and environmental loads cause a health deterioration of infrastructures such as highway bridges and viaducts [2]; this reflects in serious issues for user security. Considering that most of these structures are near, or in some cases beyond, the life for which they were designed, the risk is that they no longer meet the standards requirements. Therefore,

---

A. Cigada · F. Lucà  
Department of Mechanical Engineering, Politecnico di Milano, Milan, Italy

M. Malavisi (✉)  
Department of Structural, Geotechnical and Building Engineering, Politecnico di Torino, Torino, Italy  
e-mail: [marzia.malavisi@polito.it](mailto:marzia.malavisi@polito.it)

G. Mancini  
SafeCertifiedStructure Ingegneria s.r.l., Torino, Italy

maintenance strategies assume a central importance and they can only be effective if the health status of the structures is constantly assessed.

This article describes an interesting case study of a damaged operating bridge located in Italy. Following visual inspections, the structure was found to be in a state of advanced deterioration and strengthening works were required, through the adoption of external pre-stressing tendons. In particular, this type of intervention improves the ultimate bearing capacity and thus the performances of the bridge, increasing the lifespan and durability of the structure.

In addition, the owner of the structure decided to install a SHM system for the future assessment of the structure. Despite the short time available between the decision to carry out the strengthening works and the start of operations, a series of sensors were installed on the deteriorated structure to track its behavior during the maintenance procedure. Therefore, different accelerometers and inclinometers have been used to verify the effectiveness of the intervention from a dynamic and static point of view. These have not been installed according to a modal analysis design; the very short time needed for the restoration works only allowed to set up a line of sensors, for a check on natural frequencies and modal damping, and only roughly accounting for the mode shapes; all the same, this has been considered a very important occasion to compare a damaged and undamaged bridge behavior in short times.

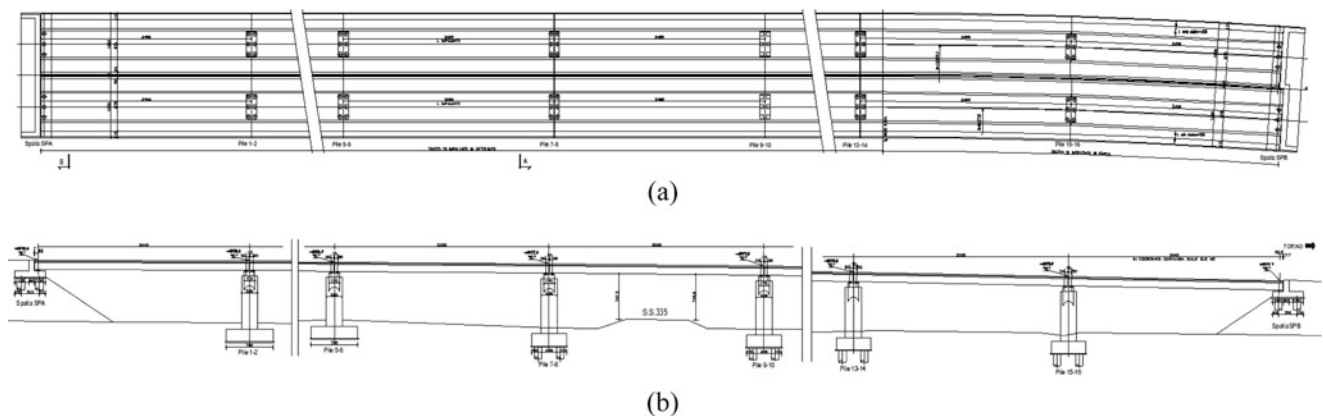
The measurements started before the strengthening works so that a dataset representative of a damaged state is now available; this is of considerable importance in a supervised learning perspective. Indeed, once a damage feature is chosen to represent the state of the structure, this family of approaches searches for damage through the correspondence between data coming from the monitored structure and data related to the damaged structure [3]. In case of civil structures, data referred to the damaged state are usually not available, apart from some case studies [4], limiting the applicability of supervised strategies.

This paper describes the application of some simple data analysis techniques applied to the data recorded before and after the strengthening works. In particular, the structure asset is derived from the clinometer data while the dynamic characteristics are obtained from the acceleration ones. Both methodologies provided very clear representations of the state of the structure before and after the maintenance works, so that it is possible to hypothesize a future development of a supervised learning SHM strategy.

## 19.2 The Monitored Structure: A Pre-Stressed Concrete Bridge

The monitored structure is a pre-stressed concrete bridge from the early 1965s, located in northern Italy. This bridge, due to its geometric and design features, can be considered as representative of many highway infrastructures in Italy. In fact, pre-stressed concrete was a very common way of designing bridges at that time.

The structure is composed by two independent roadways, each characterized by three simply supported pre-stressed concrete spans. The span is 35.0 m long and the cross-section is a pre-stressed reinforced concrete slab with a constant height in the longitudinal direction of about 1.5 m, as shown in the plan view, elevation and cross-section of Figs. 19.1 and 19.2.



**Fig. 19.1** (a) Plan view and (b) elevation of the monitored bridge

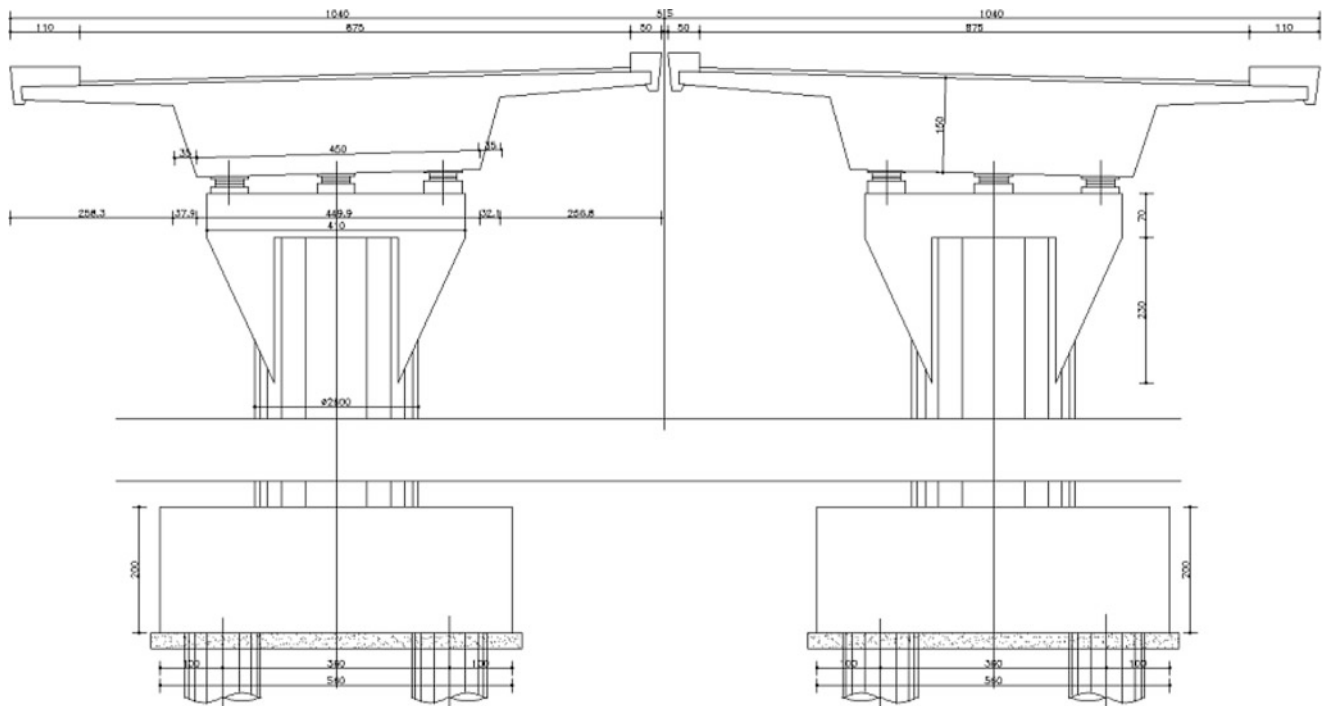


Fig. 19.2 Cross-section of the monitored bridge

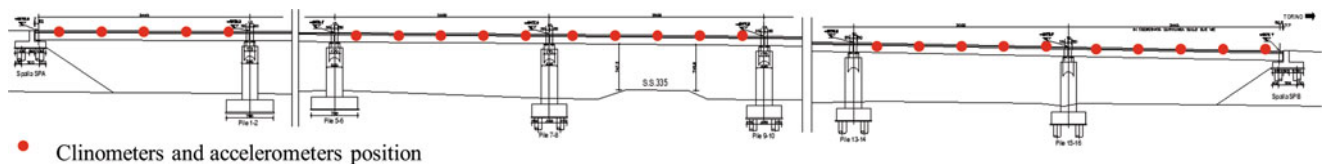


Fig. 19.3 Instrumented cross-sections

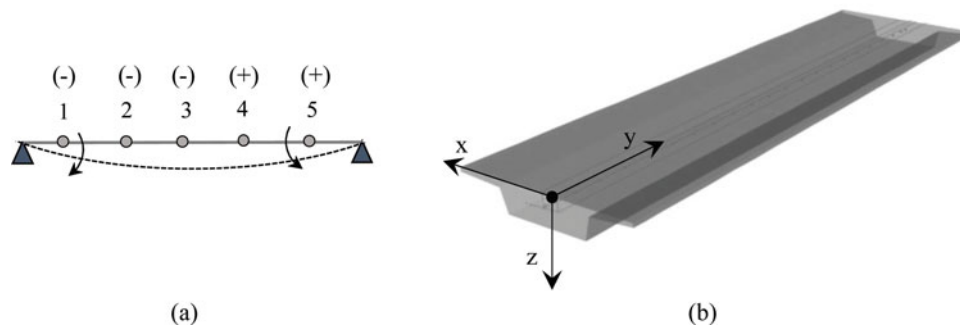
### 19.3 The Monitoring System

A structural health monitoring system composed of 90 biaxial inclinometers and 90 triaxial accelerometers has been installed on both carriageways of the viaduct. In particular, 45 inclinometers and 45 accelerometers were installed on the longitudinal beams, as reported in Fig. 19.3. The gateways, one for each carriageway, are located between spans 5 and 6. Each of the 9 spans is therefore equipped with a chain made up of 5 sensors. A power line communication has been adopted to connect all the different devices of the network.

The biaxial MEMS clinometers installed on the viaduct have two measuring axes  $x$  and  $y$ , corresponding respectively to the transversal and longitudinal direction of the bridge, meaning that the axes are respectively perpendicular and parallel to the longitudinal extension of the deck in the horizontal plane; the sign conventions adopted for the rotations are shown in Fig. 19.4a. The triaxial MEMS accelerometers installed on the viaduct have the three measuring axes  $x$ ,  $y$  and  $z$  oriented as shown in Fig. 19.4b. The  $x$  axis is the transversal direction of the deck,  $y$  axis is parallel to the longitudinal extension of the spans and  $z$  axis corresponds to the vertical direction. Both clinometers and accelerometers are equipped with a 32-bit microcontroller for data processing at sensor level.

This choice of sensors layout deserves some deepening, as the use of MEMS allows to adopt a wider number of measurement points in a trade-off against their expected performances. Preliminary laboratory testing has allowed to fix the MEMS sensors features, not so far from those of more expensive instrumentation, anyway suitable for giving the needed information. Conversely their low cost has allowed to have a very dense bridge sensing, which was considered of fundamental importance for the planned operation. Consequently, dealing with the huge data streaming represents the real challenge that forced a new data evaluation strategy.

A data processing protocol was developed to transform the readings coming from the sensors into “consistent” data, meaning significant data for the subsequent numerical modelling phases. The data acquisition from each clinometer takes



**Fig. 19.4** (a) Signs convention for clinometers; (b) measurement axes ( $x$ ,  $y$ ,  $z$ ) orientation

place sequentially starting from the gateway at a predetermined time interval, which can be modified by a remote operator. The data acquisition of the entire sensor network is executed at regular time intervals of different length, depending on the elapsed time before all the sensors are interrogated (polling cycle). Each “read” instance includes the acquisition of the signals sent by a single sensor; only at the end of this instance, the next sensor is interrogated by the gateway.

Each inclinometer acquires a record of 1 second with a sampling frequency of 208 Hz (the sampling frequency can be updated remotely); some statistical quantities such as the mean value, the standard deviation, the maximum and minimum are then evaluated for the rotation; also the temperature and the relative humidity are recorded. If an error occurs in the interrogation of a sensor, the procedure is repeated before switching to the next sensor. Therefore, the time needed in order to complete the interrogation of all sensors is variable, depending on the occurrence of communication errors in the entire sequence of readings. The gateways store the data received locally in a buffer memory and forward it via a 3G mobile network to the Cloud database.

As for the accelerometers, the acquisition is continuous, with a sampling frequency of 100 Hz on the 3 measurement axes. Only data collected in pre-defined intervals during the day are sent to the cloud, for a better energy resources exploitation, as data transfer for storage in the cloud environment waste most of the energy in the overall balance. Fifteen minutes of continuous acquisition every 4 hours are recorded and sent to the cloud (also the frequency of this process can be modified remotely). In addition, some threshold levels have been set in order to identify anomalous scenarios; in the event that these thresholds are exceeded at any time of the day, the data around the anomalous event are stored in a local cache memory, a Solid State Disk located on the gateway and subsequently transferred to the cloud, in addition to the data sent with the explained procedure.

To finish with, at the cloud level, data coming from different sensors are stored in a dedicated database; data are then progressively extracted from the database, normalized with respect to the temperature and stored back for subsequent uses. In this phase, corrupted data are discarded. In the end the algorithms developed for data analysis are used to have a picture of the health of the structure, from a static and dynamic point of view.

## 19.4 Strengthening Works of the Pre-stressed Concrete Bridge

The deterioration and the consequent performance reduction of the existing bridges, due mainly to both the structural aging and the increase in the weight and volume of traffic loads, results in localized or global damages in most of the bridge structures.

For the case study analyzed in this paper, serious structural deficiencies were identified in a particular span of the bridge following a visual inspection campaign, in which some longitudinal cracks were observed under the concrete slab. More in-depth investigations have therefore been carried out and a significant loss of pre-stressing in the investigated span of the bridge was detected due to the breakage of a significant number of pre-stressing tendons in the concrete slab.

The failure of pre-stressing tendons was probably caused by a widespread corrosive phenomenon, as shown in Fig. 19.5.

Therefore, a network of sensors was designed and installed to the purpose of monitoring the evolution of deterioration phenomena and, at the same time, checking the effectiveness of a reinforcement intervention. In fact, following the identification of the damage, the infrastructure operator decided to carry out a reinforcement intervention on the structure. In particular, the introduction of additional external pre-stressing tendons has been chosen as a method to strengthen the structure.



**Fig. 19.5** Visual inspection campaign carried out on the bridge

This method has proved to be very useful in increasing the capacity of concrete span bridges. External pre-stressing tendons were thus placed outside the concrete section in May 2019 and the pre-stressing force was transferred to the concrete by means of end anchorages. The application of external pre-stressing in strengthening should lead to a structural system in which the stiffness is increased. In fact, the application of an axial load combined with a hogging bending moment should reduce in-service deflections, consequence of an increased stiffness.

However, the effectiveness and the corresponding effect given by the introduction of external pre-stressing tendons as bridge reinforcement method is not so easily assessable after tendons installation.

In the following paragraph, the main results deriving from the monitoring of the described bridge, before and after the intervention, will be presented in order to verify the change in structural stiffness, confirming the effectiveness of the adopted intervention in improving the structural properties.

## 19.5 Static and Dynamic Monitoring During the Strengthening Works

This paragraph summarizes the main results deriving from both clinometers and accelerometers after the reinforcement installation. Into details, a comparison between the bridge behavior before and after the reinforcement has been performed.

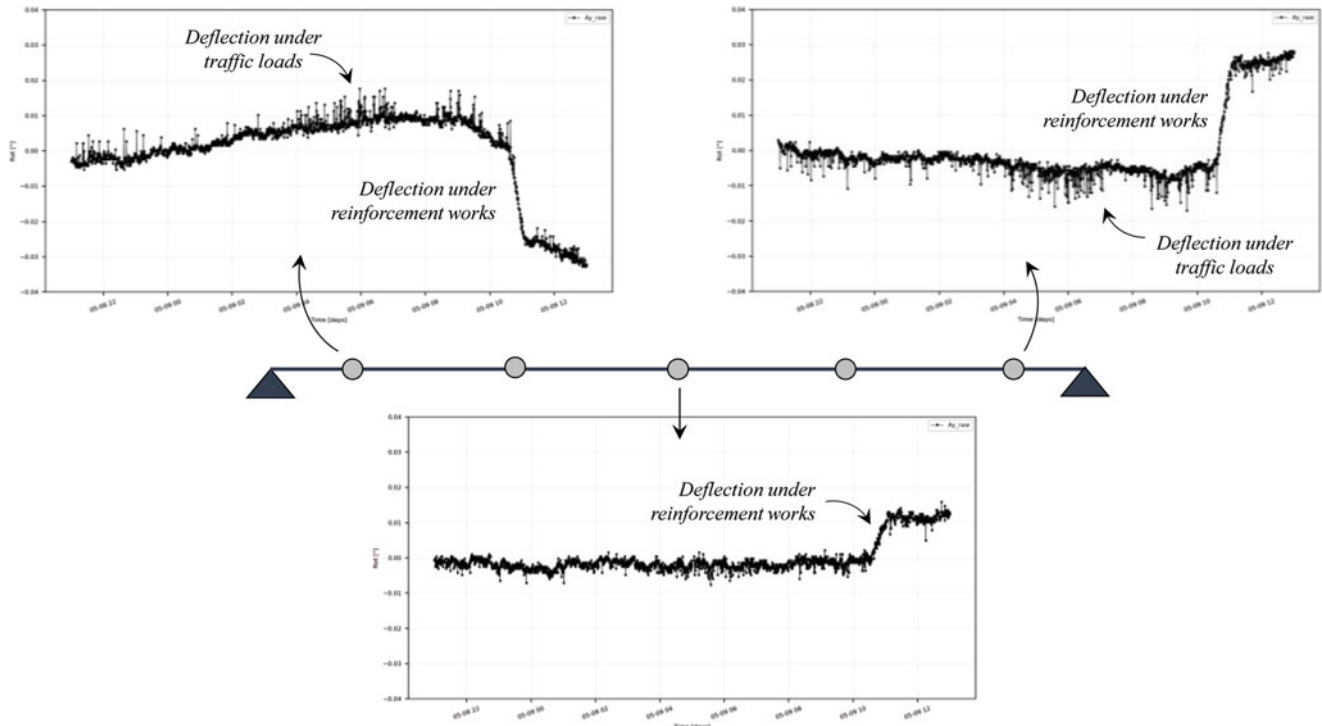
The strengthening works took place on May 9th, 2019. During the restoration works the highway was open in both directions. The event was entirely recorded by both clinometers and accelerometers.

Regarding the clinometer readings, data were recorded continuously, collecting a measurement every 30 seconds. During the works, there were no relevant temperature changes, so environmental variations can be neglected in their effect on measurements.

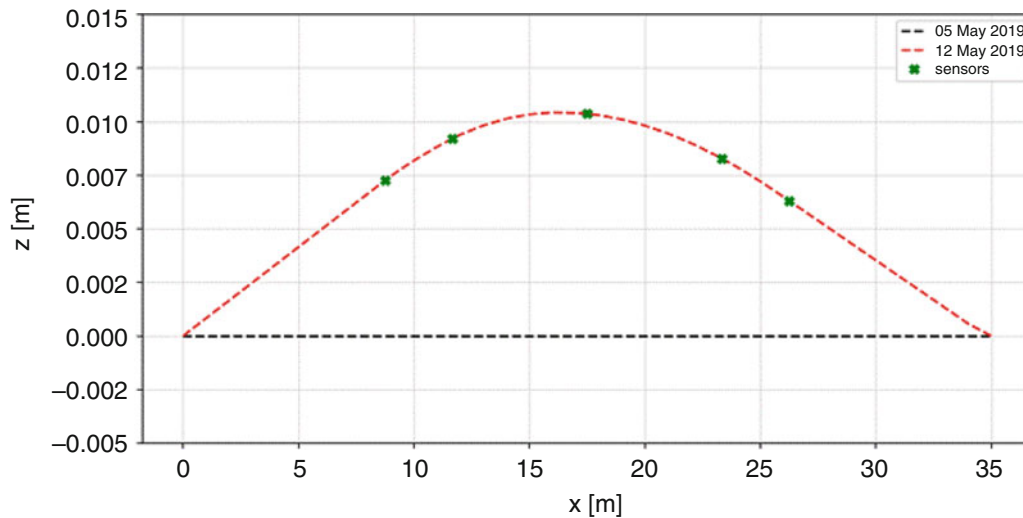
A first analysis of the clinometer raw data highlighted an instantaneous shift in the average of tilt readings when the external force was transferred to the bridge members (May 9th, 2019, morning). Figure 19.6 shows tilts data recorded on the reinforced span by the two sensors located near the span ends and by the sensor positioned at mid span, in a time interval straddling the reinforcement intervention, namely from 01 to 05 May 2019.

As clearly shown in Fig. 19.6, a significant shift in tilt values has been recorded by all the sensors. In particular, it is possible to observe that the tilt variation due to the strengthening works occurred in the opposite direction with respect to the bridge deformation under traffic loads, indicating that the external pre-stressing has caused a counter-balance in the bridge. It is also evident that the sensor located at the center of the span, from which a zero rotation value is expected under load, showed a considerable shift in the tilt average value, indicating the presence of a damaged area in the middle of the span (the presence of a plastic hinge has been hypothesized).

Starting from tilt data recorded before and after the reinforcement intervention, it was possible to calculate the deformation experienced by the bridge under the pre-stressing intervention. Figure 19.7 shows the bridge deformation, in terms of vertical displacements, experienced by the structure following the strengthening works. The red curve was obtained by linear interpolation of the tilt values recorded in the  $y$  direction by the sensors, after removing the average value measured before the intervention.



**Fig. 19.6** Tilt measurements straddling the strengthening works



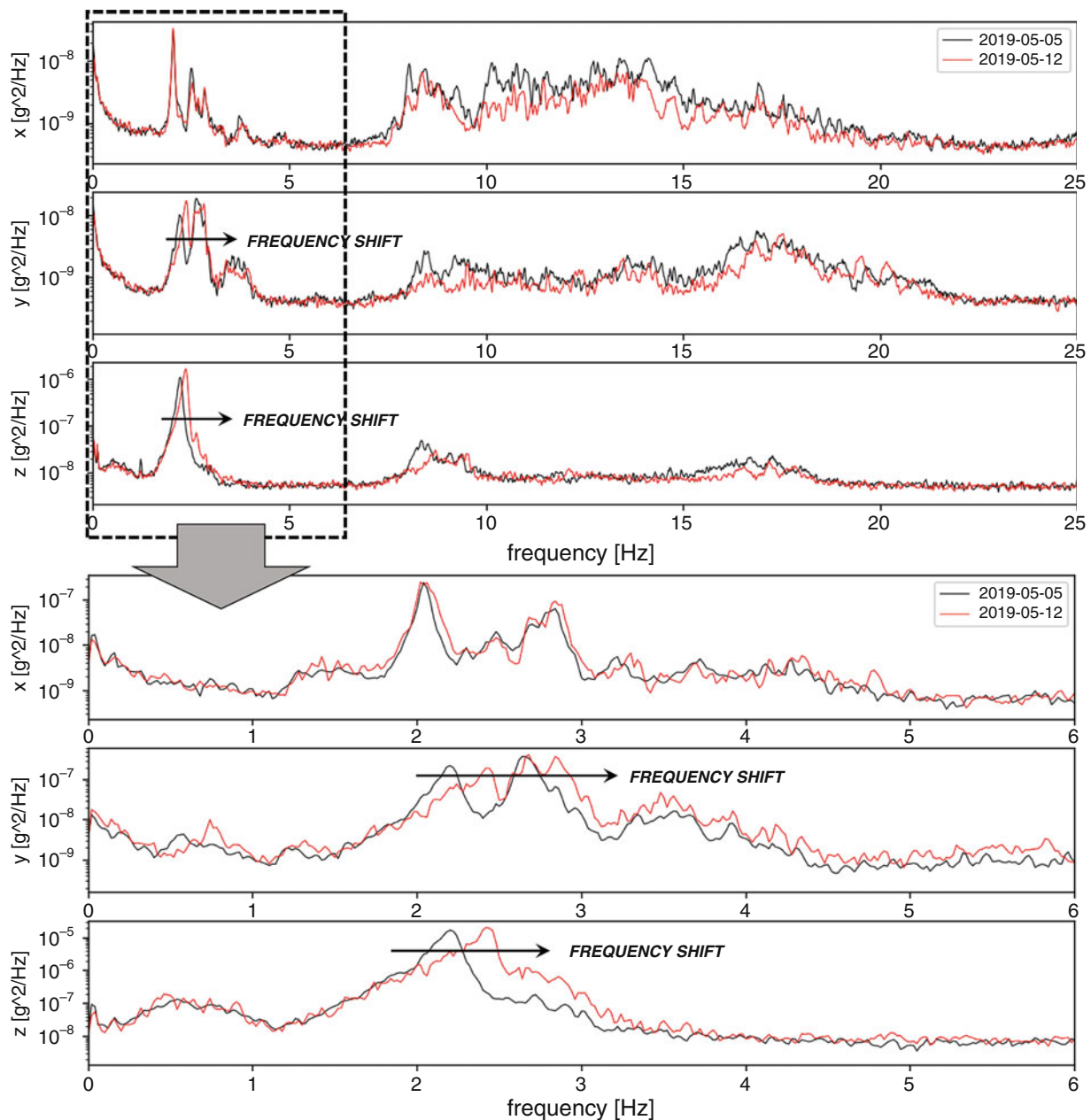
**Fig. 19.7** Deformation experienced by the bridge during the strengthening works

As can be seen from the graph, following the reinforcement intervention, the structure experienced a camber of about 1 cm at the centreline of the span.

As for dynamic readings, the use of accelerometers allowed for the evaluation of the structural behaviour under the reinforcement works by observing the dynamic response of the deck.

The fundamental assumption of vibration-based damage detection is that the damage will alter structures properties such as the stiffness, mass or energy dissipation which, in turn, will reflect in a change in the measured dynamic response of the system [5]. The most common features that can be identified from the measured response time records are the common modal properties of resonant frequencies and mode-shape vectors.

The MEMS accelerometers installed on the bridge acquired data at a sampling frequency of 100 Hz, 15 minutes every 4 hours due to streaming limitations of the entire system, resulting in a difficult application of accurate Operational Modal



**Fig. 19.8** PSD of the sensor located in the center of the span before (black) and after (red) the strengthening works

Analysis (OMA) techniques to identify mode-shape vectors. For that reason, although being conscious about the limits of this approach [5–7], resonant frequency shifts have been used as data feature for damage detection at this preliminary stage (this can be checked on all sensors).

Since the signals are of random nature, the power spectral density (PSD) was used to evaluate the system natural frequencies. The averaging process has been carried out with a sub-records length of 200 seconds, overlap of 66% (Hanning window). The peaks of the PSD correspond to the natural frequencies of the structure under examination.

Figure 19.8 shows the PSDs calculated for the sensor located at mid span in the three directions x, y, z for 2 days, before and after the strengthening works (May 5th, 2019 and May 12th, 2019). It can be observed that the stringing caused a stiffening of the system; this is proved by a shift to the right of the natural frequencies of the span. This translation is more evident in the y and z directions, while in the x direction, transversal to the longitudinal extension of the viaduct, this variation is hardly recognized. This is consistent with the observation that external pre-stressing causes a flexural stiffening of the structure mainly in the y–z plane, with minor effect in the x–y plane.

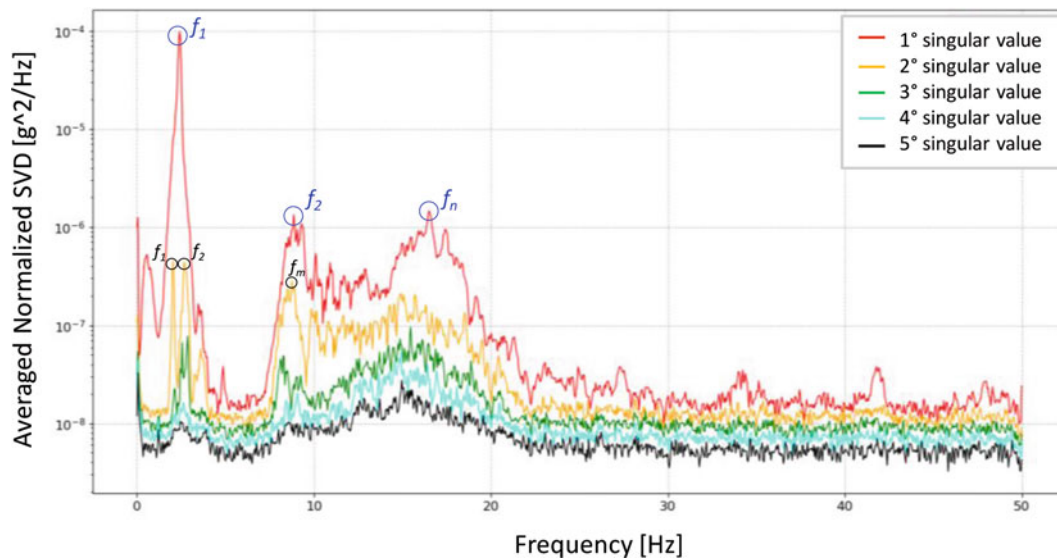


Fig. 19.9 Singular values diagram for the monitored bridge

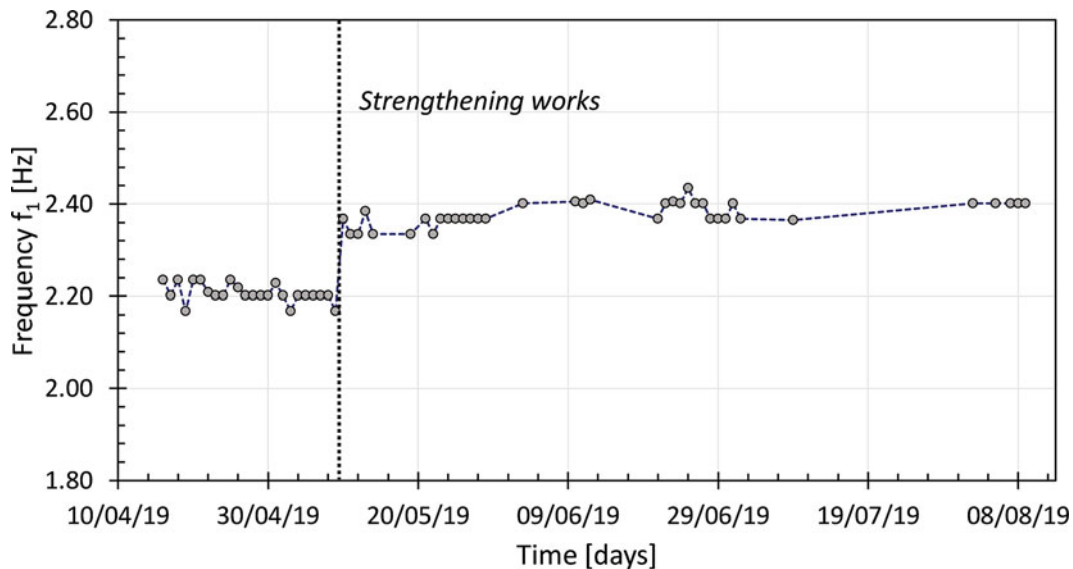


Fig. 19.10 Frequency evolution over time (before and after the reinforcement)

Although the PSD curve has been used to observe the overall effect of the strengthening works, the Frequency Domain Decomposition (FDD) has been used as OMA methodology to get a more accurate identification of the natural frequencies. The theory of this well-known technique [8] is based on the assertion that any change in the state of the structure can be seen as a linear combination of the eigenvectors, which represent the modes of the structure. It is therefore possible to decouple the components of the various modes through a singular value decomposition (SVD) of the PSD matrix. The advantage of this method lies in the fact that it is possible to accurately distinguish modes that are close in frequencies.

As shown in Fig. 19.9, the presence of coupled modes is pointed out by the co-existence of different curves, related to different singular values, in the same frequency range.

A stable peak-picking analysis has been performed in order to track the evolution of the natural frequencies over time. The peak-picking method assumes that each significant peak in the frequency-response function corresponds to exactly one natural mode. Close to a peak, the system is assumed to behave like a one-degree-of-freedom damped harmonic oscillator.

In Fig. 19.10, the trend of the first resonance frequency, corresponding to the mode at 2.2 Hz, is reported over time.

It can be clearly seen that a sharp jump in frequency is detected in correspondence of the strengthening works (May 9th, 2019), indicating a stiffening of the structure.



However, the possibility of observing such a frequency shift is strongly influenced by the frequency resolution. The uncertainty related to the identification of natural frequency values, and consequently related to the extent of the recognizable frequency variations, could be reduced by using longer windows for the estimation of the averaged PSD. Nevertheless, in this specific case study, a compromise was found between the need to have a large number of sensors to be installed on the structure in a short time and data accuracy in identifying changes in the modal characteristics of the structure before and after the reinforcement.

## 19.6 Conclusions

This paper discusses the case study of a Structural Health Monitoring system installed on a bridge in an advanced state of deterioration, where a widespread corrosive phenomenon caused the failure of a significant number of pre-stressing tendons, mainly on a specific span. Just before the beginning of the strengthening works, a series of MEMS sensors, both clinometers and accelerometers, were installed on the structure allowing to gather very significant data, mainly for two purposes.

First of all, which is the part that is mainly discussed in this paper, the sensors allowed to monitor the evolution of the structure following the maintenance works, thanks to a new architecture, privileging some items at the expenses of others. Both the evaluation of the new asset of the monitored span, obtained by the rotations acquired by the clinometers, and the changing of the dynamic properties in terms of stiffness, obtained from the acceleration data, confirmed the effectiveness of the intervention with external pre-stressing tendons.

The second very important aspect is that the data coming from the structure in damaged conditions have been observed and this represents a very rare case in the field of SHM of real operating civil structures. Therefore, knowing the outputs of the analyzes obtained when the structure was in a state of advanced and widespread deterioration, the use of supervised learning techniques can be adopted allowing to have indications on the progress of pre-stressing loss for future SHM purposes.

## References

1. Farrar, C.R., Worden, K.: An introduction to structural health monitoring. *CISM Int. Centre Mech. Sci. Courses Lect.* **520**, 1–17 (2010)
2. Wardhana, K., Hadipriono, F.C.: Analysis of recent bridge failures in the United States. *J. Perform. Constr. Facil.* **17**(3), 144–150 (2003)
3. Farrar, C.R., Worden, K.: *Structural Health Monitoring: a Machine Learning Perspective*. Wiley, Chichester (2013)
4. Bertagnoli, G., Lucà, F., Malavisi, M., Melpignano, D., Cigada, A.: A large scale SHM system: a case study on pre-stressed bridge and cloud architecture. *Conf. Proc. Soc. Exp. Mech. Ser. 2*, 75–83 (2020)
5. Farrar, C.R., Doebling, S.W., Nix, D.A.: Vibration-based structural damage identification. *Philos. Trans. R. Soc. A Math. Phys. Eng. Sci.* **359**(1778), 131–149 (2001)
6. Doebling, S.W., Farrar, C.R., Prime, M.B.: A summary review of vibration-based damage identification methods. *Shock Vib. Dig.* **30**(2), 91–105 (1998)
7. Fan, W., Qiao, P.: Vibration-based damage identification methods: a review and comparative study. *Struct. Health Monit.* **10**(1), 83–111 (2011)
8. Brincker, R., Zhang, L., Andersen, P.: Modal identification of output-only systems using frequency domain decomposition. *Smart Mater. Struct.* **10**(3), 441–445 (2001)

**Prof. Alfredo Cigada** is Full Professor in Mechanical and Thermal Measurements at Politecnico di Milano, Italy.



# Chapter 20

## Comparison of Time-Domain and Time-Frequency-Domain System Identification Methods on Tall Building Data with Noise

Ronwaldo E. R. Aquino, Mohamed Barbosh, and Ayan Sadhu

**Abstract** Dynamic properties (e.g. frequency and damping ratio) play an important role in determining the impact of natural disasters on tall buildings. A variety of system identification (SID) techniques have been developed and implemented on response measurement data from full-scale structures for condition assessment, where modal parameters were used as the condition indicators. Previous research has demonstrated the strengths and limitations of the Random Decrement Technique (RDT) as a time-domain SID technique. In this paper, the Time-Varying Filtering based Empirical Mode Decomposition (TVF-EMD), a new time-frequency-domain analysis method, is used on a suite of synthetic building response data to demonstrate how the RDT results can be further improved in lieu of bandpass filtering. The two techniques are then used together to extract the dynamic properties from a full-scale tall building and the results are compared against the use of bandpass filtering. It can be observed that RDT alone or in conjunction with an appropriate filter design is able to extract damping better in most cases. The current results suggest that TVF-EMD may provide accurate results but only if the noise level is low. On the other hand, the bandpass filtering only works better with appropriate filter design.

**Keywords** System identification · Time-domain · Time-frequency-domain · Random decrement technique · Empirical mode decomposition · Time-varying filtering-based empirical mode decomposition

### 20.1 Introduction

It is well known that the dynamic properties (e.g. natural frequency and damping ratio) are important parameters in determining environmental impacts (wind, earthquake, etc.) on tall buildings. There are a number of system identification (SID) techniques that can be applied to full-scale response measurements of these buildings to determine these dynamic properties. Earlier papers have demonstrated the efficacy of the Random Decrement Technique (RDT) as a time-domain SID technique [1, 2], applied to random response data such as ambient vibrations and wind response. The natural frequency is not difficult to obtain – errors are normally small. But the SID framework that is typically used to arrive at the damping ratio is presented in Fig. 20.1. To properly evaluate damping, the raw data needs to be pre-processed and converted into a format suitable for direct damping extraction; namely, as a free decay function or as an amplitude spectrum.

The traditional RDT process can be illustrated using this SID framework, shown in Fig. 20.2. Previous research [1–3] has recommended the use of curve fitting techniques (CFT) over the logarithmic decrement technique (LDT), which also facilitates error evaluation to assess how reliable is the resulting damping value which is included in the generic framework shown in Fig. 20.1. Other methods that are used for direct damping extraction include the decay envelope method (DEM), Hilbert-Huang Transform (HHT) [5, 6], and basic frequency domain methods (BFDM) such as half-power bandwidth (HPB) and peak-picking (PP). As part of the pre-processing and signal conditioning, typically a Fast Fourier Transform (FFT) is applied. In some cases, empirical mode decomposition (EMD) [7] and the use of power spectral densities (PSD) and singular value decomposition (SVD) [8] may be used. Lastly, resampling, demeaning or detrending may be employed but more often than not, some bandpass filtering is carried out.

---

R. E. R. Aquino (✉)  
RWDI, Guelph, ON, Canada  
e-mail: [ron.aquino@rwdi.com](mailto:ron.aquino@rwdi.com)

M. Barbosh · A. Sadhu  
Department of Civil and Environmental Engineering, Western University, London, ON, Canada

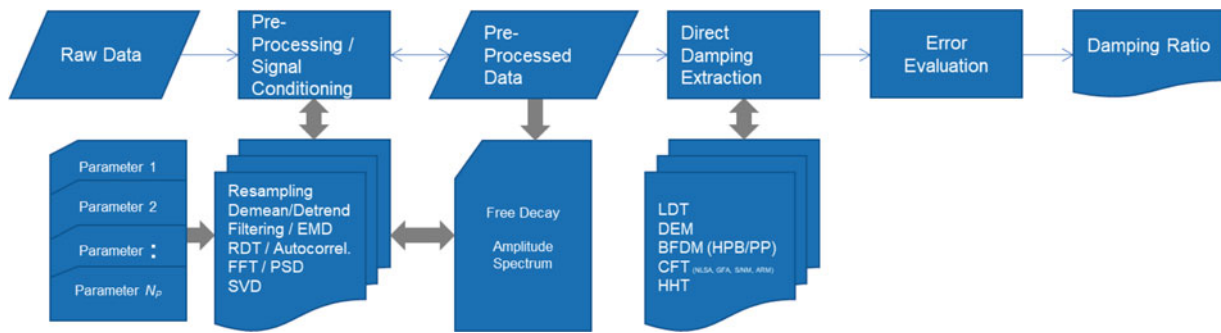


Fig. 20.1 Generic system identification framework to obtain damping ratio from raw data

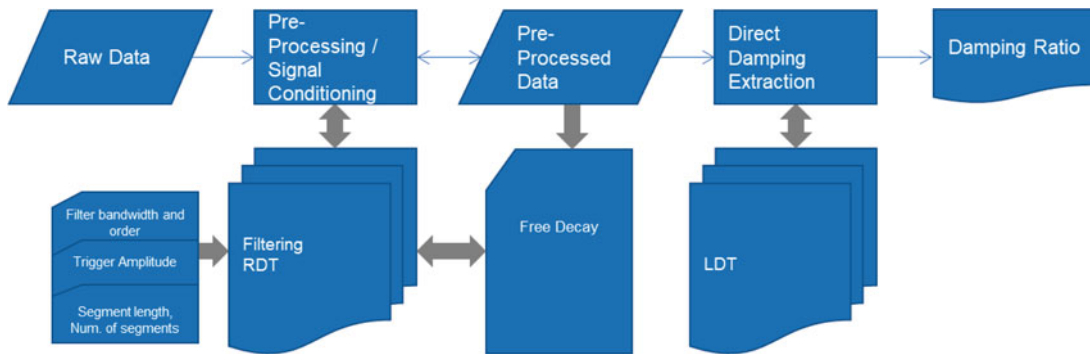


Fig. 20.2 Traditional random decrement technique (RDT) process

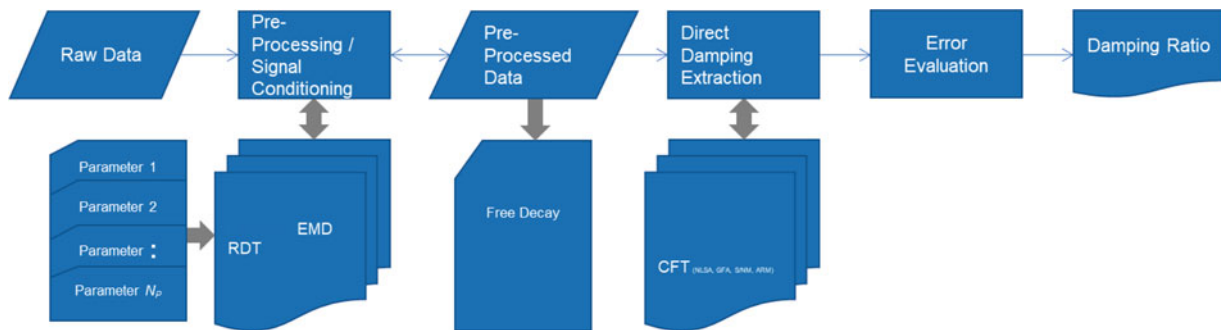


Fig. 20.3 TVF-EMD + RDT + CFT process being investigated in the current paper

However, an issue that has been brought up [1] is that the use of filtering often distorts the data, directly affecting the end result. In this regard, the current paper then looks to evaluate the Time-Varying Filtering based Empirical Mode Decomposition (TVF-EMD), a new time-frequency-domain analysis method, to see its contribution in improving the accuracy of the RDT + CFT method (see Fig. 20.3). This is illustrated by applying it to the same suite of synthetic and similar full-scale building response data as RDT has been subjected to in the earlier research.

## 20.2 Background of TVF-EMD

In the past, several SID techniques have been used to extract the modal parameters of structures. These techniques can work either in time, frequency or time-frequency domain simultaneously. While time-domain methods are the basic SID methods, representing the signal in time domain only, frequency-domain methods convert the time history of a recorded signal into its frequency spectrum [8]. On the other hand, time-frequency domain methods have gained popularity, especially in civil and mechanical systems applications since they can present time and frequency information of the measured signals at the same

time. The most common time-frequency techniques are wavelet transform (WT) [9], blind source separation (BSS) [10], and empirical mode decomposition (EMD) [6] which were used widely as a modal identification method.

Empirical mode decomposition (EMD) [5–7, 11] is a time-frequency method that can deal with both nonlinear and nonstationary signals. The EMD method decomposes the signal into a group of oscillatory signals named as intrinsic mode functions (IMFs). In TVF-EMD [7], a B-spline approximation is adopted as criteria to select a time-varying filter. While most of the present work use B-splines as an interpolation tool with polynomial spline, TVF-EMD however uses B-spline functions which are piecewise polynomials with time-varying cut-off frequencies. With such a property, the TVF-EMD can deal with single vibration measurement to identify all frequencies without any mode-mixing issue in the modal responses. In order to form the desired signal, the polynomial portions are joined together. The joining points of the polynomial sections are denoted as knots. Each signal in B-spline can be expressed by [12, 13].

$$s_z^n(t) = \sum_{i=-\infty}^{+\infty} q(i)\beta^n\left(\frac{t}{z} - i\right) \quad (20.1)$$

Where  $q(i)$  is the B-spline coefficients and it is enlarged by a factor of  $z$ . The signal (or approximation result) is determined by  $n$ ,  $z$ , and  $q(i)$ . The B-spline approximation is used to determine the B-spline coefficients  $q(i)$  that minimizes the approximation error. Let's assume  $f_z^n(t) = \beta^n\left(\frac{t}{z}\right)$  and the asterisk denotes the convolution operator. For an original signal  $y(t)$ ,  $q(i)$  is determined by minimizing the approximation error  $\delta_z^2$ :

$$\delta_z^2 = \sum_{t=-\infty}^{+\infty} (y(t) - \{q\} * f_z^n(t))^2 \quad (20.2)$$

Where  $\{-\}_{\uparrow z}$  is the up-sampling operation by  $z$ . After introducing the concept of B-spline approximation (i.e., revealing its low-pass filtering property), the solution of  $q(i)$  is

$$q(i) = \{l_z^n * y\}_{\downarrow z}(q) \quad (20.3)$$

Where  $\{-\}_{\downarrow z}$  is the down-sampling operation by  $z$  and  $l_z^n$  is the pre-filter defined by

$$l_z^n = \left\{ \left( \{f_z^n * f_z^n\}_{\downarrow z} \right)^{-1} \right\}_{\uparrow z} * f_z^n \quad (20.4)$$

$s_z^n(t)$  can be expressed now as:

$$s_z^n(t) = \{l_z^n * y\}_{\downarrow z} * f_z^n(t) \quad (20.5)$$

There are three steps to carry out the B-spline approximation of a signal. The signal  $y$  is first band-limited through a pre-filter  $f_z^n$ . Next, by a factor of  $z$ , the band-limited signal is decimated. Finally, the approximation is reconstructed using a post-filter  $f_z^n$ .

### 20.3 Analysis

The various data sets listed in Table 20.1 are subjected to three analysis procedures: directly analyzing using RDT + CFT, pre-bandpass-filtering prior to RDT + CFT, and performing TVF-EMD prior to RDT + CFT. Table 20.1 also lists the SNRs for the processed data sets subjected to RDT + CFT in the selected IMF obtained from the TVF-EMD.

All data sets have a sampling rate of 50 Hz. The synthetic data was generated using Gaussian excitation on a single-degree-of-freedom (SDOF) system with an undamped natural frequency 0.18 Hz and a damping ratio of 2.00%.

Figure 20.4 shows the time histories and Fourier spectra of the synthetic data (Data #1 to #3). Figure 20.5a, b shows the time history and Fourier spectrum of the full-scale tall building data (Data #4), while Fig. 20.5c shows a Fourier Spectrum of the selected IMF. Figure 20.6a–c show the Random Decrement Signature (RDS) generated by RDT for Data #1 for the unfiltered, filtered, and selected IMF cases, and the resulting SDOF curve fits.

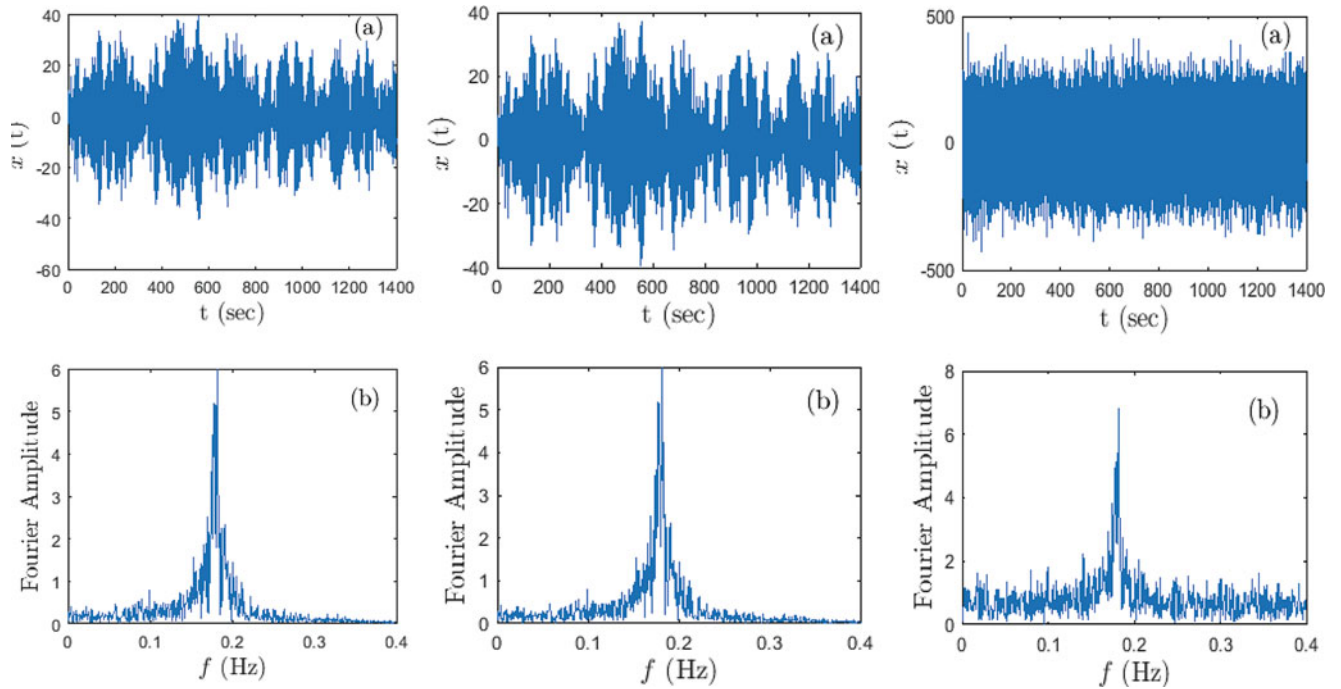
**Table 20.1** Description of data used in the analyses

Data #	Data filename	System response	Descriptive noise level	Record length (h)	Unfiltered SNR <sup>a</sup> (dB)	Filtered SNR <sup>a, b</sup> (dB)	IMF SNR <sup>a, c</sup> (dB)
1	synth7prenoise	Linear SDOF	None	4	-8.298	-8.352	0.836
2	synth77e	Linear SDOF	Low	4	-8.326	-8.353	7.570
3	synth77a	Linear SDOF	High	4	-24.812	-8.020	-1.305
4	fullscaledata3	Full-scale	High	4	N/A	-5.660	-10.682

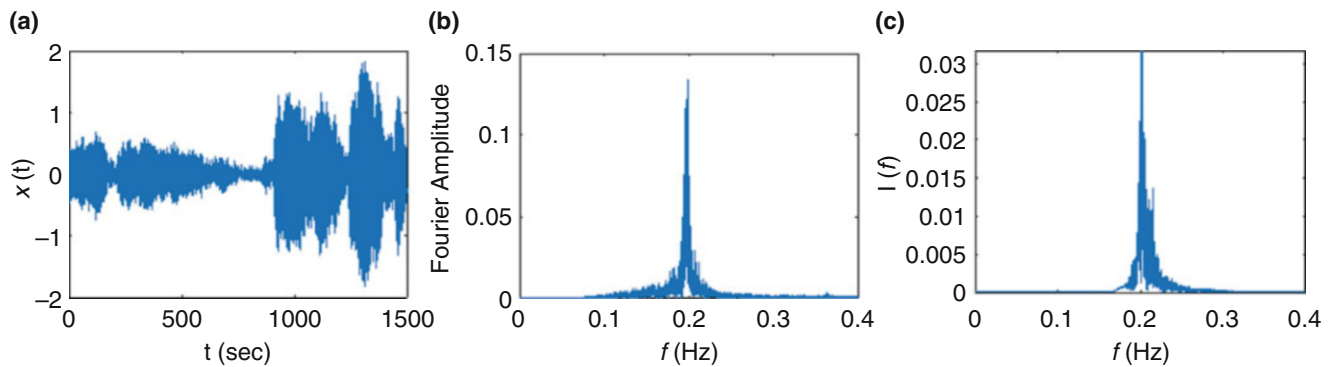
<sup>a</sup>The signal-to-noise (SNR) ratio is obtained using the MATLAB SNR command with default parameters [4]

<sup>b</sup>The filter used is a Butterworth bandpass filter for a frequency band between 0.1 and 0.26 Hz, and filter orders of 5 and 9, respectively, for the synthetic data files. The full-scale data is already pre-bandpass-filtered between 0.05 and 1 Hz

<sup>c</sup>The SNR shown is for the IMF selected for the RDT + CFT analysis



**Fig. 20.4** Time histories (top plots) and Fourier spectra of IMF (bottom plots) of data #1, #2, and #3 (left to right)



**Fig. 20.5** (a) Time history, (b) Fourier spectrum, and (c) IMF extracted from TVF-EMD of Data #4

The results are summarized in Table 20.2 based on application of CFT after performing RDT. The results for the unfiltered case are slightly different from the previous work [2] due to the curve fitting being performed on 20 free decay cycles now from 4 before. The Least Squares Error (LSE), as defined in [1, 2] as a measure of goodness of fit of the curve fitting, is in this case an indication of how close to a theoretical SDOF response the RDS is.

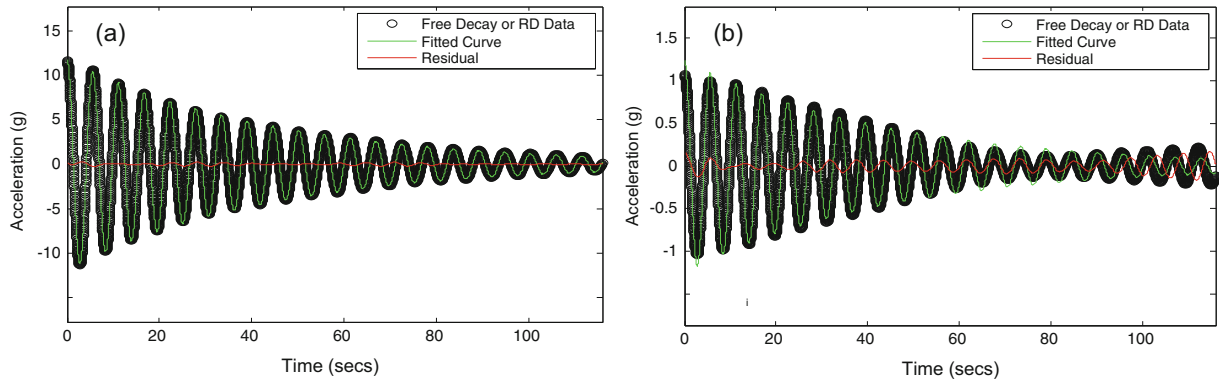


Fig. 20.6 Random decrement signatures generated from (a) unfiltered, and (b) selected IMF for Data #1

Table 20.2 Comparison of damping ratios and least squares errors between unfiltered data, bandpass-filtered data, and selected IMF after TVF-EMD

Data #	Damping ratio			Damping ratio error			Least squares error		
	Unfiltered (%)	Filtered (%)	IMF (%)	Unfiltered (%)	Filtered (%)	IMF (%)	Unfiltered (%)	Filtered (%)	IMF (%)
1	1.99	2.02	2.05	-0.5	1.0	2.5	2.9	2.7	8.2
2	1.87	2.11	1.29	-6.5	5.5	-36	4.8	2.2	16
3	N/A	2.47	1.82	N/A	24	-9.0	N/A	11	14
4	N/A	0.78	1.41	N/A	N/A	N/A	N/A	2	16

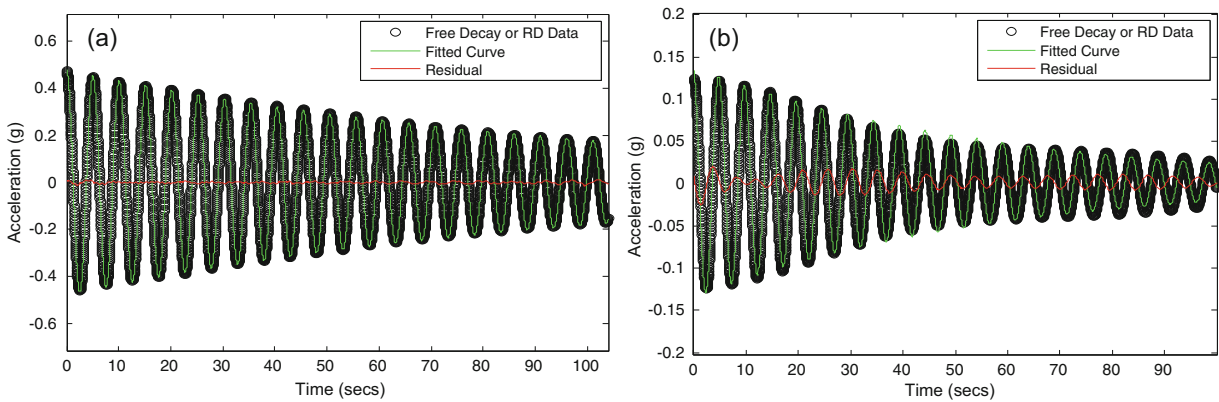


Fig. 20.7 Random decrement signatures generated from (a) filtered, and (b) selected IMF for Data #4

### 20.4 Discussion

Table 20.1 shows that, in terms of SNR, TVF-EMD can significantly reduce a good portion of the noise, except for Data #4. However, from Table 20.2, it can be observed that the TVF-EMD results in more accurate outputs with no noise, but not so with higher noise levels. Additionally, the LSQ errors are larger with the selected IMF in all cases – suggesting that TVF-EMD does not necessarily reveal the modal response itself. Figure 20.6 illustrates this where the generated RDS for Data #1 is a clear SDOF response while it appears to be a nonlinear multi-DOF response for the selected IMF. In Table 20.2, the band-pass filtering appears to provide the better result. But it should be noted that the results can change significantly depending on the band-pass filter parameters. Therefore, the filter design is very important to the overall process.

For the full-scale data, the pre-filtered data results in 0.8% while the IMF results in a 1.4% damping ratio. There is no knowledge of “ground truth” – that is, what is the correct answer and therefore, the error cannot be evaluated. However, the LSE reveals a very good fit to SDOF response using the pre-filtered data directly, and the same apparent nonlinear multi-DOF response if using the TVF-EMD, which is evident in Fig. 20.7. It is possible that the pre-filtering has impacted the TVF-EMD process and therefore the resulting IMF.

## 20.5 Conclusion

The paper has studied the impact of using TVF-EMD in lieu of bandpass filtering on random response data with a certain noise level. RDT + CFT was used to arrive at the damping ratio, as applied to the unfiltered data, bandpass-filtered data, and the selected IMF after the TVF-EMD. The results were compared for four different data sets; 3 synthetic with an increasing level of noise, from none to one with a very high level.

The finding in the current paper suggests that TVF-EMD may provide sufficiently accurate results but only if the noise level is low. As well, the calculated Least Squares Error indicate that the resulting RDS after TVF-EMD does not fully reveal the modal response of interest. However, it is emphasized that bandpass filtering only works with appropriate filter design.

**Acknowledgements** The second author would like to thank the University of Tripoli for funding the research through Libyan Ministry of Education.

## References

1. Aquino, R.E.R., Tamura, Y.: Potential pitfalls in the practical application of the random decrement technique. In: Proceedings 5th International Structural Specialty Conference, 2016 CSCE Annual Conference. Canadian Society of Civil Engineering, London/Ontario, June (2016)
2. Aquino, R.E.R., Tamura, Y.: Using the random decrement technique on short records with varying signal-to-noise ratios. In: Pakzad, S. (ed.) Dynamics of Civil Structures: Conference Proceedings of the Society for Experimental Mechanics Series, vol. 2. Springer, Cham (2019)
3. Tamura, Y., Sugauma, S.: Evaluation of amplitude-dependent damping and natural frequency of buildings during strong winds. *J. Wind Eng. Ind. Aerodyn.* **59**(2), 115–130 (1996)
4. Mathworks®, Signal Processing Toolbox™: User's guide (R2019b). Retrieved 2 Oct 2019 from [www.mathworks.com/help/pdf\\_doc/signal/signal\\_tb.pdf](http://www.mathworks.com/help/pdf_doc/signal/signal_tb.pdf) (2019)
5. Huang, N.E., Long, S.R., Shen, Z.: The mechanism for frequency downshift in nonlinear wave evolution. *Adv. Appl. Mech.* **32**, 59–111 (1996)
6. Huang, N.E., Shen, Z., Long, S.R., Wu, M.C., Shih, H.H., Zheng, Q., Yen, N.C., Tung, C.C., Liu, H.H.: The empirical mode decomposition and the Hilbert spectrum for nonlinear and non-stationary time series analysis. *Proc. Roy. Soc. Math. Phys. Eng. Sci.* **454**(1971), 903–995 (1998)
7. Tang, J., Zhao, L.J., Yeu, H., Yu, W., Chai, T.: Vibration analysis based on empirical mode decomposition and partial least square. *Procedia Eng.* **16**, 646–652 (2011)
8. Brincker, R., Zhang, L., Anderson, P.: Modal identification of output-only systems using frequency domain decomposition. *Smart Mater. Struct.* **10**(3), 441–445 (2001)
9. Dziedziech, K., Staszewski, W., Uhl, T.: Wavelet-based modal analysis for time-variant systems. *Mech. Syst. Signal Process.* **50–51**, 323–337 (2015)
10. Sadhu, A., Narasimhan, S., Antoni, J.: A review of output-only structural mode identification literature employing blind source separation methods. *Mech. Syst. Signal Process.* **94**, 415–431 (2017)
11. Barbosh, M., Sadhu, A., Vogrig, M.: Multisensor-based hybrid empirical mode decomposition method towards system identification of structures. *Struct. Control. Health Monit.* **25**(5), e2147 (2018)
12. Li, H., Li, Z., Mo, W.: A time varying filter approach for empirical mode decomposition. *Signal Process.* **138**, 146–158 (2017)
13. Lazhari, M., Sadhu, A.: Decentralized modal identification of structures using an adaptive empirical mode decomposition method. *J. Sound Vib.* **447**, 20–41 (2019)

**Ronwaldo** has a Bachelor and Master of Science in Civil Engineering from the University of the Philippines in 1999 and 2007, and a Doctor of Engineering from the Graduate School of Wind Engineering, Tokyo Polytechnic University in 2013. He is currently senior engineer at RWDI in Canada since 2013.



# Chapter 21

## Fatigue Life Analysis of Main Shaft Bearings in Wind Turbines Using Strain Measurements Collected on Blades

Bridget Moynihan, Sauro Liberatore, Babak Moaveni, and Usman Khan

**Abstract** Main shaft thrust bearing failures are a major source of unplanned maintenance and downtime for wind turbines. Turbines are typically designed to operate for at least a 20-year lifetime, but the variable-amplitude loading of changing wind conditions promotes a high rate of early bearing failure, requiring maintenance work and increasing the cost of energy. The monitoring of bearing loading conditions plays a crucial role in determining design parameters and optimizing bearing life. It can also play a significant role in estimating the remaining lifetime of bearings, enabling the repair or replacement of these components before failure occurs, or in extending bearing lifetimes for existing turbines. In this study, a method for monitoring axial loading in the main shaft bearing is suggested using strain sensor data on the blades. The method is based on using the available strain time history measurements at the base of the three blades to calculate the internal forces and moments in the main shaft. The method is implemented using data from a Clipper C96 Liberty wind turbine instrumented with interferometric strain sensors placed at the blade roots. The forces and moments acting on each blade are calculated using the data collected from the sensors. Through a rigid body equilibrium analysis, the resultant forces and moments acting on the main shaft bearing of the wind turbine are found. This data, in conjunction with SCADA data, is used to analyze the effect of strong and weak wind events on the fatigue life of the main shaft bearing. Results show that the method can be used to successfully identify wind conditions which produce axial forces beyond the bearing design assumptions.

**Keywords** Wind turbine · Fatigue analysis · Main shaft bearing · Condition monitoring · Strain sensors

### 21.1 Introduction

The main shaft bearings of wind turbines are constantly subjected to irregular, cyclical forces and moments due to changing wind conditions. These loading patterns and the resulting fatigue caused in main shaft bearings can lead to premature failure or damage. Bearing failures lead to unexpected downtime and increased operation and maintenance (O&M) costs for wind turbine owners, increasing the cost of energy over a turbine's lifetime.

O&M costs can constitute up to 25% of a turbine's levelized energy cost over its lifetime [1]. Unplanned downtime for maintenance is especially problematic for wind turbine owners [2]. Main shaft bearing failures have been found to make up 15% of onshore wind turbine downtime [3]. This represents the third leading cause for downtime, yet main bearing failure rates are significantly lower than the failure rates of most other turbine components [4, 5]. By improving bearing reliability, the levelized cost of energy produced by wind turbines can be reduced.

Condition monitoring and preventative maintenance can reduce downtime and maintenance due to breakages and bearing failure. Many sophisticated condition monitoring systems are costly and cannot be implemented after a wind turbine is installed and running [6]. Other maintenance techniques such as breakdown maintenance or time-based maintenance are options, though condition monitoring of the bearings in wind turbines is favorable, as excessive downtime and stoppages lead to loss of output and increased costs [2]. Preventative or predictive condition monitoring is useful in reducing costs and limiting downtime [2].

---

B. Moynihan (✉) · B. Moaveni · U. Khan  
Tufts University, Medford, MA, USA  
e-mail: [bridget.moynihan@tufts.edu](mailto:bridget.moynihan@tufts.edu)

S. Liberatore  
MIDE Technology Corporation, Woburn, MS, USA



This paper presents a method for the monitoring of bearing fatigue life in wind turbines using measurements from strain sensors. An analysis was done on the main bearing of a clipper C96 Liberty wind turbine using data from sensors placed on the blades of the turbine. This method is a simple way to monitor bearing fatigue life using more easily accessible sensors, where the use of costly condition monitoring systems isn't possible or practical.

## 21.2 Instrumentation and Data

The data used in this paper is of a Clipper Liberty C96 2.5 MW wind turbine from a wind farm in Cohocton, NY. The Clipper C96 turbine has a 96 m rotor diameter, blade lengths of 46.7 m, and the hub stands at a height of 80 m [7].

The wind turbine is instrumented with four interferometric strain sensors at the root of each blade, each paired with a temperature sensor. The sensors placement, labeled based on their location on the blades as high pressure (HP), low pressure (LP), leading edge (LE), and trailing edge (TE), are shown in Fig. 21.1. The blade of a turbine is circular at the root where the sensors are located, before transforming into the airfoil shape traced in Fig. 21.1.

The sensors collected strain and temperature data at 100 Hz in 1-hour intervals. The turbine is also instrumented with a supervisory control and data acquisition (SCADA) system. The SCADA system collects data on wind speed, blade pitch angle, blade torque and a number of other variables at a frequency of 0.5 Hz. The SCADA data was interpolated using the MATLAB spline function to match the sensor data's sampling rate of 100 Hz.

A number of assumptions about the turbine's geometry and other properties had to be made due to the lack of detailed structural information available from Clipper. The turbine blades are made of fiberglass, and it was assumed that the modulus of elasticity for each blade was 35 GPa [8]. The cross-sectional area of the blade at its root was not known. The shape of the blade at this section is circular, and given an approximate outer diameter of 1.5 m, it was assumed that the cross-sectional area was 2 m<sup>2</sup>.

It was assumed that the main shaft bearing in the turbine is a spherical roller thrust bearing, a common bearing type for this function in turbines. According to SKF, their spherical roller thrust bearings are the most common bearing used in wind turbine main shafts [9], thus this bearing was used as a reference for life cycle estimations. The bearing selected from SKF is an Explorer series spherical roller thrust bearing with the following parameters [10]:  $d = 1060$  mm (Inner Diameter),  $D = 1770$  mm (Outer Diameter),  $B = 426$  mm (Thickness), and  $C = 33,400$  kN (Dynamic Load Rating).

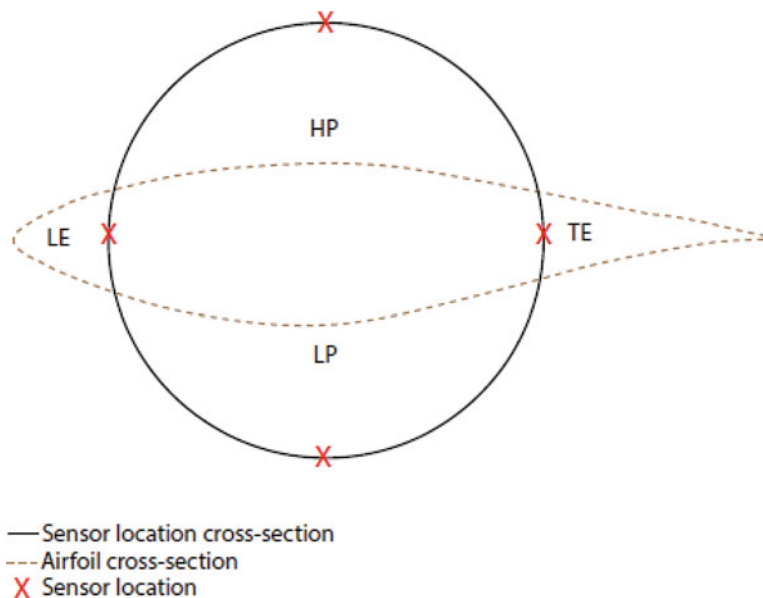


Fig. 21.1 Location of sensors placed at blade root of turbine [11]

### 21.3 Methodology

The strain sensor data was first temperature compensated using the corresponding temperature sensor data. This compensated strain data was used in calculating the bending moments on the blades. The bending moments in the flapwise and edgewise direction on each blade can be calculated directly from the strain measurements. The following equations were used to calculate the bending moments acting on each of the blades. The constant  $k$  used in these equations was provided by the interferometric strain sensor.

$$M_{Flapwise} = (HP - LP) * k_1 \quad (21.1)$$

$$M_{Edgewise} = (TE - LE) * k_2 \quad (21.2)$$

Each blade's angular position around the rotor has an important effect on the resultant forces and moments. This angle could be found by analyzing the flapwise bending moment. The flapwise moment is cyclical and is largely affected by gravity's effect on the blades as they each go through a full rotation around the turbine rotor.

The flapwise moment data was smoothed using MATLAB's Sgolayfit function, and its peaks were found with the function findpeaks. The peaks of the flapwise moment correlate to the points at which each blade is pointing vertically up. Using the peaks of the flapwise moment in conjunction with the hub speed of the turbine, the angle describing the position of each blade with respect to the vertical was calculated.

Based on the coordinate axes defined in a previous work [11] and shown in Fig. 21.2, the flapwise and edgewise bending moments were resolved into the x and z directions. The moments in the x and z directions are calculated from the components of the flapwise and edgewise moments acting in each direction based on the pitch angle of the blades. This relationship is described in the equations below, and the pitch angle was retrieved from the SCADA data. The blade torque moment (bending moment in the y direction) is also found in the SCADA data.

$$M_x = M_{Edgewise} * \cos(\text{pitch}) - M_{Flapwise} * \sin(\text{pitch}) \quad (21.3)$$

$$M_z = M_{Flapwise} * \cos(\text{pitch}) + M_{Edgewise} * \sin(\text{pitch}) \quad (21.4)$$

The strain data and the bending moments were used to calculate the forces in each blade in all three directions. In addition to the bending moments, the strain measurements were used to estimate the blade axial forces by summing and averaging the two opposite components (i.e.  $(TE + LE)/2$  and  $(HP + LP)/2$ ).

In order to calculate the "shear" forces in the non-axial directions, some assumptions were made. Since there is no information available on the profile of the Clipper blades, the lift and drag forces from an equivalent blade profile were estimated. An assumption of a FX67-K-170-17 blade profile, which is a reasonable assumption for this kind of turbine, was adopted. For this profile, the lift and drag coefficients can be found [12] and by using the SCADA data where the wind speed and rotational frequency are available, an estimated lift and drag distribution along the blade was obtained.

This force distribution was then used to estimate the application point of an equivalent single resultant force in the blade. These calculations were repeated for different wind conditions and thus an estimated range of the equivalent single resultant application point in the blade was obtained. This range was estimated to be within 3 m of 22.01 m in the direction of lift forces, and 20.88 m in the direction of drag forces.

Once this application point was estimated, it was used to apply an equivalent load on the bending moments retrieved from the strain measurements. These distances are defined as  $d_L$  and  $d_D$  in the equations below. Using these distances, the shear forces acting on the blades which cause the bending moments in the x and z directions, could be calculated.

$$F_n = AvgStrain * E * A \quad (21.5)$$

$$F_v = \frac{M_z}{d_L} \quad (21.6)$$

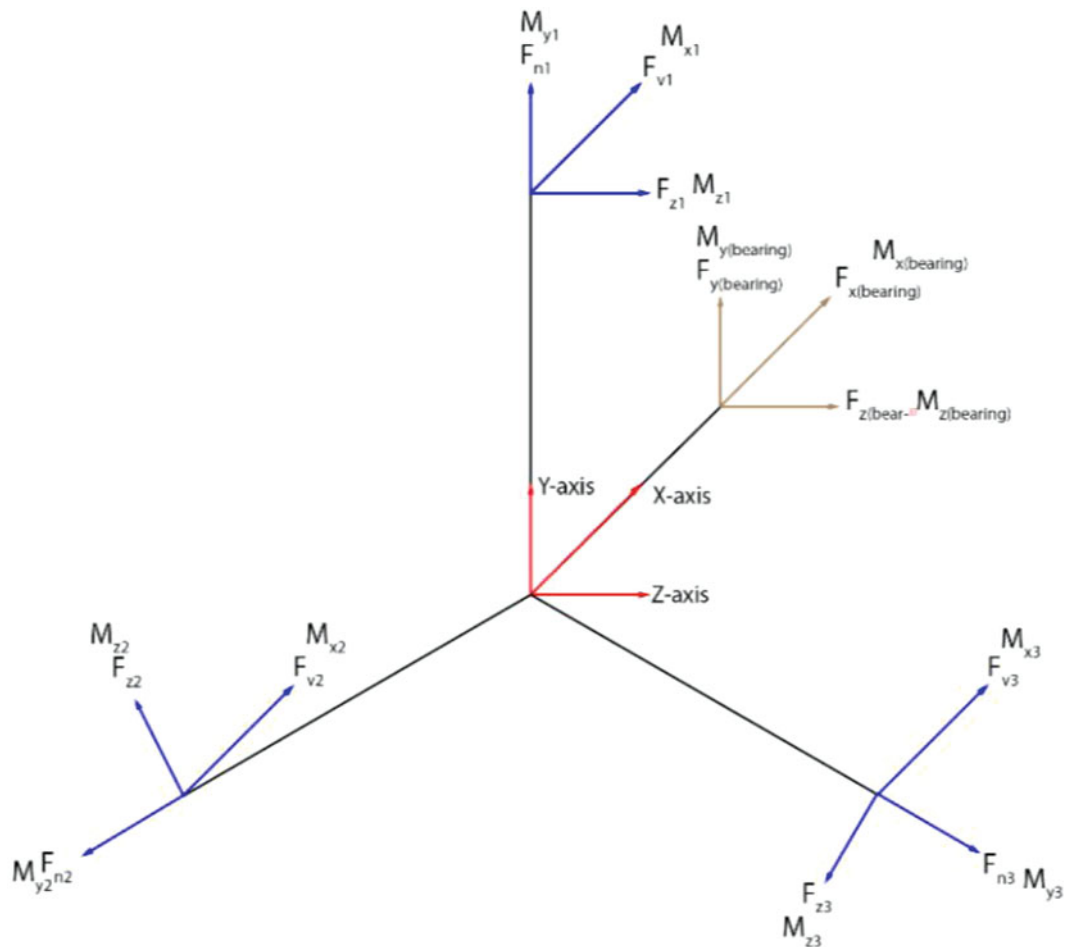


Fig. 21.2 Coordinate axes for blades and main shaft bearing [11]

$$F_z = \frac{M_x}{d_D} \tag{21.7}$$

Where  $d_L = 22.01\text{ m}$ ,  $d_D = 20.88\text{ m}$ ,  $E = 35\text{ GPa}$ , and  $A = 2\text{ m}^2$ .

Using a method formulated in a previous work [11], the resultant forces and moments acting on the main shaft of the turbine were calculated based on the forces and moments acting on each blade. The equations derived in the previous work were verified using a SAP2000 model, and were rederived for this paper. The equations for this method were derived and verified by completing a rigid body equilibrium analysis of the nacelle and blades of the turbine, making some assumptions about the geometry of the turbine. It was assumed that the rotor hub has a radius of 1.3 m, and that the distance from the end of the nacelle to the main bearing of the main shaft is 2 m.

The equations resulting from the equilibrium analysis describe the resultant forces and moments on the main shaft of the turbine as a function of the forces and moments acting on each blade as well as the angle of each blade around the rotor hub. The equilibrium analysis was completed by setting the total forces and moments in each direction on the body equal to zero, and solving for the forces and moments through the main shaft.

Figures 21.3 and 21.4 show an example of the resultant forces acting on the main bearing during a low wind and high wind event. It is clear from these results that the shape of  $F_x$  acting on the bearing loosely follows that of the wind speed. While the axial force through the bearing,  $F_x$ , appears to be affected mostly by wind speed, the radial forces,  $F_y$  and  $F_z$ , are more affected by cyclical forces, such as the blades rotating around the rotor.

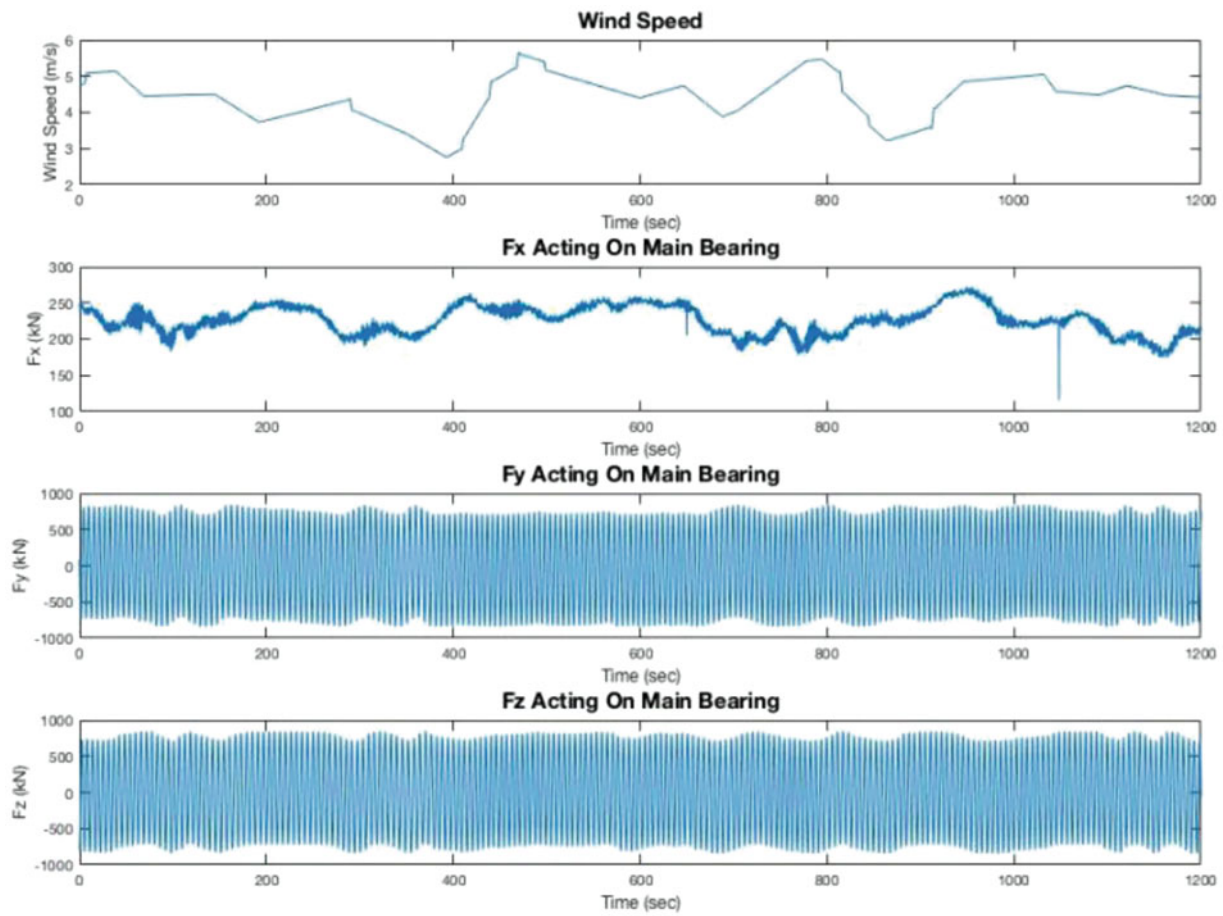


Fig. 21.3 Main bearing resultant forces for low wind event

## 21.4 Fatigue Analysis

To analyze the fatigue life of the main shaft bearing, Miner's rule for linear damage can be applied to the data. Miner's rule states that failure is expected when the sum of damages reaches 1, or 100% [13]. The sum of damages is defined by Eq. (21.8) below.

$$D = \sum_{i=1}^k \frac{n_i}{N_i} \quad (21.8)$$

Where  $k$  represents the number of constant-amplitude loading bins,  $n_i$  is the number of cycles at loading level  $i$ , and  $N_i$  is the number of cycles to failure at loading level  $i$ . The fraction  $n_i/N_i$  is the damage ratio, and is considered the fraction of life consumed by  $n_i$  cycles. This is why failure is expected when  $D = 1$ .

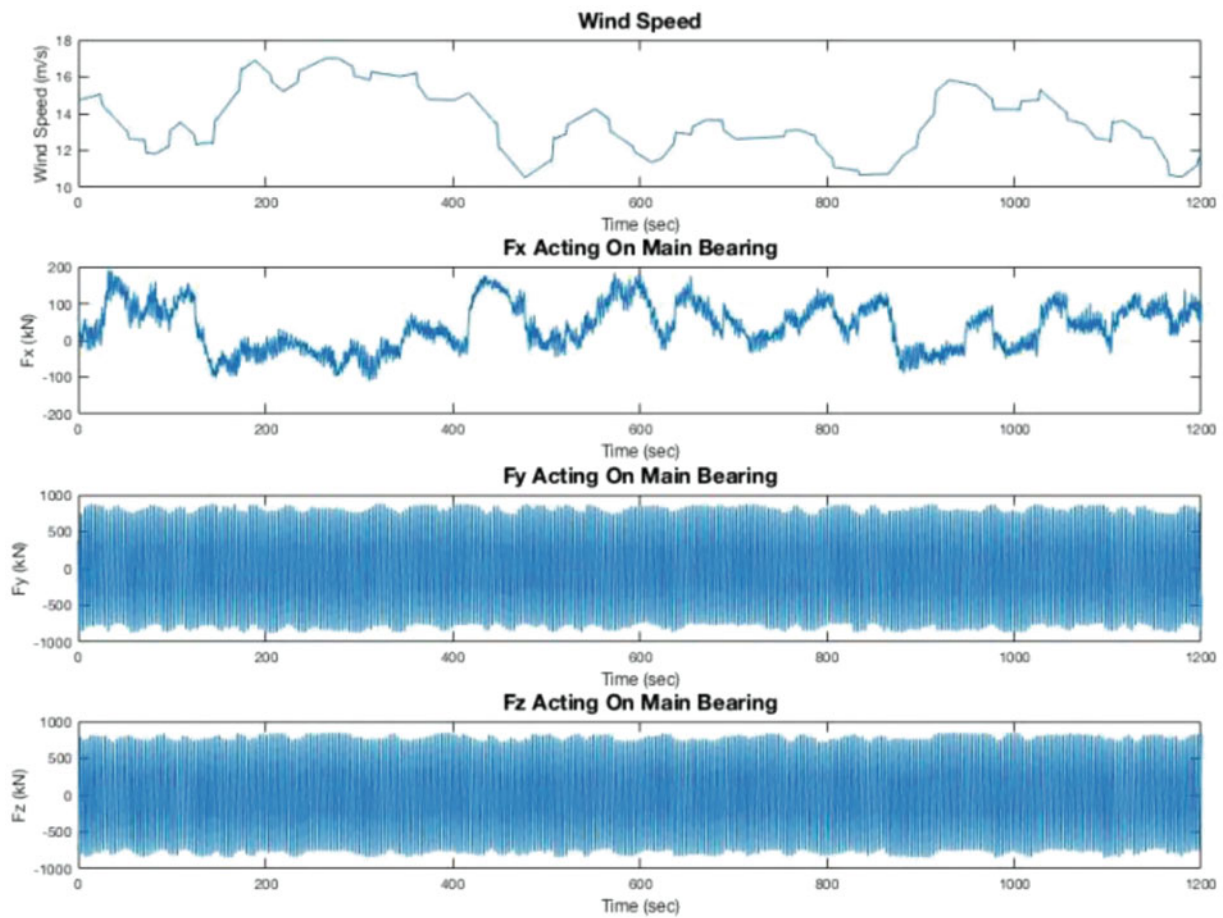
The number of cycles to failure  $N_i$ , can be found by calculating the rating life at each loading level. The following equation defines the rating life of a bearing,  $L_{10}$ , which is the fatigue life that 90% of bearings under constant loading conditions should attain [14].

$$L_{10} = \left( \frac{C}{P} \right)^p \quad (21.9)$$

$L_{10}$ : Basic rating life [millions of revolutions]

$C$ : Dynamic Load Rating, a bearing property [kN]

$P$ : Dynamic Equivalent Load (constant) [kN]



**Fig. 21.4** Main bearing resultant forces for high wind event

$p$ : Exponent of life equation, equal to 10/3 for roller bearings [14]

The dynamic equivalent load is a hypothetical load used in many bearing lifetime calculations which acts radially on radial bearings, and axially on thrust bearings [14]. The dynamic equivalent load has the same effect on a bearing's lifetime as the loads that contribute to it [14]. The equivalent load is calculated following Eq. 21.10.

$$P = XF_r + YF_a \quad (21.10)$$

$F_r$ : Radial Load

$F_a$ : Axial Load

X: Radial Load Factor,  $X = 1.14$

Y: Axial Load Factor,  $Y = 0.88$

Using SKF's website, the values of the radial and axial load factors for a spherical roller thrust bearing of the assumed bearing size were found. SKF provides a dynamic equivalent load calculator, and using this, the load factors could be solved for by inputting two scenarios and solving the resultant system of equations. This allowed for the dynamic equivalent load through time to be calculated. The axial load through the bearing is  $F_x$ , and the radial load was found by combining  $F_y$  and  $F_z$  using the Pythagorean theorem, since these forces are orthogonal to each other and both act radially on the bearing.

In order to compute the total damage, the rainflow counting method was applied to the time history of dynamic equivalent load to obtain constant-amplitude loading blocks. This was done using MATLAB's rainflow function which computes the cycle counts according to the ASTM E 1049 standard [15]. Constant-amplitude loading blocks are required to compute the total damage experienced by the bearing.

Figure 21.5 shows an example of the resultant histogram of the dynamic equivalent load after the rainflow method was applied to a data set representing 1 hour of turbine activity. As shown in the histogram, most of the loading cycles occurred

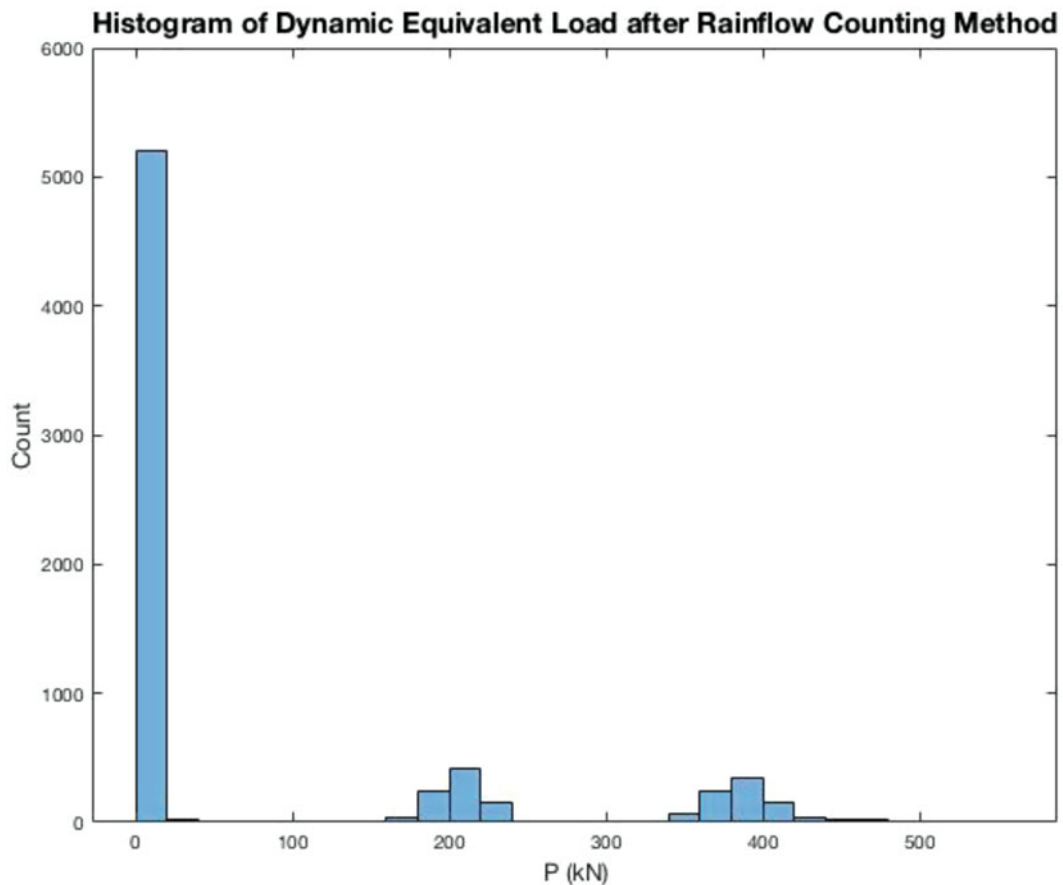


Fig. 21.5 Example of rainflow counting method on dynamic equivalent load, P

below 100 kN, but a small set of loads were much higher, reaching up to 420 kN. These sets of loads would affect the bearing's fatigue life more than lower magnitude loads, so it is important that they are represented here.

The total damage accumulated can be calculated once the dynamic equivalent load time history is computed and then broken down into constant-amplitude loading blocks. For each loading block, the rating life will need to be computed, and with this, the total fraction of life consumed can be calculated.

## 21.5 Conclusion

This paper presents a method which can serve as a simple, accessible way to monitor the health of the main shaft bearing. This method outlines the possibility of using sensors placed at the blade root to estimate the forces experienced by the main shaft bearing, and to analyze the effect of these forces on its lifetime. This method can be applied to any wind turbine with strain sensors at these locations to serve as a way to monitor the condition of the main shaft bearing. Analyzing patterns in the fraction of life consumed by different ranges of wind speed and dynamic equivalent load could provide wind turbine owners a better understanding of the damage that will be applied by different weather conditions. The accuracy of the estimations in this method can be greatly improved upon with more detailed structural information on the wind turbine.

**Acknowledgements** Partial support of the study by the National Science Foundation grant 1350264 and 1903972 is gratefully acknowledged. The opinions, findings, and conclusions expressed in this paper are those of the authors and do not necessarily represent the views of the organizations involved in this project.

## References

1. SKF wind news: black oxide bearings. <http://windfarmmanagement.skf.com/black-oxide-bearings/> (2017, May 8)
2. Reder, M.D., et al.: Wind turbine failures – tackling current problems in failure data analysis. *J. Phys. Conf. Ser.* **753**, 072027 (2016)
3. McMillan, D., Ault, G.: Condition monitoring benefit for onshore wind turbines: sensitivity to operational parameters. *IET Renew. Power Gener.* **2**, 60 (2008)
4. Faulstich, S., et al.: Wind turbine downtime and its importance for offshore deployment. *Wind Energy.* **14**, 327 (2011)
5. Li, Y., et al.: Research and development of the wind turbine reliability. *Int. J. Mech. Eng. Appl.* **6**(2), 35 (2018)
6. May, A., et al.: Economic analysis of condition monitoring systems for offshore wind turbine sub-systems. *IET Renew. Power Gener.* **9**, 900 (2014)
7. Clipper Windpower Plc: Liberty 2.5 MW Wind Turbine: Facts and Specifications. Clipper Windpower Plc. United States of America, Carpinteria, California (2009)
8. Steigmann, R., et al.: Determination of mechanical properties of some glass fiber reinforced plastics suitable to wind turbine blade construction. In: 7th International Conference on Advanced Concepts in Mechanical Engineering, IOP Conference Series: Materials Science and Engineering **146**, p. 012140. IOP Publishing Ltd Philadelphia, United States (2016)
9. SKF: SKF spherical roller bearings for wind turbine main shafts. [skf.com](http://skf.com) (2018, July)
10. Bearing size. <https://www.skf.com/group/products/bearings-units-housings/principles/bearing-selection-process/bearing-size/index.html>
11. Fava, G., et al.: Estimating Fatigue in the Main Bearings of Wind Turbines Using Experimental Data: Conference Proceedings of the Society for Experimental Mechanics Series. Springer, Basel, Switzerland (2018)
12. NACA 4 digit airfoil generator. <http://airfoiltools.com/airfoil/naca4digit>
13. Long, H., et al.: Fatigue analysis of wind turbine gearbox bearings using SCADA data and miner's rule. In: European Wind Energy Association Conference. Curran Associates, Inc. Red Hook, NY, USA (2011)
14. Bearing rating life. <https://www.skf.com/group/products/bearings-units-housings/principles/bearing-selection-process/bearing-size/size-selection-based-on-rating-life/bearing-rating-life/index.html>
15. MATLAB R2017a, MathWorks Inc., Natick, 2019

**Bridget Moynihan** is from St. Paul, MN and is currently in her junior year at Tufts University where she studies Civil Engineering and Astrophysics.



# Chapter 22

## Towards the Detection and Localization of Multiple Occupant Footsteps from Vibroacoustic Measurements

Sa'ed Alajlouni, Murat Ambarkutuk, and Pablo Tarazaga

**Abstract** Tracking occupants indoors has important applications such as intruder detection and tracking. It has been shown that a vibration measurement system of underfloor accelerometer sensor network can detect, localize, and track occupants in a non-intrusive manner. In the literature, little attention has been given to studying the problem of detecting occupant foot-fall impacts in a real-life scenario, and its effect on footstep impact localization, especially in the case of multiple occupants walking on the same instrumented area. Therefore, in this paper, a footstep detection algorithm is proposed and analyzed. The performance of the proposed algorithm is evaluated using occupant walking experiments on an instrumented floor section, inside an operational smart building. Additionally, the detected footsteps are localized using an energy-based localization method. Footstep detection and localization performances are compared between single occupant and multiple occupant cases.

**Keywords** Footstep impact detection · Multi-occupant footstep localization · Underfloor accelerometers · Sensor networks · Matched filters

### 22.1 Introduction

Indoor occupant tracking is important for security reasons, emergency evacuation, and for smart management (automation) of building systems; such as lighting and air-conditioning. Instrumenting building floors with hidden accelerometers provides a tamper-proof, and a non-intrusive system to track occupants.

Methods in the literature are available, dealing with the problem of indoor footstep localization and occupant tracking using accelerometers [1, 2]; however, these methods overlook footstep detection, which is a pre-requisite for localization, and assume that most foot-falls can be successfully detected inside an instrumented floor area, which as will be shown in this study, is not always a reasonable assumption, especially in the case of multiple-occupant tracking.

Footstep detection using seismic sensors is a challenging problem. The challenges include the fact that the footstep-generated floor wave is highly attenuated with the traveled distance [3], and the fact that higher frequency components of the traveling wave—which give a footstep signature a great level of detail—die out faster with the traveled distance compared to the lower frequency components [2, 4]. To make things worse, due to dispersion, the shape of the floor wave gets distorted with the traveled distance [4–6], especially for the lower frequency components [2]. It is worth mentioning that footstep floor impacts generate an excitation force, with a variable frequency content, mainly in the range 1–75 Hz, depending on the type of shoe wear, gait style, and floor material [7, 8]. In addition, wave reflections off floor boundaries can potentially complicate the footstep detection problem.

---

S. Alajlouni (✉)  
Department of Mechatronics Engineering, The Hashemite University, Zarqa, Jordan

Department of Mechanical Engineering, Virginia Tech, Blacksburg, VA, USA  
e-mail: [saed@hu.edu.jo](mailto:saed@hu.edu.jo); [saed13@vt.edu](mailto:saed13@vt.edu)

M. Ambarkutuk · P. Tarazaga  
Department of Mechanical Engineering, Virginia Tech, Blacksburg, VA, USA  
e-mail: [murata@vt.edu](mailto:murata@vt.edu); [ptarazag@vt.edu](mailto:ptarazag@vt.edu)



As a result, it is not surprising that some popular signal features used for event detection cannot be accurately utilized in the case of footstep detection. For example, *kurtosis* is a popular identifying feature of signals; however, Succi et al. [9] and Xing et al. [10] showed that kurtosis values for footsteps vary depending on sensor-footstep distance, which makes kurtosis impractical for detecting footsteps.

Furthermore, the authors in [11, 12] mention that a matched filtering approach [13] is not suitable for detecting footstep impacts using accelerometer measurements. The authors mention, that in some cases, when match-filtering accelerometer data containing a single footstep, multiple nearby peaks were observed; instead of just one defined peak. Nevertheless, the authors do not clarify nor show examples of the observed phenomenon. A detection scheme similar in principle to matched filtering was suggested in [14] using linear predictive modeling.

A more recent study [15] considers the problem of footstep detection using Laplacian distribution, but it is not clear from the study if the authors used acoustic or seismic sensors. Also, the study does not mention the effect of sensor-footstep distance on the detection accuracy.

### 22.1.1 Contribution and Organization of Paper

In this paper, we investigate the use of a prominence-based peak-picking approach for detecting footsteps from accelerometer measurements. The proposed method is detailed in Sect. 22.2. Using experiments involving single and multi-occupant walking trials on an instrumented floor (Sect. 22.3), the performance of the proposed footstep detection algorithm is evaluated quantitatively based on the number of footstep detections per trial, and qualitatively, by looking at occupant tracking results. In Sect. 22.3.1, detected footsteps from the experimental trials will be used to track occupant paths, utilizing the single occupant tracking method in [16].

It is shown that the proposed footstep detection method is more effective for the detection of single occupant footsteps compared to the multi-occupant case (see Sects. 22.3 and 22.4 for details). Furthermore, in Sect. 22.4, an example is given showing the shortcoming of using a conventional matched filtering approach for footstep detection. Lastly, Sect. 22.5 states the conclusions of this study.

## 22.2 Methodology

Assume a floor is instrumented with  $N$  accelerometers, and an estimate of the per-sensor noise power  $\sigma_i^2$  ( $i = 1, 2, \dots, N$ ) is obtained. In the case of sampled sensor data, noise power estimates are calculated as the mean squares of data sample points during a period of no activity on (and nearby) the instrumented area. Further assume that sensor data is buffered to generate consecutive data time-frames of suitable length (e.g., 1 s), where synchronous data frames are denoted by  $z_i$ ,  $i = 1, 2, \dots, N$ . Also assume that the accelerometer signature for a single footstep will not exceed a time duration of  $T = 0.15$  s.

Moreover, in the context of footstep localization, the minimum number of sensors,  $N_{\min}$ , required to efficiently estimate the location of a detected footstep, must be determined before running the algorithm. For example, in the case of the occupant tracking algorithm in [16], which will be used for tracking in Sect. 22.4,  $N_{\min}$  is set to a value of 5.

Then, the proposed detection algorithm works in the following sequence

1. Calculate  $\sigma_{\text{avg}} = 1/N \cdot \sum_i^N \sigma_i$
2. Calculate  $g = 1/N \cdot \sum_i^N |z_i|$ .
3. Evaluate a smoothed envelope of the signal  $g$  using spline interpolation over local maxima [17], smoothed over a time period equivalent to  $T$ .
4. Pick prominent peaks in the calculated envelope to be the detected footsteps. Using the `findpeaks` function in matlab [18], only local maxima that satisfy the following peak requirements are chosen
  - (a) Peak height ( $PH$ ) must satisfy  $PH \geq N_{\min} \cdot \sigma_{\text{avg}}$ .
  - (b) Peak distance ( $PD$ ) must satisfy  $PD \geq T/2$ .
  - (c) Peak prominence ( $PP$ ) must satisfy  $PP \geq 3 \cdot N_{\min} \cdot \sigma_{\text{avg}}$ . Peak *prominence* is a measure of how much a peak stands out among neighboring peaks [18]. According to [18], “the prominence of a peak, is the minimum distance that the signal must drop on either side of the peak before climbing back to a higher level”. The  $PP$  requirement helps rule out peaks that appear in the data as a result of wave reflections.

5. Finally, the time instance corresponding to a detected footstep, is stored as the footstep detection time (FDT).

It is worth mentioning that the proposed detection algorithm in its presented form cannot distinguish a peak due to a footstep from a peak due to a similarly-looking impulsive event (e.g., ball drop on the instrumented floor); therefore, the algorithm must be supplemented with a means of classifying the selected prominent peaks as corresponding to a “footstep”, or “not a footstep”. This classification task can be done by match-filtering the data around the FDT (using a previously recorded footstep template), and then enforcing a minimum amplitude (or signal power) threshold on the match-filtered data to decide if the impulsive event is a footstep; or not.

## 22.3 Experimental Results

Several occupant walking trials were conducted on an instrumented floor, to provide a data-set for evaluating the proposed footstep detection algorithm. The trials were as follows

- Trial 1 (T1): single occupant (female) wearing high heel shoes.
- Trial 2 (T2): single occupant (male) wearing formal shoes.
- Trial 3 (T3): single occupant (male) wearing soft-soled running shoes.
- Trial 4 (T4): two occupants walking in a corridor; a male wearing formal shoes, and a female wearing high heels.

In each trial, test subject(s) walked exactly 40 footsteps, with a footstep impact frequency of about 2 Hz per test subject. Test subject weights fell in the range of 140–180 pounds. Experiments took place on the 4th floor of a 5-story building (Goodwin Hall of Virginia Tech). Floor was made of concrete, and instrumented with 10 PCB accelerometers (model 352B). The accelerometers were placed under structural steel girders carrying the floor. For more details, on the sensor installation, wiring, and data acquisition in Goodwin Hall, the interested reader is referred to [19]. Figure 22.1 shows the sensor layout, and occupant walking paths in the single and multi-occupant cases.

For the single occupant trials T1 and T2 (high heels, and formal men shoes), the footstep-generated peaks in the accelerometer data were prominent enough to yield a perfect detection of all 40 footsteps in each of T1 and T2. Figure 22.2 shows a sample data from T2, and the footstep detections made by the proposed algorithm.

Only 18 footsteps were detected in the case of the single occupant wearing soft-soled shoes (T3), due to the reduced footstep signal to noise ratio. For the multi-occupant case (T4), 23 footsteps (out of 40) were detected due to reasons explained in Sect. 22.4.

### 22.3.1 Occupant Tracking Results

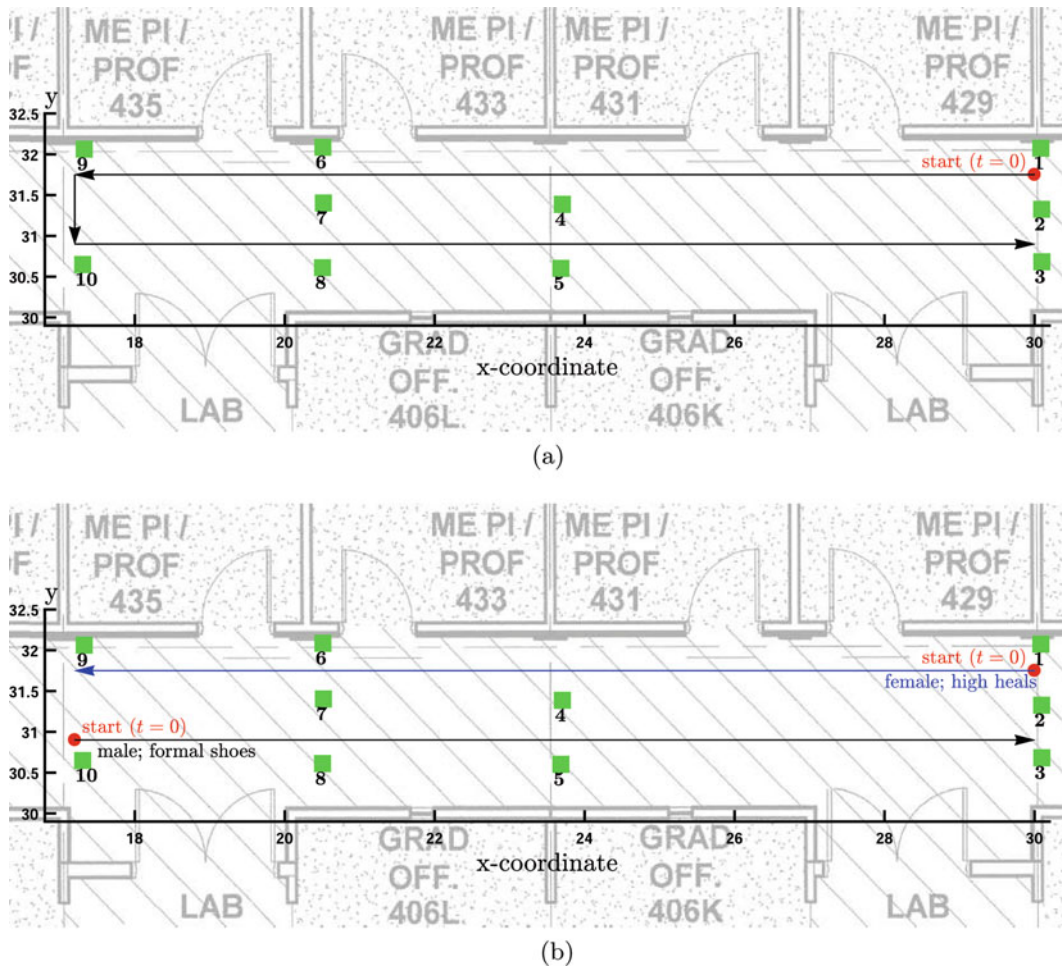
As a qualitative performance measure of the proposed footstep detection algorithm, occupant path tracking is done. By looking at occupant tracking results from the detected footsteps, we would get an idea of the accuracy of the footstep detection algorithm, since bad (or missed) detections would affect the quality of path tracking.

A matlab implementation of the energy-based occupant tracking technique in [16] is used. The tracking technique—designed for single occupant tracking—utilizes a passive accelerometer sensor network, and does not require knowledge of floor-dependent parameters (calibration-free method). The technique in [16] feeds initial footstep location estimates to a Kalman filter to yield the final occupant’s path.

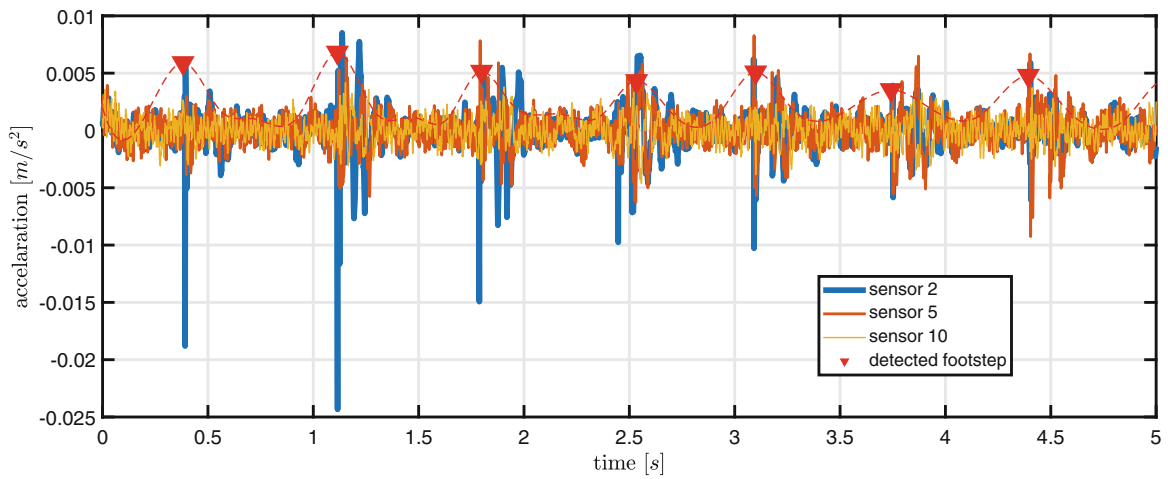
Figure 22.3 shows the tracking results of the three single occupant walking trials, while Fig. 22.4 illustrates the results for the multi-occupant case (T4), where only the estimated footstep locations are shown in the order of footstep detection. Occupant paths are not generated for the multi-occupant case because the algorithm in [16] cannot directly deal with the case of multi-occupant tracking. If the tracking algorithm in [16] is to be used for generating multi-occupant paths, then additional routines are required providing an estimate of the number of walking occupants, and assigning each detected/localized footstep to a corresponding occupant.

## 22.4 Discussion

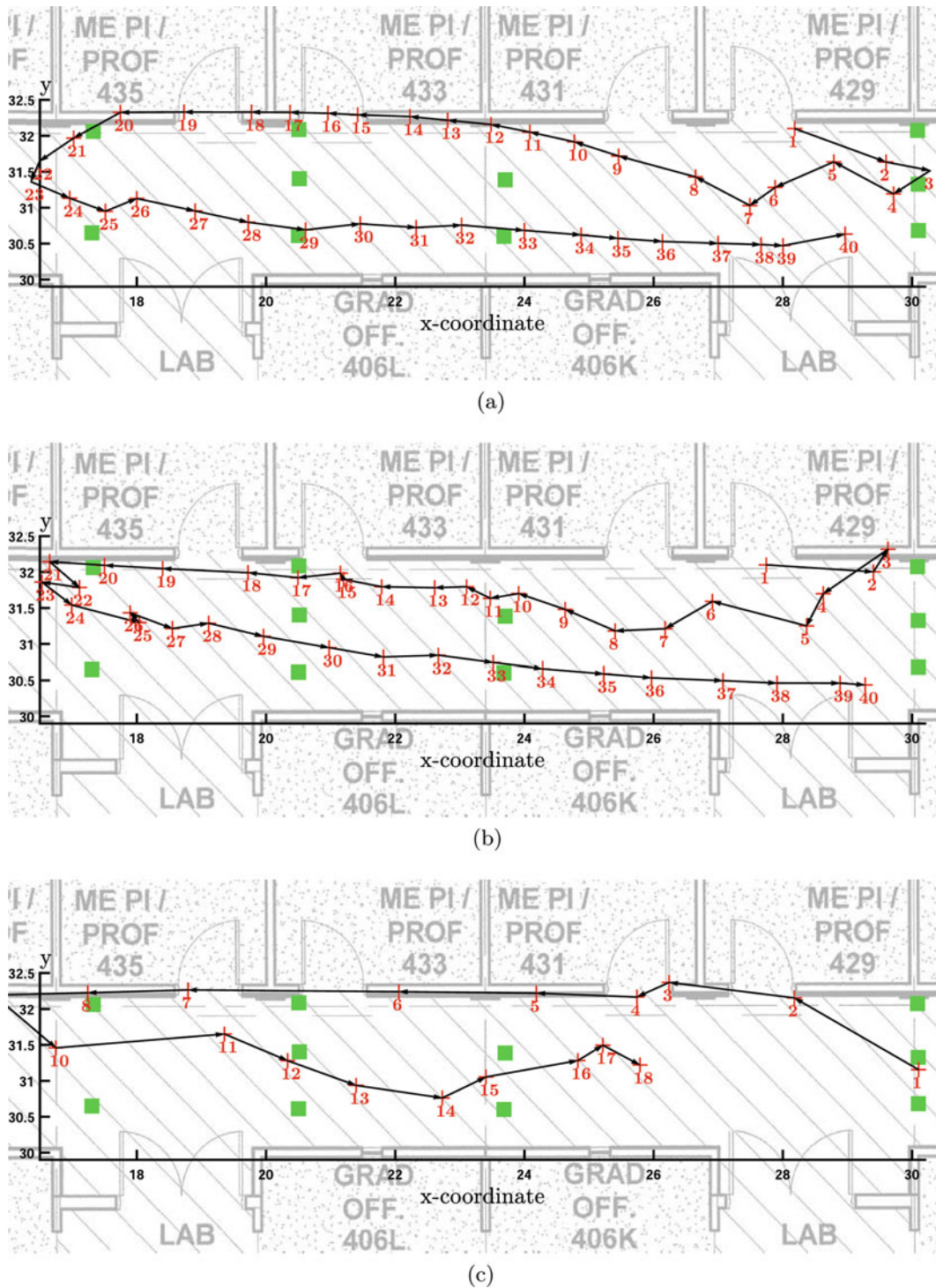
Analyzing the experimental results, it can be seen that the proposed detection algorithm had a flawless performance in the case of single occupant footstep detection, when hard-soled shoes were worn (relatively high signal to noise ratio) compared



**Fig. 22.1** (a) Sensor layout and Walking path of the single occupant trials. (b) Multi-occupant walking path



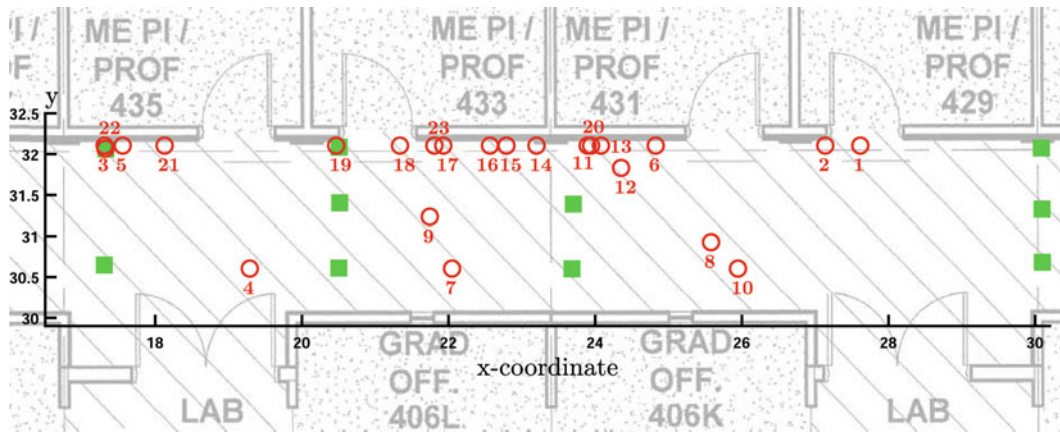
**Fig. 22.2** Sample data recorded during Trail 2, showing data from three distant sensors. Plot shows the detected footsteps obtained from the proposed algorithm



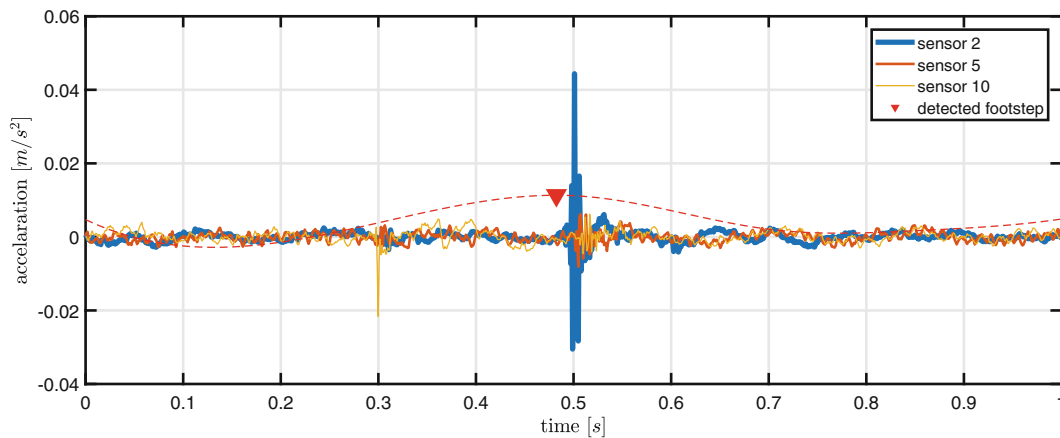
**Fig. 22.3** Single occupant tracking results using the algorithm in [16], and based on footstep impact detections by the proposed algorithm. (a) Trial 1: female; high heels. (b) Trial 2: male; formal shoes. (c) Trial 3: male; running shoes

to the soft-soled shoes; therefore, more signal analysis is required to denoise the data in the case of walkers wearing soft-soled shoes, or stealthy walkers in general.

In addition to the previous observation, in the case of multiple occupants walking in the instrumented area, it has been noticed that the footstep detection accuracy is expected to improve if



**Fig. 22.4** Multi-occupant footstep localization. Each detected footstep was localized and annotated with a number in the order it was detected



**Fig. 22.5** A case of a missed-detection in the multi-occupant trial (T4). The 1st footstep taken by the male test subject is not detected at time  $t = 0.3$  s

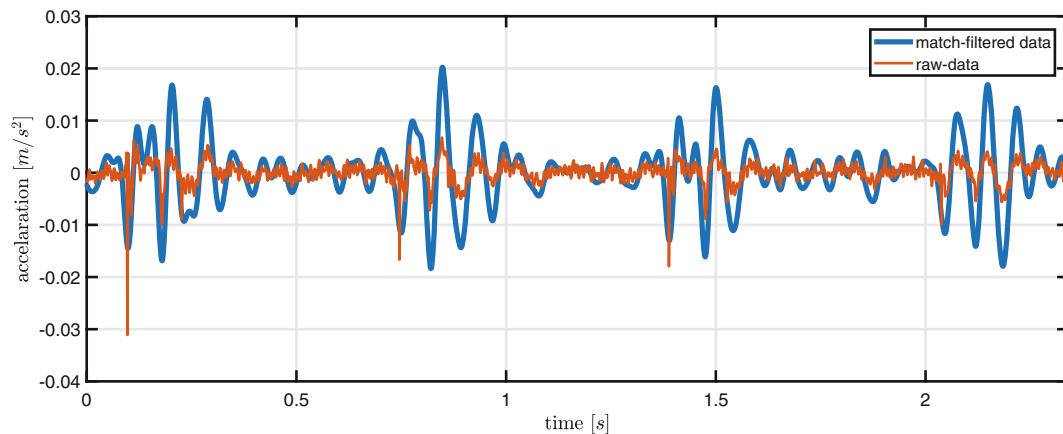
- Foot falls (heel-strikes) tend to be more separated in time (minimum time separation period is  $T/2 = 0.075$  s).
- Similar type of shoe-wear is worn, and simultaneous walkers have similar walking speeds.

Inspection of Fig. 22.4 shows a bias towards detecting the female footsteps, who was wearing high heels, compared to the other test subject. The reason for the bias is that high heels generated more prominent impacts compared to the hard-soled shoes the male was wearing. Figure 22.5 shows a sample data from the multi-occupant case (T4), with a clear missed detection at time instance  $t = 0.3$  s.

### 22.4.1 Note on Detection Using Matched Filters

Initially, before developing the proposed prominence based footstep detection algorithm, the authors found it worthy to test a matched filtering approach for detecting footsteps. Two filter templates were created from accelerometer walking data. The templates were generated in the same instrumented area on the 4th floor of Goodwin Hall, using accelerometer footstep signatures from a different test subject. Each filter template consisted of the first 2 main lobes (lower and upper) seen from an accelerometer response to a footstep impact.

The authors noticed that after match-filtering accelerometer data containing a single footstep, multiple nearby peaks were observed; instead of just one defined peak. This observation matches what the authors in [11, 12] have reported. Figure 22.6 gives an example of the observed phenomenon.



**Fig. 22.6** Portion of the raw measurements of sensor No. 4 (thin line), recording during Trial 2 (one male wearing formal shoes). Raw data is compared to the match-filtered data from the same sensor. Match-filtered data (thick line) is amplitude-scaled, and phase-delay compensated, for better visualization

## 22.5 Conclusion

The authors presented a prominence based peak-picking algorithm for the purpose of detecting footstep impacts from accelerometer data. The algorithm was designed to eventually aid in footstep localization, and occupant path tracking. The detection algorithm was found to be accurate and effective in single occupant walking scenarios, and even with many missed-detections, it was possible to generate a reasonably accurate walking path.

Detection accuracy degrades in a multiple occupant walking scenario, especially if there is a difference in the sharpness of impacts generated by any two different occupants walking simultaneously on the instrumented floor (detections are biased towards walkers with sharper (and/or harder) shoe heels (and/or heel-strikes)).

Future work will include attempts to increase detection accuracy, especially in the case of multiple walkers. Furthermore, given an a priori estimate of the number of walkers in an instrumented area (eg., using a camera), future work will include using artificial intelligence (pattern-matching) to assign detected footsteps with a corresponding (most probable) walker.

**Acknowledgments** The authors are thankful for the support and collaborative efforts provided by our sponsors VTI Instruments, PCB Piezotronics, Inc.; Dytran Instruments, Inc.; and Oregano Systems. The authors are particularly thankful for the support provided by the College of Engineering at Virginia Tech through Ed Nelson and Dean Richard Benson as well as Capital Project Manager Todd Shelton. The authors would also like to acknowledge the collaboration with Gilbane, Inc.; in particular members David Childress and Eric Hotek. We are especially thankful to the Hashemite University of Jordan and the Student Engineering Council at Virginia Tech for their support. The authors would also like to recognize the support provided by the John R. Jones III faculty fellowship. The work was conducted under the patronage of the Virginia Tech Smart Infrastructure Laboratory and its members.

## References

1. Poston, J.D.: ILoViT: indoor localization via vibration tracking. Thesis (2018)
2. Alajlouni, S., Albakri, M., Tarazaga, P.: Impact localization in dispersive waveguides based on energy-attenuation of waves with the traveled distance. *Mech. Syst. Signal Process.* **105**(15), 361–376 (2018) ISSN:0888-3270. <https://doi.org/10.1016/j.ymssp.2017.12.007>, <http://www.sciencedirect.com/science/article/pii/S0888327017306428>, <https://www.sciencedirect.com/science/article/pii/S0888327017306428?via%3Dihub>
3. Alajlouni, S., Tarazaga, P.A.: Evaluation of a new energy-based human tracking method in a smart building using floor vibration measurements. In: Pakzad, S. (ed.) *Dynamics of civil structures*, Vol. 2, pp. 289–292. Springer International Publishing, Cham (2019). ISBN:978-3-319-74421-6
4. Bahroun, R., Michel, O., Frassati, F., Carmona, M., Lacoume, J.L.: New algorithm for footstep localization using seismic sensors in an indoor environment. *J. Sound Vib.* **333**, 1046–1066 (2014). ISSN:0022-460X
5. Graff, K.F.: *Wave Motion in Elastic Solids*. Dover Publications, Inc., New York (1991). isbn:978-0-486-66745-4
6. Ziola, S.M., Gorman, M.R.: Source location in thin plates using cross-correlation. *J. Acoust. Soc. Am.* **90**, 2551–2556 (1991) ISSN:0001-4966
7. Racic, V., Pavic, A., Brownjohn, J.M.W.: Experimental identification and analytical modelling of human walking forces: Literature review. *J. Sound Vib.* **326**(1), 1–49 (2009) ISSN:0022-460X. [http://ac.els-cdn.com/S0022460X09003381/1-s2.0-S0022460X09003381-main.pdf?\\_tid=44e6a2d6-8719-11e6-a71c-00000aacb35f&acdnat=1475245508\\_5fd0a8a612aac6a4a7b91741d8ca8c16](http://ac.els-cdn.com/S0022460X09003381/1-s2.0-S0022460X09003381-main.pdf?_tid=44e6a2d6-8719-11e6-a71c-00000aacb35f&acdnat=1475245508_5fd0a8a612aac6a4a7b91741d8ca8c16)

8. Simon, S.R., Paul, I.L., Mansour, J., Munro, M., Abernethy, P.J., Radin, E.L.: Peak dynamic force in human gait. *J. Biomech.* **14**(12), 817–822 (1981). ISSN:0021-9290). <https://www.ncbi.nlm.nih.gov/pubmed/7328088>
9. Succi, G.P., Clapp, D., Gampert, R., Prado, G. Footstep detection and tracking. In: *Unattended Ground Sensor Technologies and Applications III*, Vol. 4393, pp. 22–29. International Society for Optics and Photonics, SPIE (2001). <https://doi.org/10.1117/12.441277>
10. Xing, H.-F., Li, F., Liu, Y.-L.: Wavelet denoising and feature extraction of seismic signal for footstep detection. In: *2007 International Conference on Wavelet Analysis and Pattern Recognition*, Vol. 1, pp. 218–223. IEEE (2007)
11. Poston, J.D., Buehrer, R.M., Woolard, A.G., Tarazaga, P.A.: Indoor positioning from vibration localization in smart buildings. In: *2016 IEEE/ION position, location and navigation symposium (PLANS)*, pp. 366–372. IEEE (2016)
12. Poston, J.D., Buehrer, R.M., Tarazaga, P.A.: Indoor footstep localization from structural dynamics instrumentation. *Mech. Syst. Signal Process.* **88**(1), 224–239 (2017). ISSN:0888-3270. <http://dx.doi.org/10.1016/j.ymssp.2016.11.023>, <http://www.sciencedirect.com/science/article/pii/S0888327016305015>, [http://ac.els-cdn.com/S0888327016305015/1-s2.0-S0888327016305015-main.pdf?\\_tid=c8aab7a8-c0ba-11e6-b364-00000aacb35f&acdnat=1481582094\\_380ce34ce8b635ef8a0b7549c1a74390](http://ac.els-cdn.com/S0888327016305015/1-s2.0-S0888327016305015-main.pdf?_tid=c8aab7a8-c0ba-11e6-b364-00000aacb35f&acdnat=1481582094_380ce34ce8b635ef8a0b7549c1a74390)
13. Veen, J., van der Wiellen, P.C.J.M.: The application of matched filters to pd detection and localization. *IEEE Elect. Insul. Mag.* **19**(5), 20–26 (2003). ISSN:0883-7554. [10.1109/MEI.2003.1238714](https://doi.org/10.1109/MEI.2003.1238714)
14. Bland, R.E.: Acoustic and seismic signal processing for footstep detection. Ph.D. thesis, Massachusetts Institute of Technology (2006)
15. Shah, R.S., Shah, R.S., Kumar, A.L., Abhijith, S., Badiger, S.D.: Footstep detection using Laplacian distribution. In: *2017 International Conference on Energy, Communication, Data Analytics and Soft Computing (ICECDS)*, pp. 821–824. IEEE. ISBN:1538618877
16. Alajlouni, S., Tarazaga, P.: A passive energy-based method for footstep impact localization, using an underfloor accelerometer sensor network with Kalman filtering. *J. Vib. Control.* **26**(11–12), 941–951 (2020). <https://doi.org/10.1177/1077546319890520>
17. Analytic Envelopes of Decaying Sinusoid Example, (Oct 2019). <https://www.mathworks.com/help/signal/ref/envelope.html>. Online; Accessed 20 Oct 2019
18. Find Peaks in a Vector Example, (Oct 2019). <https://www.mathworks.com/help/signal/ref/findpeaks.html>. Online; Accessed 21 Oct 2019
19. Hamilton, J.M.: Design and implementation of vibration data acquisition in goodwin hall for structural health monitoring, human motion, and energy harvesting research. Thesis, Virginia Polytechnic Institute and State University (2015)

**Sa'ed Alajlouni** is an assistant professor in the Department of Mechatronics Engineering at the Hashemite University; Jordan. He holds a PhD degree in Electrical Engineering from Virginia Tech, USA.



# Chapter 23

## An Augmented Risk-Based Paradigm for Structural Health Monitoring

Aidan J. Hughes, Robert J. Barthorpe, Charles R. Farrar, and Keith Worden

**Abstract** The notion of risk is comprised of *two* components: the likelihood of an adverse event occurring, and the severity of the consequences. Probabilistic risk assessment (PRA) is an established methodology for quantifying risks, used by engineers in a range of industries to inform decisions regarding the design and operation of safety-critical or high-value structures and systems.

In comparison, a salient motivation for implementing a structural health monitoring (SHM) system is to facilitate the decision-making process throughout the lifetime of a structure. Oftentimes, there is uncertainty when assessing the damage state of a structure. As such, a statistical pattern recognition (SPR) approach to structural health monitoring is employed in which data acquired from a structure of interest are processed to yield features indicative of the damage state. The current paper details how decision-making under uncertainty can be aided by augmenting the established structural health monitoring paradigm to incorporate risk, utilising a framework based on probabilistic graphical models.

The modelling of failure events as fault trees is a core process in conducting a PRA and, by modelling key failure modes of interest for a given structure in this way, provides a convenient and rigorous basis for formulating risk-based SHM problems. As statements in Boolean logic, fault trees are limited to representing binary damage states. Fortunately, it is possible to map fault trees into Bayesian networks which are capable of representing multi-state variables whilst also affording other benefits.

Risk is incorporated into the framework by introducing utility nodes into the probabilistic graphical model, thereby attributing costs to failure events. Decision nodes are also included, enabling the evaluation of potential courses of action such that a strategy that maximises utility may be determined.

**Keywords** Structural health monitoring · Probabilistic risk assessment · Probabilistic graphical models

### 23.1 Introduction

*Probabilistic Risk Assessment* (PRA) is a method for identifying potential adverse events and quantifying the associated likelihood of occurrence and the severity of the consequences. For decades, PRA has been employed in a range of industries, including nuclear and aerospace, to inform decision-making regarding the design and operation of safety critical systems and structures, such as nuclear power plants [1] and reusable space vehicles, like the space shuttle [2].

In comparison, *Structural Health Monitoring* (SHM) is a field of engineering concerned with the detection of damage within aerospace, civil or mechanical infrastructure via continual acquisition and online processing of data [3]. A primary incentive for the development and implementation of SHM systems is to gain the ability to make informed decisions regarding the operation and management of structures so as to improve safety and/or reduce costs. A decision-making agent in the context of SHM is required to specify action policies whilst being robust to uncertainties that arise due to having imperfect information regarding the damage state of a structure. Additionally, structures can be complex and a decision maker may have to take into account multiple failure modes and/or manage a population of structures simultaneously. The problem of decision-making for SHM is highly involved and therefore demands a rigorous and structured approach.

---

A. J. Hughes (✉) · R. J. Barthorpe · K. Worden  
Department of Mechanical Engineering, Dynamics Research Group, University of Sheffield, Sheffield, UK  
e-mail: [ajhughes2@sheffield.ac.uk](mailto:ajhughes2@sheffield.ac.uk); [r.j.barthorpe@sheffield.ac.uk](mailto:r.j.barthorpe@sheffield.ac.uk); [k.worden@sheffield.ac.uk](mailto:k.worden@sheffield.ac.uk)

C. R. Farrar  
Engineering Institute, Los Alamos National Laboratory, Los Alamos, NM, USA  
e-mail: [farrar@lanl.gov](mailto:farrar@lanl.gov)



Thus far, the majority of research in the field of SHM has been focussed on the identification, localisation and classification of damage. There have been fewer attempts to address decision-making processes and to incorporate risk into SHM problems. Flynn and Todd successfully applied a Bayes risk approach to the decision problem of sensor placement for an SHM system on square, gusset and T-shaped plates in [4]. The approach considered the risk of false positives and false negatives of damage identification in discrete regions of the plates. An approach proposed in [5], facilitates cost-efficient reliability-based maintenance. As it is a reliability-based approach rather than a risk-based approach, the costs of failure events and maintenance are not explicitly modelled. Hence, whilst the maintenance strategies developed may be cost-efficient for given safety parameters, they are not necessarily cost-optimal. There has been some research into the risk-based operation and maintenance of structures and components. Nielsen details a risk-based approach that is utilised for the operation and maintenance of off-shore wind turbines in [6], using probabilistic graphical modelling. Similarly, Hovgaard and Brincker provide a case study demonstrating a risk-based approach to the monitoring and maintenance of a finite element model of a wind turbine tower experiencing circumferential cracking in [7]. In [8] a continuous-state partially observable Markov decision process (POMDP) was demonstrated on artificial data for maintenance planning on a deteriorating bridge.

The current paper aims to address the lack of a generalised framework for conducting risk-based monitoring of structures at the full-system scale by augmenting the current SHM paradigm with practices employed in probabilistic risk assessment and thereby facilitating the decision-making processes that motivate the implementation of SHM systems. An overview is given of the current paradigms for conducting PRA and SHM as outlined in the literature. Also provided is background theory regarding the key technologies required for mapping PRA onto SHM; namely, probabilistic graphical models in the form of Bayesian networks and influence diagrams. A notation is established before the augmented risk-based paradigm for SHM is detailed. Finally, a discussion around the framework is made and further challenges in the SHM decision-process are identified.

## 23.2 Current Structural Health Monitoring Paradigm

Structural health monitoring is a field of engineering that is concerned with determining the health state of a structure over time via a damage identification strategy. Due to the uncertainties that arise when dealing with problems in engineering, statistical pattern recognition (SPR) is a natural approach to SHM that has been the focus of much research over the past three decades. The established SPR paradigm for an SHM system is composed of four procedures [3]:

1. Operational Evaluation.
2. Data acquisition.
3. Feature selection.
4. Statistical modelling for feature discrimination.

### 23.2.1 Operational Evaluation

The operational evaluation process seeks to answer questions regarding the implementation of an SHM system, specifically:

- What is the justification (safety and/or economic) for implementing an SHM system?
- How is damage defined for the system and what are the critical damage states?
- What are the environmental and operational conditions that the monitoring system is required to perform under?
- How does the operational environment limit data acquisition?

A large amount of information is required for the operational evaluation process, and significant effort may be necessary to obtain a sufficient amount. Examples of required information include: the financial cost and reliability of the proposed SHM system; possible damage states of the structure and thresholds at which they can be considered to have occurred; and the temperature variation experienced by the structure.

### 23.2.2 Data Acquisition

The data acquisition process is informed by the operational evaluation. The process aims to finalise the types, number and locations of sensors to be used in the SHM system. The data acquisition, storage and transmittal hardware must also be selected. The process is constrained by both economic restrictions and the limitations enforced by the expected environmental conditions; for this reason, the data acquisition process is context dependent and relies heavily on the information gathered during the operational evaluation stage.

### 23.2.3 Feature Selection

Once the data have been acquired, a set of features must be constructed that indicate whether or not there is damage present in the structure. This procedure often involves processing the data acquired from the structure; common practices include domain transformation, dimensionality reduction, and normalisation.

### 23.2.4 Statistical Modelling for Feature Discrimination

Statistical models must be developed to exploit the discrepancy between features that indicate differing damage states. The degree of knowledge regarding the damage state obtained from an SHM system is highly dependent on the statistical model employed and can be evaluated in terms of Rytter's Hierarchy [9]:

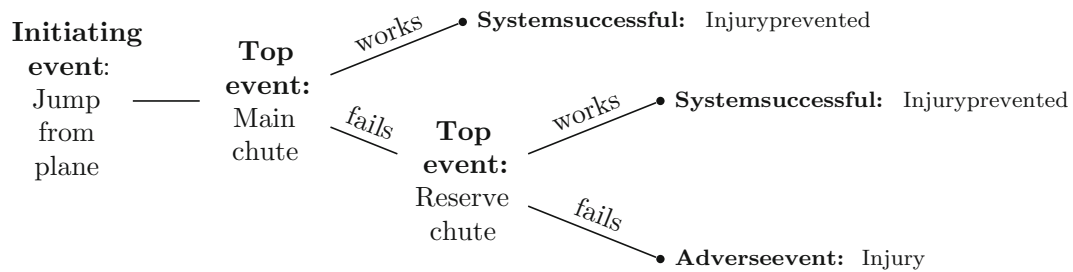
1. Is there damage in the system?
2. Where is the damage located?
3. What type of damage is present?
4. How severe is the damage?
5. How much useful life remains?

Whilst Rytter's hierarchy, in itself, does not lead to decisions being made, as SHM systems progress up the hierarchy, the information they yield becomes increasingly useful to agents tasked with deciding upon a course of action for a structure. Within the field of decision theory, cost and utility are metrics used ubiquitously for the comparison of courses of action and their consequences. By combining the cost/utility of a given consequence with the respective likelihood, one can arrive at the notion of *risk*.

## 23.3 Probabilistic Risk Assessment Paradigm

Probabilistic risk assessment (PRA) is a method that is widely used for evaluating risks and making decisions associated with the design and management of safety-critical systems and high-value assets. In the context of PRA, risk is characterised by the likelihood of an adverse event occurring and the severity of the consequences of the event. The likelihood of occurrence for uncertain adverse events is quantified through probabilistic event sequence and system modelling. The consequences and expected costs/gains are compared and evaluated by finding an appropriate utility metric – obvious examples include financial cost and loss of human life; however, in many applications these are overly simplistic [10]. Probabilistic risk assessment is applied in a range of industries including nuclear, aerospace and chemical process. Whilst the exact methodology used for conducting PRA differs between industries, they generally adhere to the key steps as outlined by the US Nuclear Regulatory Commission (USNRC) and the International Atomic Energy Agency (IAEA) [1]:

1. Initial information collection.
2. Event-tree development.
3. System modelling.
4. Reliability modelling.
5. Failure sequence quantification.
6. Consequence analysis.



**Fig. 23.1** An example event tree for a parachute system to prevent fall injuries [11]

Further detail is provided for each step in the following subsections.

### 23.3.1 Initial Information Collection

Information regarding the design and operation of the structure in question is collated. Details such as component specifications, loading and environmental conditions are considered. The information gathered at this stage is used to inform the subsequent steps. Given the large quantity of information required for conducting PRA, an important factor to be considered at this stage is the method by which the necessary information is represented, stored and managed. A common practice is to utilise a database [10].

### 23.3.2 Event-Tree Development

Event trees outline potential accident sequences – combinations of initiating events and the subsequent system failures or successes that may result in an adverse consequence. The sequences of system failures and successes are known as *top events*. The system failures identified in the event-tree development stage are subsequently modelled as fault trees. An example event tree for a system designed to prevent injury following a jump from a plane is shown in Fig. 23.1.

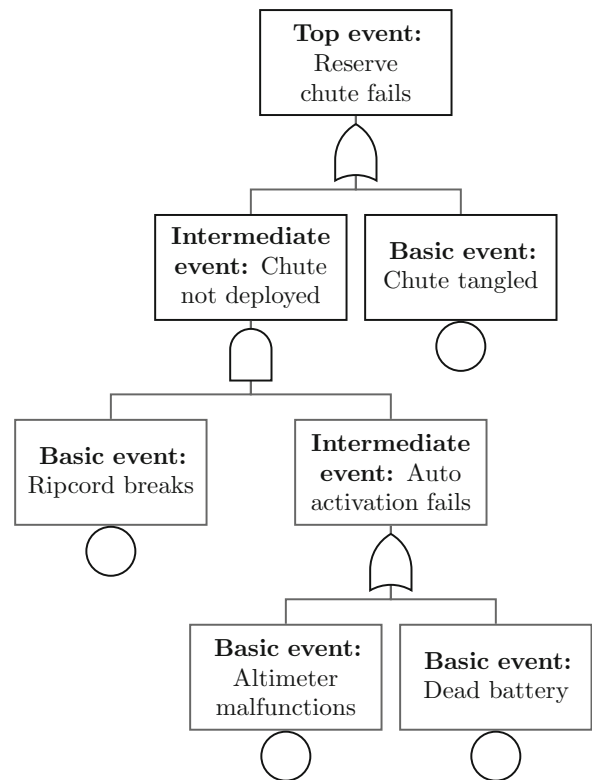
### 23.3.3 Fault Tree Development

Fault trees are used in PRA to facilitate the quantification of system failure probabilities. The development of fault trees involves expressing the causal relationships between component failures and subsystem failures using Boolean logic gates. The level of detail captured in the fault tree (the level of components which are incorporated) is determined by the component level for which meaningful reliability data can be obtained. An example fault tree for the deployment of a reserve parachute is shown in Fig. 23.2.

### 23.3.4 Reliability Modelling

Information regarding the reliability of system components and the frequency of initiating events is necessary to quantify the probabilities of top events. This is typically gleaned from data and applying appropriate reliability models.

**Fig. 23.2** An example fault tree for a reserve parachute system [11]



### 23.3.5 Failure Sequence Quantification

By assigned the components in the fault trees with failure rates, the probability of top events may be computed. Propagating the probabilities of the initiating events and top events through the event tree allows the probability of each possible outcome in the event tree to be calculated.

### 23.3.6 Consequence Analysis

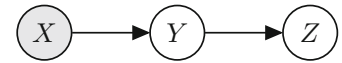
With the probability of an adverse event quantified, a cost/utility metric must be chosen so that the risk associated with the failure sequence may be assessed. The risk assessment may then be used to inform design decisions, such as increasing safety by introducing additional redundancies in the system, or optimising cost by removing components that do not cause the risk to fall below an acceptable threshold. The risk assessment may also be used to inform risk-based inspection for a system that is in operation.

## 23.4 Probabilistic Graphical Models

Probabilistic graphical models (PGMs) are a powerful framework for reasoning and decision-making under uncertainty – a core problem in SHM. Probabilistic graphical models are representations of joint probability distributions, in which nodes denote a set of random variables and edges connecting nodes imply dependency between variables. The probabilistic graphical model representation provides benefits over a flat (non-graphical) representation [12]:

- They provide a compact and intuitive representation of complex probability distributions which makes them easier to understand, communicate and learn.
- They facilitate efficient computation by exploiting local independence structures.

**Fig. 23.3** An example Bayesian network



A PGM over a set of  $N$  variables  $X$  may be specified by a set of  $M$  local functions  $f(Y_i)$ , where  $Y_i$  is some subset of  $X$ , and a graph  $G$  comprised of nodes/vertices  $V$  and edges  $E$ . The joint probability distribution represented by the graph is obtained by:

$$P(X_1, X_2, \dots, X_N) = K \prod_{i=1}^M f(Y_i) \quad (23.1)$$

where  $K$  is a normalisation factor ensuring the probabilities sum to unity.

There are two classes of problem associated with PGMs: *inference* and *learning*. Inference is concerned with obtaining the marginal or conditional probabilities of a subset of variables  $Z$  given any other subset  $Y$ . i.e.  $P(Z|Y)$ . Learning is concerned with obtaining the graph structure and parameters given a complete, or incomplete, set of observed data values for  $X$ . i.e.  $G, f(Y_i)|X$ . The remainder of the current paper will be primarily concerned with inference problems and their application in a risk-informed SHM framework.

### 23.4.1 Bayesian Networks

Bayesian networks (BNs) are a form of PGM. Specifically, they are directed acyclic graphs (DAGs) in which nodes represent random variables and edges connecting nodes represent conditional dependencies between variables. For discrete random variables, the local functions that describe the conditional probability distributions (CPDs) between variables are conditional probability tables (CPTs), and in the case of continuous random variables are conditional probability density functions (CPDFs).

Figure 23.3 shows a simple Bayesian network where  $X$  is a parent of  $Y$  and an ancestor of  $Z$ ;  $Z$  is said to be the child of  $Y$  and a descendant of  $X$ . Node  $X$  is independent of other nodes and so is specified by the unconditional distribution  $P(X)$ . Observed variables are shaded grey.

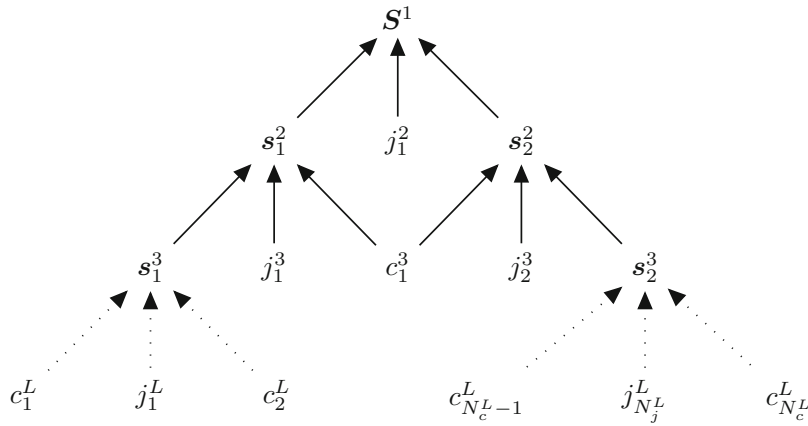
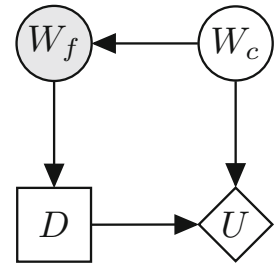
Given observations on a subset of nodes in a BN, inference algorithms can be applied to obtain posterior distributions over the unobserved random variables. In some cases, analytical solutions of posterior distributions may be found by using exact inference methods. To solve the inference problem using direct computation from the joint probability distribution, the computational complexity increases exponentially with the size of the graph and quickly becomes intractable. Fortunately, algorithms have been developed that allow efficient computation [13].

### 23.4.2 Influence Diagrams

Bayesian networks can be augmented to represent decision processes by incorporating nodes for decision variables and utility functions – these augmented networks are known as *influence diagrams*. Decision nodes are denoted by squares and utility nodes are denoted by rhombi, as shown in Fig. 23.4. Edges connecting random variables to utility nodes denote that the utility function is dependent on the state of that variable. Similarly, edges connecting decision nodes to utility nodes denote that the utility function has a dependence on the action decided upon. Edges connecting random variables or decision nodes to other decision nodes denote order, that is to say the random variable or decision is observed prior to the decision being made; such edges are referred to as *informational links* as they do not imply a functional dependence but rather that the information regarding the state of the variable is required for the decision to be made.

The influence diagram shown in Fig. 23.4 can be interpreted as a binary decision process regarding whether to go out for a walk or stay in and watch TV under uncertainty in the future weather condition  $W_c$  given an observed weather forecast  $W_f$ . The nodes  $W_f$  and  $W_c$  can be considered as binary random variables representing the weather forecast and actual weather condition, respectively, with possible states  $domain(W_f) = domain(W_c) = \{bad, good\}$  and the weather forecast is dependent on the weather condition. The possible actions can be summarised as  $domain(D) = \{TV, walk\}$ . The utility  $U$  achieved is then dependent on both the weather condition experienced and the decided action.

**Fig. 23.4** An example influence diagram representing the decision of whether to go outside or stay in under uncertainty in the future weather condition given an observed forecast



**Fig. 23.5** A hierarchical graphical representation of a generic structure  $S$ . Superscripts denote the level in the hierarchy and subscript indexes each type of constituent unit in a given level. Dotted edges imply an arbitrary structuring between levels

In general, a policy  $\delta$  is a mapping from all possible observations to possible actions. The problem of inference in influence diagrams is to determine an optimal strategy  $\Delta^* = \{\delta_1^*, \dots, \delta_n^*\}$  given a set of observations on random variables where  $\delta_i^*$  is the policy for the  $i$ th decision to be made in a strategy  $\Delta^*$  that yields the *maximum expected utility (MEU)*. The expected utility is a function of probability and utility; and by this definition is equivalent to risk.

### 23.5 Definitions

To establish a framework for mapping PRA onto SHM, some fundamental concepts will first be defined. In addition, a notation will be established for describing structures that can be expressed as hierarchical graphs.

One must start with a physical structure or system of interest  $S$ . It is assumed that  $S$  may be defined in terms of constituent units; components  $c$ , joints  $j$  and substructures  $s$ . Components and joints are considered irreducible base units of  $S$  whereas substructures are compound units and may be comprised of joints, components and other substructures.

Figure 23.5 depicts a graphical representation of a hierarchical structure that may be considered without loss of generality. Nodes represent the global structure and its constituent units and edges represent the dependence of a (sub)structure on its constituent units. At the top, or level 1, of the hierarchy is the global structure with the hierarchy level denoted in the superscript. It can be seen that the global structure  $S^1$  is comprised of two substructures  $s_1^2, s_2^2$  and a joint  $j_1^2$ , i.e.  $S^1 = \{s_1^2, j_1^2, s_2^2\}$ . These units form the second level of the hierarchy.  $s_1^2$  and  $s_2^2$  may in turn be expanded to yield  $S^1 = \{s_1^3, j_1^3, c_1^3, j_2^3, s_2^3\}$ . Progressing down the hierarchy levels, one can continue to expand the substructures into constituent units until the  $L$ th level of the hierarchy which is comprised solely of base units. By taking the expansion of  $S^1$  into its constituent base units and discarding the repeated units arising from substructures that share components, one obtains a list of the base units that form a given structure  $S$ . Within each level of the hierarchy, units are numbered via a subscript from 1 to  $N_u^i$  where  $N_u^i$  is the number of a constituent unit type  $u$  in the  $i$ th level of the hierarchy. The notation  $u_n^i$  where  $i$  is an integer from 1 to  $L$  and  $n$  is an integer from 1 to  $N_u^i$  provides a unique identifier for each unit within a structure.

It is assumed that there exists a set of features  $\mathbf{v}$ , observable from  $\mathbf{S}$ , that are produced according to a generative latent state model with latent state  $\mathbf{H}^*(t)$ , where  $\mathbf{H}^*(t)$  is the true health state of  $\mathbf{S}$  and may be expressed in terms of the true health states of the constituent components and joints  $h^*c_n^i(t)$  and  $h^*j_n^i(t)$ , respectively, i.e.  $\mathbf{H}^*(t) = \{h^*c_1^2(t), \dots, h^*c_{N_c}^L(t), h^*j_1^2(t), \dots, h^*j_{N_j}^L(t)\}$ .

The structure  $\mathbf{S}$  also has a predicted time-dependent health state vector  $\mathbf{H}(t) = \{hc_1^2(t), \dots, hc_{N_c}^L(t), hj_1^2(t), \dots, h^{j_{N_j}^L}(t)\}$ . Health-state vectors can be constructed from any subset of components and joints.

For the structure/system  $\mathbf{S}$ , there must exist a set of failure modes of interest  $\mathbf{F} = \{F_1, \dots, F_{N_F}\}$  whereby  $\mathbf{S}$  ceases to be fit for purpose. It is assumed that a given failure mode is dependent on the health states of a subset of components, joints and substructures for which a health-state vector can be constructed. In addition, each failure state has an associated utility  $U_{F_n}$ .

Finally, for the structure  $\mathbf{S}$ , there also exists a set of decisions  $\mathbf{d} = \{d_1, \dots, d_{N_d}\}$  which affect  $\mathbf{H}^*$ , each having an associated utility  $U_{d_i}$ . In addition, there will exist some set of environmental conditions  $\mathbf{e} = \{e_1(t), \dots, e_{n_e}(t)\}$  that will alter the distribution of  $\mathbf{v}$ .

## 23.6 Mapping PRA Onto SHM

Upon examination, it becomes apparent that there are both differences and similarities between the paradigms for SHM and PRA that can be examined to determine which aspects of PRA will be useful for SHM. Whilst it is clear that both SHM and PRA are utilised for the purpose of making decisions in the face of uncertainty, PRA is conducted offline for a system experiencing a set of anticipated initiating events. In contrast, the decision processes for which SHM is implemented are online and require continual predictions of the damage state of the structure. It is for this reason that the event-tree development stages and failure sequence quantification stages in PRA are less applicable to SHM.

Both paradigms begin with collating information regarding the structure and defining the context in which decisions are to be made. In fact, the first three stages of the PRA paradigm involve expressing the structure and context in a logical way which facilitates the quantification of risk and the decision-making process. It is in this formal expression of the structure that the decision-making process in the SHM paradigm stands to benefit. An overview of the risk-based SHM paradigm is as follows:

1. Operational evaluation.
2. Failure-mode modelling.
3. Decision modelling.
4. Data acquisition.
5. Feature selection.
6. Statistical modelling for feature discrimination.

### 23.6.1 Operational Evaluation

With the aim of justifying the use and defining the context of a risk-based SHM system, the operational evaluation stage seeks to answer many of the same questions as in the standard paradigm. However, some questions require an approach that facilitates the failure-mode modelling and decision-modelling stages.

Foremost, information regarding the components  $\mathbf{c}$ , joints  $\mathbf{j}$ , substructures  $\mathbf{s}$ , and the dependencies between them is required.

When identifying the critical damage states of the structure  $\mathbf{S}$ , one should aim to identify the failure modes of interest  $\mathbf{F}$ . Critical components, joints and substructures/subsystems that contribute to  $\mathbf{F}$  should also be identified at this stage. The predicted damage states of these components  $\mathbf{h}$  should be defined. The damage states of the critical substructures/subsystems  $\mathbf{H}$  should be defined as a vector in terms of  $\mathbf{h}$ .

For each failure mode in  $\mathbf{F}$ , potential decisions  $\mathbf{d}$  should be identified and the ways in which the actions influence the structure or likelihood of failure modes occurring should be determined. Utility values  $U_F$  and  $U_d$  for all  $\mathbf{F}$  and all  $\mathbf{d}$ , respectively, should be quantified. The selection of utility values will determine the behaviour of the decision-making agent, and is analogous to setting a decision threshold in a standard SHM paradigm.

Environmental influences  $e$  should also be identified. It should also be decided whether the SHM system is to evaluate the health of the structure at static, independent instances in time, or predict future health states, thereby requiring a model forecasting the degradation of the structure.

For large, complex structures it may be beneficial to borrow the data management techniques used in PRA, such as databases, to organise the information obtained during the Operational Evaluation stage. This will allow for a rigorous and structured approach to the information collection and allow for the identification of aspects of the SHM system that require further specification or more information. Having a formal information structure will also expedite the subsequent failure-mode modelling step which requires detailed knowledge of the physical structure.

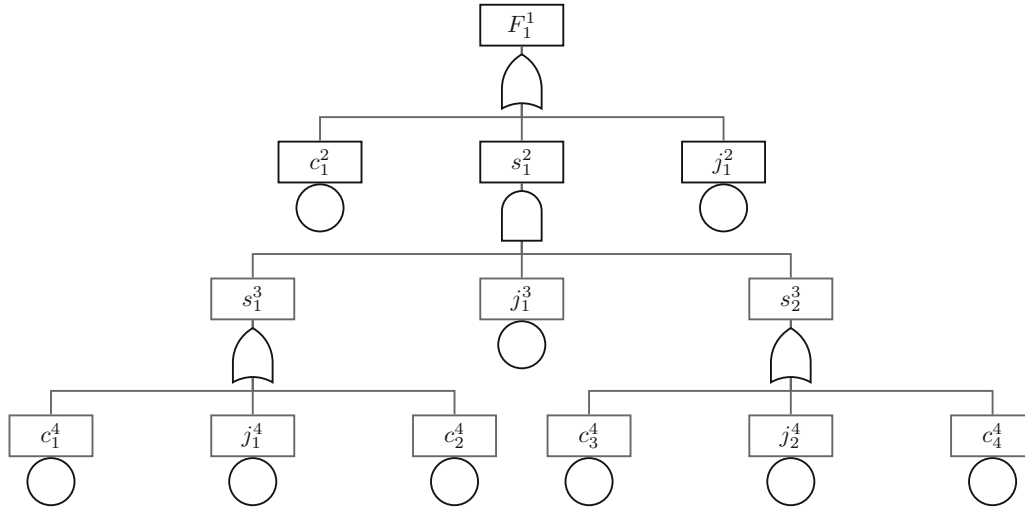


Fig. 23.6 A fault tree of a failure mode  $F_1$  where the superscript denotes the hierarchy level and the subscript is an identifier

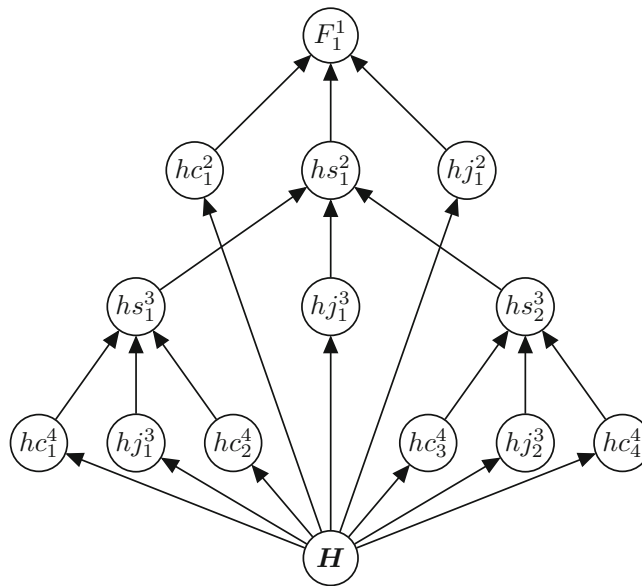


Fig. 23.7 A Bayesian network of failure mode in  $F_1$



### 23.6.2 Failure-Mode Modelling

For each of the failure modes of interest in  $F$ , one should proceed to construct a fault tree, such as that shown in Fig. 23.6, based upon the health states of the relevant components, joints and substructures/subsystems. It should be noted here that, in many cases, the exact nature of the failure modes will be unknown and so a best estimate based on engineering judgement may be used.

Fault trees offer a rigorous and consistent structure for expressing the failure modes; however, as statements in Boolean logic they are limited in their flexibility. In the context of SHM, it is desirable to represent the components in a fault tree as having multiple damage states, and it is for this reason that one should map the constructed fault trees into Bayesian networks. Bobbio et al. outline a convenient mapping from fault trees into Bayesian networks in [14], whilst also highlighting the additional flexibility that is granted by doing so. Additionally, Bayesian networks are used to represent structural failures in [15].

In the example shown in Fig. 23.7, the component health states, substructure health states and failure event are represented as random variables where the substructure health states are conditioned on the component health states and the failure events is conditioned on the substructure health state. The random variables are defined using a conditional probability distribution (CPD) which may be discrete or continuous.

A node representing the health-state vector of the critical components and joints  $H$  should be included in the fault tree, as this latent state will be predicted during the statistical modelling process. To define the vector  $H$  within the Bayesian network, the conditional dependence between the nodes representing the local health states of the components and joints and  $H$  are expressed as a binary logic table.

One function of the failure-mode Bayesian network is to allow the flow of information from the statistical model to the decision, whilst parsing the information in a way that facilitates the defining of the failure events  $F$ . The network also allows the computation of marginal distributions for the probability of failure in each component, joint, or substructure allowing for damage localisation.

### 23.6.3 Decision Modelling

Modelling the decision process involves augmenting the Bayesian network developed in the failure modelling stage with nodes for each decision in  $d$  and for utilities  $U_F$  and  $U_d$  to produce an influence diagram. Decision nodes in which the actions alter the probability of a state or event should modify the CPDs accordingly. Utility nodes are constrained to be leaf nodes and should be dependent on the appropriate failure events or decisions.

For static problems, it may be convenient to model the decision process in a separate influence diagram which receives information regarding failure probabilities from the fault tree. This issue is because it is implicit that the decision is made after observations are made; if one attempts to solve a network in which a decision is made that yields a state that is inconsistent with the observed state, a conflict arises.

### 23.6.4 Data Acquisition

The data acquisition process should not differ from that in the standard SHM paradigm. Here, there is a subtlety that the data acquisition system should be designed so as to optimise the decision-making rather than damage identification.

### 23.6.5 Feature Selection

The feature selection process should not differ from that in the standard SHM paradigm. Again, there is the subtlety that the features should be selected so as to optimise the decision-making.

### 23.6.6 Statistical Modelling

The purpose of the statistical model is to predict the critical health states  $\mathbf{H}$  given the selected feature set  $\mathbf{v}$ . As aforementioned, it is assumed that  $\mathbf{x}$  is produced through a generative latent state model, with latent-state  $\mathbf{H}$ . Probabilistic classifiers that output a probability distribution over all possible states of  $\mathbf{H}$ , such as relevance vector machines (RVMs) and Gaussian mixture models (GMMs), are compatible. Probabilistic classifiers are instrumental in building robustness to the uncertainty surrounding the true health state of  $\mathbf{S}$  into the decision process. Ideally, the chosen statistical model will be capable of consistently identifying the actual health state under all identified operating and environmental conditions  $e$ , or at least appropriately reflect the uncertainty caused by varying conditions in the prediction.

Finally, if a model describing the degradation of  $\mathbf{S}$  (i.e. a transition model for  $\mathbf{H}$ ) is required for forecasting failure events in the time-dependent case, the CPDs defining  $P(\mathbf{H}_t | \mathbf{H}_{t-1}, \mathbf{d})$  should be specified accordingly.

## 23.7 Discussion

The framework described provides an approach to conducting risk-based SHM that incorporates useful stages of the PRA procedure into the SHM paradigm. Decision-making is facilitated through the inclusion of risk, thereby allowing for the comparison of actions and the selection of one that maximises expected utility.

By considering the nature of the decision problems associated with PRA and SHM, inapplicable aspects of the PRA procedure were identified. Specifically, due to fact that the decision process for SHM are required to be online and continual, the event-tree development, reliability modelling and failure sequence quantification stages were deemed unnecessary.

On the other hand, PRA provided a numbers of methods that facilitate the implementation of SHM systems capable of informed decision-making. Firstly, formalising the operational evaluation procedure by organising the information specifying the structure and monitoring system in a database will assist with ensuring all the necessary information required for subsequent stages is acquired and it will provide a structured method for the retrieval of applicable information at each stage. The fault tree development process of PRA provides the key novelty of this risk-based approach to SHM. Targeting selected failure modes of interest for a structure and modelling them as fault trees allows the scope of the decision-maker to be limited thereby making the problem more approachable. Mapping the fault trees into Bayesian networks enables the framework to retain information regarding the uncertainties in the health states thereby allowing robustness in the decision-making. Finally, the consequence analysis process of PRA motivates the explicit incorporation of risk into the SHM framework. Utilities are attributed to the selected failure events and possible courses of action enabling the computation of expected utilities within an influence diagram and the comparison of strategies so that a utility-optimal decision can be made.

Whilst the framework presented addresses some of the problems surrounding the SHM decision process, there remain a number of challenges. One challenge, that has been widely acknowledged in the SHM community, is that data from the damage states of interest for a structure are seldom available prior to the implementation of an SHM system. This poses an issue in the development of the probabilistic classifiers on which the decision process is highly dependent and a choice must be made regarding the approach to the statistical modelling. One option is to take a model-driven approach [16] that utilises outputs from physics-based models of the structure in its damage states of interest to learn a classifier in a supervised manner pre-implementation of the SHM system. Subsequently, the classifier can be continuously updated and validated with data obtained during the monitoring campaign. Alternatively, a semi-supervised approach can be taken in which a clustering algorithm is applied to the data acquired throughout the monitoring campaign. Clusters are attributed damage state labels through the incorporation of labelled data into the clustering algorithm [17]; damage state labels for data points may be obtained through inspection of the structure [18].

In addition to being dependent on the statistical classifier used, the optimality of decisions in temporal processes is highly contingent on the appropriateness of the transition model used; if the degradation of the structure is not accurately modelled, erroneous actions may be taken. Facing a similar issue to the statistical modelling process, oftentimes, data describing the transitions between the health states of interest are not held a priori. Again, one is faced with the choice of taking a model-driven approach involving the simulation of the degradation, or a data-driven approach that utilises data obtained during the monitoring campaign.

A necessary step in the risk-based framework is to assign utilities/costs to failure events and actions. Currently, within the literature there is no formal approach to how these values should be elicited, nor is there a consensus on how the risk preferences of an SHM decision-maker should be specified; should an agent be risk averse, risk neutral, or risk seeking? The issue at hand is one of both a technical and ethical nature, and whilst it will not be discussed in further detail in the current

paper, it is highlighted to stimulate the conversations required for progress in the area of risk-informed decision-making for SHM.

In summary, a risk-based framework for structural health monitoring was presented. Borrowing practices frequently used in probabilistic risk assessment, such as the use of fault trees to model system failures, the framework facilitates robust decision-making under uncertainty.

**Acknowledgments** The authors would like to acknowledge the support of the UK EPSRC via the Programme Grant EP/R006768/1. KW would also like to acknowledge support via the EPSRC Established Career Fellowship EP/R003625/1.

## References

1. US Nuclear Regulatory Commission. PRA procedure guide, Vol. 1. US Nuclear Regulatory Commission (1983)
2. Fragola, J.R., Maggio, G.: Space shuttle operational risk assessment. *AIP Conf. Proc.* **361**(May), 719–720 (1996)
3. Farrar, C.R., Worden, K.: *Structural Health Monitoring: A Machine Learning Perspective*. Wiley, Chichester (2013)
4. Flynn E.B., Todd, M.D.: A Bayesian approach to optimal sensor placement for structural health monitoring with application to active sensing. *Mech. Syst. Signal Process.* **24**(4), 891–903 (2010)
5. Gobbato, M., Kosmatka, J.B., Conte, J.P.: A recursive Bayesian approach for fatigue damage prognosis: an experimental validation at the reliability component level. *Mech. Syst. Signal Process.* **45**(2), 448–467 (2014)
6. Nielsen, J.S.: Risk-based operation and maintenance of offshore wind turbines. Ph.D. thesis, Aalborg University (2013)
7. Hovgaard, M.K., Brincker, R.: Limited memory influence diagrams for structural damage detection decision-making. *J. Civil Struct. Health Monit.* **6**(2), 205–215 (2016)
8. Schöbi, R., Chatzi, E.N.: Maintenance planning using continuous-state partially observable Markov decision processes and non-linear action models processes and non-linear action models. *Struct. Infrastruct. Eng.* **12**(8), 977–994 (2016)
9. Rytter, A.: Vibration based inspection of civil engineering structures. Ph.D. thesis, Aalborg University (1993)
10. Bedford, T., Cooke, R.: *Probabilistic Risk Analysis: Foundations and Methods*. Cambridge University Press, Cambridge (2001)
11. US Nuclear Regulatory Commission. Probabilistic Risk Assessment (PRA) (2018)
12. Sucar, L.E.: *Probabilistic Graphical Models: Principles and Applications*. Springer, London (2015)
13. Pearl, J.: Fusion, propagation and structuring in belief networks. *Artif. Intell.* **29**(3), 241–288 (1986)
14. Bobbio, A., Portinale, L., Minichino, M., Ciancamerla, E.: Improving the analysis of dependable systems by mapping fault trees into Bayesian networks. *Reliab. Eng. Syst. Saf.* **71**(3), 249–260 (2001)
15. Mahadevan, S., Zhang, R., Smith, N.: Bayesian networks for system reliability reassessment. *Struct. Saf.* **23**(3), 231–251 (2001)
16. Barthorpe, R.J.: On model- and data-based approaches to structural health monitoring a thesis submitted to the university of sheffield for the degree of. Ph.D. thesis, The University of Sheffield (2011)
17. Bull, L.A., Rogers, T.J., Wickramarachchi, C., Cross, E.J., Worden, K., Dervilis, N.: Probabilistic active learning: an online framework for structural health monitoring. *Mech. Syst. Signal Process.* **134**, 106294 (2019)
18. Rogers, T.J., Worden, K., Fuentes, R., Dervilis, N., Tygesen, U.T., Cross, E.J.: A Bayesian non-parametric clustering approach for semi-supervised structural health monitoring. *Mech. Syst. Signal Process.* **119**, 100–119 (2019)

**Aidan J. Hughes** received his MEng in Mechanical Engineering with Nuclear Technology from the University of Sheffield in the summer of 2018. Remaining at Sheffield to undertake a PhD, in the following autumn he began researching the application of probabilistic graphical models for decision-making in the context of structural health monitoring (SHM).



# Chapter 24

## Running Safety Analysis Considering Track Irregularities on an Open-deck Steel Plate Girder Bridge Using Finite Element Multibody Dynamics

Sanghyun Choi, Sooho Chae, Kyoungho Kim, and In-Chul Back

**Abstract** The open-deck steel plate girder bridge in service has been an issue due to noise and vibration as well as its damage-prone structural characteristics of direct connection between a bridge beam and a track panel. Recently in Korea, to cope with the issue, a more economical method of installing CWR (Continuous Welded Rail) is being conducted using a stiffer sleeper-beam fastener installation, appropriate support arrangement and bridge substructure reinforcement. In this paper, using the finite element multibody dynamic analysis technology, running safety analysis is conducted considering track irregularities, and the appropriateness of the current track geometry standards is reviewed. The dynamic analysis is performed using commercial programs, ABAQUS and VI-Rail. A 30 m long open-deck plate girder bridge is utilized in the analysis. From the analysis, it is observed that the modification of the current geometry standard on track irregularities needs be considered.

**Keywords** Open-deck steel plate girder bridge · Finite element multibody dynamics · Track irregularity · CWR

### 24.1 Introduction

As metropolitan area expands, demands for less noise and more pleasant environment is arising. Due to the energy-efficient and mass-transport characteristics, more and more cities and countries adopt the railroad as their solution for traffic problems. The open-deck steel plate girder bridge has been built as a more economic railroad bridge type, and still in use in many countries. However, the open-deck steel bridge has its own problem of generating high-level noise and impact, and providing less lateral stiffness [1]. Recently, researches on installing CWR to the open-deck steel bridge are being conducted [2], but little research attention has been paid to how to maintain track geometries on the bridge considering its weaker lateral stiffness.

In this paper, the finite element multibody dynamic analysis is conducted to identify the appropriateness of the current track maintenance standard. Commercial programs the ABAQUS and the VI Rail are utilized for the purpose of the study. One of the most utilized trains in Korea, i.e., the Semaetul train, is used in the analysis. The train and track irregularities including twist, gauge, alignment, cross level and longitudinal level are simulated using the VI Rail, and a simply-supported open-deck bridge with 30 m length is modeled using the ABAQUS. The vehicle responses when passing the track with irregularities on the bridge, on the flexible ballast and on the rigid ground are compared each other, and, based on the lateral force, the derailment coefficient, and the bogie acceleration, the appropriateness of the current track geometry standards is assessed.

---

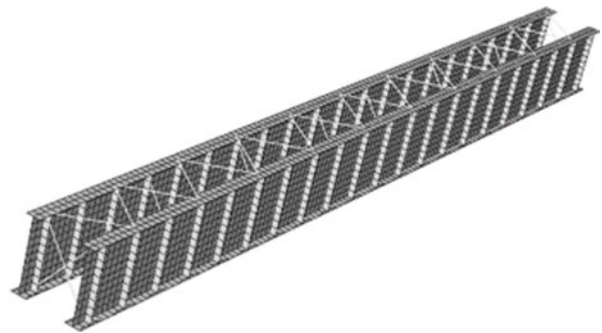
S. Choi (✉) · S. Chae  
School of Railroad Engineering, Korea National University of Transportation, Uiwang, South Korea  
e-mail: [schoi@ut.ac.kr](mailto:schoi@ut.ac.kr)

K. Kim  
Abest Co., Seoul, South Korea

I.-C. Back  
Korail Co., Daejeon, South Korea

**Table 24.1** Track geometry maintenance limits (unit, mm)

Limit values	Longitudinal	Alignment	Gauge	Cross level	Twist
Construction (CV)	4	4	5	3	3
Target (TV)	5	5	11	5	5
Warning (WV)	13	12	17	10	10
Action (AV)	19	16	30	20	15
Speed reduction (SV)	26	22	35	–	21

**Fig. 24.1** Numerical model for a 30 m long open deck steel railway bridge

## 24.2 Background

The current track geometry maintenance standards is summarized in Table 24.1, which are categorized to five maintenance limits, i.e., construction, target, warning, action and speed reduction limits. Recently, Coudert et al. [3] conducted a study for relaxation of geometry standards of France, but little research result has been reported on a track of the open deck steel railroad bridge. Note that, in Table 24.1, the abbreviations for maintenance limits are provided.

## 24.3 Analysis

For the purpose of the analysis, an open-deck steel plate girder bridge is modeled using the ABAQUS. The simply-supported bridge with a length of 30 m is modeled using shell and beam elements, as shown in Fig. 24.1. The modal parameters of the bridge is then transferred to the VI Rail, which simulates train running and track irregularities. The vehicle responses including lateral force, derailment coefficient, and bogie acceleration are assessed for tracks on the bridge, on the flexible ballast and on the rigid ground. The train speed is simulated as 80 km/h and the wavelength of all track irregularities is 10 m. The allowable values of the vehicle response are determined based on the UIC 518 [4].

The analysis results are depicted in Figs. 24.2, 24.3, 24.4, 24.5, and 24.6. For longitudinal level irregularity in Fig. 24.2, the vehicle responses of three cases are similar and much smaller than the UIC 518 limits. However, for alignment irregularity in Fig. 24.3, the vehicle responses on the track on the open-deck steel bridge rapidly increase at SV. For track gauge irregularity, as shown in Fig. 24.4, the vehicle responses on the track of the open-deck steel bridge are far greater than the other tracks. Notably, the derailment coefficient increases greater than the UIC 518 limit at SV. For cross level and twist irregularities, the vehicle responses of three track cases are similar and much smaller than the UIC 518 limit, as presented in Figs. 24.5 and 24.6.

## 24.4 Conclusion

In this paper, the vehicle responses of three track types, on the open-deck bridge, on the flexible ballast, and on the rigid ground with irregularities are assessed and compared using the finite element multibody dynamic simulation. Based on the analysis results, the following conclusions can be drawn.

- Based on much less vehicle responses, reducing the track irregularity limits for longitudinal, cross level and twist needs to be considered.

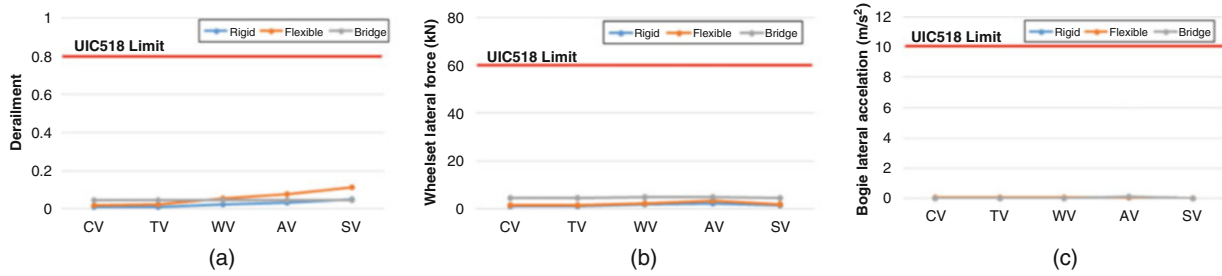


Fig. 24.2 Maximum vehicle response for longitudinal level irregularity. (a) Derailment coefficient. (b) Lateral force. (c) Bogie acceleration

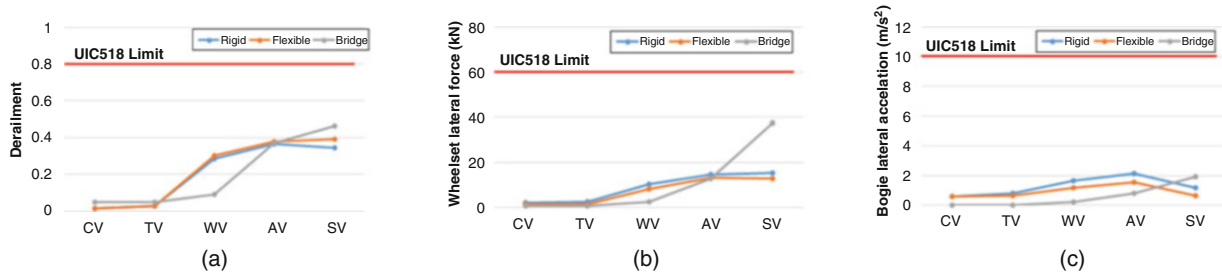


Fig. 24.3 Maximum vehicle response for alignment irregularity. (a) Derailment coefficient. (b) Lateral force. (c) Bogie acceleration

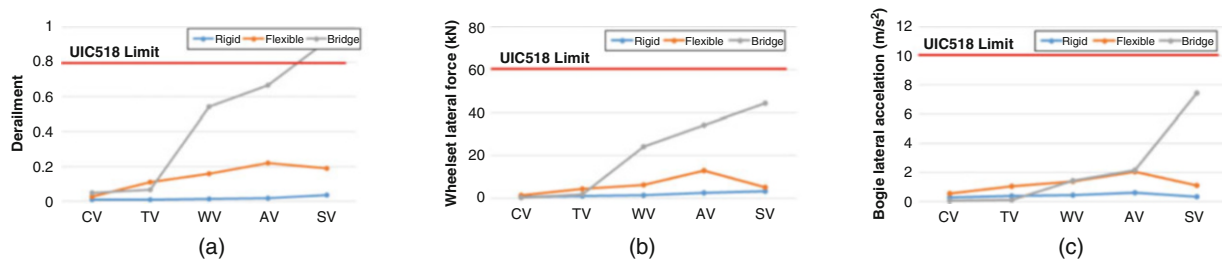


Fig. 24.4 Maximum vehicle response for track gauge irregularity. (a) Derailment coefficient. (b) Lateral force. (c) Bogie acceleration

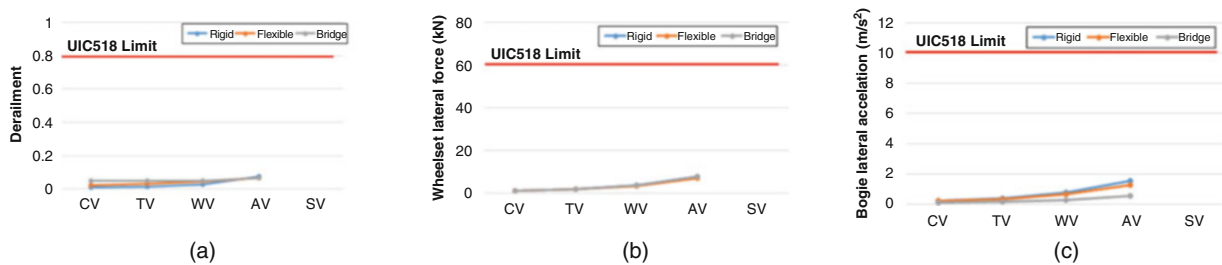


Fig. 24.5 Maximum vehicle response for cross level irregularity. (a) Derailment coefficient. (b) Lateral force. (c) Bogie acceleration

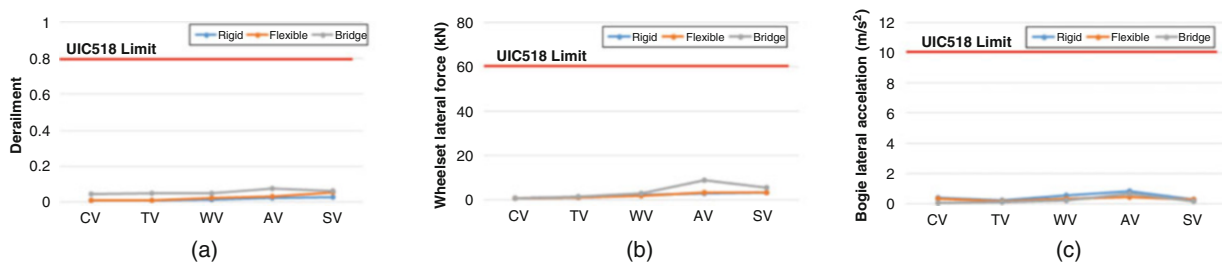


Fig. 24.6 Maximum vehicle response for twist irregularity. (a) Derailment coefficient. (b) Lateral force. (c) Bogie acceleration

- For alinement and track gauge standard, vehicle responses for a track on the open-deck steel bridge become much greater than other two track cases.
- Based on the vehicle response for alinement and track gauge, track geometry standard of the open-deck bridge for the two irregularities may need to be modified.

**Acknowledgements** This research was supported by a grant (18RTRP-B137866-02) from Railroad Technology Research Program funded by Ministry of Land, Infrastructure and Transport of Korean government.

## References

1. Chae, S., Yoo, Y., Park, Y., Choi, S.: Dynamic response analysis of a ballastless steel plate girder bridge due to a rail joint. *J. Kor. Soc. Railw.* **21**(11), 1–12 (2018)
2. Chae, S., Yoo, Y., Lim, C., Choi, S.: Applicability analysis of a continuous welded rail construction method on an open deck steel railway bridge using displacement control. *J. Kor. Soc. Railw.* **22**(2), 158–168 (2019)
3. Coudert, F., Causse, J., Kraft, S.: Optimization of track maintenance standards based on simulation. In: *World Congress on Railway Research* (2013)
4. UIC 518: Testing and approval of railway vehicles from the point of view of their dynamic behavior safety – track fatigue – ride quality, 4th edn, UIC (Union Internationale des Chemins de fer, International Union of Railways), Paris, France (2009)



# Chapter 25

## Influence of State-Switching Rotational Inertia Dampers on the Natural Frequencies and Response of Structures

Abdollah Javidialesaadi and Nicholas Wierschem

**Abstract** Rotational inertia dampers have been proposed as passive vibration absorbers. Traditional rotational inertia dampers come in different configurations, but all feature a mechanical device called an inerter. The inerter is a two terminal device that can produce a large effective mass via the transformation of translational motion to the rotation of a flywheel. Despite the effectiveness of rotational inertia dampers at reducing the response of structures, their use has potential drawbacks. The inerter increases the effective mass of a system and, therefore, reduces the natural frequencies of that system; this shift in natural frequency is not always desirable. Furthermore, energy that is transferred to the inerter as rotational kinetic energy is transferred back to the structure when the structure's motion slows, which can drive the response of the structure. To address these issues, one-way rotational inertia dampers have recently been proposed and investigated. In the one-way rotational damper, energy is transferred to a flywheel as rotational kinetic energy in a manner in which it cannot transfer back to the structure. In addition, the one-way rotational damper is not always engaged with the structure; thus, the effective mass of the system changes during its response. Due to these changes, also known as state-switching, it is not straightforward to evaluate the response of the system or its effective frequency. In this study, the effect of the one-way rotational inertia damper on the frequency and response of the base structure is investigated with numerical analyses.

**Keywords** Passive control · Rotational inertia damper · Resonance frequency

### 25.1 Introduction

The inerter is a two terminal mechanical device featuring a rotational inertia mass that can produce an equal and opposite force proportional to the relative acceleration between its terminals [1]. Inerters have been studied to increase the effectiveness of mass dampers, including the tuned mass damper (TMD) [2], three element vibration absorber [3], and nonlinear energy sink [4]. The rotational inertia viscous damper (RIVD), which consists of an inerter with a flywheel that rotates in a viscous material, has been proposed and used for control of single-degree of freedom (SDOF) structures [5]. Despite the effectiveness of devices like the RIVD at reducing the dynamic response of structures, these devices have drawbacks including that energy can transfer back to the structure from them and that the use of these devices results in significant, and undesirable at times, shifts in the natural frequencies of the structures they are utilized in [6]. To improve the RIVD, the one-way rotational inertia damper has been proposed recently as an effective alternative [7]. While the RIVD is based on the traditional inerter, the one-way rotational inertia damper is based on a one-way mechanism that switches between states where the device's flywheel is engaged and not engaged. This study investigates the effect that state-switching in a one-way rotational inertia damper has on the resonance frequency of the SDOF structure it is attached to.

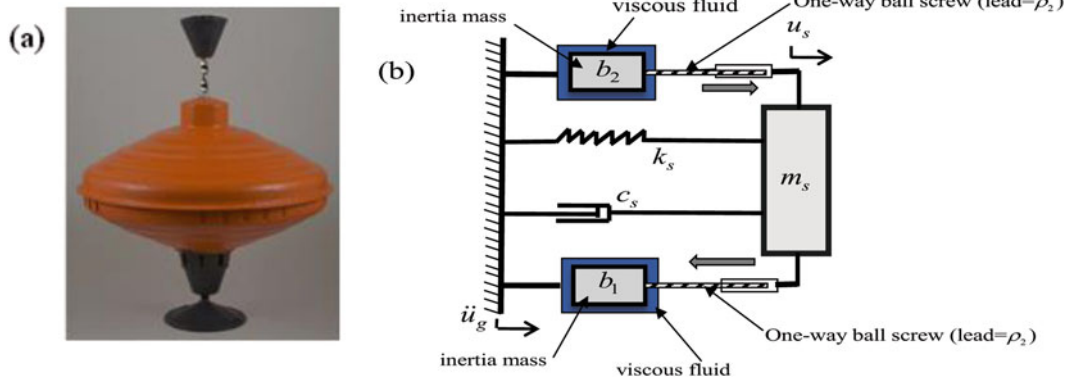
### 25.2 One-Way Rotational Inertia Damper

A spinning top toy, Fig. 25.1a, presents a physical realization of the state switching one-way rotational inertia damper. When the shaft is pushed down with a resulting velocity at an interaction point higher than that of the rotational mass, the rotational

---

A. Javidialesaadi (✉) · N. Wierschem  
Department of Civil and Environmental Engineering, The University of Tennessee, Knoxville, TN, USA  
e-mail: [ajavidia@vols.utk.edu](mailto:ajavidia@vols.utk.edu); [nwiersch@utk.edu](mailto:nwiersch@utk.edu)





**Fig. 25.1** (a) Spinning top toy as a physical realization of the one-way state switching device, (b) dynamic model of SDOF structure with one-way state switching dampers

mass will increase in rotational velocity. In all other cases, including whenever the shaft moves up, the rotational mass does not engage and spins freely. Figure 25.1b shows a SDOF system with two one-way rotational inertia dampers. The structural mass, stiffness and damping are equal to  $m_s$ ,  $k_s$ , and  $c_s$ , respectively.  $b_1$  and  $b_2$  denote the inertia of each rotational inertia damper,  $D_1$  and  $D_2$  are the device's damping coefficients, and  $\rho_1$  and  $\rho_2$  are the leads of the ball screws.

The equation of motion of the system when each of the inertia masses are engaged can be expressed as follows:

$$\left(m_s + J_i \frac{4\pi^2}{\rho_i^2}\right) \ddot{u}_s + D_i \frac{4\pi^2}{\rho_i^2} \dot{u}_s + k_s u_s = -m_s \ddot{u}_g \quad (i = 1, 2) \quad (25.1)$$

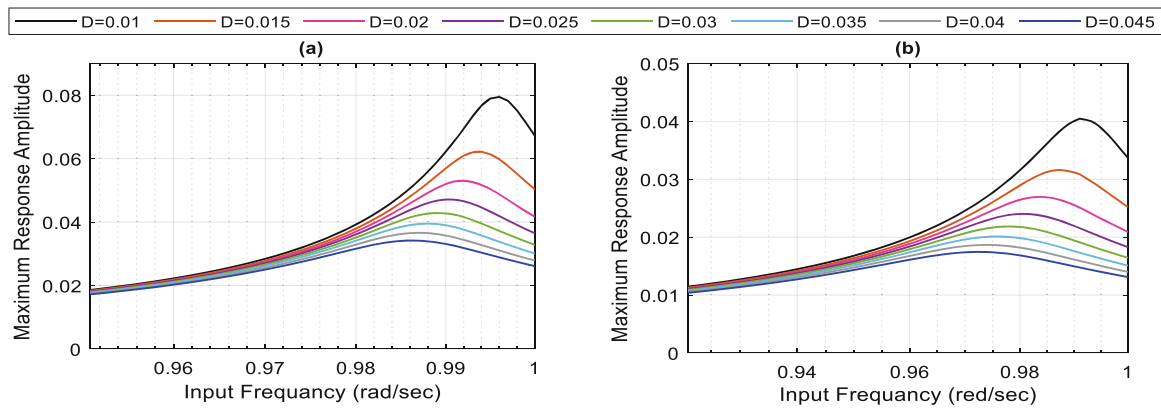
where  $J_i$  represent the moment of inertia of the inertia mass. The equation of motion of the damper when it is not engaged to the structure can be expressed as follows:

$$J_i \ddot{\theta} + D_i \dot{\theta} = 0 \quad (i = 1, 2) \quad (25.2)$$

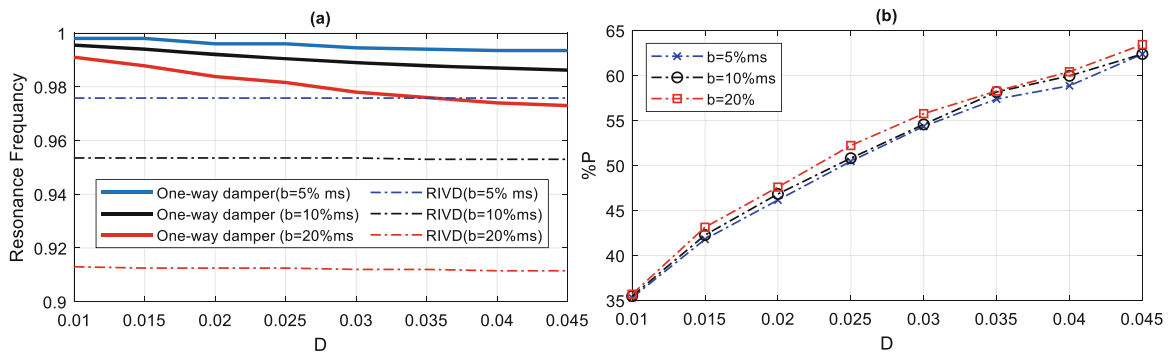
where,  $\theta$  is the rotation angle of the rotational mass.

### 25.3 Analysis and Results

To show the effect of the one-way rotational inertia damper on the resonance frequency of an undamped SDOF structures with  $m_s = k_s = 1$ , the frequency response of the SDOF structure with different inertia mass ( $b_1 = b_2$ ,  $b = b_1 + b_2$ ) and damping coefficient ( $D$ ) are investigated. These resonance frequencies are obtained by identifying the resulting maximum displacement of steady state response from a series of numerical analyses in which a harmonic load is applied to the system with a range of excitation frequencies. Figure 25.2 shows the results of this analysis. These results show that, in the cases of 10% and 20% rotational inertia mass, the resonance frequency and amplitude decrease with increases in the damping. In addition, at a given level of damping, the resonance frequency decreases with increasing rotational inertia mass ratio. Figure 25.3a shows the effect of the inertia mass and damping level of the RIVD and the one-way rotational inertia damper on the resonance frequency of a SDOF structure. As shown in this figure, when a RIVD is used with a SDOF structure, increasing the inertia mass ratio of the device significantly decreases the system's resonance frequency. Meanwhile, increasing the damping level and inertia mass in the one-way rotational inertia damper decreases the resonance frequency, but this reduction is not as significant as in the RIVD case. Considering the percentage of time when the structure is engaged to the rotational inertia mass as (P), Fig. 25.3b shows the effect of the level of the damping on the percentage of time which the inertia mass and structure are engaged. It is found that the percentage of time engaged increases as the damping is increased.



**Fig. 25.2** Frequency response of SDOF structure with one-way rotational inertia damper with (a)  $b = 0.1m_s$  (b)  $b = 0.2m_s$



**Fig. 25.3** (a) Effect of damping and inertia mass ratio on the resonance frequency of the RIVD and one-way rotational inertia damper (b) Effect of the level of the damping on the percentage of time that the inertia mass of the one-way rotational inertia damper and structure are engaged

## 25.4 Conclusion

In this study, the effect of the level of inertia mass and damping on the resonance frequency of a SDOF structure controlled with a one-way rotational inertia damper is investigated. It was found that increasing the level of damping leads to a reduction in the resonance frequency of the structure. In addition, increasing the inertia mass decreases the resonance frequency slightly in the one-way rotational inertia damper, while it leads to significant reductions in the resonance frequency in the case of the RIVD. It was also found that by increasing the damping of the one-way rotational inertia damper, the percentage of engagement of this device with the structure increases significantly; however, significant engagement does not correlate with significant changes in natural frequency.

## References

1. Smith, M.C.: Synthesis of mechanical networks: the inerter. *IEEE Trans. Autom. Control.* **47**, 1648–1662 (2002). <https://doi.org/10.1109/TAC.2002.803532>
2. Marian, L., Giaralis, A.: Optimal design of a novel tuned mass-damper–inerter (TMDI) passive vibration control configuration for stochastically support-excited structural systems. *Probab. Eng. Mech.* **38**, 156–164 (2014). <https://doi.org/10.1016/j.probengmech.2014.03.007>
3. Javidialesaadi, A., Wierschem, N.E.: Three-element vibration absorber–inerter for passive control of single-degree-of-freedom structures. *J. Vib. Acoust.* **140**, 11 (2018). <https://doi.org/10.1115/1.4040045>
4. Javidialesaadi, A., Wierschem, N.E.: An inerter-enhanced nonlinear energy sink. *Mech. Syst. Signal Process.* **129**, 449–454 (2019). <https://doi.org/10.1016/j.ymssp.2019.04.047>
5. Hwang, J.-S., Kim, J., Kim, Y.-M.: Rotational inertia dampers with toggle bracing for vibration control of a building structure. *Eng. Struct.* **29**, 1201–1208 (2007). <https://doi.org/10.1016/j.engstruct.2006.08.005>
6. Chen, M.Z.Q., Hu, Y., Huang, L., Chen, G.: Influence of inerter on natural frequencies of vibration systems. *J. Sound Vib.* **333**, 1874–1887 (2014). <https://doi.org/10.1016/j.jsv.2013.11.025>
7. Javidialesaadi, A., Wierschem, N.E.: Energy transfer and passive control of single-degree-of-freedom structures using a one-directional rotational inertia viscous damper. *Eng. Struct.* **196**, 109339 (2019). <https://doi.org/10.1016/j.engstruct.2019.109339>

# Chapter 26

## Towards Population-Based Structural Health Monitoring, Part VI: Structures as Geometry



Keith Worden

**Abstract** One of the requirements of the population-based approach to Structural Health Monitoring (SHM) proposed in the earlier papers in this sequence, is that structures can be represented by points in an abstract space. Furthermore, these spaces should be metric spaces in a loose sense; i.e. there should be some measure of distance applicable to pairs of points; similar structures should then be ‘close’ in the metric. This geometrical structure is not enough for the framing of problems in data-based SHM, as it leaves undefined the notion of feature spaces. Interpreting the feature values on a structure-by-structure basis as a type of field over the space of structures, it seems sensible to borrow an idea from modern theoretical physics, and define feature assignments as sections in a vector bundle over the structure space. With this idea in place, one can interpret the effect of environmental and operational variations as gauge degrees of freedom, as in modern gauge field theories. One can then regard data normalisation procedures like cointegration as gauge-fixing operations. This paper will discuss the various geometrical structures required for an abstract theory of feature spaces in SHM, and will draw analogies with how these structures have shown their power in modern physics.

**Keywords** Population-based structural health monitoring ((PB)SHM) · Differentiable manifolds · Fibre bundles · Confounding influences

### 26.1 Introduction

This paper is the sixth in a sequence devoted to introducing new technology for *Population-based Structural Health Monitoring* (PBSHM) [1–5]. The aim of the new technology is to facilitate the principled transfer of information between disparate structures, specifically for SHM diagnostic purposes. In the first paper, the idea of a *homogenous population* (Hom-P) was introduced, and the concept of the *form* appeared as a means of representing populations of nominally-identically structures [1]. The next papers in the sequence introduced the more challenging *heterogeneous population* (Het-P), in which the population is formed of disparate structures [2–4]. In order to impose some mathematical order on the Het-P, the Irreducible Element (IE) model and its associated Attributed Graph (AG) were introduced as abstract representations of structures, with the population then taking the form of a complex network [2, 3]. In this framework, the physical structures of interest appear as points in a (mathematically) structured set, which has metric properties which allow a judgement of the closeness of resemblance of the physical structures. This metric is a key element in deciding whether two structures are ‘close’ enough to allow the transfer of diagnostic information or capability [4].

In reality, the ‘transfer’ of information will take the form of maps and associations between the feature spaces associated with the SHM problem specified for the structures. The feature spaces themselves will usually be vector spaces. In abstract terms, one might think of the population itself as having a total feature space, which is the union of all the individuals. In rough terms, one can think of this object as a type of vector bundle [6, 7] over the space of structures, with ‘transfer’ being a map within the bundle space. The aim of the current paper is to look at whether this level of abstraction is sensible – or even possible – and to speculate on whether it might bring practical benefits for PBSHM.

Vector bundles, or more generally fibre bundles, most often appear in algebraic or differential geometry, and are often constructed from *differentiable manifolds*, which are spaces where notions of smoothness and differentiability – the ability to meaningfully do calculus – are important. The ‘spaces’ of structures mentioned above, the complex networks of attributed

---

K. Worden (✉)

Department of Mechanical Engineering, Dynamics Research Group, University of Sheffield, Sheffield, UK  
e-mail: [k.worden@sheffield.ac.uk](mailto:k.worden@sheffield.ac.uk)

graphs, do not have such properties of smoothness; however, in order to explore the possibility of using fibre bundles in PBSHM, the discussion here will begin with some problems in structural dynamics in which the spaces of structures are indeed manifolds. This will lead to the idea of feature spaces as bundles above manifolds, and then finally to the general mathematical structures of interest in PBSHM.

The layout of the paper is as follows. Section Two will provide basic introductions to fibre bundles, while Section Three will provide some examples of how fibre bundles might arise in structural dynamics. Section Four introduces the idea of feature spaces as vector bundles and Section Five extends the discussion to include confounding influences and data normalisation. Section Six discusses how the feature bundles might arise in the context of spaces of structures for PBSHM, and the paper then concludes.

## 26.2 Fibre Bundles

The basic idea of the fibre bundle is explained well in [6]; however, only really the definitions are covered. The two ‘classic’ mathematical texts are [8] and [9]; however, these are more concerned with topology than geometry. A more geometrical classic is the two-volume [10], which is particularly detailed on connections on bundles, which are essential in discussing differentiation. The survey paper [11] is a wonderful resource and serves as an introduction to how many aspects of differential geometry are used in gravitational physics and gauge theories. A more modern text on gauge theories, which also manages to be very readable is [7]. The material presented requires an understanding of some basic ideas of topology and geometry, particularly in relation to *differentiable manifolds*. For convenience, a very limited summary is given in the appendix here.

### 26.2.1 Fibre Bundles: Basic Definitions

A fibre bundle is fundamentally composed of two objects: a *base manifold*  $M$  (e.g. spacetime), and a *total manifold*  $E$ , which essentially contains the ‘fields on  $M$ ’. In order that movement on the base manifold induces movement in the total manifold, the two manifolds need to be glued together, and this is accomplished by means of a projection  $\pi$  which is a map from  $E$  to  $M$ . Now, thinking in terms of the number of components one needs to specify for a vector field, it is clear that  $E$  must have a *higher dimension* than  $M$ . This in turn means that the inverse map  $\pi^{-1}(x)$  at any point  $x \in M$  must be multi-valued. The first requirement in defining a fibre bundle  $\pi : E \rightarrow M$  is that all the sets  $\pi^{-1}(x) = F_x \in E$  are all homeomorphic to each other; these sets are denoted  $F$  and termed *the fibre above  $x$* .

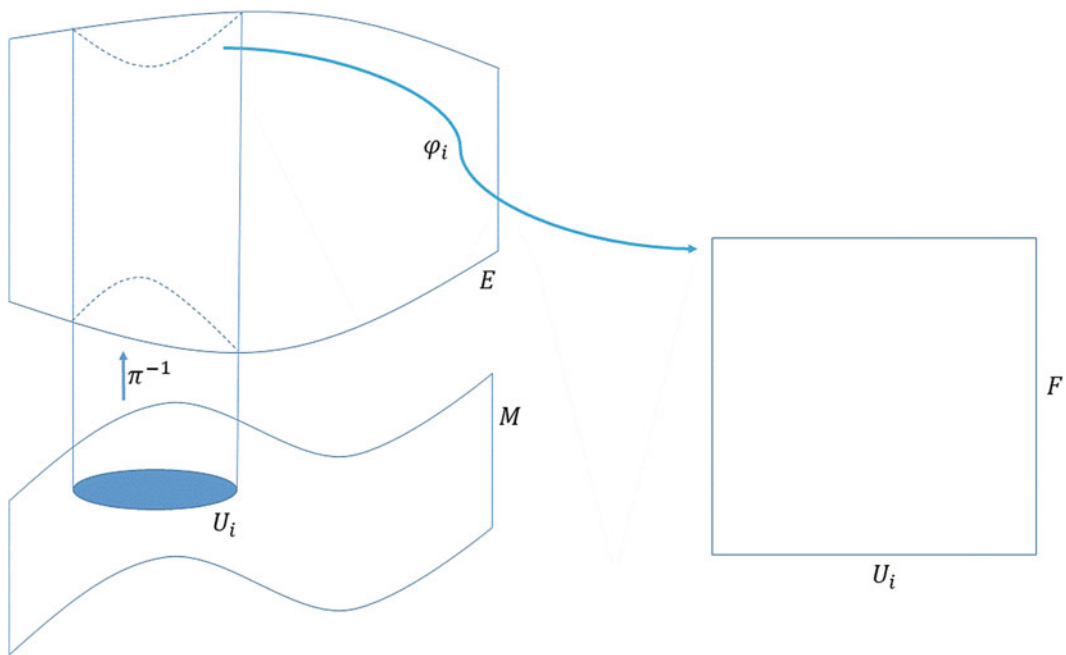
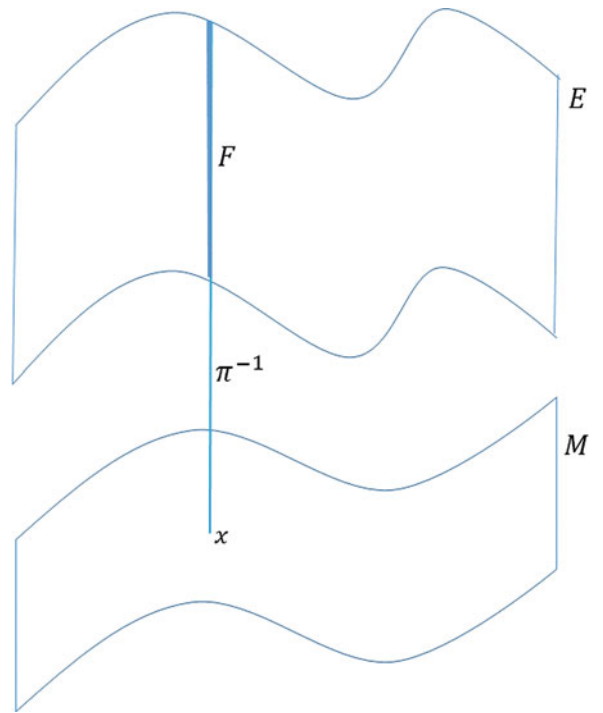
So far, the fibre bundle could be defined as the set of objects  $\{M, E, \pi, F\}$  as depicted in Fig. 26.1; however, one needs a little more precision. If there is a copy of  $F$  above each point of  $M$ , a simple way to define  $E$  would be as the Cartesian product  $M \times F$ , then the projection is simply  $\pi(x, f) = x$  and one obtains  $\pi^{-1}(x) = F$ , exactly as required. However, there is no new structure here, it really is just a Cartesian product, and one can allow  $E$  to have much more general structures by using the same kind of trick that allowed the definition of a manifold in the first place (see Appendix A). Suppose that one is working within a specific coordinate domain  $U$  on  $M$ , there is then the local homeomorphism into  $\mathbb{R}^n$  (where  $n$  is the dimension of  $M$ ). To mimic all of the appropriate flat-space vector calculus, one can assume that  $\pi^{-1}(U) = U \times F$  locally, but as in the case of  $M$  itself, one does not have to assume that the single homeomorphism extends across all  $M$  e.g.  $\pi^{-1}(M) \neq M \times F$ .

In fact, in much the same way that a manifold is only *locally homeomorphic* to  $\mathbb{R}^n$  (Appendix A), one can require that the total space  $E$  is only *locally homeomorphic* to the product space. One extends the definition of the bundle to the set of objects  $\{M, \{U_i\}, E, \{\varphi_i\}, \pi, F\}$  where  $\{U_i\}$  is a coordinate atlas on  $M$  and for each  $U_i$  on  $M$ ,  $\varphi_i$  is a homeomorphism (Fig. 26.2),

$$\varphi_i : \pi^{-1}(U_i) \rightarrow U_i \times F \quad (26.1)$$

In reality, things are a little more complicated. In much the same way that coordinate patches have to glue together in a particular way in order to respect the topology of a manifold, via appropriately smooth changes of coordinates, the locally-trivial regions of the fibre bundle need to be glued together; this is accomplished by means of *structure functions*. The structure functions do not play a role in the following discussion, in order to find out more, the reader can consult [11].

**Fig. 26.1** Schematic of basic objects in a fibre bundle



**Fig. 26.2** Local triviality property in a fibre bundle

At this point, one can define the objects that correspond to ‘fields’ in the theory. Supposing the base manifold to be spacetime, a vector field (for example), would be the assignment of a single vector to each point in spacetime. If the fibre space is a vector space of the appropriate dimension, a vector field is thus a map from points  $x$  in the base manifold, to points in the fibres above  $x$ . Such maps  $s(x) \in F$  are called *sections* and are defined by the condition  $\pi(s(x)) = x$  or alternatively by  $\pi \circ s = Id$ . Clearly, this definition is too general as it stands, so it is always supplemented by conditions on the map like smoothness of some degree. According to these ideas, a vector field is a section of the tangent bundle.

When the fibre is a vector space, the origin of the space is a special point and thus generates a special section – the *zero section* – when the image of  $s(x)$  in each fibre is the origin [11].

### 26.3 Some Fibre Bundles in Structural Dynamics

Fibre bundles have been used extensively in the past in the mathematical theory of nonlinear dynamics [12] and in gauge theories of particle physics [7]. However, they have not really featured in structural dynamics at all. The purpose of this section will be to show that some problems in structural dynamics can be framed in terms of bundles; in particular, some of the structures that would appear to be desirable from the point of view of population-based Structural Health Monitoring (PBSHM) have abstract formulations in those terms [1–4]. One of the main aims of PBSHM is to allow the transfer of SHM inferences between different structures, in situations where data for training machine learners are available for some structures – *source structures* – but not others – *target structures* [4]. A mathematical formulation of PBSHM can be defined in terms of an abstract representation of structures, as discussed in [2, 3]. One way to build such a representation theory would be to have the structures of interest as *points in a space of structures*; the feature data that are then used for inference can be envisaged as points in a bundle space over the space of structures. As will be seen later, this may require quite a lot of generalisation, as the ‘space of structures’ might not be a manifold.

To provide an illustration of the use of bundles, one can consider the simplest dynamical situation possible – the Single-Degree-of-Freedom (SDOF) oscillator, governed by the equation of motion,

$$m\ddot{y} + c\dot{y} + ky = 0 \quad (26.2)$$

for the situation of unforced or free motion. This ‘structure’ is uniquely fixed by the values of  $m$ ,  $c$  and  $k$ , so the space of structures is simply  $S = \mathbb{R}^3$  with points  $(m, c, k)$ . Furthermore, on physical grounds, all the parameters have to be positive, so in fact the appropriate space is  $S = \mathbb{R}_+^3$ , which is a manifold with boundary.

Consider now, what sort of physics one might be interested in analysing. In this case, an obvious choice is the *free decay* of the system when it is displaced from the origin and released. If the initial condition for the motion is  $(Y_0, 0)$ , the subsequent motion is described by [13],

$$y(t) = Y_0 e^{-\zeta \omega_n t} \cos(\omega_d t) \quad (26.3)$$

where the *damping ratio*  $\zeta$  is defined by,

$$\zeta = \frac{c}{2\sqrt{mk}} \quad (26.4)$$

the *undamped natural frequency*  $\omega_n$  by,

$$\omega_n = \sqrt{\frac{k}{m}} \quad (26.5)$$

and the *damped natural frequency*  $\omega_d$  by,

$$\omega_d^2 = \omega_n^2 (1 - \zeta^2) \quad (26.6)$$

Now, the important quantities in equation (26.3) are all *ratios* of the physical quantities  $(m, c, k)$ , so transforming the point to the scaled quantity  $(m\alpha, c\alpha, k\alpha)$ , where  $\alpha \in \mathbb{R}$ , produces a different equation of motion,

$$m\alpha\ddot{y} + c\alpha\dot{y} + k\alpha y = 0 \quad (26.7)$$

but *does not change the observed physics* of the free decay. This is true even if  $\alpha < 0$ . It would appear sensible to rule this out on physical grounds, so in fact one restricts to  $\alpha \in \mathbb{R}_+$ . Now,  $\mathbb{R}_+$  is actually a *group* under multiplication, where the defining properties of a general group are as follows [14].

A group  $G$  is a set of objects  $g$ , with a multiplication operator  $\times$ , such that:

1.  $G$  is *closed* under the operation  $\times$  i.e. if  $g_1, g_2 \in G$  then  $g_1 \times g_2 \in G$ .
2.  $G$  contains a unique *identity*  $e$  such that  $e \times g = g \times e = g \quad \forall g \in G$ .
3. For each  $g \in G$ , there is an *inverse*  $g^{-1}$  such that  $g \times g^{-1} = g^{-1} \times g = e$ .

Where there is no ambiguity, the  $\times$  operator will be omitted from equations as in normal multiplication.

Now an *action*  $A$  of the group  $G$  on a space  $X$  is defined as a map,

$$A : G \times X \longrightarrow X \quad (26.8)$$

So, what has been defined in the space  $S$  above is a *right action* of the group  $G = \mathbb{R}_+$  via  $(m, c, k) \longrightarrow (m\alpha, c\alpha, k\alpha)$ . Furthermore this action of the group *leaves the observed physics of interest unchanged*. Following the definitions in particle physics, one can say that  $S$  is *gauge invariant* under the action of the *gauge group*  $\mathbb{R}_+$ .

Now, as far as the physics is concerned, there is considerable redundancy in the definition of  $S$ , the space can be simplified accordingly. It is easy to see that, by scaling  $y$  and  $t$  in equation (26.2), the equation can be transformed into,

$$\ddot{y} + 2\zeta\dot{y} + y = 0 \quad (26.9)$$

which one can regard as the *canonical representation* of an SDOF system. Obviously, many systems can share the same canonical representation.

Unfortunately, this doesn't amount to a simple coordinate transformation on  $S$ ; however, it can be made into one by going to three scaling parameters  $(\alpha, \beta, \gamma)$  which are elements of the group  $\mathbb{R}_+^3$ , and defining the action of the group via  $(m, c, k) \longrightarrow (m\alpha, c\beta, k\gamma)$ . Note that the  $\alpha, \beta$  and  $\gamma$  are not independent, but are related by the scaling parameters for  $y$  and  $t$ . With a single scaling parameter  $\alpha$ , the best one can do in simplifying equation (26.2), is to reduce it to,

$$\ddot{y} + 2\zeta\omega_n\dot{y} + \omega_n^2 y = 0 \quad (26.10)$$

One can now think in terms of a right action of  $\mathbb{R}_+^3$  on  $S$  which leaves the physics invariant, so the gauge group is  $\mathbb{R}_+^3$ <sup>1</sup> This leads to the first example of a fibre bundle in dynamics (Fig. 26.3); although not a very complicated one, this is nonetheless interesting as it is also the first example showing spaces of structures, and relationships between them.<sup>2</sup>

In this example, the fibre  $F = \mathbb{R}_+^3$  is actually the gauge group of interest; such a bundle can be referred to as a *principal bundle* [11].

One can also characterise the redundancy in  $S$  in a more geometrical way.

Define the *orbit* of a point  $s = (m, c, k) \in S$  as the set of all points  $s'$  such that  $s' = (m\alpha, c\beta, k\gamma)$  i.e. all the points reachable from  $s$  via the action of  $G = \mathbb{R}_+^3$ .

Now, define an *equivalence relation* on  $S \times S$  as follows.

$\sim$  is an equivalence relation on  $S \times S$  if the following are true:

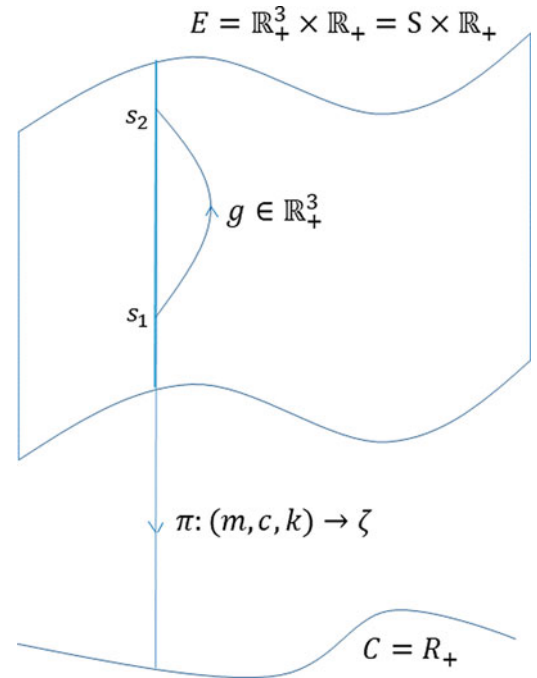
1. *Identity*:  $s \sim s$ .
2. *Reflexivity*:  $s_1 \sim s_2 \implies s_2 \sim s_1$ .
3. *Transitivity*:  $s_1 \sim s_2$  and  $s_2 \sim s_3$  implies  $s_1 \sim s_3$ .

Now, an equivalence class  $[s]$  is defined as the set of all points  $s'$  such that  $s' \sim s$ . The set of equivalence classes is called the *quotient space under*  $\sim$  and is denoted  $S/\sim$ . Under certain specific circumstances, the quotient space inherits the structure of  $S$ , e.g. the quotient space may be a manifold if the original space is. For the sake of simplicity, it will be assumed here that quotient spaces, manifolds, groups etc. are appropriately well behaved.

<sup>1</sup>In fact, things are a little more complicated, because the scaling operations on  $y$  and  $t$  force a condition  $\gamma/\beta = \beta/\alpha$  or  $\alpha\gamma = \beta^2$ .

<sup>2</sup>Note that one should not strictly call the construction in Fig. 26.3 a *vector bundle*, because  $\mathbb{R}_+$  is not a vector space; for all points  $x$  in  $\mathbb{R}_+$  except zero,  $-x$  is not in the space. It is perhaps only a minor abuse to talk of vector bundles because one could always work with the logarithms of the parameters, then they would be in  $\mathbb{R}$ . The  $\alpha$  etc. parameters could also be represented by logarithms; the group would then simply act additively.

**Fig. 26.3** Space of SDOF systems as a bundle over the space of ‘canonical’ representations of SDOF systems



In the space of SDOF structures  $S$ , one can define an equivalence relation such that  $s_1 \sim s_2$  if  $s_1$  is on the same orbit of the group action of  $\mathbb{R}_+^3$  as  $s_2$ . In this case,  $S/\sim \cong C$ , where the symbol  $\cong$  denotes homeomorphism. The orbits of the group action on points in the bundle space are the fibres, so  $S/\sim$  can also be thought of as the set of fibres. The important thing is that  $S/\sim$  has only a single point for all gauge-equivalent structures, so redundancy has again been removed, and it is simpler to work with as a ‘space of structures’.

This construction is an example of *gauge-fixing*. Another way of removing the redundancy would be to work with a single representative sample for each class of gauge-equivalent structures. Such a choice amounts to taking a section of  $E$ ; if the section is continuous, then it will be homeomorphic to  $C$  again.

One can also extend this analysis to Multi-Degree-of-Freedom (MDOF) systems as follows. The general equation for a free (unforced)  $n$ -DOF system is,

$$[m]\{\ddot{y}\} + [c]\{\dot{y}\} + [k]\{y\} = 0 \quad (26.11)$$

where  $[m]$ ,  $[c]$  and  $[k]$  are the  $n \times n$  mass, damping and stiffness matrices respectively.  $[m]$  and  $[k]$  are symmetric, and proportional (Rayleigh) damping,  $[c] = \alpha[m] + \beta[k]$ , will be assumed, so that  $[c]$  will also be symmetric.

The space of structures  $S_n$  will be parameterised by the upper triangles of  $[m]$  and  $[k]$ , so it has dimension  $n(n+1)/2 + n(n+1)/2 = n(n+1)$ .

The first question to address here is, what are the canonical forms here corresponding to those obtained for SDOF systems. Using standard techniques of modal analysis [13] (and assuming Rayleigh damping), one can simultaneously diagonalise  $[m]$ ,  $[c]$  and  $[k]$  using the same diagonalising matrix – the modal matrix  $[\psi]$ . The system of equations in (26.11) is decoupled, and the equations of motion become,

$$m_i \ddot{y}_i + c_i \dot{y}_i + k_i y_i = 0 \quad i = 1, \dots, n \quad (26.12)$$

and the space of these systems is  $\mathbb{R}^{3n}$  and will be denoted  $C'_n$ .

One should note that the columns of  $[\Psi]$  – the *modeshapes* are only unique up to scale. The simplest way to *normalise* is to make the column vectors  $\{\psi_i\}$  have unit length i.e.  $\|\{\psi_i\}\| = 1$ .

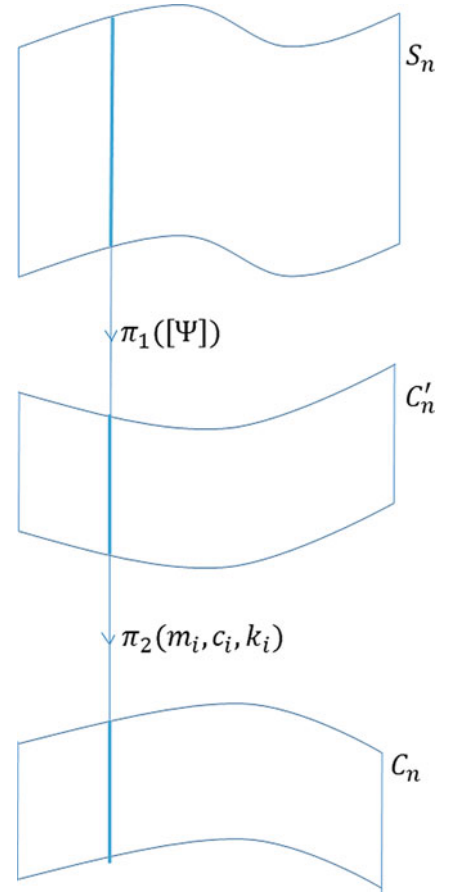
Now, for each of the decoupled equations, one has the same gauge-invariance as in the SDOF case. This means that there is an action of the group  $(\mathbb{R}_+^3)^n = \mathbb{R}_+^{3n}$  on  $C'_n$  which generates the system of equations,

$$\ddot{y}_i + 2\zeta_i \dot{y}_i + y_i = 0 \quad i = 1, \dots, n \quad (26.13)$$



where the  $\zeta_i = c/(2\sqrt{mk})$  are the *modal damping ratios*.<sup>3</sup>

**Fig. 26.4** Sequence of spaces of representation of MDOF systems as vector bundles over the space of ‘canonical’ representations of MDOF systems



This means the space of canonical representations of structures, denoted here by  $C_n$  has dimension  $n$ ; this is the result of factoring through,

$$S_n \xrightarrow{[\Psi]} C'_n \xrightarrow{R_+^{3n}} C_n \quad (26.14)$$

and  $C_n \cong \mathbb{R}_+^n$ .

As before, one has a representation of the sequence of spaces in terms of fibre bundles (Fig. 26.4), where  $\dim(S_n) = n^2 + n$ ,  $\dim(C'_n) = 3n$  and  $\dim(C_n) = n$ .

This is all interesting in terms of representing structures as points in spaces; however, it isn't immediately of use for learning in populations of structures, which is the aim of data-based PBSHM. The next section will consider how fibre bundles can be used to represent collective feature spaces over populations of structures.

<sup>3</sup>If one takes the option of scaling each equation and reparameterising time – which is shared between all the equations – the best one can do in terms of simplification is,

$$\ddot{y}_1 + 2\zeta_1 \dot{y}_1 + y_1 = 0; \quad y_i + 2\zeta_i \omega_{ni} \dot{y}_i + \omega_{ni}^2 y_i = 0 \quad i = 2, \dots, n$$

where  $\omega_{ni} = \sqrt{k_i/m_i}$  is the  $i$ th *undamped natural frequency*.

### 26.4 Fibre Bundles as Feature Spaces Over Populations of Structures

Suppose that one has identified the population of structures of interest and embodied that as a ‘space’ of structures  $S$ . Now, further suppose that the objective is to carry out data-based SHM on and across this space i.e. the ultimate aim will be to allow data-based inferences to transfer between the structures [4]. Each member of the population  $s_i$  will have an associated feature space  $F_i$  (it is serendipitous that one can use the same symbol as for ‘fibre’). For the moment, it will be assumed that all the feature spaces are *dimensionally equivalent* and *physically equivalent*, which means they can all be assigned the same fibre space  $F$ .

To make things specific, it will be assumed that the features in each case are the first four natural frequencies of the structure in question. In this case, one can regard the totality of feature spaces as an  $\mathbb{R}_+^4$  vector bundle over  $S$ . As mentioned earlier, it will not always be possible to insist that  $S$  is a manifold, but this will hold for first simple example here. Assume that  $S$  is the space of cantilever beams made of homogeneous and isotropic materials. In this case, the cantilever is uniquely specified by its physical dimensions (length  $l$ , width  $w$  and thickness  $t$ ), and material constants (density  $\rho$ , Young’s modulus  $E$  and Poisson’s ratio  $\nu$ ), so  $S \cong \mathbb{R}_+^6$ . So  $S$  is again a (flat) manifold with boundary, and the *feature bundle* associated with the problem is as shown in Fig. 26.5.

The first question one might ask is why is a bundle needed, why not a single set of natural frequencies for each  $s \in S$ ? The answer is that the problem of interest is SHM and the features will change as damage occurs; the feature space is needed to cover the range of health states of  $S$ . Again, to make things specific, assume that the damage can be characterised as loss of stiffness, and this can be modelled as loss of Young’s modulus. One defines  $d \in [0, 1]$  such that  $E_d = (1 - d)E$  such that  $d = 0$  corresponds to *normal condition* and  $d = 1$  corresponds to maximal damage. So, the fibre above  $s = (l, w, t, \rho, E, \nu)$  is the set of natural frequencies of all beams with properties  $(l, w, t, \rho, E_d, \nu)$ . Now, the theoretical natural frequencies are actually the solutions to an eigenvalue problem determined by  $s$ , so it is not immediately clear that the fibres will glue together so that the natural frequencies for a given state form a nice section of the bundle.

Before considering this problem a little further, it is necessary to point out another simplification that is implicitly being made here – which is that the features associated with (above a) given structure  $s$  can be considered to be a ‘point’ in  $F$ . In fact, a fundamental part of any data-based SHM strategy is the existence of training data. This means that the feature space above  $s$  will actually contain many points, and there will need to be points for each damage state one seeks to classify. For simplicity again, assume that the SHM problem is *novelty detection* i.e. one seeks only to establish if damage is present within the structure. This is an unsupervised learning problem and can be accomplished if data are known, characteristic of the normal (undamaged) state [15]. A basic outlier analysis would require enough data to construct a sample mean vector

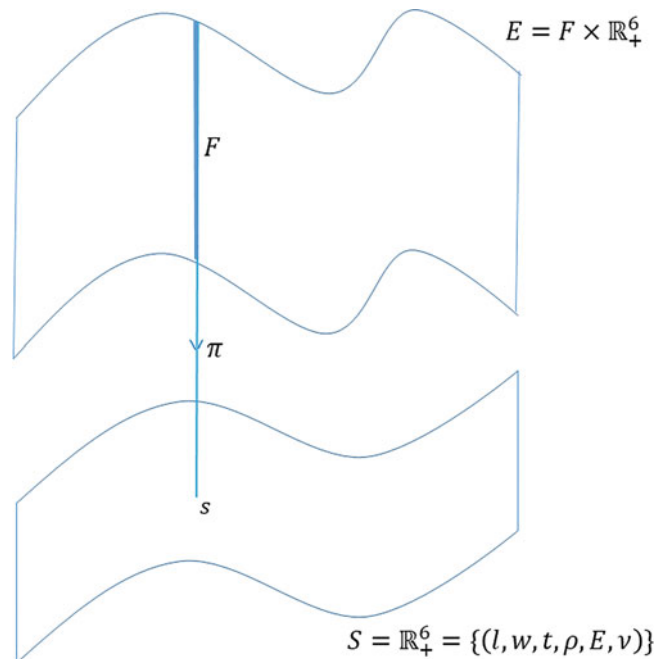
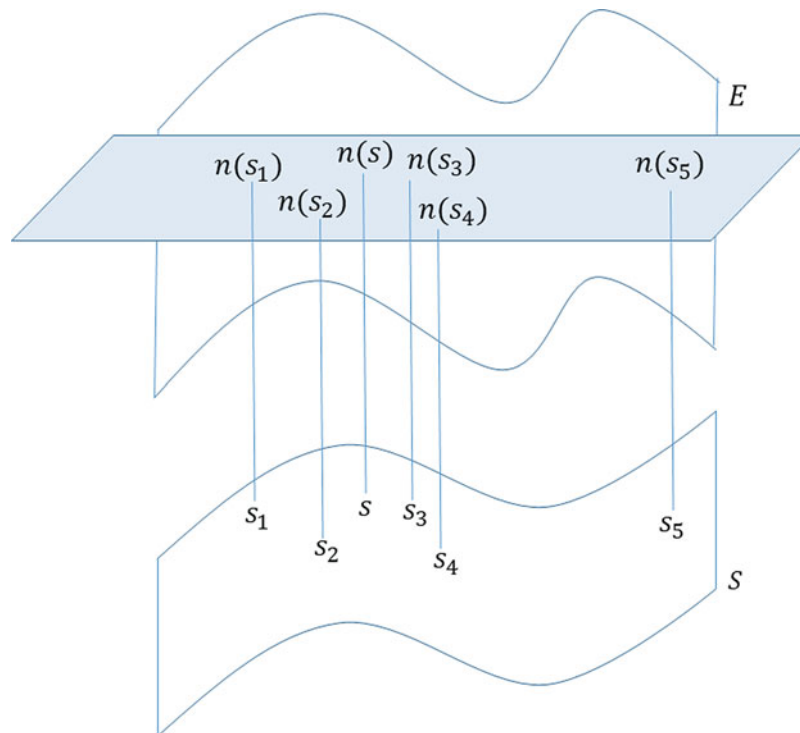


Fig. 26.5 Collected feature spaces across a population of structures  $S$  considered as a vector bundle

for the normal damage features, and a sample covariance matrix. If one then regards the mean and covariance as fixed feature data characteristic of the normal condition, one can regard them as points in an *associated* feature space which contains ‘deterministic’ quantities. If one had a univariate feature space with feature  $x$ , the associated feature space would be parametrised by  $\bar{x}$  and  $\sigma_x$ . The alternative approach would be to take a fully probabilistic view of the bundles, and it is not immediately clear how to accomplish that, although it will be the subject of future research. For the sake of simplifying the geometry here, it will be assumed that a health state of  $s$  will be represented by a single point in the fibre over  $s$ .

This discussion points to the existence of an important, if not critical structure in the problem. If one is to carry out novelty detection at any structure in  $s$ , one needs training data or feature data which characterise the normal condition of  $s$ . Assuming that this can be characterised by a single point, it is clear that the normal condition states over the whole population, determine a section of the feature bundle; this will be referred to as the *normal section* for the population (Fig. 26.6). Another way of characterising the basic damage detection problem boils down to the problem of specifying the normal section across the population from normal condition data measured on only a subset of the population. In the simplest terms, one might regard this as an interpolation problem. In the univariate case discussed above, suppose that the data  $\bar{x}$  and  $\sigma_x$  are known at sufficiently many training structures that the values can be interpolated onto neighbouring structures with no training data; in this case, the interpolated values can be used for outlier analysis when monitored data become available at the structures without training data. Of course, the problems will generally involve multi-class classification, and even novelty detection will need more sophisticated approaches than basic outlier analysis; in these cases, the idea will be to use transfer learning [4]. This discussion raises an important point; while interpolation/transfer might be a powerful tool here, one must be careful not to *extrapolate*. This issue means that any transfer from a structure  $s$  to a ‘neighbouring’ structure  $s'$ , should only be allowed if  $s$  and  $s'$  are *sufficiently close* to each other, as measured in some appropriate metric on  $S$ . All of the spaces of structures discussed so far have been flat, as in fact, have all the bundle spaces, so the standard Euclidean metric could be employed. For more complicated spaces of structures, which may not even be manifolds, it will be necessary to establish a ‘metric’ of some form.

A further remark on interpolation and approximation in curved spaces, is that the derivatives will be covariant derivatives and these will need to be estimated from (potentially sparse) data. There is theory available for such numerical analysis in manifolds, and it is discussed briefly in the context of SHM in [16]. Again, all the bundles discussed here so far have been flat and globally trivial.



**Fig. 26.6** Normal section  $n(s)$  of a feature bundle over a space of structures  $S$ . It is assumed that normal condition data are not known for the point  $s$ . Interpolation/transfer of the normal condition from any neighbouring points  $s_i$  should only be considered if they are sufficient close to  $s$  in some metric on  $S$ . In this diagrammatic example,  $s_5$  might be considered ‘too far away’; for transfer

One can now briefly return to the problem alluded to earlier, that the feature spaces may not glue together nicely to form a bundle with nice sections. Consider the problem of mode-swapping. One normally orders the natural frequencies of a structure in order of magnitude; to simplify matters suppose that there are only two modes: a bending mode and a torsional mode. It may happen, that as one varies the structure  $s$  continuously in  $S$  (i.e. by smoothly varying  $E$  in the case of the cantilever beams), the natural frequencies may cross each other i.e. one might go from the bending mode as lowest frequency, to the torsional mode. If one does not track this bifurcation, and simply keeps the order of frequencies from the eigenvalue problem, the normal section will appear to have a  $C^1$  discontinuity. This exchange of modes could also occur as damage progresses in a single structure  $s$  e.g. in the cantilever case discussed above, as  $d$  is varied. For the moment, it will be assumed that these problems do not occur; feature bundles and the sections of interest will be assumed to be well-behaved. Even if singularities like those mentioned do not cause basic problems with the geometry, they would be likely to cause issues with interpolation/transfer, and should be avoided if possible.

In all the cases considered so far, the overall construction of the bundles is not an issue; this is because they are all trivial bundles i.e. the total spaces are all globally trivial. In fact, all bundles over *contractible* base spaces are trivial [11].<sup>4</sup>

## 26.5 Feature Bundles and Confounding Influences

It is important to discuss how another important issue in SHM might impact on a geometrical formulation, this is the issue of *confounding influences*. In order for feature data to be useful for SHM purposes, it must clearly be sensitive to damage. The natural frequencies discussed so far are candidate features because they are damage sensitive. For example, when a crack grows in a structure, it will reduce the stiffness locally and there may also be friction because of rubbing of the crack interfaces; both of these mechanisms will reduce the natural frequencies. The problem is that many *benign* variations in the operational conditions and/or environment may also reduce the natural frequencies e.g. an increase in temperature, or traffic on a bridge will reduce frequencies. If one is using novelty detection for SHM, one is essentially only looking for changes in the features; if the features change because of benign changes to the environment, one will potentially produce a false alarm for damage. This problem has long been recognised [15], a good review in the context of standard SHM can be found in [17]. In general, one needs to remove the effects of benign variations before applying the diagnostic algorithm, this is a process often called *data normalisation*. In broad terms, one can divide data normalisation algorithms into *subtraction* and *projection* schemes [18].

In order to discuss these matters, the example earlier of the space of cantilever beams will suffice. Suppose that some subset of the properties of the beams are temperature dependent (in fact, they all are). For simplicity, it will be assumed that only the Young's modulus  $E(\theta)$  is a function of the temperature  $\theta$ . In practice the temperature variations will be restricted to some interval  $[\theta_{\min}, \theta_{\max}]$ . If the natural frequencies are now denoted by  $\{f(s)\}$ , it is clear that they will also be functions of  $\theta$ . In fact, because this is an SHM problem, the frequencies are also functions of  $d$ , the damage severity variable. So  $\{f(s)\} = \{f(s, \theta, d)\}$ , by virtue of the fact that  $E = E(s, \theta, d)$ . Now, the points on the normal section of the feature bundle are those points corresponding to  $d = 0$ , but they are still functions of  $\theta$ . When one is measuring features for SHM, the 'physics of interest' is whether the structure is damaged or not; this means that the variations due to temperature (or any other confounding variable) can be regarded as *gauge variations*. The difference here is that one cannot easily assign a group action to the variations; in the first place  $\theta$  takes values on an interval, so can not be given a group structure directly (although one could monotonically transform that range onto the whole of  $\mathbb{R}$ ); secondly, the effect of temperature on the natural frequencies is complicated, so the action will not generally allow an analytical formulation. Putting aside these issues, one can still regard confounding variables as gauge degrees of freedom. Apart from the simplicity of removing gauge variables, they are actually a nuisance in this problem. It is clear that a form of gauge-fixing is needed, and this is essentially what data normalisation is.

One approach to this data normalisation problem in this context, is essentially a subtraction scheme; it assumes that measurements of the temperature are available, so that points  $\{f(s_i, \theta, 0)\}$  are known on some subset of structures  $s_i$ ; if this is the case, one can fit a series of regression models like the linear,

$$\{f(s_i, \theta, 0)\} = \{f(s_i, 0, 0)\} + \{f_1\}\theta + \dots \quad (26.15)$$

<sup>4</sup>A space is contractible, if it can be continuously deformed (shrunk) to a point within the space; this is essentially trivial topology. All  $\mathbb{R}_+^n$  are contractible, as are  $\mathbb{R}^n$ .

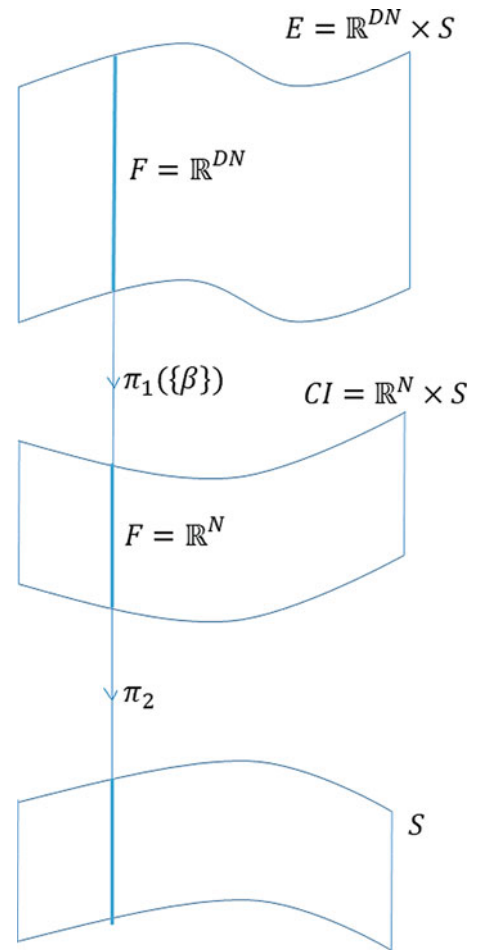
where  $\{f_1\}$  is a vector of regression coefficients. This allows one to gauge fix to the normal condition features  $\{f(s_i, 0, 0)\}$ , and these can, in principle, be transferred onto neighbouring members of the populations – systems  $s$  – which do not have training data.

Projection methods offer a more geometrical solution to the problem; this also allows for the discussion of time-series features, which have not appeared up to now. Suppose that the feature data for a given system  $s_i$  are multivariate time series, which have been sampled over a time  $[0, T_i]$  and have  $N_i$  samples. The features are thus represented by an  $N_i \times D_i$  matrix  $[X]$  where  $D_i$  is the number of time series variables. This is too general for immediate use, so it will be assumed that  $T_i = T$ ,  $N_i = N$  and  $D_i$ . This is quite a high-dimensional feature space; it is  $\mathbb{R}^{DN}$ , where  $N$  might be large.<sup>5</sup> In general, the quantities measured in structural dynamics: displacements, velocities, accelerations etc. will be zero-mean as stochastic processes, so the feature spaces and thus fibres in the feature bundle are vector spaces in this case.

One approach to projection – and arguably the state of the art – is cointegration [19, 20]. In this approach, the confounding influences are considered to be common nonstationary trends in the data which can be removed by forming appropriate combinations of the components of the multivariate series. The details of the algorithms etc. are not relevant here – the curious reader can consult the original papers [19, 20]. Other benefits of cointegration, and projection methods in general, are that one does not require measurements of the confounding variables, and that multiple influences can be removed in one step. In the case under discussion here, cointegration, via a linear combination with coefficients  $\{\beta\}$ , reduces the  $D$  nonstationary time series – the columns of  $[X]$  – to a single stationary time series  $\{x\}$ , which has been purged of its temperature variation i.e. has been gauge-fixed. The geometry of the situation is shown in Fig. 26.7.

In this geometrical context cointegration is a *bundle map*. It is interesting, and may be important to note that, as cointegration produces a zero-mean residual time series, the normal section in  $CI$  (see Fig. 26.7), is actually the *zero*

**Fig. 26.7** Sequence of bundles arising from cointegration of time series features



<sup>5</sup>As before, the fact that there will generally be multiple samples of training data is ignored; it is assumed that each structure has a ‘point’ in the feature space corresponding to each damage state of interest.

section of the bundle [11]. In terms of interpolation/transfer, the cointegration vectors can potentially be transferred between members of the population, from a subset with training data to those with none.

It is worth considering geometrical issues which might arise in dealing with cointegrating vectors. Returning to the examples of the cantilever beams. If one considers the features that might arise from the situation where  $\theta$  and  $d$  both vary. The possible features will live on a two-dimensional submanifold of the four-dimensional fibre (four natural frequencies); however, both temperature increase and damage can cause the natural frequencies to decrease. This observation means that a feature might arise from temperature decrease alone or damage alone, so the ‘submanifold’ will actually self-intersect, so can not actually be a manifold. This observation will bear further investigation.

## 26.6 Feature Bundles and More Complicated Spaces of Structures

In order to motivate the discussion of this section, it will consider the *Irreducible Element* (IE) and *Attributed Graph* (AG) representations of structures as discussed in [2, 3].

If the population of structures of interest is *homogeneous* [1], each structure will be parameterised by the same number of continuous parameters, and all corresponding parameters will have the same physical interpretation. In this case, the situation is like the space/population of cantilever beams discussed earlier and the space of structures  $S$  will be a manifold. However, in general, one might have to deal with a *heterogeneous population*. As a simplified example of this situation, one might consider a population of *laminated cantilever beams*. Adding the number of layers  $n_L$  as an explicit parameter, this yields a set of  $6n_L + 1$  parameters per beam  $\{n_L, \{l_i, w_i, t_i, \rho_i, E_i, v_i\}, i = 1, \dots, n_l\}$ , assuming perfect interfaces. So the cantilevers do not look too strange, one can assume common values of  $l_i$  and  $w_i$ . The problem is that the set of structures is not a manifold; it is not even a topological space, because it has different dimensions in different places.

The obvious mathematical solution to the problem is to partition the set into subsets with common numbers of layers, and then one simply has multiple versions of the original cantilever problem; more parameters, but no new geometry. Unfortunately, the whole point of the exercise is to solve problems in data-based SHM; to move inferences from structures where one has training data, to structures where one does not. One can only partition the population, if each subset has enough exemplars with data for transfer to be feasible within the subset/sub-population. PBSHM is proposed in the first place to deal with the problem that data across populations may well be scarce. If pragmatism demands that one has to deal with heterogeneous populations, one has to adopt the methods appropriate to those problems i.e. to match structures and transfer inferences across more complicated populations [4].

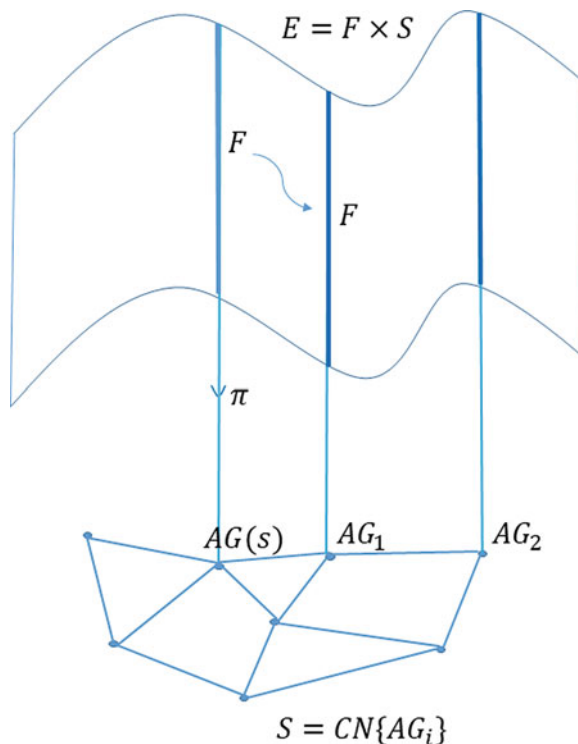
For now, it will be assumed that there is a characterisation of the population in terms of AG representations of the structures. The most general structure one can adopt in this situation is to assume a complex network with nodes comprised of the AGs [2, 3]. Transfer between structures in such a population is the detailed subject of other papers in this series [4]; the discussion here will concentrate on the geometry of the feature spaces associated with the structures. Each AG model within the population will have varying numbers of parameters, so the space  $S$  can not be a manifold. As discussed earlier, the least one can ask of this  $S$  is that it be equipped with a metric of some kind so that the ‘closeness’ of structures can be measured, and transfer is only attempted for structures that are appropriately close in the metric. Classical graph matching metrics are available [21, 22], and metrics for matching attributed graphs have been proposed based on machine learning [23].

Even if the population is heterogeneous, it may be that their feature spaces are homeomorphic e.g. it may have been decided to monitor the first  $n_f$  natural frequencies across the population. In this case, it may be possible to assemble the feature spaces into a ‘vector bundle’ over  $S$  (Fig. 26.8). Transfer will be enabled again between fibres if the source task and target task are sufficiently close in the metric of  $S$ . If a number of structures with training data are sufficiently close, multi-source transfer might be enabled [24].

An interesting possibility arises if the feature data are sufficient to allow the construction of a modal model. In this case one can also appeal to the construction of a *canonical modal model* (CMM), as discussed in [2, 3], and embodied in the sequence of spaces shown in Fig. 26.9.

The interesting point about the sequence is that the points in the spaces at the end of the sequences, are all lumped-mass modal models. The models in  $C$  are theoretical physics-based in the sense that they originated in an IE model, which passed to an AG model, and then to the CCM. The models in  $C^{OMA}$  have been extracted experimentally. The interesting situation is when the two model spaces have the same dimension i.e. number of modes; they will both be an  $\mathbb{R}^n$  and homeomorphic, and can thus be identified, and it makes sense to measure the distance between models in the superimposed space. Bearing in mind that the models in  $C$  are derived by IE schematics, they are not guaranteed to be particularly accurate, but the metric allows that accuracy to be measured. There may be implications here for Validation and Verification of computer models,

**Fig. 26.8** Feature bundle over a more complicated space of structures.  $S = CN\{AG_i\}$  is a complex network of attributed graphs. The space is equipped with a metric and transfer of SHM inferences between two structures would be enabled if they were sufficiently close in the metric. In the current schematic  $AG_1$  would be considered close enough to  $AG(s)$ , but  $AG_2$  would not



and this is being followed up. The chain structure can also be used for model-based SHM, but in doing so it has arguably arrived back at a point which could have been considered without reference to the interesting geometrical structure.

## 26.7 Conclusions

In fact, a long set of conclusions is not warranted. The object of this paper has simply been to set out some interesting geometrical structures – differentiable manifolds and fibre bundles – and frame some problems in population-based SHM which may benefit from their use. The paper is very speculative in its nature; it may turn out to be the case that only the simplest SHM problems can be formulated in such abstract terms. However, it is certainly true to say that, in many cases where problems in engineering and physics have been suited to a geometrical formulation, it has led to considerable insights into those problems. In the case of PBSHM, the formulation of a collective of feature spaces as a bundle over a space of structures, does seem a quite natural one; the problem of data normalisation then appears naturally as a form of gauge-fixing. Transfer learning, which has been proposed separately as a basis for PBSHM appears as a map between fibres in the bundle. While it is clear that considerable research remains to be done, it is hoped that the geometrical approach will provide some insights along the way.

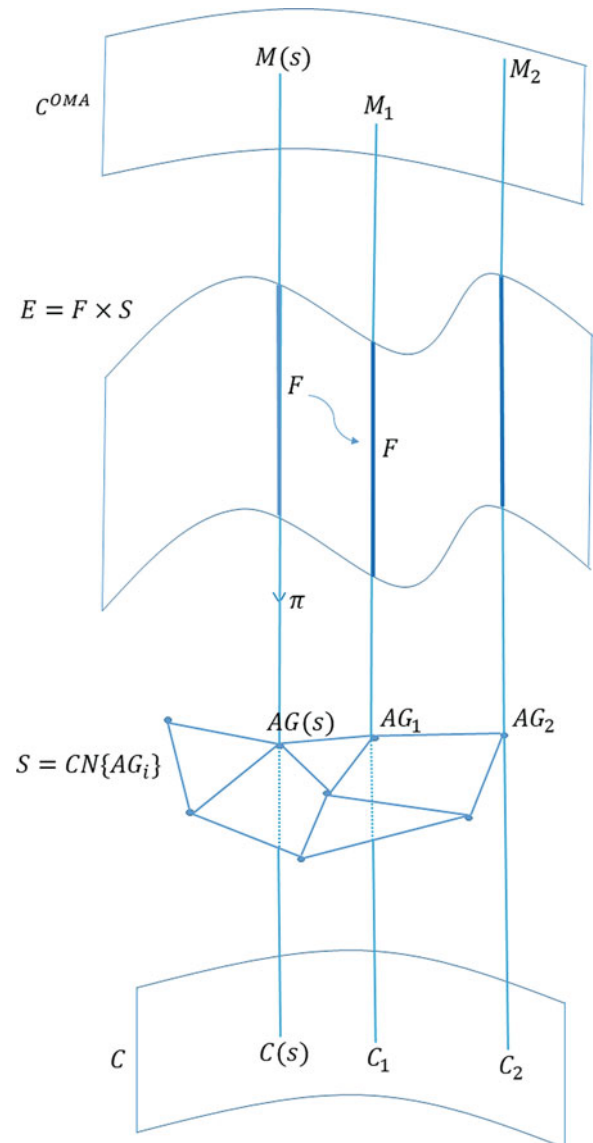
**Acknowledgments** The author would like to thank the UK EPSRC for funding through the Established Career Fellowship EP/R003645/1 and the Programme Grant EP/R006768/1.

## Appendix A

### Topology, Manifolds and Vectors: Basic Definitions

The idea of a manifold begins with the concept of a *topological space*, which is essentially a space with a notion of continuity. One also needs the idea of *homeomorphism* which is essentially a continuous map with a continuous inverse. Homeomorphisms between topological spaces exist if they are essentially the same in terms of topology e.g. have the same

**Fig. 26.9** Sequence of bundles over  $S$ , a complex network of attributed graphs. Two classes of modal models are shown. The lower set of models  $\{C_i\}$ , corresponds to the canonical modal models which are directly constructible from the AG representation; the upper set  $\{M_i\}$  corresponds to modal models directly estimated from data acquired from the structure of interest



number of holes etc. Many topological spaces are not homeomorphic – i.e. topologically equivalent – to flat Euclidean spaces  $\mathbb{R}^n$ . This inequivalence presents a problem in physics and engineering because one usually wants to go beyond notions of continuity and do calculus i.e. one needs *differentiability*. However, it is only clear how to do calculus in flat spaces; this would not be a problem if the space of interest,  $X$ , was globally homeomorphic to some  $\mathbb{R}^n$ , one would then map the calculus problem into the  $\mathbb{R}^n$ , solve it (if possible), and map back. However, many problems of interest will be on curved spaces – like the sphere. However, if one is concerned with differentiation e.g. the problem is to solve some differential equation, one can exploit the fact that differentiation is a local operation. This observation means that one only needs to map some local region of the space of interest into  $\mathbb{R}^n$ , solve the problem and map back – one only needs *local homeomorphism*. However, one may want a solution that covers  $X$ , and that means that many local homeomorphisms may be needed; furthermore, if one wishes a well-behaved solution to the problem on  $X$ , the solutions on different regions will need to knit together in some appropriate manner. Generally speaking if one has ‘solutions’ on two overlapping regions of  $X$ , the solutions should agree on the region of overlap. Despite the rather woolly nature of this discussion, it does motivate the notion of a *differentiable manifold*.

The basic theory of manifolds is explained well in [6]. From a mathematical point of view, one of the classic texts on differentiable manifolds is [25]; a discussion at a much more sophisticated (and modern) level can be found in [7], which also covers applications in gauge theories, which are mentioned in the main body of this paper.



One begins with a topological space  $X$ , and assumes that it is equipped with a family of open sets  $\{U_i\}$  such that any point  $x \in X$  also satisfies  $x \in U_i$  for at least one  $i$ .

A *chart* on  $X$  is a pair of one of the  $U_i$  together with a homeomorphism  $\psi_i$  which carries  $U_i$  onto an open set  $\psi_i(U_i) = V_i$  in  $\mathbb{R}^n$ . The homeomorphism condition ensures that there is an inverse  $\psi_i^{-1}(V_i) = U_i$ . Thus,  $\psi_i : U_i \rightarrow \mathbb{R}^n$  and  $\psi_i^{-1} : \mathbb{R}^n \rightarrow U_i$ . One can regard  $\psi_i(x) = (x_1, \dots, x_n) \in \mathbb{R}^n$  as providing a *coordinate system* on  $U_i$ .

If there is a map  $\psi_i$  for every  $U_i$  in the open cover of  $X$ , then one has coordinates for any point in  $X$ , and the set  $\{U_i, \psi_i\}$  is referred to as an *atlas* for  $X$ . This construction establishes the first thing needed, a set of local homeomorphisms from  $X$  into flat  $\mathbb{R}^n$ , that covers  $X$ . One now needs the condition that the maps interact sensibly on the regions of overlap of the charts i.e.  $U_i \cap U_j$ .

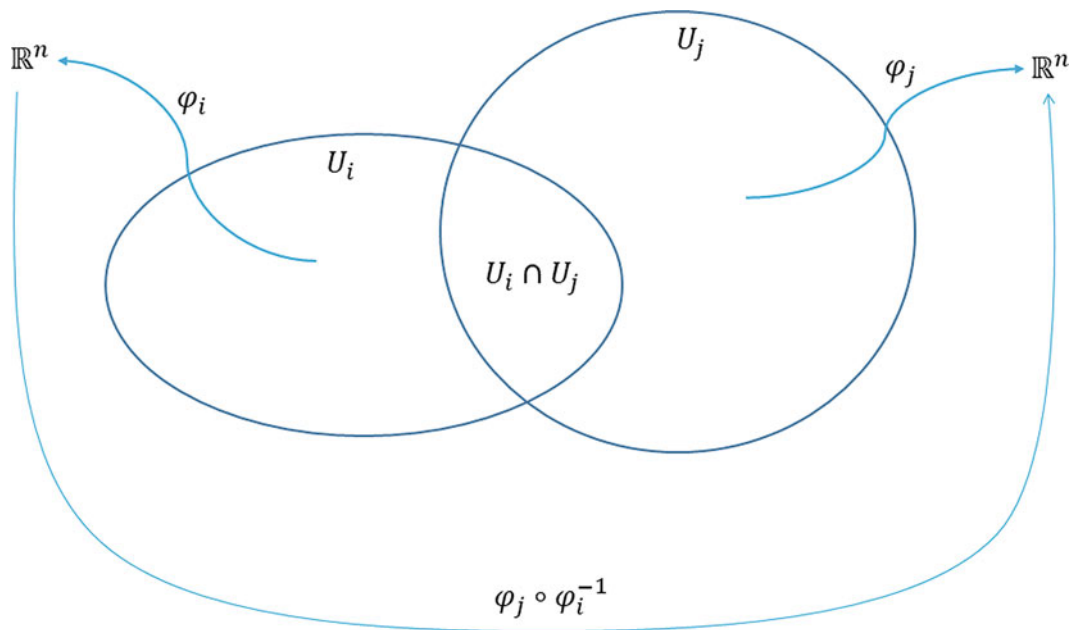
Suppose that some point  $x \in U_i \cap U_j$ . As  $U_i$  and  $U_j$  are both open, so then is  $U_i \cap U_j$  ( $X$  is a topological space). Furthermore both  $\psi_i$  and  $\psi_j$  restrict to homeomorphisms on  $U_i \cap U_j$ . These facts mean that both  $\psi_{ij} = \psi_i \circ \psi_j^{-1}$  and  $\psi_{ji} = \psi_j \circ \psi_i^{-1}$  are both flat-space homeomorphisms i.e.  $\psi_{ij} : \mathbb{R}^n \rightarrow \mathbb{R}^n$ . Thus both  $\psi_{ij}$  and  $\psi_{ji}$  are subject to normal flat space calculus rules.

So, staying on  $U_i \cap U_j = U_{ij}$ , one can denote the coordinate system induced by  $\psi_i$  as  $\psi_i(x \in U_{ij}) = \{x\} = (x_1, \dots, x_n) \in \mathbb{R}^n$ . (Throughout this paper, curved brackets will denote vectors, while square brackets will denote matrices.) If one similarly denotes the coordinate system induced by  $\psi_j$  by  $\psi_j(x \in U_{ij}) = \{x'\} = (x'_1, \dots, x'_n) \in \mathbb{R}^n$ , it is clear that  $\psi_{ji}(\{x\}) = \{x'\}(\{x\}) = (x'_1(\{x\}), \dots, x'_n(\{x\}))$  is nothing more than a *change of coordinates* on  $U_{ij}$  (Fig. 26.10).

Now, the only condition ensured on the maps so far (because they are homeomorphisms) is that they are continuous. However, because they are maps/functions on flat space, it is straightforward to determine their level of *differentiability*. The maps are referred to as  $C^m$  if they are  $m$ -times differentiable under the conditions of normal flat-space calculus. The charts are *compatible* if all the maps  $\psi_{ij}$  are  $C^m$ , and one can then say that the atlas is  $C^m$ , and gives  $X$  the structure of a  $C^m$  *differentiable manifold*. Some special cases are:

- $C^0$  denotes a *continuous* manifold, so no real extra structure over the topology.
- $C^1$  is a differentiable manifold.
- $C^\infty$  indicates an infinitely-differentiable manifold.
- $C^\omega$  denotes an *analytic* manifold ( $C^\infty$  and all Taylor series converge).

It is now necessary to define vectors on/in manifolds. If one thinks of a vector at a point as an actual straight line segment pointing in the direction of interest with a certain magnitude, curved manifolds present a problem; the line would leave the manifold. Only an infinitesimal line would stay in the manifold, and in the limit of zero length, would clearly be tangent to the manifold at the point of interest. In order to define vectors at a point more generally, one assumes that a vector space is



**Fig. 26.10** Coordinate mappings on open sets of a manifold, and the corresponding ‘change of coordinates’ on the region of overlap

attached to the manifold at the point of interest; this is then where vectors ‘live’, and the space is called the *tangent space*. At a point  $x$  in a manifold  $M$ , the tangent space is denoted  $T_x(M)$ .

In order to do any sensible physics or engineering, one actually needs the idea of a *vector field*. Suppose that the manifold of interest  $M$  is spacetime; in order to look at fluid mechanics for example, one needs a way of defining vectors at all points within the flow field. Furthermore, if one is going to use calculus on the vector fields, it will be necessary to impose ideas of continuity etc. of the fields as one moves between points on  $M$ . What is needed is a means of collecting together the tangent spaces of all points in  $M$  in such a way that one can move between the tangent spaces smoothly, as one moves on the manifold  $M$ . Gluing the tangent spaces together leads to the idea of the *tangent bundle*  $T(M)$ ; however, one can make the construction more general, and this leads to the concept of the *fibre bundle*.

## References

1. Bull, L.A., Gardner, P.A., Gosliga, J., Maguire, A.E., Campos, C., Rogers, T.J., Haywood-Alexander, M., Dervilis, N., Cross, E.J., Worden, K.: Towards population-based structural health monitoring, part I: homogeneous populations and forms. In: Proceedings of IMAC XXXVIII – the 38th International Modal Analysis Conference, Houston (2020)
2. Gosliga, J., Gardner, P.A., Bull, L.A., Dervilis, N., Worden, K.: Towards population-based structural health monitoring, part II: heterogeneous populations and structures as graphs. In: Proceedings of IMAC XXXVIII – the 38th International Modal Analysis Conference, Houston (2020)
3. Gosliga, J., Gardner, P.A., Bull, L.A., Dervilis, N., Worden, K.: Towards population-based structural health monitoring, part III: graphs, networks and communities. In: Proceedings of IMAC XXXVIII – the 38th International Modal Analysis Conference, Houston (2020)
4. Gardner, P.A., Worden, K.: Towards population-based structural health monitoring, part IV: heterogeneous populations, matching and transfer. In: Proceedings of IMAC XXXVIII – the 38th International Modal Analysis Conference, Houston (2020)
5. Lin, W., Worden, K., Maguire, A.E., Cross, E.J.: Towards population-based structural health monitoring, part VII: EoV fields: environmental mapping. In: Proceedings of IMAC XXXVIII – the 38th International Modal Analysis Conference, Houston (2020)
6. Schutz, B.F.: Geometrical Methods of Mathematical Physics. Cambridge University Press, Cambridge (1980)
7. Hamilton, M.J.D.: Mathematical Gauge Theory. Springer, Cham (2017)
8. Steenrod, N.: The Topology of Fibre Bundles. Princeton University Press, Princeton (1951)
9. Husemoller, D.: Fibre Bundles. Springer, Berlin (1994)
10. Kobayashi, S., Nomizu, K.: Foundations of Differential Geometry, Vol. I, II. Wiley Interscience, New York (1963)
11. Eguchi, T., Gilkey, P.B., Hanson, A.J.: Gravitation, gauge theories and differential geometry. Phys. Rep. **66**, 213–393 (1980)
12. Abraham, R., Marsden, J.E.: Foundations of Mechanics. American Mathematical Society, Providence (2008)
13. Worden, K., Tomlinson, G.R.: Nonlinearity in Structural Dynamics. Institute of Physics Press, Bristol (2001)
14. Birkhoff, G., Mac Lane, S.: A Survey of Modern Algebra. Routledge, London (2008)
15. Farrar, C.R., Worden, K.: Structural Health Monitoring: A Machine Learning Perspective. Wiley, Hoboken (2011)
16. Mihaylov, G., Spallanzani, M.: Emergent behaviour in a system of industrial plants detected via manifold learning. J. Prognost. Health Manag. **7**, 1–16 (2016)
17. Sohn, H.: Effects of environmental and operational variability on structural health monitoring. Philos. Trans. R. Soc. A **365**, 539–560 (2007)
18. Worden, K., Baldacchino, T., Rowson, J., Cross, E.J.: Some recent developments in SHM based on nonstationary time series analysis. Proc. IEEE **106**, 1589–1603 (2016)
19. Cross, E.J., Worden, K., Chen, Q.: Cointegration; a novel approach for the removal of environmental trends in structural health monitoring data. Proc. R. Soc. Ser. A **467**, 2712–2732 (2011)
20. Cross, E.J., Worden, K., Manson, G., Pierce, S.G.: Features for damage detection with insensitivity to environmental and operational variations. Proc. R. Soc. Ser. A **468**, 4098–4122 (2012)
21. Bunke, H., Shearer, K.: A graph distance metric based on the maximum common subgraph. Pattern Recogn. Lett. **19**, 255–259 (1998)
22. Fernández, M.-A., Valiente, G.: A graph distance metric combining maximum common subgraph and minimum common supergraph. Pattern Recogn. Lett. **22**, 753–758 (2001)
23. Li, Y., Gu, C., Dullion, T., Vinyals, O., Kohli, P.: Graph matching networks for learning the similarity of graph structured objects. Technical Report arXiv:1904.1278v2 [cs.LG] (2019)
24. Sun, S., Shi, H., Wu, Y.: A survey of multi-source domain adaptation. Inf. Fusion **24**, 84–92 (2015)
25. Auslander, L., MacKenzie, R.E.: Introduction to Differentiable Manifolds. Dover Publications, Mineola (1963)

# Chapter 27

## Comparison of Modal Parameters of a Concrete Slab Floor from EMA and OMA



Ellis Kessler, Vijaya V. N. Sriram Malladi, Rodrigo Sarlo, Luke A. Martin, and Pablo A. Tarazaga

**Abstract** In this study, the modal parameters of a hallway floor in Goodwin Hall are compared with experimental modal analysis (EMA) and operational modal analysis (OMA). A set of 17 high sensitivity accelerometers mounted to structural beams under the floor of the hallway will be used to measure the floor response. In EMA an instrumented hammer was used to measure the input, while in OMA ambient excitation was used to excite the floor. The natural frequency, damping ratio, and mode shape estimates for the first five modes of the floor will be compared between the two methods. Despite limitations with generating enough energy to excite standing waves, the modal parameters between EMA and OMA match well. Frequency differences are less than 10%, and all the damping ratio estimates between 2% and 10%. Mode shapes also match well visually, and the MAC shows agreement between methods. Both EMA and OMA show the ability to extract modal parameters from the floor, where the mode shapes show global motion of the floor instead of only local motion between supports.

**Keywords** Floor vibrations · Human structure interaction · Smart infrastructure · EMA · OMA

### 27.1 Goodwin Hall and Experimental Methods

Goodwin Hall on the Virginia Tech campus is the most instrumented building in the world for vibrations. There are 225 high sensitivity accelerometers permanently mounted to the steel structure of the over 160,000 square foot building. Since its construction, Goodwin Hall has served as a test bed for research into various human structure interaction topics such as localization [7, 10], occupant classification [1, 5], and gait analysis [3, 4]. All of these research areas have one thing in common: they rely on the vibration signals generated from human walking patterns to learn something about the occupant. The structural dynamics of the floor in different buildings will cause different responses to an identical input, making it difficult to extend research on human structure interaction to a different building or even to a different part of the same building. If the full structural dynamics of the floor on which an occupant is walking are understood, a comprehensive algorithm could be developed for all buildings. In this study, the first five estimated natural frequencies and mode shapes of a hallway on the fourth floor of Goodwin Hall are compared from multiple methods. Experimental modal analysis (EMA), as well as operational modal analysis (OMA) are used to extract modal parameters. The estimated modal parameters will be extracted for a set of 17 sensors which span a length of about 100 ft along a hallway. The floor in Goodwin Hall is a concrete slab supported by a series of steel beams which are in turn supported by girders and columns. A diagram of the hallway and

---

E. Kessler (✉) · P. A. Tarazaga

Department of Mechanical Engineering, Virginia Polytechnic Institute and State University, Blacksburg, VA, USA  
e-mail: [ellisk1@vt.edu](mailto:ellisk1@vt.edu); [ptarazag@vt.edu](mailto:ptarazag@vt.edu)

V. V. N. Sriram Malladi

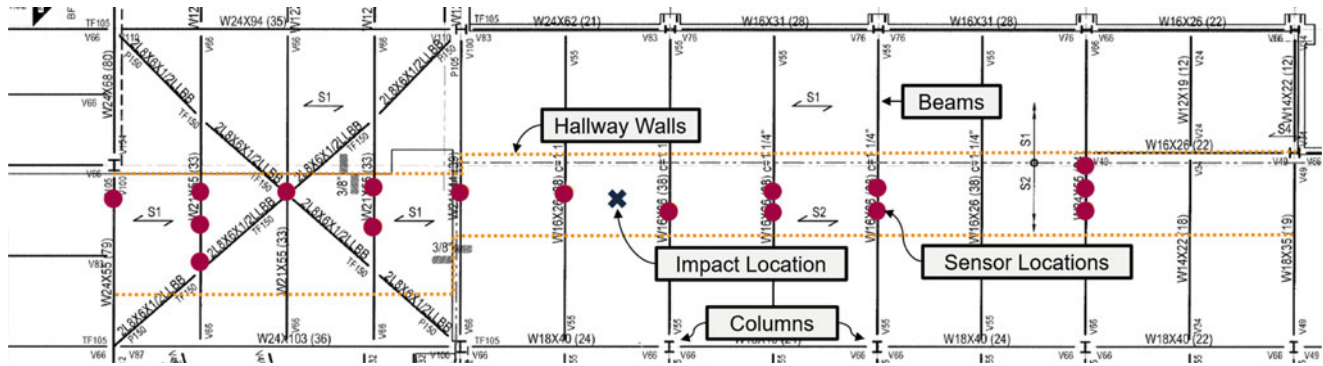
Department of Mechanical Engineering-Engineering Mechanics, Michigan Tech, Houghton, MI, USA  
e-mail: [smalladi@mtu.edu](mailto:smalladi@mtu.edu)

R. Sarlo

Department of Civil Engineering, Virginia Polytechnic Institute and State University, Blacksburg, VA, USA  
e-mail: [sarlo@vt.edu](mailto:sarlo@vt.edu)

L. A. Martin

Naval Surface Warfare Center, Dahlgren, VA, USA  
e-mail: [luke.a.martin@navy.mil](mailto:luke.a.martin@navy.mil)



**Fig. 27.1** Structural layout of the floor in Goodwin Hall under the hallway being studied. The 17 sensor locations and impact location are shown, as well as structural information about the building such as locations of columns, beams, and the walls of the hallway

sensors is shown in Fig. 27.1. The sensors in Goodwin are on mounts which are welded to the steel beams at the locations indicated by dots.

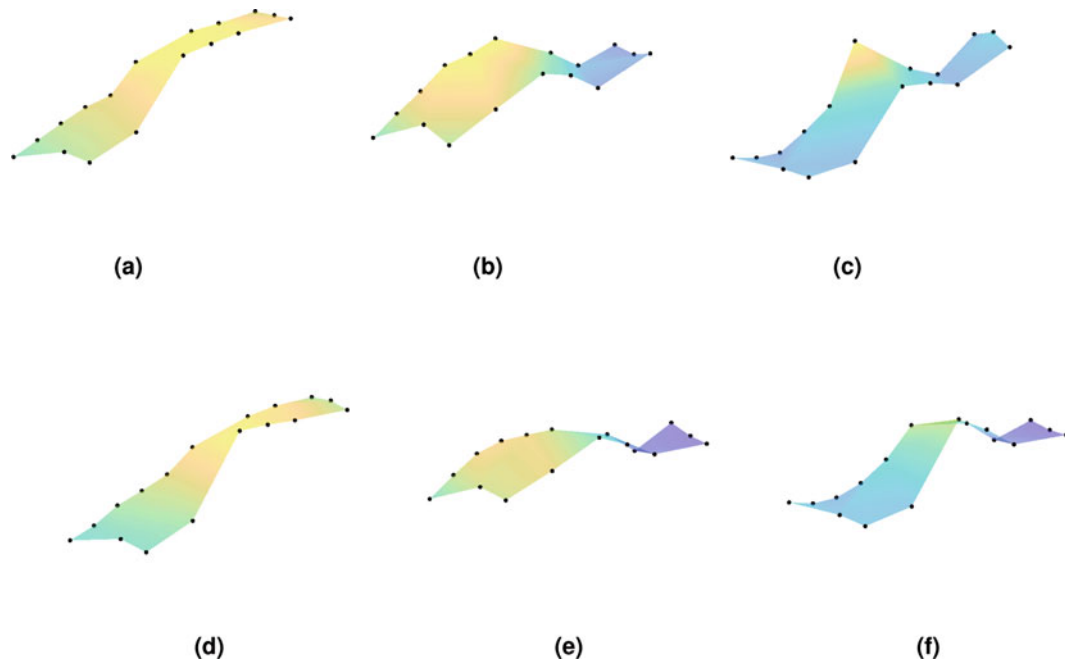
For the EMA, a 12.1 pound hammer with a maximum force of 5,000 lbf was used. The softest tip was used for the main EMA presented in this study, as it concentrated more energy at the low frequencies of the modes of interest compared to a harder tip with the same maximum force. The hardest tip was also used, but is not presented. The hammer was used to measure the force as it was used to impact the floor at the position marked in Fig. 27.1. The input from the hammer and the output of the 17 floor mounted accelerometers were used to estimate the frequency response functions (FRFs), from which the modal parameters were extracted.

For the OMA, it was important to find a time period where the hallway being studied experienced as much ambient excitation as possible. During an unplanned fire alarm, the entire building was required to evacuate. As all the occupants of the building walked towards the exits, there was a period of approximately 8 min where the hallway experienced continuous inputs from the walking occupants. This time period showed more prominent peaks in the frequency content than other times with less activity in the building, allowing the best estimation of modal parameters. Covariance driven Stochastic Subspace Identification [6] and automated modal selection based on clustering [8] have been successfully applied in Goodwin Hall [9], and are used here on the set of 17 hallway sensors to estimate the modal parameters in this study.

## 27.2 Comparison of EMA and OMA

The first five vibration modes of the hallway were extracted using both EMA and OMA, and are shown in Fig. 27.2. The modal parameters estimated from each method are compared in Table 27.1. The estimated frequencies of each mode are similar, with differences under 10% between the methods. The frequencies estimated by OMA are all lower than those of the matching mode from EMA. This is possibly due to the presence of several people in the hallway during the evacuation, adding mass, which would lower the natural frequencies. The estimated damping ratio is almost always lower in the EMA, although all damping estimates from both methods are between 2% and 10%. The modal assurance criterion, MACs, between the methods show that while there is good visual agreement between modes, there are some differences. The MAC for the first mode is high, however the MAC values get progressively lower for higher modes. The additional mass from the evacuating occupants could have affected the mode shape, although it is expected that the estimates from both techniques would get worse at higher frequencies as the input power rolls off, which would also degrade the comparison of higher order modes.

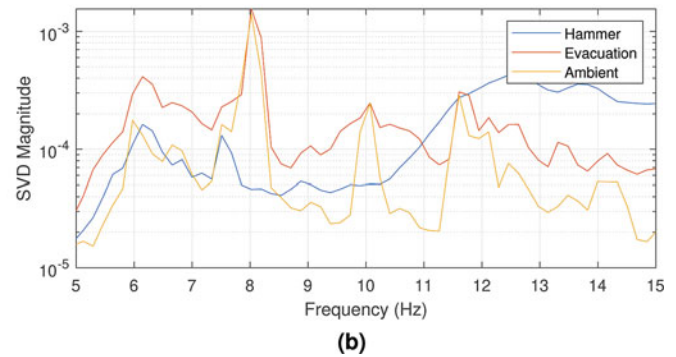
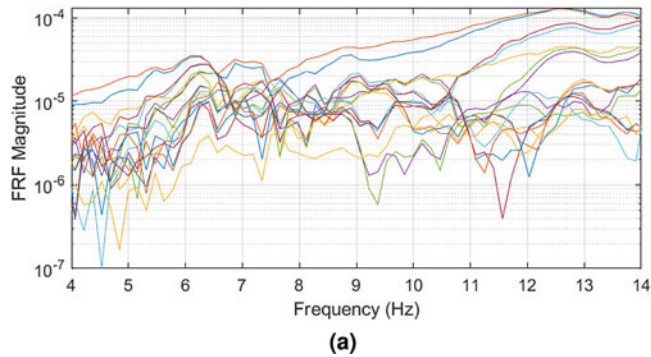
The FRFs from EMA in Fig. 27.3a show another limitation of this study. For the FRFs, it can be seen that two of the FRFs are the highest for all frequencies. These FRFs came from sensors that were closest to the impact location, which suggests that even the large hammer used in this study was not able to generate steady state standing waves throughout the whole hallway. In order to get a direct comparison of the excitation levels of the hammer and walking occupants, we compared output-only data from the hammer excitation to occupant excitation. The raw acceleration data with hammer excitation used was the same length as the occupant excitation data, and contained 30 hammer impacts spread out between 6 locations along the hallway. The singular value decomposition (SVD) of the output spectral density matrix was extracted for each dataset [2], and are shown in Fig. 27.3b to compare the frequency content from each excitation method. Additionally a separate occupant excitation is also shown during a time of normal building activity, with less occupant activity than the



**Fig. 27.2** Estimated mode shapes for the first three modes from EMA (a–c) and OMA (d–f). (a) EMA Mode 1 Estimate. (b) EMA Mode 2 Estimate. (c) EMA Mode 3 Estimate. (d) OMA Mode 1 Estimate. (e) OMA Mode 2 Estimate. (f) OMA Mode 3 Estimate

**Table 27.1** Modal parameter comparison between EMA and OMA. MACs shown are between the EMA and OMA estimated mode shape for each mode order

Mode	EMA		OMA		MAC
	$f$	$\zeta$	$f$	$\zeta$	
1	6.39	0.046	6.14	0.100	0.85
2	7.46	0.021	7.42	0.100	0.51
3	8.72	0.034	8.16	0.031	0.49
4	10.85	0.024	10.25	0.060	0.37
5	12.61	0.039	12.01	0.070	0.42



**Fig. 27.3** FRFs between the input location and all 17 output locations (a), and comparison of the average SVD of the spectral matrix from each excitation type (b)

evacuation. The occupant excitation during the evacuation has the highest levels of excitation at low frequencies, being passed by the hammer excitation around 12 Hz. Even the ambient occupant excitation provided as much or more excitation at low frequencies when compared to the hammer. The power of occupant excitation is not surprising, as OMA of civil structures often relies on this type of excitation. This result does however highlight the difficulty of providing enough energy to perform a proper EMA on large structures, with the 12 pound hammer used in this study not providing enough excitation.

## 27.3 Conclusion

Although there were limitations with getting enough input excitation to generate standing waves along the whole floor, estimated modal parameters via EMA and OMA were very similar. It is a significant result that along this hallway there are global modes instead of each bay responding as an isolated system, instead of the slab-beam connections creating significant boundary conditions or nodal lines in the modes. Another significant result is that for estimating modal parameters, there did not appear to be significant differences between EMA and OMA. In fact, for very low frequencies, excitation from distributed occupant excitation provided more excitation than the hammer used in this study.

**Acknowledgments** Dr. Tarazaga would like to acknowledge the financial support of the John R. Jones Faculty Fellowship.

The work is supported in part by the National Science Foundation via grant no. DGE-1545362, UrbComp (Urban Computing): Data Science for Modeling, Understanding, and Advancing Urban Populations. Any opinions, findings, and conclusions or recommendations expressed in this material are those of the authors and do not necessarily reflect the views of the National Science Foundation.

The authors wish to acknowledge the support as well as the collaborative efforts provided by our sponsors, VTI Instruments, PCB Piezotronics, Inc.; Dytran Instruments, Inc.; and Oregano Systems. The authors are particularly appreciative for the support provided by the College of Engineering at Virginia Tech through Dean Richard Benson and Associate Dean Ed Nelson as well as VT Capital Project Manager, Todd Shelton, and VT University Building Official, William Hinson. The authors would also like to acknowledge Gilbane, Inc. and in particular, David Childress and Eric Hotek. We are especially thankful to the Student Engineering Council (SEC) at Virginia Tech and their financial commitment to this project. The work was conducted under the patronage of the Virginia Tech Smart Infrastructure Laboratory and its members.

## References

1. Bales, D., Tarazaga, P.A., Kasarda, M., Batra, D., Woolard, A.G., Poston, J.D., Malladi, V.V.N.S.: Gender classification of Walkers via underfloor accelerometer measurements. *IEEE Internet Things J.* **3**(6), 1259–1266 (2016)
2. Brincker, R., Ventura, C., Andersen, P.: Damping estimation by frequency domain decomposition. In *Proceedings of IMAC 19. Society for Experimental Mechanics*, 698–703 (2001)
3. Fagert, J., Mirshekari, M., Pan, S., Zhang, P., Noh, H.Y.: Characterizing structural changes to estimate walking gait balance. In *Dynamics of Civil Structures*. Springer International Publishing, **2**, 333–335 (2019)
4. Kessler, E., Malladi, V.V.S., Tarazaga, P.A.: Vibration-based gait analysis via instrumented buildings. *Int. J. Distrib. Sensor Netw.* **15**(10), 1550147719881608 (2019)
5. Pan, S., Yu, T., Mirshekari, M., Fagert, J., Bonde, A., Mengshoel, O.J., Noh, H.Y., Zhang, P.: FootprintID: indoor Pedestrian identification through ambient structural vibration sensing. *Proc. ACM Interact. Mob. Wearable Ubiquitous Technol.* **1**(3), 89:1–89:31 (2017)
6. Peeters, B., de Roeck, G.: Reference-based stochastic subspace identification for output-only modal analysis. *Mech. Syst. Signal Process.* **13**(6), 855–878 (1999)
7. Reuland, Y., Pai, S.G.S., Drira, S., Smith, I.F.C.: Vibration-based occupant detection using a multiple-model approach. In *Dynamics of Civil Structures*. Springer International Publishing, **2**, 49–56 (2017)
8. Reynders, E., Houbrechts, J., de Roeck, G.: Fully automated (operational) modal analysis. *Mech. Syst. Signal Process.* **29**, 228–250 (2012)
9. Sarlo, R., Tarazaga, P.A., Kasarda, M.E.: High resolution operational modal analysis on a five-story smart building under wind and human induced excitation. *Eng. Struct.* **176**, 279–292 (2018)
10. Woolard, A.G., Tarazaga, P.A.: Applications of dispersion compensation for indoor vibration event localization. *J. Vib. Control* **24**(21), 5108–5117 (2018)

**Ellis Kessler** is a PhD student at Virginia Tech working with Dr. Pablo Tarazaga in the Virginia Tech Smart Infrastructure Laboratory on topics of human structure interaction.

# Chapter 28

## Modeling Human Jumping Force on a Flexible Structure Using Control Models



Ahmed T. Alzubaidi and Juan M. Caicedo

**Abstract** Live loads on structures such as dance halls, fitness centers, and malls can generate excessive vibrations causing serviceability problems. Several models were used to model force generated by human jumping on a flexible structure such as semi-sinusoidal pulse force, Fourier series, statistical model of the dynamic loads, and pseudo-variable mass models. While these models are able to represent the dynamics of the system in some cases, the human body is a more complex dynamic system. For example, Fourier series model and even other mentioned models are not capable to consider an external excitation like music sound as input to the overall system. This paper expands a prior model of human standing on flexible structure using control theory to a model that considers sound as the excitation to the human-structure system. Energy is added to the system when a person jumps or performing short movement up and down at the beat of a metronome. Here, the sound created by the metronome is used as input to the overall system.

A flexible cantilever structure, idealized as single degree of freedom system, is used to develop and validate the proposed model. The force exerted by people jumping as well as the acceleration records are used to determine the probability distribution functions of the model parameters. The model is validated by comparing model predictions with additional experimental records.

**Keywords** Human-structure interaction · Control theory · Human activity · Structural dynamics · Mean square error

### 28.1 Introduction

In designing a building, the live loads due to human activities such as standing up from sitting, sitting down from rising, moving, bobbing, jumping, and dancing are challenging loads because these actions generate dynamic forces larger than the human body weight. Additionally, the activities sometimes lead to a human discomfort and panic amongst the occupants as they cause excessive vibration in the building [32]. Human force considers the large portion of live load in the designing a commercial, residential building and even stadium, gyms, dance floor and theaters because the structural designers started using a new materials in the designing of lighter and more flexible members of structures above-mentioned [1, 2]. These materials provide a good strength but they are susceptible to human-induced vibration problem. Therefore, in recent years, researchers have been focused on modeling human activities on structures and developing new methodologies to deal with human induced vibration problem. Several examples of excessive vibration induced by individual walking, jumping, and bouncing have been proposed in the literature [3–6]. The oldest one was the failure of footbridge in Broughton, UK 1831 due to the soldiers unison marching [4, 7]. Another well known example is the Millennium footbridge, UK where it had excessive vibration due the people walking during its opening day [6]. The interesting example is in Seoul, South Korea where 39 floor TechnoMart building was shaking because aerobic exercise. The people living there felt the building vibrate vertically for 10 minutes. However, there was no earthquake, explosion, or even high winds. After the detailed investigations, the inspection team found the vibration was caused by people performing an aerobic sport in the fitness center on the 12th floor of the building [5].

---

A. T. Alzubaidi · J. M. Caicedo (✉)

Department of Civil and Environmental Engineering, University of South Carolina, Columbia, SC, USA  
e-mail: [alzubaa@email.sc.edu](mailto:alzubaa@email.sc.edu); [caicedo@cec.sc.edu](mailto:caicedo@cec.sc.edu)

### 28.1.1 *Human-Structure Interaction*

When people are performing activity such as jumping or bouncing over a flexible structure, the interdependence of the human and structure dynamic system can cause the phenomenon of human-structure interaction (HSI). Thus, new properties of dynamic system can be resulted by this interdependence [8]. There are two significant issues which should be taken into account. The first one, natural frequency and damping ratio of combined human structure system can make the structure prone to unacceptable vibration due the dynamic force of individual. Second, the synchronization amongst occupants is because of the crowd dynamic and interaction with structure [6, 8–10].

Modeling human-structure interaction has a lack in the fundamental knowledge where most structural engineers have not considered the influence of dynamic load of people in the structure design [11]. Several models were used to model force generated by human jumping on a flexible structure such as semi-sinusoidal pulse force, Fourier series, statistical model of the dynamic loads, and pseudo-variable mass models [12, 13]. While these models are able to represent the dynamics of the system in some cases, the human body is a more complex dynamic system. For example, Fourier series model and even other mentioned models are not capable to consider an external excitation like music sound as input to the overall system.

This study expanded the model proposed by Ortiz and Caicedo [1] to model HSI when individual jumping over flexible structure. New controller have been designed to include the music sound as an input to overall system. We collected experimental data for people jumping to be used in fitting of proposed model. In the Sect. 28.2, we present the methodology while section has a discussion about instruments and experiments setup. The experiments testing is presented in Sect. 28.4 whereas Sect. 28.5 has the comparison between the data points generated by proposed model and experimental data. Finally, the conclusion is presented in Sect. 28.6.

## 28.2 Proposed Approach

Control theories are divided into three essential categories which are classical, modern and robust control theories. Several applications such as robotics, space-vehicle systems, radar antenna, and automobile steering control work based on control theory [14–16]. In 1940, the researchers developed the frequency-response methods which allow engineers to design linear control system [15]. One of these systems is a closed-loop control which fundamentally uses the concept of feedback. Classical control theory developed for single input single output system and based on frequency-domain whereas modern control theory developed for multiple input multiple output system and deals with time-domain analysis of the differential equation [14, 15]. The simplicity of designing control system comes from the fact that modern control theory is based on the model of real control system. The principle of the feedback control was developed for engineering and non-engineering fields and found to reduce the difference between output and input system. Control systems can be classified as open and closed-loop control system (feedback control system). The idea of using feedback is not new. The Greeks used feedback in 300 B.C. in developing the float regulator mechanisms [14, 16]. More than 50% of industrial controllers that have been used are PID controllers. The usefulness of the PID controller is to provide satisfactory control [15].

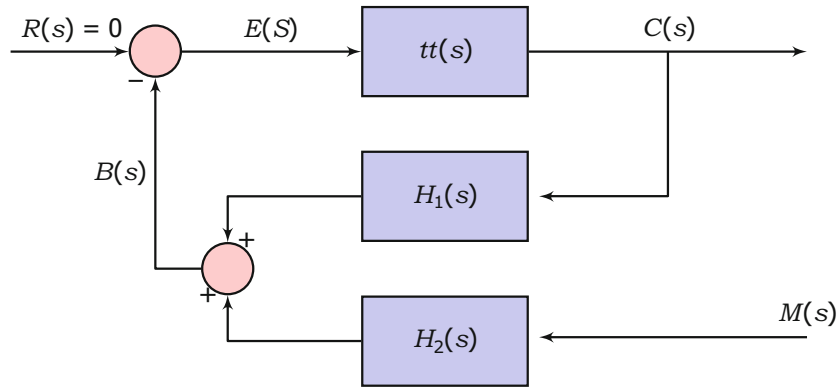
Many authors in different disciplines have been modeling the human body using a control system in last three decades [17–22]. For example, Kimura and Jiang have applied the control system to robotics and compared it with human body performance in terms of keeping stability for different activities, such as standing and jumping [19]. In the same scope, they have proposed and developed PID controller in modeling the balance, keeping control of humans, and found that a PID controller can be utilized to understand the standing process [17]. Result shows that the Derivative term (Kd) is remarkably lower when the humans close their eyes. However, the controller models are not main stream in HSI problems.

Ortiz et al. were the first researchers to utilized a closed-loop control system to represent a model of the interaction between the human and structure.

### 28.2.1 *Human-Structure Model*

Control systems are not only applied in the mechanical and electrical engineering fields but also in civil, chemical, and environmental engineering [14]. The fundamental concepts of control system were developed for linear systems using feedback concept. Control systems are based on input and output relationship and could be open or closed-loop control systems. In this research, we focused on a closed loop control system to model human-structure interaction.. Closed loop control systems use an output of the plant (system to be controlled) and a feedback loop to achieve the desired behavior [14].





**Fig. 28.1** Block diagram of a closed-loop control system

The underlying aim of the feedback concept is to reduce the error between the input and output in the system. Figure 28.1 shows the block diagram of the proposed model. The term  $G(s)$  is the transfer function of the structural system whereas the terms  $H_1(s)$  and  $H_2(s)$  are the transfer function of the first and second controllers respectively. The input force for empty and occupied structure is represented with terms  $R(s)$  whereas the second excitation when people are jumping on the structure which is the sound of music is represented by the term  $M(s)$ . The output acceleration is represented by the term  $C(s)$  whereas the terms  $B(s)$  and  $E(s)$  represent the force utilized to control the structure and the actuating error. A measure from the plant is used as input to the controller and control device which provides an additional input to the plant. In this study, we modeled HSI using the same concepts where the structure is modeled as the plant of the system and the human is modeled as the controller. Equation (Eq. 28.1) describes the combined structure and human system.

$$TF(s) = \frac{H_2(s)}{1 + G(s)H_1(s)} \quad (28.1)$$

### 28.2.2 Structural Model

A cantilever structure was built at the Department of Civil and Environmental Engineering at the University of South Carolina and has been used to experimentally test the proposed model. This structure consists of a steel frame and concrete blocks as shown in Fig. 28.2. This structure has a mobile support and masses which are used to change the dynamic properties of the system and the live to dead load ratio. For simplicity, the structure  $G(s)$  has been modeled as a single degree of freedom system. The transfer function of structure  $G(s)$  is defined as:

$$G(s) = \frac{\frac{s^2}{m}}{s^2 + 2\zeta\omega_n s + \omega_n^2} \quad (28.2)$$

where  $m$ ,  $\zeta$ ,  $\omega_n$  are the mass, damping ratio, and natural frequency of the system. The poles which are the root of denominator of transfer function are expressed in terms of the natural frequency ( $\omega_n$ ) and damping ratio  $\zeta$  of the structure as shown in the following equation [15]

$$p_{1,2} = -\zeta\omega_n \pm \sqrt{(\zeta\omega_n)^2 - \omega_n^2} \quad (28.3)$$

Based on the SDOF model shown in (28.5), the model parameters for the structure are  $\Theta = \{m, \omega_n, \zeta\}$ .



Fig. 28.2 Experimental structure

### 28.2.3 Controller of the Model

Proportional, Integrative, and Derivative (PID) controller is one of the most widely utilized in industry. A PID controller is supported by Laplace transform and has operation form in time domain. Each term of the controller can shape the response of the system and change response characteristics such as overshoot. The wide availability and ease of use are the two main reasons to make the PID controller a significant control tool [23]. PID has been used in most of the engineering fields such as electrical [24], biochemical [25], aerospace [26], and civil engineering [27, 28]. A PID controller has three terms which are Proportional, Integrative, and Derivative, and has two derivations which are PI and PD controller. PID controller has transfer function:

$$H_1(s) = K_p + \frac{K_i}{s} + K_d s \quad (28.4)$$

In this research,  $H_1(s)$  which represents the dynamics of the person due to floor motion is represented by PID controller, and  $H_2(s)$  represents dynamics of the person due to sound excitation as shown in Fig. 28.1. We designed new controller which is denoted by the following equation:

$$H_2(s) = \frac{\alpha s + \beta}{s^2 + \gamma s + \psi} \quad (28.5)$$

### 28.2.4 Optimization Process

Optimization is one of the deterministic numerical methods where it used to estimate the parameters value of complex model [29]. One of optimization technique is the Mean Square Error (MSE) which was used to estimate the model parameter by using the model parameter that give a minimum mean square error [30]. MSE is to measure the mean square different between the experimental data points and the data points generated by proposed model. MSE is denoted by equation Eq. 28.6.

$$MSE = \frac{1}{n} \sum_{i=1}^n (Y - \hat{Y})^2, \quad (28.6)$$

where the  $Y$  is the experimental data points and  $\hat{Y}$  is the data points generated by proposed model. The parameter which gave a minimum mean square error were used to fit the model the experimental data.

## 28.3 Experimental Testing

### 28.3.1 Lab Specimen

The structure utilized in the experiments has been designed, built, and retrofitted in structural lab of the Civil and Environmental Engineering Department in the University of South Carolina. This structure has steel frame and concrete blocks where they are used to inspect the dynamic properties of flexible slabs. The concrete blocks are made using normal concrete whereas the steel frame which is composed using  $5 \times 4 \times 1.4$  steel tube is a cantilever truss shown in the Fig. 28.3.

The structure is a cantilever slab and has four supports. Two supports are hinge support which allow the rotation about  $y$ -axis cannot move along  $x$ -axis. The other two which are mobile supports are roller supports and can move along  $x$ -axis to change the cantilever length which in turn can change the structure dynamic characteristics. However, the concrete blocks can also change the dynamic properties of structure.



Fig. 28.3 Experimental structure

The dynamic properties of the structure are modified from rigid ( $\omega_n = 62$  rad/s) to flexible structure ( $\omega_n = 18.5$  rad/s) by changing the mass and stiffness. The actual live to dead load ratio of structure susceptible to human-induced vibration is represented in the lab specimen by making the structure light and flexible. The length of the cantilever used in this study is 124 in as shown in the Fig. 28.3.

### 28.3.2 Instrumentation and Experiments

In the practical aspect, we used a PCB 096D50 impact hammer with a sensitivity of 0.2198 mV/N and a PCB 333B50 accelerometer with a sensitivity of 1019 mV/g. We used the accelerometer to measure the vertical acceleration at the tip of the cantilever whereas the impact hammer was used to excite the empty structure. In addition, we developed a force plate to measure the force exerted by the individual jumping on the flexible structure. A PCB 130F20 microphone with a sensitivity of 40.2 mV/Pa and was utilized to measure the sound created by a metronome and. The data was collected using an NI 9234 data acquisition system. Data was collected in 20 s records at a sampling frequency of 6400 Hz. While this frequency is high for the structure, it was required to correctly describe the pressure captured by the microphone.

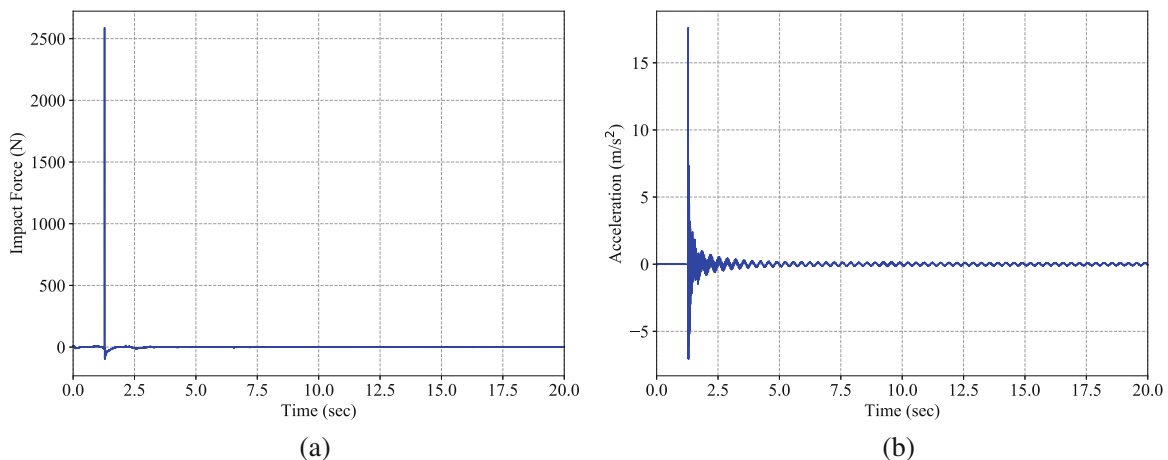
## 28.4 Modeling the Jumping Force

To compare the force generated by person jumping over the flexible structure and force predicted by the proposed model, we conducted three experiments described below where the experiments involved empty, occupied structure and individual jumping on the flexible structure.

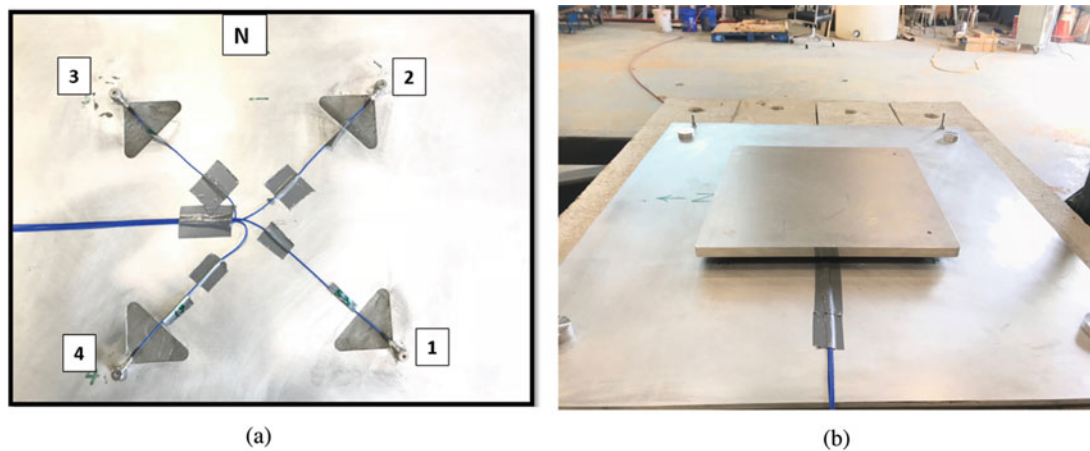
### 28.4.1 Empty Structure

The impact hammer is used to excite the structure. Figure 28.4a shows the input force of the hammer and Fig. 28.4b shows the acceleration response. The structure is modeled as single degree of freedom and this model has three parameters ( $\omega_n$ ,  $\zeta$ ,  $m$ ).

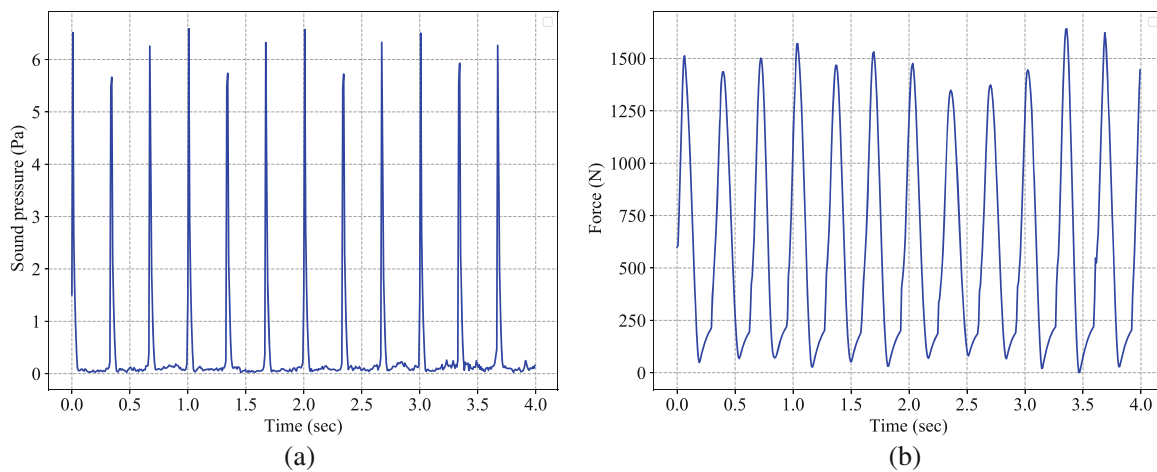
The experimental transfer function of empty structure which is calculated using frequency response function [31]. where the value of first single predominant peak is 18.5 rad/s. The parameters ( $\omega_n$ ,  $\zeta$ ,  $m$ ) were calculated using optimization technique to be used for the model of the human-structure system of the individual jumping.



**Fig. 28.4** Acceleration and impact force-time history of empty structure. (a) Impact force-time history. (b) Acceleration-time history



**Fig. 28.5** Force plate for jumping. (a) Force sensor. (b) Top part of the force plate



**Fig. 28.6** Sound and dynamic load-time history of jumping at 3 Hz. (a) Sound pressure-time history. (b) Dynamic load-time history

### 28.4.2 Occupied Structure

Single individual was standing over the structure with bent knees to test the flexible structure where the test was similar to that of the empty structure. The experimental transfer function of occupied structure is calculated using frequency response function [31]. The parameters of the occupied structure ( $\omega_n$ ,  $\zeta$ ,  $m$ ,  $K_p$ ,  $K_d$ ,  $K_i$ ) were calculated using optimization technique to be used for the model of the human-structure system of the individual jumping.

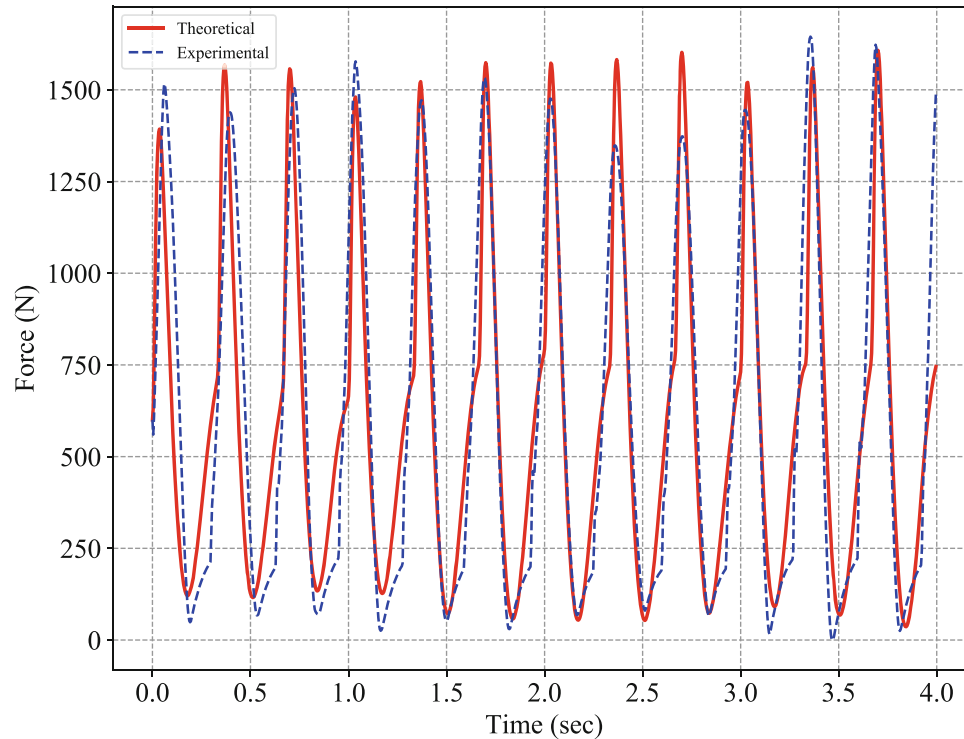
### 28.4.3 Individual Jumping on Flexible Structure

To understand the interaction between the human jumping and the flexible structure, we conducted a test using the force plate. Figure 28.5 shows the force plate designed and developed in Civil and Environmental Engineering Department at University of South Carolina. Here the force generated by the person jumping is measured to compare with theoretical force produced by the proposed model in Fig. 28.1. During jumping the subject move her/his body up and down and loss the contact with the floor.

A metronome or music beats was set to 180 bpm and the person standing in the structure was asked to excite the structure by moving his/her body at the frequency of the sound. The sound pressure produced by the metronome, acceleration, and load applied by the person were acquired using data acquisition system and shown in Fig. 28.6.

**Table 28.1** The parameters value of the human, music and structure

Parameter	$\omega_n$ [rad/s]	$\zeta$	$m$ [kg]	$K_p$	$K_d$	$K_i$	$\alpha$	$\beta$	$\gamma$	$\psi$
Values	18.0	0.04	730	34	2000	6	11,000	10	11	300

**Fig. 28.7** Fitting theoretical to experimental response of dynamic force

## 28.5 Results

The parameter of the empty structure was optimized with the empty structure data whereas the parameter of PID controller was optimized using the data of person standing. Then, the overall system was optimized using the data of individual jumping over flexible structure. The beat of metronome was assumed to be 180 bpm and the force generated by person jumping was calculated to compare with model. Mean square error technique was used to estimate the parameters of proposed model. The parameters of model were  $(\omega_n, \zeta, m, K_p, K_d, K_i, \alpha, \beta, \gamma, \psi)$ . The parameters  $K_p, K_d,$  and  $K_i$  belong to the PID that simulates the dynamics of the person due to floor motion whereas the parameters  $\alpha, \beta,$  and  $\psi$  belong to the new controller  $H_2$  that simulates the dynamics of the person due to sound excitation.

Table 28.1 shows the parameters values which gave minimum mean square error. Figure 28.7 shows the fitting model to the experimental data of dynamic force of individual jumping one flexible structure.

## 28.6 Conclusion

This paper presents a new deterministic force model for a person jumping on flexible structure and to understand the interaction between the human and structure. The overall model is based on one control theory and has two controllers. The first controller is PID and used to represent the dynamic of person due to floor motion whereas the second was designed to represent the dynamics of the person due to sound excitation. Not only the feedback between the structure and individual was included by the model but also the additional input (Music sound) to human. The parameters of the overall model were estimated using optimization process by taking the parameters that minimize the mean square error. The data points of individual force generated by deterministic model match well with experimental data points.

**Acknowledgments** The author would like to acknowledge the higher education and scientific research ministry of Iraq to support this research as well as the University of South Carolina.

## References

1. Ortiz-Lasprilla, A.R., Caicedo, J.M.: Comparing closed loop control models and mass-spring-damper models for human structure interaction problems. In: *Dynamics of Civil Structures*, vol. 2, pp. 67–74. Springer, Cham (2015)
2. Lasprilla, A.R.O.: Modeling human-structure interaction using a controller system. Ph.D. dissertation (2016)
3. Racic, V., Pavic, A.: Mathematical model to generate near-periodic human jumping force signals. *Mech. Syst. Signal Process.* **24**(1), 138–152 (2010)
4. Tilly, G., Cullington, D., Eyre, R.: Dynamic Behaviour of Footbridges, pp. 13–24. IABSE Surveys S-26/84 (1984)
5. Lee, S.-H., Lee, K.-K., Woo, S.-S., Cho, S.-H.: Global vertical mode vibrations due to human group rhythmic movement in a 39 story building structure. *Eng. Struct.* **57**, 296–305 (2013)
6. Dallard, P., Fitzpatrick, T., Flint, A., Low, A., Smith, R.R., Willford, M., Roche, M.: London millennium bridge: pedestrian-induced lateral vibration. *J. Bridg. Eng.* **6**(6), 412–417 (2001)
7. Kerr, S.C.: Human induced loading on staircases. Ph.D. thesis, University of London (1998)
8. Jones, C., Reynolds, P., Pavic, A.: Vibration serviceability of stadia structures subjected to dynamic crowd loads: a literature review. *J. Sound Vib.* **330**(8), 1531–1566 (2011)
9. Madarshahian, R., Caicedo, J.M., Zambrana, D.A.: Benchmark problem for human activity identification using floor vibrations. *Expert Syst. Appl.* **62**, 263–272 (2016)
10. Alzubaidi, A.T., Caicedo, J.M.: Modeling human-structure interaction using control models: External excitation. In: *Dynamics of Civil Structures*, vol. 2, pp. 183–190. Springer, Cham (2019)
11. Živanović, S., Pavic, A., Reynolds, P.: Vibration serviceability of footbridges under human-induced excitation: a literature review. *J. Sound Vib.* **279**(1–2), 1–74 (2005)
12. Nhleko, S., Zingoni, A., Moyo, P.: A variable mass model for describing load impulses due to periodic jumping. *Eng. Struct.* **30**(6), 1760–1769 (2008)
13. Martínez, J.F., Hermanns, L., de Lerma, A.F., Álvarez, E.A.: Jumping load models applied on a gymnasium floor. *Eng. Struct.* **125**, 26–38 (2016)
14. Dorf, R.C., Bishop, R.H.: *Modern Control Systems*. Pearson, Essex (2011)
15. Ogata, K.: *Modern control engineering*. Book Rev. **35**(1181), 1184 (1999)
16. Nise, N.S.: *Control Systems Engineering*, (With CD). Wiley, New York (2007)
17. Hidenori, K., Jiang, Y.: A pid model of human balance keeping. *IEEE Control. Syst. Mag.* **26**(6), 18–23 (2006)
18. Kwon, T., Hodgins, J.: Control systems for human running using an inverted pendulum model and a reference motion capture sequence. In: *Proceedings of the 2010 ACM SIGGRAPH/Eurographics Symposium on Computer Animation*, pp. 129–138. Eurographics Association (2010)
19. Kimura, Y.J.H.: Balance-keeping control of upright standing in biped human beings and its application for stability assessment. In: *Humanoid Robots: New Developments*. IntechOpen (2007)
20. Melzer, I., Benjuya, N., Kaplanski, J.: Postural stability in the elderly: a comparison between fallers and non-fallers. *Age Ageing.* **33**(6), 602–607 (2004)
21. Winter, D.A.: Human balance and posture control during standing and walking. *Gait Posture.* **3**(4), 193–214 (1995)
22. Bocian, M., Macdonald, J.H., Burn, J.F., Redmill, D.: Experimental identification of the behaviour of and lateral forces from freely-walking pedestrians on laterally oscillating structures in a virtual reality environment. *Eng. Struct.* **105**, 62–76 (2015)
23. Johnson, M.A., Moradi, M.H.: *PID Control*. Springer, London (2005)
24. Privara, S., Široký, J., Ferkl, L., Cigler, J.: Model predictive control of a building heating system: The first experience. *Energy Build.* **43**(2–3), 564–572 (2011)
25. Ying, H.: Theory and application of a novel fuzzy PID controller using a simplified Takagi–Sugeno rule scheme. *Inf. Sci.* **123**(3–4), 281–293 (2000)
26. Smith, J.W., Montgomery, T.: Biomechanically Induced and Controller Coupled Oscillations Experienced on the f-16x1 Aircraft during Rolling Maneuvers. National Aeronautics and Space Administration, Washington, D.C. (1996)
27. Dyke, S.J., Caicedo, J.M., Turan, G., Bergman, L.A., Hague, S.: Phase I benchmark control problem for seismic response of cable-stayed bridges. *J. Struct. Eng.* **129**(7), 857–872 (2003)
28. Caicedo, J.M., Dyke, S.J., Moon, S.J., Bergman, L.A., Turan, G., Hague, S.: Phase II benchmark control problem for seismic response of cable-stayed bridges. *J. Struct. Control.* **10**(3–4), 137–168 (2003)
29. Robert, C., Casella, G.: *Monte Carlo Statistical Methods*. Springer Science & Business Media, New York (2013)
30. Bendat, J.S., Piersol, A.G.: *Random Data: Analysis and Measurement Procedures*, vol. 729. Wiley, New York (2011)
31. Ewins, D.: *Modal Testing: Theory, Practice and Application* (Mechanical Engineering Research Studies: Engineering Dynamics Series). Research Studies Press, Philadelphia (2003)
32. Alzubaidi, A.T., Caicedo, J.M.: Modeling human-structure interaction using control models when bobbing on a flexible structure. In: *Dynamics of Civil Structure*, vol. 2, pp. 27–34. Springer, Cham (2020)

**Ahmed T. Alzubaidi** obtained his B.Sc. and M.Sc. degree in civil engineering in 2008 and 2011 respectively from Babylon University. He earned a M.Sc. in Engineering Management from the University of South Carolina in 2018. He is a Ph.D. student at the University of South Carolina working on Human-Structure interaction.

# Chapter 29

## Control of Traffic-Induced Ground Vibrations in a Residential Structure



Brad Pridham, Tom Normile, Christian Kronenwetter, Paul Reynolds, and Emma Hudson

**Abstract** Ground-borne vibrations from roadway traffic are a common source of disturbance in urban areas. These vibrations are often due to poor road conditions combined with heavy vehicle movements near the receiving structure. Mitigation of vibration disturbances in existing structures usually requires a combination of added mass, added stiffness, and/or added damping to limit vibrations to acceptable levels. The suitability and feasibility of solutions will largely depend on site conditions, performance, and cost.

This paper presents a case study on control of traffic-induced ground motion disturbances in a historic residential structure. The building was previously occupied by commercial space but was known to have lively floors subjected to perceptible levels of motion induced by vehicle movements on the adjacent roadway. The desire of the owners to convert the commercial space to residential use raised concerns regarding impacts of traffic on comfort in the home. To assist with the renovation, the authors were engaged to investigate the problem and develop solutions for control. Site testing was completed to quantify existing vibration levels and structural dynamic properties. This was followed by an investigation of solutions including structural retrofits, passive dampers, and active control. Ultimately the owner proceeded with structural retrofits and following the renovation there was opportunity to complete performance measurements for verification of the solution.

**Keywords** Ground vibration · Active control · Passive control · Active mass damper

### 29.1 Introduction

Traffic vibrations can be a great source of annoyance to building occupants, particularly in cases where sleep disturbance is a concern. These vibrations are usually caused by a combination of poor roadway conditions and heavy vehicle traffic (trucks, buses etc.). Ground vibrations from cars, trucks, and buses are caused by axle hopping over discontinuities and obstructions in the drive surface. The frequency of these forces typically falls in a 10–15 Hz frequency range depending on vehicle suspension characteristics. Vehicle speed and weight and the efficiency of soil transmission are also determining factors in the vibration amplitudes at the receptor.

On projects involving land use planning and new construction, vibration impacts can be managed in design using commonly accepted approaches to assessment, such as those published by the Federal Transit Administration in the US [1]. Mitigation typically includes increased setback between building foundation and roadway, increased foundation mass/stiffness, attenuation barriers/trenches in the transmission path, and/or vibration isolation. The effectiveness of the selected scheme largely depends on measured or predicted vibration amplitudes at the receptor, comfort criteria, and the frequency content of traffic vibrations.

In cases when the receptor is an existing building mitigation is often challenging. Foundation isolation or attenuation trenches may be impractical or infeasible due to site constraints (e.g., location of site services, proximity to roadway,

---

B. Pridham (✉)  
SLR Consulting (Canada) Ltd., Guelph, ON, Canada  
e-mail: [bradp@novusenv.com](mailto:bradp@novusenv.com)

T. Normile · C. Kronenwetter  
Keast & Hood Structural Engineers, Philadelphia, PA, USA

P. Reynolds · E. Hudson  
Full Scale Dynamics Limited, Exeter, UK





**Fig. 29.1** Photos of the residence and adjacent roadways discussed in the study

interruption of pedestrian traffic etc.). In some cases, preservation of historic or heritage elements may preclude such invasive actions. Therefore, controls to address the source or the receiving structure must be considered.

In this paper we discuss the results from an investigation of traffic vibration control in a residential building. Originally a single-unit wood and masonry framed residence, it was renovated 10 years prior to the study to accommodate a public art gallery operated by the owners. This featured new steel framing and new concrete on metal pan floor systems. Following operation as an art gallery, the owners wished to return the building to its prior residential use. A photo of the home and adjacent roadways is shown in Fig. 29.1.

During the planning discussions with the structural team, it was learned that certain areas of the floor respond to traffic vibrations at levels that would be uncomfortable to the owners. This warranted a vibration study to establish if feasible mitigation measures could be developed. The authors were engaged to investigate control solutions. Strategies considered in the study included: structural framing upgrades; added mass; passive control (tuned mass dampers); and, active control (active mass dampers).

The paper is organized as follows: a discussion on baseline data collection and assessment is followed by details on control strategies investigated. Implementation and validation testing are then discussed, followed by concluding remarks.

## 29.2 Vibration Testing

At the onset of the study vibration testing was completed to quantify existing conditions and identify dynamic properties for use in the impact assessment and mitigation development. Site measurements were completed over an 8-hour period and included: modal testing of the floors; footfall response measurements; and, traffic vibration response measurements.

Traffic vibrations were measured for a 1.5-hour period during the afternoon rush, ensuring a good sampling of vibrations due to heavy vehicles on the roadway. Footfall paths were aligned along mid-span locations on the floor and footfall tests were completed for fast and slow pacing rates (90 and 120 steps/min). Six channels of data were acquired in two test setups. The locations of accelerometers and the impact test grid are shown in Fig. 29.2. During the ambient/traffic vibration testing, two of the accelerometers were installed outside of the building on ground to measure ground motion inputs to the structure. Modal test data were processed to identify the fundamental bay frequencies, damping, and mode shapes. A summary of identified frequencies and damping ratios is given in Table 29.1.

Peak-hold spectra from the ambient/traffic response measurements are shown in Fig. 29.3. The data shown in the plots is the maximum measured levels outside on ground, on level one, and on level two. The modal data and measured traffic responses indicate floor resonances at frequencies within the same range as ground motions from vehicles. The highest traffic responses were measured on the floor at the front on level two, which was the planned location for the master bedroom. Qualification of the measured responses from an occupant comfort perspective is discussed in the following section.

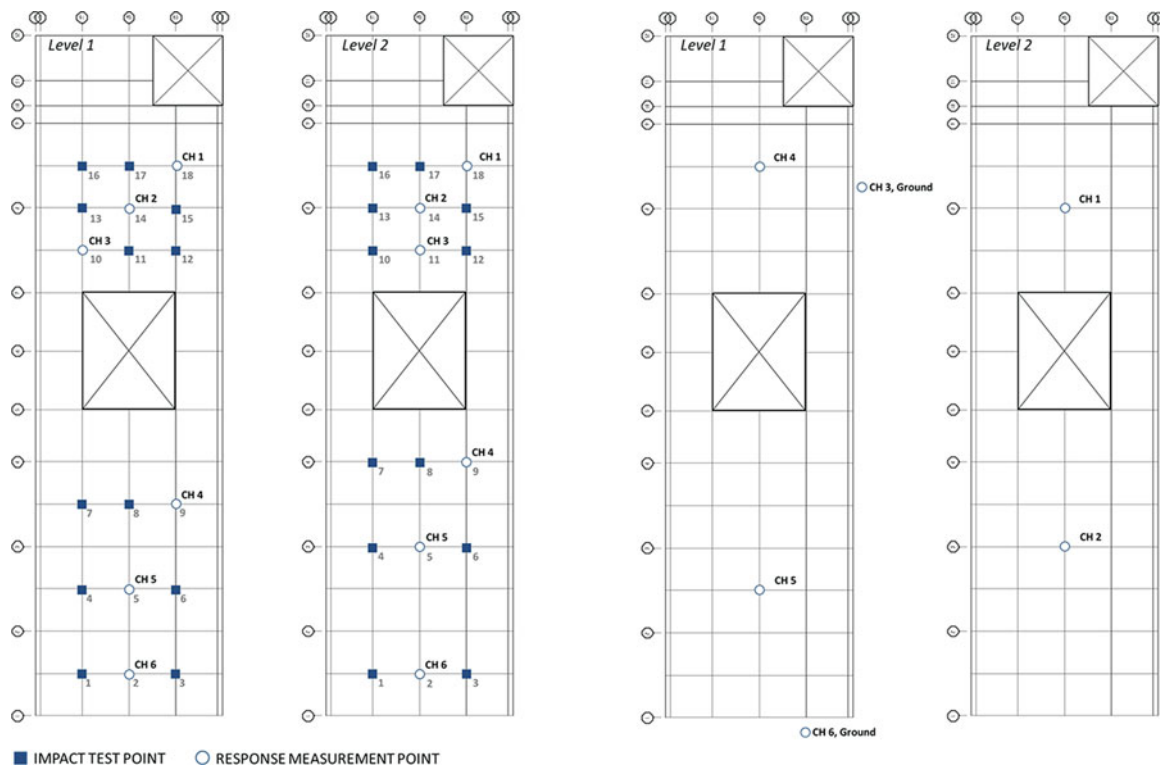


Fig. 29.2 Vibration testing measurement setup – modal and footfall setup at left, ambient setup at right

Table 29.1 Identified frequencies and damping for fundamental modes of each floor area

Location	Fundamental bay frequency (Hz)	Fundamental mode damping estimate (%)
Level 1, front	16.3	4.3
Level 1, back	20.9	3
Level 2, front	11.5	6
Level 2, back	13.8	5

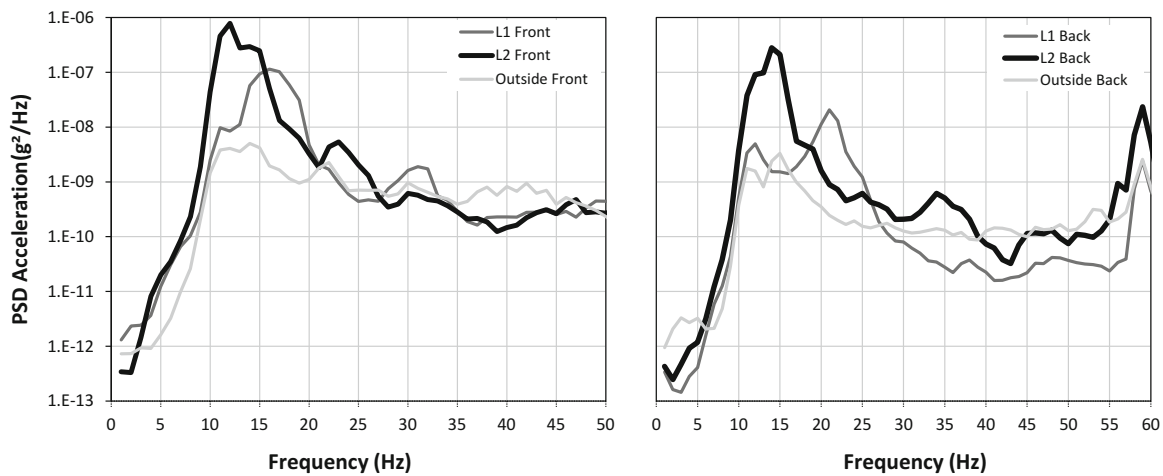


Fig. 29.3 Maximum measured ambient/traffic responses at the front (left), and the back (right) of the building

## 29.3 Baseline Performance Assessment

### 29.3.1 Vibration Criteria

Design criteria related to human comfort are typically specified in units of peak acceleration (%g), root-mean-square (RMS) acceleration (%g), response factors (ratio of measured RMS acceleration to the threshold of perception), and/or RMS vibration velocity ( $\mu\text{-in/s}$ ). Criteria for peak acceleration are suggested by some design guidelines, including AISC DG11 [2], and published RMS criteria are based on the ‘human perceptibility curves’ published by the ISO. The use of RMS metrics is typically appropriate to comfort assessments as they more appropriately reflect the sensitivity of humans to time-averaged floor motions. Spurious peaks are common in the measurement of transient response from traffic and can be misleading to assessment of comfort.

The basis for the criteria applied in this study is the ISO Base Curve, also referred to as the ISO-Operating Theatre criterion, which is the threshold of human perception expressed as a function of frequency and RMS vibration level. Multiples, or vertical shifts, of the base curve are commonly applied in reference to acceptable use and occupancy (i.e., operating rooms, residences, workshops etc.). The response factor is a convenient way of quantifying response as a multiple of the base curve [3]. For example, a response factor of 2 indicates vibration levels that are twice as high as the base curve. Its use requires specification of a suitable ISO Weighting Function, which for the current study was specified as the  $m$ -weighting function ( $W_m$ ) recommended by the ISO [4]. For residential uses the ISO suggests the use of the ISO-Residential criteria, which requires that maximum 1/3rd octave band RMS vibration velocity level and Response Factors be limited to the following ranges:

- Maximum 1/3rd Octave Band RMS velocity: 5600–8000  $\mu\text{-in/s}$
- Maximum Permissible Response factor ( $R$ ): 1.4–2

The lower bound on these ranges is associated with nighttime sleep areas, whereas the upper bound is associated with daytime use. In the author’s experience, these levels typically provide a comfortable vibration environment in residences with low risk of complaint. However, it is recognized that comfort is highly subjective and that vibrations in the defined range are typically perceptible.

### 29.3.2 Performance Assessment – Existing Structure

The traffic response data were post-processed to compute the peak-hold one-third octave spectra and response factors. An integration time of 1-second was applied during the calculations. The resulting maximum measured  $R$  factors and 1/3rd octave band RMS velocity levels are summarized in Table 29.2. The maximum measured footfall and traffic responses occurred at the front area on level two. The measured traffic vibration levels on Level 1 were 1/3rd – 1/6th of the levels measured on and marginally higher than the recommended thresholds for residential use. The measured footfall levels exceed recommended residential thresholds by a factor of 1.5–2 at all measurement locations.

Based on the assessment of existing vibration levels, it was recommended that mitigation measures be designed to reduce traffic vibrations by 1/3rd – 1/4th the measured values, and to reduce footfall vibrations by approximately half of their measured levels for compliance with comfort criteria. Following the assessment and a discussion with the owners, the authors proceeded to investigate mitigation solutions.

**Table 29.2** Maximum measured response levels during footfall and ambient/traffic testing

Location	Footfalls @ 90 SPM		Footfalls @ 120 SPM		Ambient/traffic	
	$R$ max	Max 1/3rd Oct RMS Vel ( $\mu\text{-in/s}$ )	$R$ max	Max 1/3rd Oct RMS Vel ( $\mu\text{-in/s}$ )	$R$ max	Max 1/3rd Oct RMS Vel ( $\mu\text{-in/s}$ )
Level 1, front	<b>3.3</b>	<b>15,079</b>	3.9	14,963	2.1	9721
Level 1, back	2.7	12,220	3.4	15,318	0.7	2447
Level 2, front	2.6	8581	<b>4.4</b>	<b>15,725</b>	<b>6.2</b>	<b>30,623</b>
Level 2, back	2.9	10,112	3.6	13,446	2.7	11,782

## 29.4 Vibration Control Investigation

Performance studies were completed to evaluate various mitigation strategies. Strategies that included vibration isolation of the building, installation of attenuation trenches, and resurfacing of the road were not considered due to costs, site constraints, and uncertainty regarding long-term performance (e.g., reliance on the municipality to maintain any roadway fixes). The investigation of mitigation therefore focused on:

- structural stiffening (new framework);
- added mass;
- tuned mass dampers; or,
- active mass dampers.

### 29.4.1 Numerical Modeling

Both experimental and numerical finite element models of the structure were developed for use in the control investigation. Construction of a reliable FEM proved challenging as the existing steel framing interfaces with a combination of original masonry elements and steel reinforcing elements, that result in unique boundary conditions. The boundary conditions were adjusted through trial and error until a reasonable match between measured and modelled fundamental bay modes was attained. The model was then updated to account for massing of future fit-out (furniture etc.) and used to evaluate performance of new framing schemes. Table 29.3 lists the measured and modeled frequencies, as well as predicted fit-out frequencies. Since fit-out would consist primarily of new furnishings, the effects on system dynamics were modelled as added mass only (no changes to inherent/system damping).

The investigation of added mass and supplementary damping systems was completed using an experimental model of the front area of level two – the location of maximum response to traffic and footfalls. Curve fitting was applied to the measured FRF data and the parameter estimates were used to re-synthesize the FRF. The results of this procedure are shown in Fig. 29.4. A total of six modes were included in the re-synthesized system, the parameters for which are listed in Table 29.4.

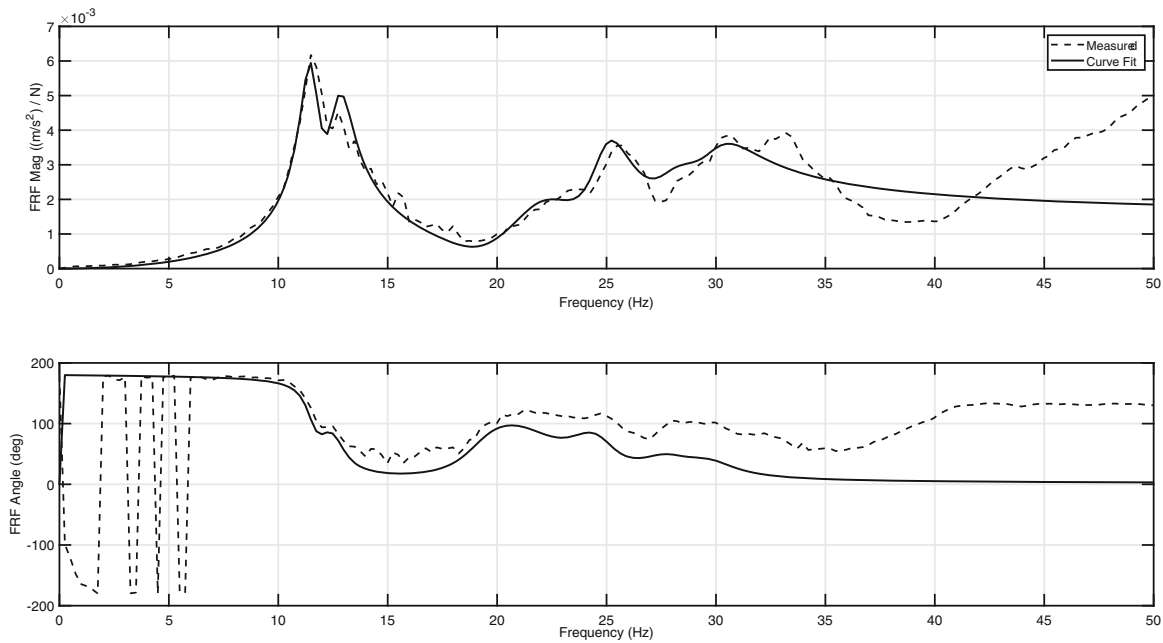
The experimental model and measured acceleration responses were used to synthesize pseudo-force time histories that produce the measured footfall and traffic acceleration responses. In this way, the model could then be manipulated to examine added mass and supplemental damping, and simulations conducted with the pseudo-forces in a comparative performance assessment. The results are discussed below.

**Table 29.3** Measured and modeled FEM floor frequencies

First bay mode location	Measured frequency (Hz)	Modelled frequency – existing (Hz)	Modelled frequency – fit-out (Hz)	Modelled change, existing/fit-out (Hz)
Level 1, front	16.3	16.8	16.2	–4%
Level 1, back	20.9	18.7	18.1	–3%
Level 2, front	11.5	13.2	12.7	–3%
Level 2, back	13.8	15.0	14.3	–4%

**Table 29.4** Curve fit parameters for the experimental model (level two, front, mid-bay point FRF)

Mode number	Frequency (Hz)	Damping (%)	Mass (kg)
1	11.5	4.0	2500
2	12.8	5.0	2500
3	22.0	9.0	3500
4	25.0	4.0	5000
5	28.0	5.0	9000
6	30.0	5.0	7000



**Fig. 29.4** Measured and re-synthesized FRF – level two, front

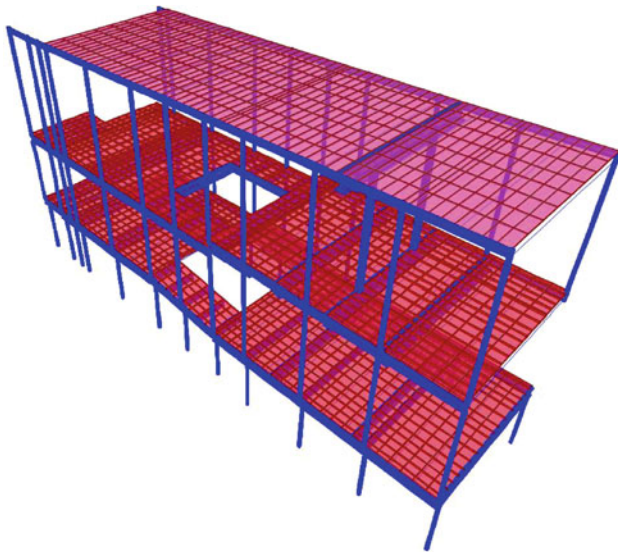
### 29.4.2 Control Option 1: Structural Stiffening

The FEM was used to investigate performance of structural upgrades to sufficiently de-tune the system from traffic excitations, whilst also improving footfall performance. Ground accelerations measured on ground outside of the residence were applied as inputs (base excitation analysis). The Columns were fully restrained at their bases and soil-structure interaction effects were not included in the analysis. Multiple structural schemes were evaluated, and a final scheme selected that was predicted to comply with performance criteria.

Figure 29.5 is a snapshot of the FEM and lists the framing upgrades. Framing upgrades at the front area of level two included hanger elements to engage truss action from new roof and floor beams supported off the masonry walls. The new floor beams were modelled to provide fully composite action but free to rotate at the end connections to masonry. The roof beam would be installed above the finished ceiling but would not be connected to the roof deck. Any out-of-plane vibrations of the beam would be controlled with intermittent bracing members connecting the beam to the deck. Simulations included the first two bending modes of each floor area (i.e., level one and two, front and back), and inputs from four heavy vehicle pass-bys on the roadway and footfall forces as specified by the Steel Construction Institute [3].

### 29.4.3 Control Option 2: Added Mass

The existing structure was determined to have capacity available to support an additional 20 lb/sqft of weight, which could be added to the underside of the floors in key areas. The experimental model developed for the level two front floor system was used to predict the effects of added mass on system dynamics and performance. Uncertainty exists in the added mass estimates due to the low levels of energy in the FRFs at the new system frequency (9.3 Hz fundamental mode frequency versus 11.5 Hz for the base system). The inversion procedure produced low levels of pseudo force in this range, which subsequently resulted in small response estimates. Additionally, damping was assumed to remain unaffected by added mass, which may not be the case. Nonetheless, the addition of mass would be much less invasive and costly and needed to be considered.



**Framing additions:**

L1 Front:	add 2 x W14x30 floor beams
L1 Back:	add 1 x W14x30 floor beam
L2 Front:	3 x W16x77 floor beams 2 x HSS 3.5x3.5x0.375 hangers 1 x W18x97 roof beam
L2 back:	add 3 x W14x30 floor beams

**Fig. 29.5** Image of SAP2000 FEM and details of proposed structural upgrades

#### **29.4.4 Control Option 3: Passive Supplemental Damping Devices**

Tuned mass dampers are a well-established means of floor vibration control and have been shown to perform well in certain cases (see for example reference [5]). The use of TMDs was investigated based on simulations using the experimental model. The TMD was specified with a 10 Hz frequency, a 662 lbs (300 kg) moving mass, and supplemental damping equal to 10%. The generated traffic and footfall pseudo-forces were applied as inputs to the TMD system model for comparison of performance with other strategies. Due to the relatively low forces and high tuning frequency of the system, the predicted displacement of the TMD was very small (0.8 mils, or 0.02 mm), and therefore the level of attenuation achievable in implementation was expected to be low. Increasing the damping in the TMD did not prove effective as it further reduces the displacements in the system and hence further degrades performance.

#### **29.4.5 Control Option 4: Active Supplemental Damping Devices**

Active mass damping devices (AMDs) are a relatively new control strategy that has been implemented with success on floor systems subjected to pedestrian excitation [6, 7]. The attractiveness of such systems includes much smaller moving mass than would be required for TMD devices, as well as a greater frequency range of control. TMDs are tuned to a specific mode, whereas AMDs effectively attenuate the target mode and adjacent modes within the stable range of feedback gains in the controller. For the performance assessment a system was designed having a 3.0 Hz actuator frequency, a moving mass of 66 lbs (30 kg), low and high pass filters at 40 and 2.1 Hz, and a feedback gain of 250.

Notable current challenges with implementation of AMDs include power availability and draw, maintenance requirements, and displacement amplitudes required for control. As was the case for the TMD, the high-frequency nature of the system and excitation source results in very low displacements of the active mass. Any assumptions on linearity of performance in the small amplitude range would require verification for both TMD and AMD solutions. Although this is generally more of a concern for TMDs due to their passive nature and limitations on commercially available damping elements.

**Table 29.5** Change in response factor ( $[(\text{measured} - \text{mitigated})/\text{mitigated}]$ )

Excitation condition	Structural stiffening (%)	20 lb/sqft added mass (%)	Tuned mass damper (%)	Active mass damper (%)
Ambient/traffic	-84	-71	-57	-78
Footfalls	-75	13	-7	-40

**Table 29.6** Summary of measured frequencies and response factors pre- and post-renovation

Location	First mode frequency (Hz)		Max measured response factor ambient/traffic		Max measured response factor footfalls	
	Pre-reno	Post-reno	Pre-reno	Post-reno	Pre-reno	Post-reno
Level 1, Front	16	19	3.0	3.7	3.3	1.7
Level 1, Back	13	22	0.7	1.4	2.7	2.3
Level 2, Front	12	16	6.1	2.4	2.6	0.8
Level 2, Back	14	19	3.8	2.0	2.8	1.1

### 29.4.6 Performance Assessment

The performance of the evaluated control schemes is summarized in Table 29.5. The numbers listed in the table are the computed change in response factor based on the measured and predicted amplitudes in the front area of level two. A negative value indicates an estimated reduction in response.

Based on the investigation, on the structural stiffening and AMD solutions were found to satisfy performance targets for both traffic and footfall excitations. The added mass solution is shown to result in significant improvements in the vibrations caused by ambient traffic. However, the impulsive and multi-harmonic nature of pedestrian walking means that this modification does not yield any improvements with the walking time histories considered.

These results were conveyed to the owners whom opted to proceed with the stiffening solution. Although the AMD was appealing due to its performance and compactness, at the time of the study there was uncertainty regarding frequency of maintenance and requirements for access. The owners opted for a permanent solution that did not require future access.

## 29.5 Validation Testing

Structural upgrades were implemented during the previously planned renovations. Careful detailing of connections to existing structure was an important step to achieving the desired composite action and end restraint at connections to existing elements. Once the upgrades were implemented, it was possible to conduct another round of testing for performance verification. Table 29.6 is a summary of measured frequencies and response levels pre- and post-renovation.

As indicated by the results in the table, the new framing resulted in a significant increase in first mode frequencies of the four floor areas. Footfall response levels are lower at all locations post-renovation. However, higher levels of traffic response were measured on level one after the framing upgrades. This was due partially to higher ground motions measured during the post-renovation survey (possibly due to stiffer soil in the winter) but is also likely a result of vibration flanking across the foundation (soil-structure interaction effects). These effects could not be quantified but could be investigated if further improvements to performance were desired. However, given the site constraints, it is expected that any feasible modifications to the foundation would have limited effects on vibration attenuation.

## 29.6 Concluding Remarks

Following implementation an additional post was added beneath the front area of level one to address residual vibration from the roadway. Qualitatively the improvements were noted to result in acceptable levels of comfort during a visit to the site, and the owners have expressed satisfaction with the results. Although the owners chose not to pursue AMDs as a final solution, the results from the study indicate superior performance of the AMD compared with a traditional passive supplemental damping system (TMD). As the AMD technology advances, it is anticipated that these devices will soon become a feasible option for implementation on floors in residential buildings.

## References

1. Transit noise and vibration impact assessment manual. Federal Transit Administration (FTA), FTA Report No. 0123 (2018, Sept)
2. Murray, M.M., Allen, D.E., Ungar, E.E., Davis, D.B.: *Floor Vibrations Due to Human Activity*, AISC/CISC Steel Design Guide Series 11, 2nd edn. American Institute of Steel Construction, Chicago, IL, USA (2016)
3. Smith, A.L., Hicks, S.J., Devine, P.J.: *Design of Floors for Vibration: A New Approach*, SCI Publication 354. The Steel Construction Institute, Silwood Park, Ascot, Berkshire UK (2007)
4. ISO 2631-2: *Evaluation of Human Exposure to Whole-Body Vibration Part 2: Continuous and Shock-Induced Vibration in Buildings (1 to 80 Hz)*. International Organization for Standardization, Geneva, Switzerland (2003)
5. Setareh, M., Ritchey, J.K., Baxter, A.J., Murray, T.M.: Pendulum tuned mass dampers for floor vibration control. *J. Struct. Eng.* **20**(1), 64–73 (2006)
6. Pereira, E., Díaz, I.M., Hudson, E.J., Reynolds, P.: Optimal control-based methodology for active vibration control of pedestrian structures. *Eng. Struct.* **80**, 153–162 (2014)
7. Hudson, E.J., Reynolds, P., Nelson, M., Christie, N., Salcedo, V.: *Active Control of Concert-Induced Vibrations*, Geotechnical and Structural Engineering Congress 2016 – Proceedings of the Joint Geotechnical and Structural Engineering Congress 2016, pp. 1729–1741. American Society of Civil Engineers, Phoenix, AZ (2016)

**Brad** is a Technical Director with SLR Consulting in Guelph, Ontario. He has practiced as an acoustics and vibration consultant for over 15 years and has worked on hundreds of high profile projects. Notably, he was actively involved in the design of Dubai Creek Harbor Tower, which will be the tallest observation tower in the world.